Cronfa
Swansea University's Research Repository

Graphene-Based Electronic Sensors for Gas Detection

Danielle Marie Goodwin



Swansea University
Prifysgol Abertawe

Submitted to Swansea University in fulfilment of the requirements for the Degree of Doctor of Engineering

Swansea University

2024

Copyright: The Author, Danielle Marie Goodwin, 2024

Abstract

This thesis describes the development of graphene-based sensor arrays, focusing on signal enhancement through innovative surface modification techniques, whilst leveraging graphene's unique properties. Awareness of the dangers posed by toxic gases has increased the demand for advanced gas sensors, which are critical for monitoring harmful gases. Gas sensor arrays, or "electronic noses," offer advantages over single sensors, including the ability to detect multiple analytes simultaneously with greater accuracy.

Since its discovery in 2004, graphene has attracted significant interest due to its exceptional mechanical, chemical, and electrical properties, which make it ideal for miniaturized, low-cost sensors with high sensitivity and selectivity. However, graphene's high sensitivity poses a challenge, as it interacts with a wide range of molecules. Managing this sensitivity and selectivity through advanced surface modification techniques is crucial for enhancing the performance of graphene-based sensors.

In this thesis, various surface modification techniques were explored to enhance the selectivity and sensitivity of graphene-based sensors, specifically targeting the detection of nitrogen dioxide, ammonia, nitric oxide, methane, and carbon dioxide. These modifications aimed to improve sensor selectivity while maintaining a strong response. One notable technique involved integrating metal phthalocyanines, known for their gas sensitivity, with graphene to create a hybrid sensor. For instance, a graphene sensor functionalized with tetra-tert-butyl copper phthalocyanine was developed for real-time detection of nitrogen dioxide (NO_2), achieving a linear response and a detection limit of 31 ppb, showcasing its potential as a highly selective and effective NO_2 detector.

Polymers of intrinsic microporosity (PIMs), although well-established in gas separation, have not been extensively explored for gas sensing. This thesis presents a PIM-modified graphene sensor array that demonstrated high selectivity and sensitivity towards NO_2, with a detection limit of 0.7 ppb, indicating its suitability for highly sensitive NO_2 detection.

The development of the graphene sensor array began with exploring electrochemical functionalization across different pixels, allowing each graphene element to respond to the same gas with different magnitudes. This proof-of-concept array demonstrated that these distinct responses could potentially be integrated with pattern recognition software to identify unknown gases. Beyond detecting environmental gases, the graphene sensors can also be adapted for the detection of volatile organic compounds (VOCs).

To test the arrays, a gas sensing system was developed to enable simultaneous, real-time resistance measurements for each graphene pixel. The iterative development of this system is reported, highlighting challenges and limitations.

A proof-of-concept bioelectronic nose based on a graphene resistor has been fabricated and evaluated. Functionalized with 1,5-diaminonaphthalene and immobilized with human olfactory receptor 2AG1, it selectively detected amyl butyrate at 0.5 pM, indicating the potential of bioelectronic noses using olfactory receptors, which can recognize multiple VOCs, thus reducing the required number of sensors in an array.

Declarations

This work has not previously been accepted in substance for any degree and is not being concurrently submitted in candidature for any degree.

Signed [redacted].....

Date .....13/09/2024.....

This thesis is the result of my own investigations, except where otherwise stated. Other sources are acknowledged by footnotes giving explicit references. A bibliography is appended.

Signed [redacted].....

Date .....13/09/2024.....

I hereby give consent for my thesis, if accepted, to be available for electronic sharing.

Signed[redacted].....

Date .....13/09/2024.....

The University's ethical procedures have been followed and, where appropriate, that ethical approval has been granted.

Signed [redacted].....

Date .....13/09/2024.....

Acknowledgements

First and foremost, I would like to express my gratitude to my supervisor, Professor Owen Guy, for his support and guidance throughout my EngD journey. I am also incredibly thankful to my co-supervisor, Dr. Mariolino Carta, for his consistent support and willingness to assist whenever needed.

My sincere thanks go to all the M2A staff for their ongoing support and guidance. A special mention to Thomas Lewis, Rhys Faulkner, and Ben Cockings, my project coordinators, who provided much-needed reassurance and encouragement when I needed it most.

I would also like to extend my thanks to the technical teams at the Centre for Nanohealth (now CISM) and the Electronics Lab. Your assistance was invaluable in completing my research. I am especially grateful to my colleagues Daniel Gillard, Jonathon Evans, and Muhammad Munem Ali for their help in getting the gas sensing rig operational. A special thank you to Muhammad, who answered my endless questions on graphene devices, XPS, Raman, and much more!

To my friends from Swansea University—Daniel Gillard, Kiran Mistry, Geraint Howells, Daniel Britton, Emily Holding, Anton Marusenko, Muhammad Ali, and April Tang—thank you for the much-needed companionship, the well-deserved nights out, and the countless laughs along this crazy journey!

Thank you to my dad, who was always eager to read my next publication. Well, Dad, you now have my thesis to read!

Finally, my deepest thanks go to my husband, Ryan Goodwin, for his unwavering support throughout this challenging journey. Thank you for standing by me through all the ups and downs, believing in me, and constantly encouraging me. Without your support, I'm not sure I would have completed my EngD.







The author would like to acknowledge the COATED M2A funding from the European Social Fund via the Welsh Government (c80816) and the Engineering and Physical Sciences Research Council (Grant Ref: EP/S02252X/1) that has made this research possible.

I dedicate this thesis to my Mom, who
passed away during the course of my research.

June Marie Peel
June 12th, 2021

Thank you for always believing in me
before I believed in myself first.
Love you forever
xx

When it looks impossible, look deeper. And then fight like you can win.

- Rost, Horizon Forbidden West

Contents

Abstract i

Declarations iii

Acknowledgements iv

Contents vii

List of Conferences & Publications xiv

List of Figures xvi

List of Tables xxx

List of Abbreviations xxxii

Chapter 1 : Introduction 1

1.1. Background & Motivation 1

1.2. Thesis Outline 3

Chapter 2 : Literature Review 5

2.1. Introduction 5

2.2. Gas Sensing 5

2.2.1. Gases and VOCs Detected by Gas Sensors 6

2.2.2. Overview of Gas Sensor Technologies 9

2.2.3. Gas Sensor Arrays 12

2.3. Overview of Graphene 13

2.3.1. Electronic Structure 13

2.3.2. Doping of Graphene 14

2.4. Graphene Fabrication 19

2.5. Graphene Surface Modification 21

2.5.1. Covalent Functionalization 21

2.5.2. Non-covalent Functionalization 23

2.6. Graphene-based Sensors 31

2.6.1. Biosensors 31

2.6.2. Electrochemical Sensors 33
2.6.3. Electrical Sensors 33
2.7. Contamination of Graphene Surfaces 36
2.8. Variability Between Devices 36
2.9. Polymers of Intrinsic Microporosity 37
Chapter 3 : Materials & Methods 39
3.1. Materials 39
3.1.1. For Chapter 4 39
3.1.2. For Chapter 5 40
3.1.3. For Chapter 6 40
3.1.4. For Chapter 7 40
3.1.5. For Chapter 8 41
3.1.6. For Chapter 9 41
3.2. Graphene Sensor Fabrication 42
3.2.1. Rapid Thermal Annealing 43
3.2.2. Spin Coater 43
3.2.3. Plasma Etcher 44
3.2.4. Mask Aligner 44
3.2.5. Physical Vapour Deposition 45
3.2.6. Molecular Vapour Deposition 46
3.2.7. Mask Design 47
3.3. Graphene Sensor Functionalization 47
3.3.1. Equipment 47
3.4. Characterization 49
3.4.1. Keyence Optical Microscope 49
3.4.2. Scanning Electron Microscopy (SEM) 49
3.4.3. Energy Dispersive Spectroscopy (EDS) 50
3.4.4. Atomic Force Microscopy (AFM) 50
3.4.5. Raman Spectroscopy 52

3.4.6. X-ray Photoelectron Spectroscopy (XPS) 56
3.4.7. Fourier Transform Infrared Spectroscopy (FT-IR) 57
3.4.8. Ultraviolet-Visible (UV-VIS) Spectroscopy 58
3.4.9. Ellipsometry 58
3.5. Electrical Measurements 59
3.5.1. Probe Station 59
3.5.2. Back-gated Measurements 61
3.5.3. Real-time Measurements 62
3.6. Gas Sensing Performance Metrics 66
3.6.1. Sensor Response 66
3.6.2. Response and Recovery Time 66
3.6.3. Percentage Recovery 68
3.6.4. Selectivity 68
3.6.5. Sensitivity 68
3.6.6. Signal-to-Noise Ratio 69
3.6.7. Limit of Detection 69
3.6.8. Limit of Quantification 70
3.6.9. Principle Component Analysis (PCA) 70
Chapter 4 : Fabrication and Design of Graphene Sensors 72
4.1. Introduction 72
4.2. Device Designs Used in this Research 72
4.2.1. Graphene 3-channel ‘DipChipX’ 72
4.2.2. Graphene 2-channel ‘Hall Bar’ 74
4.3. Design of the 3x3 Graphene Pixel Array 75
4.3.1. Overview and Motivation 75
4.3.2. Metal Tracks and Contact Pads 76
4.3.3. Graphene Pixels 77
4.4. Sensor Fabrication Process 79
4.4.1. Sample Preparation 79

4.4.2. Graphene Patterning 80
4.4.3. Metal Deposition and Lift-off 83
4.4.4. Passivation and Al_2O_3 Etch 87
4.4.5. Resistance Measurements 90
4.4.6. Wafer Dicing 92
4.5. USB-C PCB Connector Design, Optimization and Limitations 92
4.6. Back-gated Measurements 96
4.6.1. Electrical Measurements 96
4.7. Comparison of Sensor Performance Across Different Device Design 100
4.8. Device Aging and Impact on Sensor Performance 102
4.9. Conclusions and Future Work 105
Chapter 5 : Gas Sensing System 107
5.1. Introduction 107
5.2. Gas Sensing System Requirements 107
5.3. Phase 1 Iteration: Glass Jar 109
5.3.1. System Limitations 111
5.4. Phase 2 Iteration: Flow-through Gas Sensing System 112
5.4.1. System Components 113
5.4.2. Operation 115
5.4.3. Experimental Set-up 115
5.4.4. System Limitations 116
5.5. Phase 3 Iteration: Development of the Gas Sensing Rig 117
5.5.1. System Components 117
5.5.2. Experimental Set-up 132
5.6. Optimization of Experiments 133
5.6.1. Baseline sensing 133
5.6.2. Sensor Recovery Testing 137
5.7. Conclusions 146

Chapter 6 : Gas Detection Using Metal Phthalocyanine Modified-Graphene Sensors 147

6.1. Introduction 147

6.2. Summary of Sensor Designs, Phthalocyanines, and Gas Sensing System Iterations 147

6.3. Electrical Measurements 148

6.4. Graphene Functionalization via Drop-Casting 149

6.5. Drop-cast Phthalocyanine Gas Sensing Performance 152

6.5.1. Copper Phthalocyanine 152

6.5.2. Cobalt, Iron, Zinc and Metal-free Phthalocyanine 159

6.6. Synthesis of Copper (II) 2,9,16,23-Tetra-tert-butyl phthalocyanine 164

6.6.1. Motivation 164

6.6.2. Synthesis 166

6.6.3. Characterization 169

6.7. Gas Sensing with $CuPc(t\text{-}Bu)_4$ 178

6.7.1. Nitrogen Dioxide Sensing and Recovery Performance 178

6.7.2. Selectivity 184

6.7.3. Gas Sensing Performance Comparison 185

6.8. Conclusions 189

Chapter 7 : Enhanced Nitrogen Dioxide Detection Using Graphene Sensors Modified with Polymers of Intrinsic Microporosity 191

7.1. Introduction 191

7.2. Polymers Employed in this Study 192

7.3. Graphene Functionalization with PIMs and Matrimid 193

7.4. Sensor Recovery Methods 193

7.4.1. UV exposure 194

7.4.2. Methanol Treatment 194

7.4.3. Heating 194

7.5. Surface Morphology and Film Thickness 194

7.5.1. Atomic Force Microscopy 194
7.5.2. Ellipsometry 197
7.6. Gas Sensing Performance 198
7.6.1. Nitrogen Dioxide Sensing 198
7.6.2. Sensor Recovery 202
7.6.3. Selectivity 206
7.6.4. Gas Sensing Performance Comparison 207
7.7. Mixed Matrix Membranes 209
7.7.1. Graphene Functionalization and Preparation of MMMs 209
7.7.2. Gas Sensing Performance 210
7.8. Conclusions 212
Chapter 8 : Electrochemical Functionalization of Graphene Sensors 213
8.1. Introduction 213
8.2. Electrochemical Polymerization of 1,5-diaminonapthalene 213
8.2.1. Cyclic Voltammetry Methodology 214
8.2.2. Characterization of pDAN films 219
8.2.3. Gas Sensing Performance 232
8.3. Electrochemical Oxidation 236
8.3.1. Cyclic Voltammetry Methodology 237
8.3.2. Cyclic Voltammetry Profile 239
8.3.3. Surface Chemistry 240
8.3.4. Gas Sensing Performance 245
8.4. Device Damage 252
8.4.1. Pinhole Investigation 255
8.5. Conclusions 262
Chapter 9 : Detection of Odorants Using Human Olfactory Receptor 2AG1 264
9.1. Introduction 264
9.2. Graphene Functionalization 265
9.2.1. DAN functionalization 265

9.2.2. Olfactory Receptor Attachment 265
9.2.3. Blocker Attachment 267
9.3. Electrical Measurements 268
9.4. Surface Characterization 269
9.4.1. Atomic Force Microscopy 269
9.4.2. Raman Spectroscopy 270
9.5. Real-time Functionalization 272
9.6. Detection of Amyl Butyrate 274
9.7. Conclusions 277
Chapter 10 : Conclusions and Future Work 278
10.1. Summary of Key Results 278
10.2. Comparison of Nitrogen Dioxide Sensor Performance 280
10.3. Future Work 281
Appendix 283
Bibliography 293

List of Conferences & Publications

Conferences

COATED M2A Annual Conference 2023, Swansea; "Graphene based electronic sensors for gas and volatile organic compound detection" (Oral presentation).

Graphene Conference 2023, Manchester; "Graphene based electronic sensors for gas and volatile organic compound detection" (Poster presentation).

Graphene Flagship Conference 2023, Gothenburg, Sweden; "A Room Temperature Graphene-based Electronic Gas Sensor for the Sensitive Detection of Nitrogen Dioxide" (Poster presentation).

Scandinavian Sensor Summit 2023, Horton, Norway; "A Room Temperature Graphene-based Electronic Gas Sensor for the Sensitive Detection of Nitrogen Dioxide" (Poster presentation).

BioMedEng Conference 2023, Swansea; "Graphene Bioelectronic Nose for the Detection of Odorants with Human Olfactory Receptor 2AG1" (Poster presentation).

SEMI Talent Forum 2024, Swansea; "Graphene-Based Electronic Sensors for Gas Detection" (Oral presentation).

Publications

D. M. Goodwin, F. Walters, M. M. Ali, E. Daghigh Ahmadi, and O. J. Guy, "Graphene bioelectronic nose for the detection of odorants with human olfactory receptor 2ag1," *Chemosensors*, vol. 9, no. 7, pp. 1–12, 2021, doi: 10.3390/chemosensors9070174.

Submitted Manuscripts

"Enhanced Nitrogen Dioxide Detection Using Graphene-based Sensors Modified with Polymers of Intrinsic Microporosity" to *ACS Sensors*

Manuscripts in Preparation

"Electrochemical Functionalization of Graphene-based Sensor Arrays for Selective Detection of NO_2, NO and NH_3"

“Enhanced Nitrogen Dioxide Sensitivity of a Graphene Sensor Modified with a Substituted Copper Phthalocyanine at Room Temperature"

List of Figures

Figure 2.1: Schematic of a typical metal oxide semiconductor sensor. Reproduced from reference [57].

Figure 2.2: Lattice structure of graphene.

Figure 2.3: Schematic representation of the electronic band structure of graphene (Dirac cones of conduction and valence bands touching), metals with overlapping bands, semiconductors with a small band gap and insulators with a large band gap.

Figure 2.4: Schematic representation of graphene's Fermi level in relation to surface adsorbate's HOMO and LUMO. **a)** demonstrates p-doping and **b)** represents n-doping. Reproduced from reference [95].

Figure 2.5: Distribution of the Dirac point for graphene on each dielectric substrate under four different conditions. The upper and lower squares represent the average Dirac points observed during the backward and forward sweeps, respectively. Error bars indicate the standard deviation of each measurement. Reproduced from reference [101].

Figure 2.6: **(a)** metal-free phthalocyanine and **(b)** copper phthalocyanine (CuPc)

Figure 2.7: Illustration of **(a)** CuPc molecule and **(b)** proposed interaction site between NO_2 and CuPc molecule. Reproduced from reference [175].

Figure 2.8: Schematic representation of signal transduction in a biosensor. Reproduced from reference [190].

Figure 2.9: **(a)** Schematic illustration of a resistive CVD graphene sensor and **(b)** Response and recovery curves of the graphene-based sensor in different NO_2 concentration. Reproduced from reference [206].

Figure 2.10: Schematic of a graphene field-effect transistor (GFET) biosensor. Reproduced from reference [210].

Figure 3.1: **(A)** Wafer is annealed to improve graphene adhesion. **(B)** Application of a photoresist etch mask. **(C)** The mask is exposed to UV light and developed, leaving photoresist to cover the graphene pixels. **(D)** Plasma etch removes the excess graphene. **(E)** Photoresist mask is removed. **(F)** Application of a photoresist mask for metal contacts/tracks. **(G)** The mask is exposed to UV light and developed, removing the resist in areas where metal deposition will occur. **(H)** Deposition of the 30 nm Cr/200 nm Pd stack. **(I)** Excess metal lift-off and photoresist removal. **(J)** Deposition

of the 50 nm Al_2O_3 passivation layer. **(K)** Application of a photoresist mask. **(L)** The mask is exposed to UV light and developed, removing the resist in areas where the wet etch will occur. **(M)** Wet etch using TMAH is performed, exposing graphene pixels and metal contact pads* (*not shown). **(N)** Photoresist is removed – finished sensor.

Figure 3.2: Jipelec Jetfirst 200 Rapid Thermal Annealing furnace.

Figure 3.3: PE-75 Plasma Asher.

Figure 3.4: SUSS MicroTec MA8 Gen 3 mask aligner.

Figure 3.5: **(a)** PVD 75 physical vapour deposition system. **(b)** Inside the deposition chamber. Reproduced from reference [237].

Figure 3.6: Images of **(a)** L2001A3 Ossila spin coater and **(b)** custom chuck designed to fit the 3x3 graphene pixel array sensors with dimensions of 18100 µm x 6200 µm x 500 µm (L x W x D).

Figure 3.7: Hitachi S4800 SEM.

Figure 3.8: (a) JFK Nanowizard 3 atomic force microscope and **(b)** Bruker Dimension icon XR scanning probe microscope.

Figure 3.9: Schematic of G- and D-vibrations within sp^2 carbons.

Figure 3.10: The G-band position as a function of layer thickness. As the number of layers increase the band shifts to lower wavenumber. Reproduced from reference [246].

Figure 3.11: An increase in G-band intensity is observed as the number of layers increase. Reproduced from reference [246].

Figure 3.12: The 2D-band changes shape and position as the number of layers increase. Reproduced from reference [246].

Figure 3.13: Graph displaying the D-band or defect peak in graphene.

Figure 3.14: KRATOS AXIS SUPRA XPS system.

Figure 3.15: J.A. Woollam M-2000 Ellipsometer.

Figure 3.16: **(a)** Semiprobe Lab Assistant probe station with wafer of devices positioned under probes and **(b)** microscope TV screen and Keithley 2612B SourceMeter.

Figure 3.17: **(a)** Pegasus S200FA-HV Semi-automatic analytical probe station. **(b)** Microscope view and chuck position controls. **(c)** Keysight B1505A Power Device Analyzer/Curve Tracer.

Figure 3.18: Schematic of the 'DipChipX' graphene sensor.

Figure 3.19: **(a)** Real-time resistance measurement set-up, **(b)** header pins on the underside of the connector, and **(c)** Biovici 'Sensor-Connect' connector with a DipChipX sensor.

Figure 3.20: Schematic of the '3x3 graphene pixel array' sensor.

Figure 3.21: **(a)** USB-C PCB connector with USB-C male to female adapter and wire connections for D-sub electrical feedthrough and **(b)** USB-C male to USB-C female adapter with 3x3 graphene array sensor.

Figure 3.22: Calculation of the response time according to the definition. Reproduced from reference [258].

Figure 3.23: PCA bi-plot demonstrating the eigenvectors of the sensor array response to the VOCs. Reproduced from reference [74].

Figure 4.1: **(a)** Schematic of the 'DipChipX' device and **(b)** dimensions of the graphene channels, passivation window (located over graphene channels), and metal contact pads.

Figure 4.2: Schematic of the 'Hall Bar' device including dimensions of the graphene channels, graphene passivation windows and metal contact pads.

Figure 4.3: Schematic of the '3x3 graphene pixel array' devices.

Figure 4.4: Schematic and dimensions of the metal contact pads on the 3x3 graphene pixel array sensor.

Figure 4.5: Schematic of graphene pixel array including dimensions of individual pixels and the passivation window.

Figure 4.6: Graphene pixel identification key.

Figure 4.7: 3x3 graphene pixel array device fabrication schematic. **(A)** CVD monolayer graphene on Si/SiO_2 substrate. **(B)** Application of a photoresist etch mask. **(C)** After O_2 plasma etching and photomask removal. **(D)** Coating and patterning photoresist for metal electrodes. **(E)** Metal deposition and lift off. **(F)** Deposition of Al_2O_3 passivation layer using MVD technique. **(G)** Coating and patterning photoresist for selective etching to expose graphene and metal contacts. **(H)** Al_2O_3 is etched, and photomask removed – finished sensor.

Figure 4.8: 5-inch chrome photomask design for the graphene pixels for the '3x3 graphene pixel array' design (reproduced from JD Photo Data check plot). Black features represent the chrome.

Figure 4.9: Optical images of **(a)** a graphene-Si/SiO_2 wafer pre-etch. Darker region contains the corner of a graphene pixel with photoresist on top. Lighter region contains the graphene to be removed via the plasma etching process. **(b)** a graphene-Si/SiO_2 wafer post-etch. Si/SiO_2 region contains no visible graphene.

Figure 4.10: **(a)** The use of one positive photoresist and metal deposition (grey). Photoresist remover cannot penetrate underneath the metal layer, lift-off is unsuccessful. **(b)** Negative photoresist (green) forms an undercut allowing successful lift-off after metal deposition. **(c)** Bilayer photoresist consisting of two positive photoresists, the bottom forming the undercut. Photoresist remover can successfully get underneath excess metal, remove the photoresist, and perform lift-off. **(d)** SEM image of undercut formation.

Figure 4.11: 5-inch chrome photomask design for the metal tracks and contacts for the '3x3 graphene pixel array' design (reproduced from JD Photo Data check plot). Black features represent the chrome.

Figure 4.12: Wafer fragments **(a)** in the PVD substrate holder post-metal deposition and **(b)** during the lift-off process.

Figure 4.13: Optical images of a graphene wafer following metal lift-off. **(a)** Graphene pixels and metal tracks, **(b)** metal contact pads and **(c)** identifying numbers on metal contacts.

Figure 4.14: 5-inch chrome photomask design for the passivation windows for the '3x3 graphene pixel array' design (reproduced from JD Photo Data check plot). Black features represent the chrome.

Figure 4.15: Optical images of a graphene wafer post-etch. **(a)** Graphene pixels and metal tracks and **(b)** Cr-Pd metal contact pads.

Figure 4.16: SEM images of a 3x3 graphene pixel array device demonstrating the passivation windows on a **(a)** graphene pixel and **(b)** metal contact pads.

Figure 4.17: **(a)** Scatter plot of resistance (logarithmic scale) of graphene pixels pre- and post-passivation. **(b)** Box and whisker plot displaying the resistances of graphene pixels pre- and post-passivation. (Extreme outliers have been removed.)

Figure 4.18: **(a)** 4-inch completed graphene pixel array wafer. **(b)** Diced graphene pixel array sensors.

Figure 4.19: Images of the **(a)** top view and **(b)** sideview of the USB-C PCB connector.

Figure 4.20: Images displaying the **(a)** graphene sensor slotted into the USB-C PCB connector, **(b)** damaged contact pins in USB-C plug, **(c)** damaged 3x3 graphene pixel array sensor and **(d)** variations in width between the contact pins of USB-C plugs.

Figure 4.21: Cross-sectional schematic of the graphene transistor.

Figure 4.22: Dirac curve measurement (I_D-V_{GS}) of one graphene pixel on a 3x3 pixel array device, acquired by sweeping the gate-source voltage (V_{GS}) from -50 V to 50 V whilst fixing the drain-source voltage (V_{DS}) to 1 V.

Figure 4.23: **(a)** Dirac curve measurement (Id-Vbg) and **(b)** substrate current (Ibg-Vbg) for p-type Si substrate graphene phototransistors in the dark and illuminated state. Where Id = drain current, Vbg = back gate voltage, and Ibg =back gate current. Reproduced from reference [208].

Figure 4.24: Dirac curve measurement (I_D-V_{GS}) of one graphene pixel on a 3x3 pixel array device, acquired by sweeping the gate-source voltage (V_{GS}) from -60 V to 60 V whilst fixing the drain-source voltage (V_{DS}) to 1 V.

Figure 4.25: Box chart displaying the area-specific response versus the exposed graphene area for different devices.

Figure 4.26: Box charts demonstrating the impact of device age on sensor response (%) for **(a)** 5 ppm NO_2 and **(b)** 50 ppm NH_3 for 3x3 graphene pixel array sensors.

Figure 5.1: Schematic of the glass jar gas sensing system.

Figure 5.2: Nitrogen gas exposure in glass jar using a bare graphene DipChipX device.

Figure 5.3: Carbon dioxide gas exposure in glass jar using a bare graphene DipChipX device.

Figure 5.4: Schematic of the flow-through gas sensing system.

Figure 5.5: **(a)** DipChipX sensor slotted into custom-made Biovici connector. Wires soldered to 'Channel 1' header pins and metal areas covered in electrical tape to prevent shorting inside chamber. **(b)** Electrical feedthrough; **(c)** Schematic of the DipChipX sensor inserted into the connector inside the 25 mm stainless steel tube sensing chamber.

Figure 5.6: Schematic of the gas sensing rig. The vacuum is optional and can be replaced with the exhaust for flow-through applications.

Figure 5.7: Overview of FlowView interface.

Figure 5.8: Ideal Vacuum Cube (gas sensing chamber).

Figure 5.9: **(a)** 6" x 6" Ideal Vacuum Cube™ frame. **(b)** Removeable 6" x 6" plate.

Figure 5.10: **(a)** three separate gas input lines and **(b)** all gas input lines merged into a single line to allow mixing prior to entering sensing chamber.

Figure 5.11: **(a)** flow-through system set-up and **(b)** vacuum system set-up.

Figure 5.12: **(a)** 9-pin D-sub electrical feedthrough, **(b)** 25-pin D-sub electrical feedthrough and **(c)** USB-C PCB connector with sensor inside the gas sensing chamber.

Figure 5.13: **(a)** 265 nm UV LED positioned above a sensor and **(b)** ceramic power resistor functioning as a heater with a sensor resting on top.

Figure 5.14: **(a)** bubbler and **(b)** valves installed to accommodate the bubbler.

Figure 5.15: Wiring scheme of the DAQ and SMU for real-time measurements of graphene array devices.

Figure 5.16: Real-time resistance measurements of a 3x3 graphene array device when subsequently exposed to nitrogen (N_2), air (80% nitrogen/20% oxygen) and argon (Ar). $\Delta R/R_0$ is given as the average of the pixels tested.

Figure 5.17: Humidity sensing set-up.

Figure 5.18: **(a)** Change in resistance ($\Delta R/R_0$) versus relative humidity (%) as dry nitrogen and humidified nitrogen are pumped through the sensing chamber. **(b)** Real-time resistance and relative humidity (RH) measurements of a 3x3 graphene array device when exposed to the RH range of 15% to 92%. **(c)** Bar chart comparing the sensor response of N_2, air, Ar and water vapour ($H_2O_{(g)}$).

Figure 5.19: Bar chart comparing the different recovery methods investigated following a 10-minute exposure to 100 ppm NH_3.

Figure 5.20: Real-time resistance measurements from a graphene pixel array sensor demonstrating a 10-minute exposure to 100 ppm NH_3 followed by an 8-minute vacuum assisted exposure to UV light.

Figure 5.21: Real-time resistance measurements from a graphene pixel array sensor demonstrating a 10-minute exposure to 5 ppm NO_2 followed by an 8-minute vacuum assisted exposure to UV light.

Figure 5.22: Schematic representation of the position of the UV LED for both experiments, with the dashed purple line representing the most intense portion of the beam.

Figure 5.23: **(a)** Real-time resistance measurements of a graphene Hall Bar exposed to UV light in two different positions followed by exposures to 100 ppm NO_2. **(b)** Bar chart illustrating the sensor response (%) of Channel 1 and 2 for both experiments.

Figure 5.24: **(a)** Bar chart displaying the sensor response to 50 ppm NH_3 for each repeat at each temperature tested. **(b)** Variation in sensor response across different temperatures.

Figure 6.1: **(a)** Unsubstituted copper phthalocyanine molecule. **(b)** Copper 2,9,16,23-Tetra-tert-butylphthalocyanine (substituted).

Figure 6.2: Drop-cast functionalization of a DipChipX graphene sensor using copper phthalocyanine (CuPc).

Figure 6.3: SEM images of cobalt, copper, iron, zinc and metal-free phthalocyanine drop-cast on graphene-Si/SiO_2 wafers.

Figure 6.4: Gas sensing data from a CuPc functionalized 3-channel DipChipX device. **(a)** Real-time resistance measurements of two consecutive exposures to 100 ppm nitrogen dioxide gas **(b)** Sensor response of both exposures (i.e., 'Test 1 and 2'). **Inset:** Response time graph where response time is defined as 'time required for the sensor to reach 90% of the maximum response' [257].

Figure 6.5: Real-time resistance measurements of a **(a)** bare and **(b)** CuPc-functionalized DipChipX graphene sensor (1 channel) exposed repeatedly to 100 ppm NO_2 and subsequent UV light exposure. **(c)** Bar chart displaying a comparison of sensor response (%) over nine repeats of the bare and CuPc-functionalized DipChipX graphene sensors.

Figure 6.6: Real-time resistance measurements of a **(a)** bare and **(b)** CuPc-functionalized DipChipX graphene sensor (1 channel) exposed repeatedly to 100 ppm NH_3 and subsequent UV light exposure. **(c)** Bar chart displaying a comparison of sensor response (%) over nine repeats of the bare and CuPc-functionalized DipChipX graphene sensors.

Figure 6.7: Real-time resistance measurements of a bare and CuPc-functionalized DipChipX graphene sensor (1 channel) exposed repeatedly to 100 ppm CH_4.

Figure 6.8: Real-time resistance measurements of individual Hall Bar sensors functionalized with different metal phthalocyanines (cobalt, copper, iron, metal-free and zinc) exposed to **(a)** 50 ppm NO_2, **(b)** 10 ppm NO, **(c)** 50 ppm NH_3, **(d)** 100 ppm CH_4, and **(e)** 580 ppm CO_2.

Figure 6.9: Bar chart displaying the sensor response (%) for bare graphene and the different metal phthalocyanine-functionalized sensors (cobalt, copper, iron, metal-free and zinc) exposed to different gas species (NO_2, NO, NH_3, CH_4, and CO_2).

Figure 6.10: Bar chart displaying the response times (s) for bare graphene and the different metal phthalocyanine-functionalized sensors (cobalt, copper, iron, metal-free and zinc) exposed to different gas species (NO_2, NO and NH_3).

Figure 6.11: SEM image demonstrating the uneven distribution of drop-cast metal-free phthalocyanine on a 3-channel graphene 'DipChipX' device.

Figure 6.12: Reaction scheme for the synthesis of Copper (II) 2,9,16,23-Tetra-tert-butylphthalocyanine.

Figure 6.13: **(a)** Reaction mixture inside a 25 mL round bottomed flask using nitrogen inert atmosphere balloon. **(b)** The TLC plate demonstrates how the reaction's progress was monitored. The image shows that the reaction is not yet complete at this point, as traces of 4-tert-butyl phthalonitrile are still present in the reaction mixture.

Figure 6.14: Images depicting the following steps: **(a)** filtering the resulting green precipitate, **(b)** purifying $CuPc(t\text{-}Bu)_4$ using silica gel column chromatography, and **(c)** using a TLC plate to monitor the product eluting from the column.

Figure 6.15: Dark blue powder; tetra tert-butyl copper phthalocyanine.

Figure 6.16: Experimentally obtained FT-IR spectrum of tetra tert-butyl copper phthalocyanine.

Figure 6.17: Experimentally acquired UV-Vis spectrum of tetra tert-butyl copper phthalocyanine.

Figure 6.18: Image demonstrating complete coverage of the graphene pixels using a spun film on a 3x3 graphene pixel array sensor.

Figure 6.19: AFM morphology of **(a)** bare graphene wafer (5 µm spot size). $CuPc(t\text{-}Bu)_4$ spin coat graphene wafer **(b)** 5 µm spot size and **(c)** 1 µm spot size.

Figure 6.20: **(a)** Experimentally obtained Raman spectrum of pristine (bare) graphene and tetra tert-butyl copper phthalocyanine functionalized graphene. **(b)** Scatter plot displaying the G- and 2D-peak positions in the bare graphene and $CuPc(t\text{-}Bu)_4$-functionalized samples.

Figure 6.21: 60 µm x 60 µm Raman maps displaying the intensity ratio of the D-peak/G-peak (I_D/I_G).

Figure 6.22: Distribution plot displaying the resistance of graphene pixels from 3x3 graphene sensor array devices before and after functionalization with CuPc(t-Bu)$_4$.

Figure 6.23: **(a)** Seven repeat real-time resistance measurements (expressed as $\Delta R/R_0$) of a 3x3 graphene pixel array sensor exposed to 5 ppm NO_2 and subsequent exposure to UV light for 8 minutes (not shown). **(b)** Bar chart comparing the sensor response to nitrogen dioxide of a drop-cast CuPc and spin-coat CuPc(t-Bu)$_4$ sensor following repeat exposures to UV light.

Figure 6.24: **(a)** Real-time resistance response profile of a CuPc(t-Bu)$_4$-functionalized 3x3 graphene pixel array sensor exposed to different concentrations of NO_2. **(b)** Sensor response (%) versus parts per billion (ppb) NO_2 concentration at various concentrations ranging from 100 ppb to 5000 ppb of a CuPc(t-Bu)$_4$-functionalized 3x3 graphene pixel array sensor. **Inset**: Sensor response (%) versus ppb NO_2 concentration displayed on a logarithmic scale.

Figure 6.25: Graphical representation of recovery time estimation. The graph illustrates the average normalized resistance ($\Delta R/R_0$) of each graphene pixel during the following exposure sequence: (1) 10 minutes N_2, (2) 10 minutes 5 ppm NO_2, (3) 5 minutes N_2 and (4) 8 minutes UV exposure. From these data points, the recovery time—when the baseline resistance is restored—can be approximated.

Figure 6.26: Bar chart demonstrating the selectivity of the CuPc(t-Bu)$_4$-functionalized 3x3 graphene pixel array sensor exposed to various gases: 5 ppm nitrogen dioxide (NO_2), 25 ppm ammonia (NH_3), 5 ppm nitric oxide (NO), 100 ppm methane (CH_4), and 450 ppm carbon dioxide (CO_2).

Figure 6.27: Box plot showing the sensor response (%) of three different 3x3 graphene pixel array sensors: bare graphene, CuPc drop-cast, and CuPc(t-Bu)$_4$ spin-coat.

Figure 6.28: Average response times (s) for repeated measurements of bare graphene, CuPc-functionalized, and CuPc(t-Bu)$_4$-functionalized 3x3 pixel array sensors.

Figure 7.1: Molecular structure of the three polymers used in this study: PIM-1, PIM-EA-TB and Matrimid.

Figure 7.2: AFM images with accompanying 3D images for a 250 nm spot size of **(a)** PIM-1 **(b)** PIM-EA-TB and **(c)** Matrimid and. **(d)** bare Silicon wafer.

Figure 7.3: Real-time resistance measurements of three 3x3 graphene pixel array sensors functionalized with PIM-1, PIM-EA-TB and Matrimid exposed to 5 ppm

nitrogen dioxide expressed as $\Delta R/R_0$, where $\Delta R/R_0 = [R_{device} - R_0]/R_0$, and R_0 is the resistance at T = 0.

Figure 7.4: Bar chart displaying the **(a)** average sensor response (%) and **(b)** response time (s) of polymer-functionalized 3x3 graphene pixel arrays sensors exposed to 5 ppm NO_2 compared to the response of a bare graphene sensor.

Figure 7.5: Sensor response (%) versus parts per million (ppm) NO_2 concentration at various concentrations ranging from 1 ppm to 50 ppm for PIM-1, PIM-EA-TB and Matrimid-functionalized 3x3 graphene pixel array sensors.

Figure 7.6: Bar chart comparing the sensor responses of various recovery methods for the polymer-functionalized 3x3 graphene pixel array sensors.

Figure 7.7: Bar chart displaying the sensor response (%) of polymer-functionalized 3x3 graphene pixel array devices exposed to 5 ppm NO_2 and recovered using UV exposure. 'Test 0' represents the initial exposure to the target gas with no prior exposure to UV light.

Figure 7.8: Bar chart comparing the selectivity of bare graphene and $CuPc(t\text{-}Bu)_4$, PIM-1, PIM-EA-TB and Matrimid-functionalized 3x3 graphene pixel array sensors exposed to various gases: 5 ppm nitrogen dioxide (NO_2), 5 ppm ammonia (NH_3), 5 ppm nitric oxide (NO), 100 ppm methane (CH_4), and 450 ppm carbon dioxide (CO_2).

Figure 7.9: Bar chart demonstrating the sensor response (%) of four mixed matrix membranes (50:50 v/v, 80:20 v/v, 50/50 w/w and 80:20 w/w PIM-EA-TB:$CuPc(t\text{-}Bu)_4$) compared to the response of bare graphene, $CuPc(t\text{-}Bu)_4$ and PIM-EA-TB.

Figure 8.1: Proposed mechanism for the synthesis of pDAN from DAN monomers. Reproduced from reference [373].

Figure 8.2: 3-electrode cell electrochemical set-up for the polymerization of DAN onto **(a)** CVD graphene on Si/SiO2 and **(b)** 3x3 graphene pixel array sensors. The working electrode (WE) is highlighted by pink circled areas in both setups.

Figure 8.3: Schematic illustrating the number of scan cycles applied to each row of the 3x3 graphene pixel array devices during electrochemical functionalization in both experiments.

Figure 8.4: Cyclic voltammograms of **(a)** the electropolymerization of 1,5-diaminonapthalene at a scan rate of 50 mV/s over 15 cycles and **(b)** zoomed in region of the voltammogram revealing additional oxidation and reduction peaks.

Figure 8.5: Image of a bare and pDAN functionalized graphene-SiO_2/Si wafers.

Figure 8.6: Optical images of bare graphene, 5-cycles, 10-cycles, and 20-cycles of pDAN on the surface.

Figure 8.7: SEM images of **(a)** bare graphene and **(b)** 5 cycles of pDAN on graphene.

Figure 8.8: AFM surface morphology of bare graphene, 5-cycle, and 20-cycle pDAN functionalized samples.

Figure 8.9: Thickness of pDAN films measured on CVD graphene samples with 5, 10, 15, 20, 25 and 30 cycles.

Figure 8.10: **(a)** Raman spectra of bare graphene, 10-cycle, 15-cycle, and 20-cycle pDAN samples. **(b)** Raman spectra of pDAN on silicon: relevant spectra circled and labelled (reproduced from Supplementary Information, reference [372].

Figure 8.11: **(c)** Full width at half maximum (FWHM) of the G- and 2D-peaks of bare graphene and 5, 10, 15, 20, 25, 30 cycles of pDAN. **(d)** 60 µm x 60 µm Raman maps displaying the intensity ratio of the D-peak/G-peak (I_D/I_G).

Figure 8.12: Wide scan XPS spectra of bare graphene and 30-cycle pDAN samples.

Figure 8.13: High resolution XPS spectra of **(a)** C 1s, **(b)** O 1s of bare graphene and 5 to 30-cycle pDAN samples.

Figure 8.14: **(c)** High resolution XPS spectra of **(c)** N 1s of bare graphene and 5 to 30-cycle pDAN samples.

Figure 8.15: **(a)** Box plot displaying the resistance of graphene pixels from 3x3 graphene sensor array devices before and after functionalization with pDAN. **(b)** I-V sweep of a graphene pixel before and after pDAN functionalization.

Figure 8.16: Real-time resistance measurements, expressed as $\Delta R/R_0$, of a 3x3 graphene pixel array sensor functionalized with pDAN exposed to **(a)** 5 ppm NO_2, **(b)** 10 ppm NO, **(c)** 50 ppm NH_3, **(d)** 5000 ppm CH_4, and **(e)** 580 ppm CO_2.

Figure 8.17: Comparison of sensor response (%) of a 3x3 graphene array sensor exposed to NO_2, NH_3, NO, CH_4 and CO_2.

Figure 8.18: PCA bi-plot demonstrating the eigenvectors of the sensor array response to NO, NO_2 and NH_3 gases. Origin 'Multivariate Analysis' Principle Component Analysis tool was used to generate PCA results.

Figure 8.19: Schematic depicting the electrochemical oxidation setup, featuring a Hall Bar sensor and a graphene-Si/SiO_2 wafer as the control

Figure 8.20: Cyclic voltammogram of the electrochemical oxidation of a graphene Hall Bar sensor in 0.5 M H_2SO_4 for 20 cycles.

Figure 8.21:High resolution C 1s XPS spectra of bare graphene-SiO_2/Si and graphene-SiO_2/Si wafers exposed to 0.1 M, 0.25 M, 0.5 M and 0.75 M H_2SO_4 (labelled '0 cycles').

Figure 8.22: High resolution C 1s XPS spectra of **(a)** Graphene 'Hall Bar' sensors exposed to 0.1 M and 0.25 M H_2SO_4, with each channel on individual sensors exposed for 10- and 20 cycles. **(b)** Graphene 'Hall Bar' sensors exposed to 0.5 M and 0.75 M H_2SO_4, with each channel on individual sensors exposed for 10- and 20 cycles.

Figure 8.23: High resolution O 1s XPS spectra of **(a)** bare graphene-SiO_2/Si and graphene-SiO_2/Si wafers exposed to 0.1 M, 0.25 M, 0.5 M and 0.75 M H_2SO_4 (labelled '0 cycles'). **(b)** Graphene 'Hall Bar' sensors exposed to 0.1 M, 0.25 M, 0.5 M and 0.75 M H_2SO_4, with each channel on individual sensors exposed for 10- and 20 cycles.

Figure 8.24: Real-time resistance measurements, expressed as $\Delta R/R_0$, of electrochemically oxidized Hall Bar sensors sensors—oxidized in four different concentrations of H_2SO_4 (0.1 M, 0.25 M, 0.5 M, and 0.75 M) with either 10 or 20 cycles—when exposed to **(a)** 50 ppm NH_3 and **(b)** 5 ppm NO_2.

Figure 8.25: Bar charts illustrating the sensor response (%) of bare graphene sensors and electrochemically oxidized graphene Hall Bar sensors—oxidized in four different concentrations of H_2SO_4 (0.1 M, 0.25 M, 0.5 M, and 0.75 M) with either 10 or 20 cycles—when exposed to **(a)** 50 ppm NH_3 and **(b)** 5 ppm NO_2.

Figure 8.26: Schematic illustrating the number of scan cycles applied to each row of the 3x3 graphene pixel array devices during electrochemical oxidation in both experiments.

Figure 8.27: Bar chart illustrating the sensor response (%) of two different 3x3 graphene pixel array sensors exposed to 50 ppm NH_3, following electrochemical oxidation in 0.1 M and 0.01 M H_2SO_4, with varying scan cycles per row (0, 10 and 30 cycles).

Figure 8.28: SEM images of damage observed on Hall Bar and 3x3 graphene pixel array devices during electrochemical functionalization of pDAN and electrochemical oxidation. **(a)** – **(c)** 3x3 graphene pixel array devices and **(d)** Hall Bar device.

Figure 8.29: **(a)** CV profile of the electrochemical oxidation, electrodissolution, and ionic absorption of a palladium electrode, adapted from Grden, et al. [390]. **(b)** CV profile from this study, with labels highlighting similarities to **(a)**.

Figure 8.30: SEM images of graphene devices revealing potential defects in the Al_2O_3 passivation layer over the metal tracks.

Figure 8.31: EDS mapping images of a graphene pixel and metal tracks on a 3x3 graphene pixel array device. **(a)** Overlaid elemental SEM image and **(b)** individual elemental maps for Si, Pd, Al, and Cr.

Figure 8.32: EDS mapping images of a metal track on a 3x3 graphene pixel array device. **(a)** Overlaid elemental SEM image and **(b)** individual elemental maps for Si, Pd, Al, and Cr.

Figure 8.33: AFM images of the passivation layer above a metal track on a Hall Bar device (10 μm x 10 μm): **(a)** surface topography and **(b)** corresponding conductive measurements of the same area.

Figure 9.1: Functionalization of graphene: **(a)** schematic of graphene resistor chip (18,200 μm × 9700 μm), **(b)** 1,5 diaminonaphthalene chemical modification of the bare graphene surface, **(c)** addition of glutaraldehyde, **(d)** immobilization of olfactory receptor 2AG1.

Figure 9.2: Image of a passivated chip in the Biovici 'Sensor-Connect' connector for real-time resistance measurements.

Figure 9.3: Schematic representation of signal transduction in the bioelectronic nose.

Figure 9.4: AFM morphology of the **(a)** the non-functionalized (intrinsic graphene) surface, and **(b)** the functionalized graphene surface with DAN.

Figure 9.5: **(a)** Raman spectroscopy of unmodified graphene (red) and graphene after each functionalization step (drop-casting of DAN (blue), followed by glutaraldehyde attachment (green) and lastly OR2AG1 protein receptor (pink). **(b)** Scatter plot showing the shifting in the G-peak and 2D-peak positions, at each functionalization stage, unmodified graphene (red), drop-cast DAN (dark blue), glutaraldehyde attachment (green) and OR2AG1 protein receptor (light blue), indicative of changes in doping and applied strain of the graphene structure, after each functionalization stage.

Figure 9.6: Real-time resistance measurements of the graphene functionalization process, where $\Delta R/R_0 = [R_{device} - R_0]/R_0$, and R_0 is the resistance at T = 0 (resistance of bare (intrinsic) graphene).

Figure 9.7: Structure of **(a)** amyl butyrate (target odorant), **(b)** pentyl valerate, **(c)** butyl butyrate and **(d)** propyl butyrate.

Figure 9.8: **(a)** Real-time resistance measurements of the OR2AG1 functionalized sensor, where $\Delta R/R_0 = [R_{device} – R_0]/R_0$, and R_0 is the resistance at T = 0 (resistance of OR2AG1 functionalized graphene). A concentration range of 10^{-15} to 10^{-6} M in PBS was used for the target odorant, amyl butyrate (AB), and 10^{-6} M in PBS was used for pentyl valerate (PV) and butyl butyrate (BB) controls (all prepared using 1 M stock solutions in DMSO). **(b)** Picomolar amyl butyrate concentration (logarithmic scale) plotted against resistance with inset error bars.

Figure 9.9: **(c)** Picomolar amyl butyrate concentration (logarithmic scale) repeats with additional concentrations (0.1, 0.2, 0.3, 0.4, 0.75, 250, 500 pM) plotted against resistance with inset error bars. **(d)** Real-time reaction time graph showing response time after adding the target odorant (amyl butyrate, 0.5 pM). **(e)** Selectivity graph of the negative controls (1 μM PV, BB, PB) and target odorant (1 μM AB) with respect to PBS.

List of Tables

Table 1: Detection of various gases and volatile organic compounds (VOCs) using gas sensors and their associated applications.

Table 2: Gas sensor technologies and their basic operating principles.

Table 3: Metal oxide semiconductor (MOS) sensors identified in the literature.

Table 4: Gas sensor arrays identified in published literature.

Table 5: Advantages and disadvantages of different methods for synthesizing graphene.

Table 6: Metal phthalocyanine-carbon nanomaterial hybrid sensors identified in the literature.

Table 7: Graphene-based resistive and FET sensors identified from the literature.

Table 8: Various functionalization techniques utilized in this thesis.

Table 9: Characteristic bands of graphene and the properties expressed.

Table 10: Primary XPS region and approximate binding energies for silicon, carbon, nitrogen and oxygen.

Table 11: Iterations of the USB-C PCB connector, outlining challenges and solutions for each iteration.

Table 12: Summary of the graphene channel dimensions, exposed area and target gas concentration for comparison across the three unique device designs.

Table 13: Gas sensing system requirements and justifications for testing 3x3 graphene pixel array sensors.

Table 14: The limitations, challenges, and necessary requirements of the gas sensing system.

Table 15: Duration, flow rates and concentration of test gas for a typical experiment using the flow-through gas sensing rig.

Table 16: The limitations, challenges, and necessary requirements of the gas sensing system.

Table 17: Technical specifications of MFCs used. Acknowledgement: Bronkhorst UK Ltd webpage.

Table 18: Description and use of each plate installed on the sensing chamber.

Table 19: Kickstart software parameters kept constant during gas sensing experiments.

Table 20: Duration, flow rates and concentration of test gas for a typical experiment using the flow-through gas sensing rig.

Table 21: Summary of sensor designs, phthalocyanines, and gas sensing system iterations used in this chapter.

Table 22: Peak positions and peak assignments of acquired spectrum compared to literature values [329].

Table 23: Peak positions of acquired spectrum compared to literature values [333], [336].

Table 24: Recovery times (s) for three repetitions of the CuPc(t-Bu)$_4$-functionalized sensors exposed to 5 ppm NO_2 and recovered with UV light.

Table 25: Comparison of NO_2 sensors using different sensing materials.

Table 26: Average roughness and RMS roughness measurements from three measurements on bare silicon, PIM-1, PIM-EA-TB and Matrimid.

Table 27: Average film thickness of spin-coat PIM-1, PIM-EA-TB and Matrimid films on Si substrates.

Table 28: Percentage recovery of the initial response of the polymer-functionalized sensors. The formula for calculating percentage recovery is provided in **Chapter 3.6.3**.

Table 29: Recovery times (s) for three repetitions of the polymer-functionalized sensors exposed to 5 ppm NO_2 and recovered with UV light.

Table 30: Comparison of graphene-based NO_2 sensors using different sensing materials.

Table 31: Estimated Limit of Detection (LOD) and Limit of Quantification (LOQ) for each polymer-functionalized 3x3 graphene pixel array sensor.

Table 32: Atomic concentrations of carbon, oxygen, and nitrogen in bare graphene and pDAN samples.

Table 33: Atomic concentrations of the carbon-only and oxygen-containing peaks in C 1s carbon peak.

Table 34: Summary of electronic interactions with each functionalization technique.

Table 35: Comparison between the top-performing NO_2 sensors developed in this work and notable NO_2 sensors reported in the literature.

List of Abbreviations

2D Two Dimensional

AB Amyl Butyrate

AFM Atomic Force Spectroscopy

BB Butyl Butyrate

Bi-Layer A two-layer photoresist system for lift-off processes

CE Counter Electrode

CNTs Carbon Nano Tubes

CoPc Cobalt Phthalocyanine

CuPc Copper Phthalocyanine

CV Cyclic Voltammetry

CVD Chemical Vapour Deposition

DAN 1,5-diaminonaphthalene

DAQ Data Acquisition System

DI Deionised

Dip Chip Design name for a chip that can be partially submerged in solution

EDS/EDX Energy Dispersive X-ray Spectroscopy

FePc Iron Phthalocyanine

FTIR Fourier Transform Infrared Spectroscopy

FWHM Full Width at Half Maximum

GO Graphene Oxide

H_2Pc Metal-free Phthalocyanine

I_D/I_G intensity ratio of graphene's D-peak and G-peak

IPA Propan-2-ol

IV Current – Voltage

LOD Limit of Detection

LOQ Limit of Quantification

MMM Mixed Matrix Membrane

MPc Metal Phthalocyanine

MVD Molecular Vapour Deposition

n-type majority charge carriers are electrons (negative charge)

p-type majority charge carriers are holes (positive charge)

PB Propyl Butyrate

Pc Phthalocyanine

pDAN poly(1,5-diaminonaphthalene)

PIM Polymer of Intrinsic Microporosity

ppb parts per billion

ppm parts per million

ppt parts per trillion

PV Pentyl Valerate

PVD Physical Vapour Deposition

RE Reference Electrode

rGO Reduced Graphene Oxide

RMS Root Mean Square Surface Roughness

RPM Revolutions per minute

RSF Relative Sensitivity Factor

RT Room Temperature

RTA Rapid Thermal Annealing

SEM Scanning Electron Microscope

SMU Source Measure Unit

SPM Scanning Probe Microscopy

swCNT Single-Walled Carbon Nano Tube

TLC Thin-Layer Chromatography

TMA Trimethylaluminum

TMAH Trimethylaluminum hydroxide

UV Ultraviolet

UV-Vis Ultraviolet – Visible

v/v volume per volume solution

VOCs Volatile Organic Compounds

WE Working Electrode

w/w weight per weight solution

XPS X-ray Photoelectron Spectroscopy

ZnPc Zinc Phthalocyanine

Chapter 1 : Introduction

1.1. Background & Motivation

As countries around the world adopt stricter regulations on environmental pollutants and greenhouse gas emissions, and as efforts to combat climate change intensify, the demand for reliable detection of harmful gases—such as nitrous oxides, sulphur dioxide, carbon dioxide, carbon monoxide, and methane—is increasing. Growing public awareness of the risks associated with these emissions is driving the need for sensors that are versatile, accurate, reliable, reusable, and multifunctional. Often, the "allowable" limits of exposure are established based on the capabilities of current detection technologies. As technology advances, these limits are typically lowered accordingly [1]. Despite progress, modern gas sensing technologies still face significant challenges, including limited selectivity and sensitivity, prolonged response and recovery times, and environmental interferences such as fluctuations in temperature, humidity, and pressure [2], [3]. This underscores the ongoing necessity for the development of highly sensitive and selective gas sensors.

The requirement for gas sensors extends across various sectors, including agriculture, food safety, security, healthcare, and industrial applications. Industrial gases such as carbon dioxide, methane, hydrogen, and oxygen are odourless and tasteless, posing significant risks to humans, animals, and the environment [4]. Detecting these gases at low concentrations is crucial for identifying and containing leaks before they become hazardous. In healthcare settings, the ability to detect ultra-low concentrations is essential for identifying medical biomarkers. For instance, patients with asthma often have elevated levels of nitric oxide (NO) in their breath. While healthy individuals typically exhibit NO levels around 7-14 parts per billion (ppb), asthmatic individuals show levels ranging from 14-31 ppb [5]. Accurate detection of such low concentrations, necessary for precise diagnosis using point-of-care devices, remains a significant area for development and innovation.

Graphene's exceptional electrical properties make it an ideal candidate for sensing applications. As an 'all-surface' material, it has even demonstrated the ability to detect

single gas molecules [6], demonstrating its potential for highly sensitive gas detection. Although graphene has been integrated into various sensing platforms, there remains significant room for improvement, particularly in addressing challenges such as the manufacture of high-quality graphene [7], [8], long recovery times or incomplete sensor recovery [9], and issues related to its extreme sensitivity and selectivity, which can cause noise and variability in measurements.

The aim of this thesis was to develop integrated sensors by combining semiconductor fabrication processes with chemical and biochemical surface modifications. These sensors were based on a graphene platform and utilized various functionalization techniques to achieve sensitive and selective gas detection at room temperature. By focusing on signal enhancement through innovative surface modification strategies, the project sought to optimize graphene's electrical properties while managing its sensitivity and selectivity. Additionally, the thesis included the design and fabrication of a sensor array device, with the goal of selectively functionalizing each graphene pixel of the array to varying degrees. By employing diverse surface modification techniques across the array, the device has the potential to the simultaneously detect multiple analytes. This approach enhances the sensor's discrimination capabilities, leading to improved accuracy, reliability, and overall robustness.

1.2. Thesis Outline

This thesis is organised into ten chapters.

Chapter 1: Introduction

This chapter outlines the background, motivation, and objectives of the thesis, and provides an overview of its structure.

Chapter 2: Literature Review

This chapter presents an overview of the literature on graphene, graphene-based sensors, gas sensors, and various functionalization methods.

Chapter 3: Materials & Methods

This chapter details the materials and equipment used throughout this thesis, covering the tools and techniques employed in the fabrication, functionalization, and characterization processes.

Chapter 4: Fabrication and Design of Graphene Sensors

This chapter describes the design and fabrication of a 3x3 graphene pixel array sensor, as well as the design of other sensors used in this thesis. It also includes an analysis of back-gated measurements performed on these devices. A comparison of sensor performance across various designs and an examination of device aging is also discussed.

Chapter 5: Gas Sensing System

This chapter presents the development and optimization of the gas sensing system, highlighting the challenges and shortcomings encountered in each iteration.

Chapter 6: Gas Detection Using Metal Phthalocyanine Modified-Graphene Sensors

This chapter reports on the gas sensing performance of graphene sensors functionalized with various phthalocyanines. Tetra-tert-butyl copper phthalocyanine was synthesized to provide enhanced solubility of the copper phthalocyanine and used to modify the graphene sensors. The gas sensing performance of these functionalized

sensors is compared with that of other sensors discussed in this chapter and similar sensors in the literature.

Chapter 7: Enhanced Nitrogen Dioxide Detection Using Graphene Sensors Modified with Polymers of Intrinsic Microporosity

This chapter examines the gas sensing performance of PIM-functionalized graphene sensors, exploring their potential to enhance the functionality of graphene-based sensors in various gas detection scenarios. Additionally, the chapter investigates the use of a hybrid material (copper phthalocyanine + PIM), specifically a Mixed Matrix Membrane (MMM), for gas sensing applications.

Chapter 8: Electrochemical Functionalization of Graphene Sensors

This chapter discusses two electrochemical functionalization techniques applied to graphene-based sensors. The goal was to explore the potential of using a single functionalization method to modify graphene pixels on the same sensor to varying degrees. Additionally, the chapter addresses device damage observed during the functionalization process, exploring possible causes and proposing solutions.

Chapter 9: Detection of Odorants Using Human Olfactory Receptor 2AG1

This chapter reports the fabrication and evaluation of a graphene-based bioelectronic nose sensor employing human olfactory receptor 2AG1. The sensor's performance was assessed by exposure to various odorant molecules.

Chapter 10: Conclusions and Future Work

This chapter summarizes the key findings of this thesis discusses future work.

Chapter 2 : Literature Review

2.1. Introduction

This chapter includes a review and comparison of various gas sensors, highlighting their applications across different fields. It continues with a comprehensive overview of graphene, detailing its properties, fabrication methods, surface modifications, and applications in sensor technology. Despite its discovery in 2004, ongoing research is essential to advance the development of selective, sensitive, and reliable sensors based on graphene. The chapter concludes with an examination of the specific surface modification techniques employed in this thesis and evaluates their performance in other sensor technologies.

2.2. Gas Sensing

The demand for advanced gas sensing technologies has surged recently, driven by escalating concerns about environmental and public health [10]. The global push to reduce greenhouse gas emissions and achieve carbon neutrality has further heightened the need for effective gas sensing solutions [11], [12]. In 2023, the global gas sensor market was valued at USD 2.9 billion and is projected to grow at a compound annual growth rate (CAGR) of 9.5% through 2030 [13], [14].

This growing interest across industries such as manufacturing, agriculture, automotive, and healthcare is fuelled by the need to monitor critical factors including operational efficiency, pollution levels, air quality, environmental compliance, and medical biomarkers [1]. Advancements in gas sensing technology are essential for obtaining more accurate, reliable, and real-time data. These improvements are crucial for addressing environmental challenges, enhancing quality of life, and advancing diagnostic capabilities in healthcare.

Gas sensing involves detecting and measuring specific gases within an environment. Gas sensors, or gas detectors, are specialized devices designed to identify the presence, concentration, and type of gases in the air. These sensors are extensively utilized

across various fields, including food safety [15]–[18], industrial [19] and environmental monitoring [20], [21] and medical diagnostics [22], [23].

2.2.1. Gases and VOCs Detected by Gas Sensors

As awareness grows about the dangers of various gases humans are exposed to—many of which can be harmful or even fatal—there is a rising demand for advanced gas sensors [24]. These sensors are crucial for monitoring and controlling exposure to toxic gases in various environments. For example, ammonia (NH_3) is widely used in industries such as agriculture (fertilizers), water treatment, refrigeration, and in the chemical, food, and pharmaceutical sectors [25]. Despite its utility, ammonia is a toxic gas that poses significant risks to both human health and the environment. Exposure to concentrations as low as 25 ppm can cause severe damage to the respiratory system, skin, eyes, and other organs [26], making it essential to detect NH_3 at low levels.

Similarly, nitrogen dioxide (NO_2), a toxic gas emitted by vehicle exhausts and industrial processes, can cause mild respiratory symptoms at low concentrations and become fatal at higher levels [27]. The World Health Organization (WHO) has set an annual exposure limit as low as 21 ppb [28], underscoring the critical need for highly sensitive NO_2 detectors to protect public health.

Gas sensors are designed to detect a wide range of gases and volatile organic compounds (VOCs), serving specific applications across various industries and playing a crucial role in our everyday lives. For instance, carbon monoxide (CO) detectors, commonly found in households, are equipped to detect CO concentrations in the range of 25-70 ppm [29]–[31]. When these detectors sense CO within this range over a certain period, they trigger an alarm. The sensor typically employs electrochemical technology, where the presence of CO leads to a chemical reaction in the sensor compartment. This reaction causes a change in the electric current of the electrolyte, with the current increase directly correlating to the concentration of CO detected [30].

Another example is the breathalyser, a device used to measure an individual's blood alcohol content (BAC). Modern handheld breathalysers typically use electrochemical

fuel cell technology, while evidential breathalyser machines often employ infrared spectroscopy [32], [33].

In a fuel cell alcohol sensor [34], the device consists of two electrodes separated by a proton-exchange membrane. Alcohol enters the device at the anode, where it undergoes electrocatalytic oxidation, producing various by-products (e.g., acetic acid), protons, and electrons. These electrons travel to the cathode, where they react with oxygen to form water. The resulting chemical reaction generates an electric current, which is proportional to the BAC.

In contrast, infrared spectroscopy breathalysers [35] detect alcohol vapor in a person's breath by measuring the absorption of infrared (IR) energy. Alcohols have distinctive IR absorption peaks related to O-H, C-O, and C-H bond stretching vibrations. By analysing these absorption patterns, the device can determine the presence and concentration of alcohol.

Table 1 provides an overview of typical gases and VOCs detected by gas sensors, along with their respective applications.

Table 1: Detection of various gases and volatile organic compounds (VOCs) using gas sensors and their associated applications.

Gas	Applications	Reference
Carbon monoxide (CO)	• Industrial safety • Residential safety • Vehicle emissions monitoring	[27], [36], [37]
Oxygen (O_2)	• Industrial safety • Medical oxygen monitoring	[23]
Carbon dioxide (CO_2)	• Environmental air quality monitoring • Indoor air quality monitoring • Medical diagnostics (respiratory function)	[38]
Methane (CH_4)	• Natural gas leak detection • Landfill gas monitoring	[39]
Hydrogen sulphide (H_2S)	• Oil and gas industry safety • Wastewater treatment • Chemical manufacturing process	[40]
Sulphur dioxide (SO_2)	• Environmental air quality monitoring • Industrial safety	[41]
Nitrogen dioxide (NO_2)	• Environmental air quality monitoring • Vehicle emissions control • Industrial safety	[42], [43]
Ozone (O_3)	• Air quality assessment • Industrial safety	[42]
Ammonia (NH_3)	• Agricultural fertilizers • Water treatment systems • Medical diagnostics (liver and kidney health)	[25], [44]
Nitric oxide (NO)	• Medical diagnostics (biomarker for asthma and other inflammatory conditions)	[45]
Acetone (C_3H_6O)	• Medical diagnostics (biomarker for diabetes) • Industrial safety	[23], [46]
Toluene ($C_6H_5CH_3$)	• Industrial safety • Environmental pollution monitoring	[47], [48]

2.2.2. Overview of Gas Sensor Technologies

Various types of gas sensors are currently used commercially and are also the focus of ongoing research. **Table 2** provides a summary of some of these gas sensors and their basic operating principles. The sensors described below find extensive use in diverse fields such as environmental monitoring, food processing, agriculture, automotive, industrial process control and medical diagnostics [22].

__Table 2__: Gas sensor technologies and their basic operating principles.

Gas Sensor	Operation	Ref.
Electrochemical	Detects gases through a chemical reaction between the gas and an electrolyte solution, generating an electrical current proportional to the gas concentration.	[49]
Metal Oxide	Utilizes a metal oxide semiconductor (e.g., tin dioxide, titanium dioxide) whose electrical resistance changes in the presence of gases, determining the gas concentration.	[50]
Infrared (IR)	Based on the absorption of infrared light by gases. Different gases absorb different IR wavelengths, and the sensor measures the reduction in light intensity to quantify gas concentration.	[51]
Photoionization Detectors (PID)	Detects volatile organic compounds (VOCs) and other gases by ionizing the gas molecules using ultraviolet (UV) light. The resulting ions generate a current proportional to the gas concentration.	[52]
Catalytic Bead	Detects combustible gases by catalysing a reaction on a heated bead, causing a temperature change. This change alters the bead's resistance, indicating the presence of gas.	[51]
Thermal Conductivity	Compares the thermal conductivity of the target gas to a reference gas. The difference in thermal conductivities is used to identify and measure the gas concentration.	[51]
Acoustic Wave	Gas molecules interact with an acoustic wave on a piezoelectric material. Changes in the wave's frequency or amplitude indicate the presence and concentration of the gas.	[51]
Optical	Detects gas molecules through light absorption, fluorescence, or light scattering. Specific gases are identified based on their unique optical properties.	[51]
Chemiresistive	Based on changes in the resistance of a material when exposed to gas.	[22]

Various gas sensors operate on different principles, such as electrochemical reactions, infrared absorption, photoionization, and catalytic reactions. Each type has its own strengths and limitations depending on the application. For instance, electrochemical sensors are widely used for detecting toxic gases such as NO_2, SO_2, CO and H_2S [51], [53], while infrared sensors excel in identifying specific gas molecules (e.g. H_2O, CO_2, O_3, NO_X, SO_2, etc.) through their unique absorption spectra [54], [55].

Among these various technologies, chemiresistive and metal oxide semiconductor sensors are particularly noteworthy due to their sensitivity, cost-effectiveness, and compatibility with a wide range of gases [56]. Considering the similarities in their operational principles, these sensors are often directly compared in the literature. Given the use of chemiresistive sensors in this thesis, the following sub-section will provide a review of metal oxide semiconductor sensors, offering a comparison with the chemiresistive sensors developed in this work as a competing technology.

2.2.2.1. Metal Oxide Semiconductor Gas Sensors

Metal oxide semiconductor (MOS) sensors operate based on changes in electrical resistance caused by the adsorption of gas molecules on their surface, leading to redox reactions. Typically, these sensors consist of a metal oxide sensing layer positioned between two electrodes on a substrate, accompanied by a heating element (**Figure 2.1**). Commonly used metal oxides in gas sensors include tin dioxide (SnO_2), zinc oxide (ZnO), tungsten oxide (WO_3), titanium dioxide (TiO_2), copper oxide (CuO), and indium oxide (In_2O_3) [57].

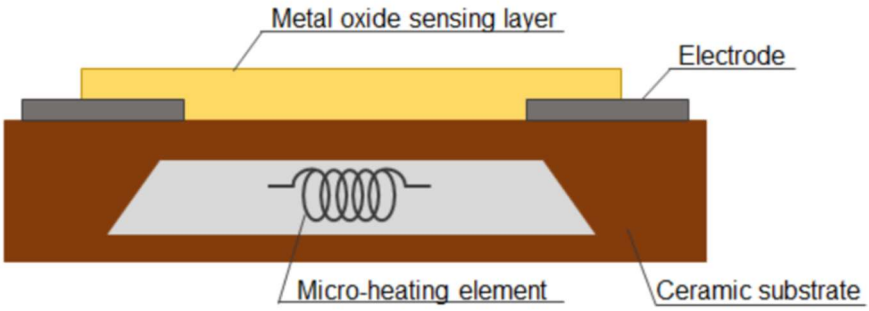


***Figure 2.1**: Schematic of a typical metal oxide semiconductor sensor. Reproduced from reference* [57].

Metal oxide sensors can be classified as either p-type or n-type, depending on the primary charge carriers—holes for p-type and electrons for n-type. The resistance of these sensors changes based on the type of gas they are exposed to and the doping present in the semiconductor. For example, in an n-type metal oxide sensor, exposure to oxidizing gases like nitrogen dioxide (NO_2) results in the loss of electrons, leading to an increase in resistance [57]. The operational mechanism is driven by charge transfer between the semiconductor and the adsorbed gas molecules, which directly impacts the sensor's resistance.

Despite their advantages, including low cost, robustness, high sensitivity, and simple operation, metal oxide sensors face challenges that require further research. Several studies [19], [43], [56]–[59] highlight issues such as high operational temperatures and poor selectivity. Additionally, slow response times [22], [43], as well as limited shelf-life [56], [59], have been noted as areas needing improvement. Nevertheless, these sensors have been widely used across various applications. **Table 3** below summarizes several MOS sensors reported in the literature.

***Table 3**: Metal oxide semiconductor (MOS) sensors identified in the literature.*

Metal Oxide	Target Gas	Operating Temperature (°C)	Sensitivity (ppm)	Recovery time (s)	Ref.
ZnO	H_2S	RT	0.03 *(30 ppb)*	90-120	[60]
CuO-ZnO hybrid	H_2S	200	1	50	[61]
SnO_2	CO_2	240	20,000	47	[62]
SnO_2	Ethanol (C_2H_6O)	285	0.05 *(50 ppb)*	76	[63]
Pt- SnO_2 hybrid	CO_2	100	100	30	[64]
Co_3O_4	Toluene ($C_6H_5CH_3$)	190	100	750	[65]
Pt-ZnO hybrid	Acetylene (C_2H_2)	300	1000	81	[66]
Au-In_2O_3 hybrid	Formaldehyde (CH_2O)	200	100	135	[67]
SnO_2-ZnO hybrid	NO_2	RT	1	300	[68]
TiO_2	NH_3	250	500	110	[69]

2.2.3. Gas Sensor Arrays

Gas sensor arrays consist of multiple sensors working together to simultaneously detect, analyse, and determine the concentrations of gaseous mixtures. These arrays mimic the olfactory system, with different sensing components acting like olfactory receptors in mammals, which is why they are often called "electronic noses." [15], [70], [71] Sensor arrays have several advantages over traditional sensors. By using multiple sensing elements, they can detect a broader range of analytes with greater accuracy and reliability. The combined responses from different sensors enhance selectivity, allowing for the differentiation of similar compounds [15]. Additionally, sensor arrays, unlike traditional sensors that target a single analyte, can detect multiple substances simultaneously. This capability, enhanced by pattern recognition, makes them particularly valuable in complex applications such as environmental monitoring, medical diagnostics, and industrial processes. [72].

The first sensor array device, reported by Seiyama et al. [73] in 1962, consisted of a single silicon chip capable of detecting hydrogen sulphide, methane, and carbon monoxide [74]. Since then, research has focused on developing sensor arrays to advance gas sensor technology. **Table 4** highlights some of the gas sensor arrays documented in the literature.

***Table 4**: Gas sensor arrays identified in published literature.*

Sensor Description	Sensing Component(s)	Target Gases	Sensing Mechanism	Ref.
Metal oxide	WO_3, SnO_2 and NiO decorated with Au nanoparticles (NPs)	Acetone, toluene, NH_3, and H_2S	Change in electrical resistance	[75]
Perovskite-type oxide	Ag-doped LaFeO3	Acetone, benzene and formaldehyde	Change in electrical resistance	[76]
Graphene	cobalt porphyrin	NH_3	Change in electrical resistance	[77]
Single-walled carbon nanotubes	Pd, Pt, Rh, and Au NPs	H_2, CH_4, CO, and H_2S	Change in electrical resistance	[78]
Optical	14 unique polymers (see reference)	Benzene, toluene, xylene, pentyl acetate, butyl acetate, propyl acetate, pentyl alcohol, butyl alcohol, propyl alcohol,	Fluorescence changes	[79]
Single-walled carbon nanotubes	single-stranded DNA	ethylhexanol, linalool, tetradecene, and phenylacetaldehyde	Change in electrical resistance	[80]

2.3. Overview of Graphene

Since graphene's discovery by Novoselov and Geim in 2004 [81], the nanomaterial continues to be a rising star in the scientific community due to its extraordinary properties including unparalleled mechanical strength (Young's modulus of 1 TPa and intrinsic strength of 130 GPa), large surface area, remarkable thermal and electrical conductivity and high electron carrier mobility (2.5 x 10^5 cm^2 V^{-1} s^{-1}) [82]. Graphene, an allotrope of carbon, is described as a two-dimensional (2D) single layer of sp^2 hybridised carbon atoms arranged in a honeycomb shape [83], [84] (**Figure 2.2**). Attributable to the exceptional properties, graphene presents opportunities for applications in a diverse range of fields such as: medical [85], solar cells [86], energy storage [87], transparent electrodes [88], transistors [89] and nanocomposites [90].

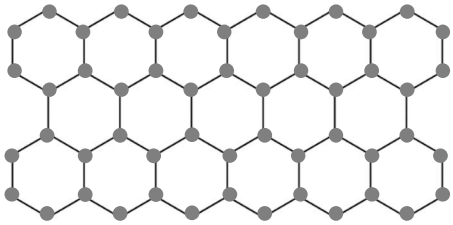


***Figure 2.2**: Lattice structure of graphene.*

2.3.1. Electronic Structure

In graphene, every carbon atom forms robust sp^2 'sigma' (σ) bonds with three neighbouring atoms, a result of hybridizing the 2s, 2px, and 2py orbitals. The electronic band structure of graphene is then shaped by the remaining 2pz orbital, giving rise to two pi (π) bands: the bonding band (lower energy valence band) and the anti-bonding band (higher energy conduction band). [91].

Pristine graphene, as a zero-band gap semiconductor, exhibits conduction and valence bands in direct contact, and the point where these bands touch is referred to as the 'Dirac point'. The band structure of graphene sets it apart from other materials, with semiconductors typically having a small band gap, insulators possessing an even larger band gap, and metals exhibiting overlapping bands (**Figure 2.3**). In graphene devices, the substrate often induces a band gap, a topic that is discussed in detail in **Section 2.3.2.2.1**.

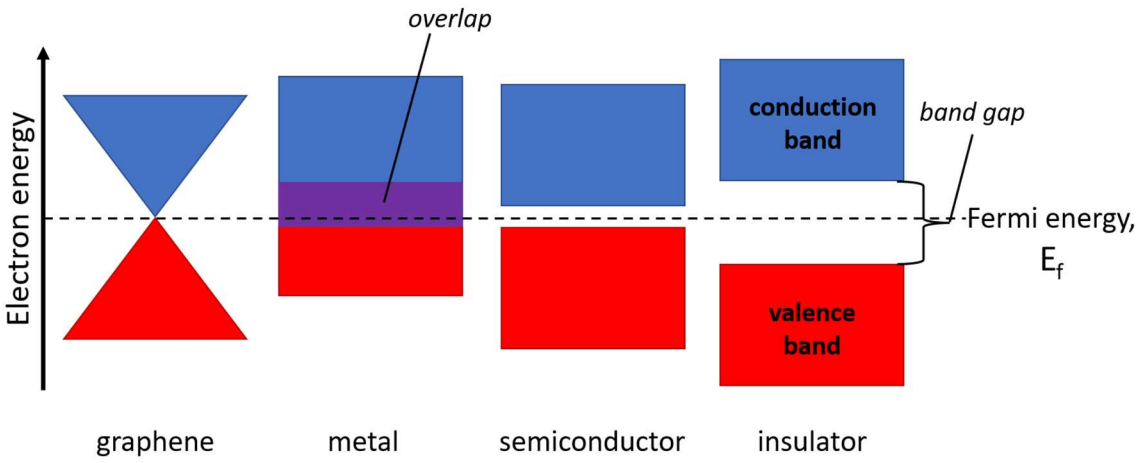


***Figure 2.3**: Schematic representation of the electronic band structure of graphene (Dirac cones of conduction and valence bands touching), metals with overlapping bands, semiconductors with a small band gap and insulators with a large band gap.*

2.3.2. Doping of Graphene

Doping refers to the process of intentionally introducing impurities or chemical modifications to alter graphene's electronic properties, tailoring its electrical behaviour. Due to graphene's ambipolar nature, the type of charge carrier—electrons or holes—depends on external conditions [92]. The Dirac point in graphene is where the valence and conduction bands intersect, and this point also corresponds to graphene's Fermi level. Shifting the Fermi level above or below the Dirac point results in n-type or p-type doping, respectively [93]. Liu et al. [92] categorize graphene doping into two types: electrical and chemical. Electrical doping is achieved by adjusting the gate voltage, while chemical doping involves more complex methods, such as introducing specific chemical species.

2.3.2.1. Electrical Doping

Electrical doping of graphene can be achieved by applying a gate voltage to a field-effect transistor (FET). Numerous studies [81], [93]–[95] have shown that this reversible process can switch the polarity of a graphene channel by simply adjusting the gate voltage, allowing the channel to transition between p-type and n-type conduction. The type of induced carriers is opposite to the sign of the applied gate voltage: a positive gate voltage leads to the generation of electrons, whereas a negative gate voltage results in the formation of holes [95]. A negative shift in the Dirac point

voltage indicates n-type doping, while a positive shift indicates p-type doping [81], [93].

2.3.2.2. Chemical Doping

Controlling and fine-tuning graphene's electronic structure by introducing holes and electrons is necessary to create useful electronic devices. In addition to electrical doping, this can also be achieved through chemical doping. Research [95], [96] has shown that graphene can either be p- or n-doped depending on the atoms or molecules in contact with the graphene surface. This type of doping is non-destructive and involves charge transfer between the adsorbed species and graphene. Whether graphene is p- or n-doped depends on graphene's Fermi level with respect to the adsorbed species' highest occupied molecular orbital (HOMO) and lowest unoccupied molecular orbital (LUMO) (**Figure 2.4**). If the HOMO of the surface adsorbate is higher than graphene's Fermi level, then electrons will transfer to graphene from the adsorbate with graphene becoming n-doped. If graphene's Fermi level is higher than the LUMO, then electrons will transfer from graphene to the surface adsorbate, and graphene becomes p-doped. In general, molecules with an electron-withdrawing nature interacting with graphene will induce p-type doping, while electron-donating molecules will result in n-type doping of graphene [92]. This type of doping is particularly relevant to gas sensing.

Finally, similar to other semiconductor materials, graphene can be doped through substitutional doping [92], where carbon atoms in the lattice are replaced by other atoms. P-type doping is typically achieved by substituting carbon with atoms like boron, which has fewer valence electrons than carbon. Conversely, n-type doping is accomplished by replacing carbon with atoms such as nitrogen, which has an extra valence electron.

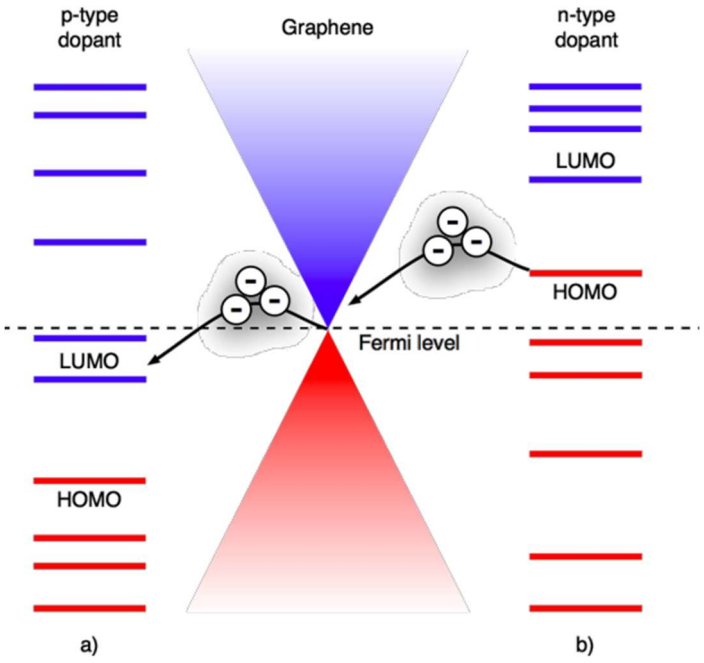


***Figure 2.4**: Schematic representation of graphene's Fermi level in relation to surface adsorbate's HOMO and LUMO. **a)** demonstrates p-doping and **b)** represents n-doping. Reproduced from reference* [95].

2.3.2.2.1. Doping Effects of Substrates

Graphene's properties are heavily affected by its interactions with the surrounding environment, particularly the substrate it rests on. As a result, the interaction between graphene layers and various substrates has been extensively studied [95], [97]–[100], revealing significant changes in graphene's electronic properties.

Silicon dioxide/silicon (SiO_2/Si) is a commonly used substrate for graphene-based devices, where graphene typically experiences p-type doping [95]. Kang et al. [100] attribute this effect to electron transfer from graphene to oxygen dangling bonds on the SiO_2 surface. Beyond SiO_2, the choice of dielectric significantly influences graphene's electronic properties. For example, one study [101] demonstrates that graphene on Al_2O_3 (aluminum oxide), h-BN (hexagonal boron nitride), and Si_3N_4 (silicon nitride) exhibits varying degrees of p-type doping. **Figure 2.5** illustrates the Dirac point of graphene on four different substrates, highlighting the variations in doping levels experienced on each substrate. Conversely, graphene placed on SiC substrates typically experiences n-type doping. Given the importance of controlling graphene's electronic properties for effective device performance, understanding how

different substrates and environmental factors impact graphene is crucial for engineering its properties in a targeted manner.

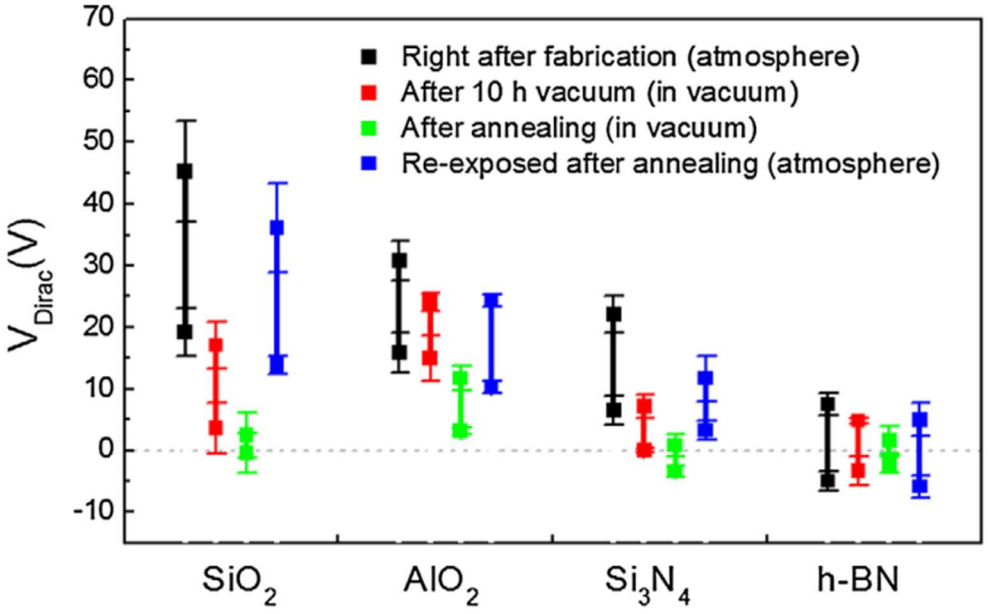


***Figure 2.5**: Distribution of the Dirac point for graphene on each dielectric substrate under four different conditions. The upper and lower squares represent the average Dirac points observed during the backward and forward sweeps, respectively. Error bars indicate the standard deviation of each measurement. Reproduced from reference* [101].

2.3.2.2.2. Doping Effects of Ambient Air Absorbates

Graphene's two-dimensional nature means that every atom is exposed on its surface, making it highly sensitive to its environment. However, this extreme sensitivity poses a challenge, as graphene tends to respond to all surrounding molecules. Understanding the impact of these environmental factors is crucial for optimizing sensor performance in practical gas sensing applications.

Graphene's sensitivity to ambient air absorbates, such as oxygen (O_2) and humidity, has been well-documented in various studies [102]–[106]. For example, Hayasaka et al. [102] demonstrated that graphene field-effect transistors (FETs) exhibit significant sensitivity to both humidity and O_2 at low operational temperatures. As the temperature increases, the sensitivity to humidity diminishes, whereas the sensitivity to O_2 initially decreases and then increases. Another study [105] confirmed that both oxygen and water induce hole-doping in graphene. Interestingly, the study also revealed that the improvement or degradation in carrier mobility is influenced by substrate impurities [103], [105]. Additionally, oxygen and water absorbates can

become trapped at the interface between graphene and the underlying substrate during the fabrication process, with O_2 doping being particularly enhanced in humid environments [106]. While doping by ambient absorbates is generally unavoidable, it can be managed through techniques such as thermal annealing during fabrication [103], [104] and surface passivation [106].

2.4. Graphene Fabrication

There are various methods for fabricating graphene, each with its own advantages and limitations, and the choice of method depends on the intended application and desired properties of the graphene. These fabrication techniques can be broadly categorized into two approaches: top-down and bottom-up. Top-down approaches include mechanical exfoliation, chemical exfoliation, and chemical synthesis, while epitaxial growth and chemical vapour deposition (CVD) are bottom-up approaches [107]. **Table 5** summarises the different synthesis techniques, including the advantages and disadvantages of each.

***Table 5**: Advantages and disadvantages of different methods for synthesizing graphene.*

Synthesis Technique	Description	Advantages	Disadvantages	Ref.
Mechanical exfoliation	'Scotch tape method', layers of graphene are peeled off from a graphite crystal using adhesive tape.	High quality and purity samples of monolayer graphene	Not scalable, time consuming and low yield	[107], [108]
Chemical exfoliation	Dispersion of graphite in a solvent followed by sonication to exfoliate the layers	Scalable, high yield, compatible with solution-based processing techniques, tuneable properties	Quality – functional groups can be introduced during the process and size and thickness of graphene flakes can be hard to control	[109], [110]
Chemical synthesis	Process involves oxidation of graphite using strong acids/oxidants, ultrasonication to separate layers and reduction of graphene oxide to reduced graphene oxide	Compatible with solution-based processing techniques, easily modifiable surface functional groups	Use of toxic chemicals during process, graphene contains some defects and oxygen-containing functional groups	[107], [111]
Epitaxial growth	High temperature growth of graphene on a silicon carbide (SiC) substrate	High quality, scalable	High cost, low yield	[112]
Chemical vapour deposition	Decomposition of hydrocarbons or other carbon-containing gases to form a graphene layer on a metal substrate	High quality large graphene sheets	Low yield, precise control over layers has not been achieved	[113], [114]

Exfoliation of graphene refers to the process of isolating individual layers of graphene from a bulk material or precursor (i.e. graphite). Mechanical exfoliation, or micromechanical cleavage, is a process that uses adhesive tape to remove graphene monolayers from a graphite crystal [115]. Although this method produces high quality graphene flakes, it is not scalable for commercial sensor applications. Chemical exfoliation and chemical synthesis utilize solvents and strong acids/oxidants, and subsequently, sonication of the solution to separate layers [116]. While both techniques are scalable and produce easily modifiable surfaces, the quality of graphene is low, as it contains defects and functional groups introduced during the manufacturing process [110]. Such defects and functional groups cause disorder in graphene electronic structure, resulting in reduced electrical conductivity [107].

Epitaxial growth is a method used to synthesize graphene by growing it directly on a crystal substrate (e.g. SiC) in a way that aligns the graphene lattice with the lattice of the underlying substrate. In homoepitaxial growth, the arrangement of atoms in the growing material (graphene) mimics the structure of the crystalline substrate, resulting in a well-ordered and high-quality graphene layer [112], [117]. Single- and multi-layer epitaxially grown graphene has been used in several gas sensors, and report high sensitivity, selectivity, and low limits of detection [118]–[121].

Chemical Vapor Deposition (CVD) is a widely used technique for synthesizing graphene. The process involves placing a substrate, typically copper foil (although nickel is sometimes used), into a tube furnace at high temperatures [122]. Carbon-containing precursor gases, primarily methane (CH_4) with occasional use of acetylene (C_2H_2) and ethylene (C_2H_4), are introduced into the chamber [123]. The precursor gases decompose at the elevated temperature, and the carbon species adsorb onto the substrate surface, where they start to nucleate and form graphene domains. After the desired graphene layer is formed, the sample is transferred from the growth substrate to a different substrate (e.g. silicon wafer) for further processing or device fabrication.

In addition to the low yield, the substrate and chemicals used during the transfer process can introduce contaminants to CVD graphene [113]. Furthermore, the absence of standardized quality control for graphene production results in variability among products from different manufacturers [124]. Despite these challenges, it is still possible to fabricate large, high-quality graphene sheets. This makes CVD graphene a

dependable resource for manufacturing devices on a large scale. (CVD graphene has been utilized in this work.)

2.5. Graphene Surface Modification

Graphene functionalization, or the chemical modification of the surface is essential to obtaining highly selective and sensitive devices. Selectivity, or the ability for a sensor to discriminate between multiple interfering analytes, producing a higher response for a specific target analyte, is a vital characteristic for an effective sensor. Graphene's electrical conductivity fluctuates when exposed ambient air absorbates and due to its electronic band structure, can lead to quite significant changes [95]. This issue can be overcome by modifying the graphene surface to target a specific analyte, therefore, immobilising the desired species [125]. Functionalization of graphene can be performed via two primary routes: covalent (covalent bond formation) and non-covalent (Van der Waals forces). Both functionalization techniques can lead to charge transfer and the subsequent p- or n-doping of graphene depending on whether the modification species is electron-donating or -withdrawing, and therefore, plays a key role in the resulting sensor performance [125].

2.5.1. Covalent Functionalization

Covalent functionalization of graphene alters the nature of the bonding, shifting hybridisation from sp^2 to sp^3. Consequentially, this modifies the electrical transport properties of graphene due to the decrease of free electrons available. Although covalent bonding results in a disruption of the sp^2 bonding of the carbon atoms, converting them to sp^3 configuration, this can be advantageous as the electronic properties can be controlled [126]. Furthermore, covalent functionalization methods ensure that biomolecules, such as antibodies, are oriented in such a way that the receptor site is unhindered, allowing for effective binding. Some commonly used covalent functionalization techniques on graphitic surfaces include: oxidation and reduction, radical reactions/ diazo-coupling, and single-atom introductions [127], [128].

2.5.1.1. Oxidation and Reduction of Graphene

Graphene oxide (GO) and reduced graphene oxide (rGO) are valuable derivatives of graphene, widely used in various applications. While the surface modification of graphene into GO and rGO alters its electronic properties, these materials have gained significant attention due to their straightforward preparation, the introduction of oxygen-containing functional groups, and their versatility. These functional groups can be utilized directly or further modified by attaching additional groups, allowing for precise control over the surface's hydrophilicity and enabling their use in a range of applications such as energy storage [129], gas sensors [130], biomedical [131].

In several studies, human chorionic gonadotropin (hCG), a biomarker for certain cancers, was detected using immunosensors based on oxidized carbon nanotubes (CNTs) [132] and graphene [133], [134]. After oxidation, the surfaces of these materials were modified through silanization with 3-triethoxysilylpropylamine (APTES) [132], [133] or by electrodeposition of chitosan gold nanoparticles [134]. These modifications react with the hydroxyl groups on the surfaces, creating amine-terminated ($-NH_2$) groups. These amine groups then serve as binding sites for hCG antibodies, enabling the detection of the biomarker.

2.5.1.2. Radical Reactions

Radical reactions, such as diazo coupling, are highly effective for achieving extensive functionalization with the added advantage of versatility across various conditions. During these reactions, diazonium salts are reduced to form aryl radicals that attack the sp^2-hybridized carbon framework of graphene, creating new chemical bonds. However, the inherent unpredictability of radical reactions can complicate the control over the composition of the attached functional groups. As noted in research by Park and Yan [135], the radicals often engage in side reactions with each other and/or the solvent, making it challenging to accurately determine grafting density and composition.

Sinitskii et al. [136] demonstrated that grafting diazonium salts onto graphene nanoribbons alters both chemical and electrical properties due to changes in hybridization. Consistent with these findings, a decrease in current across a graphene channel was observed when nitrophenol or aniline compounds were bound to

diazonium-grafted surfaces. In a related study, diazonium compounds were covalently attached to the graphene surface to introduce nitrobenzene or aniline moieties, facilitating the immobilization of antibodies for detecting cancer risk biomarkers [85], [137], [138].

2.5.1.3. Single-atom Introductions

Single-atom introduction is an effective method for tuning the electrical properties of graphene. This involves incorporating individual atoms—such as hydrogen, chlorine, fluorine, or oxygen—into the graphene lattice. Techniques for this process include exposing graphene to gases containing the desired atoms or employing plasma treatment to achieve precise doping. This covalent functionalization technique is appealing due to its high degree of functionalization and the largely reversible nature of the processes. Studies [139]–[141] have demonstrated that by adjusting experimental parameters, one can control the doping density and increase the band gap of graphene with single-atom additions. However, the single-atom doping approach has drawbacks, including the potentially harsh conditions that may damage sensitive biomolecules and the need for specialized equipment and expertise for successful functionalization [128].

Previous research has shown that doping graphene with hydrogen, chlorine, or fluorine can introduce defects that disrupt its structure, potentially transforming it into an insulator. In contrast, Wu et al. [140] found that carefully controlling chlorine plasma treatment can enhance graphene's conductivity. Their study compared the kinetics of hydrogen and fluorine plasma doping—which introduced defects and disorder within seconds—with chlorine doping, where defects and disorder developed more slowly, over minutes. This investigation concluded that the duration of exposure significantly influences whether graphene undergoes destructive or non-destructive changes.

2.5.2. Non-covalent Functionalization

Non-covalent functionalization methods are advantageous because they introduce functional groups to the graphene surface while preserving the underlying electronic properties of the graphene lattice. These methods utilize π-π interactions, electrostatic

interactions, or Van der Waals forces, which maintain the sp^2 hybridization of carbon atoms and the material's electrical mobility [142]–[144]. This preservation of the graphene crystal structure and its inherent sp^2 hybridization ensures that its exceptional electronic properties remain largely unaffected.

2.5.2.1. Metal Nanoparticles

The incorporation of metal nanoparticles onto graphene surfaces is an effective method for functionalizing graphene without altering its hybridization. This largely reversible process has gathered significant interest from researchers due to its ability to achieve high levels of functionalization and its potential to create semi-metallic, semiconductor, or insulating materials [128]. This technique can enhance graphene's catalytic, sensing, and electronic properties. Additionally, it offers versatility, as a wide range of metals can be employed to tailor the functionalization for various applications.

In one instance, gold nanoparticles were employed to decorate the surface of graphene, creating a binding site for sulphur-terminated bioreceptor, as well as increasing the sensitivity due to the creation of further binding sites [84]. In another example, a graphene-gold hybrid sensor to detect hepatitis B surface antigen was fabricated [145]. In addition to oligomers adsorbed to planar graphene, single-stranded DNA (ssDNA) bonded to gold nanoparticles via a thiol bond and were anchored to the graphene surface by way of π-π interactions. The hybrid sensor benefited from an increased bioreceptor surface area and a variety of unique angles available to facilitate antigen attachment.

2.5.2.2. Conductive Polymers

Conducting polymers have alternating single and double carbon-carbon bonds along their polymer chains, creating aromatic, conjugated systems. These systems are particularly valuable because their reversible chemical, electrochemical, and physical properties can be precisely controlled through a doping and de-doping process [146]. Additionally, applying a layer of conductive polymer is an effective way to preserve

the sp^2 hybridization of graphene, protecting its electronic properties while creating a hybrid material that combines the advantages of both components.

It's also important to note that the additional of a π-stacked polymer can cause doping of the graphene layer. For instance, Cheng et al. [147] created a p-n junction by noncovalently functionalizing graphene with two π-stacking polymers, one electron-donating and the other electron-withdrawing: 1,5-diaminonaphthalene and 1-nitropyrene, respectively. This approach demonstrates how the interaction between graphene and conductive polymers can be used to engineer electronic properties.

Conducting polymers have been utilized in various biosensor applications, demonstrating their versatility beyond enhancing graphene's properties. For instance, one report [148], details the development of an immunosensor capable of detecting picogram levels of human chorionic gonadotropin (hCG) was fabricated using electro-polymerization of aniline creating a polyaniline film on graphene followed by attachment of hCG antibody. Another example used in biosensor development is 1,5 diaminonaphthalene (DAN) which can be deposited using electro-polymerization and utilised in its polymeric form (pDAN) to create thin film conducting surfaces. Modifying the parameters during electro-polymerization enables control over the thickness of the DAN layers, and thus the amine groups present, indicating the level of functionalization achieved [149]. These graphene-pDAN nanocomposites have been used to detect Alzheimer's beta amyloid peptides Ab(1–42) [150], lactose [151], lead [152] and enhance enzymatic electrochemical sensing [149].

2.5.2.3. Drop-cast Method

Aromatic compounds, with their π-conjugated systems that can overlap with graphene's π-orbitals, are ideal candidates for non-covalent functionalization methods [153]. The strong π-π stacking interactions between graphene and these aromatic molecules result in stable surface modifications that are relatively resistant to rinsing or processing in solution [154]. These compounds are especially well-suited for the drop-cast functionalization technique.

A quick and easy drop-cast method of introducing DAN to graphene devices was demonstrated by Walters et al. [155] and was shown to remain immobilised on the

graphene surface even after multiple solvent washes. As DAN orients itself flat on graphene, π-π interactions between the naphthalene entity and aromatic structure of graphene secure the molecule in place, achieving amine functionalization [156]. The availability of amine groups means that further crosslinking chemistries like EDC-NHS (EDC(N-(3-Dimethylaminopropyl)-N'-ethylcarbodiimide hydrochloride)-NHS(N-Hydroxysuccinimide)) can be employed to attach biomolecules via peptide bonds [157]. This method was also employed by Lee et al. [158] to immobilise a human olfactory receptor, hOR2AG1, on a single-walled carbon nanotube sensor (swCNT) for the detection of a known odorant, amyl butyrate. Following the drop-casting of DAN, a condensing agent, glutaraldehyde was used to activate the swCNTs to immobilise the olfactory receptor in the correct orientation.

2.5.2.4. Metal Phthalocyanines

Phthalocyanines, or metal phthalocyanines (MPcs), are p-type metal-organic semiconductors that consist of an 18π-electron conjugated structure surrounded by sixteen hydrogen atoms and can have a metal-free centre (H_2Pc) or contain a metal atom [26], [159], [160]. The hydrogen atoms can be readily substituted for other organic groups, and the hole in the centre of the ring can accommodate a variety of metals thus creating different types of metal phthalocyanines [26] (**Figure 2.6**).

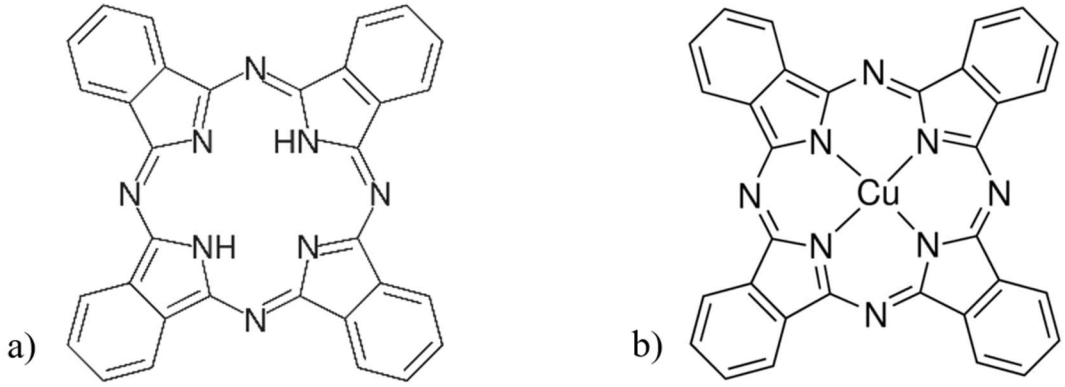


***Figure 2.6**: **(a)** metal-free phthalocyanine and **(b)** copper phthalocyanine (CuPc)*

Although originally used as dyes [161] due to their outstanding colour, phthalocyanines have been investigated for other applications such as catalysis [162], batteries [163], solar cells [164] and gas sensing [26], [165], [166]. Phthalocyanines

are good conductors of electricity, stable at high temperatures (400 – 500°C) and although insoluble in most solvents, are easily sublimed and deposited into thin films making them attractive candidates for gas sensing applications [167]. The aromatic nature of the molecule means that non-covalent functionalization of graphene is possible through π-π stacking. The facile substitution of groups on the ring and metal centre means that sensitivity and selectivity of gas sensor performance can be fine-tuned. The electrical conductivity of phthalocyanines changes when exposed to oxidizing, electron-withdrawing, gases (e.g. NO_2, SO_2, O_2, CO) [168] or reducing, electron-donating, gases (e.g. NH_3, H_2) [169]. Conductivity gains are observed with exposure to oxidizing gases as they generate holes, contrastingly, current losses occur with reducing gases as they donate electrons, trapping holes [166].

2.5.2.4.1. Interaction of Gases with Phthalocyanine Molecules

The interaction mechanism between gases and phthalocyanine (Pc) molecules has been a subject of significant debate. The specific site of interaction between an analyte and MPc depends on various factors, including the metal centre, ring substituents (if present), crystal form, and defects in the material [170]. The interactions between gases and copper phthalocyanine (CuPc) have been extensively studied. Some research suggests that electronegative compounds (electron acceptors) adsorb onto the phthalocyanine macrocycle, interacting with the large electron cloud at the molecule's periphery [170]–[172]. On the other hand, electropositive compounds (electron donors) are believed to form coordination complexes with the positively charged metal ion at the centre of the molecule [170]. Contrarily, studies by Lozzi et al. [173] and Park et al. [174] propose that nitrogen dioxide (NO_2) specifically interacts with the metal centre rather than the macrocycle.

To clarify the interaction mechanism, Chia et al. [175] conducted an extensive investigation using in-situ X-ray absorption spectroscopy (XAS) to study the interactions of copper phthalocyanine (CuPc) with the oxidizing gas NO_2 and the reducing gas ammonia (NH_3). Their findings revealed that both gases interact primarily with the Pc macrocycle rather than the metal centre. They explained that the hybridization of orbitals between the copper ion and the Pc macrocycle leads to the highest occupied molecular orbital (HOMO) and lowest unoccupied molecular orbital

(LUMO) of CuPc being dominated by the Pc character, largely due to the nearly filled d-orbital of copper. Through XAS [175], they confirmed this hypothesis and observed that NO_2 interacts with the pyrrole moiety of the macrocycle, evidenced by a compression of the Cu-N bond (**Figure 2.7**). In contrast, NH_3 was found to interact with either the benzo moiety or the bridging atom of the Pc macrocycle, as there was no evidence to suggest interaction with the metal centre.

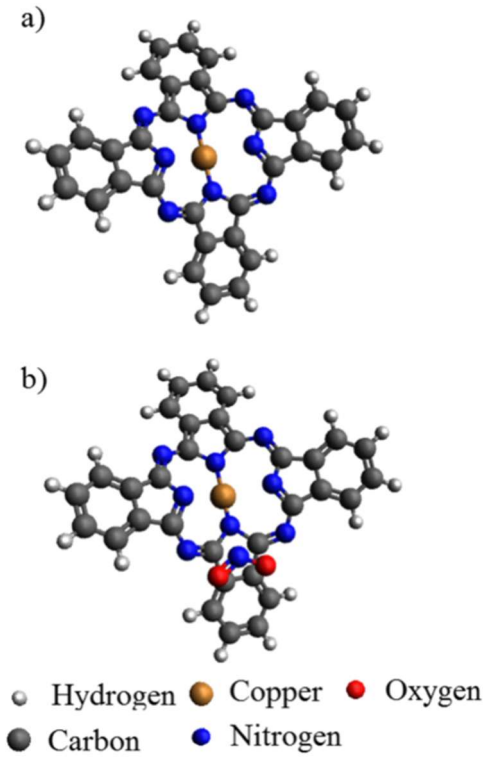


***Figure 2.7**: Illustration of **(a)** CuPc molecule and **(b)** proposed interaction site between NO_2 and CuPc molecule. Reproduced from reference* [175].

2.5.2.4.2. Tuning the Gas Sensitivity

Substituting different functional groups on the phthalocyanine ring and varying the metal centre enables the design of highly selective and sensitive metal phthalocyanine sensors. Numerous studies [26], [176] have shown that altering the molecular structure of phthalocyanines significantly influences their selectivity and sensitivity toward various gases.

For example, Bohrer et al. [166] compared the gas sensitivities of cobalt (Co), nickel (Ni), copper (Cu), zinc (Zn), and metal-free (H_2) phthalocyanines. They found that sensitivity toward gaseous electron donors correlated exponentially with binding

enthalpy. Additionally, the sensitivities of metal-containing phthalocyanines correlated with Lewis base enthalpies, while H_2Pc sensitivity correlated best with hydrogen bond base enthalpies.

The impact of functional substituents on the phthalocyanine ring was highlighted by Guo et al. [26], who reported a fully recoverable cobalt phthalocyanine-reduced graphene oxide (CoPc-rGO) sensor capable of detecting ammonia (NH_3) at 100 ppb with 60-day stability. In their study, different phenoxyl substituents on the CoPc macrocycle were investigated, and they identified the tetra-β-carboxylphenoxyl derivative as the phthalocyanine with superior gas sensing performance. The electron-withdrawing carboxyl groups on the ring provided multiple sites for NH_3 adsorption. Notably, their adsorption energy comparison (-23.1 kcal mol^{-1}, more negative than the others) emphasized the importance of the carboxyl group in enhancing gas sensitivity [26].

Similarly, three reduced graphene oxide-cobalt phthalocyanine ammonia gas sensors were fabricated, including two with different amino substituents: tetra-α-(p-aminobenzyloxy)phthalocyanine cobalt (ABO-CoPc-rGO), tetra-α-aminophthalocyanine cobalt (A-CoPc-rGO), and one substituent-free cobalt phthalocyanine (F-CoPc-rGO) [176]. The study demonstrated that phthalocyanine derivatives with amino substituents exhibited increased sensitivity toward NH_3.

2.5.2.4.3. Metal Phthalocyanine Gas Sensors

Due to their versatility, compatibility with carbon nanomaterials, and exceptional gas sensitivities, phthalocyanines have been employed in various gas sensing platforms. A few examples reported in published literature is summarized below in **Table 6**.

***Table 6**: Metal phthalocyanine-carbon nanomaterial hybrid sensors identified in the literature.*

Carbon Nanomaterial	Phthalocyanine	Operational Temperature (°C)	Target Gas	Sensitivity (ppb)	Ref.
Reduced graphene oxide (rGO)	tetra-a-(p-aminobenzyloxy) and tetra-a-aminophthalocyanine **cobalt** phthalocyanine derivatves	RT	NH_3	400	[168]
rGO	1-[N-(2-ethoxyethyl)-4-pentynamide]-8(11),15(18),22(25)-tris-{2-[2-(2-ethoxyethoxy) ethoxy]-1-[2-((2-ethoxy ethoxy)-ethoxy)methyl]ethyloxy}**zinc** (II) phthalocyanine	RT	NH_3	10,000 *(10 ppm)*	[177]
rGO	tetra-b-carboxylphenoxyl **cobalt** phthalocyanine	RT	NH_3	100	[26]
graphene quantum dots (GQDs)	hexafluoroisopropanol (HFIP) and hexafluorbisphenol A (6FBPA) **cobalt** phthalocyanine derivatives	RT	Dimethyl methyl phosphonate (DMMP)	100	[178]
Carbon nanotubes (CNTs)	**copper** phthalocyanine	40	NO_x	500	[179]
GQDs	2,9,16,23-tetracarboxylic **cobalt** phthalocyanine	100 – 700	NO_2	500	[180]
rGO	hexadecafluorinated **copper** phthalocyanine	RT	Cl_2	500	[181]
CNTs	**lead** 2,9,16,23-tetra-iso-pentyloxyphthalocyanine	RT	NH_3	150	[182]
rGO	4-trifluoromethylphenoxy **cobalt** phthalocyanine	RT	H_2S	1000	[183]

The gas sensitivity and modifiability of metal phthalocyanines underscore their importance in this thesis, where they are investigated in depth to assess their potential for enhancing the gas sensing performance of graphene-based devices.

2.6. Graphene-based Sensors

Graphene holds promise as an extremely sensitive gas sensor, with some suggesting its capability to detect individual gas molecules [184], [185]. The sensitivity is attributed to several factors: (1) the two-dimensional planar structure of graphene maximises the surface area and enables all carbon atoms to be exposed to the environment, (2) π-bonding structure providing high electrical conductivity and high charge carrier mobility and (3) minimal crystal defects allowing for a low level of noise [184]. Graphene has been proven to exhibit sensitivity to various gases, including those present in the surrounding environment. The presence of adsorbed molecules has the capacity to modify graphene's carrier mobility or electron mobility, leading to quantifiable changes.

Due to its exceptional physiochemical and biological characteristics, graphene has attracted attention for its potential applications in sensor technology [186]. Mass-producing high-quality graphene and manufacturing sensors through conventional photolithography methods offer a cost-effective and high-yield enhancement to sensing applications. Integrating graphene with sensors brings numerous benefits, such as miniaturization, robustness, rapid results, point-of-care diagnostics, high sensitivity, accessibility to users and ease of functionalization [187]. Graphene has been incorporated in various types of sensors including biosensors, electrochemical sensors, and resistive/chemiresistive sensors.

While graphene has been incorporated into various sensing platforms, there is still considerable potential for improvement. Key challenges include the production of high-quality graphene [7], [8], lengthy recovery times or incomplete sensor recovery [9], and problems associated with its extreme sensitivity and poor selectivity, which can lead to noise and measurement variability.

2.6.1. Biosensors

A biosensor is a device that integrates a biological component with a physicochemical detector to detect, monitor, or measure a specific biological or biochemical substance. Typically, a biosensor contains a bioreceptor, such as a cell, enzyme, aptamer, DNA, or nanoparticles that interact with the target analyte and produces a signal (**Figure**

2.8). Interaction of the target analyte with the bioreceptor usually generates a sensitive and selective response, allowing the analyte to be detected and quantified [188]. The transducer (e.g. photodiode, thermistor, pH electrode, etc.) converts the biological recognition event into a measurable signal [189]. Signal conditioning is performed by the electronics and translates the signal into a readable output, such as an electrical signal, and is commonly displayed on a computer screen.

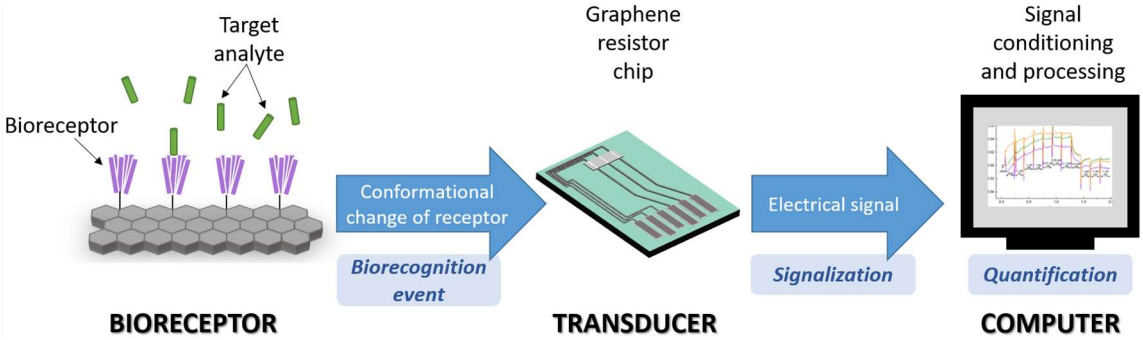


***Figure 2.8**: Schematic representation of signal transduction in a biosensor. Reproduced from reference* [190].

Biosensors are widely used in various fields, including medical diagnostics, drug discovery, security, environmental monitoring, food safety, and biotechnology [44], [188]. The advantages of biosensors include their specificity, sensitivity, simple preparation, and potential for real-time monitoring. Graphene biosensors have applications in glucose monitoring for diabetes [191], detection of pathogens such as E. coli [192], cancer biomarkers [138], [193], and COVID-19 [194], pollution [195] and environmental monitoring [196]. Additionally, graphene's inherent biocompatibility suggests it could serve as an excellent platform for gas detection. For instance, the biomolecules such as DNA [197] or haemoglobin [198] could be immobilized on graphene surfaces to detect gases like nitrogen dioxide and carbon monoxide, respectively. The development of biosensors continues to be an active area of research, aiming to improve their performance, expand their applications, and make them more accessible for various uses.

2.6.2. Electrochemical Sensors

An electrochemical sensor is a device that measures the concentration of a specific chemical or substance by detecting the electrical signals generated by a redox reaction. These sensors convert a chemical reaction, typically involving the transfer of electrons, into a measurable electrical signal [49]. Electrochemical sensors are widely used in various fields, including environmental monitoring, medical diagnostics, food safety, and industrial process control [199].

Since its discovery, graphene has been extensively employed in various electrochemical devices, including those for detecting DNA, proteins, and in immunosensors. Electrochemical graphene-based sensors have also been reported for the detection of acetaminophen [200], [201], paracetamol [202] and dopamine [203]. In one study, Du, M. et al. [204] presented an electrochemical DNA sensor fabricated using gold nanoparticles and reduced graphene oxide (AuNP-rGO), which successfully detected synthetic sequence-specific DNA and distinguished between single- and double-base mismatched DNA. Additionally, another study [193] developed an electrochemical immunoassay system capable of detecting a gastric cancer biomarker using a platinum/gold-diaminonaphthalene graphene aptasensor nanocomposite.

2.6.3. Electrical Sensors

A chemiresistive sensor is a type of chemical sensor that detects the presence of specific gases or chemical compounds by measuring changes in electrical resistance [205]. These sensors are commonly used in gas detection, environmental monitoring, and various industrial applications due to their simplicity, sensitivity, and ability to be miniaturized.

Resistive sensors are often considered the simplest type of sensor, comprising two electrodes—commonly referred to as the source and drain—with the sensor material, or "channel," positioned between them. When the target analyte interacts with the sensor material, it causes a measurable change in resistance. Their straightforward fabrication and simple electrical measurements make resistive sensors an appealing choice for gas sensor design. **Figure 2.9** provides a schematic of a graphene-based resistive sensor.

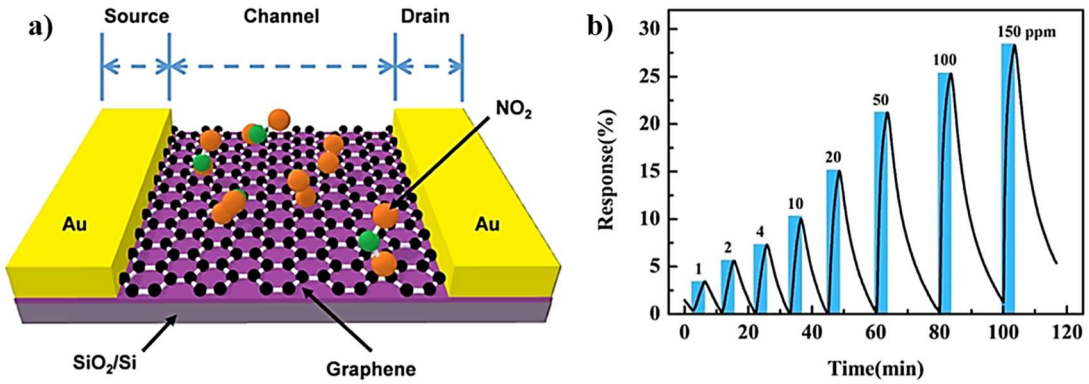


***Figure 2.9**: **(a)** Schematic illustration of a resistive CVD graphene sensor and **(b)** Response and recovery curves of the graphene-based sensor in different NO_2 concentration. Reproduced from reference* [206].

Another type of electrical sensor utilizing graphene is the field-effect transistor (FET). While FETs share a similar sensing mechanism with resistive sensors, they have a slightly different construction. FETs consist of source, drain, and gate electrodes, where the current between the source and drain is modulated by the gate electrode [207]. **Figure 2.10** provides a schematic of a graphene-based FET biosensor functionalized with antibodies. FET sensors allow for the measurement of the Dirac point in graphene, providing valuable insights into the level of doping and electronic properties of the material [208]. Compared to resistive sensors, FET sensors are often preferred because they provide more measurement parameters and have generally have higher sensitivity due to current amplification from the induced electric field, which in turn provides more information about gas sensing [207], [209]. **Table 7** provides a summary of various chemiresistive and FETs found in published literature.

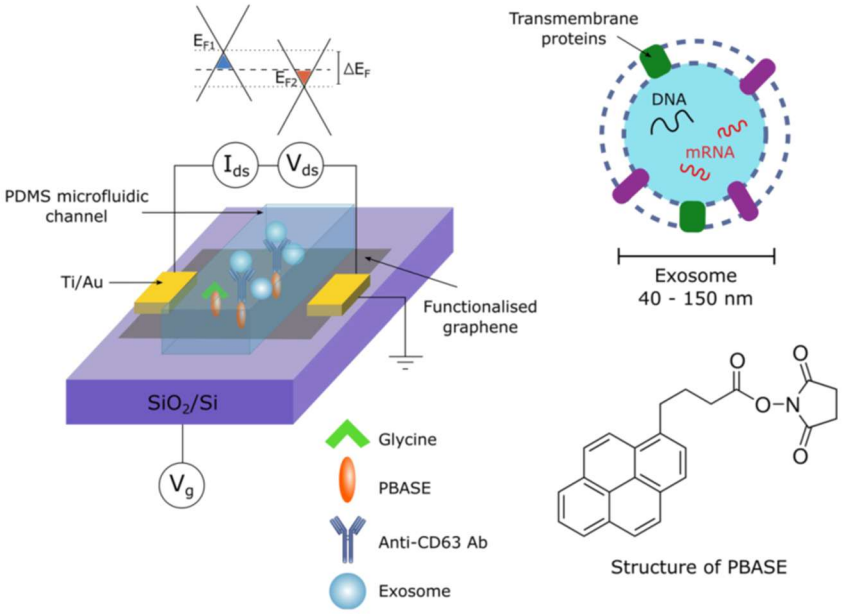


***Figure 2.10**: Schematic of a graphene field-effect transistor (GFET) biosensor. Reproduced from reference* [210].

***Table 7**: Graphene-based resistive and FET sensors identified from the literature.*

Sensor type	Graphene type	Functionalization	Target	Sensitivity	Ref.
Resistive	CVD monolayer	N/A	NO_2	1-100 ppm	[206]
Resistive	CVD monolayer	cobalt porphyrin ($Co(tpfpp)ClO_4$)	NH_3	20-160 ppm	[77]
Resistive	Reduced graphene oxide (rGO)	N/A	SO_2	5 ppm	[211]
Resistive	Reduced graphene oxide (rGO)	Palladium (Pd)	NO	2-420 ppb	[45]
FET	CVD monolayer	anti-CD63 antibodies	exosomes	0.1 µg/mL	[210]
FET	CVD monolayer	N/A	O_2 & H_2O	NR	[102]
FET	CVD monolayer	N/A	H_2O, methanol & ethanol	NR	[212]
FET	CVD monolayer	single-stranded DNA (ssDNA) aptamer	Hg^{2+}	40-100 pM	[213]
FET	CVD monolayer	N/A	SO_2	50 ppm	[214]

***NR** = Not Reported

2.7. Contamination of Graphene Surfaces

Contamination is an unavoidable consequence of graphene processing, often occurring during the fabrication and functionalization processes, and it inadvertently impacts graphene's electrical properties. Common contaminants include poly(methyl methacrylate) (PMMA) residues left after the graphene transfer process, trace metals from chemical vapour deposition (CVD) [215], [216], photoresists from the photolithography process [217] and water trapped at the graphene-substrate interface [218], [219]. These impurities have a significant impact on device performance, especially for graphene, where the surface dominates the overall properties. Impurities such as PMMA can cause carrier scattering, reducing the overall carrier mobility [220] and induce charges and structural deformations causing local doping [219]. Pirkle et al. [220] observed a twofold increase in carrier mobility—from 1400 to 2700 cm^2/Vs—after removing such residues.

Although complete elimination of these contaminants is challenging, extensive solvent cleaning [219] and vacuum thermal annealing [99], [219] have been employed to reduce contamination. However, there remains a critical need for innovative strategies to achieve pristine, high-quality graphene for advanced applications.

2.8. Variability Between Devices

Variability in graphene devices, driven by both intrinsic and extrinsic factors, presents a significant challenge to the commercialization of graphene-based technologies. Xu et al. [221] categorize this variability into two main categories: (1) environmental disturbances and (2) material imperfections. Environmental disturbances encompass factors such as interface traps, charged impurities, adsorbed molecules, resonant scatterers, surface roughness, and contact doping [221]. Material imperfections include edge disorders, structural defects away from the edge, ripples, curvatures, and other deviations inherent to graphene's structure [221], [222].

Additionally, several studies report various factors that can affect the electrical conductivity and, consequently, the performance of graphene-based devices. These factors include geometry [194], [195], graphene channel dimensions [109], [196], grain and grain boundaries [197]– [199], and underlying oxide thickness [109], all of

which impact graphene's carrier mobility. For instance, one study shows that mobility increases with channel length but then saturates at a constant value for channel lengths of several micrometres. As channel width increases, mobility initially rises due to the reduction of edge scattering, but then decreases significantly, influenced by oxide thickness [223]. Grain boundaries and the size of domains, which are sensitive to slight changes in growth parameters, also play a critical role in affecting graphene's conductance [224].

Grain boundaries [225], edge sites [226], and defects [227], [228] in graphene not only influence its electrical properties but also serve as active adsorption sites for gas molecules. While these features can enhance adsorption capacity under certain conditions, they can also affect selectivity, sensitivity, and other critical performance parameters of sensors. Therefore, a thorough understanding and precise control of these factors are essential for optimizing the performance of graphene-based sensors.

Despite advancements in graphene fabrication processes that have led to higher quality materials, significant device-to-device variations persist [229]. While in some cases, variability has been exploited to enhance sensing performance [221], [222], it remains a major obstacle to the scalability of graphene technologies. Addressing this issue may require the establishment of standardized fabrication processes to minimize variability and make graphene-based devices commercially viable.

2.9. Polymers of Intrinsic Microporosity

Polymers of intrinsic microporosity (PIMs) are long chain, rigid polymers used in various applications including gas separation, membrane separation, adsorption and catalysis [230]. This distinctive group of polymers possesses a structure characterised by intermolecular voids, called ‘micropores’, a direct result of their high rigidity and restricted rotational freedom. Micropores, as defined by IUPAC [231], are pores less than 2 nm in size. The rigid polymer backbone in PIMs primarily consists of rings, inhibiting the macromolecules from undergoing conformational rearrangements that could lead to the collapse of the micropore structure [232].

Gas separation is a compelling focus for this thesis, as the enhanced selectivity of these polymers could significantly improve the performance of gas sensors. PIMs have

demonstrated superior gas separation capabilities compared to other polymers. Notably, the Robeson plot, a widely used tool for evaluating membrane performance, currently features upper bounds defined by the performance of PIMs [233]. Extensive research has since focused on developing various PIMs to optimize both permeability and selectivity, which are typically seen as trade-offs, in order to improve the separation efficiency of common industrial gas pairs.

In this thesis, PIMs are utilized due to their exceptional gas separation properties, particularly in enhancing selectivity. The exploration of PIMs in this context aims to demonstrate their potential for improving sensor accuracy in detecting specific gases. Future research is increasingly focusing on the development of hybrid materials and the synthesis of PIMs using diverse monomer precursors [234] to further enhance their performance in gas separation and other applications, indicating a promising direction for advanced materials development.

Chapter 3 : Materials & Methods

3.1. Materials

The following materials were used in the fabrication, functionalization and testing of graphene devices in this work.

3.1.1. For Chapter 4

- Graphene:

CVD monolayer graphene on 90/300 nm thermal oxide SiO_2-381/525 µm Si wafers (<100> orientation, 1–10 Ω.cm resistivity and P-type/Bor) and monolayer graphene on 90 nm thermal oxide SiO_2/381 µm Si wafers (<100> orientation, 1–10 Ω.cm resistivity and P-type/Bor) was supplied by *Graphenea* (Spain).

- Photoresists, Developers and Removers:

Microposit LOR 3A Photoresist and Microposit S1805 G2 positive photoresist were supplied by *DOW Electronics Materials* (USA). TechniStrip NI555, 25% TMAH etchant, AZ nLof 2070 photoresist and TI prime were supplied by *MicroChemicals GmbH* (Germany). Microposit MF-CD-26 Developer and Microposit 1165 Remover were supplied by *A-Gas Electronic Materials* (UK).

- PVD Targets:

Chromium and palladium PVD targets were supplied by *Kurt J. Lesker Company Ltd.* (UK).

- MVD Precursors:

Trimethylaluminium (TMA) precursor was supplied by *Pegasus Chemicals* (UK).

- DI Water:

Type II DI water with the ASTM D1193 standard and a resistance of 18 MΩ.cm was produced using a Merck Millipore Elix 3 water purification system (*Merck*, Germany).

3.1.2. For Chapter 5

Process gases were supplied by *BOC Limited* (UK).

3.1.3. For Chapter 6

- Process Gases:

Process gases were supplied by *BOC Limited* (UK).

- Phthalocyanine Functionalization:

Copper phthalocyanine, cobalt (II) phthalocyanine, iron (II) phthalocyanine, phthalocyanine, zinc phthalocyanine were supplied by *Thermo Fisher Scientific* (USA).

- Copper (II) 2,9,16,23-Tetra-tert-butyl phthalocyanine Synthesis:

Dichloromethane, silica gel and magnesium sulphate were supplied by *Thermo Fisher Scientific* (USA). Dimethyl sulfoxide (DMSO) was supplied by *Regency Organics Ltd* (UK). Copper (II) acetate, 2-dimethylamino ethanol and 1,8-Diazabicyclo[5.4.0]undec-7-ene were supplied by *Sigma Aldrich Company Ltd* (UK). 4-tert-Butylphthalonitrile was supplied by *TCI Europe N.V.* (Belgium).

- DI Water:

Type II DI water with the ASTM D1193 standard and a resistance of 18 MΩ.cm was produced using a Merck Millipore Elix 3 water purification system (*Merck*, Germany).

3.1.4. For Chapter 7

- Process Gases:

Process gases were supplied by *BOC Limited* (UK).

- Polymer Functionalization:

PIM-1 and PIM-EA-TB were synthesized by Dr Mariolino Carta's research group (*Swansea University*, UK) [233]. Matrimid was supplied by *Huntsman Corporation* (UK). Chloroform was supplied by *Fisher Scientific UK Ltd* (UK).

3.1.5. For Chapter 8

- Process Gases:

Process gases were supplied by *BOC Limited* (UK).

- Electrochemical Functionalization:

Sulphuric acid, 95% was supplied by *Fisher Scientific UK Ltd* (UK). 1,5 diaminonaphthalene was supplied by *Sigma Aldrich Company Ltd* (UK).

- DI Water:

Type II DI water with the ASTM D1193 standard and a resistance of 18 MΩ.cm was produced using a Merck Millipore Elix 3 water purification system (*Merck*, Germany).

3.1.6. For Chapter 9

- Olfactory Receptor Functionalization:

1,5 diaminonaphthalene, glutaraldehyde and bovine serum albumin (BSA) were supplied by *Sigma Aldrich Company Ltd* (UK). Human olfactory receptor 2AG1 was supplied by *Abnova* (Taiwan). Ethanol and phosphate buffered saline (PBS) containing 0.01 M phosphate, 0.0027 M KCl, and 0.137 M NaCl, pH 7.4 were supplied by *Fisher Scientific UK Ltd* (UK).

- Odorants:

Pentyl valerate, amyl butyrate, propyl butyrate and dimethyl sulfoxide (DMSO) were supplied by *Sigma Aldrich Company Ltd* (UK). Butyl butyrate was supplied by *Fisher Scientific UK Ltd* (UK).

- DI Water:

Type II DI water with the ASTM D1193 standard and a resistance of 18 MΩ.cm was produced using a Merck Millipore Elix 3 water purification system (*Merck*, Germany).

3.2. Graphene Sensor Fabrication

The following equipment was used in the fabrication of graphene devices in this work.

Figure 3.1 illustrates the process flow for creating graphene devices.

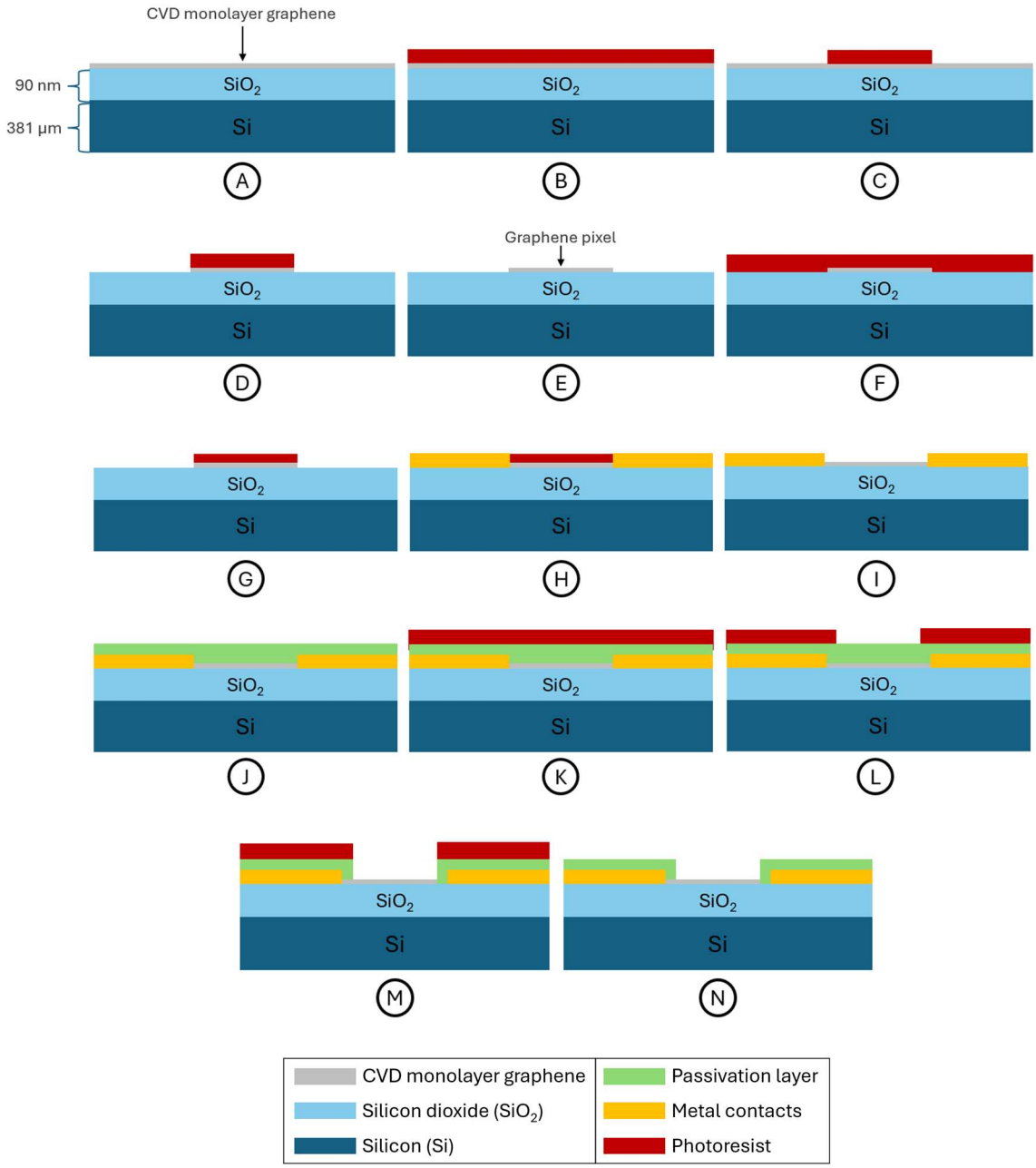


***Figure 3.1**: **(A)** Wafer is annealed to improve graphene adhesion. **(B)** Application of a photoresist etch mask. **(C)** The mask is exposed to UV light and developed, leaving photoresist to cover the graphene pixels. **(D)** Plasma etch removes the excess graphene. **(E)** Photoresist mask is removed. **(F)** Application of a photoresist mask for metal contacts/tracks. **(G)** The mask is exposed to UV light and developed, removing the resist in areas where metal deposition will occur. **(H)** Deposition of the 30 nm Cr/200 nm Pd stack. **(I)** Excess metal lift-off and photoresist removal. **(J)** Deposition of the 50 nm Al_2O_3 passivation layer. **(K)** Application of a photoresist mask. **(L)** The mask is exposed to UV light and developed, removing the resist in areas where the wet etch will occur. **(M)** Wet etch using TMAH is performed, exposing graphene pixels and metal contact pads* (*not shown). **(N)** Photoresist is removed – finished sensor.*

3.2.1. Rapid Thermal Annealing

Rapid thermal annealing (RTA) (Process A, **Figure 3.1**) was performed using a Jipelec Jetfirst 200 rapid annealing furnace (**Figure 3.2**) (*Qualiflow, France*) prior to device fabrication. Samples are placed in the chamber which was pumped down under vacuum to start the heating process. Annealing was performed at 550°C with a ramp rate of 10°C/s, while argon was introduced into the chamber at a flow rate of 50 sccm. The samples were annealed for 15 minutes, followed by a 3-minute ramp-down period. This process aimed to eliminate any trapped moisture at the graphene-SiO_2 interface, thereby enhancing adhesion. The *Annealsys* software was utilized to execute the specified annealing recipe.

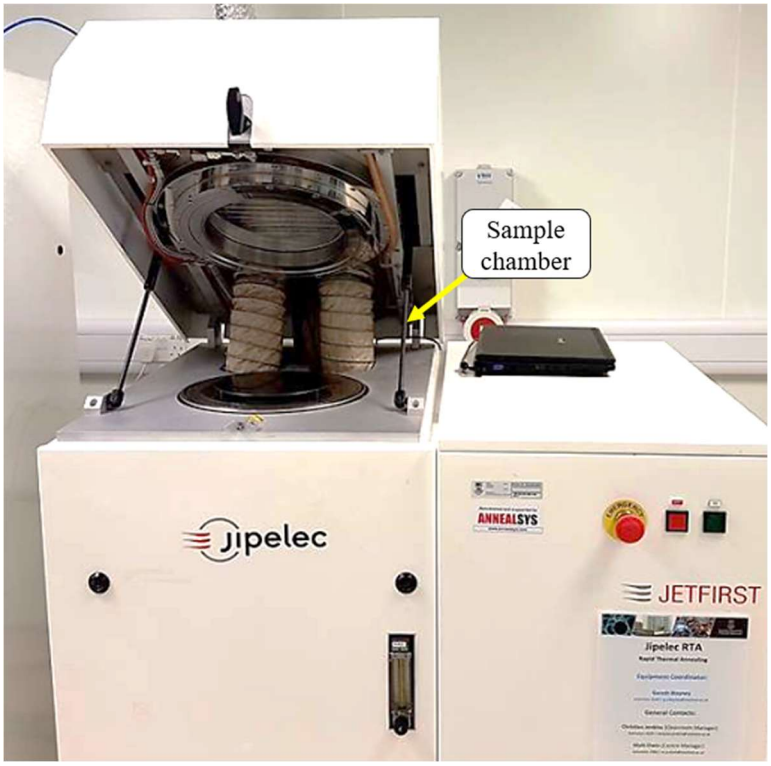


***Figure 3.2**: Jipelec Jetfirst 200 Rapid Thermal Annealing furnace.*

3.2.2. Spin Coater

Spin coating (Process B, F and K, **Figure 3.1**) was conducted using a Laurell Spin Coater 200 mm (*Laurell Technologies Corporation,* USA). Spin coating was used to deposit the photoresist on wafers to pattern the graphene channels and metal tracks. The wafers were positioned on the spin chuck, and the vacuum was activated.

Photoresist was then applied to the wafer, and the lid was closed. The desired spin coating recipe was selected and executed.

3.2.3. Plasma Etcher

A PE-75 Plasma Asher (*Plasma Etch, Inc.,* USA) (**Figure 3.3**) was used to remove excess graphene from wafers (Process D, **Figure 3.1**). The wafers were placed into the etch chamber and subjected to a 2-minute oxygen plasma etch, with a flow rate of 10 cc/min, a radiofrequency (RF) power of 90 W, and a vacuum level between 150 and 300 mTorr.

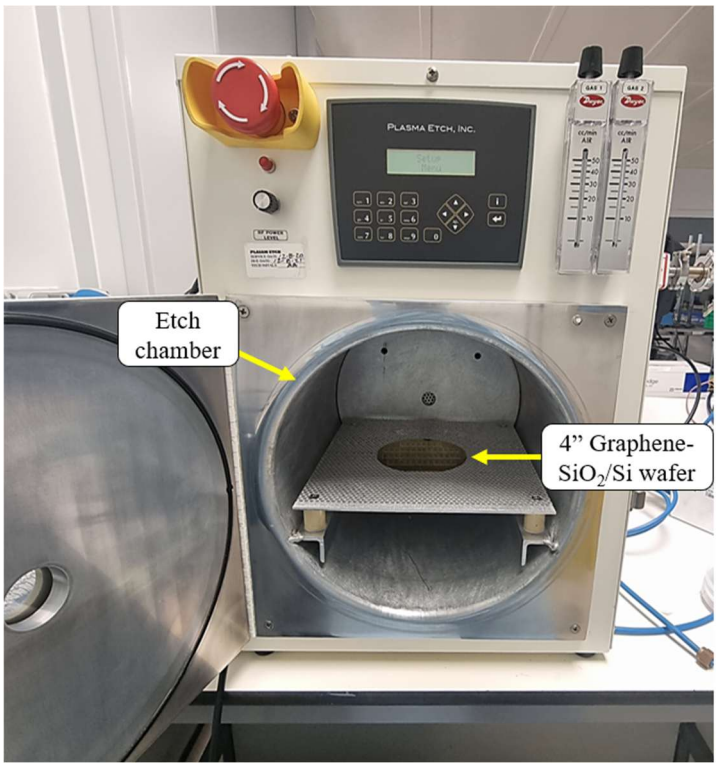


***Figure 3.3**: PE-75 Plasma Asher.*

3.2.4. Mask Aligner

Following the application of the photoresist, a SUSS MicroTec MA8 Gen 3 mask aligner (*SUSS MicroTech,* Germany) (**Figure 3.4**) was used to transfer the desired pattern onto the graphene-SiO_2/Si wafer (Process C, G and L, **Figure 3.1**). The wafers were placed on the sample stage, and the vacuum was activated to hold them in place. The mask was secured in a holder and positioned above the wafer. Micromanipulators

on the sample stage were used to precisely align the mask with the wafer. Once aligned, the substrate was selectively exposed to UV light. Depending on the type of photoresist used, the exposed areas either became more soluble (positive photoresist) and were washed away using a developer solution, or became insoluble (negative photoresist) while the surrounding unexposed areas were washed away during development [235].

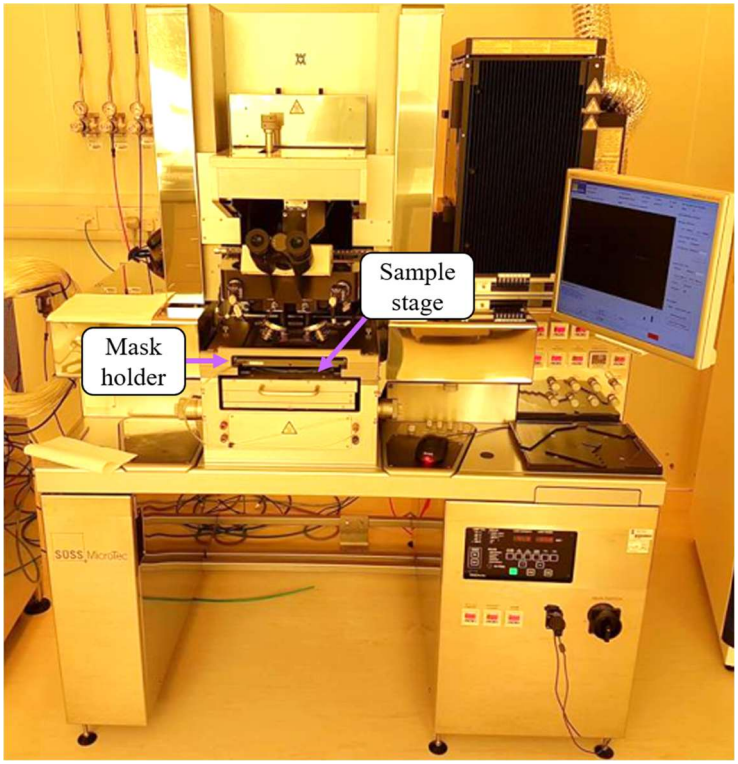


***Figure 3.4**: SUSS MicroTec MA8 Gen 3 mask aligner.*

3.2.5. Physical Vapour Deposition

To deposit the metal tracks and contacts (Process H, **Figure 3.1**) on the graphene-SiO_2/Si wafers, a PVD 75 Physical Vapor Deposition system (*Kurt J. Lesker, Sussex, UK*) (**Figure 3.5**) was used. Wafers were placed in a substrate holder and positioned at the top of the chamber in a rotating holder to ensure even metal coverage. During the deposition process, argon (Ar) gas was pumped into the chamber and ionized by an electric field. The ionized Ar ions were attracted to the negatively charged source gun containing the desired metal target. The bombardment of Ar ions on the target ejected metal particles, which were then deposited onto the substrate [236]. The chamber contained a quartz crystal microbalance (QCM) that resonated at a specified

frequency. As particles were deposited on the surface of the QCM, the frequency changed. This change was detected by the system and used to calculate the deposition rate of the metal. Once the desired thickness was reached, the deposition process was stopped. If needed, another target could be utilized from one of the other source guns to achieve the required metal contact structure.

The chamber was pumped down to 10^{-5} torr, and the chromium (30 nm)/palladium (200 nm) stack was deposited using magnetron sputtering. Deposition of the chromium layer was carried out with an argon flow rate of 30 sccm and a power of 80 W, while the palladium layer was deposited with an argon flow rate of 60 sccm and a power of 50 W. The approximate deposition rates were 1–3 Å/s for chromium and 2–5 Å/s for palladium.

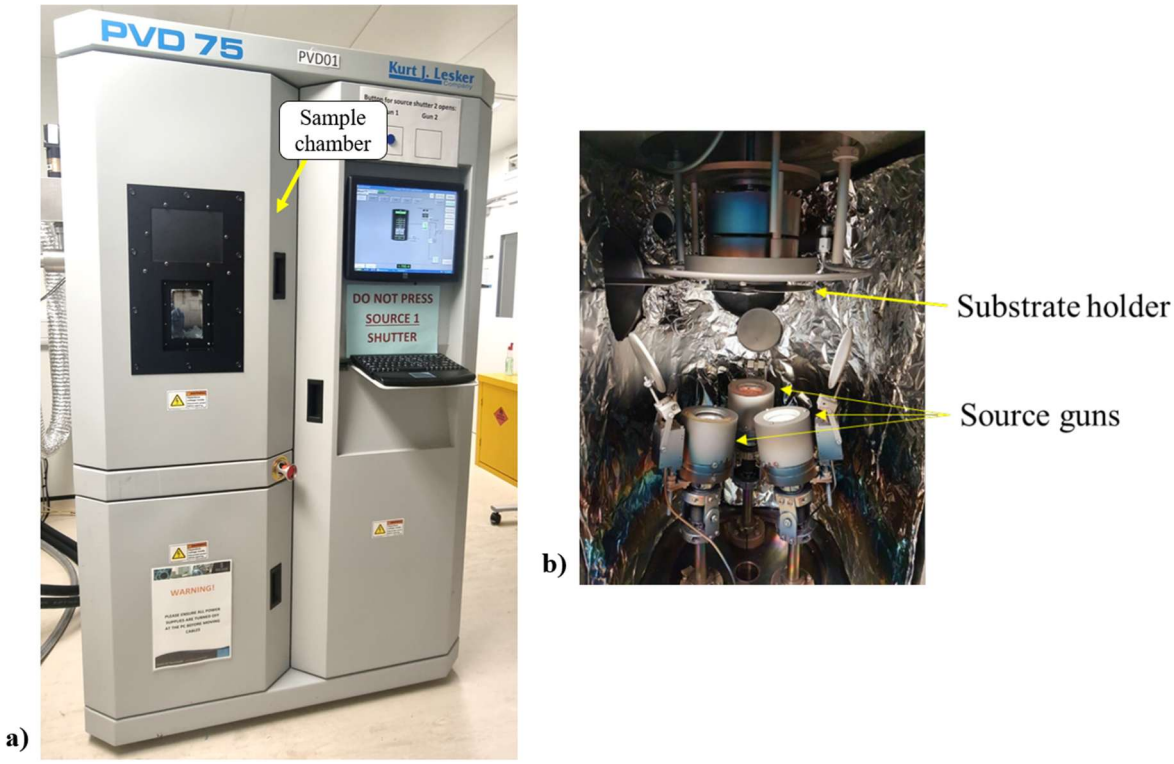


***Figure 3.5**: **(a)** PVD 75 physical vapour deposition system. **(b)** Inside the deposition chamber. Reproduced from reference* [237].

3.2.6. Molecular Vapour Deposition

To deposit the aluminium oxide (Al_2O_3) passivation layer on graphene-SiO_2/Si wafers (Process J, **Figure 3.1**), using a SPTS MVD300 system (*SPTS Technologies (KLA),*

Newport, UK). The deposition was performed by Daniel Gillard at 100°C using trimethylaluminium (TMA) and water vapour precursors.

3.2.7. Mask Design

Mask design was carried out using *KLayout* software, and photomasks were purchased from *JD Photodata* (UK). The 127 mm x 127 mm chrome-on-quartz glass masks featured a resolution of 2 µm, with the smallest designed feature being 50 µm.

3.3. Graphene Sensor Functionalization

As this thesis employed various functionalization methods, each method is detailed in its respective chapter. The different surface modification techniques used are listed in **Table 8**.

***Table 8**: Various functionalization techniques utilized in this thesis.*

Functionalization	Chapter
Metal Phthalocyanines (MPcs)	**6.4**
Polymers of Intrinsic Microporosity (PIMs)	**7.3**
1,5-diaminonapthalene	**8.2**
Oxidation	**8.3**
Human Olfactory Receptor 2AG1	**9.2**

3.3.1. Equipment

The following equipment was used for the functionalization processes listed in **Table 8**.

3.3.1.1. Weighing Scale

A *KERN ABS-N_ABJ-NM* (*Kern & Sohn, Germany*) analytical balance was used to weigh the functional molecules for preparing solutions for surface modification.

3.3.1.2. Spin Coater

Spin coating was conducted using an *L2001A3 Ossila spin coater* (*Ossila Ltd*, UK) (**Figure 3.6a**) with a custom-made chuck. Spin coating was used to deposit functional molecules (MPcs/PIMs) in Chapters 6 and 7 onto the graphene pixels of the '3x3 graphene pixel array' sensors. The wafers were placed on a custom-made chuck, and the prepared solution was applied to the graphene pixels. After closing the lid, the desired spin coating recipe was selected and executed.

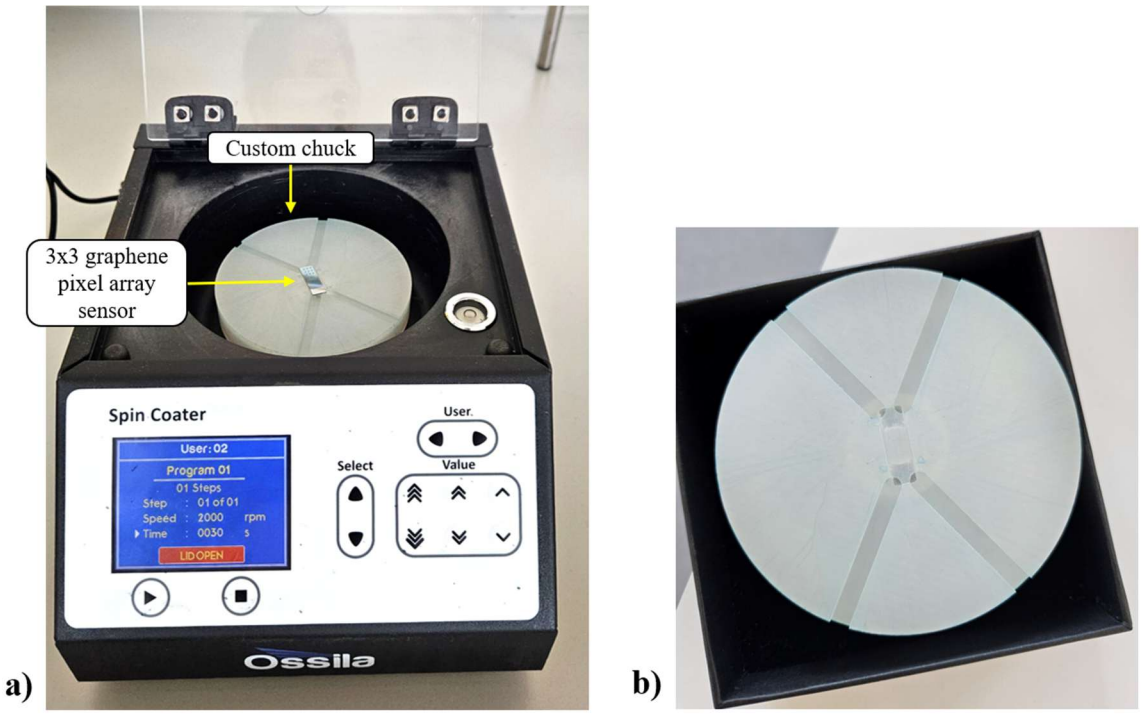


***Figure 3.6**: Images of **(a)** L2001A3 Ossila spin coater and **(b)** custom chuck designed to fit the 3x3 graphene pixel array sensors with dimensions of 18100 µm x 6200 µm x 500 µm (L x W x D).*

3.3.1.3. Potentiostat-Galvanostat

The electrochemical functionalization described in Chapter 8 was carried out using a *PGSTAT30 Autolab* (*Metrohm Ltd*, UK). *Nova 2.1.2* software was used to operate the Autolab and to create and execute recipes. Depending on the procedure, 2-3 electrodes were used, and the experimental parameters were entered into the software.

3.4. Characterization

The following characterization methods were used the fabrication and functionalization of graphene devices in this work.

3.4.1. Keyence Optical Microscope

Keyence VHX-950F and *VHX-7000* Digital Microscopes (*Keyence Corporation,* UK) were used to image graphene devices during and after the fabrication and functionalization processes. Magnifications ranging from x20 to x6000 were available and were selected based on specific requirements.

3.4.2. Scanning Electron Microscopy (SEM)

In this research, a *Hitachi S4800* Scanning Electron Microscopy (SEM) (*Hitachi High-Tech Europe GmbH*, Germany) (**Figure 3.7**) was used to image graphene devices with accelerating voltages of between 5 keV-10 keV after fabrication and functionalization. In contrast to light microscopes, SEM utilizes a focussed electron beam to image samples. The beam of electrons is produced by an electron gun and is focussed on the sample using a variety of electromagnets and lenses. Scanning coils deflect the beam in x and y directions, ensuring it scans the sample in a raster pattern. Once the high energy beam hits the sample, electrons and x-rays are emitted and detected. There are different types of electrons that can be ejected from the sample: secondary and backscatter electrons. Secondary electrons are loosely bound electrons with low energy that provide information about the surface topography with good resolution. Backscatter electrons are high energy and can provide both topographic and compositional information [238]. X-rays emitted from samples can be detected using energy-dispersive x-ray spectroscopy (EDS) and provide information about chemical composition.



Figure 3.7: Hitachi S4800 SEM.

3.4.3. Energy Dispersive Spectroscopy (EDS)

In this work, Energy Dispersive Spectroscopy (EDS) was performed using a detector on the *Zeiss Evo LS25* scanning electron microscope (*Zeiss*, Germany) belonging to the *Advanced Imaging of Materials* facility (AIM) at Swansea University, UK. EDS mapping measurements were used for the elemental analysis of graphene devices to investigate the presence of pinholes in the passivation layer. EDS requires the sample to be excited by an energy source, for example, an electron beam, and is therefore, used in conjunction with electron microscopy systems. The high energy beam of electrons ejects core-shell electrons from the sample and subsequently, a higher shell electron moves down to take its place. This transition releases energy in the form of x-rays, which are unique to the atom it came from. The position of the peaks in the characteristic spectrum is a 'fingerprint' for a particular element, and the intensity is related to the concentration [239].

3.4.4. Atomic Force Microscopy (AFM)

In this thesis, atomic force microscopy (AFM) was employed to examine the surface topography of graphene devices during the functionalization process. Additionally, conductive AFM measurements were performed to investigate the presence of pinholes in the passivation layer on graphene devices. AFM operates by scanning a

cantilever probe with a sharp tip across the sample surface under a constant force. A laser beam is directed onto the cantilever, and its deflection is detected by a photodetector, producing a topographical image of the surface.

To examine the surface topography, AFM measurements were performed using a *Bruker Dimension icon XR* scanning probe microscope (*Bruker Corporation,* USA) (**Figure 3.8a**) equipped with a 'SCANSYST-AIR' silicon nitride probe. This probe had a resonant frequency of 70 kHz and a tip radius of 2 nm. Scans were conducted in tapping mode at a line rate of 1.00 Hz, covering scan sizes ranging from 500 nm to 5 µm.

For conductive (Kelvin probe) measurements, a *JFK Nanowizard 3* AFM system (*Bruker Corporation,* USA) (**Figure 3.8b**) was utilized. It featured a gold SHR300 probe with a resonant frequency of 300 kHz, a spring constant of 40 N/m, and a tip radius of 1 nm. Scans were conducted in tapping mode at a line rate of 0.6 Hz, with acquisitions obtained for 10 x 10 µm scans at a resolution of 1024 x 1024 pixels.

Data analysis and presentation were carried out using *Gwyddion* software, which facilitated the determination of film roughness for graphene functionalization.

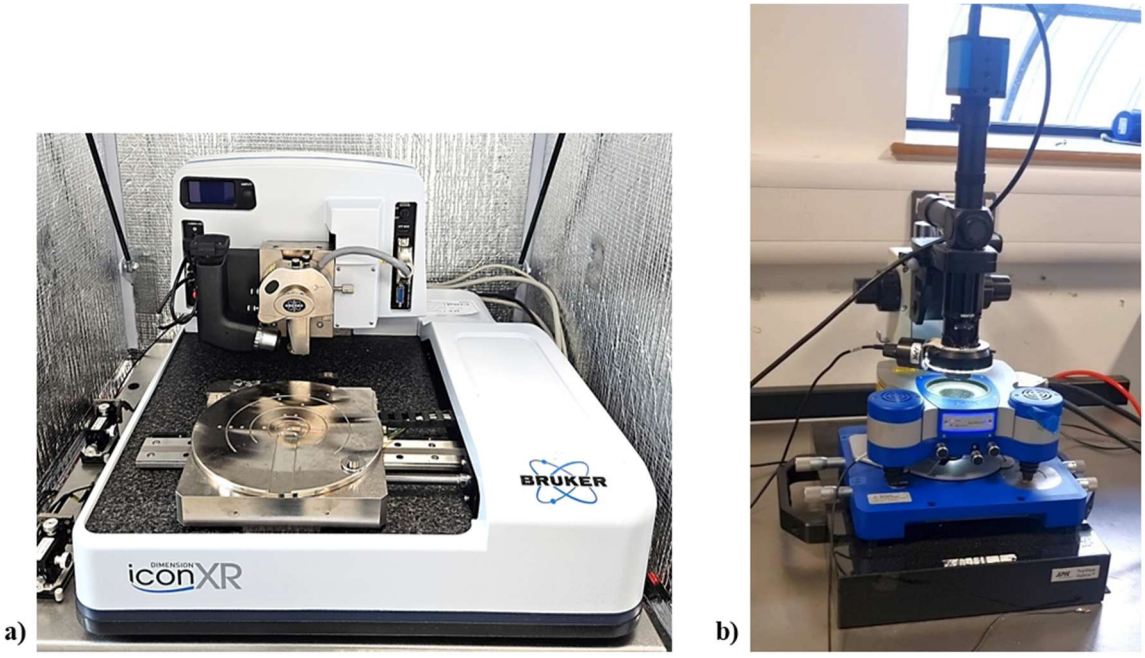


***Figure 3.8**: (a) JFK Nanowizard 3 atomic force microscope and **(b)** Bruker Dimension icon XR scanning probe microscope.*

3.4.5. Raman Spectroscopy

In this thesis, a *Renishaw inVia* Raman microscope was used to perform measurements on graphene before and after functionalization. A 532 nm laser was used with a power of 10% and a 50x or 100x objective lens. Extended scans were acquired from 1100 to 3000 cm^{-1} and static scans used for Raman mapping (60 µm x 60 µm) were taken at 1500 cm^{-1} and 2500 cm^{-1}. *WiRE 4.4* software was used to operate the Raman system and additionally, to create intensity, peak position, and ratio maps.

Raman spectroscopy is a powerful technique for analysing graphene and determining its properties. A Raman spectrometer uses monochromatic light, typically a green laser of wavelength 532 nm, to illuminate the sample. Light is scattered elastically, 'Rayleigh scattering' and inelastically, 'Raman scattering', and it is this inelastic scattering of light this is detected. Raman scattering occurs when molecular bonds, which are constantly vibrating within the sample, absorb light energy and vibrate further. As different bonds vibrate at different frequencies, the scattered light that returns has a different frequency and wavelength than it did previously [240]. Each vibrational frequency is unique to individual bonds, and therefore, the geometric structure and bonding within the sample can be determined. Comparing Raman spectra before and after surface modification often reveals a peak shift. This shift in wavenumber is described as either a 'red' or Stokes shift, or a 'blue' or anti-Stokes shift. A Stokes or red shift refers to a decrease in frequency (wavenumber), resulting in a positive wavenumber shift. This occurs when the scattered photon has less energy than the incident photon. Conversely, an anti-Stokes or blue shift indicates an increase in frequency (wavenumber), resulting in a negative wavenumber shift. This occurs when the scattered photon has more energy than the incident photon [241], [242].

The Raman spectrum of graphene consists of three important bands: G-band and 2D-band, the third band, the D-band can be present when defects in graphene exist. G-vibrations, or the in-plane stretching vibrations, vibrate laterally and D-vibrations, or the 'breathing mode' involve vibrations along the bonds (**Figure 3.9**) [243].

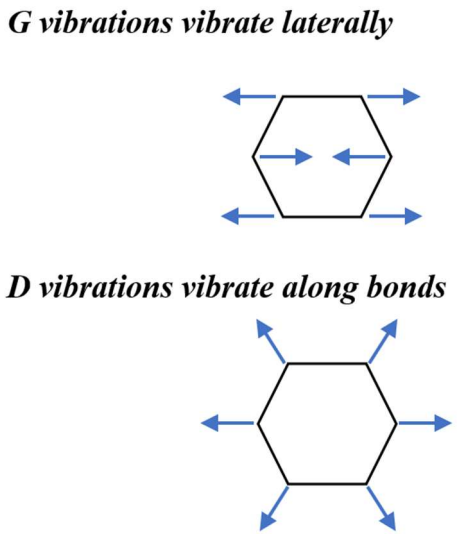


Figure 3.9: Schematic of G- and D-vibrations within sp^2 carbons.

The three bands can provide an extensive amount of information about graphene and is summarised in **Table 9** below [244]–[246].

Table 9: Characteristic bands of graphene and the properties expressed.

Band	Relative position (cm^{-1})	Properties	Figure
G	1580	• Position is affected by the number of layers present. • Greater number of layers, the lower the wavenumber. • Greater number of layers, the larger the peak intensity • Position is also sensitive to strain, temperature, and doping.	3.10 and 3.11
2D	2700	• Also referred to as the G' band • Indicative of the numbers of layers present • As the layers increase, the band changes shape and position.	3.12
D	1350	• Indicative of defects in the sample • The higher the intensity, the higher the level of disorder • Must be adjacent to a defect to be Raman active.	3.13

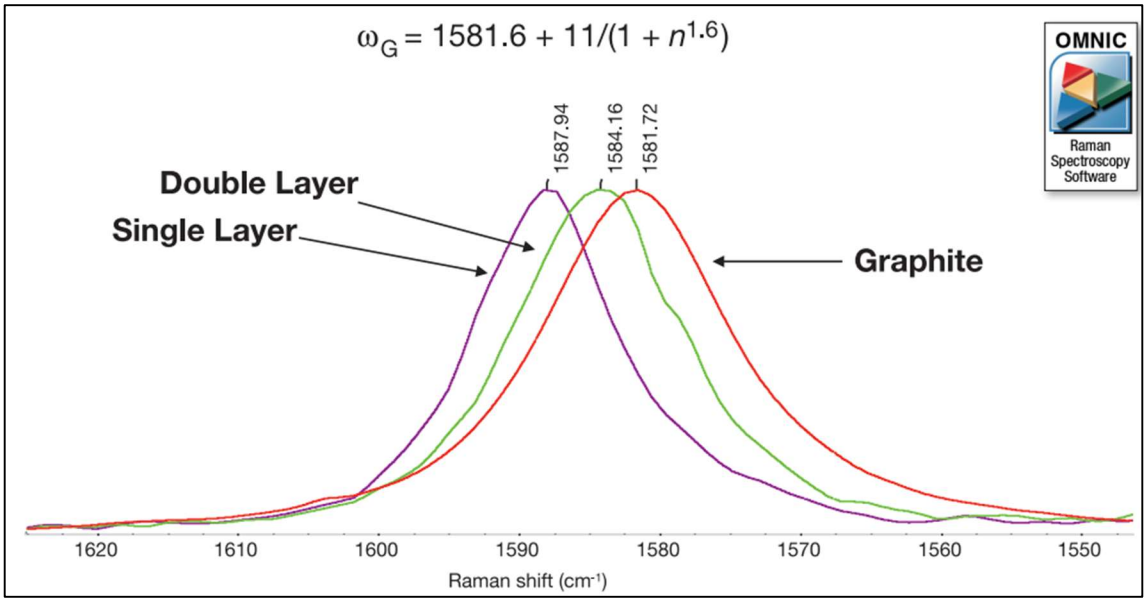


***Figure 3.10**: The G-band position as a function of layer thickness. As the number of layers increase the band shifts to lower wavenumber. Reproduced from reference* [246].

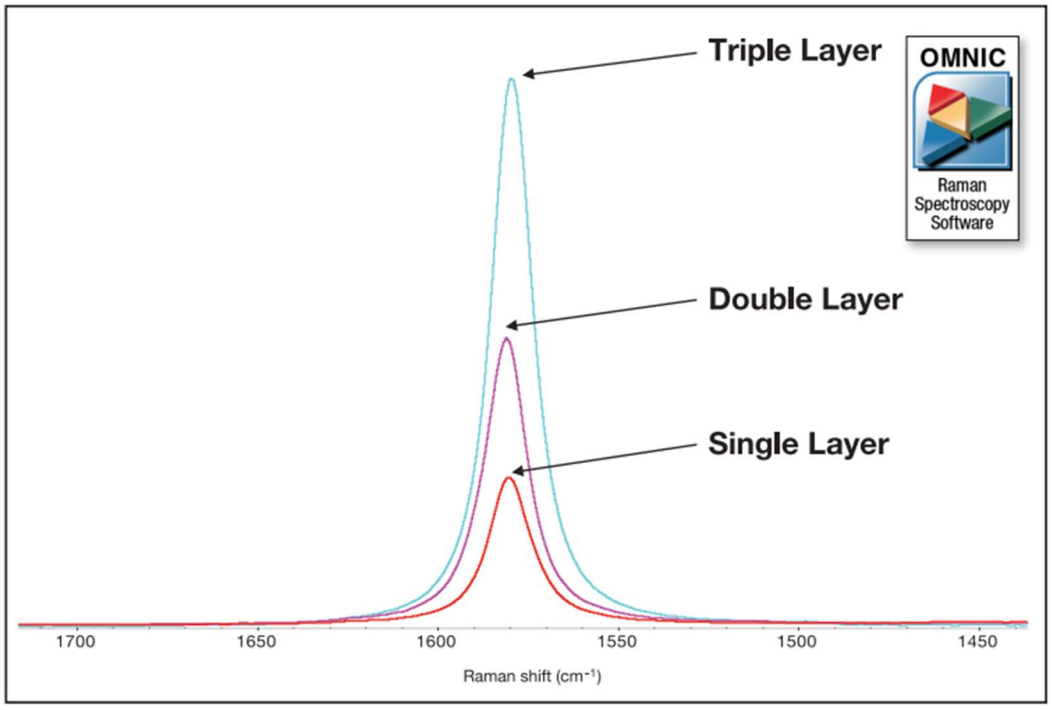


***Figure 3.11**: An increase in G-band intensity is observed as the number of layers increase. Reproduced from reference* [246].

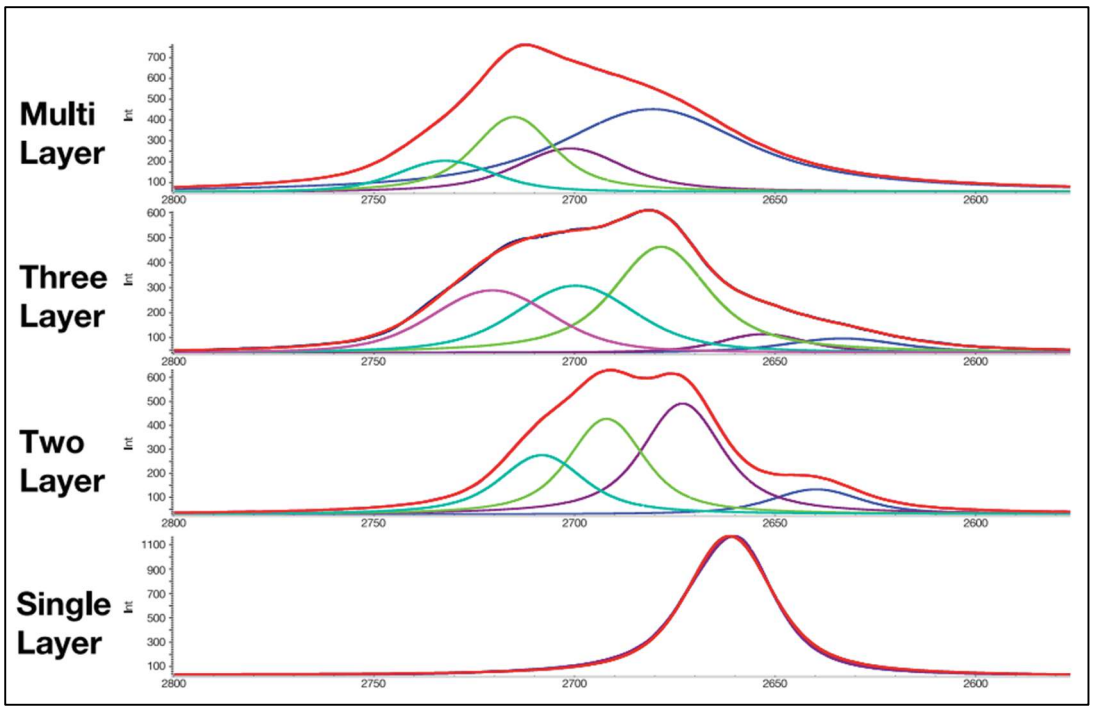


***Figure 3.12**: The 2D-band changes shape and position as the number of layers increase. Reproduced from reference* [246].

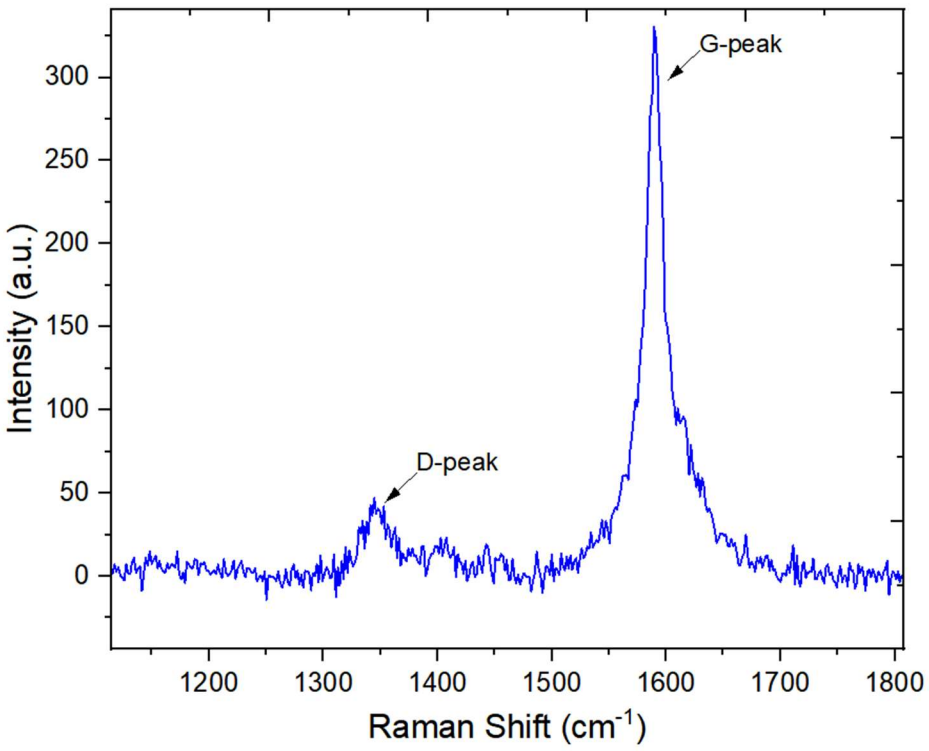


***Figure 3.13**: Graph displaying the D-band or defect peak in graphene.*

3.4.6. X-ray Photoelectron Spectroscopy (XPS)

XPS is a surface analysis technique that enables the investigation of a material's elemental composition, chemical structure, and electronic state. XPS begins with the irradiation of a material's surface with high energy X-ray photons. The photons interact with the inner shells of the atoms on the top 1-10 nm of the material and can cause electrons to be ejected from the sample. Emitted photoelectrons have an energy directly related to the binding energy of the electron in its original shell [247]. As the binding energy is influenced by the chemical environment of the atom, information about the elements and their chemical states on the material's surface can be obtained. A detector analyses the kinetic energy and intensity of the emitted photoelectrons and therefore, the binding energy can be deduced [248]. The resulting spectrum displays peaks corresponding to different elements in the material, revealing their presence and chemical states. The position and shape of these peaks help identify the elemental composition and chemical bonding of the material.

In this work, X-ray Photoelectron Spectroscopy (XPS) analysis was performed using a *KRATOS AXIS SUPRA* system (*Kratos Analytical Ltd.*, UK) (**Figure 3.14**) and *ESCApe* software. Experiments were executed under ultra-high vacuum (~10^{-9} torr) using a monochromated aluminium X-ray source (1487 eV). The analysis area was selected according to the sample analysed. A 300 μm x 700 μm area was utilized for graphene wafer fragments, while a spot size of 110 μm x 110 μm was employed for graphene pixels. A wide scan between binding energies of 0 and 1200 eV was performed first, using a pass energy of 160 eV. The purpose of this scan is to identify the elements present, aiding in the selection of elements for inclusion in the subsequent high-resolution scans. High resolution scans were performed at a pass energy of 20 eV to increase the resolution of each peak. High resolution scans were performed for silicon, carbon, nitrogen and oxygen and **Table 10** shows the primary XPS regions and the approximate binding energies (eV) for these elements [249], [250].

CasaXPS software was used for peak fitting and data analysis. Atomic concentrations were calculated based on the relative sensitivity factor (RSF) of the element. XPS reference pages [250] and the *NIST database* [251] were used to advise curve fitting procedures and identify peaks.

***Table 10**: Primary XPS region and approximate binding energies for silicon, carbon, nitrogen and oxygen.*

Element	Primary XPS Region	Binding Energy (eV)
Silicon	Si 2p	~99
Carbon	C 1s	~284
Nitrogen	N 1s	~399
Oxygen	O 1s	~532



***Figure 3.14**: KRATOS AXIS SUPRA XPS system.*

3.4.7. Fourier Transform Infrared Spectroscopy (FT-IR)

In this work, an *Alpha Bruker benchtop* FT-IR spectrometer (*Bruker*, UK) was used to obtain the infrared spectrum of synthesized copper (II) 2,9,16,23-tetra-tert-butylphthalocyanine. Infrared spectroscopy involves passing IR radiation through a sample, where some radiation is absorbed, and some is transmitted. The IR photons

have sufficient energy to induce vibrational transitions in the atoms and bonds of the molecules. These vibrational modes have distinct energies and characteristic frequencies. When the sample is exposed to IR radiation, it absorbs the radiation at frequencies that correspond to these vibrational modes [252]. The resulting spectrum serves as a unique 'fingerprint' for the sample, as no two compounds have the same atomic arrangement and vibrational characteristics.

3.4.8. Ultraviolet-Visible (UV-VIS) Spectroscopy

In this work, a *LAMBDA 365* UV/Vis spectrophotometer (*PerkinElmer*, USA) with *WinLab* software was used to obtain the UV-Vis spectrum of synthesized copper (II) 2,9,16,23-tetra-tert-butylphthalocyanine. UV-Vis spectroscopy is an analytical technique used to measure the absorbance or transmittance of a sample in the ultraviolet and visible regions of the electromagnetic spectrum. UV-Vis spectroscopy is based on the principle that molecules absorb light at specific wavelengths corresponding to the electronic transitions between molecular orbitals. When a molecule absorbs UV or visible light, electrons are promoted from a lower energy level to a higher energy level [253]. The resulting absorbance spectrum provides information about the electronic structure of the molecule, allowing for the identification of different compounds.

3.4.9. Ellipsometry

In this thesis, an M-2000 ellipsometer (*J.A. Woollam,* USA) (**Figure 3.15**) and *CompleteEASE* software was utilized to estimate the thickness of organic films (copper (II) 2,9,16,23-tetra-tert-butylphthalocyanine and polymerized 1,5-diaminonapthalene) deposited on graphene for functionalization purposes.

Ellipsometry is an optical technique used to determine the thickness and optical properties (such as refractive index and extinction coefficient) of thin films. The method involves measuring the change in polarization as light reflects off the surface of a material [254]. To estimate film thickness, a model incorporating layers with known or assumed optical properties is used and fitted to the collected data [255].

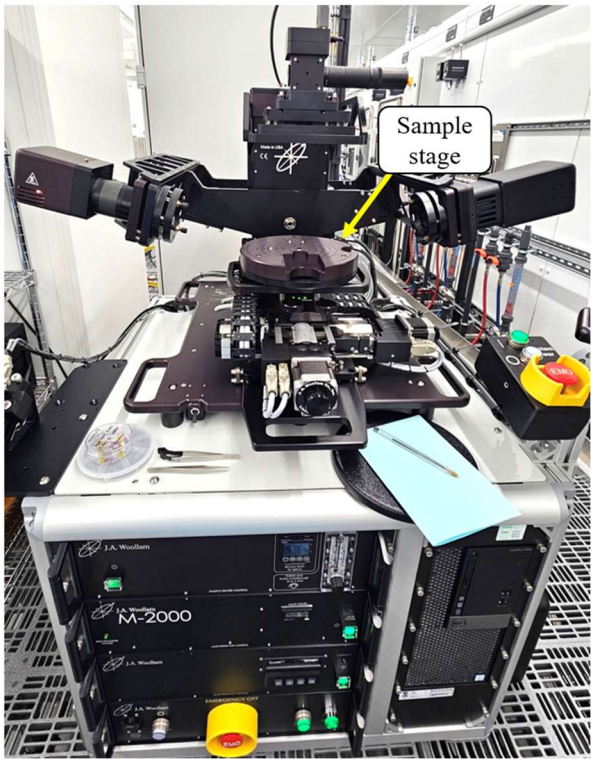


***Figure 3.15**: J.A. Woollam M-2000 Ellipsometer.*

3.5. Electrical Measurements

This section describes electrical measurements and the equipment utilized to conduct these measurements on graphene devices.

3.5.1. Probe Station

Electrical measurements using an *LA200-DC Semiprobe Lab Assistant* probe station (*Inseto Ltd*, UK) and *Keithley 2612B SourceMeter (Tektronix,* USA*)* were performed on all graphene devices utilised in this research (**Figure 3.16a**). Individual sensors or an entire 4-inch wafer was placed on a platform positioned below tungsten probes. Using the manipulators, the probes were adjusted to connect with the device contacts. This was visualised using a microscope and TV screen (**Figure 3.16b**). Voltage (V) sweeps were performed using *TSP Express* software on each device from -1 to 1 V and current (I) was measured. The I-V data was plotted using Excel and the resistances calculated using the slope of the graph. The probe station was used during device

fabrication and functionalization to ensure devices were working appropriately and to document resistances.

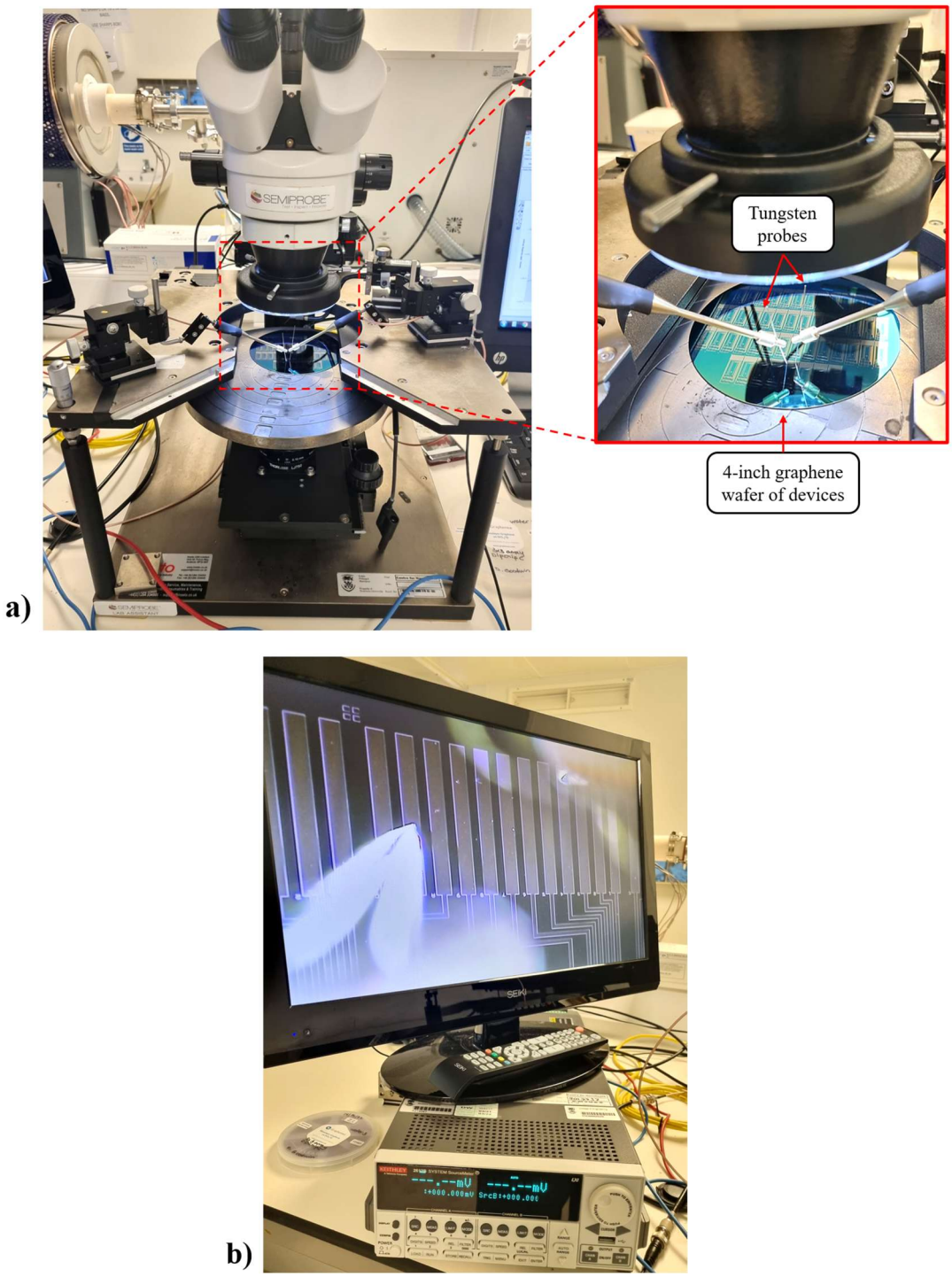


Figure 3.16: ***(a)*** *Semiprobe Lab Assistant probe station with wafer of devices positioned under probes and* ***(b)*** *microscope TV screen and Keithley 2612B SourceMeter.*

3.5.2. Back-gated Measurements

Back-gated measurements were performed using a *Pegasus Semiautomatic S200FA-HV* Semi-automatic analytical probe station (*Wentworth Laboratories*, UK) (**Figure 3.17a**) and a *Keysight B1505A Power Device Analyzer/Curve Tracer* (*Keysight Technologies*, USA). Individual sensors were placed on a vacuum chuck positioned below tungsten probes. The chuck was positioned in the X, Y and Z positions using *LabMaster FA 15.1.2* software. Using the manipulators, the probes were adjusted to connect with the device contacts. This was visualised using a microscope and TV screen (**Figure 3.17b**). For back-gated measurements, a potential (V) is also applied to the chuck. Parameters for the electrical measurement were entered into the Keysight interface (**Figure 3.17c**).

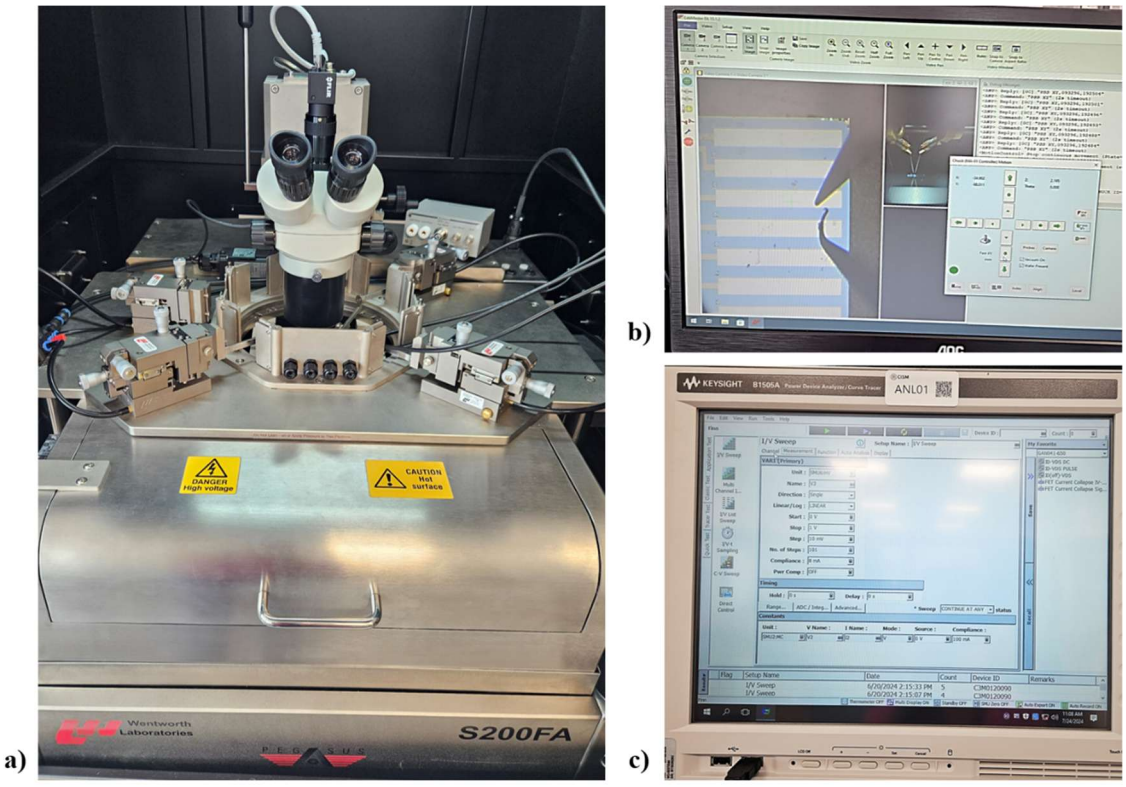


***Figure 3.17**: **(a)** Pegasus S200FA-HV Semi-automatic analytical probe station. **(b)** Microscope view and chuck position controls. **(c)** Keysight B1505A Power Device Analyzer/Curve Tracer.*

3.5.3. Real-time Measurements

Real-time 2-point resistance measurements were performed with the 3-channel 'DipChipX' and the 9-pixel '3x3 graphene pixel array' devices.

3.5.3.1. DipChipX

DipChipX sensors were designed and fabricated for compatibility with an electrical connector and for liquid sensing applications (**Figure 3.18**). Additional details on the design are provided in **Chapter 4.2.1**.

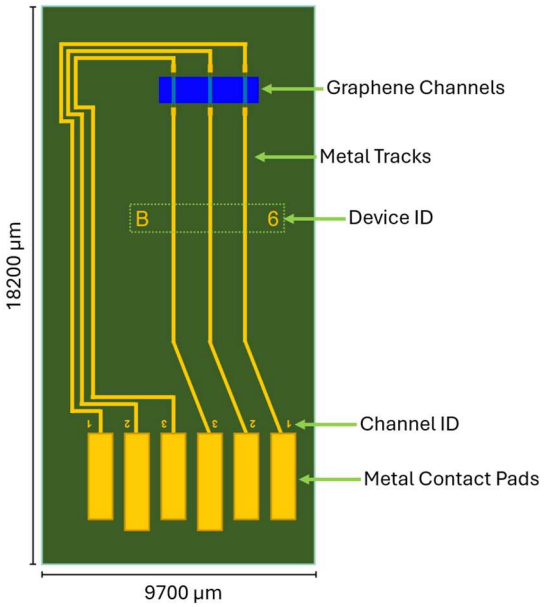


***Figure 3.18**: Schematic of the 'DipChipX' graphene sensor.*

The DipChipX sensors were slotted into a 'Sensor-Connect' connector (**Figure 3.19c**) (supplied by *Biovici Ltd*) to provide the electrical connections between the device contact pads and measurement instruments. The connector contained header pins which were connected to by hook clips to two *Keithley 2636B SourceMeters* (**Figure 3.19a-b**). Real-time measurements were taken using *TSP Express* software on the 3 graphene channels simultaneously using a fixed voltage of 40 mV. The current was measured, and the resistance was calculated from the data and presented as $\Delta R/R_0$, where $\Delta R = R_{device} - R_0$ and R_0 is the initial resistance of the device in ambient conditions. Real-time testing was performed during the functionalization processes and during testing to demonstrate real-time resistance changes as they occur.

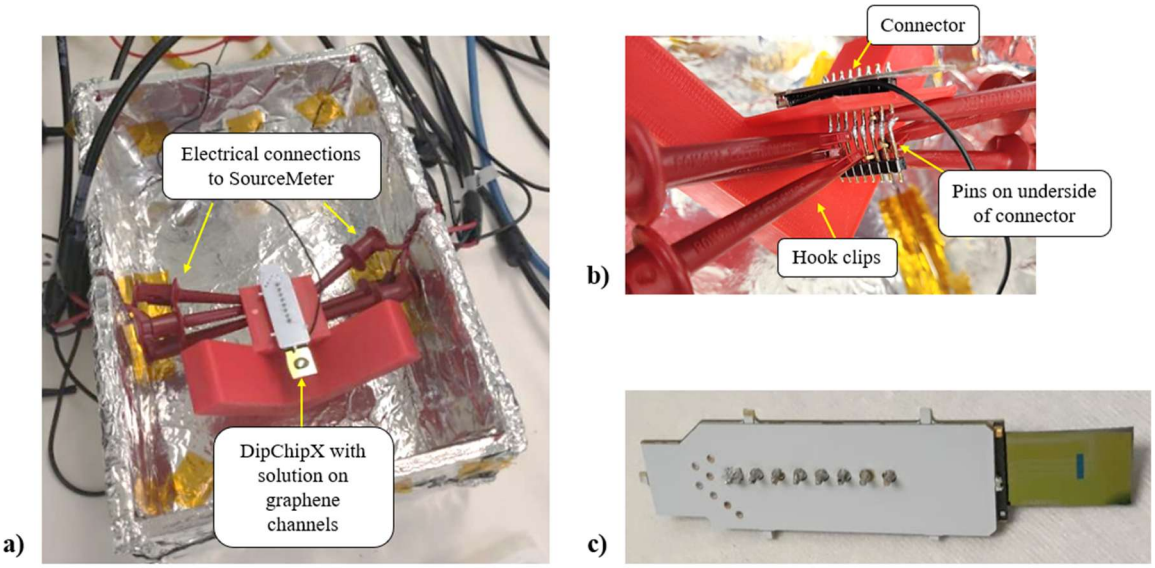


***Figure 3.19**: **(a)** Real-time resistance measurement set-up, **(b)** header pins on the underside of the connector, and **(c)** Biovici 'Sensor-Connect' connector with a DipChipX sensor.*

3.5.3.2. 3x3 Graphene Pixel Array

The 3x3 graphene pixel array sensors were designed and fabricated to be compatible with a USB-C type plug and to simultaneously detect multiple analytes (**Figure 3.20**). Additional details on the design are provided in **Chapter 4.3.**

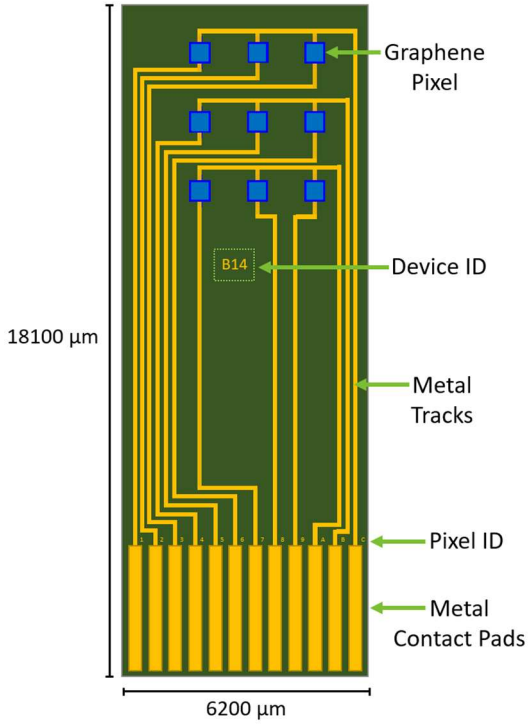


***Figure 3.20**: Schematic of the '3x3 graphene pixel array' sensor.*

The 3x3 graphene pixel array sensors were placed into a USB-C male to female adapter (purchased from *Amazon*, brand: *Duttek*) then connected to custom-made USB-C PCB connectors purchased from *Electronics* (UK) to provide the electrical connection between the metal contact pads and measurement equipment (**Figure 3.21**). The PCB connectors contained screw clamp terminal blocks which were used to connect to the D-sub connection at the back of the gas sensing rig (more information on the gas sensing rig is provided in **Chapter 5.5**).

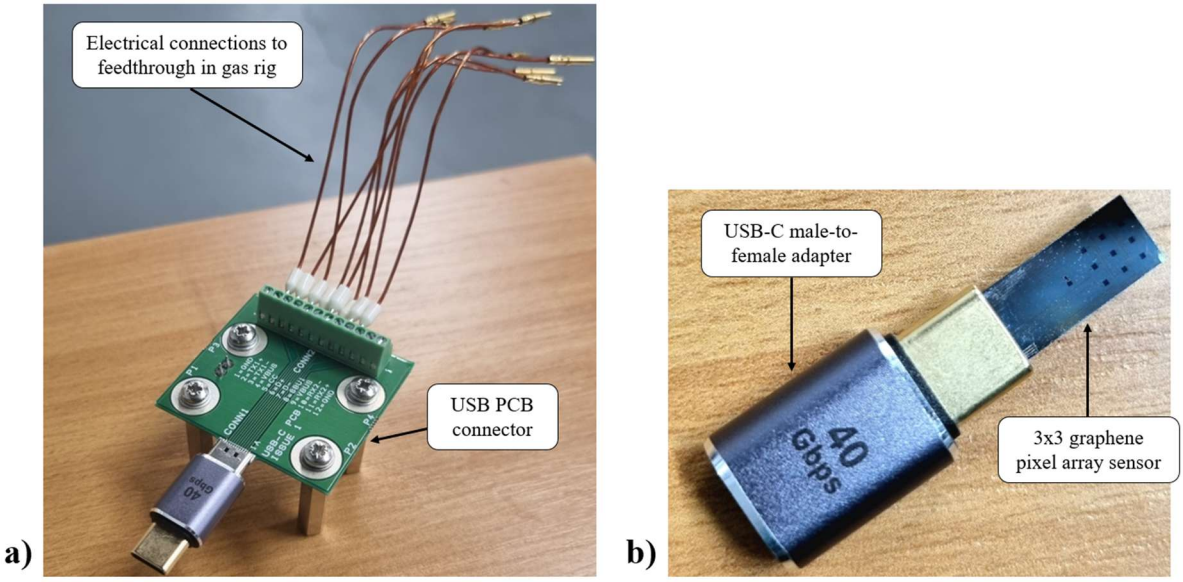


***Figure 3.21**: **(a)** USB-C PCB connector with USB-C male to female adapter and wire connections for D-sub electrical feedthrough and **(b)** USB-C male to USB-C female adapter with 3x3 graphene array sensor.*

Real-time measurements were taken using a *Keithley 2602A SourceMeter*, *Data Acquisition/Multimeter System 6510* and *KickStart* software using the *IV Characteriser* and *Data Logger* apps. A fixed voltage of 1 V was used and the change in voltage of all the selected channels (system is capable of measuring up to 40) across a fixed resistor was measured. Device resistance was calculated using the following formula:

$$R_d = \frac{V_f - V_m}{\frac{V_m}{R_f}}$$

Where:

R_d = device resistance V_m = measured voltage

R_f = fixed resistance V_f = fixed voltage

***Equation 1**: Formula to calculate device resistance using the DAQ.*

Following calculation of device resistance (R_d), the data is presented as $\Delta R/R_0$, where $\Delta R = R_{device} - R_0$ and R_0 is the initial resistance of the device in ambient conditions. Real-time testing measurements were performed during ultra-violet (UV) assisted vacuum treatments, baseline sensing and target gas sensing to demonstrate the change in resistance of devices as it occurs.

3.6. Gas Sensing Performance Metrics

The evaluation of gas sensor performance involves reporting various parameters, including sensor response, response time, recovery time, selectivity, sensitivity, signal-to-noise ratio (SNR), Limit of Detection (LOD), and Limit of Quantification (LOQ). This section aims to define each parameter and describe how they are determined.

3.6.1. Sensor Response

Sensor response, often expressed as a percentage of the relative response, is calculated by taking the difference between the maximum resistance in the presence of the target gas (R_g) and the resistance in the absence of the target gas (R_i), divided by R_i.

Sensor response was calculated using the following formula:

$$Sensor\ response\ (\%) = \frac{R_g - R_i}{R_i}\ x\ 100$$

Where:

R_g = resistance in target gas R_i = resistance in air or inert gas

***Equation 2**: Sensor response formula.*

3.6.2. Response and Recovery Time

Response and recovery times are defined as “the time needed for achieving 90% change of the electrical resistance in the target gas and air, respectively” [256], [257]. **Figure 3.22** demonstrates how these values are calculated.

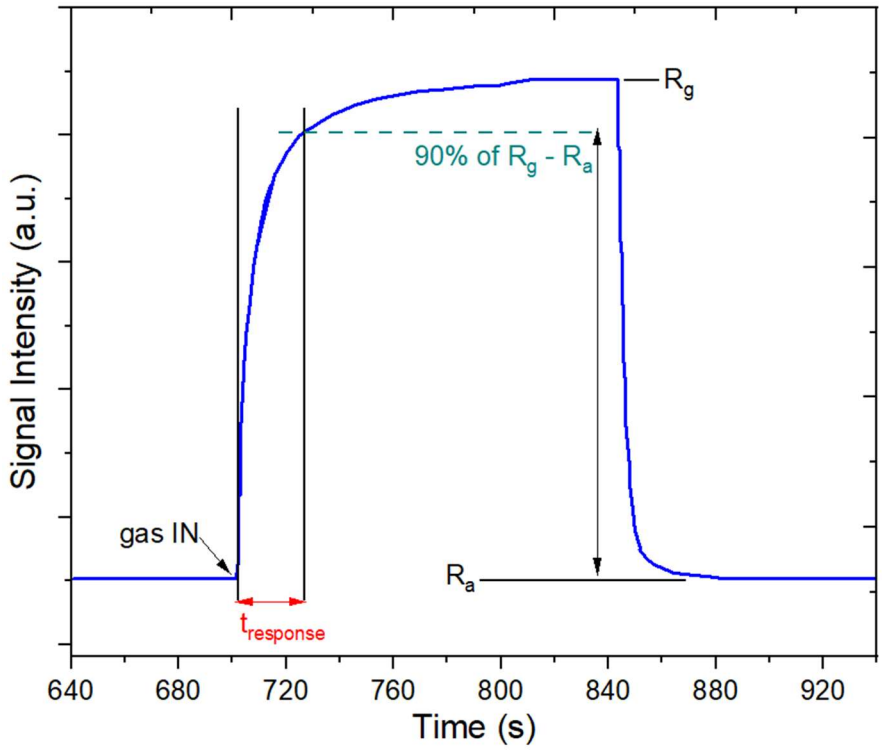


***Figure 3.22**: Calculation of the response time according to the definition. Reproduced from reference* [258].

Sensor recovery refers to the process of returning a sensor to its baseline state after it has been exposed to a target gas. This involves desorbing the adsorbed gas molecules from the sensor's surface, thereby restoring its original electrical properties and ensuring it is ready for subsequent measurements [259]. Effective sensor recovery is crucial for maintaining accuracy and consistency in repeat measurements.

Although gas sensor recovery is typically evaluated by comparing the electrical resistance before and after applying the recovery method, in this work, sensor response repeat measurements were often used as an indicator of recovery. This approach served as a simple method to evaluate recovery, as the recovery methods used remove adsorbed gases indiscriminately, making it challenging to achieve the exact same resistance value after recovery. In all experiments conducted for this research, the recovery time was consistently set at 8 minutes using vacuum-assisted UV exposure, as this method proved to be the most effective.

3.6.3. Percentage Recovery

The percentage recovery of a gas sensor is a metric used to evaluate how effectively a sensor returns to its baseline state after exposure to a target gas. It is an important parameter to assess the reusability and stability of the sensor in practical applications. The percentage recovery can be calculated using the following formula:

$$\%\ Recovery = \frac{Sensor\ Response_f}{Sensor\ Response_i}\ x\ 100$$

Where:

$\text{Sensor Response}_i = \text{initial sensor response}$

$\text{Sensor Response}_f = \text{Sensor response following recovery}$

***Equation 3**: Percentage recovery formula.*

3.6.4. Selectivity

Selectivity is the ability of a sensor to distinguish between different gases. A sensor with high selectivity can produce a strong response to the target gas even in the presence of other interfering gases that may also elicit a response [58]. Selectivity is often represented by a chart comparing the sensor's response to the target gas against its response to other interfering gases.

3.6.5. Sensitivity

Sensitivity in gas sensing refers to the ability of a sensor to detect and quantify small changes in the concentration of a gas [58]. It is a measure of how much the sensor's output signal changes in response to a change in the gas concentration. Higher sensitivity indicates that the sensor can detect smaller changes in gas concentration more effectively.

Sensitivity can be expressed as:

$$Sensitivity = \frac{\Delta Response}{\Delta Concentration}$$

Where:

$$\Delta\text{Response} = \text{change in sensor response (\%)}$$

$$\Delta\text{Concentration} = \text{change in gas concentration}$$

***Equation 4**: Sensitivity formula.*

Sensitivity can be readily determined by the slope of the calibration curve, which is created by plotting the sensor response against different concentrations of the target gas. In cases where the relationship is linear, the slope directly provides the sensitivity. For non-linear relationships, the slope is determined from the linear segment of the curve to estimate sensitivity.

3.6.6. Signal-to-Noise Ratio

The signal-to-noise ratio (SNR) is an important gas sensing performance parameter where a high SNR value indicates a high-performing sensor. The signal-to-noise ratio (SNR) indicates the relative gas signal intensity over noise intensity and can be defined as:

$$SNR = \frac{Height\ of\ signal}{Height\ of\ noise}$$

Where:

$$\text{Height of signal} = \text{sensor response in target gas} \qquad \text{Height of noise} = \text{sensor response in air or inert gas}$$

***Equation 5**: Signal-to-Noise (SNR) formula.*

3.6.7. Limit of Detection

The Limit of Detection (LOD) is the lowest concentration or amount of analyte that can be reliably detected by an analytical procedure [260]. It represents the smallest

signal or concentration that can be distinguished from the background noise. LOD is often based on the standard deviation of the response (signal) of the blank sample, a defined SNR (3:1 is typically used [261]) and the slope of the calibration curve (sensitivity). The LOD can be estimated as:

$$LOD = 3\ x\ \frac{\sigma}{S}$$

Where:

σ = standard deviation of response of blank signal

S = sensitivity, or slope of the calibration curve

***Equation 6**: LOD formula* [262], [263].

3.6.8. Limit of Quantification

The Limit of Quantification (LOQ) is the lowest concentration or amount of analyte that can be accurately quantified. The LOQ is estimated in a similar manner to the LOD, with a higher signal-to-noise ratio (10:1) [261].

$$LOQ = 10\ x\ \frac{\sigma}{S}$$

Where:

σ = standard deviation of response of blank signal

S = sensitivity, or slope of the calibration curve

***Equation 7**: LOQ formula* [262], [263].

3.6.9. Principle Component Analysis (PCA)

Principal Component Analysis (PCA) is a statistical technique used for dimensionality reduction, data compression, and pattern recognition, particularly useful in analysing gas sensing data from arrays [74], [264]. PCA reduces the number of variables in a dataset while retaining as much variance as possible, revealing patterns or trends that might not be apparent in the original high-dimensional space. In PCA, the principal components form an orthogonal set of dimensions, where each axis is independent of

the others. This orthogonality allows for clear separation of different sources of variance, making it easier to analyse and interpret the contributions of each original variable or sensor element [264].

A typical PCA bi-plot includes eigenvectors, represented by lines with arrowheads, which illustrate how strongly each feature contributes to the principal components (PCs) [265], [266]. This visualization is especially valuable in gas sensing applications, as it allows users to assess the sensitivity of each sensing element to specific gases [74]. Additionally, a bi-plot incorporates data points that, when representing gases, reveal the effectiveness of the sensor array in distinguishing between them.

Figure 3.23 [74] exemplifies a standard PCA plot where eigenvectors (e.g., 2600, 2602, 2610) correspond to various commercially available sensors, while the data points represent different volatile organic compounds (VOCs) tested. In this plot, the red eigenvector (2600) is located in the upper left quadrant, indicating its sensitivity to gases such as decane, acetone, and methyl i-butyl ketone (MiBK). This spatial arrangement highlights how the eigenvectors and data points interact to provide insights into the sensor array's performance.

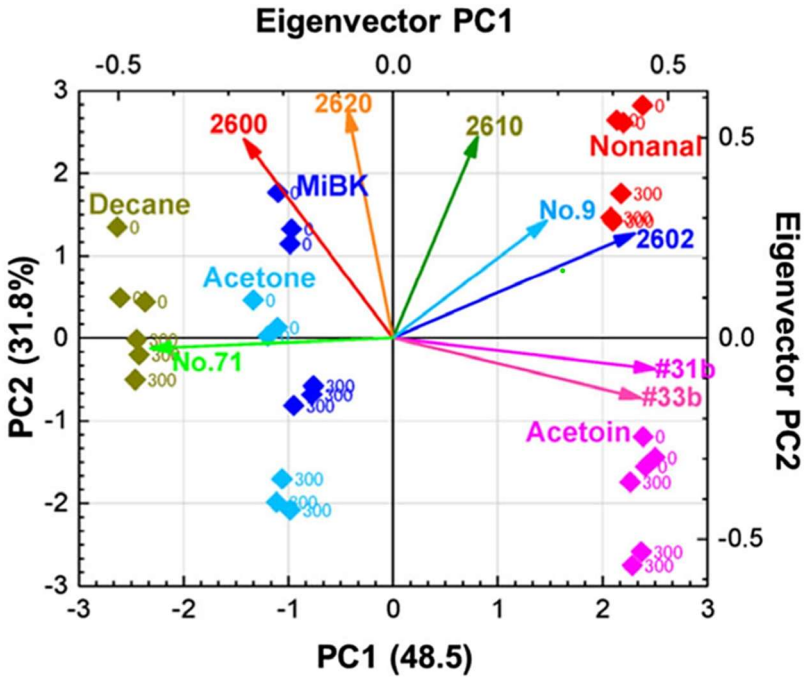


Figure 3.23: PCA bi-plot demonstrating the eigenvectors of the sensor array response to the VOCs. Reproduced from reference [74].

Chapter 4 : Fabrication and Design of Graphene Sensors

4.1. Introduction

The following chapter describes the fabrication process to create the graphene sensor devices. The optimized fabrication method for devices was established by previous post-doctoral and PhD students within the research group [237], [267], [268]. Three unique device designs were employed in this research for sensing purposes. The 'DipChipX' and 'Hall Bar' devices were developed by Jacob Mitchell [268], while the graphene 3x3 pixel array, depicted in this work, was specifically created for multiplexing purposes and will be discussed in greater detail. The same methods and materials used to create the 'DipChipX' and 'Hall Bar' graphene devices were also employed in the fabrication of the 3x3 graphene array devices. Additionally, the design and limitations of the 3x3 array devices, the USB PCB connector, and back-gated measurements will be discussed. Finally, this chapter explores a comparison of sensor performance of different device designs and discusses the influence of device aging on sensor functionality.

4.2. Device Designs Used in this Research

The 'DipChipX' and 'Hall Bar' designs, developed by Jacob Mitchell [268], were utilized in this research for initial gas sensing.

4.2.1. Graphene 3-channel ‘DipChipX’

The ‘DipChipX’ is an 18200 µm x 9700 µm device consisting of three (1500 µm x 100 µm) graphene channels, connecting metal tracks, and six metal contact pads at the bottom in a ‘MicroSD card’ style arrangement (**Figure 4.1**).

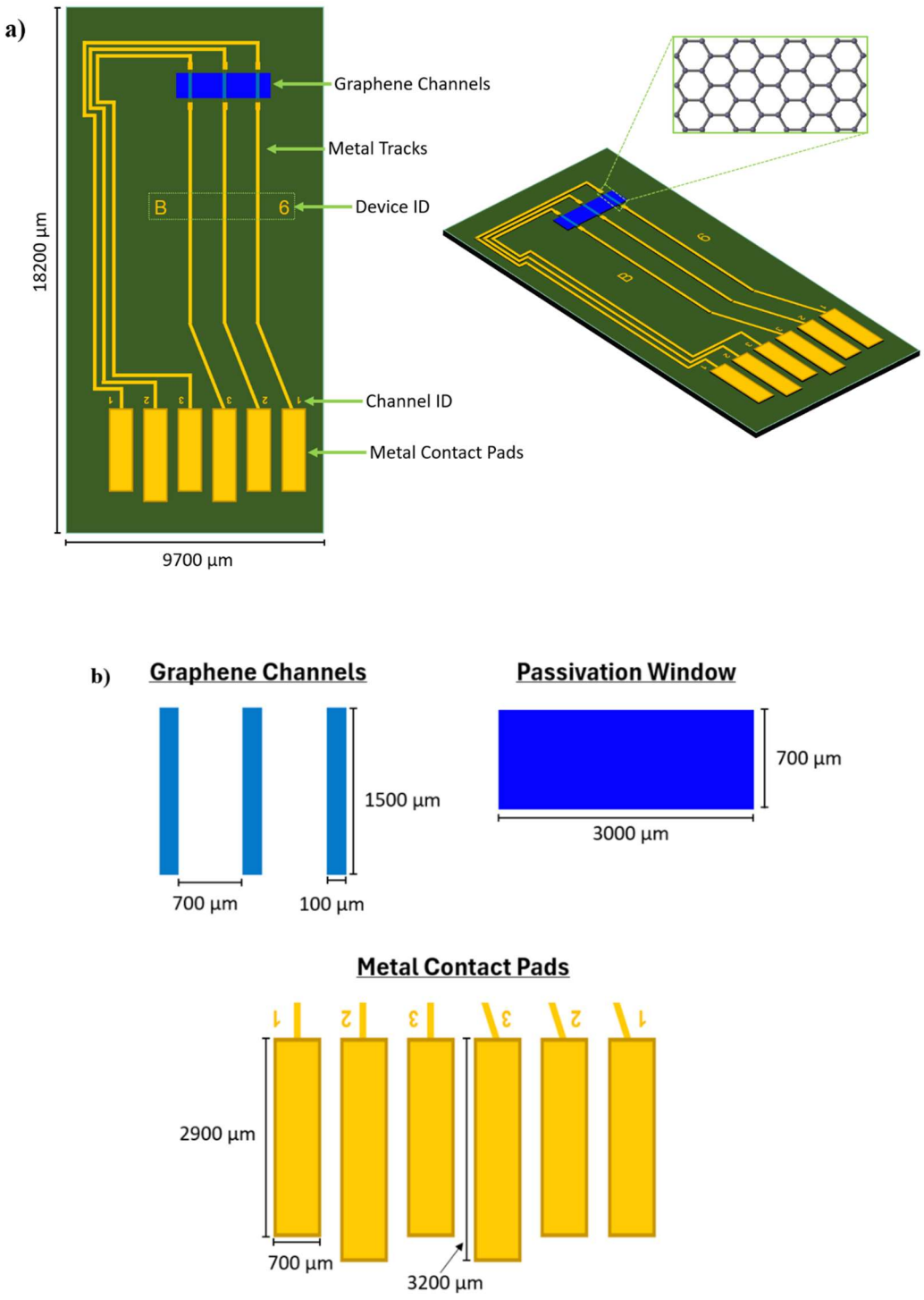


***Figure 4.1**: **(a)** Schematic of the 'DipChipX' device and **(b)** dimensions of the graphene channels, passivation window (located over graphene channels), and metal contact pads.*

Devices were fabricated using chemical vapour deposited (CVD) monolayer graphene grown on copper (Cu) substrate and transferred on 300 nm thermal SiO_2/525 µm Si wafers using polymethyl methacrylate (PMMA)-based wet transfer. Graphene devices

were also coated in a ~50 nm aluminium oxide (Al_2O_3) passivation layer to protect the metal tracks. The 'DipChipX' was primarily used in liquid-based sensing, and therefore, was commonly referred to as a 'Dip Chip'. The MicroSD card style devices enabled convenient real-time sensing measurements to be performed by utilizing a 'connector' that devices could easily slide into for testing. An image of the connector can be seen in **Chapter 3.5.3.1** (**Figure 3.19c**).

4.2.2. Graphene 2-channel 'Hall Bar'

The 'Hall Bar' is an 18200 µm x 9700 µm device consisting of two (1150 µm x 250 µm) graphene channels, connecting metal tracks, and eight metal contact pads at the bottom in a 'MicroSD card' style arrangement (**Figure 4.2**). Devices were fabricated using CVD monolayer graphene on 300 nm thermal SiO_2/525 µm Si wafers and were coated in a ~50 nm aluminium oxide (Al_2O_3) passivation layer to protect the metal tracks. Hall measurements were not performed with this device; instead, it was used for real-time resistance measurements. Similar to the 'DipChipX,' these devices could easily slot into the MicroSD card connector.

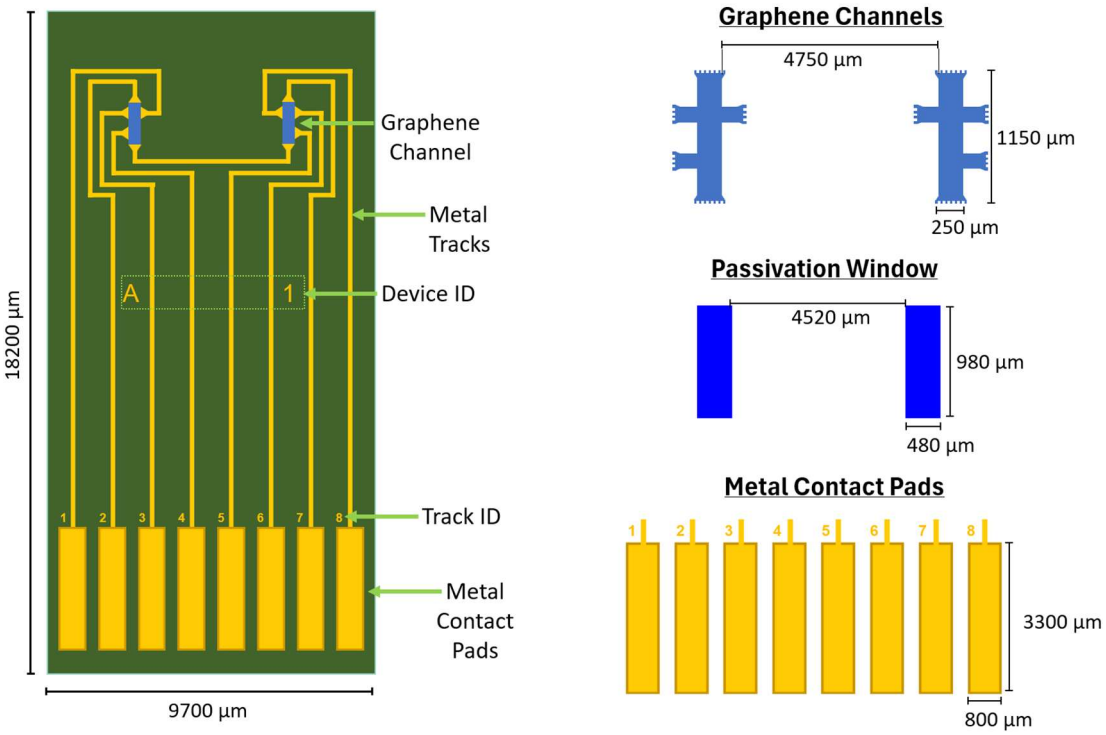


Figure 4.2: Schematic of the 'Hall Bar' device including dimensions of the graphene channels, graphene passivation windows and metal contact pads.

4.3. Design of the 3x3 Graphene Pixel Array

This section describes the design and dimensions of the '3x3 graphene pixel array' devices, which were created specifically for the research presented in this thesis.

4.3.1. Overview and Motivation

Gas sensor arrays, often known as 'electronic noses,' offer significant advantages over single sensors. These arrays can simultaneously detect multiple analytes and provide superior discrimination between them, resulting in more robust sensors with enhanced accuracy and reliability. With these benefits in mind, the 3x3 graphene pixel array was designed. The '3x3 graphene pixel array' is an 18100 µm x 6200 µm device consisting of nine graphene pixels, connecting metal tracks, and twelve metal contact pads at the bottom in a 'USB-C' compatible arrangement (**Figure 4.3**). Devices were fabricated using CVD monolayer graphene on 90 nm thermal SiO_2/381 µm Si wafers and were coated with a ~50 nm aluminium oxide (Al_2O_3) passivation layer to protect the metal tracks from any subsequent chemical processing. The dimensions of the USB-C style devices were established by Muhammad Munem Ali to ensure compatibility with the USB-C plug receptacle.

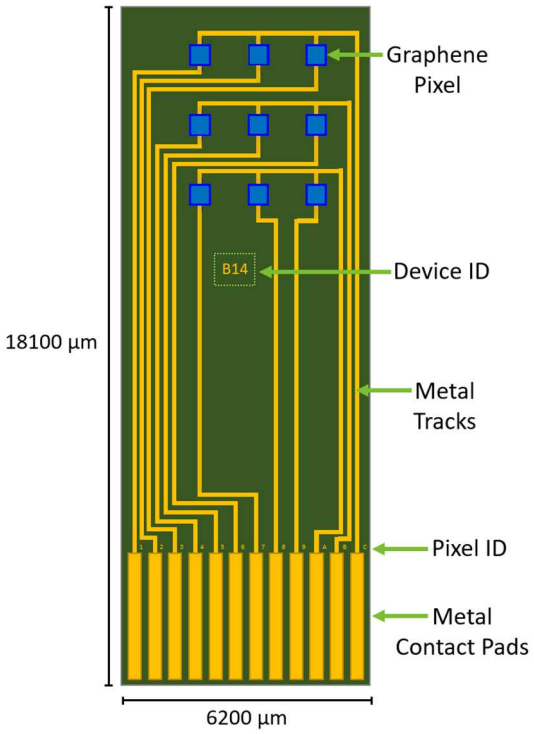


Figure 4.3: Schematic of the '3x3 graphene pixel array' devices.

4.3.2. Metal Tracks and Contact Pads

Each device contains twelve 300 µm x 3300 µm contact pads, spaced 200 µm apart, resembling 'USB-C style' contacts (**Figure 4.4**). Twelve 100 µm wide metal tracks connect each graphene pixel to the contact pads and each row is grounded together by a single track. As devices are passivated to preserve the metal tracks, 280 µm x 3280 µm windows are etched exposing the contact pads enabling an electrical connection to the sensors. Tracks are numbered sequentially from left to right and labelled A, B, and C to identify the corresponding graphene pixels to which they are connected.

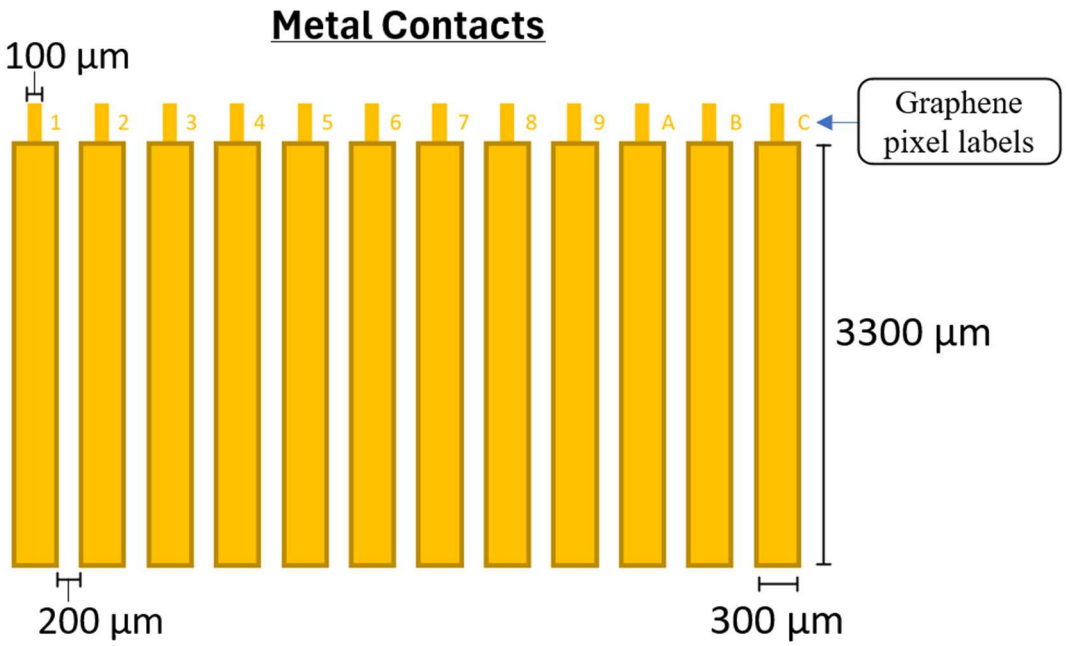


***Figure 4.4**: Schematic and dimensions of the metal contact pads on the 3x3 graphene pixel array sensor.*

4.3.3. Graphene Pixels

Each graphene array consists of nine 500 µm x 500 µm pixels and includes a 150 µm x 100 µm feature at each end to ensure adequate contact with the metal tracks (**Figure 4.5**). Devices undergo passivation to shield the metal tracks, including the metal-graphene interface, from environmental factors like air, moisture, and contaminants. Additionally, protecting metal contacts from functionalization chemistries is crucial. Following device passivation, 400 µm x 400 µm windows are etched to expose the graphene pixels, enabling sensing.

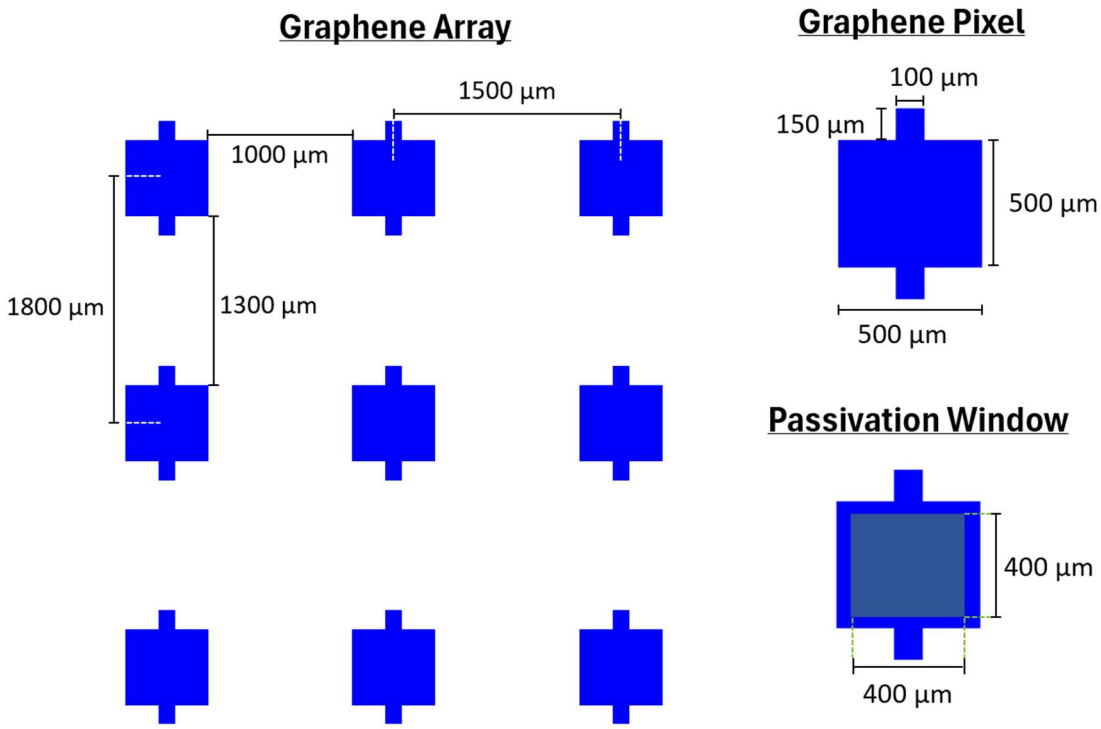


***Figure 4.5**: Schematic of graphene pixel array including dimensions of individual pixels and the passivation window.*

Pixels on the sensor are labelled near the metal contact pads at the bottom of the device. Each pixel is identified by its row and pixel number (**Figure 4.4**). The row closest to the metal contact pads is labelled 'Row A', the middle row as 'Row B', and the top row as 'Row C'. Pixels are then numbered sequentially from left to right, descending down the sensor (**Figure 4.6**).

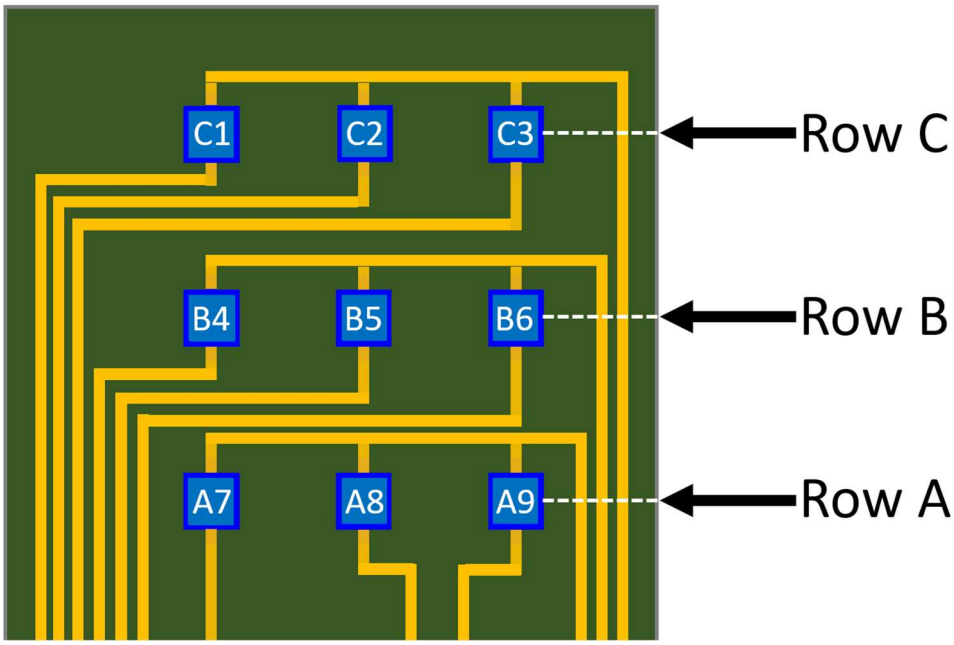


***Figure 4.6**: Graphene pixel identification key.*

4.4. Sensor Fabrication Process

Figure 4.7 presents a schematic representation of the fabrication process, preceding a detailed explanation of each step.

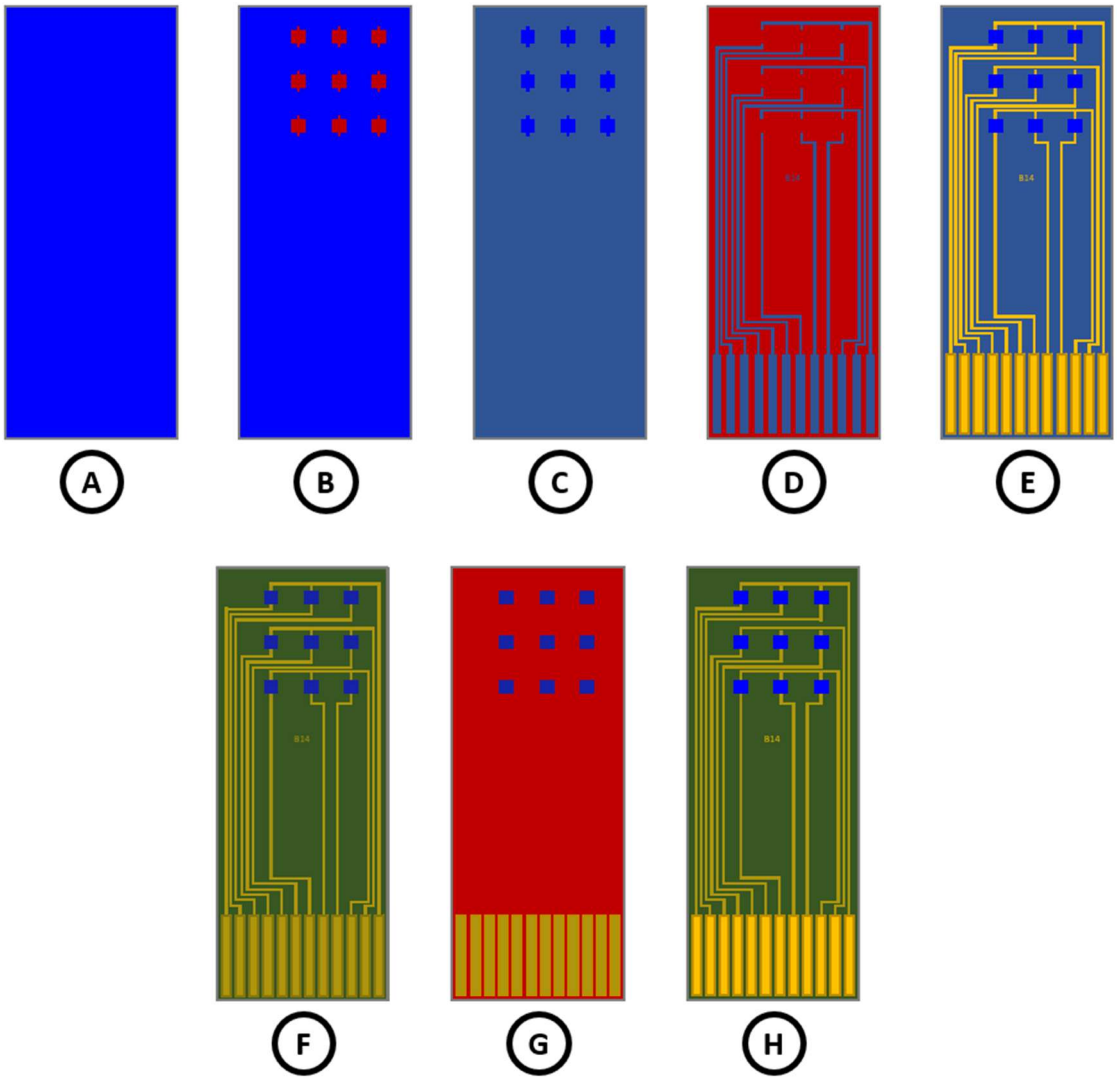


***Figure 4.7**: 3x3 graphene pixel array device fabrication schematic. **(A)** CVD monolayer graphene on Si/SiO_2 substrate. **(B)** Application of a photoresist etch mask. **(C)** After O_2 plasma etching and photomask removal. **(D)** Coating and patterning photoresist for metal electrodes. **(E)** Metal deposition and lift off. **(F)** Deposition of Al_2O_3 passivation layer using MVD technique. **(G)** Coating and patterning photoresist for selective etching to expose graphene and metal contacts. **(H)** Al_2O_3 is etched, and photomask removed – finished sensor.*

4.4.1. Sample Preparation

Graphene resistor devices were fabricated using 4" (100 mm) chemical vapour deposition (CVD) graphene wafers (90 nm thermal SiO_2/381 µm Si). To begin, wafers were cleaned for 10 minutes in acetone, 5 minutes in isopropyl alcohol (IPA) and dried

with a nitrogen (N_2) gun before placing on a hot plate at 130°C for 15 minutes. The cleaning process aids in the removal of any polymer residues left on the surface following the graphene transfer process [269].

Following the cleaning procedure, wafers were placed in a susceptor and annealed at 550°C under vacuum for 15 min with 50 sccm argon (Ar) flow using a Rapid Thermal Annealing system. After a cool down period, wafers were removed from the annealing system and photolithography processes are used to pattern the wafers. Annealing removes any moisture trapped at the silicon-graphene interface which can cause delamination and impact the electronic properties of graphene [218], [270].

4.4.2. Graphene Patterning

A bilayer photoresist method was used consisting of two positive photoresists: LOR 3A and S1805. The intended thickness of LOR 3A and S1805 was approximately 0.3 µm and 0.5 µm, respectively. Wafers were initially spin coated with LOR 3A using a Laurell Spin Coater followed by 2 minutes of curing using EMS 1200 precision hot plate at 180°C. A 15-minute hydration period was required after curing before the next photoresist was added. The second photoresist, S1805, was spin coated onto the wafer followed by 1 minute on the hot plate at 115°C and another 15-minute hydration period. Spin coating parameters are identical for both photoresists:

	Step 1	**Step 2**
Time (s):	5.0	45.0
Spin speed (rpm):	500	3000
Acceleration (rpm/s):	250	10000

UV exposure, using an exposure dose of 75 mJ/cm^2, and mask alignment for the graphene pixel design (**Figure 4.8**) were performed first using SUSS MicroTec MA/BA8 Mask Aligner. As a positive photoresist was used, the transparent regions of the quartz mask (show in white in **Figure 4.8**) will allow UV light to pass through, solubilising the photoresist underneath. Chrome regions (shown in black) will not allow UV light through, and therefore, will remain insoluble when exposed to the developer solution.

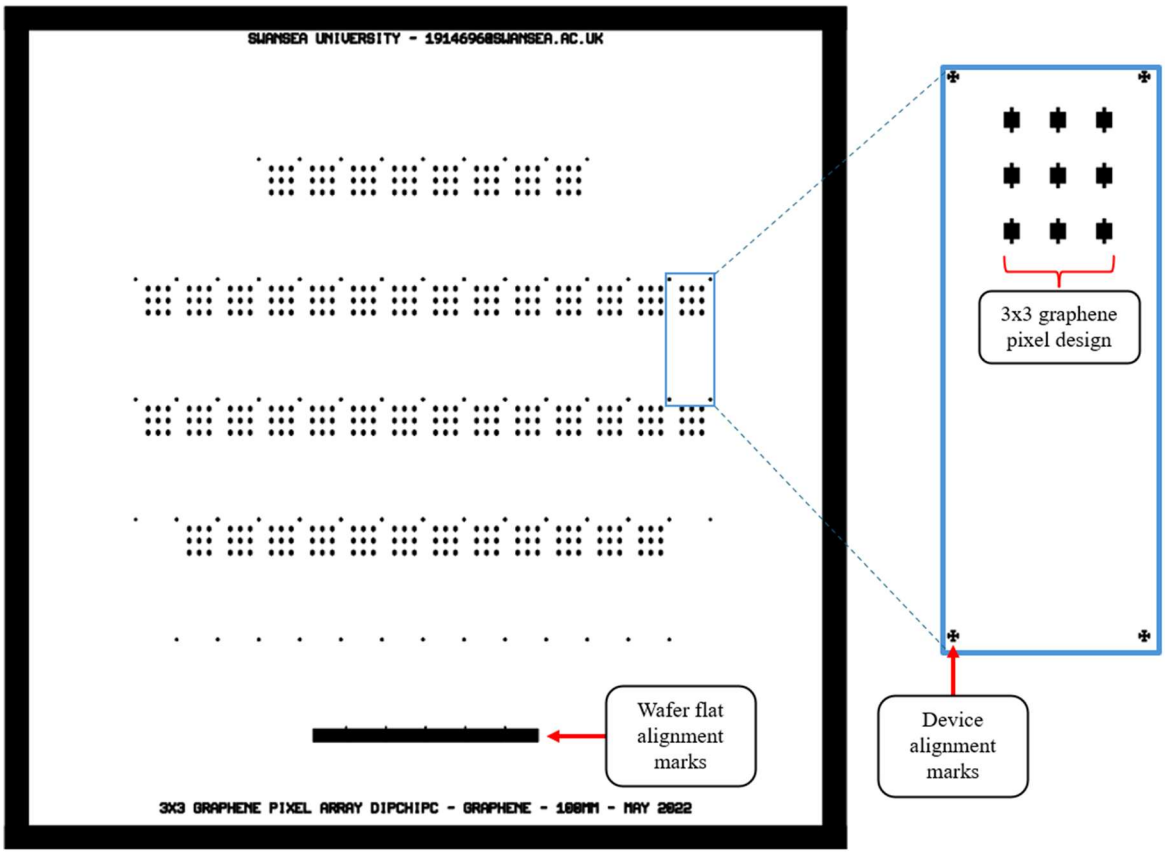


***Figure 4.8**: 5-inch chrome photomask design for the graphene pixels for the '3x3 graphene pixel array' design (reproduced from JD Photo Data check plot). Black features represent the chrome.*

After UV exposure, wafers were placed in pure MF-CD-26 Developer for 30 seconds and two subsequent washes in deionised (DI) water were performed to reveal the graphene pixel pattern. Next, the wafers were placed in the Plasma Etcher for 1 minute (RF power = 50 W) prior to the residual resist being removed. The photoresist remains over the graphene pixels, acting as a protective layer during the etching process. After ensuring the excess graphene had been successfully etched using a VHX Digital Microscope (**Figure 4.9**), wafers were placed in 1165 Remover on a hot plate at 60°C for 3 hours total (1.5 hours in the first beaker, 1.5 hours in a second) to remove the photoresist remaining on the graphene pixels.

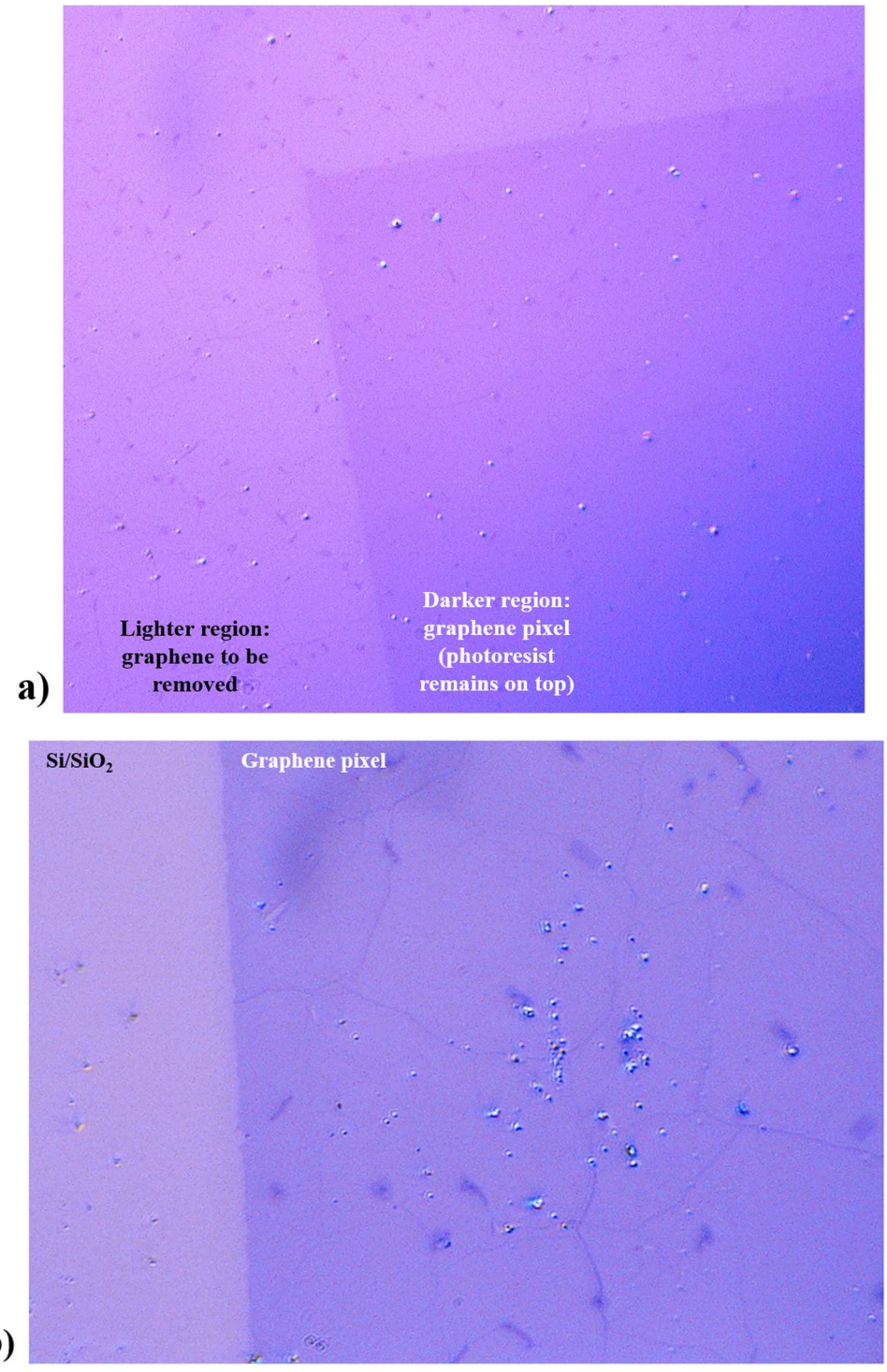


*Figure 4.9: Optical images of **(a)** a graphene-Si/SiO_2 wafer pre-etch. Darker region contains the corner of a graphene pixel with photoresist on top. Lighter region contains the graphene to be removed via the plasma etching process. **(b)** a graphene-Si/SiO_2 wafer post-etch. Si/SiO_2 region contains no visible graphene.*

Figure 4.9 displays optical images of a graphene-Si/SiO_2 wafer pre- and post- plasma etch. The top image (pre-etch) displays the corner of a graphene pixel with a photoresist mask on top (darker region) next to the lighter region containing the

graphene to be etched. Surface features from the graphene are visible over the entire surface shown. Contrastingly, the post-etch image (**b**), with the absence of surface features demonstrates the graphene in the exposed region has been removed.

4.4.3. Metal Deposition and Lift-off

Following photoresist removal, the wafers are placed in IPA for 5 minutes and then dried with the N_2 gun no ensure a clean surface prior to spin coating. Wafers were spin coated using the same bi-layer photoresist method using LOR 3A and S1805 for a second time employing the same spin parameters, curing and hydration times. The bilayer photoresist method forms an 'undercut' which enables a successful lift-off process by allowing photoresist remover to get underneath the metal pattern (**Figure 4.10**).

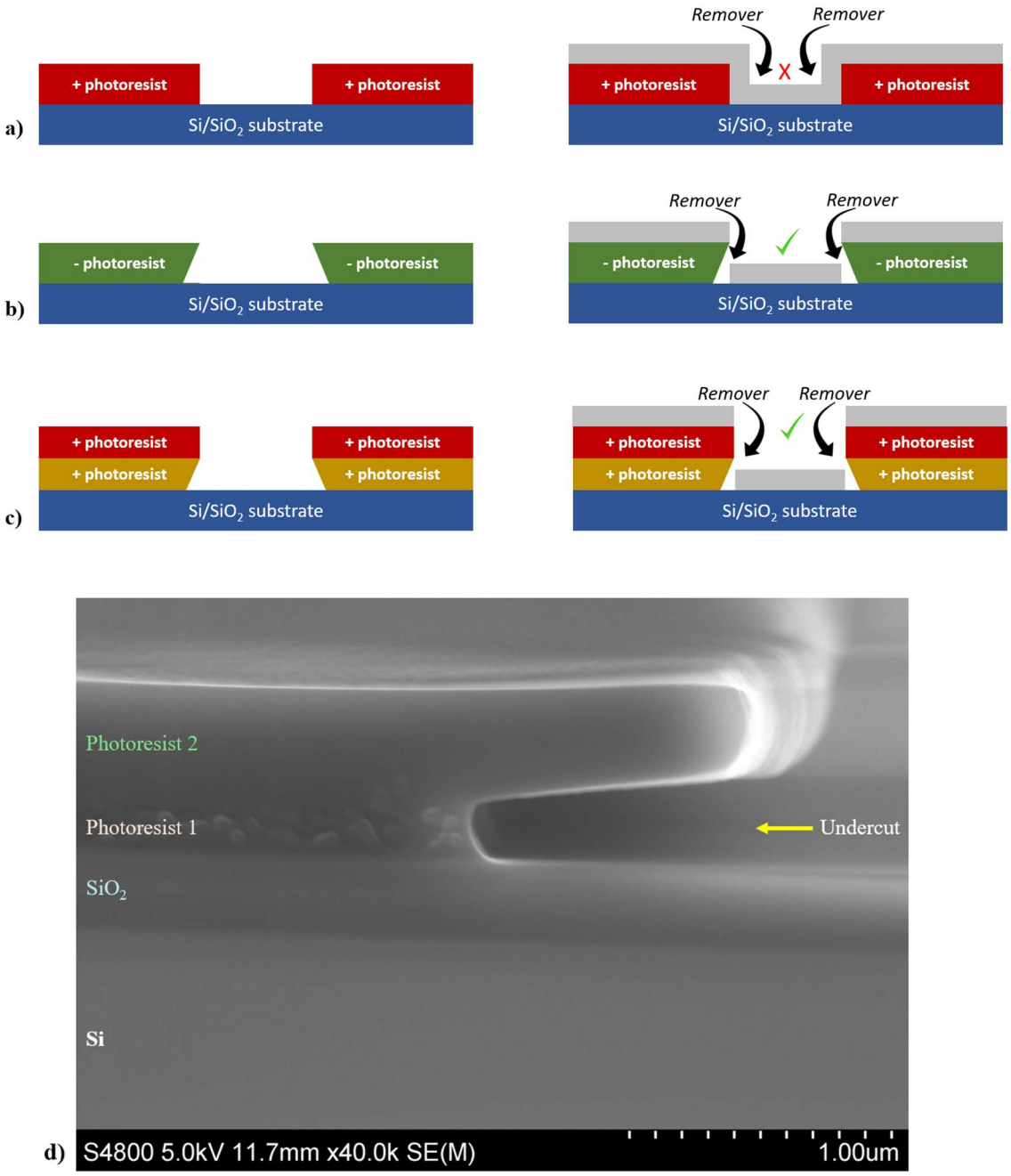


***Figure 4.10**: **(a)** The use of one positive photoresist and metal deposition (grey). Photoresist remover cannot penetrate underneath the metal layer, lift-off is unsuccessful. **(b)** Negative photoresist (green) forms an undercut allowing successful lift-off after metal deposition. **(c)** Bilayer photoresist consisting of two positive photoresists, the bottom forming the undercut. Photoresist remover can successfully get underneath excess metal, remove the photoresist, and perform lift-off. **(d)** SEM image of undercut formation.*

After spin coating, the wafers were placed in the mask aligner, using the same parameters as before, for the second exposure which patterns the metal tracks and contacts. The transparent regions on the second mask (shown in white in **Figure 4.11**) represent the pattern of the metal tracks and contact pads. As a positive photoresist

was used, the transparent regions will be solubilised and subsequently removed by the developer solution to allow for metal deposition.

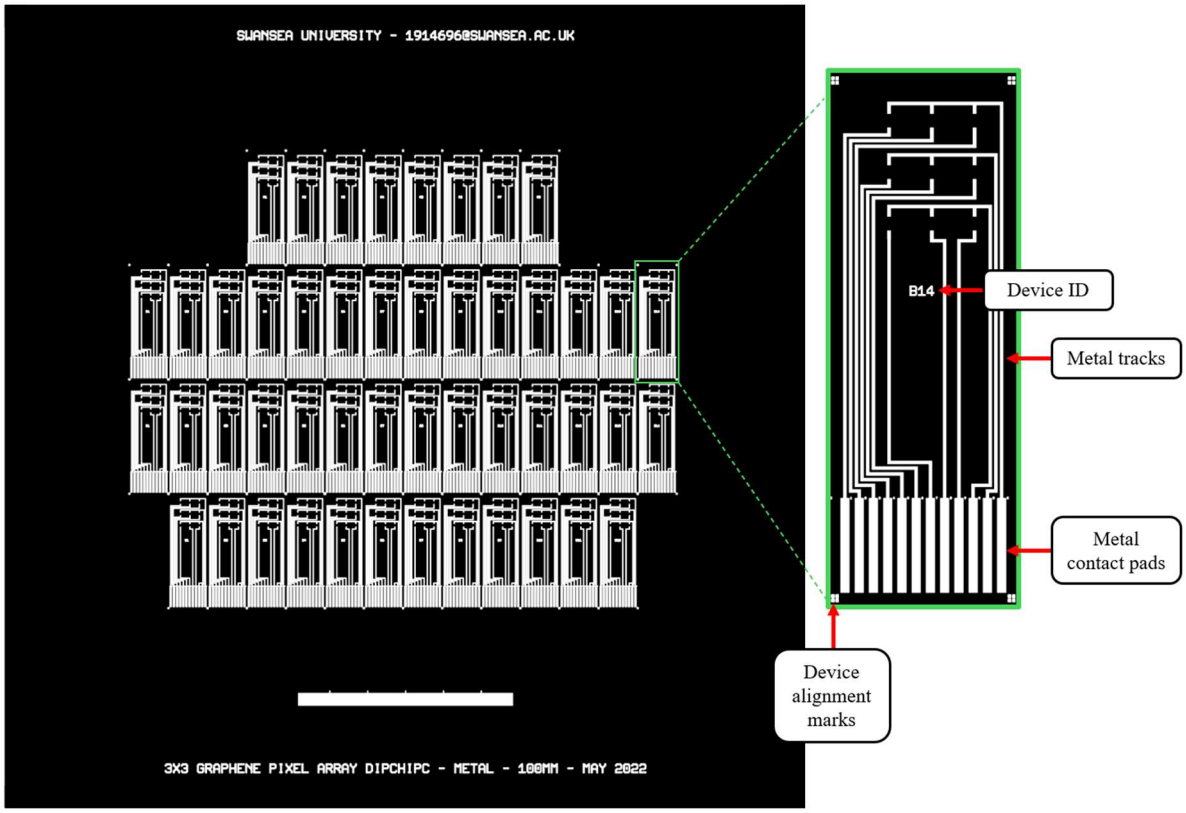


***Figure 4.11**: 5-inch chrome photomask design for the metal tracks and contacts for the '3x3 graphene pixel array' design (reproduced from JD Photo Data check plot). Black features represent the chrome.*

The chromium (30 nm)/palladium (200 nm) stack was deposited using a magnetron sputtering source in a Physical Vapour Deposition (PVD) system by Kurt J. Lester. After metal deposition, the wafer was placed in a beaker submerged in 1165 Remover on a hot plate at 60°C for 1 hour. The lift-off process was used to remove the excess metal from the wafer, leaving behind the patterned metal contacts and tracks. **Figure 4.12** below displays the wafer following metal deposition (left) and the same wafer submerged in remover during the lift-off process (right). Patterned metal tracks and contacts become visible as the excess metal is removed from the wafer.

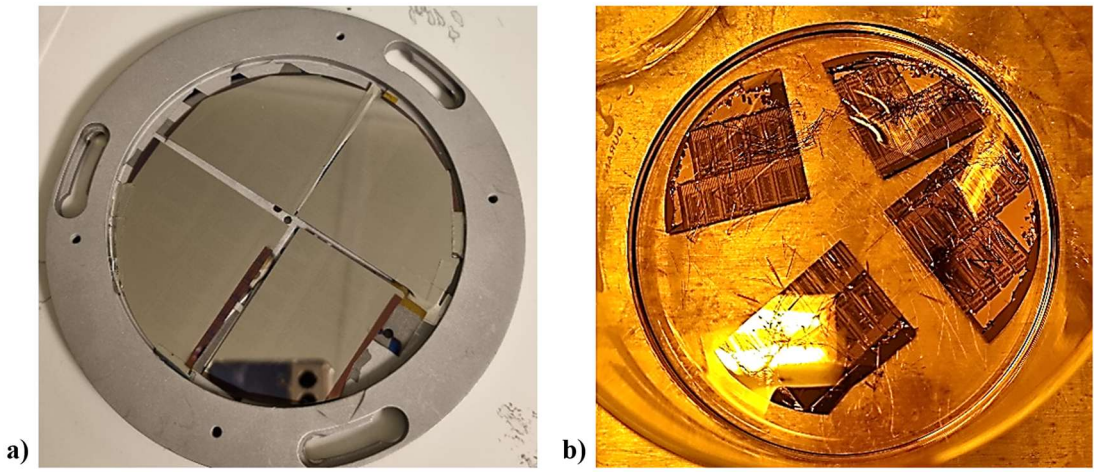


*Figure 4.12: Wafer fragments **(a)** in the PVD substrate holder post-metal deposition and **(b)** during the lift-off process.*

Following the lift-off process, wafers are examined under an optical microscope to ensure that all the excess metal has been successfully removed and identify any flaws or defects (**Figure 4.13**).

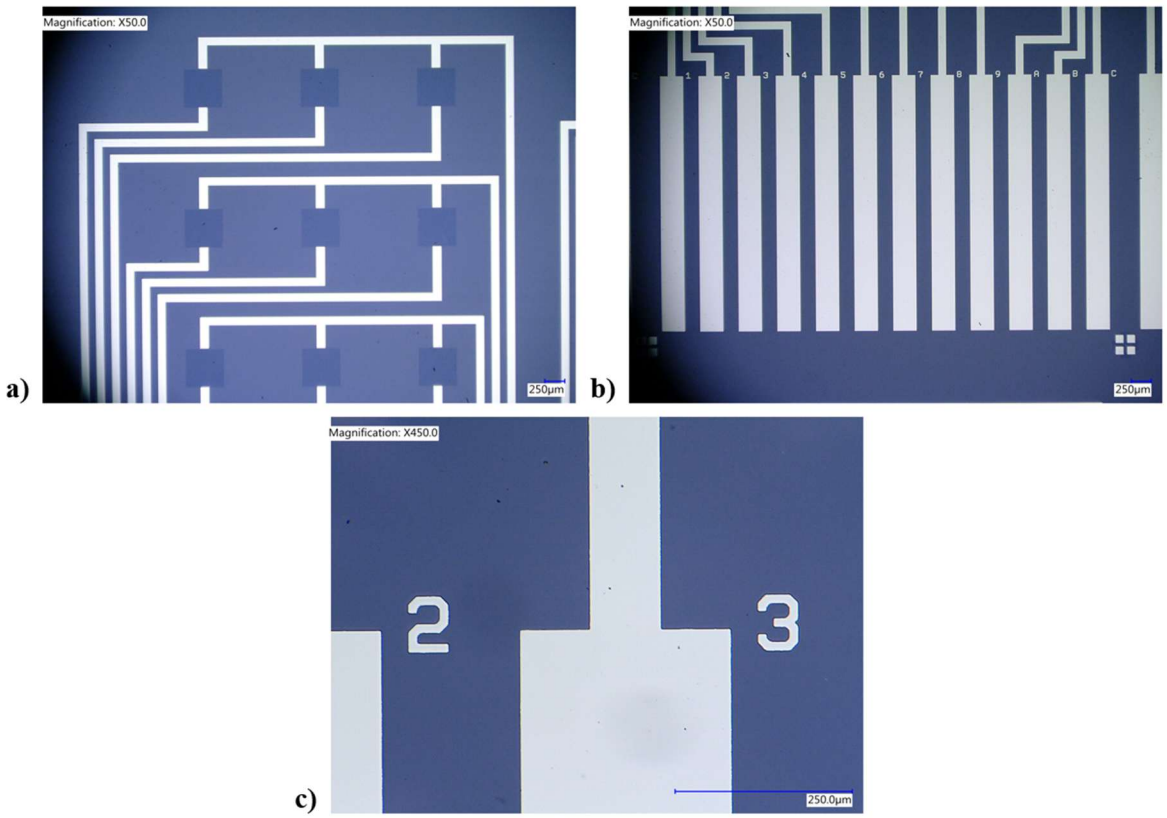


*Figure 4.13: Optical images of a graphene wafer following metal lift-off. **(a)** Graphene pixels and metal tracks, **(b)** metal contact pads and **(c)** identifying numbers on metal contacts.*

4.4.4. Passivation and Al_2O_3 Etch

Once lift-off was complete, the passivation layer, ~50 nm aluminium oxide (Al_2O_3), was deposited at 100°C using trimethylaluminium (TMA) and water vapour precursors using a SPTS MVD300 system [267]. This process covers the entire wafer, including all pattern features, in Al_2O_3. To enable sensing with the devices, it's necessary to etch passivation windows, revealing the graphene pixels and metal contact pads. After the deposition of the passivation layer, an adhesive layer, TI prime, and subsequently, a negative photoresist, nLof 2070 (thickness ~ 7 µm), was used to pattern the windows for the graphene pixels and metal contacts (**Figure 4.14**).

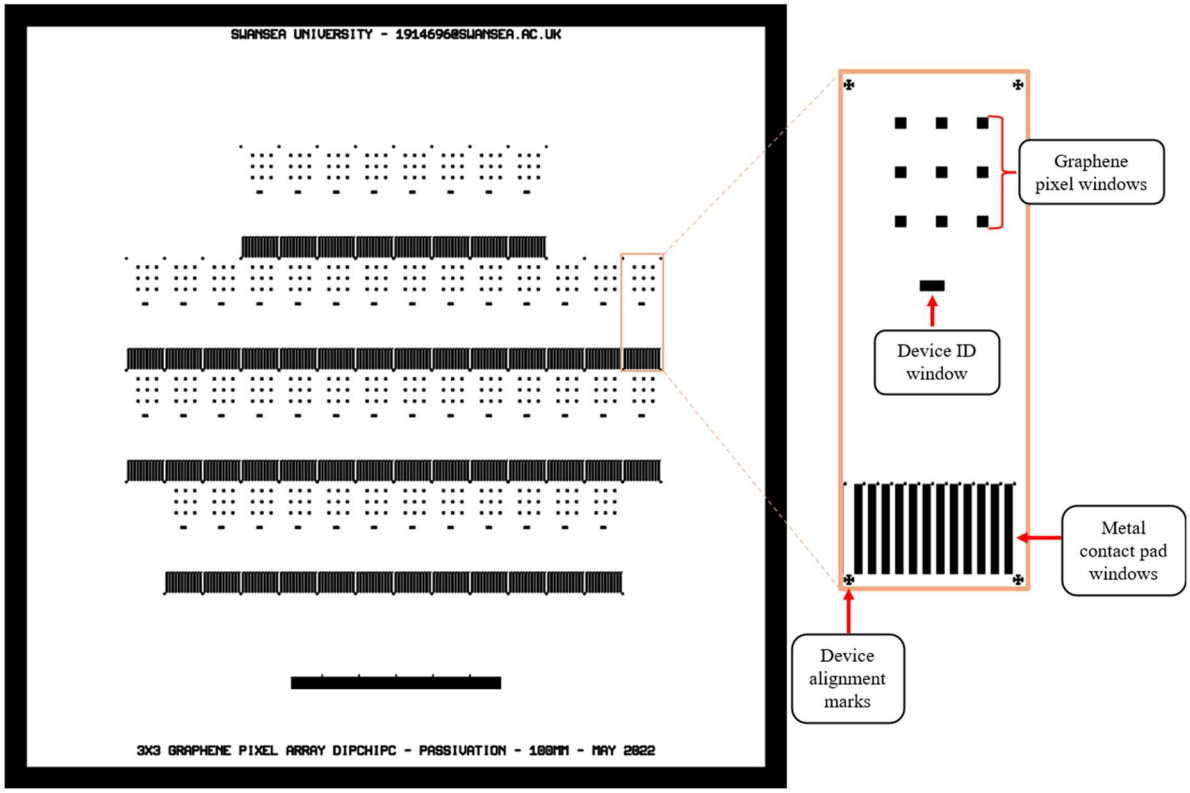


***Figure 4.14**: 5-inch chrome photomask design for the passivation windows for the '3x3 graphene pixel array' design (reproduced from JD Photo Data check plot). Black features represent the chrome.*

Spin coating parameters are as follows:

	TI Prime	**nLof 2070**
Time (s):	20.0	50.0
Spin speed (rpm):	4000	2500
Acceleration (rpm/s):	1000	700

After spin coating TI prime, wafers were cured on a hot plate at 120°C for 2 minutes. Once the wafers cooled down, they were spin coated with the nLof 2070 and placed on a hot plate for the soft bake (pre-exposure bake) at 100°C for 9 minutes. The wafers were exposed using the mask aligner 350mJ/cm^2 and subsequently placed on a hot plate for the hard bake (post-exposure bake) at 110°C for 3 minutes. As a negative photoresist was used this time, the transparent regions of the mask (shown in white in **Figure 4.14**) will allow UV through, making the photoresist underneath insoluble. The wafers were placed in AZ 726 Developer for 2 minutes. Once the development was complete, wafers were rinsed with IPA, dried with a N_2 gun, and then immersed in 1.25% tetramethylammonium hydroxide (TMAH) etchant for 35 minutes to remove the Al_2O_3, creating the passivation windows. Once the passivation windows had been etched, the wafers were immersed in NI555 Remover and placed on a hot plate at 80°C for 1 hour to remove the photoresist, revealing the completed graphene pixel array devices (**Figure 4.15**).

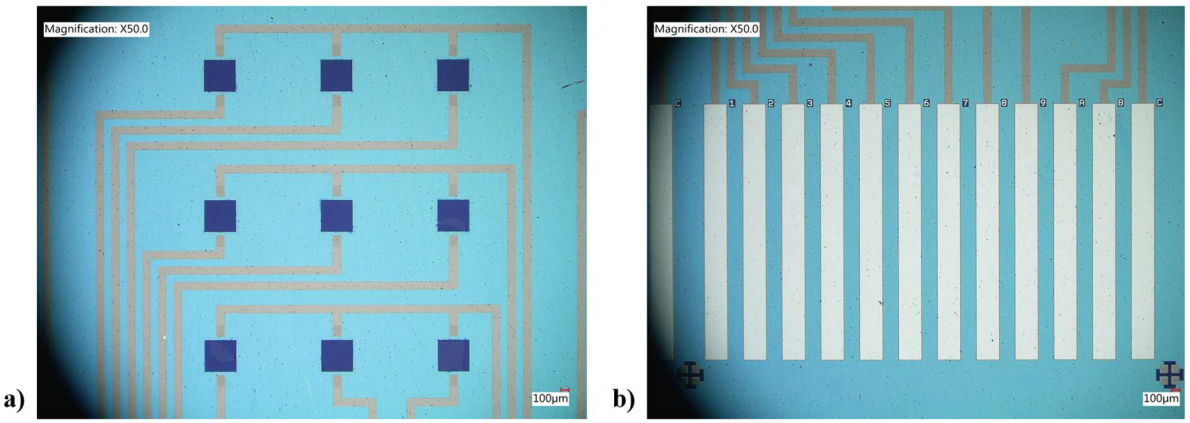
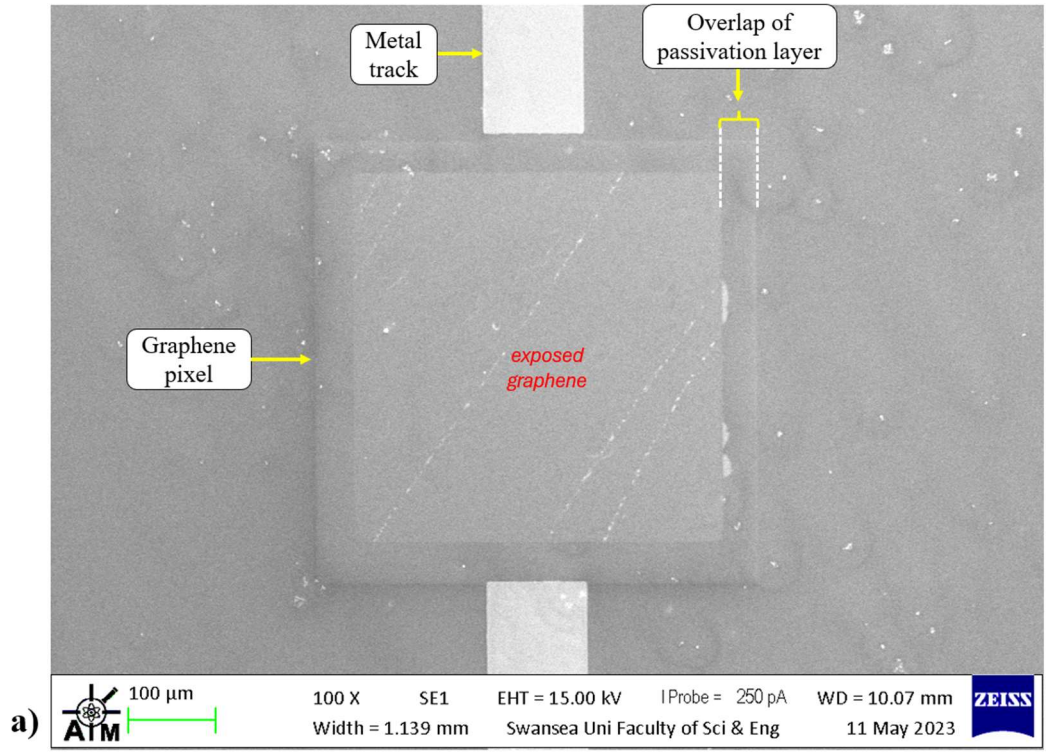


***Figure 4.15**: Optical images of a graphene wafer post-etch. **(a)** Graphene pixels and metal tracks and **(b)** Cr-Pd metal contact pads.*

The SEM images below (**Figure 4.16**) show the post-etch passivation windows on a graphene pixel and metal contact pads. The alumina passivation overlaps by ~100 µm on all sides of the graphene pixels and by ~20 µm on the metal contact pads. SEM images were obtained using a *Zeiss Evo LS25* scanning electron microscope (*Zeiss*, Germany) belonging to the *Advanced Imaging of Materials* facility (AIM) at Swansea University, UK.



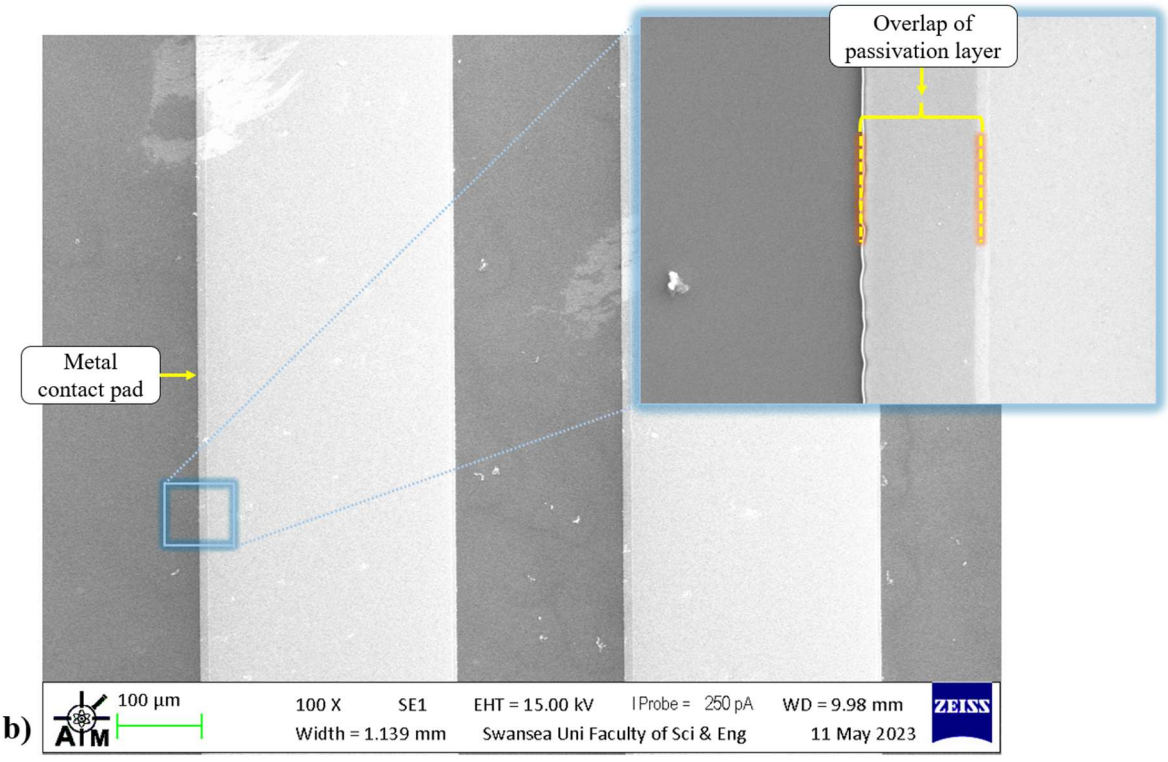


***Figure 4.16**: SEM images of a 3x3 graphene pixel array device demonstrating the passivation windows on a **(a)** graphene pixel and **(b)** metal contact pads.*

4.4.5. Resistance Measurements

Resistance measurements of all devices on the wafer were performed before and after passivation to verify the functionality of each device. For further information regarding how these measurements are taken, see **Chapter 3.5.1** (**Figure 3.21**).

Figure 4.17 demonstrates the change in resistance before and after device passivation (addition of Al_2O_3 layer). A small increase in resistance (~1.39 kΩ) of pixels is observed following deposition and etch of the passivation layer. The average resistance (excluding outliers) was 2.53 kΩ with a standard deviation of 0.43 and 3.92 kΩ with a standard deviation of 0.80 for graphene pixels before and after passivation, respectively. The change in resistance can be attributed to the slight n-doping effect of the Al_2O_3 passivation layer which was deposited directly on top of an already p-doped graphene [267], [271]. It is known that graphene deposited on SiO_2 is p-doped [101]; the addition of electrons from Al_2O_3 will effectively neutralize some of the positively charged holes. This process reduces the overall concentration of charge carriers available for conduction, leading to a decrease in conductivity. Although a passivation window was etched to expose the underlying graphene, a 100 μm overlap exists on all sides of the pixel to protect the metal-graphene interface.

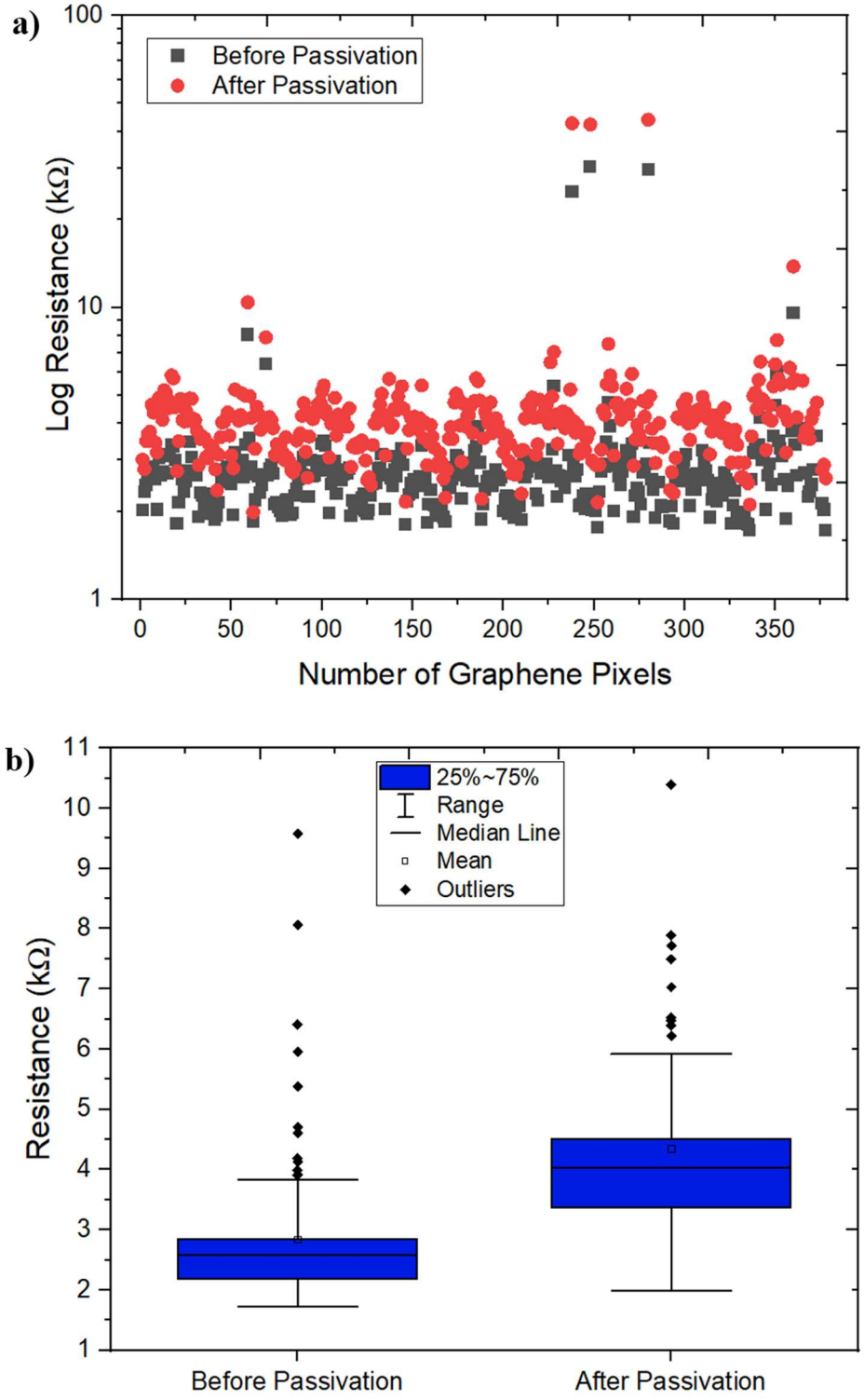


***Figure 4.17**: **(a)** Scatter plot of resistance (logarithmic scale) of graphene pixels pre- and post-passivation. **(b)** Box and whisker plot displaying the resistances of graphene pixels pre- and post-passivation. (Extreme outliers have been removed.)*

4.4.6. Wafer Dicing

The final step of the fabrication process involves sending the completed graphene wafers to be diced. As there was no equipment available on-site for dicing the wafers at the time, they were sent to *DISCO HI-TEC EUROPE GmbH* in Germany. **Figure 4.18** displays images of the wafers before and after dicing. Each 4-inch wafer yields 48 graphene pixel array devices, each measuring 18,100 µm x 6,200 µm.

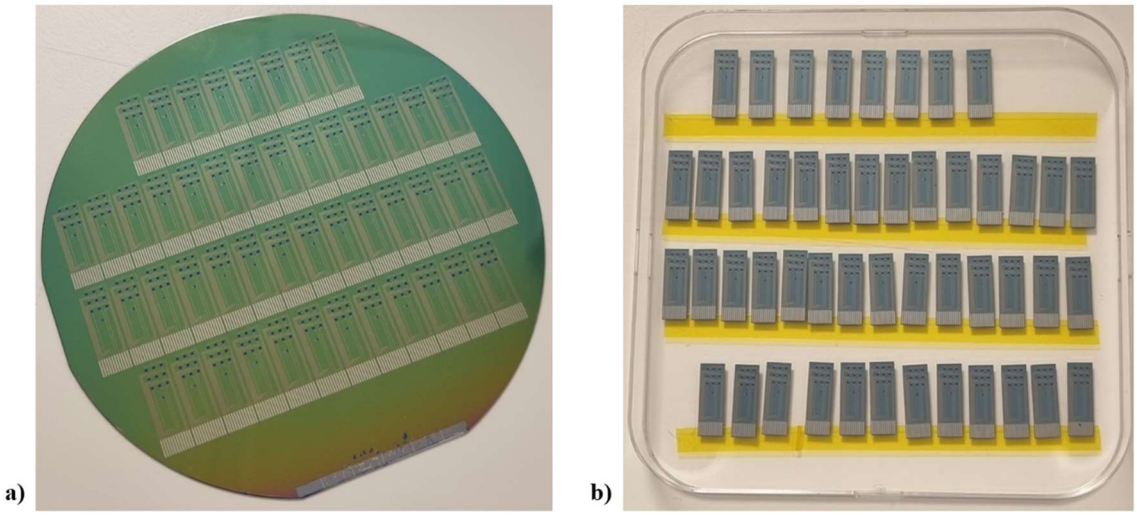


***Figure 4.18**: **(a)** 4-inch completed graphene pixel array wafer. **(b)** Diced graphene pixel array sensors.*

4.5. USB-C PCB Connector Design, Optimization and Limitations

The USB-C PCB connector played a vital role in enabling convenient, plug-and-play real-time resistance measurements of the 3x3 graphene pixel arrays to be performed. Its primary function was to establish a direct link between the gas sensing rig, electrical equipment, and each sensor. Each PCB connector consisted of a USB-C plug, 12-contact screw terminal and 4 mm x 25 mm standoffs (**Figure 4.19**). The PCB was designed to connect to each graphene pixel individually, allowing simultaneous resistance measurements of different pixels to be performed. Due to the absence of on-site facilities capable of producing a high-quality PCB connector, the connectors were designed and procured from an outside company (*Newbury Electronics*, UK).

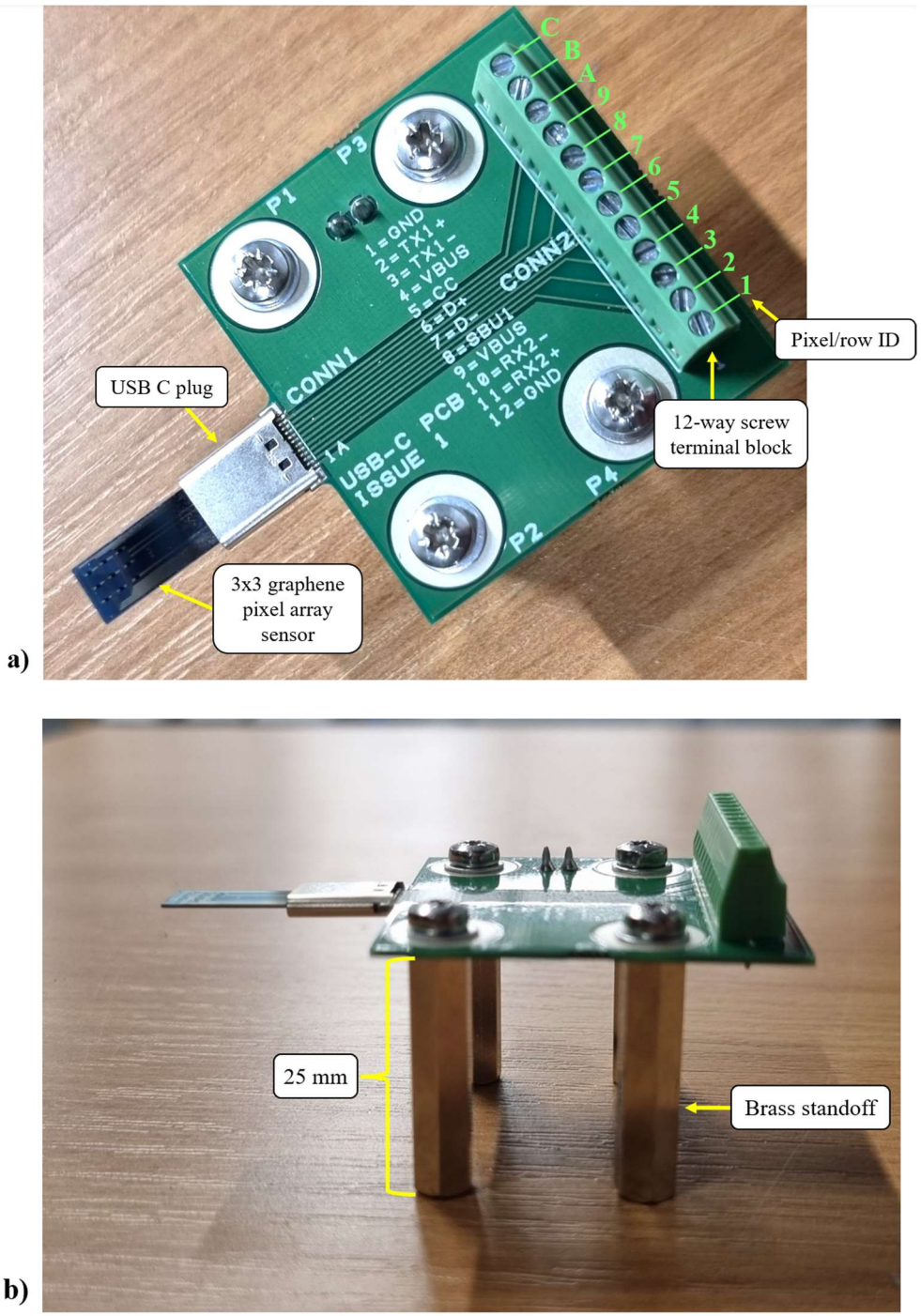


***Figure 4.19**: Images of the **(a)** top view and **(b)** sideview of the USB-C PCB connector.*

The connector underwent two revisions before achieving a dependable USB-C PCB design. In the initial iteration (as depicted above in **Figure 4.19**), the outer metal tracks served as grounds, rendering Pixel C1 redundant. Furthermore, inserting sensors into the USB-C plug proved challenging, resulting in damaged contact pins and device chips. Despite the expectation of a standard width between contact pins in USB-C

plugs from different manufacturers, variations were discovered (**Figure 4.20**). A second iteration of the USB-C PCB became imperative to address these issues.

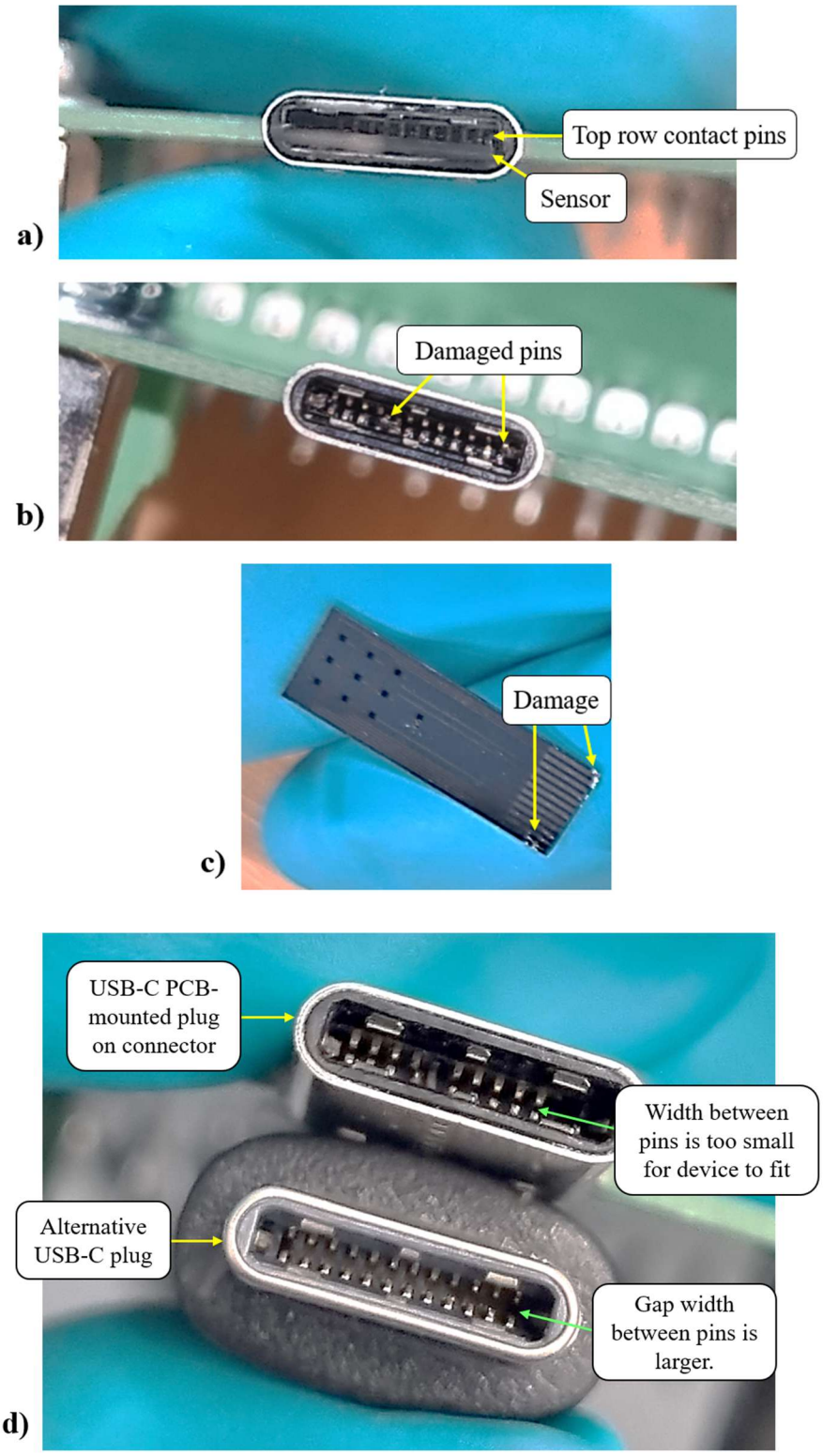


***Figure 4.20**: Images displaying the **(a)** graphene sensor slotted into the USB-C PCB connector, **(b)** damaged contact pins in USB-C plug, **(c)** damaged 3x3 graphene pixel array sensor and **(d)** variations in width between the contact pins of USB-C plugs.*

Given the unavailability of a suitable PCB-mounted USB-C plug, a USB-C female-to-male adapter with the correct dimensions was sourced to fit the sensors. This adapter allowed the sensors to slide in effortlessly without causing damage to either the device or the plug. Images of the adapter can be seen in **Chapter 3.5.3.2.**

Although the second iteration reallocated the outer metal tracks as signal pathways, a sensor design flaw was discovered upon further examination of the USB-C plug datasheet. Conventionally, standard USB-C plugs designate the outer contact pins as grounds, creating an impediment to measurements when these pathways are linked. Ultimately, this unforeseen complication rendered Pixel C1 ineffective for resistance measurements. Given the time constraints of the research scope, a sensor redesign was deemed impractical. Consequently, eight pixels were retained for real-time resistance measurements.

Table 11 provides a summary of the two distinct iterations and the corresponding modifications made.

***Table 11**: Iterations of the USB-C PCB connector, outlining challenges and solutions for each iteration.*

Iteration	Challenge	Solution
1	• Outer metal tracks on PCB designated as grounds.	• Designate outer metal tracks as signal pathways.
	• USB-C plug width not suitable for sensors, causing damage.	• Replace USB-C plug with an alternative.
2	• A suitable USB-C PCB-mounted plug cannot be sourced.	• USB-C female-to-male adapter employed.
	• USB-C plug outer contact pins designated as grounds.	• Sensor redesign (not performed).

4.6. Back-gated Measurements

As a two-dimensional material, graphene is highly sensitive to its surrounding environment, including surface adsorbates and molecules adsorbed onto the underlying SiO_2 layer [208]. These molecules can dope the graphene and affect its electronic properties. Doping shifts the Dirac point of graphene, with the direction of the shift depending on the type of dopant [95], [98], [272]. Consequently, the response of graphene sensors can vary due to these factors. Therefore, the ability to measure the Dirac point of individual graphene pixels on a device can provide valuable insights into their electronic properties and the type and level of doping each pixel is experiencing.

During the design and fabrication of the 3x3 graphene pixel array devices, the wafers (p-type doped silicon) were processed with the intent to create devices that did not require back-gated measurements, as no equipment was available to access the backside of the wafers without damaging the topside. Consequently, these devices were not originally designed for back-gated measurements. However, the backside of the wafer was plasma etched (through the backside oxide layer), making it possible to attempt these measurements in the future. **Figure 4.21** displays a cross-sectional schematic of the graphene transistor.

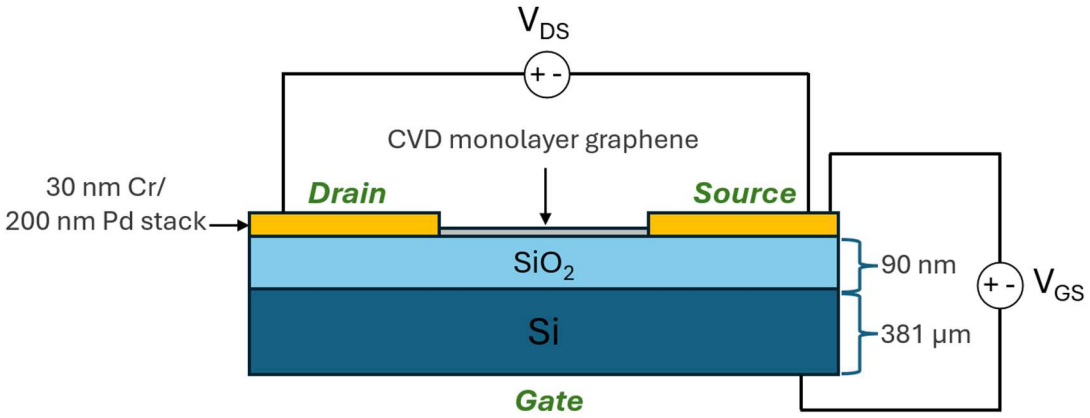


Figure 4.21: Cross-sectional schematic of the graphene transistor.

4.6.1. Electrical Measurements

Back-gated measurements on the 3x3 graphene pixel array devices were performed using a *Pegasus Semiautomatic S200FA-HV* Semi-automatic analytical probe station

and a *Keysight B1505A Power Device Analyzer/Curve Tracer*. Photos of the setup are provided in **Chapter 3.5.2** (**Figure 3.17**).

The electrical properties of the graphene pixels were measured by fixing the drain-source voltage (V_{DS}) at 1 V and sweeping the gate-source voltage (V_{GS}) from -50 to 50 V. Measurements were carried out under ambient conditions (temperature 20 °C, normal atmospheric pressure). **Figure 4.22** presents the attempted Dirac curve measurements on a single graphene pixel of a 3x3 graphene pixel array device.

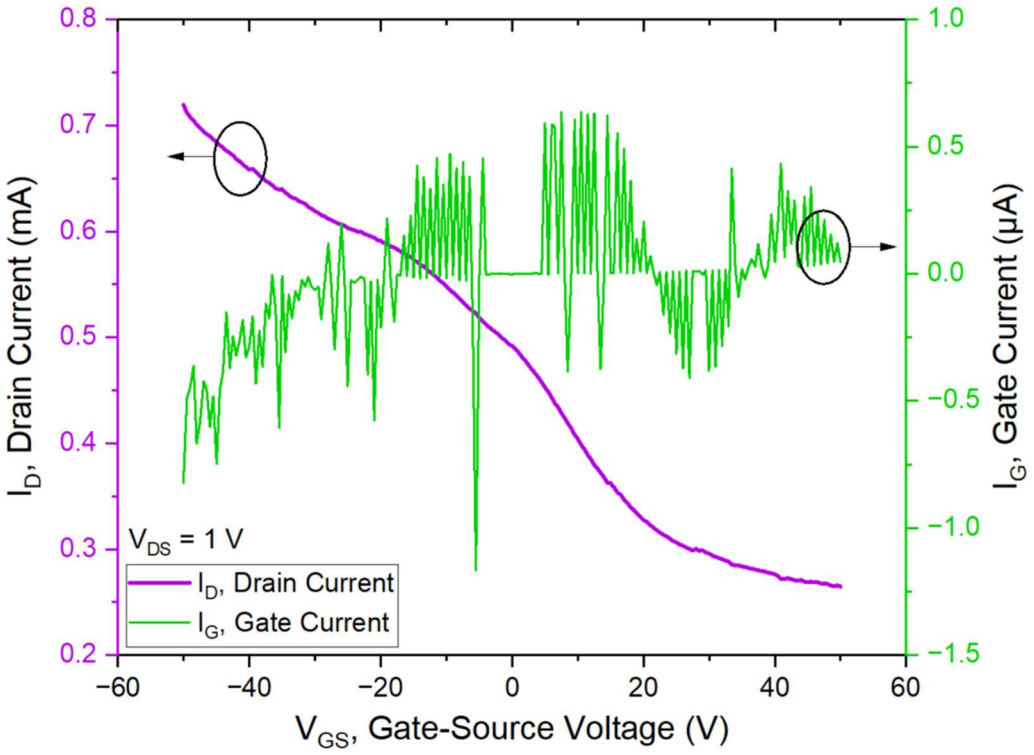


***Figure 4.22**: Dirac curve measurement (I_D-V_{GS}) of one graphene pixel on a 3x3 pixel array device, acquired by sweeping the gate-source voltage (V_{GS}) from -50 V to 50 V whilst fixing the drain-source voltage (V_{DS}) to 1 V.*

Figure 4.22 (I_D, purple line) depicts a trend similar to a Dirac curve measurement, with the notable exception of current recovery on the right side of the curve. The curve suggests that the Dirac point might be located between approximately 50 V and 60 V. The gate current (I_G, green line) indicates minimal current flow through the gate, with a slight spike around -5.5 V.

For comparison, **Figure 4.23a** presents a Dirac curve measurement from published literature. When compared with the experimental plot obtained in this study, some

similarities are observed. However, it is crucial to highlight that, despite the similar trends, the gate current in this work is higher (in the microampere range) than that reported in the literature, which was in the picoampere range (**Figure 4.23b**).

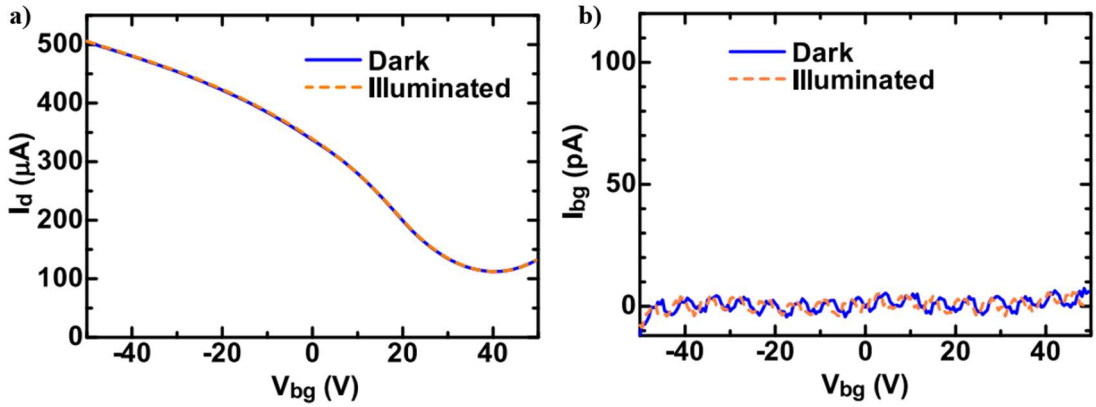


***Figure 4.23**: **(a)** Dirac curve measurement (Id-Vbg) and **(b)** substrate current (Ibg-Vbg) for p-type Si substrate graphene phototransistors in the dark and illuminated state. Where Id = drain current, Vbg = back gate voltage, and Ibg =back gate current. Reproduced from reference* [208].

To assess whether the suspected Dirac curve would recover beyond 50 V, the potential range was extended from -60 V to 60 V. **Figure 4.24** illustrates the Dirac curve measurement over this broader range. The gating response (ID-VGS) exhibits a similar trend to that in Figure 4.22. However, increasing the voltage to 60 V did not result in current recovery; instead, the current decreased further. Notably, the gate current (I_G, green line) shows an increase compared to the first test (**Figure 4.22**), with current spikes observed near both -60 V and 60 V. This increase in current suggests that the gate oxide (SiO_2) is undergoing stress and degradation, leading to increased current leakage from the gate.

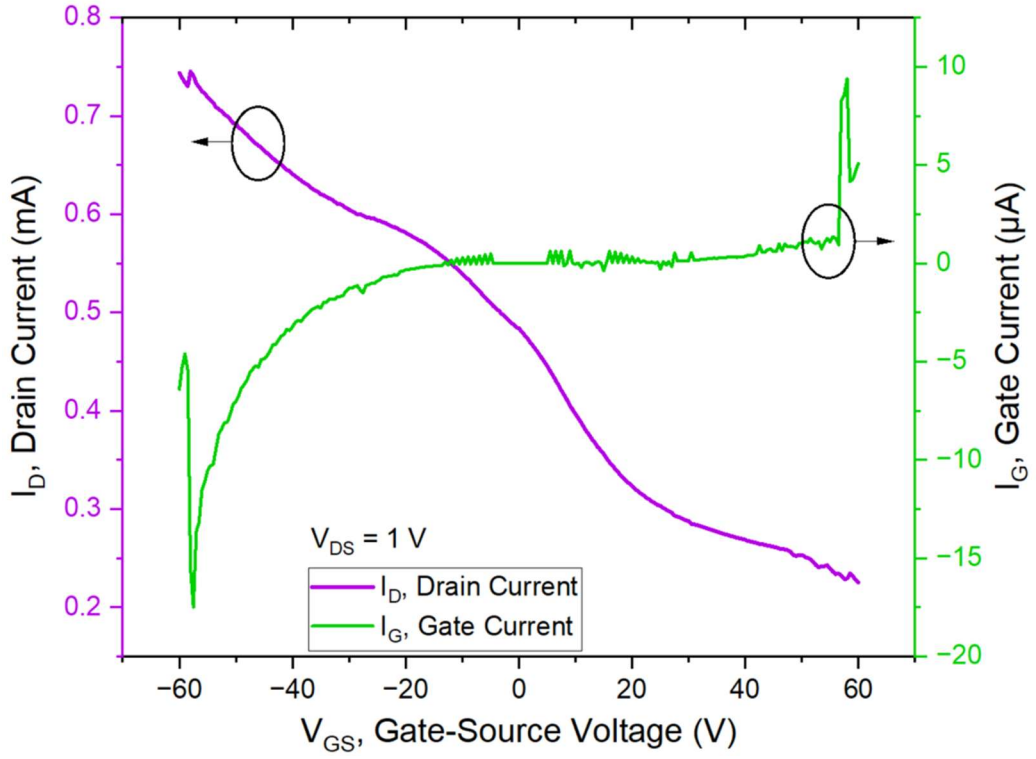


***Figure 4.24**: Dirac curve measurement (I_D-V_{GS}) of one graphene pixel on a 3x3 pixel array device, acquired by sweeping the gate-source voltage (V_{GS}) from -60 V to 60 V whilst fixing the drain-source voltage (V_{DS}) to 1 V.*

To further investigate whether the current would recover and reveal the Dirac point, the potential range was extended to -70 V to 70 V. However, the test reached the software compliance limit, which was set at a gate current of 1 mA, causing the test to fail. Subsequent attempts to reduce the potential range to -65 V to 65 V and finally back to -50 V to 50 V also exceeded the software compliance threshold, indicating potential breakdown of the gate oxide. Repeating these tests on two additional devices yielded similar results.

The inability to detect the Dirac point, along with the significant current flow from the gate, strongly suggests that the gate oxide has degraded. This implies that the 90 nm SiO_2 layer is too thin to support effective back-gated measurements, leading to vertical current leakage through the device. Although obtaining Dirac measurements was not feasible with these devices, and sensor redesign fell outside the time constraints of this research, these findings offer valuable insights for future device design. For instance, using a thicker oxide layer, such as 300 nm, may be more suitable for this application [98], [208].

4.7. Comparison of Sensor Performance Across Different Device Design

Using data collected from gas sensing experiments over the course of this research, a comparison of sensor performance across the three different device designs was explored. To evaluate performance, experiments with the same target gas exposure time (5-minute) and target gas concentration were selected. As ammonia is a reducing gas and readily donates electrons to p-type graphene (due to its placement on SiO_2 [97]), an increase in sensor resistance is expected [273]. In this scenario, donor electrons deplete the holes in the p-type graphene, reducing carrier concentration and thereby increasing resistance. **Table 12** summarizes the graphene channel dimensions, exposed area, SiO_2 oxide thickness and target gas concentration for the three devices.

***Table 12**: Summary of the graphene channel dimensions, exposed area and target gas concentration for comparison across the three unique device designs.*

Device	SiO_2 oxide thickness (nm)	Length (µm)	Width (µm)	Exposed area (µm²)	Exposed area (mm²)	Target gas: NH_3 (ppm)
DipChipX	300	700	100	70000	0.70	100
Pixel Array	90	400	400	160000	1.60	50 and 100
Hall Bar	300	980	250	245000	2.45	50

The exposed area was determined based on the theoretical dimensions of the wet-etched passivation window, as defined by the mask design.

$$Theoretical\ Exposed\ Area\ (A_p) = L_p\ x\ W_p$$

Where:

L_p = length of passivation window

W_p = width of passivation window

***Equation 8**: Exposed area calculation.*

The ‘area-specific response’, shown in the box chart below (**Figure 4.25**), was calculated as follows:

$$Area\ Specific\ Response = \frac{A_P}{Sensor\ response}$$

Where:

A_p = area of passivation window

***Equation 9**: Area-specific response calculation.*

Figure 4.25 suggests that a smaller graphene exposed area results in a higher area-specific response, indicating that the DipChipX devices exhibit the best performance in sensing ammonia. According to several studies, various factors can affect the electrical conductivity and, consequently, the sensor response of a graphene channel. These factors include geometry [274], [275], channel dimensions [223], [276], grain and grain boundaries [277]–[279], and underlying oxide thickness [223], all of which impact graphene's carrier mobility. However, in this situation, the increased sensor response in the smaller graphene channel might be attributed to the greater impact of the NH_3 dopant on the channel resistance due to the reduced surface area.

Although the initial investigation into sensor performance suggests that smaller graphene channels yield better performance and some observed phenomena in the literature can explain the demonstrated data, additional data is required to verify these results. Furthermore, the factors influencing graphene carrier mobility need to be evaluated and controlled to better assess the performance of the different device designs.

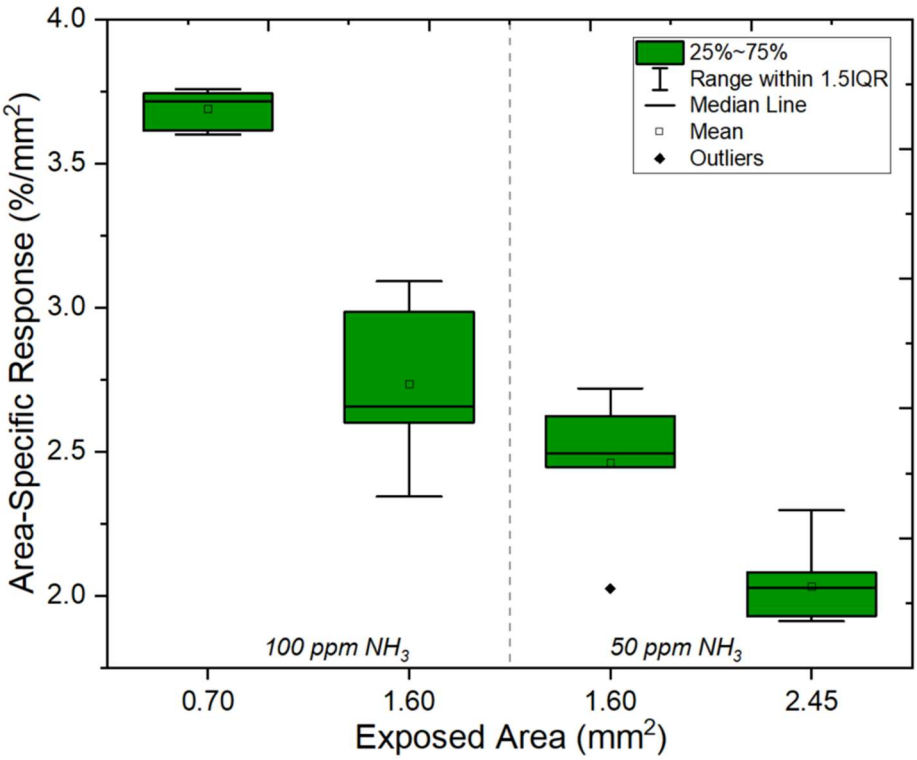


***Figure 4.25**: Box chart displaying the area-specific response versus the exposed graphene area for different devices.*

4.8. Device Aging and Impact on Sensor Performance

The lifespan of graphene sensors can vary depending on several factors such as their application, operational conditions, and the specific characteristics of the graphene material used [102], [280]. Due to graphene's exceptional mechanical strength and chemical stability [281], graphene sensors have the potential for a relatively long lifespan, similar to that of traditional sensors. However, their longevity can be influenced by factors such as exposure to harsh chemicals [282], mechanical stress [281], and electrical properties degradation over time [283].

Device aging of the 3x3 graphene pixel array devices was examined by comparing their gas sensing performance when exposed to 5 ppm nitrogen dioxide (NO_2) and 50 ppm ammonia (NH_3) over a 12-month period. The first sensing experiments with target gases were conducted approximately 9 months after the fabrication of the pixel array devices. This delay in testing was due to the development and optimization of

the gas sensing system (discussed in **Chapter 5**). After fabrication, the devices were stored in a vacuum desiccator; however, it should be noted that there was a 6-month period during which the vacuum pump was undergoing repairs, and the devices were kept at atmospheric pressure.

Figure 4.26 illustrates a significant decrease in sensor response to both gases over the period shown, with the response decreasing by 5.5% for NO_2 and 3.0% for NH_3 exposure. It is widely known that ambient air absorbates, especially water (H_2O), impact gas sensing performance [97], [98], [218], [270]. Doping species such as oxygen (O_2) and H_2O trapped at the graphene-substrate interface, as well as on the graphene surface, can significantly affect carrier mobility. Therefore, this suggests that the performance of the sensors degraded rapidly due to the devices being stored in ambient conditions instead of under vacuum. If the decrease in sensor performance is indeed attributed to ambient adsorbates, vacuum annealing may offer a reversible solution, as demonstrated in some studies [218], [256], [284]. Further investigation is necessary to confirm the source of the performance degradation and optimize the lifespan of graphene sensors.

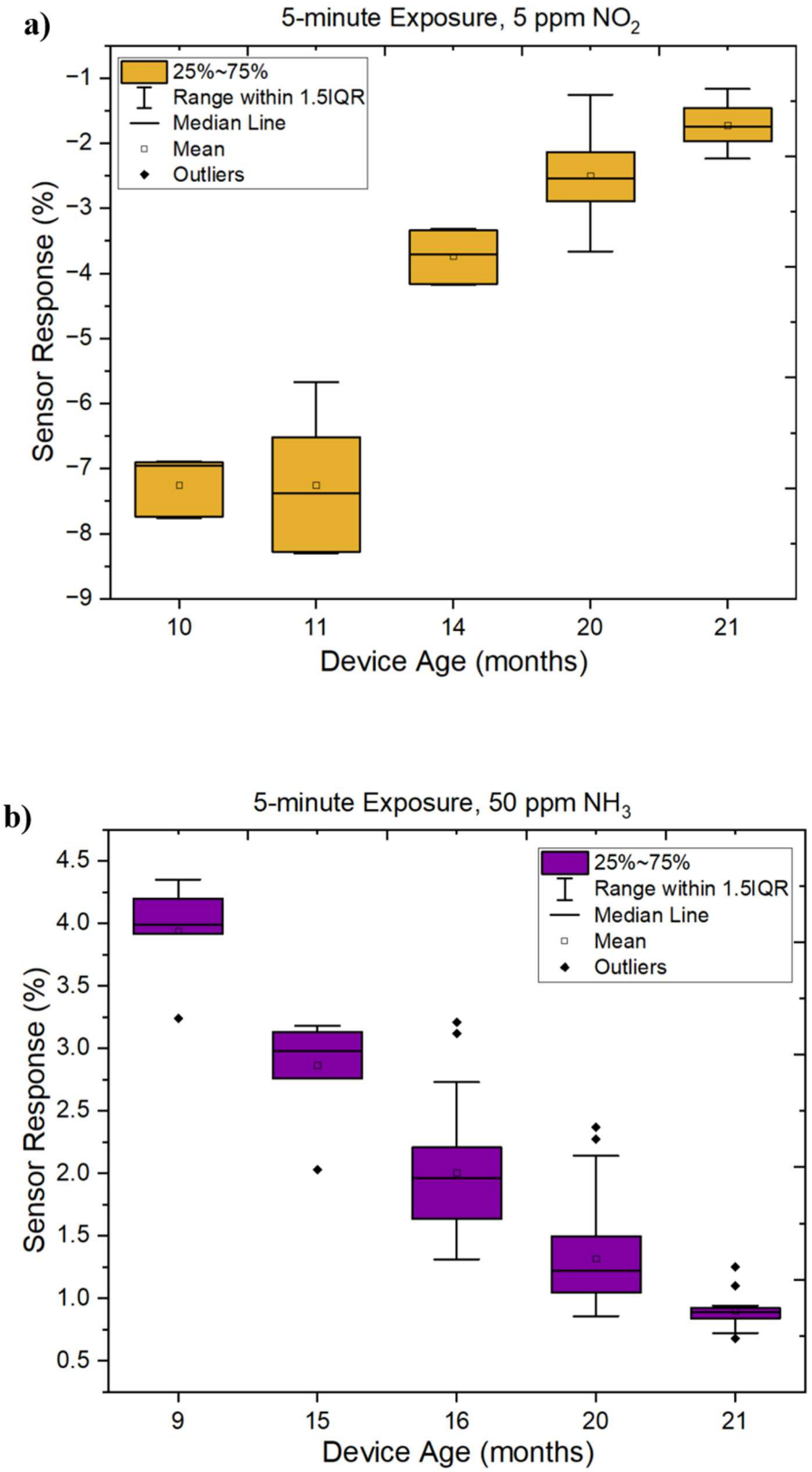


***Figure 4.26**: Box charts demonstrating the impact of device age on sensor response (%) for **(a)** 5 ppm NO_2 and **(b)** 50 ppm NH_3 for 3x3 graphene pixel array sensors.*

4.9. Conclusions and Future Work

In this chapter, the design and fabrication of the 3x3 graphene pixel array device were discussed. The fabrication process for graphene sensors was established by previous PhD students, and the same procedure was used to fabricate the 3x3 graphene pixel array devices. Fabrication of graphene sensors involves three main steps: (1) graphene patterning, (2) metal deposition, and (3) passivation. Resistance measurements conducted before and after passivation show a small average increase of 1.39 kΩ across the pixels, likely attributed to doping from the deposited Al_2O_3 passivation layer.

The sensor array, consisting of nine 400 μm x 400 μm graphene pixels, was designed to explore the potential of multiplexing, aiming to create more reliable and accurate sensors capable of detecting multiple gases simultaneously. Integration of USB-C style contact pads on the sensor, in conjunction with the USB-C PCB connector, facilitates straightforward plug-and-play real-time resistance measurements. During the optimization of the USB-C PCB connector, a design flaw was identified that rendered one graphene pixel unusable. Future sensor designs should carefully consider the type of connector or plug used to prevent similar issues.

Due to limitations in the available fabrication equipment, the 3x3 graphene pixel array devices were not originally intended for back-gated measurements. Nevertheless, the possibility of conducting such measurements was facilitated through etching on the underside of the wafers. The thin SiO_2 layer (90 nm) prevented measurement of the Dirac point due to suspected current flow through the gate. Incorporating a thicker SiO_2 layer in future designs may enable back-gated measurements, offering valuable insights into graphene's electronic properties and doping levels.

The sensor performance was assessed across various device designs used in this research. Initial results show that the DipChipX sensor, which features the smallest graphene channel, exhibited the best performance in ammonia sensing. This improvement is likely due to the increased impact of NH_3 doping on the smaller surface area of the channel. Smaller graphene channels have a higher surface-to-volume ratio, making them more responsive to minor changes in the surrounding environment [6], [185]. Additionally, these smaller channels often possess a higher proportion of edge sites and localized defects, which are more reactive than the basal

plane of graphene. These reactive sites enhance the sensor's sensitivity by providing additional adsorption sites for target molecules [285].

Moreover, various factors such as grains/grain boundaries [277]–[279], domain size, geometry [274], [275], channel dimensions [223], [276], and oxide thickness [223] can influence graphene's carrier mobility and, consequently, sensor response. Further measurements are necessary to validate these findings, maintaining constant oxide layer thickness and similar graphene quality while controlling gas concentration and exposure time.

Lastly, the impact of device aging on the 3x3 graphene pixel array's sensor performance was investigated over a 12-month period. Significant degradation was observed, with sensor responses to NO_2 and NH_3 decreasing by 5.5% and 3.0%, respectively. Ambient conditions during storage likely contributed to this degradation, affecting carrier mobility through doping by O_2 and H_2O. This underscores the critical importance of proper storage conditions to minimize the influence of ambient air absorbates and sustain optimal sensor performance. Further comprehensive studies are recommended to validate these hypotheses and explore the operational lifespan of graphene sensors.

Chapter 5 : Gas Sensing System

5.1. Introduction

The following chapter describes the development and optimization of a gas sensing system used to perform the electrical testing of sensors. The gas system developed is a completely new facility for the research group and have been created as part of this thesis. Requirements for the new gas sensing system and shortcomings of the systems used prior to the development of the final system are discussed.

5.2. Gas Sensing System Requirements

To measure the gas sensing performance of 3x3 graphene pixel array sensors, specific requirements were essential for the gas sensing system. **Table 13** provides a summary of these requirements along with their justifications.

Table 13: Gas sensing system requirements and justifications for testing 3x3 graphene pixel array sensors.

System Requirement	Justification
Sealed sensing chamber	Vacuum-compatible and facilitates flow-through testing at a constant flow rate.
Reasonably sized sensing chamber	The chamber must accommodate the sensor, sensor connector, and sensor recovery aids (e.g., UV light, heater, etc.).
Vacuum capability	Essential for reducing humidity within the sensing chamber and/or serving as a recovery aid.
Mass Flow Controllers	Enable precise control and measurement of gas flow into the sensing chamber, ensuring accurate gas dilution capabilities.
Pre-mixing of gases prior to entering the sensing chamber	Facilitates gas dilution and ensures precise concentration control before entering the chamber.
Low-noise data acquisition	Essential for detecting lower concentrations accurately.
Electrical equipment capable of real-time simultaneous measurement across multiple graphene channels	Essential for the new sensor design featuring a 3x3 graphene pixel array with 9 individual channels.

Gas sensing measurements were conducted using several developmental gas sensing systems, with each successive system designed to address the shortcomings of its predecessor. The iterative development of these gas systems included:

1) Glass Jar
2) Flow-through Gas System
3) Gas Sensing Rig

These systems are described in detail below.

5.3. Phase 1 Iteration: Glass Jar

Initial testing was performed in a glass jar with a removable glass lid containing feedthrough ports, which was clamped onto the jar using a metal clip (**Figure 5.1**). Electrical connections and gas piping inlets were fed through small holes in the rubber septa on the lid. The laboratory used had the necessary infrastructure and safety facilities for the supply of gases such as nitrogen (N_2), carbon dioxide (CO_2), and argon (Ar). Crocodile clips were used to electrically connect to the pins on the connector. These connections were attached to header pins on the sensor connector, allowing it to hang within the sensing chamber. Details on the *Biovici* 'Sensor-Connect' connector are provided in **Chapter 3.5.3.1** (**Figure 3.19c**).

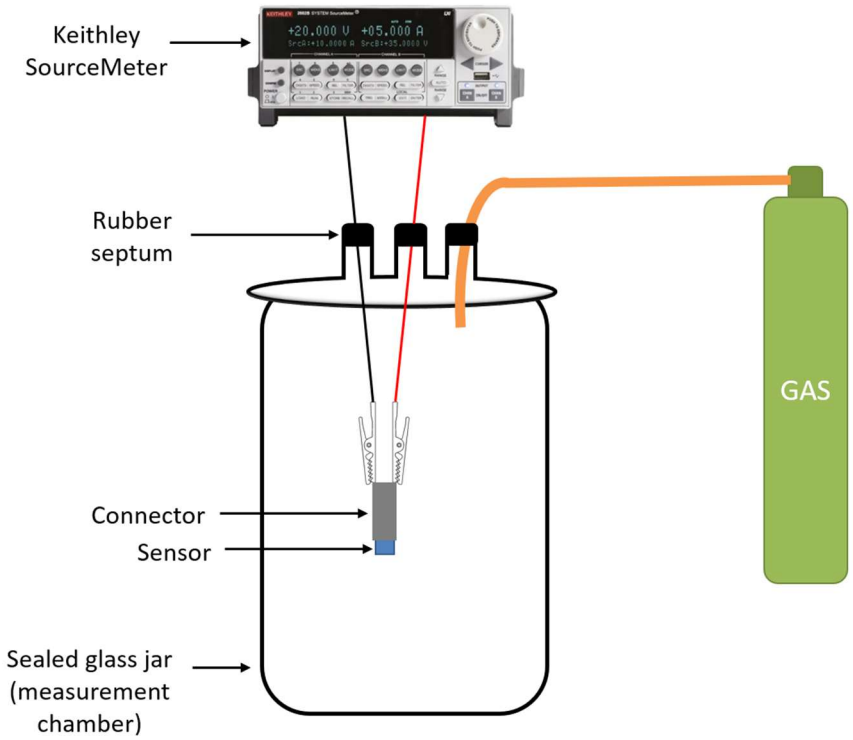


***Figure 5.1**: Schematic of the glass jar gas sensing system.*

Multiple repeat measurements were taken using N_2 and CO_2 gases to assess the integrity and viability of the system. Each test was performed using real-time electrical measurements by applying a voltage bias of 40 mV using a *Keithley 2612B SourceMeter* and measuring the current using *TSP Express* software.

Sensing was initially performed using pristine (bare) graphene 3-channel 'DipChipX' sensors. Although three graphene channels are present on these devices, only one can be measured in real-time with this configuration. The sensor's resistance changed (see **Figure 5.2**) when nitrogen gas was introduced into the sensing chamber. Although the electrical signal is noisy, a stepwise trend is observed upon each successive exposure to nitrogen.

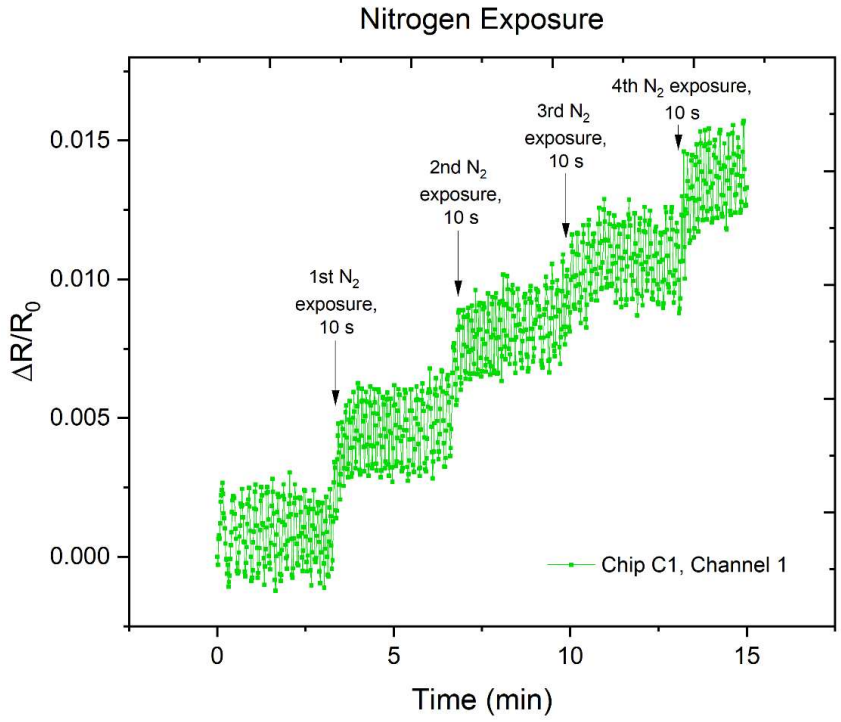


***Figure 5.2**: Nitrogen gas exposure in glass jar using a bare graphene DipChipX device.*

This experiment was repeated using CO_2 instead of N_2 gas and using a new pristine graphene DipChipX sensor. Comparable to the previous data set, a stepwise trend is evident with each successive exposure to carbon dioxide gas in the sensing chamber (**Figure 5.3**). Subsequent measurements with both nitrogen and carbon dioxide gases using the Phase 3 iteration of the gas sensing system would suggest that the sensors do not respond to these gases. The observed response was likely due to the gas exposure process itself, such as the release of gas into the chamber, rather than any specific reaction to N_2 or CO_2. This effect could be attributed to the physical pressure change in the chamber, as there is no exhaust. Measurements using N_2 and CO_2 in the

Phase 3 configuration are discussed further in **Section 5.6.1** (N_2) and **Chapters 6.7.2** and **1** (CO_2).

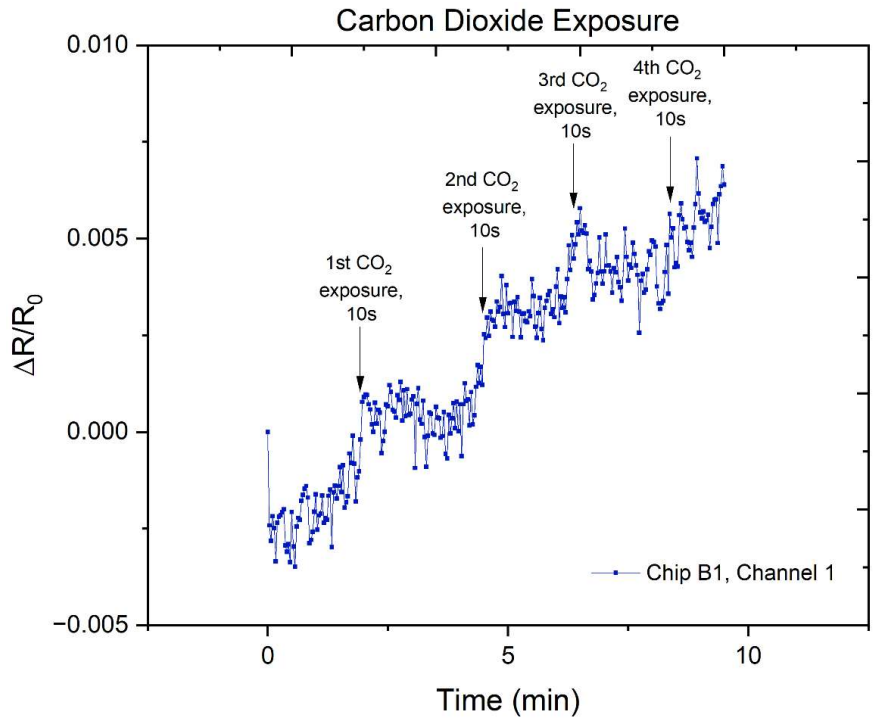


***Figure 5.3**: Carbon dioxide gas exposure in glass jar using a bare graphene DipChipX device.*

5.3.1. System Limitations

Despite the convenience and ease of setup offered by the glass jar, it became evident that a more dependable and controllable method for conducting gas sensing experiments was imperative. The sensing chamber proved impractical due to persistent leaking issues and would not be compatible with a vacuum setup. Additionally, the absence of an exhaust system resulted in pressure buildup within the jar, leading to uncontrollable leaks through the seals. Moreover, the unavailability of mass flow controllers necessitated the use of a plumbed gas supply, resulting in unpredictable gas flow into the jar. Furthermore, the limitations of the setup restricted real-time sensing to only one channel and produced noisy data, further highlighting its unsuitability for gas sensing experiments. The limitations of the glass jar would not offer the required sensitivity and ability to differentiate between various gases, making it unsuitable for future experiments. **Table 14** summarizes the limitations of this system and the necessary requirements to perform gas sensing experiments.

***Table 14**: The limitations, challenges, and necessary requirements of the gas sensing system.*

Limitation	Challenge	Requirement
Sensing chamber	Poor seal (leaking)	Sensing chamber should be sealed effectively to prevent gas leaks
Electrical feedthrough	Only 4 ports in the lid – no option to expand.	Electrical feedthrough large enough to support the simultaneous measurement of nine graphene pixels. Additional feedthrough required for UV light/heater.
Vacuum capability	With the current setup, this is not possible.	Capability for static (vacuum) and dynamic (flow-through) sensing conditions
Mass Flow Controllers	Communal plumbed gas supply, unable to modify.	Controllable flow of gases into sensing chamber.
Pre-mixing of gases prior to entering sensing chamber	Single chamber glass jar and plumbed gas supply, unable to modify.	Facilitates gas dilution and ensures precise concentration control before entering the chamber.
SourceMeter	Only two measuring units available per SourceMeter	Electrical measurement system that enables the simultaneous, real-time measurement of nine graphene pixels
Electrical signal	Noisy data	Optimal signal-to-noise ratio to enable detection of low gas concentrations

5.4. Phase 2 Iteration: Flow-through Gas Sensing System

A purpose-built gas sensing system located at Bay Campus, Swansea University, was sourced from Dr. Thierry Maffeis' research group. This system was tested with the DipChipX devices to evaluate its feasibility for gas sensing experiments.

5.4.1. System Components

This system consisted of four *Aalborg* Mass Flow Controllers (MFCs), relays, an *Arduino* microcontroller, *Keithley 6487* Picoammeter/Voltage Source and a system of ¼" stainless-steel and flexible tubing all connecting to the gas cylinders. *LabVIEW* software was used to control the gas sensing system. A diagram of the system is shown below (**Figure 5.4**).

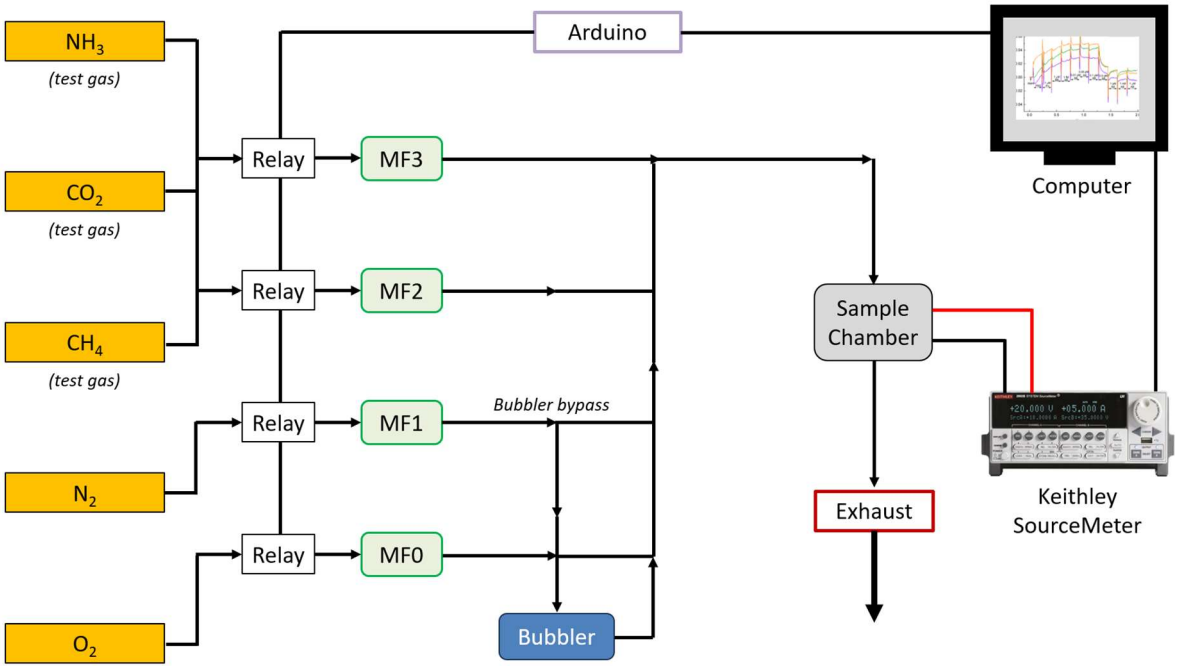


***Figure 5.4**: Schematic of the flow-through gas sensing system.*

The sensing chamber was a KF-25 stainless-steel tube (25 mm inner diameter) that the sensor, connector, and an electrical feedthrough snuggly fit into (**Figure 5.5**). Sensing was performed using the 3-channel DipChipX design. However, with this configuration, only one channel could be measured at a time due to the SourceMeter having a single measurement unit. Sensors were slotted into a custom electrical connector supplied by *Biovici Ltd* and wires were soldered onto the header pins that connected to the channel being tested. The wires were fitted with mini crocodile clips on the opposite end and clamped onto the electrical feedthrough.

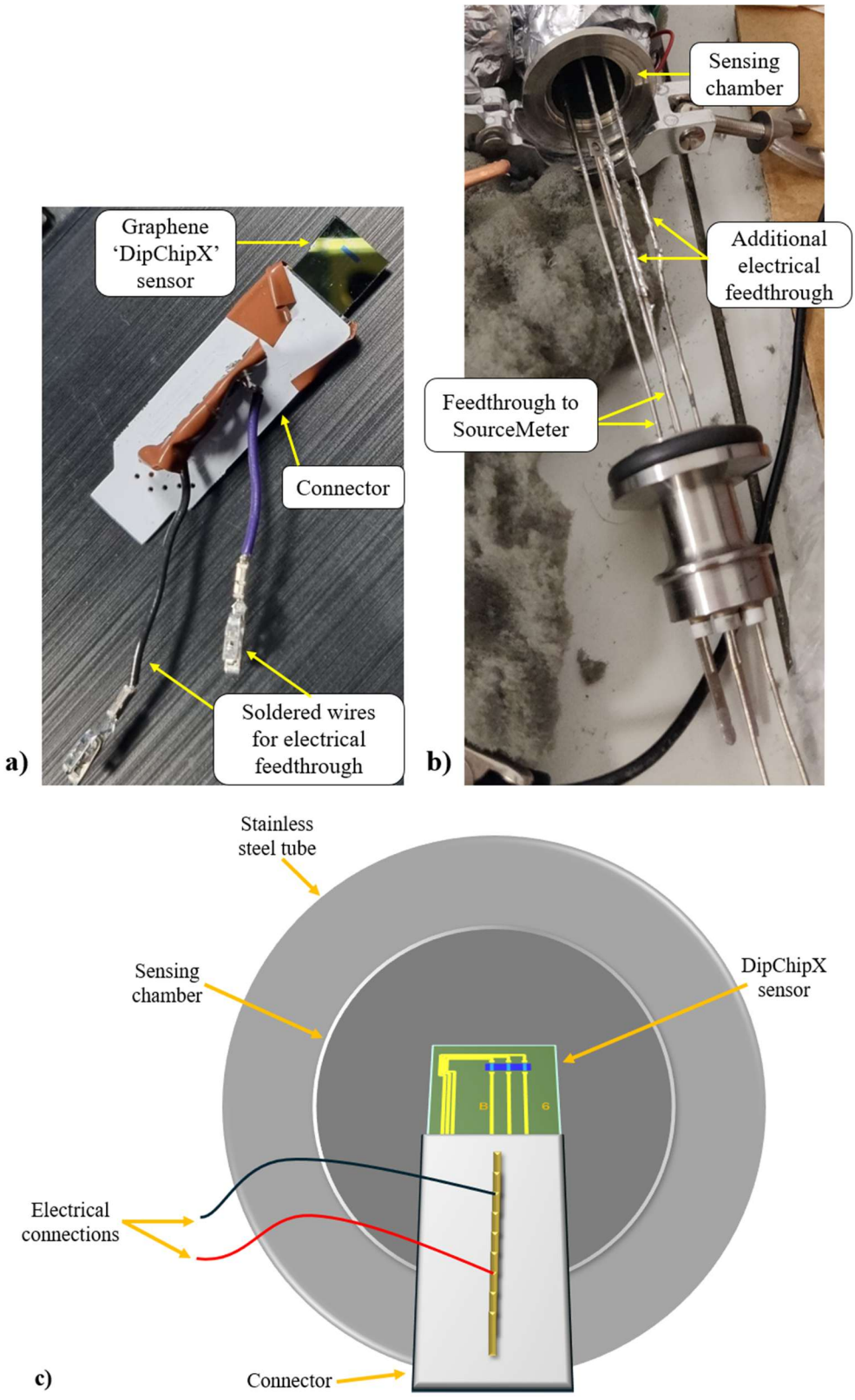


***Figure 5.5**: **(a)** DipChipX sensor slotted into custom-made Biovici connector. Wires soldered to 'Channel 1' header pins and metal areas covered in electrical tape to prevent shorting inside chamber. **(b)** Electrical feedthrough; **(c)** Schematic of the DipChipX sensor inserted into the connector inside the 25 mm stainless steel tube sensing chamber.*

5.4.2. Operation

There were three types of MFCs used on the system with different flow ranges: 0-10 mL/min, 0-100 mL/min and 0-1000 mL/min. This allowed the gases to be mixed in various ratios for testing. The stainless-steel tubing connected to each MFC merged, allowing the gases to mix prior to entering the sensing chamber. The Arduino microcontroller switched the relays connected to the MFCs ON/OFF according to the programme set by Lab VIEW. Experiments were set up by filling in various rows on LabVIEW interface, indicating the duration (Time(s)), the flow rates (MFC_0, MFC_1, MFC_2 and MFC_3) for the various gases, selected relays (REL_0 to REL_9), and voltage bias (1V used for all experiments).

5.4.3. Experimental Set-up

A typical experiment on this gas sensing system would utilize three MFCs: nitrogen (N_2), oxygen (O_2) and nitrogen + test gas (N_2 + test). Nitrogen and oxygen gases would be mixed in a ratio of 80/20 respectively to mimic ambient air composition, with a total flow rate of 1000 mL/min. Nitrogen and oxygen 80/20 was always used at the beginning and end of the experiment to establish a baseline and to reduce noise and drift.

Test gases included: 1000 ppm nitrogen dioxide (NO_2) in nitrogen, 1000 ppm ammonia (NH_3) in nitrogen and 1000 ppm methane (CH_4) in nitrogen (these gases were chosen by the research group who owned the system). The gases were all premixed and provided in gas cylinders by BOC. When a test gas was introduced, the flow rate was subtracted from the flow of nitrogen to ensure the total flow rate remained constant at 1000 mL/min. Below is an example of a typical LabVIEW setup (**Table 15**). The 80/20 N_2/O_2 would flow into the chamber at 1000 mL/min for 10 minutes. Next, the test gas flow would begin, and the flow of nitrogen would be decreased accordingly to ensure a total flow rate of 1000 mL/min. Finally, the test gas flow would cease and 80/20 N_2/O_2 would resume at 1000 mL/min to establish a baseline and flush any test gas from the chamber.

Table 15: Duration, flow rates and concentration of test gas for a typical experiment using the flow-through gas sensing rig.

Time (s)	N_2 (mL/min)	O_2 (mL/min)	N_2 + 1000 ppm test (mL/min)	Calculated concentration test gas (ppm)
600	800	200	0	-
600	700	200	100	100
600	800	200	0	-

5.4.4. System Limitations

Although this system was automated and enabled gas sensing measurements to be performed on the graphene sensors, there were several limitations. **Table 16** provides a summary of the system's limitations, the challenges it posed, and the requirements necessary to accomplish gas sensing for this researcher's thesis.

Table 16: The limitations, challenges, and necessary requirements of the gas sensing system.

Limitation	Challenge	Requirement
Sensing chamber	Too small – only enough space for the sensor and connector to fit.	Sensing chamber large enough to fit a UV light/heater.
Electrical feedthrough	Too small – only contained two electrical connections	Electrical feedthrough large enough to support the simultaneous measurement of nine graphene pixels. Additional feedthrough required for UV light/heater.
Vacuum capability	With the current setup, this is not possible.	Capability for static (vacuum) and dynamic (flow-through) sensing conditions
SourceMeter	Only one measuring unit available per SourceMeter	Electrical measurement system that enables the simultaneous, real-time measurement of nine graphene pixels

While modifying the existing system would have been possible, it was under the ownership of another research group, rendering this course of action unfeasible.

5.5. Phase 3 Iteration: Development of the Gas Sensing Rig

This section outlines the development of the gas sensing system, hereafter referred to as the "gas sensing rig," designed specifically for gas sensing experiments on the graphene devices used in this researcher's thesis. Unlike the previous iterations, the final version of the gas sensing rig meets all necessary requirements for gas sensing experiments. It supports simultaneous, real-time resistance measurements in both flow-through and vacuum setups. Additionally, the larger chamber size facilitates easy setup of experiments and the integration of other components, such as a UV light or heater for recovery, making it a significantly more advanced and capable system than its predecessors.

5.5.1. System Components

The system is composed of three mass flow controllers, a measurement chamber, electrical feedthroughs, exhaust/vacuum inlet, pressure gauge, and electrical measurement equipment. **Figure 5.6** displays a schematic of the gas sensing rig. The following section describes in detail the components, technical specifications and software used on the gas sensing rig.

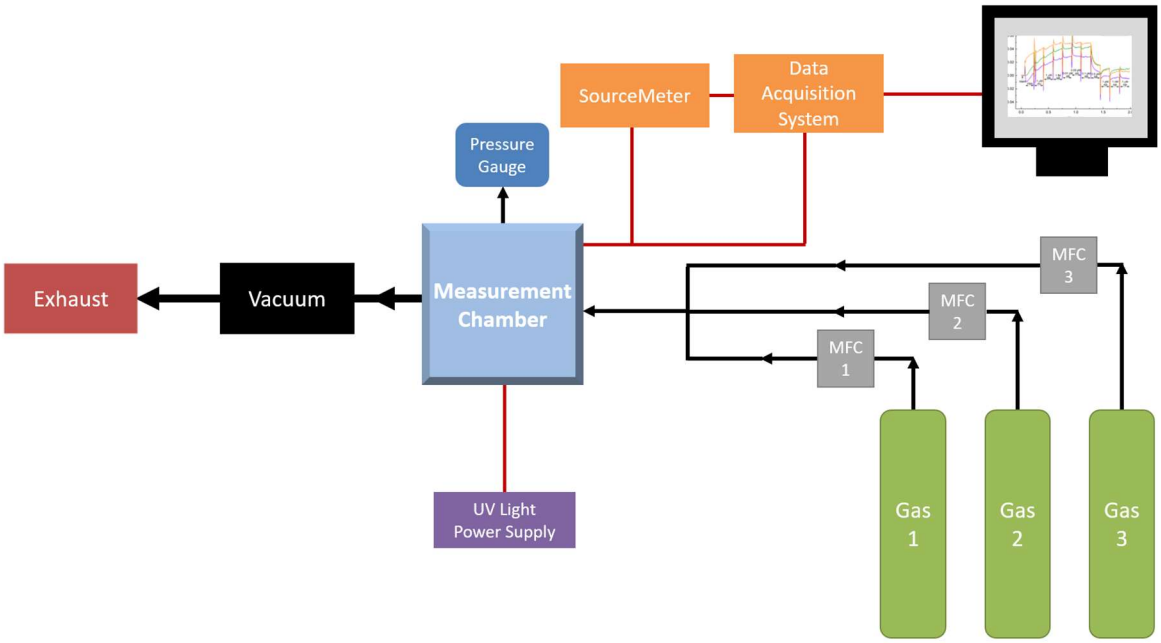


***Figure 5.6**: Schematic of the gas sensing rig. The vacuum is optional and can be replaced with the exhaust for flow-through applications.*

5.5.1.1. Mass Flow Controllers

This system consists of three Mass Flow Controllers (MFCs) purchased from *Bronkhorst UK Ltd* (UK). Two types of MFCs were employed: EL-FLOW Select F-201CV (x2) for the inert gases and LOW-ΔP-FLOW F-201DV (x1) for the corrosive gases. **Table 17** summarizes a few technical specifications of each MFC taken from the data sheet.

***Table 17**: Technical specifications of MFCs used. Acknowledgement: Bronkhorst UK Ltd webpage.*

MFC	Operating temperature (°C)	Operating Pressure	Flow range (mln/min)*
F-201CV	-10 to 70	Vacuum to 64 bar	8 to 1000
F-201DV	-10 to 70	Vacuum to 64 bar	20 to 1000

*(mln/min): millilitre normal per minute. This indicates 'normal' conditions as defined by *Bronkhorst UK Ltd*: a temperature of 0°C and a pressure of 1.013 bar.

To allow for simultaneous operation of MFCs, they were electrically connected using the 'daisy chain' wiring scheme and connected to the computer using a USB 2.0 converter. Each MFC is controlled using the *FlowView 4 V1.23* application via *FlowDDE*, both of which were provided free and downloaded from *Bronkhorst UK Ltd*'s webpage. *FlowDDE*, (Dynamic Data Exchange server) is used to initiate the connection and exchange data between digital instruments (MFCs) and *FlowView*. Using *FlowView*, the setpoint (flow rate, ml/min) is chosen by the user and the 'measured' flow rate is displayed. Each MFC is given a channel (1 to 3) which can be identified using the LED indicator light button, can be customised using the 'USERTAG', and includes information such as the model (F-201CV or F-201DV), capacity (1000 mln/min) and fluid it was calibrated for (e.g. N_2, O_2, or Mix) (**Figure 5.7**). Furthermore, *FlowView* can be opened in several different windows to enable the user to control and monitor the flow rate of each MFC simultaneously.

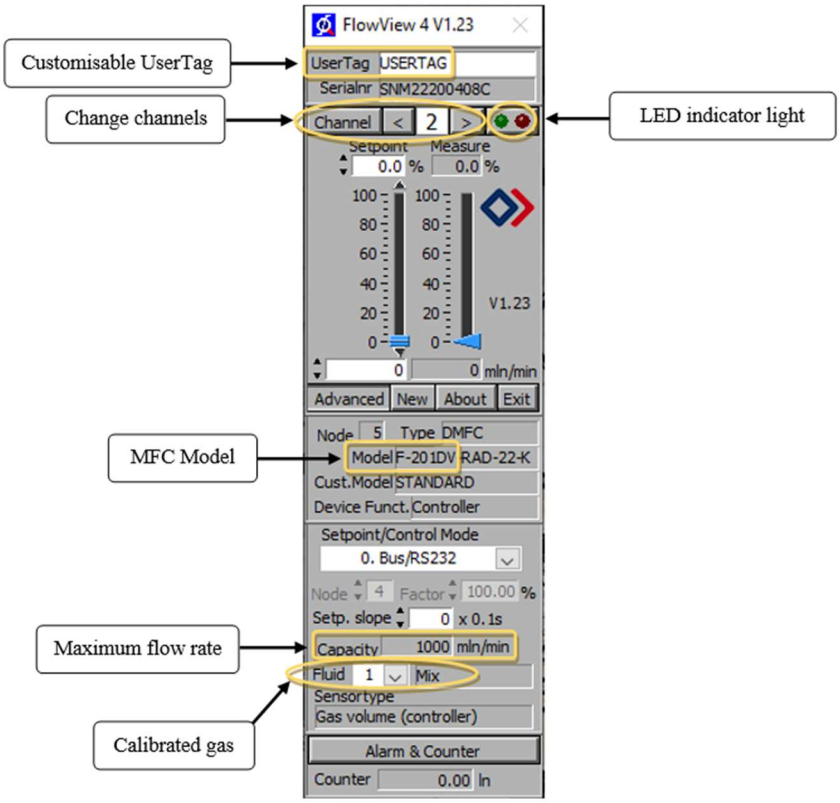


Figure 5.7: Overview of FlowView interface.

5.5.1.2. Measurement Chamber

The measurement chamber, or sensing chamber, is a 6" x 6" (15 cm x 15 cm) Ideal Vacuum Cube™ purchased from *Ideal Vacuum (Albuquerque, New Mexico, U.S.A)*. The cube, made from aluminium alloy, is a vacuum chamber consisting of a cube frame with removable plates to enable the user to modify the system based on their requirements. Below is a photo of the measurement chamber (**Figure 5.8**) and table of the plates (**Table 18**) included on this cube and their use.

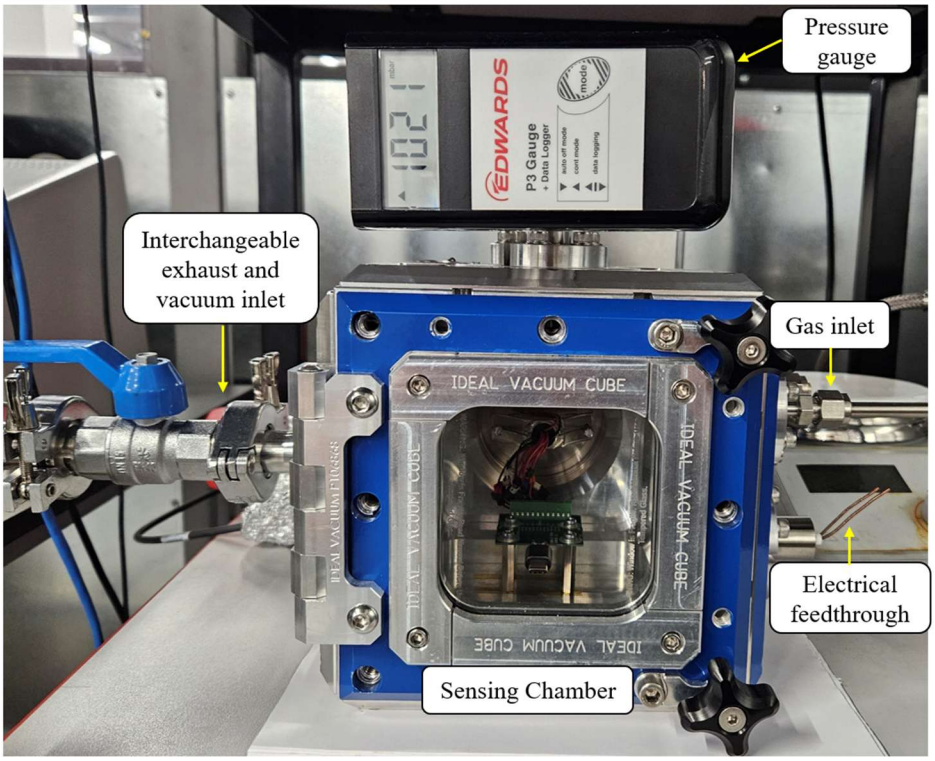


Figure 5.8: Ideal Vacuum Cube (gas sensing chamber).

Table 18: Description and use of each plate installed on the sensing chamber.

Quantity	Plate Description	Use
1	Blanking plate	N/A
1	Glass viewing window plate, fitted with a hinge and knobs	Inspection of chamber processes
1	Plate with 4x KF-16 (NW-16) feedthrough ports	3x gas feedthroughs (later modified to two to allow gas mixing) and 1x electrical feedthrough port for UV light
1	Plate with 1x KF-40 (NW-40) feedthrough port (later modified to an ISO-63 port)	Electrical 9-pin D-sub feedthrough port for electrical measurements (later modified to a 25-pin D-sub feedthrough)
1	Plate with 1x KF-16 (NW-16) feedthrough port	Pressure gauge
1	Plate with 1x KF-25 (NW-25) feedthrough port	Vacuum inlet/exhaust

Each plate is mounted onto the cube frame (**Figure 5.9**) and secured into place with bolts. Bolts are tightened in a specific 'tightening pattern', advised by *Ideal Vacuum*, and tightened at 70 in-lb (7.9 N·m) using a torque wrench to ensure a vacuum seal.

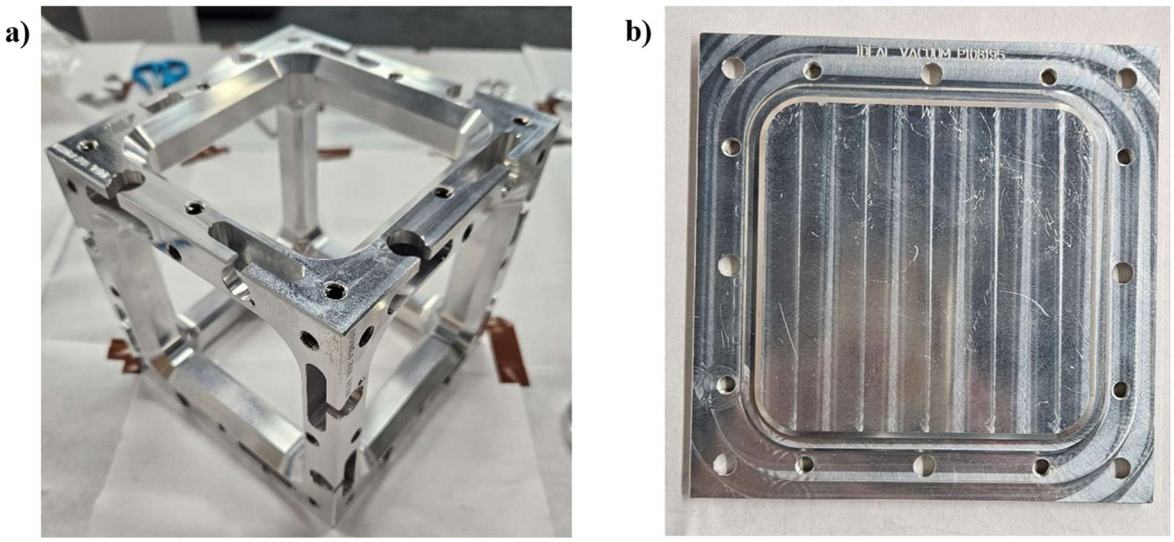


***Figure 5.9**: **(a)** 6" x 6" Ideal Vacuum Cube™ frame. **(b)** Removeable 6" x 6" plate.*

5.5.1.3. Gas Inlets

The measurement chamber is connected to three gases: (1) nitrogen or argon, (2) 20% oxygen in nitrogen and (3) one of the following test gases: 5 ppm nitrogen dioxide (NO_2), 5/10 ppm nitric oxide (NO), 50/100 ppm ammonia (NH_3), 80/580 ppm carbon dioxide (CO_2) or 1000/5000 ppm methane (CH_4). Gas cylinders were purchased from BOC and all test gases were premixed with nitrogen. Gases were connected to the cube using flexible braided tubing, ¼" stainless steel tubing and ¼" Swagelock to KF-16 adapters, all purchased from *Swagelok* (UK). Stainless steel tubing was manipulated using a hand bender, tube cutter and union tube fittings to create the required connections to the gas sensing rig. Originally, the gas sensing system consisted of three separate gas lines, each connecting a gas cylinder directly to the sensing chamber. However, as the requirement arose to dilute gases, this was later modified so that all gas lines merged into a single line, allowing the gases to mix thoroughly before entering the sensing chamber (**Figure 5.10**).

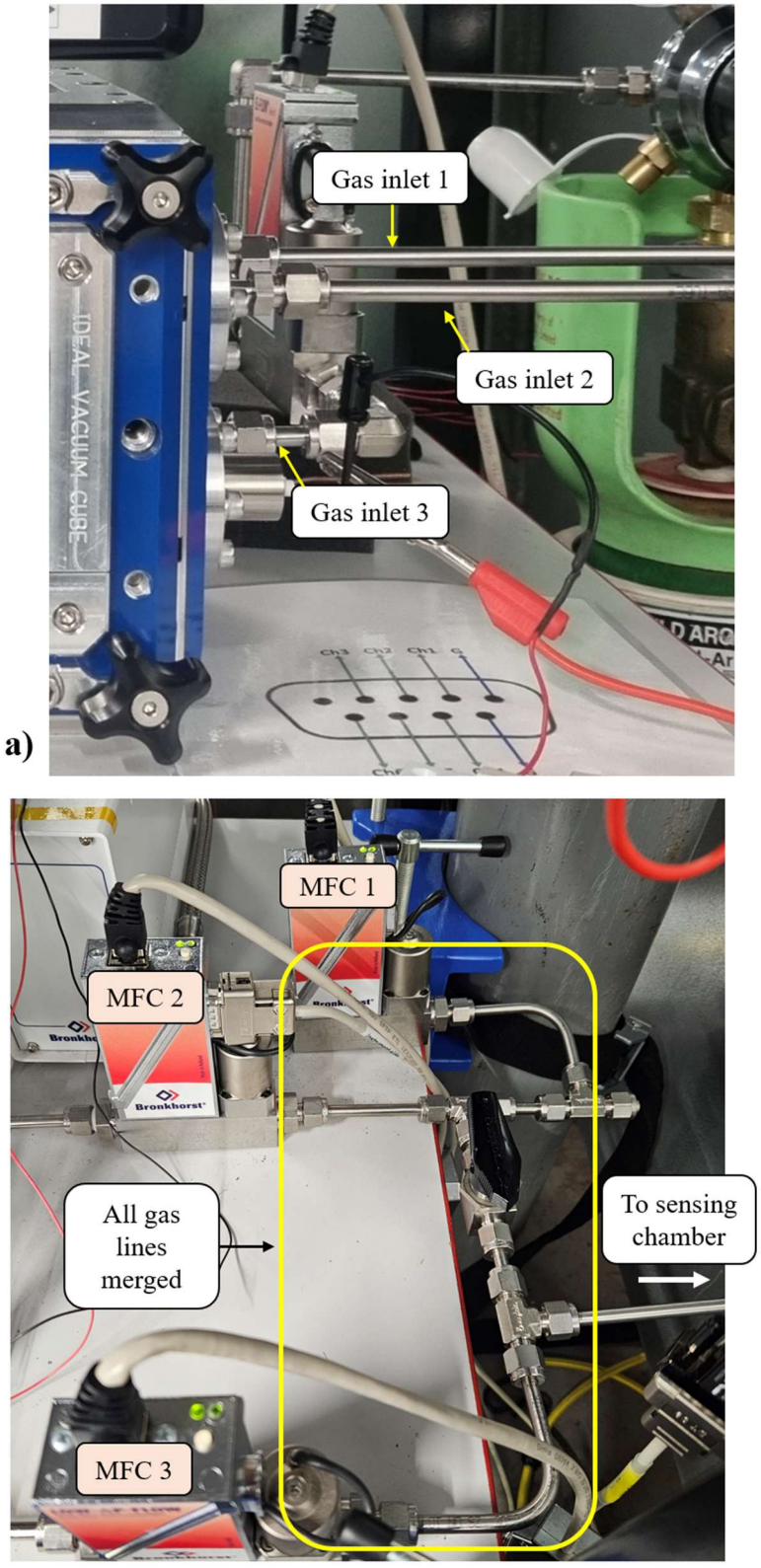


Figure 5.10: ***(a)*** *three separate gas input lines and* ***(b)*** *all gas input lines merged into a single line to allow mixing prior to entering sensing chamber.*

5.5.1.4. Vacuum Capabilities

The gas sensing system can be used in two formats: flow-through (dynamic) and vacuum (**Figure 5.11**). In the flow-through setup, the cube is connected to a steel braided flexible exhaust hose. In vacuum configuration, an Edwards RV8 rotary pump is used for the vacuum. To connect to the vacuum pump, the exhaust hose is removed via a 'quick connect' fitting and attached to the vacuum inlet. A ball valve between the cube and the vacuum inlet allows the user to isolate the cube from the vacuum pump. A pressure gauge, positioned on top of the cube, monitors the pressure during vacuum applications. The sensing chamber takes approximately five minutes to pump down and, with the current modifications, achieves a minimum pressure of 8.4×10^{-2} mbar.

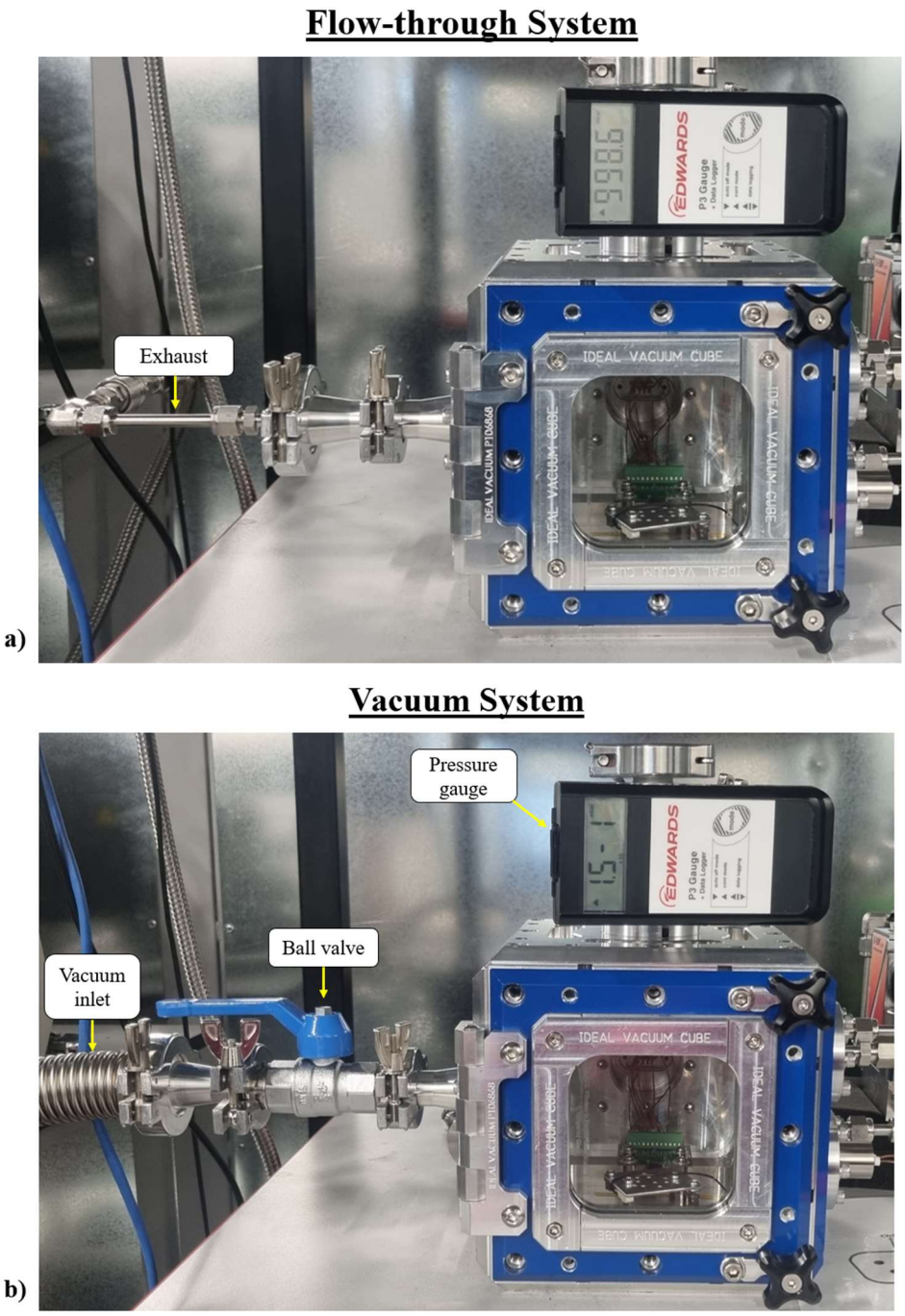


***Figure 5.11**: **(a)** flow-through system set-up and **(b)** vacuum system set-up.*

5.5.1.5. Electrical Feedthroughs

There are two electrical feedthrough ports on the cube, one located on the back of the cube and the other on the right-hand side. The feedthrough on the back contains an electrical D-sub feedthrough, connected to the electrical measurement equipment, which was eventually upgraded from a 9-pin to a 25-pin configuration, both purchased from *Ideal Vacuum* (**Figure 5.12**). Due to the new sensor design, the 3x3 graphene

array, more electrical connections (pins) were required to measure the resistance of all channels in real-time.

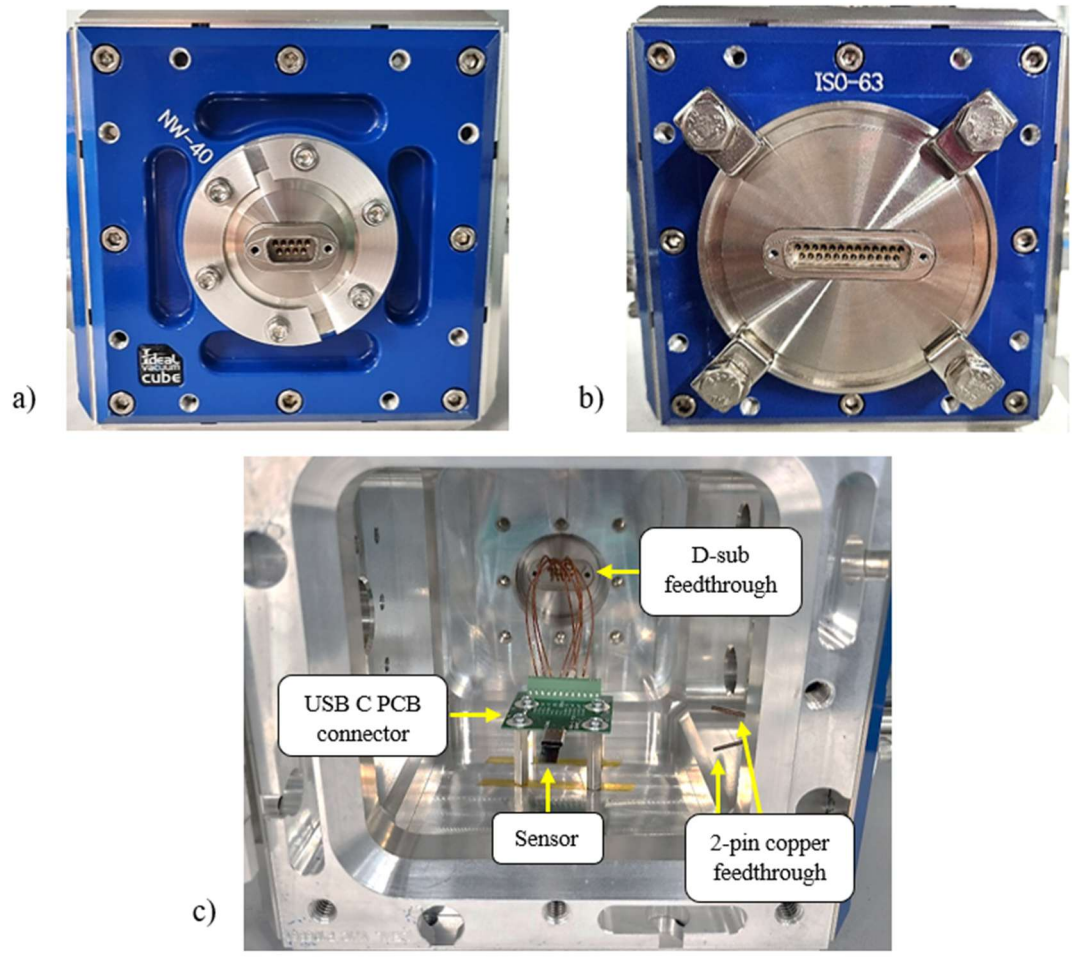


***Figure 5.12**: **(a)** 9-pin D-sub electrical feedthrough, **(b)** 25-pin D-sub electrical feedthrough and **(c)** USB-C PCB connector with sensor inside the gas sensing chamber.*

5.5.1.5.1. Sensor Recovery

Following initial gas exposure, gases adsorb onto the graphene sensor, effectively saturating its surface. To desorb these gases and recover adsorption sites for consistent repeat measurements, different techniques such as UV light [256], [284], [286], [287] and heating [6], [118], [288] can be used. These mechanisms are discussed in **Section 5.6.2**. Both techniques were explored to evaluate their potential for in situ recovery during the initial optimization of the gas sensing rig.

A 265 nm, 25 mW UVC LED, purchased from *RS Components* (UK), is connected to the sensing chamber via a 2-pin copper electrical feedthrough (purchased from *Ideal Vacuum*), located on the right-hand side of the cube. The electrical feedthrough was connected externally to a *TTi EL301R* power supply (*Aim-TTi*, UK) set to 7 V and 0.067 A to power the UV LED. The UV LED platform is mounted on threaded hexagonal spacers to maintain a fixed height. Similarly, the USB-C PCB connector, also at a fixed height, ensures that the sensor is consistently exposed to the UV light from the same distance (~1.2 cm) across multiple uses (**Figure 5.13a**). The UV LED has a beam angle of 120°, covering a lateral distance of approximately 4 cm with respect to the LED height, which is enough to expose all graphene pixels on a 3x3 graphene pixel array device simultaneously. It is also important to note that according to the polar radiation plot (**Appendix**, **Figure A1**) provided in the UV LED data specification by the manufacturer, the highest relative intensity is radiated in the middle of the LED and includes 10° on either side of the centre peak. This means that a ~2 mm lateral distance would be exposed to the maximum radiation intensity, which could lead to slight variations in intensity from pixel to pixel as the graphene pixels cover a total area of 3400 μm x 4000 μm across the surface of each device. Although the impact of varying light intensity on these devices is not fully known, this UV LED was used as it was the only suitable option available with the correct wavelength and compact size to fit inside the sensing chamber above the sensor. Sensor recovery performance using the UV LED was monitored throughout this thesis and will be reported in each respective chapter.

The 'heater' was a 25 Ω, 10 W ceramic power resistor purchased from *RS Components*. For recovery, the resistor was placed on a stand with the sensor resting on top, connected to the 2-pin electrical feedthrough inside the chamber (**Figure 5.13b**). Externally, the electrical feedthrough was connected to a *TTi EL301R* power supply. The resistor was calibrated by setting the power supply to various voltages and measuring the temperature using a *FLIR-E64501* thermal imaging camera (*Teledyne FLIR LLC*, UK). The calibration data was plotted to calculate the voltage setting required for a specific temperature **(Appendix, Figure A2**). However, without a control module to regulate the temperature, the resistor's temperature continued to rise with prolonged use, leading to device damage. Consequently, this in situ heater was

discontinued for recovery. Instead, an external hot plate was used to heat sensors for recovery, as presented later in this chapter.

Inside the sensing chamber, the configuration includes the custom-made USB-C PCB connector, the sensor, and the UV LED/ceramic resistor, each connected to its respective electrical feedthrough. All components are visible through the window plate. (**Figure 5.13**).

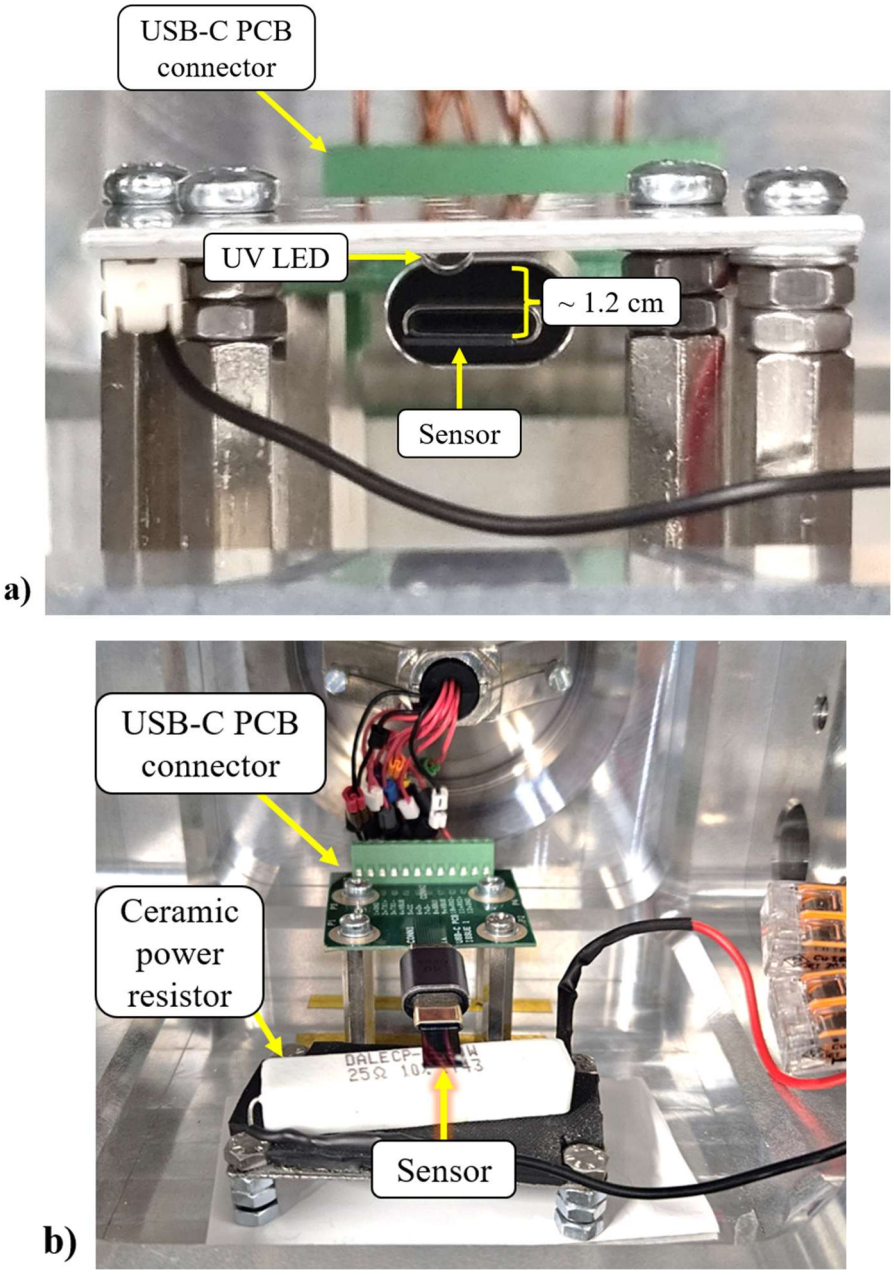
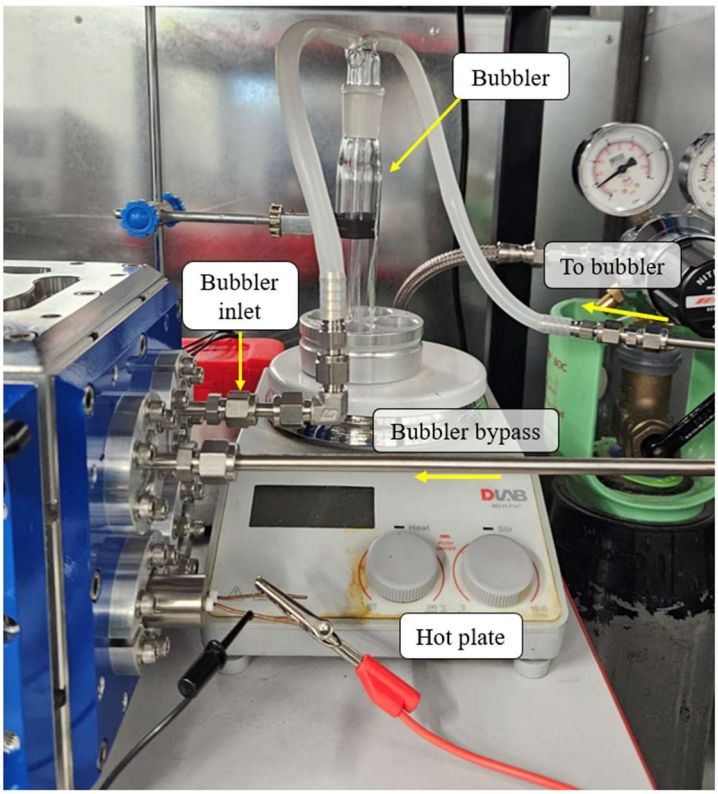


***Figure 5.13**: **(a)** 265 nm UV LED positioned above a sensor and **(b)** ceramic power resistor functioning as a heater with a sensor resting on top.*

5.5.1.6. Bubbler Installation

To investigate the impact of humidity on sensing performance, a bubbler was integrated into the setup, enabling adjustment of humidity levels inside the sensing chamber. The bubbler allows the input gas to be passed through a liquid, in this case, water, and pick up moisture A *DLAB MS-H-Pro*$^{+}$ hot plate was placed under the bubbler to provide some control over the humidity. Additionally, a *ThermPro* hygro-thermometer was acquired to monitor humidity and temperature changes during gas sensing experiments. Installing the bubbler involved adding two valves: one to direct gas flow through the bubbler and another to bypass it if needed (**Figure 5.14**). A hose-tail connector (purchased from *Swagelok*) was used to connect rubber tubing to the ¼" stainless steel tubing and attach the bubbler to the gas system.



a)

b)

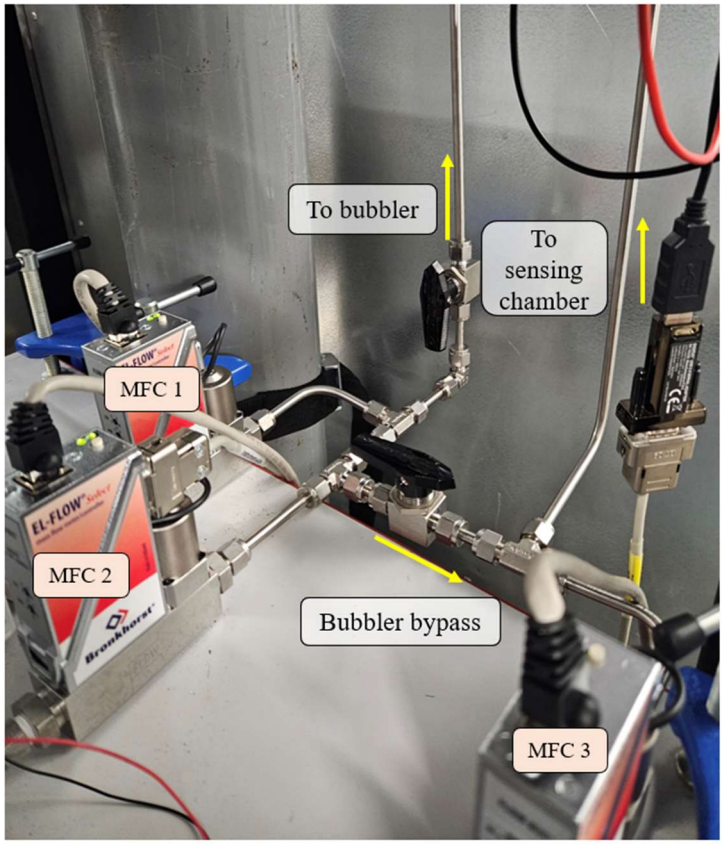


***Figure 5.14**: **(a)** bubbler and **(b)** valves installed to accommodate the bubbler.*

5.5.1.7. Electrical Measurement Equipment

To perform voltage sweeps and apply a voltage bias for real-time resistance measurements, a *Keithley SourceMeter 2602A* (SMU) was used. Enabling up to 40 channels to be measured simultaneously, the *Keithley Data Acquisition/Multimeter System 6510* (DAQ) was employed. Both units were purchased from *Tektronix,* USA.

Both units are controlled using the 'KickStart' software provided by *Tektronix*. The software works by purchasing applications to operate the equipment purchased. In this case, the 'IV-characteriser' and 'Data Logger' applications were purchased to operate the SMU and DAQ respectively. Both applications enable either unit to operate continuously for a designated number of data points or a specific duration. The Data Logger interface allows for the selection of individual channels (up to 40) for measurement, which are then measured simultaneously by a relay module card (7702) inserted into the DAQ. **Table 19** displays parameters kept constant during gas sensing experiments.

***Table 19**: Kickstart software parameters kept constant during gas sensing experiments.*

Parameter	Value
Current mode	DC
Function	Voltage bias
Level	1 V
Number of Power Line Cycles (NPLC)	1

To enable the DAQ to perform the required measurements, that is, measuring current of nine devices simultaneously, an external resistor was required in addition to the current system. The voltage drop could be measured over the resistor, and knowing the value, the resistance of devices under test (DUT) could be calculated. Furthermore, the DAQ relay module card had to be wired using a wiring scheme proposed by the Tektronix Technical Team.

Figure 5.15 displays the wiring scheme of the DAQ and the formula used to calculate the resistance of devices.

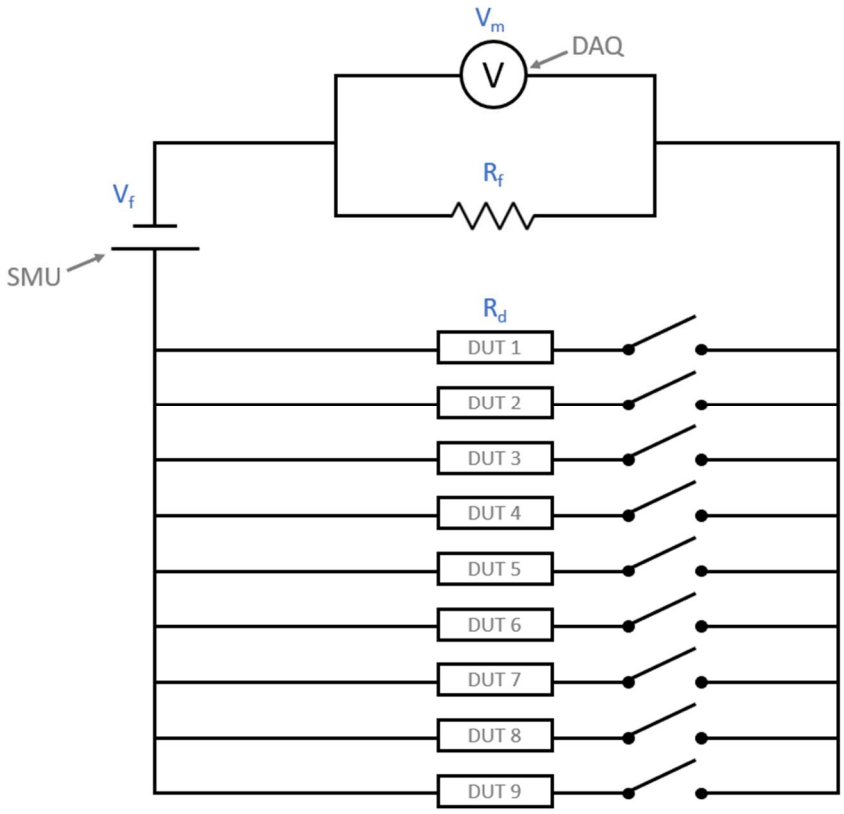


***Figure 5.15**: Wiring scheme of the DAQ and SMU for real-time measurements of graphene array devices.*

SMU: Source Measure Unit (SourceMeter)

DAQ: Data Acquisition System

DUT: Device Under Test

$$R_d = \frac{V_f - V_m}{\frac{V_m}{R_f}}$$

$\mathbf{R_d}$	=	Device Resistance
$\mathbf{R_f}$	=	Fixed Resistance
$\mathbf{V_f}$	=	Fixed Voltage (1 V)
$\mathbf{V_m}$	=	Measured Voltage

5.5.2. Experimental Set-up

This section describes the procedure for conducting a typical gas sensing measurement using the gas sensing rig. The experiment typically involves two gases: either 20% oxygen in nitrogen (air) or pure nitrogen, and a test gas. Air or pure nitrogen is used before and after test gas exposure to establish a baseline for the measurement to occur. Generally, prior to test gas exposure, the sensor would first be exposed to UV light under vacuum to desorb any gases. Next, 20 minutes of air flow would be used to condition the chamber by decreasing the humidity after it has been exposed to the atmosphere. Finally, to perform the experiment, 10 minutes of air flow, followed by 10 minutes of test gas and a further 5 minutes of air, all kept at a constant flow rate of 1000 mL/min. The voltage was kept fixed at 1 V for all experiments. As this system does not have a LabVIEW interface, the MFCs and electrical measurement equipment must be operated manually using their respective software's. Multiple versions of FlowView are opened, allowing the seamless switching between different gases, enabling the flow rate to remain constant at 1000 mL/min during experiments. To dilute test gases, the flow rate would be lowered, and air or nitrogen would be added accordingly to achieve a total flow rate of 1000 mL/min. For instance, 5 ppm nitrogen dioxide (NO_2) was diluted to 1 ppm NO_2 by lowering the flow rate of NO_2 to 200 mL/min and mixing this with 800 mL/min 20% oxygen (O_2)/80% nitrogen (N_2) (**Table 20**).

***Table 20**: Duration, flow rates and concentration of test gas for a typical experiment using the flow-through gas sensing rig.*

Time (min)	20% O_2/ 80%N_2 (mL/min)	5 ppm NO_2 (mL/min)	Calculated concentration test gas (ppm)
10	1000	0	-
10	800	200	1
5	1000	0	-

5.6. Optimization of Experiments

This section describes the optimization of experiments in order to effectively perform testing on the target gases.

5.6.1. Baseline sensing

Examining the selectivity of the sensor to the different constituents in air is an important step in evaluating sensor performance. This investigation would aid in establishing a baseline signal when no target gas is present, allowing for a better understanding of the sensor's initial state. The sensor response was characterised in 'air' (80% N_2/20% O_2), nitrogen, argon, and water vapour (in N_2 carrier gas) at room temperature and atmospheric pressure. Experiments were conducted by positioning the sensor in the middle of the gas sensing chamber and flowing gases at 1000 mL/min for 30 minutes each.

Figure 5.16 demonstrates that the resistance of the device shows no significant changes when exposed to nitrogen, air and argon. Despite the slight fluctuations in the baseline when a new gas is introduced into the chamber, the resistance only changed 0.72%, 0.44% and 0.54% over the 30-minute period for N_2, air and Ar respectively. This indicates that the resistance of the graphene device is minimally impacted by these gases. These findings are comparable to other gas sensing studies that demonstrate the insignificant effect of ambient gases on sensor resistance [288]–[290].

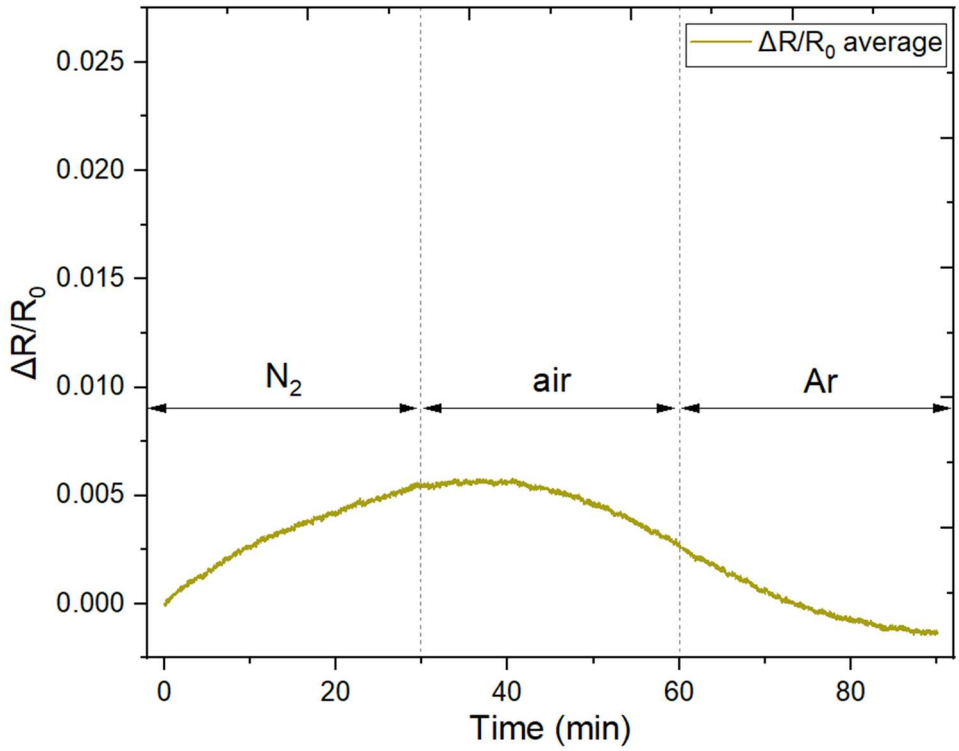


***Figure 5.16**: Real-time resistance measurements of a 3x3 graphene array device when subsequently exposed to nitrogen (N_2), air (80% nitrogen/20% oxygen) and argon (Ar). $\Delta R/R_0$ is given as the average of the pixels tested.*

5.6.1.1. Humidity Sensing

As discussed in the literature review, water vapour or humidity, influences sensor resistance [289], [291], [292]. Consequently, it was crucial to examine the impact of humidity on the graphene devices employed in this study before conducting tests with any target gases.

Humidity sensing was conducted in the range of 15% to 92% using a bubbler and a carrier gas (N_2). Humidified nitrogen was passed through the sensing chamber at 1000 mL/min while measuring the change in resistance in real time. Furthermore, a commercial humidity sensor was positioned inside the chamber with the graphene device to monitor the relative humidity (**Figure 5.17**).

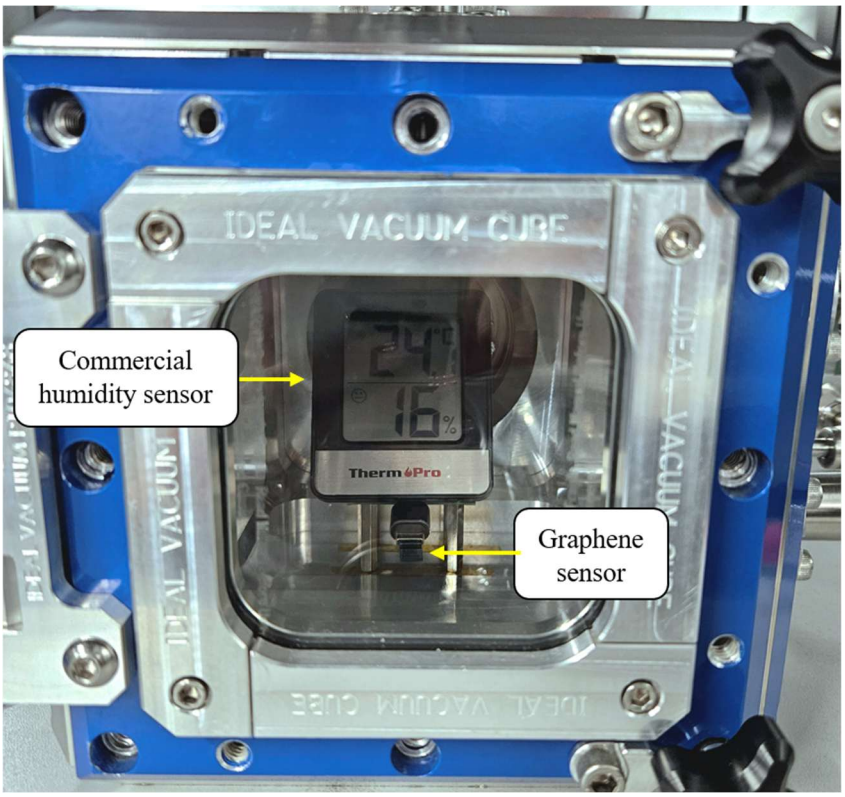
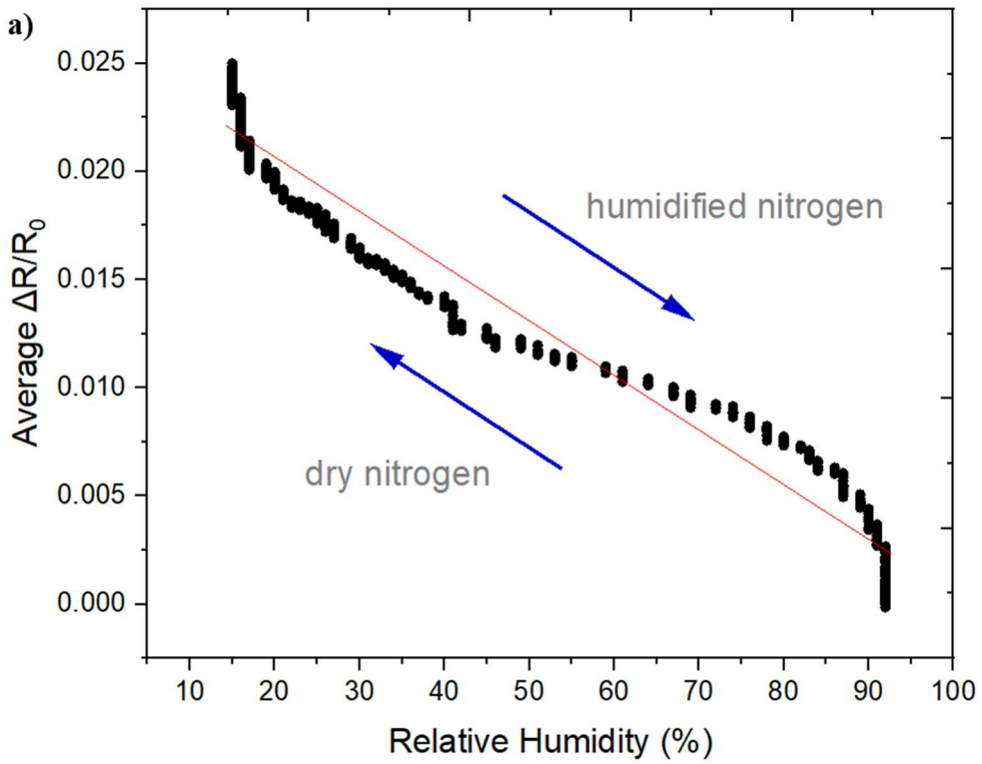
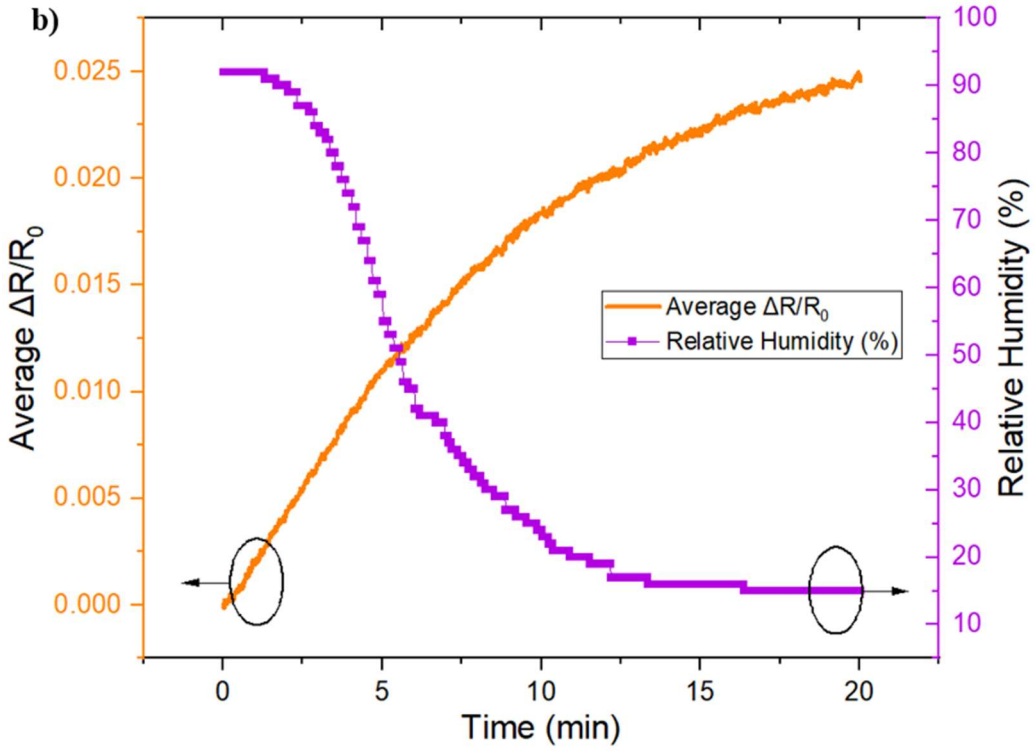


Figure 5.17: Humidity sensing set-up.

The experiment was conducted in two instances: first, by introducing water vapor into the chamber using a bubbler, and second, by employing only the flow of nitrogen to eliminate humidity from the chamber. The humidity range was established based on the capabilities of the equipment and the duration of time.

Figure 5.18 demonstrates the impact relative humidity has on sensor resistance. As the humidity increases, the sensor resistance decreases. Throughout the 20-minute duration, the relative humidity decreased from 92% to 15% with the use of dry nitrogen, resulting in a 2.5% average resistance change across the seven graphene pixels. **Figure 5.18c** presents a comparison of sensor responses to N_2, air, Ar, and humidity (water vapor, $H_2O_{(g)}$). The bar chart demonstrates that humidity has the most significant impact on sensor response compared to the baseline gases. These findings highlight the influence of humidity fluctuations on sensor resistance, highlighting the importance of maintaining consistent humidity levels during sensing.


a)
Average ΔR/R0
0.025
0.020
0.015
0.010
0.005
0.000
humidified nitrogen
dry nitrogen
10
20
30
40
50
60
70
80
90
100
Relative Humidity (%)


b)
Average ΔR/R0
0.025
0.020
0.015
0.010
0.005
0.000
Average ΔR/R0
Relative Humidity (%)
100
90
80
70
60
50
40
30
20
10
Relative Humidity (%)
0
5
10
15
20
Time (min)

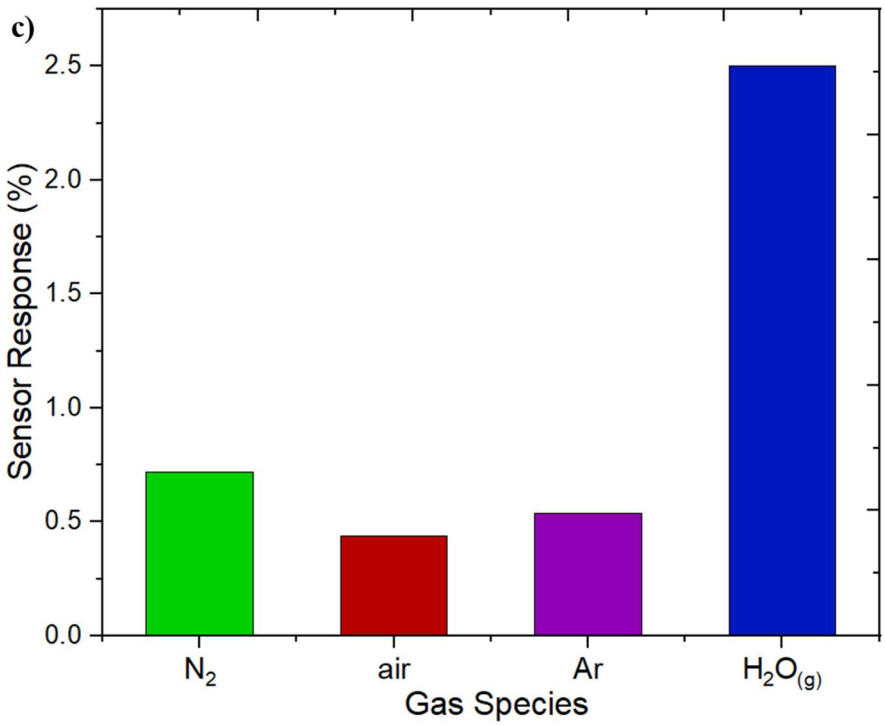


***Figure 5.18**: **(a)** Change in resistance ($\Delta R/R_0$) versus relative humidity (%) as dry nitrogen and humidified nitrogen are pumped through the sensing chamber. **(b)** Real-time resistance and relative humidity (RH) measurements of a 3x3 graphene array device when exposed to the RH range of 15% to 92%. **(c)** Bar chart comparing the sensor response of N_2, air, Ar and water vapour ($H_2O_{(g)}$).*

5.6.2. Sensor Recovery Testing

Sensor recovery serves as a crucial performance metric for gas sensing. Unlike sensors employed in biomedical applications, gas sensors are anticipated to undergo repeated use throughout their operational lifespan. Various recovery methods have been previously introduced in research, including: ultraviolet (UV) light [256], [284], [286], [287], vacuum annealing [6], [118], [288], current annealing [45], infrared (IR) light [293], ambient air flow [294] and vacuum desorption [295].

As devices (and graphene) inevitably vary, it was essential to establish a dependable method or methods for recovering the sensors utilised in this research. Bare graphene sensors were used to perform initial recovery testing to establish a basis of which methods may be beneficial. Data on the recovery of functionalized devices is located in their respective chapters.

5.6.2.1. UV Treatment and Vacuum Desorption

The first recovery method investigated was the use of a 265 nm UV LED, and the experimental set-up is depicted in **Figure 5.13** in **Section 5.5.1.5.1**. To conduct the recovery tests, the sensor was initially subjected to a 10-minute exposure of 100 ppm ammonia (NH_3) mixed with nitrogen, and its response was measured. Ammonia gas was used in this instance because it is known to elicit a response in graphene sensors [293], [296]–[298]. Subsequent tests were performed by exposing the sensor to varying durations of UV light before exposing it to 100 ppm NH_3 for 10 minutes. Additionally, the use of a vacuum on recovery was investigated for 30- and 60-minute durations before ultimately integrating both approaches.

Sensor responses (formula provided in **Chapter 3.6.1**) were calculated and compared for each experiment, operating under the assumption that complete recovery of the sensor would yield a response comparable to the initially calculated one. Comparing the initial sensor response to a target gas alongside repeated measurements can indicate sensor recovery. While typically, sensor recovery involves comparing initial resistance to resistance after recovery, this method may not always be dependable. Since recovery methods indiscriminately remove adsorbed gases from the surface, restoring the initial resistance can be challenging. However, if the sensor consistently yields a similar response magnitude to the same concentration and exposure time of a target gas, this suggests sensor recovery.

Figure 5.19 compares the sensor responses for various recovery methods tested. Initial exposure of the sensor to 100 ppm NH_3 yielded a response of 4.1% with a standard deviation of 0.42 between graphene pixels. Subsequent exposure to 2, 4 and 6 minutes of UV light after the initial exposure produced a revised response of 0.20%, 0.64% and 0.86% respectively, to 100 ppm NH_3. The decreased sensor responses to NH_3 after the initial exposure, suggests the recovery method was unsuccessful at desorbing all ammonia molecules from the surface. Likewise, 30- and 60-minute vacuum desorption (2.7% and 3.8% respectively) did not completely recover the device, recovering up to 91% of the initial response within 60-minutes (percentage recovery formula is provided in **Chapter 3.6.3)**. While vacuum desorption seems to achieve some success in eliminating adsorbed molecules, and extending the vacuum

duration may fully restore the device, this prolonged period is unfavourable for sensor recovery in a commercial sensor device.

The combination of both methods, UV exposure and vacuum desorption, termed as "vacuum-assisted UV treatment", appears to be the most effective in eliminating the adsorbed molecules from the surface, restoring the sensor to its initial state. Following treatment, the sensor response to 100 ppm NH_3 was 4.3%, slightly higher than the initial response (104% recovery). The increased response could indicate the UV light removed other desorbed gases from the sensor surface, providing more sites for the ammonia to adsorb. Vacuum-assisted UV treatment is prevalent throughout this thesis and was the most effective recovery method used for bare graphene and functionalised devices alike.

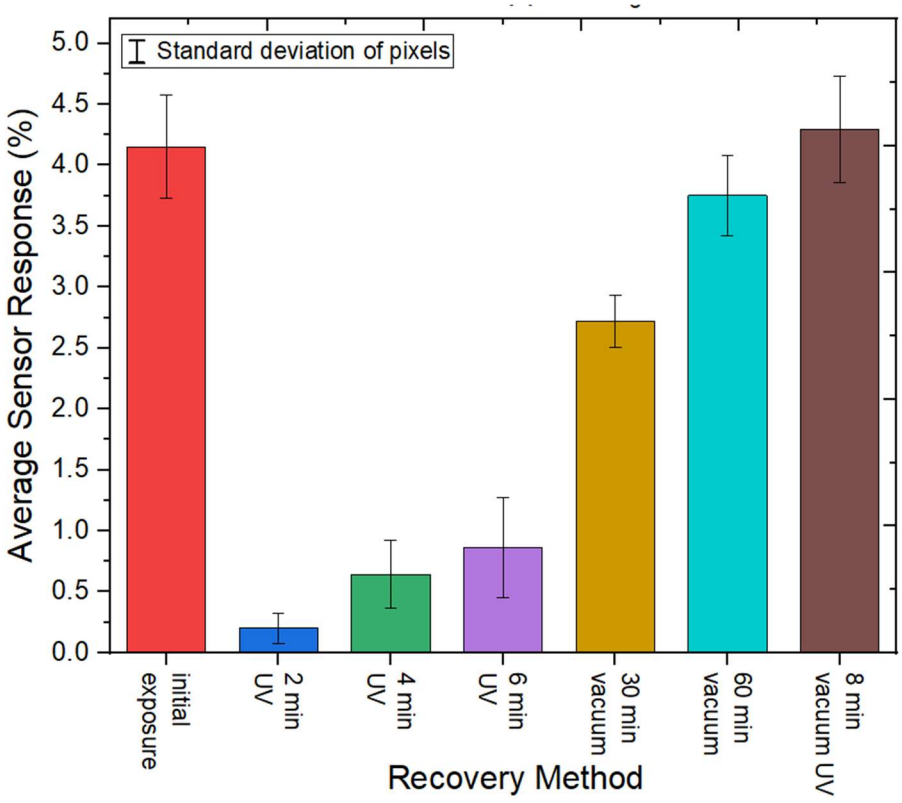


***Figure 5.19**: Bar chart comparing the different recovery methods investigated following a 10-minute exposure to 100 ppm NH_3.*

Figure 5.20 depicts the real-time resistance measurement profile for one graphene pixel during an individual UV light exposure experiment. In each instance, the sensor was exposed to: (1) 10 minutes air, (2) 10 minutes 100 ppm NH_3, (3) 10 minutes air

and (4) UV light exposure (different durations tested). After achieving a steady baseline by exposing the sensor to air, addition of 100 ppm NH_3 causes an increase in the sensor resistance ($\Delta R/R_0$ in a positive direction). Exposure to UV light causes an immediate and sharp decrease in resistance followed by a sharp increase in resistance. The change in resistance direction following UV exposure is contingent upon the gas to which it was previously exposed. In this case, ammonia is an electron donating gas, thereby increasing the resistance of p-type graphene [166], [169]. Exposure to UV removes ammonia from the surface, reducing the resistance. The subsequent increase could be caused by removal of oxygen from the surface, which is an electron withdrawing group. As adsorption of oxygen molecules to the surface would inherently decrease the resistance of p-type graphene, the removal of these molecules would cause the resistance to increase [299], [300].

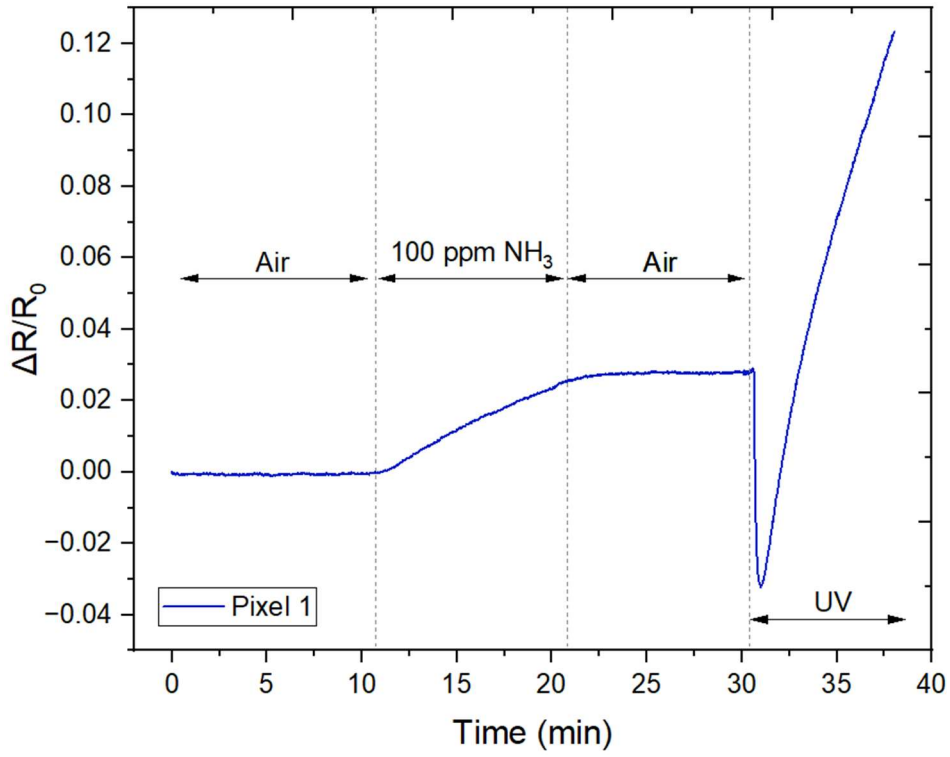


***Figure 5.20**: Real-time resistance measurements from a graphene pixel array sensor demonstrating a 10-minute exposure to 100 ppm NH_3 followed by an 8-minute vacuum assisted exposure to UV light.*

Figure 5.21 illustrates real-time resistance measurements of a graphene pixel exposed to 5 ppm nitrogen dioxide (NO_2). The experiment involved sequential exposure: 10 minutes in air, 10 minutes in 5 ppm NO_2, followed by 5 minutes in air, and finally, 8

minutes under UV light. During NO_2 exposure, the resistance of the sensor decreases. NO_2, an electron-withdrawing gas, removes electrons from p-type graphene, thereby increasing hole carrier concentration and decreasing resistance [301]. Exposure to air alone does not fully recover the sensor, but subsequent UV light exposure sharply increases resistance, rapidly restoring the sensor to its original state and beyond, by removing additional air adsorbates (O_2) from the surface.

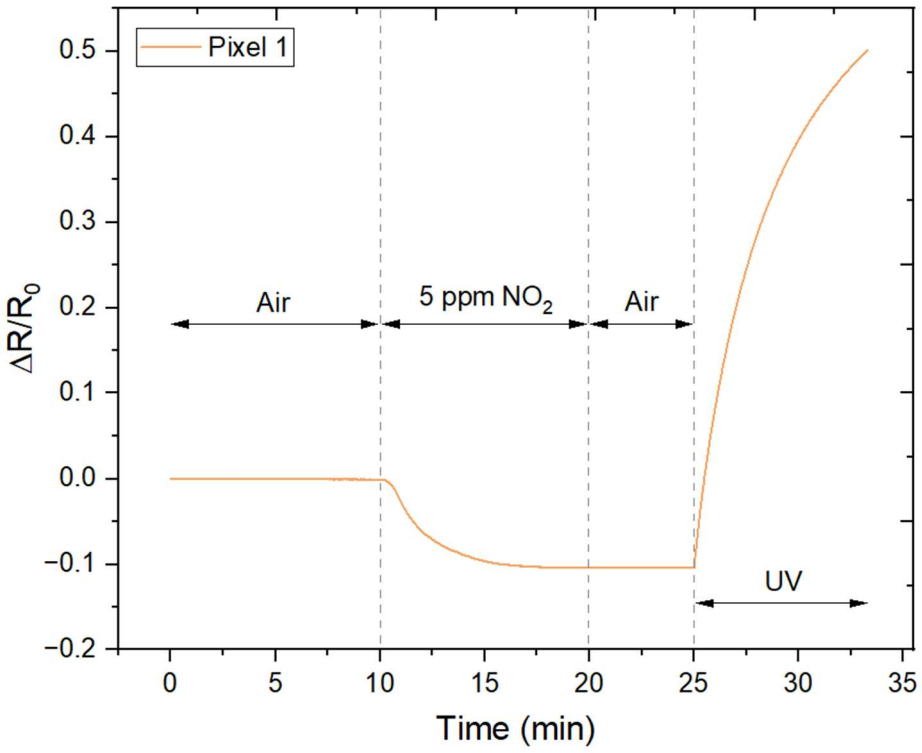


***Figure 5.21**: Real-time resistance measurements from a graphene pixel array sensor demonstrating a 10-minute exposure to 5 ppm NO_2 followed by an 8-minute vacuum assisted exposure to UV light.*

5.6.2.1.1. Challenges

As discussed in **Section 5.5.1.5.1**, the radiation intensity of the UV LED is not uniform across the beam and is most intense in the centre. To investigate the impact this may have on recovery, a Hall Bar with a spacing of 4750 µm between graphene channels was used. The following exposure sequence was employed for the experiment: (1) 8-minute UV exposure, (2) 10-minute air exposure, (3) 10-minute 100 ppm NO_2 exposure, and (4) 5-minute air exposure. This sequence was repeated twice with different UV light positions. During the first UV exposure, the light was positioned

closer to Channel 1 (on the left side of the device), and during the second UV exposure, the centre of the LED was positioned directly above Channel 1. **Figure 5.22** provides a schematic representation of both experiments.

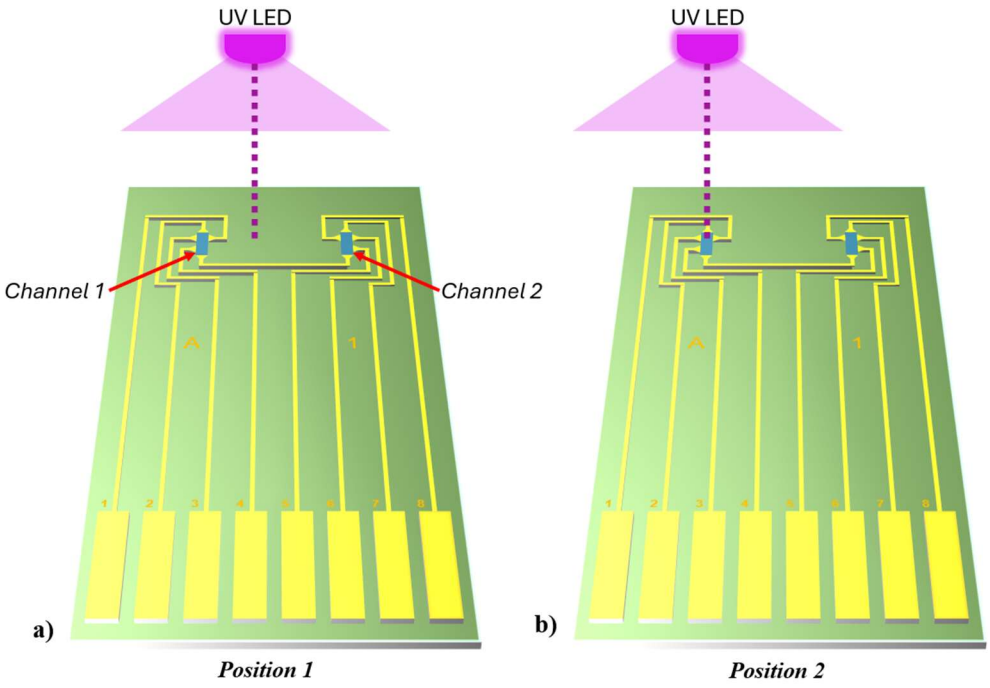


Figure 5.22: Schematic representation of the position of the UV LED for both experiments, with the dashed purple line representing the most intense portion of the beam.

Figure 5.23 suggests that the position of the UV LED for devices with large spaces between graphene channels significantly impacts recovery and, consequently, repeat testing of target gases. When the UV light was positioned closer to Channel 1 in the first experiment, there was a noticeable difference in recovery between the two channels. Subsequent exposure to NO_2 revealed a lower sensor response for Channel 2 (-30.1% compared to Channel 1 at -45.2%), the channel that received less intense UV light treatment.

In the second experiment, with the centre of the LED directly above Channel 1, an even larger difference in recovery between the two graphene channels was observed (evidenced by a larger $\Delta R/R_0$). The NO_2 exposure revealed a significant difference in sensor responses between the two channels, with Channel 1 showing a response of -51.6% and Channel 2 showing -20.3%. This indicates that more intense UV light results in more effective desorption and recovery. This conclusion is further supported

by comparing the responses of individual channels over the two experiments. The magnitude of recovery and subsequent sensor response to NO_2 increases as the position of the UV light, and thus a larger radiation intensity, is closer to a channel.

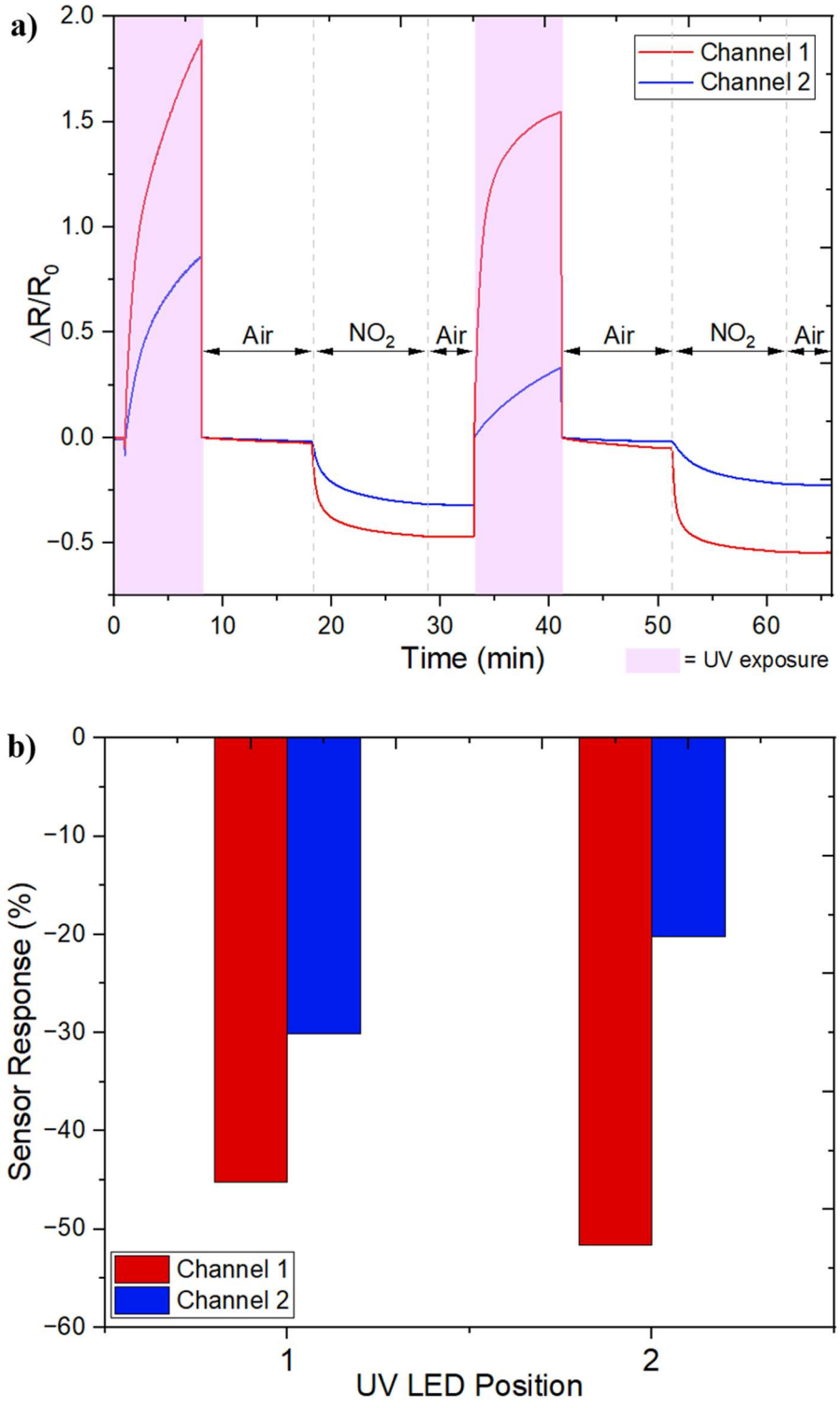


***Figure 5.23**: **(a)** Real-time resistance measurements of a graphene Hall Bar exposed to UV light in two different positions followed by exposures to 100 ppm NO_2. **(b)** Bar chart illustrating the sensor response (%) of Channel 1 and 2 for both experiments.*

5.6.2.2. Heat Treatment

Employing heat to remove adsorbed molecules is another recovery method commonly used within gas sensing [302], [303]. This investigation was conducted with 2-channel bare graphene sensors and 50 ppm ammonia. Experiments were performed by firstly exposing the sensor to air to achieve a stable baseline, followed by a 5-minute exposure to 50 ppm NH_3 and finally, a 5-minute exposure to air. At this point, sensors were removed from the sensing chamber and placed on a hot plate at various temperatures (175°C, 150°C, 125°C and 100°C) for 5 minutes (refer to **Section 5.5.1.5.1** for details of why an integrated heater was not used). Each temperature was repeated four to five times, contingent on whether there was a discernible decrease in sensor response after the previous measurement. The real-time resistance measurement profiles, response times, and sensor responses for each repeat at various temperatures are provided in the **Appendix** (**Figure A3** to **Figure A6**).

Figure 5.24 demonstrates the change in sensor response after repeated exposures to 50 ppm NH_3. The sensor response decreases at temperatures of 100°C and 125°C with successive exposures to ammonia gas, suggesting inadequate recovery and insufficient desorption of gases at these temperatures. Conversely, the sensor response remains relatively stable at 150°C, recovering an average 97% of the initial response. Optimal recovery is observed after 5 minutes at 175°C, with the sensor regaining an average 101% of its initial response.

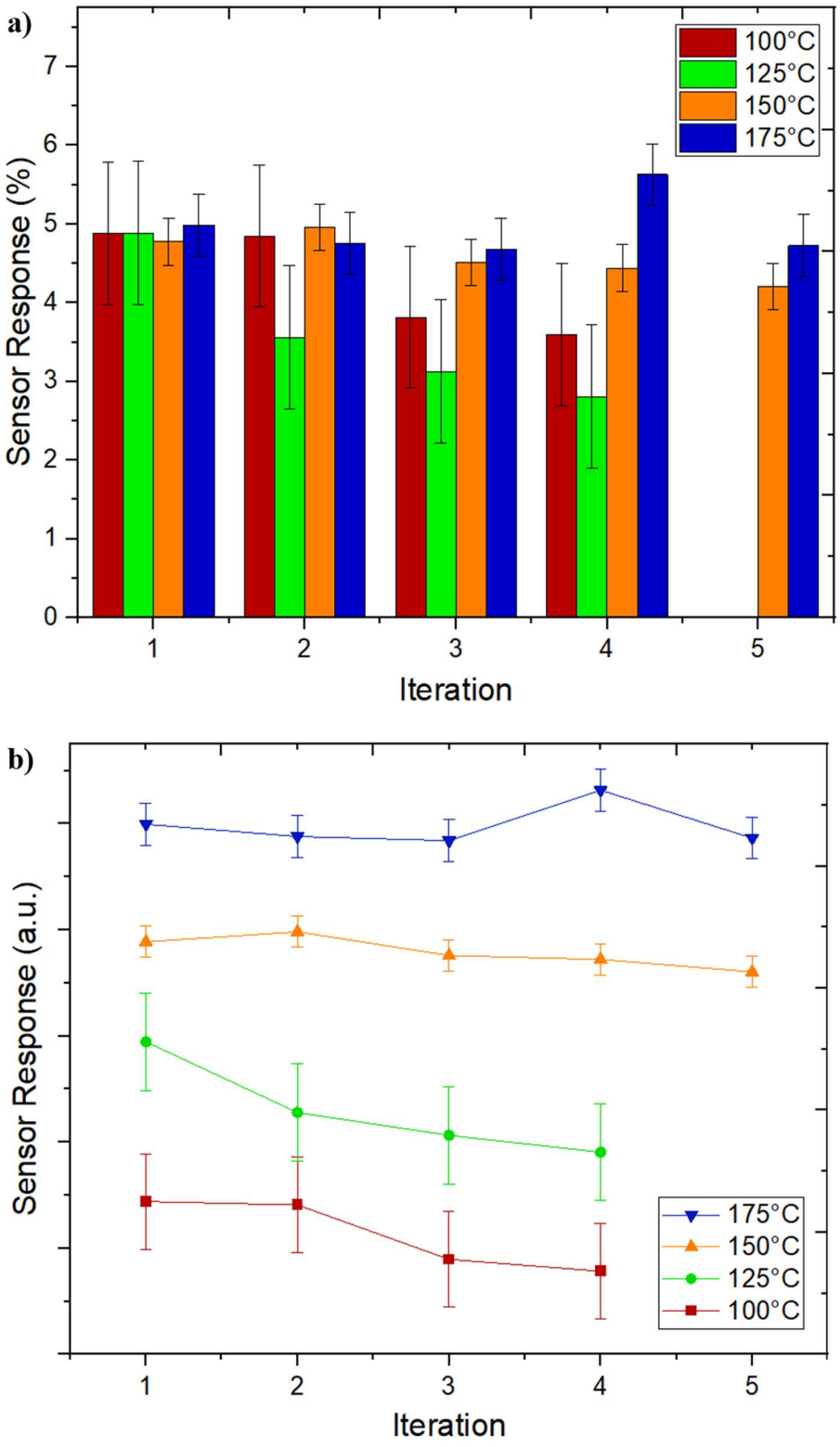


***Figure 5.24**: **(a)** Bar chart displaying the sensor response to 50 ppm NH_3 for each repeat at each temperature tested. **(b)** Variation in sensor response across different temperatures.*

5.7. Conclusions

In conclusion, the development of a new gas sensing system will enable real-time simultaneous measurements of graphene pixel arrays to be collected. The system, comprised of a sensing chamber, three mass flow controllers, three gas lines, two electrical feedthroughs, and a pressure gauge, offers flexibility for both static and dynamic gas sensing experiments.

Optimization of experiments using the new system has been paramount in establishing robust testing protocols. By examining sensor selectivity and response to different environmental conditions, a better understanding of the sensor's initial state has been determined. Notably, the investigations revealed minimal changes in sensor resistance upon exposure to nitrogen (0.72%), air (0.44%), and argon (0.54%), indicating that these gases could be used to establish a baseline prior to exposure to a target gas. Humidity testing further highlighted the impact of environmental variables on sensor behaviour. A 2.5% change in sensor resistance with a decrease in humidity from 92% to 15%, highlights the need for humidity control during gas sensing experiments.

Sensor recovery is important to ensure repeated use of gas sensors throughout their operational lifespan. Consequently, it was important to determine a reliable method(s) to recover sensors after target gas exposure. The most effective technique identified for recovering the bare graphene sensors was an 8-minute vacuum-assisted UV treatment, which achieved a 104% recovery. Another promising recovery method was a 5-minute heat treatment at 150°C and 175°C, yielding recovery rates of 97% and 101%, respectively. Since the vacuum-assisted UV treatment allowed for real-time resistance measurements and enabled sensors to remain in the sensing chamber during recovery processes, it was prioritized as the primary recovery method for pre- and post-treatment in gas sensing experiments.

Chapter 6 : Gas Detection Using Metal Phthalocyanine Modified-Graphene Sensors

6.1. Introduction

As a 2D material, graphene has its entire surface area exposed, providing a highly sensitive surface capable of detecting individual gas molecules [184]. However, this high sensitivity poses challenges for gas sensing applications, as graphene can respond to many atmospheric molecules [304]. Therefore, it is crucial to engineer the graphene surface using various functionalization techniques to tailor its properties for specific applications and induce selectivity [305]. Metal phthalocyanines (MPcs) are known gas-sensitive molecules that respond differently to gases based on interaction of the gas molecule with the metal centre and functional groups on the ring [26], [175], [261], [306]. MPcs possess an 18π-electron conjugated aromatic structure, which allows them to π-π stack with graphene, facilitating electronic coupling between the phthalocyanine and graphene. Utilizing metal phthalocyanines provides an exciting opportunity to enhance the sensitivity and selectivity of graphene-based gas sensors.

The following chapter describes and evaluates the gas sensing performance of metal phthalocyanines, using real-time resistive measurements. These MPcs are deposited onto three different graphene-based devices, previously discussed in **Chapter 4**, the 'DipChipX', 'Hall Bar', and '3x3 graphene pixel array' graphene sensors.

6.2. Summary of Sensor Designs, Phthalocyanines, and Gas Sensing System Iterations

This work involved different sensor designs, phthalocyanines, and iterations of the gas sensing system during its development (see **Table 21**). In this chapter, copper phthalocyanine was utilized in two forms: unsubstituted (CuPc) (**Figure 6.1a**) and

substituted with tert-butyl groups ($CuPc(t\text{-}Bu)_4$) (**Figure 6.1b**). The term 'unsubstituted' indicates a phthalocyanine molecule in its original form without any additional substituents or functional groups attached to its structure. A substituted copper phthalocyanine derivative was utilized to improve the solubility of the Pc molecule in organic solvents (details are provided in **Section 6.6**).

***Table 21**: Summary of sensor designs, phthalocyanines, and gas sensing system iterations used in this chapter.*

Gas System Iteration	Sensor Design	Sensing Material	Section
Phase 2	DipChipX	• Bare graphene • *Copper phthalocyanine-graphene	**6.5.1**
Phase 3	Hall Bar	• Bare graphene • *Cobalt/*Copper/*Iron/*Zinc/*metal-free phthalocyanine-graphene	**6.5.2**
	3x3 Pixel Array	• Bare graphene • *Copper phthalocyanine-graphene • Copper 2,9,16,23-Tetra-tert-butylphthalocyanine-graphene	**6.7**

*Denotes the unsubstituted phthalocyanine.

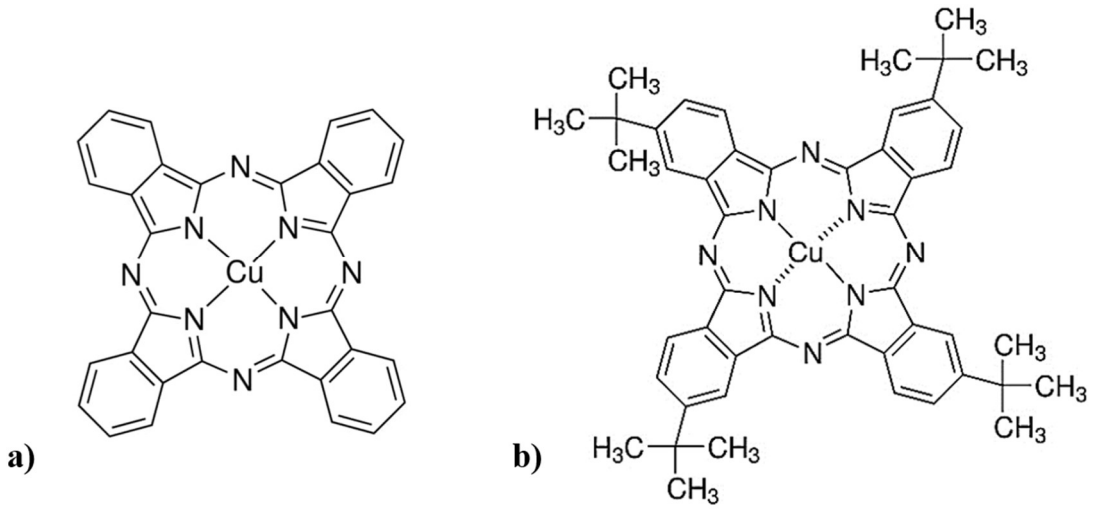


***Figure 6.1**: **(a)** Unsubstituted copper phthalocyanine molecule. **(b)** Copper 2,9,16,23-Tetra-tert-butylphthalocyanine (substituted).*

6.3. Electrical Measurements

Real-time resistance measurements were first conducted on the DipChipX graphene sensors using the Phase 2 Iteration gas sensing system following the procedure

outlined in **Chapter 5.4.1**. Due to the SourceMeter having only a single measuring channel, only one graphene channel (out of three per device) could be measured per experiment. A UV recovery procedure was developed to allow for the same graphene device to be reused after gas sensing (discussed in **Chapter 5.6.2)**. The UV recovery procedure was performed outside the sensing chamber, due to insufficient space to accommodate the UV LED inside the chamber. Therefore, resistance changes during the recovery process could not be measured in real-time.

Following the assembly and optimization of the Phase 3 Iteration gas sensing rig, the gas sensing performance of copper phthalocyanine was also investigated using the 3x3 graphene pixel array sensor. Additionally, other phthalocyanines, including cobalt, iron, zinc, and metal-free variants, were tested using Hall Bar sensors in the final iteration (Phase 3) of the gas sensing system. Details of the procedure used with this gas sensing system are outlined in **Chapter 5.5**.

6.4. Graphene Functionalization via Drop-Casting

This section describes the drop-casting procedure utilized in this section. Due to their aromatic structure, MPcs are particularly suitable for the non-covalent functionalization of graphene. The π-π interactions between graphene and MPc provide a stable surface modification without compromising the electronic properties of graphene, unlike covalent functionalization, which disrupts the sp^2 hybridization and reduces the carrier mobility of graphene [142]–[144].

The drop-casting procedure remained constant across the three different graphene sensors. To functionalize the sensors, a 1 mg/mL metal phthalocyanine solution was prepared by dissolving the MPc in dimethyl sulfoxide (DMSO). A 20 µL droplet was then drop-cast onto the graphene channel and incubated at room temperature (RT) for 30 minutes (**Figure 6.2**). Following incubation, the devices were washed with deionized (DI) water and dried with nitrogen.

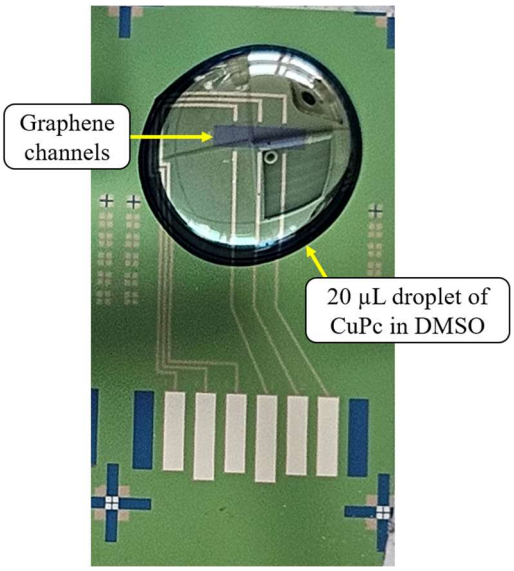


***Figure 6.2**: Drop-cast functionalization of a DipChipX graphene sensor using copper phthalocyanine (CuPc).*

SEM images were taken after drop-casting MPcs on graphene-Si/SiO_2 wafers at an acceleration voltage of 10kV (**Figure 6.3**). The SEM images show phthalocyanine crystals of different sizes and shapes with a random distribution across the surface.

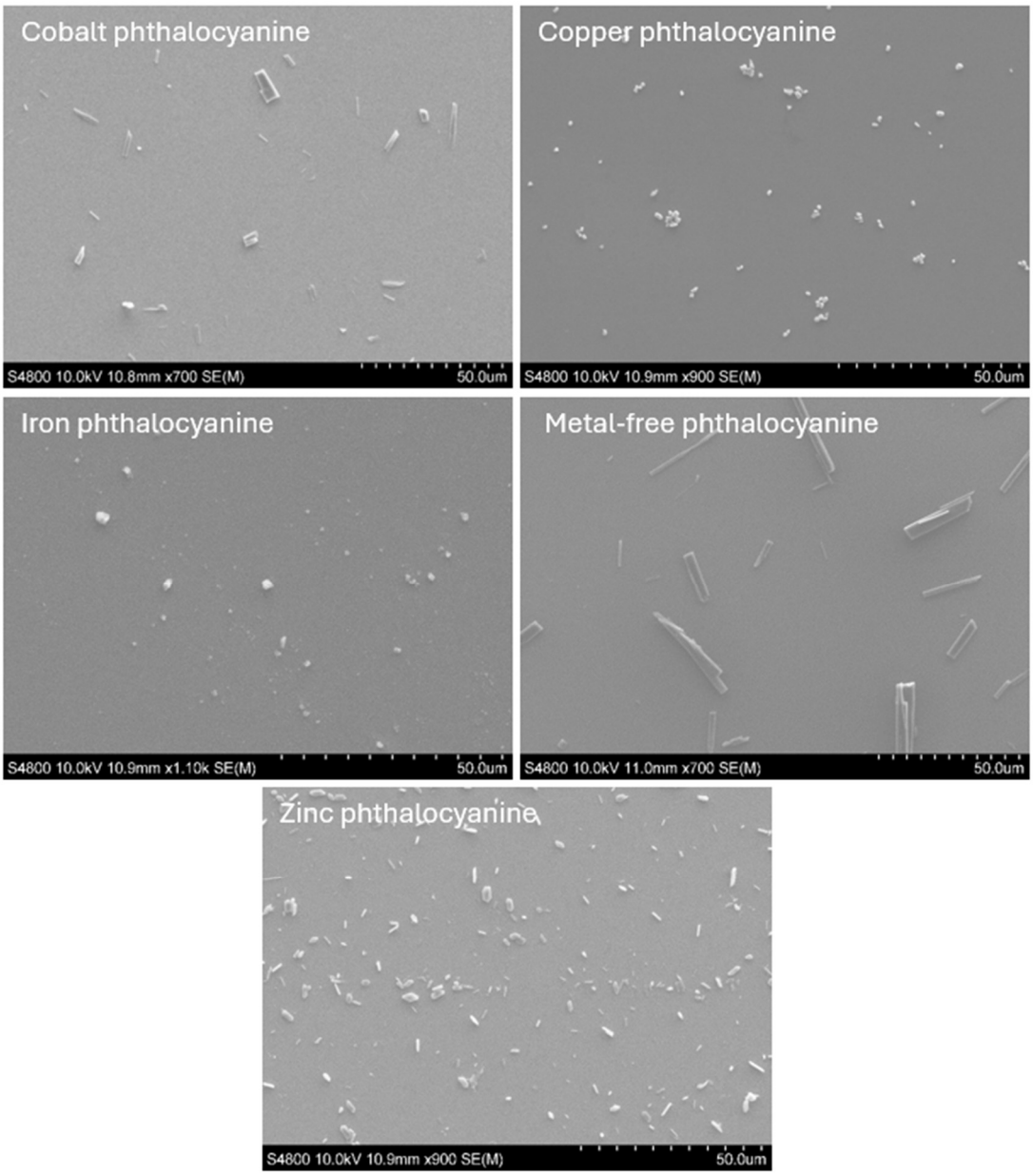


***Figure 6.3**: SEM images of cobalt, copper, iron, zinc and metal-free phthalocyanine drop-cast on graphene-Si/SiO_2 wafers.*

From the SEM images, it is apparent that the Pc crystals are distributed non-uniformly on the graphene surface. To enhance the uniformity of the coatings, a substituted Pc with increased solubility was developed. This improvement is detailed later in **Section 6.6** of this chapter.

6.5. Drop-cast Phthalocyanine Gas Sensing Performance

This section presents the gas sensing performance of different drop-casted unsubstituted metal phthalocyanines on graphene sensors. First, the sensing performance of copper phthalocyanine-functionalized DipChipX devices is discussed in detail. This is followed by an investigation of Hall Bar sensors functionalized with metal phthalocyanines having different metal centres: cobalt, iron, zinc, and metal-free.

6.5.1. Copper Phthalocyanine

The gas sensing performance of drop-cast (unsubstituted) copper phthalocyanine (CuPc) was investigated using nitrogen dioxide, ammonia, and methane gases in the Phase 2 gas system.

6.5.1.1. Nitrogen Dioxide Sensing

Initial tests with unsubstituted copper phthalocyanine (CuPc)-functionalized DipChipX graphene sensors were conducted to evaluate sensor recovery. Sensors were first exposed to air for 20 minutes to establish a baseline. Following this, the sensors were exposed to 100 ppm nitrogen dioxide (NO_2) for 10 minutes, then to air for another 10 minutes. A final 10-minute exposure to 100 ppm NO_2 was then conducted. Throughout all gas exposures, the flow rate was maintained at 1000 mL/min, and all experiments were performed at room temperature (RT) and atmospheric pressure.

Figure 6.4a displays the real-time resistance measurement profile for one graphene channel on a copper phthalocyanine-functionalized 3-channel DipChipX device. The introduction of 100 ppm NO_2 caused a sharp decrease in resistance, with sensor saturation beginning during the second exposure to 100 ppm NO_2 gas. This is evident in **Figure 6.4b**, where the sensor response drops from -5.5% in Test 1 to -1.5% in Test 2. Notably, a negative sensor response value indicates a decrease in resistance, or a drop in $\Delta R/R_0$. Additionally, the response time (details on the calculation method are

provided in **Chapter 3.6.2**) increases by 60 seconds during the second exposure period, from 403 seconds in Test 1 to 463 seconds in Test 2. Furthermore, the reduced response during the second exposure period, following air exposure, suggests that the device does not fully recover to its original baseline state.

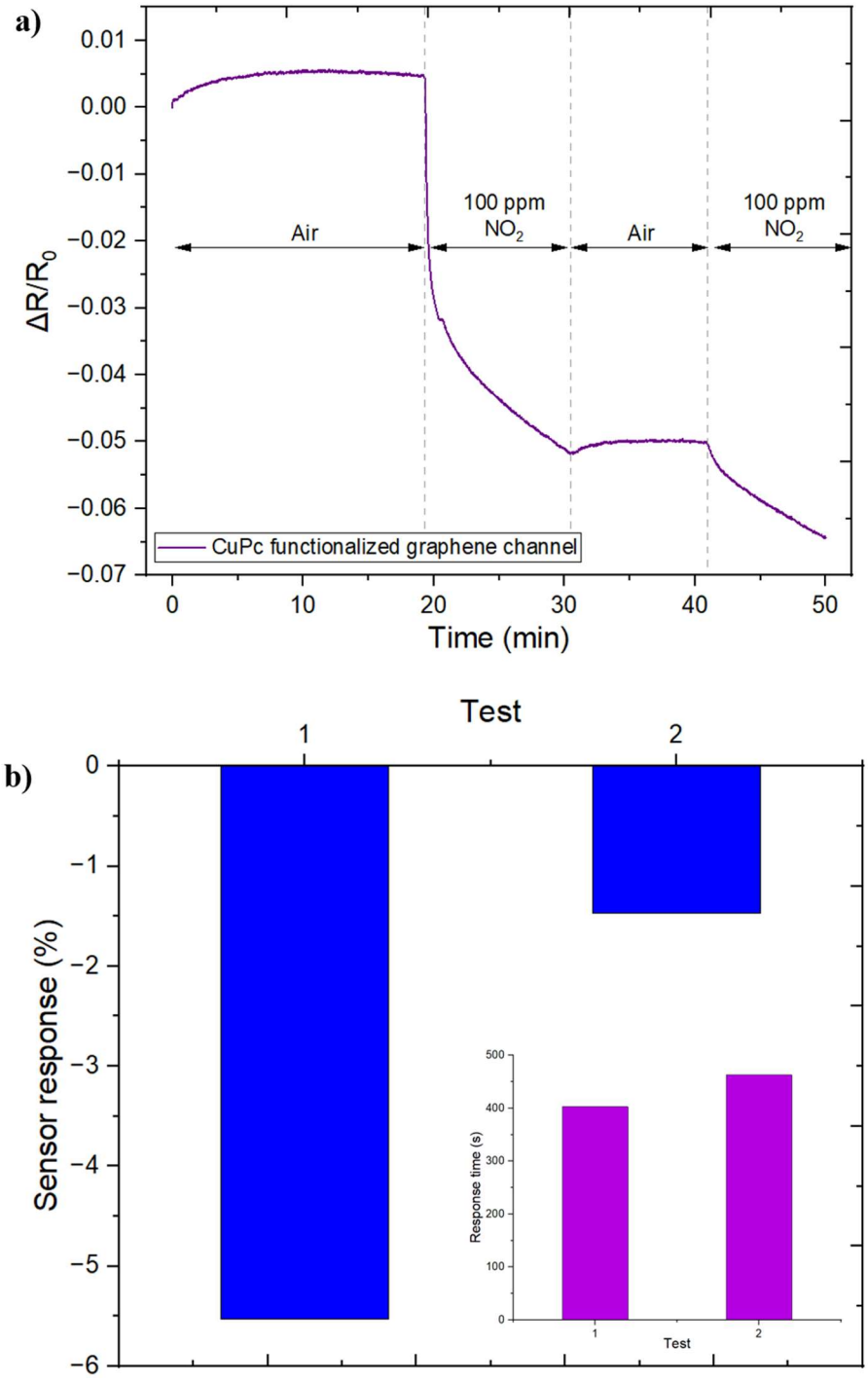


***Figure 6.4**: Gas sensing data from a CuPc functionalized 3-channel DipChipX device. **(a)** Real-time resistance measurements of two consecutive exposures to 100 ppm nitrogen dioxide gas **(b)** Sensor response of both exposures (i.e., 'Test 1 and 2'). **Inset:** Response time graph where response time is defined as 'time required for the sensor to reach 90% of the maximum response'* [257].

Next, the sensor recovery process using a 265 nm UV light was investigated. Sensors were exposed in this experiment with reduced exposure times: 5 minutes of air, 5 minutes of 100 ppm NO_2, and 5 minutes of air. After the final air exposure, the sensors were removed from the chamber and exposed to UV light for 120 seconds, a duration previously reported to successfully recover sensors [26]. This experiment was repeated nine times with both bare graphene and CuPc-functionalized graphene sensors to evaluate their recovery. Repetitions were plotted on the same graph for easy comparison (**Figure 6.5**).

Figure 6.5a presents the real-time resistance measurements of one bare graphene channel from a DipChipX sensor. Following each exposure to NO_2, the resistance sharply decreases due to the electron-withdrawing nature of the gas, which accentuates the p-type nature of graphene [307]. After each exposure to UV light, the sensor's resistance increases significantly. Subsequently, the sensor's response magnitude to NO_2 remains consistent, indicating that the NO_2 molecules have been effectively desorbed from the surface, returning the sensor to its initial baseline state. This trend is clearly observable in **Figure 6.5c**, as the sensor response averages -3.9% with a standard deviation of 0.28 across the repeats for the bare graphene sensor.

Figure 6.5b displays the real-time resistance measurements of one graphene channel functionalized with CuPc, exposed to 100 ppm NO_2. Compared to the bare graphene sensor, the sensor response is enhanced due to the presence of the CuPc molecule on the surface. For instance, the first iteration shows a sensor response of -3.3% for bare graphene, which increases to -9.7% for the CuPc-functionalized sensor. This enhanced sensor response is consistent with findings by Wang et al. [308], who constructed metal phthalocyanine-graphene oxide (MPc-GO) hybrids. The combination of the gas sensitivity of MPcs with the excellent electrical conductivity and larger surface area of graphene, which facilitates faster charge transfer, explains the improved sensor response of the CuPc-functionalized sensors.

Despite the improved sensor response with CuPc, the data also reveals that the functionalized sensor does not appear to be fully recover following UV exposure. The magnitude of the sensor response decreases with each repeated exposure to NO_2. The initial sensor response drops from -9.7% to -2.3% by the 5th repeated exposure, where it stabilizes until the final exposure. The standard deviation between repeats of the

CuPc-functionalized sensor (2.7) further evidences the variability of repeat measurements. The data suggests that the UV light is only partially desorbing the adsorbed NO_2 molecules, indicating that a longer exposure time may be necessary to achieve complete desorption.

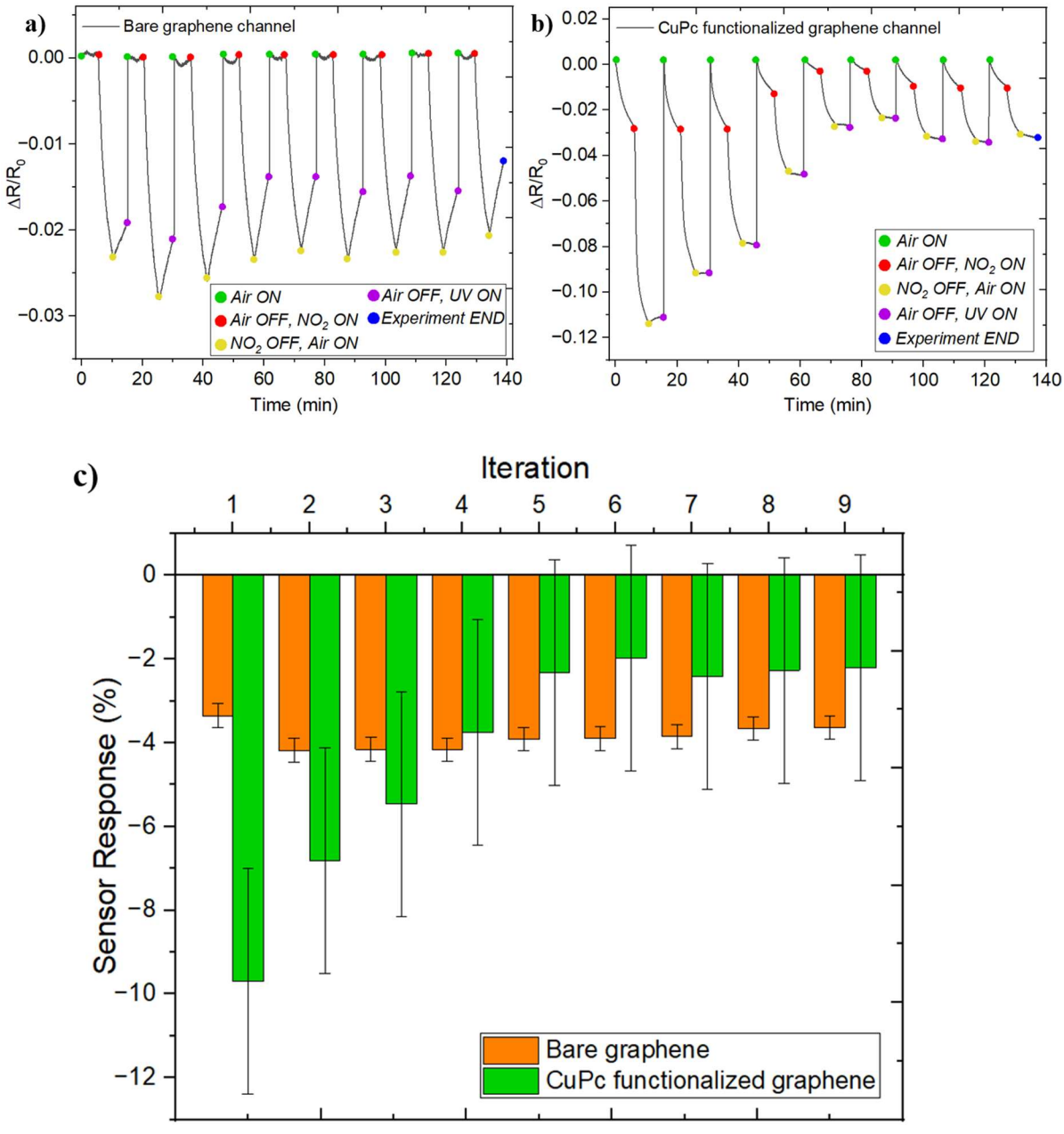


***Figure 6.5**: Real-time resistance measurements of a **(a)** bare and **(b)** CuPc-functionalized DipChipX graphene sensor (1 channel) exposed repeatedly to 100 ppm NO_2 and subsequent UV light exposure. **(c)** Bar chart displaying a comparison of sensor response (%) over nine repeats of the bare and CuPc-functionalized DipChipX graphene sensors.*

6.5.1.2. Ammonia Sensing

Using a similar procedure, the gas sensing performance of both bare and CuPc-functionalized graphene DipChipX sensors was evaluated with 100 ppm ammonia (NH_3). The sensors underwent the following sequence: (1) 5 minutes of air exposure, (2) exposure to 100 ppm NH_3, (3) another 5 minutes of air, and (4) 120 seconds of UV light exposure. Nine repeats were conducted at RT with a constant flow rate of 1000 mL/min, and the results were combined into a single graph (**Figure 6.6a**) for comparison.

Figure 6.6a shows the real-time resistance measurement profile for one bare graphene channel on a DipChipX sensor exposed repeatedly to 100 ppm NH_3, followed by 120-second UV recovery treatments. Exposure to NH_3 generates an opposite response to NO_2, with $\Delta R/R_0$ increasing positively due to ammonia's electron-donating nature. Since the graphene is p-type, electron donation reduces carrier concentration and increases resistance as the electrons combine with holes. The sensor response (**Figure 6.6c**) across the nine repeats is variable (standard deviation = 1.1), ultimately increasing over time. The initial sensor response of 2.6% rises to 5.3% by the final iteration. This increase could be attributed to the removal of ambient adsorbed gases along with NH_3, freeing up additional surface adsorption sites.

Figure 6.6b presents the real-time resistance measurement profile for the CuPc-functionalized sensor. Although the response appears less variable (standard deviation = 0.29) compared to the bare graphene sensor, the overall response is lower with CuPc on the surface. The average sensor response (**Figure 6.6c**) across nine repeats was 2.0% for the functionalized sensor, whereas the maximum response for the bare graphene sensor was 5.3%. Published literature indicates that sensor performance using phthalocyanines depends on: (1) the central metal [166], [308], (2) ring substituents [26], and (3) the nature of the target gas [167]. In this case, copper phthalocyanine is not the ideal choice for detecting NH_3. For instance, cobalt phthalocyanine (CoPc) has a higher adsorption energy (-21.7 kcal/mol) compared to CuPc (-12.4 kcal/mol), resulting in a greater affinity for NH_3 interactions with CoPc. [308]. The gas sensing performance of CoPc is investigated later in this work, detailed in **Section 6.5.2.** Moreover, the diminished sensor response may be due to the CuPc molecules obstructing NH_3 adsorption on the graphene surface.

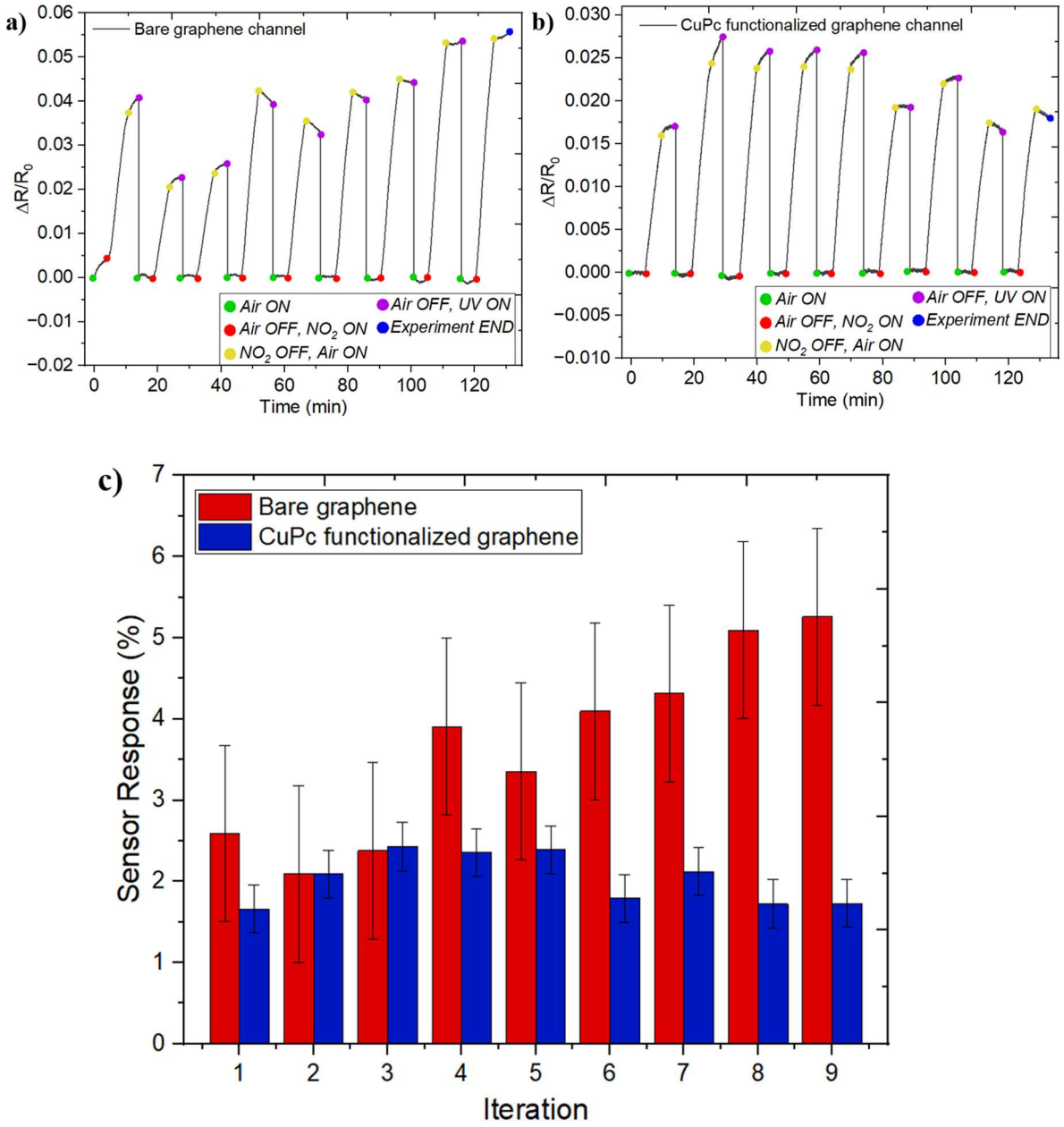


***Figure 6.6**: Real-time resistance measurements of a **(a)** bare and **(b)** CuPc-functionalized DipChipX graphene sensor (1 channel) exposed repeatedly to 100 ppm NH_3 and subsequent UV light exposure. **(c)** Bar chart displaying a comparison of sensor response (%) over nine repeats of the bare and CuPc-functionalized DipChipX graphene sensors.*

6.5.1.3. Methane Sensing

The sensing performance of both sensors were evaluated by exposing them to 100 ppm methane (CH_4). The real-time resistance measurements of bare graphene and CuPc-functionalized graphene sensors show that there is no response upon exposure to methane (**Figure 6.7**). During the 15-minute exposure period, the resistance drifted down by -1.0% and -0.71% for bare and CuPc-functionalized graphene, respectively, with no obvious changes when the methane entered the sensing chamber.

Due to the low adsorption energy of CH_4 on pristine graphene, methane does not interact strongly enough with graphene to induce noticeable changes in its electrical properties [309]. Various studies have demonstrated that surface modification [310], [311], doping [312], [313], defects [309] and increasing the number of layers [313] can alter the electronic properties of graphene, thereby enhancing its sensing performance toward CH_4. Similarly, the low binding energy of -6.20 kcal/mol reported by Rana et al. [306] could explain why no response was observed between CuPc and CH_4.

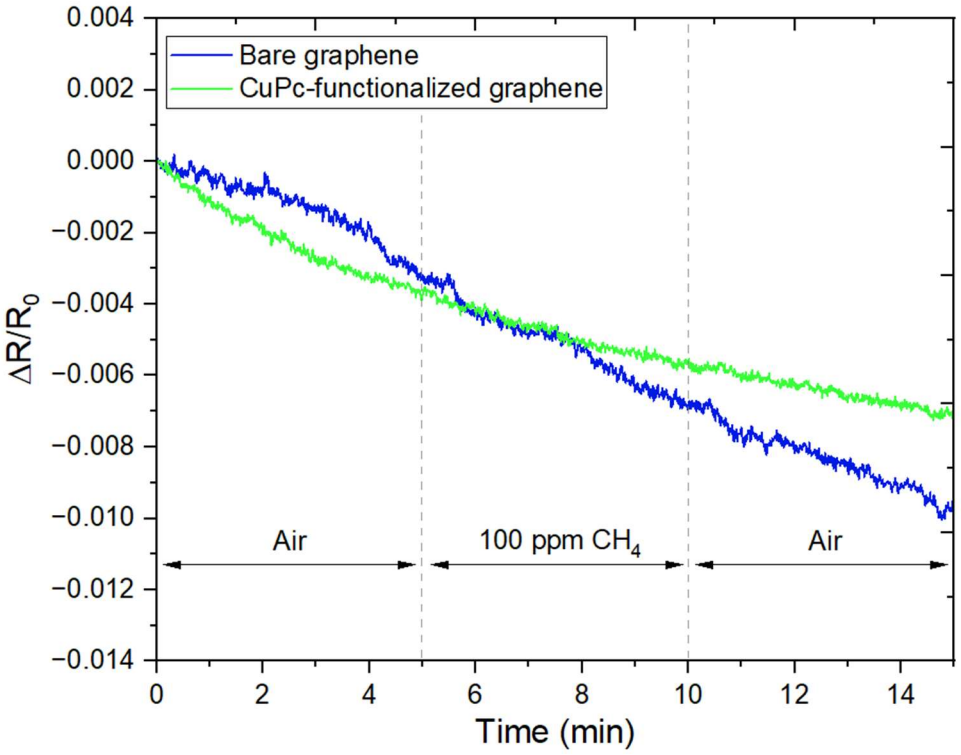


Figure 6.7: Real-time resistance measurements of a bare and CuPc-functionalized DipChipX graphene sensor (1 channel) exposed repeatedly to 100 ppm CH_4.

6.5.2. Cobalt, Iron, Zinc and Metal-free Phthalocyanine

To investigate the gas sensing performance of various metal phthalocyanines with different gases, each MPc was drop-cast onto Hall Bar sensors and tested using the Phase 3 gas sensing system. A bare graphene Hall Bar sensor was also exposed to the same gases for additional comparison. The five different metal phthalocyanines used were cobalt (CoPc), iron (FePc), zinc (ZnPc), metal-free (H_2Pc), and copper. The experiments with copper phthalocyanine (CuPc) were repeated using the Hall Bar graphene devices. The sensing tests began by exposing the sensors to nitrogen for 30 minutes to establish a baseline, with a 5-minute period shown in real-time resistance plots. Subsequently, each sensor, functionalized with different metal phthalocyanines, was exposed to the following gases in separate tests: 50 ppm nitrogen dioxide (NO_2), 10 ppm nitric oxide (NO), 50 ppm ammonia (NH_3), 100 ppm methane (CH_4), and 580 ppm carbon dioxide (CO_2). After exposure to the target gas, a final 5-minute exposure to nitrogen was performed. Throughout all gas exposures, the target gas exposure time was 5 minutes, the flow rate was maintained at 1000 mL/min, and all experiments were conducted at RT and atmospheric pressure.

Before exposing the sensors to the next target gas, they were recovered outside the sensing chamber by heating on a hot plate at 175°C for 5 minutes (see **Chapter 5.6.2.2** for details on the selected heating parameters). Since the recovery process occurred outside the sensing chamber, real-time measurements of resistance changes during recovery were not possible.

Due to the large spacing between graphene channels in the 'Hall Bar' design, using the UV LED for recovery was challenging. Consequently, heating was employed as an alternative recovery method. **Chapter 5.6.2.1.1** illustrates this issue, showing incomplete desorption on one of the channels due to the UV LED placement.

The real-time gas sensing response for each target gas is displayed below. The responses for both channels were averaged and expressed as $\Delta R/R_0$, normalized resistance. **Figure 6.8a** and **b** demonstrate that following nitrogen exposure, both NO_2 and NO exposure resulted in a sharp decrease in the resistance of all the sensors. Like graphene, the phthalocyanines are p-type semiconductors [166], which explains the decrease in resistance when exposed to oxidizing, electron-withdrawing gases [301]. In contrast, ammonia exposure (**Figure 6.8c**) increased the resistance of the devices

due to the electron-donating nature of the gas [166], [169]. The varying magnitudes of response to the same gas across different metal phthalocyanines indicate that the different metal centres impact the sensing performance. This aligns with several studies [166], [306], [308], [314] which emphasize the importance of tailoring the metal centre to the desired target gas. Finally, upon exposure to CH_4 and CO_2 (**Figure 6.8d** and **e**), neither the bare graphene nor the metal phthalocyanine-functionalized graphene sensors exhibited any response to these gases.

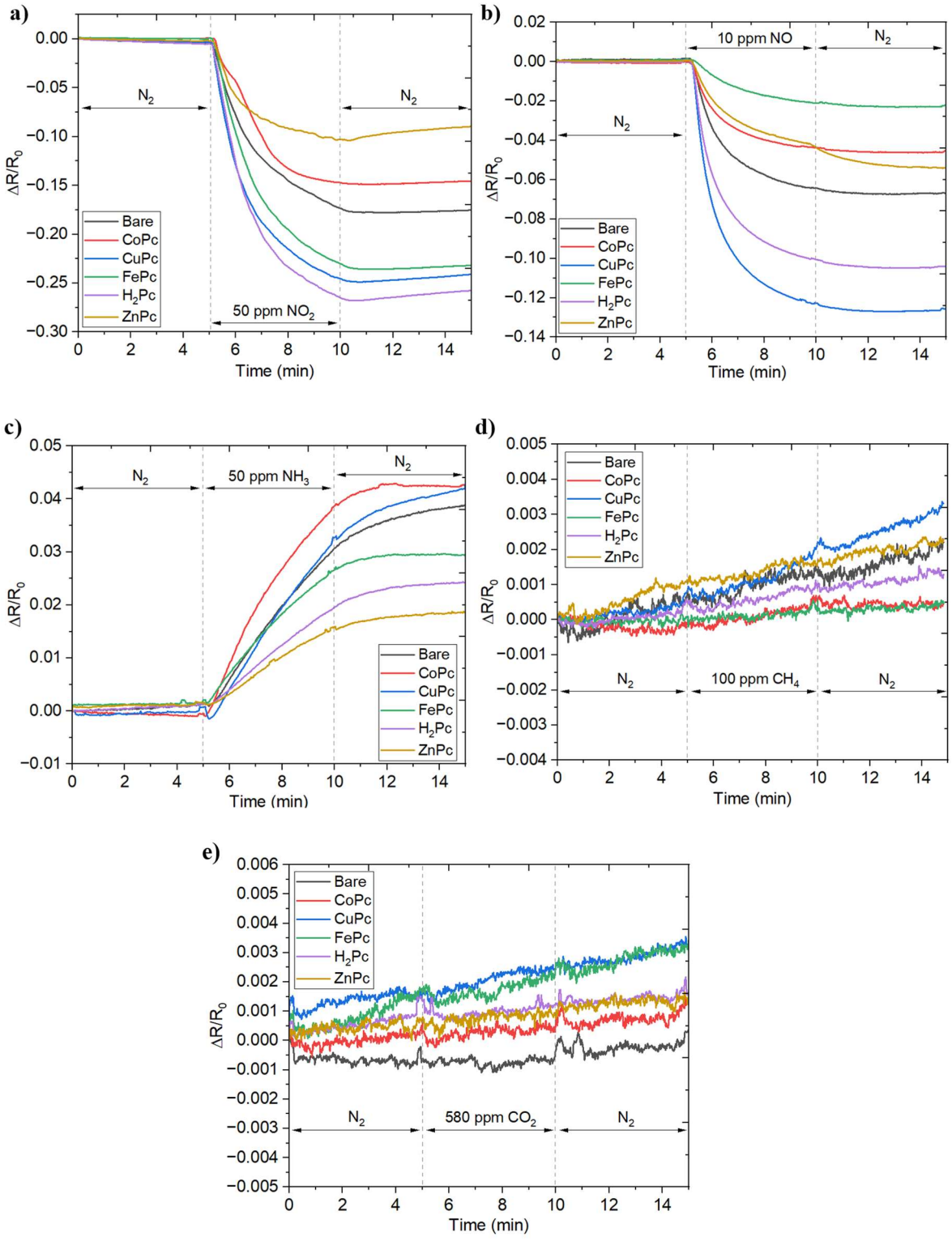


***Figure 6.8**: Real-time resistance measurements of individual Hall Bar sensors functionalized with different metal phthalocyanines (cobalt, copper, iron, metal-free and zinc) exposed to **(a)** 50 ppm NO_2, **(b)** 10 ppm NO, **(c)** 50 ppm NH_3, **(d)** 100 ppm CH_4, and **(e)** 580 ppm CO_2.*

Figure 6.9 presents the sensor response for bare graphene and each metal phthalocyanine-functionalized sensor exposed to five different gas species. Among the metal phthalocyanines, the largest response to NO_2 gas was observed with the metal-free, copper, and iron variants, demonstrating responses of -26.4%, -24.6%, and -23.5%, respectively, all of which outperform bare graphene at -17.3%. Nitric oxide exposure induced the greatest change in CuPc (-12.4%) and H_2Pc (-10.2%), both surpassing the response of bare graphene (-6.7%).

It is unclear why the H_2Pc sensor responded so well to NO_2 gas. This is contrary to findings by Bohrer et. al, who demonstrated that the higher the hydrogen bond basicity of the analyte, the greater the sensitivity to that particular entity. Typically, compounds with an electronegative atom directly bonded to a hydrogen atom (e.g., NH_3) would have higher hydrogen bond basicity than NO_2. Thus, the strong response to NO_2 was unexpected. Moreover, the sensor showed a significantly lower response (2.2%) to NH_3, which has higher hydrogen bond basicity, compared to NO_2 (-26.4%). Additionally, Pochekailov et al. [315] reported that the NO_2 molecule interacts weakly with H_2Pc via Van der Waals forces, and hence, produced a lower response than the other phthalocyanine variant tested. Further repeat experiments are necessary to investigate the unexpected response thoroughly.

For ammonia gas, cobalt phthalocyanine exhibited the highest response at 4.4%, followed closely by CuPc at 4.0% and bare graphene at 3.5%. Notably, bare graphene demonstrated a higher response to ammonia compared to several metal phthalocyanine variants, including iron, metal-free, and zinc. However, the overall response to NH_3 gas was considerably weaker than the response to the two oxidizing gases. Cobalt phthalocyanine was expected to achieve the highest response to ammonia as it is commonly chosen for ammonia sensing [26], [176], [316]. As discussed in **Section 6.5.1.2**, cobalt phthalocyanine has a higher adsorption energy with ammonia than CuPc, which explains its superior response [308]. Finally, neither the bare graphene nor the metal phthalocyanine-functionalized sensors exhibited any measurable response upon exposure to CH_4 and CO_2.

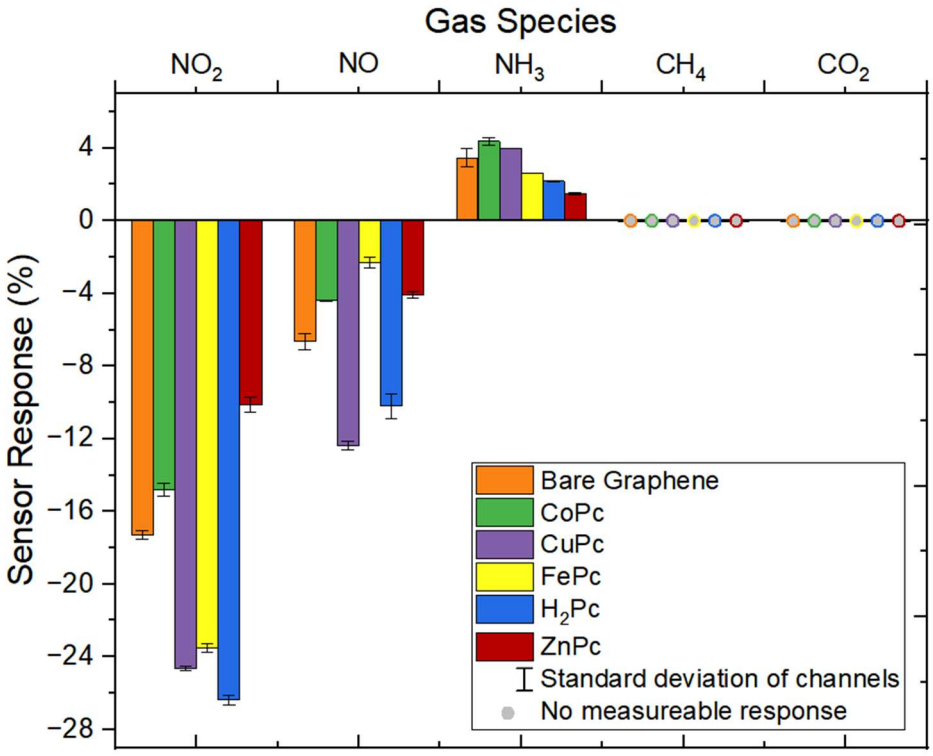


***Figure 6.9**: Bar chart displaying the sensor response (%) for bare graphene and the different metal phthalocyanine-functionalized sensors (cobalt, copper, iron, metal-free and zinc) exposed to different gas species (NO_2, NO, NH_3, CH_4, and CO_2).*

Response times of the bare graphene and metal phthalocyanine-functionalized sensors are presented in **Figure 6.10**. With a few exceptions, the response time tends to increase as the sensor response decreases. For instance, NH_3 induces the weakest response on the sensors and generally results in the longest response times.

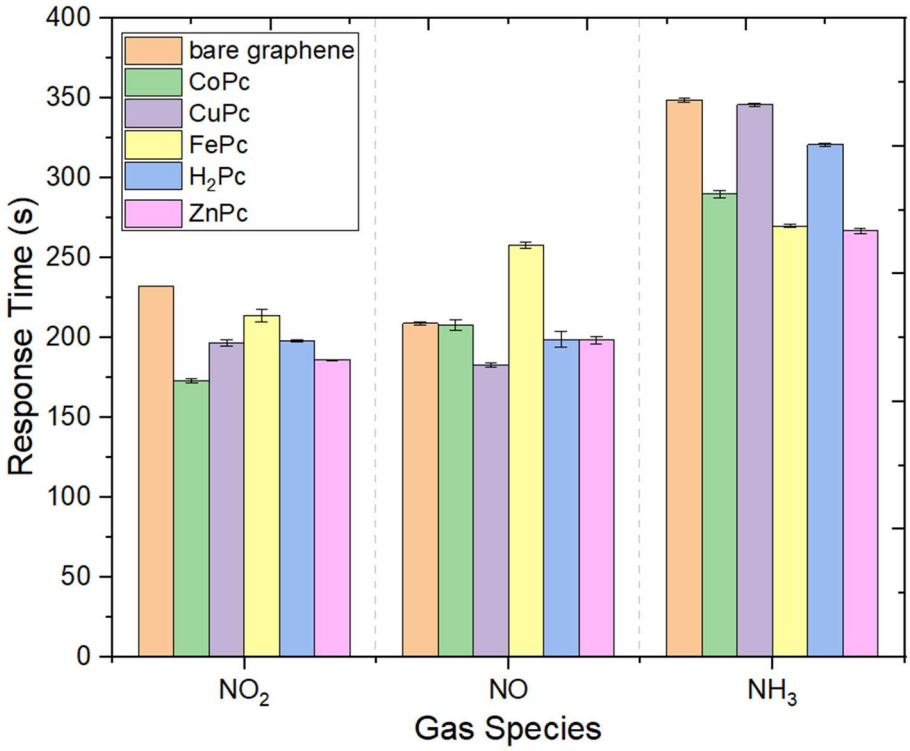


***Figure 6.10**: Bar chart displaying the response times (s) for bare graphene and the different metal phthalocyanine-functionalized sensors (cobalt, copper, iron, metal-free and zinc) exposed to different gas species (NO_2, NO and NH_3).*

6.6. Synthesis of Copper (II) 2,9,16,23-Tetra-tert-butyl phthalocyanine

The next section will describe the synthesis and characterization of copper (II) 2,9,16,23-tetra-tert-butylphthalocyanine.

6.6.1. Motivation

While drop-casting is a simple method for functionalizing graphene, it can lead to non-uniform coverage of the functional entity on the surface (**Figure 6.11**). Additionally, unsubstituted phthalocyanine molecules are known for their low solubility in most solvents [317], making spin-coating an unsuitable application method. Thermal evaporation is a widely used method for creating uniform films of phthalocyanines [318]–[320]. However, at the time of the research, this technique could not be employed due to concerns about cross-contamination of the devices with the existing

lab equipment available. Therefore, it was necessary to synthesize a soluble phthalocyanine to investigate the gas-sensing properties of a film. Solubilizing phthalocyanines involves adding substituent groups to the benzene rings. Previous studies have achieved this by incorporating octa-alkyl [321], neopentoxy [322], and tert-butyl groups [323]–[325]. Owing to the straightforward preparation, solubility in a wide variety of solvents [326], and potential for use in gas sensing [324], [327], [328], the tetra-tert-butyl copper phthalocyanine derivative was chosen for synthesis.

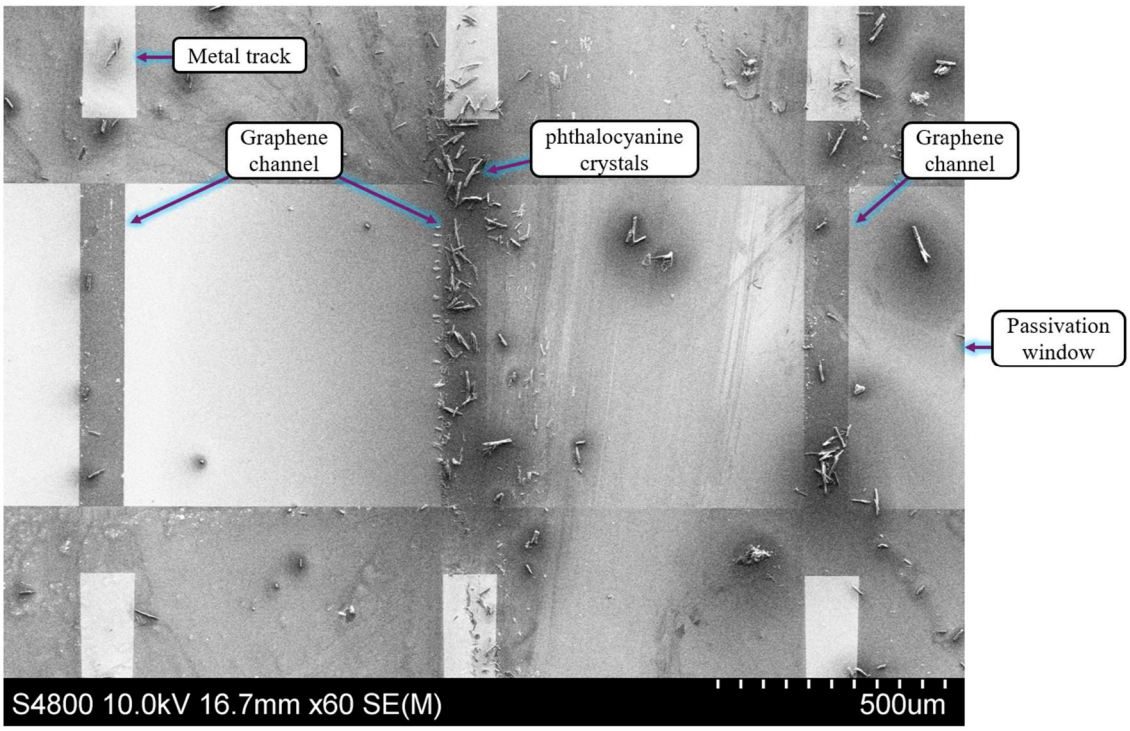


***Figure 6.11**: SEM image demonstrating the uneven distribution of drop-cast metal-free phthalocyanine on a 3-channel graphene 'DipChipX' device.*

6.6.2. Synthesis

The 2, 9, 16, 23-tetra-tert-butyl copper (II) phthalocyanine ($CuPc(t\text{-}Bu)_4$) synthesis was based on the approach outlined in a prior research publication [329]. The reaction scheme is shown below.

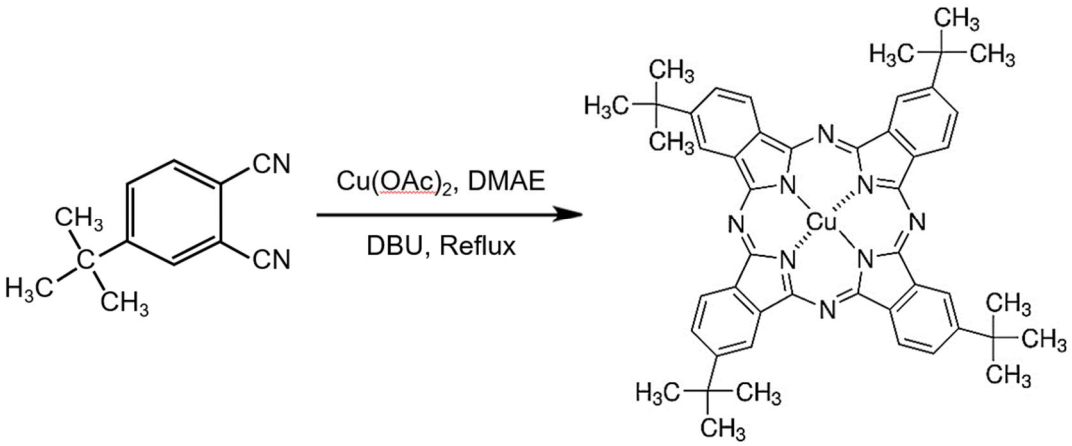


***Figure 6.12**: Reaction scheme for the synthesis of Copper (II) 2,9,16,23-Tetra-tert-butylphthalocyanine.*

Copper (II) acetate (0.25 mmol) and 4-tert-butyl phthalonitrile (1 mmol) were mixed together in a round-bottomed flask with 5 mL of dried N,N-dimethylaminoethanol. A couple of drops of the catalyst, 1,8-diazobicyclo[5.4.0]undec-7-ene (DBU) was added to the flask. The flask was equipped with a magnetic stir bar and sealed using a folded rubber septum. Nitrogen gas, contained in a balloon connected to a syringe, was then introduced into the flask through the rubber septum. The gas was bubbled through the flask for 15 minutes to ensure an inert atmosphere. The reaction mixture was heated and stirred in a nitrogen atmosphere at 160°C for 24 hours, deviating from the referenced method's suggested 6 hours. This adjustment was made as the initial reaction attempt did not reach completion. Reaction completion was confirmed using thin layer chromatography (TLC).

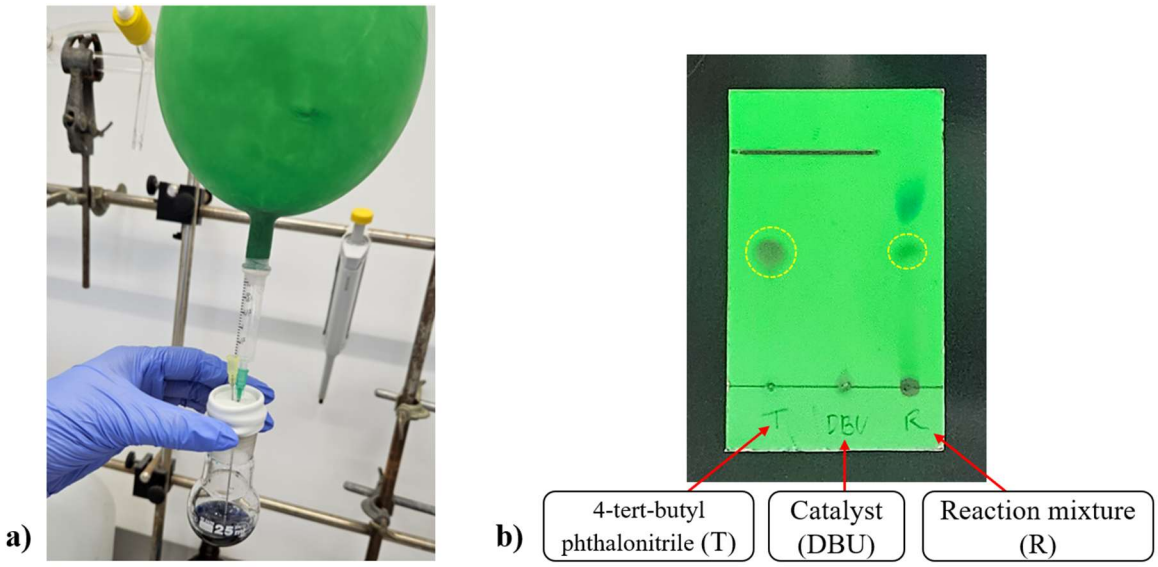


***Figure 6.13**: **(a)** Reaction mixture inside a 25 mL round bottomed flask using nitrogen inert atmosphere balloon. **(b)** The TLC plate demonstrates how the reaction's progress was monitored. The image shows that the reaction is not yet complete at this point, as traces of 4-tert-butyl phthalonitrile are still present in the reaction mixture.*

The resulting green precipitate was filtered using vacuum filtration and washed several times with water and then dried using magnesium sulphate (**Figure 6.14a**). The dried precipitate was dissolved in dichloromethane and purified using silica gel column chromatography (**Figure 6.14b**). The eluent exiting the column was collected in 50 mL increments and monitored using TLC to ensure the correct product was retained. Finally, the product was dried using a rotary evaporator and characterised using Fourier transform infrared spectroscopy (FT-IR) and ultraviolet-visible spectroscopy (UV-Vis).

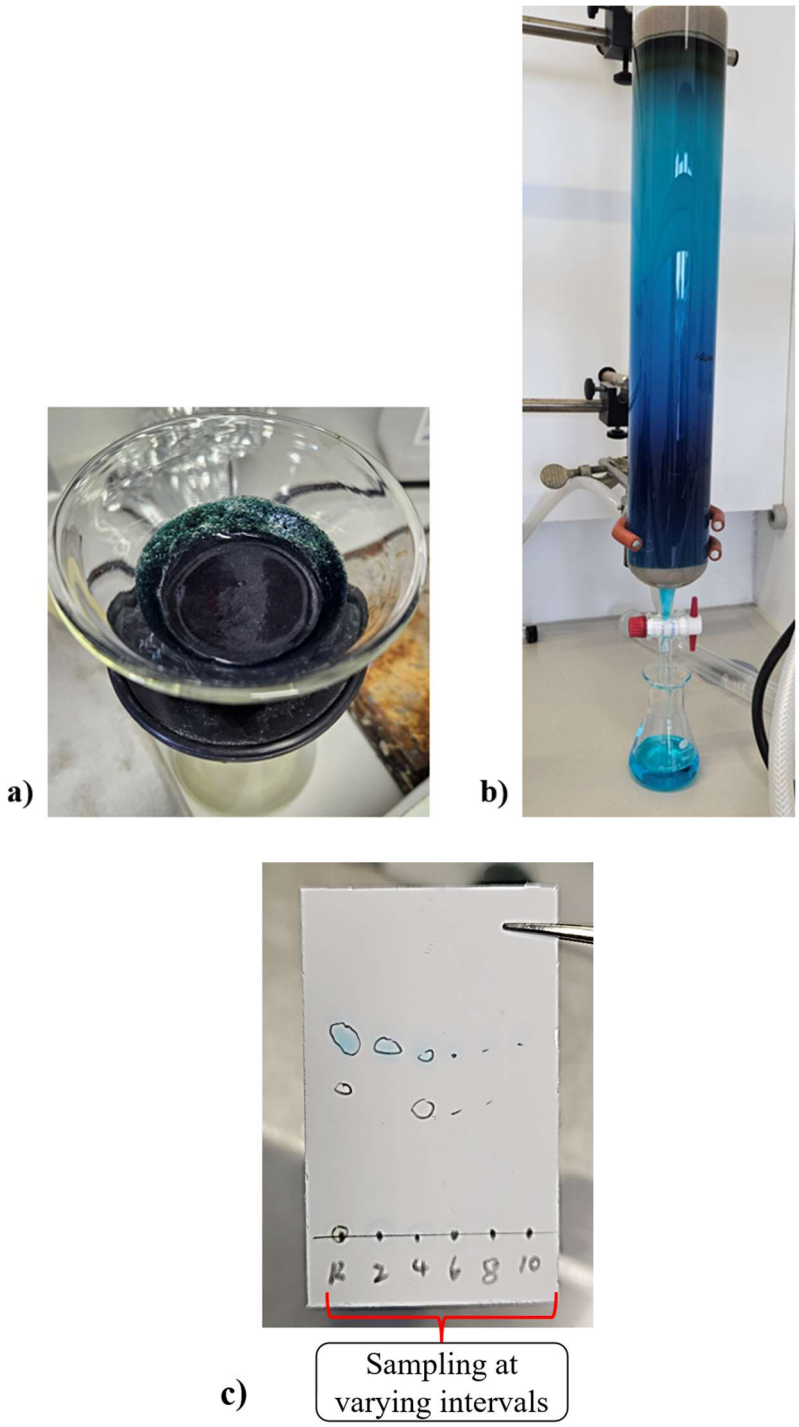


***Figure 6.14**: Images depicting the following steps: **(a)** filtering the resulting green precipitate, **(b)** purifying $CuPc(t\text{-}Bu)_4$ using silica gel column chromatography, and **(c)** using a TLC plate to monitor the product eluting from the column.*

The final product (**Figure 6.15**) was a dark blue powder exhibiting high solubility in various solvents such as dichloromethane and toluene.



***Figure 6.15**: Dark blue powder; tetra tert-butyl copper phthalocyanine.*

6.6.3. Characterization

The identity of the synthesized compound was confirmed using FT-IR and UV-Vis spectroscopy. Additionally, further characterization was performed on dissolved tetra-tert-butyl copper phthalocyanine spin-coated onto silicon wafers.

6.6.3.1. Infrared Spectroscopy

The experimental FT-IR spectrum (**Figure 6.16**) of the product was obtained using an *Alpha Bruker benchtop FT-IR spectrometer* and *OPUS* software.

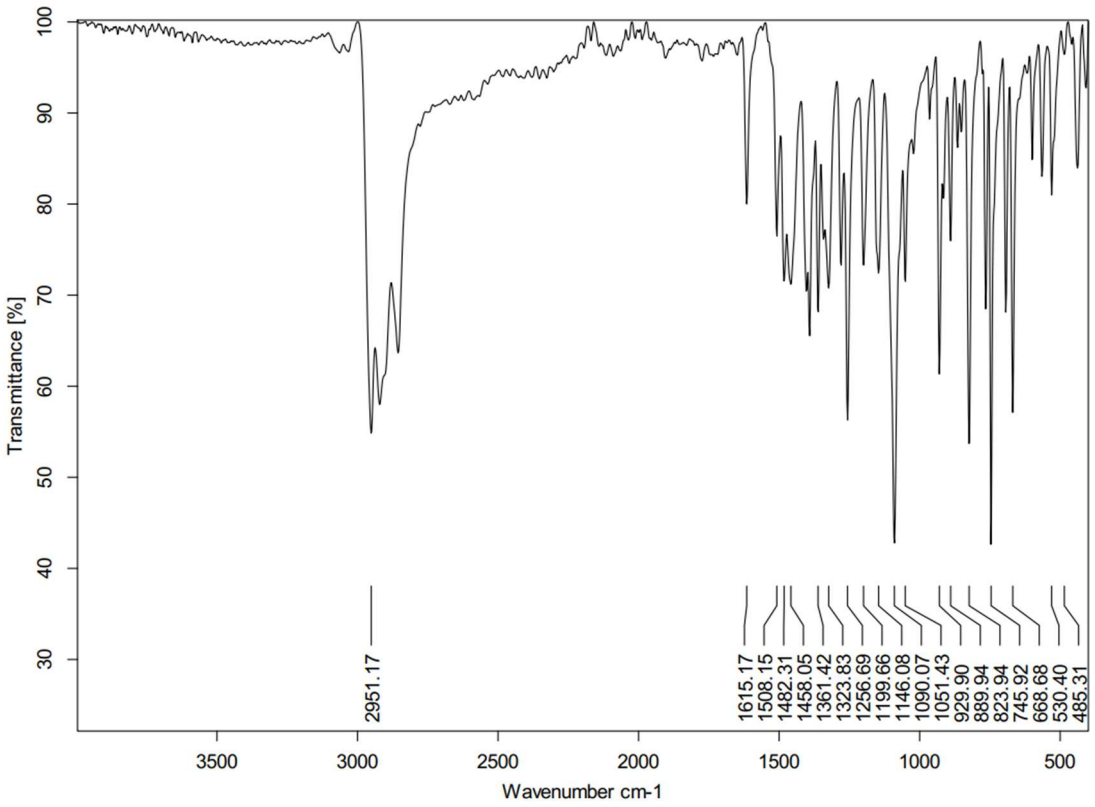


***Figure 6.16**: Experimentally obtained FT-IR spectrum of tetra tert-butyl copper phthalocyanine.*

The acquired spectrum was cross-referenced with the absorbance values reported in a paper by Yadav, K. et al. [329]. **Table 22** presents the peak positions acquired in the experimental spectrum compared to similar peaks found in reference [329].

Table 22: Peak positions and peak assignments of acquired spectrum compared to literature values [329].

Acquired spectrum (cm^{-1})	Literature (cm^{-1})	Assignment	Ref.
2951	2953	CH_3 asymmetric stretching	[325], [330]
1615	1611	Aromatic ring stretching	[331]
1458	1448	In plane pyrrole stretching, C=C stretching	[332], [333]
1361	1359	Isoindole stretching, C=C stretching	
1324	1317	C-H bending, C=C stretching	
1257	1253	C-O stretching	[198]
1200	1195	C-N-C bending	
1090	1088	Cu-N stretching	
1051	1046	In-plane C-H deformation	
824	822	Out of plane C-H vibration	[334]
746	742	Out of plane C-H deformation	[198]
669	665	*Unassigned – matched with literature spectrum	[329]
532	530		

The absorptions observed at ~2950 cm^{-1} are associated with the tert-butyl groups [325]. The band at ~1090 cm^{-1} can be attributed to the Cu-N bond stretching [333]. Bands within the region 1500 – 1300 cm^{-1} could be attributed to the C=C stretching and C=N skeletal vibrations [332]. Additionally, Kumar et al. who collected spectra from powdered and $CuPc(t\text{-}Bu)_4$ films, report a band at 1615 cm^{-1} (analogous to the collected spectrum above), ascribed to the C=C vibrations [324].

6.6.3.2. UV-Vis Spectroscopy

The UV-Vis spectrum (**Figure 6.17**) of tetra tert-butyl copper phthalocyanine was obtained by preparing a 7 x 10^{-6} M solution of $CuPc(t\text{-}Bu)_4$ dissolved in dichloromethane. Absorbance peaks at wavelengths (λ) of 339, 610, and 677 nm were observed and align closely with literature values of 340/345, 607/609, and 671/676 nm [325], [329] respectively.

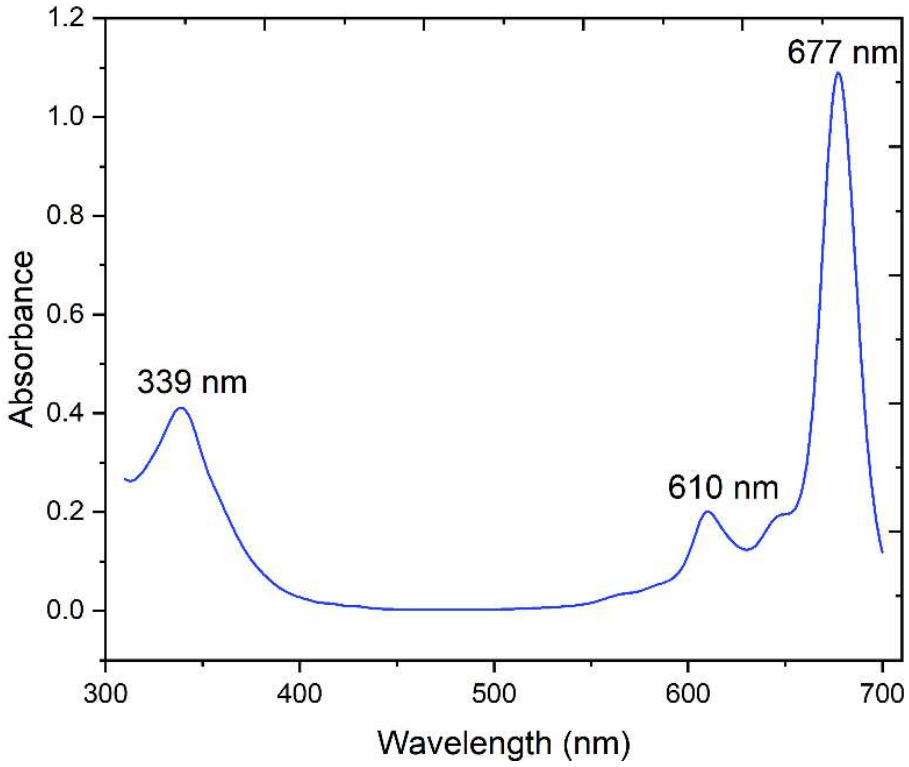


***Figure 6.17**: Experimentally acquired UV-Vis spectrum of tetra tert-butyl copper phthalocyanine.*

6.6.3.3. Graphene Functionalization via Spin-Coating

To perform additional characterization techniques such as atomic force microscopy, ellipsometry, and Raman spectroscopy, $CuPc(t\text{-}Bu)_4$ was spin-coated onto graphene-Si/SiO_2 wafer pieces. Additionally, using the same spin-coating procedure, 3x3 graphene arrays were functionalized for gas sensing experiments. The details of the spin-coating process are provided below.

Copper (II) 2,9,16,23-tetra-tert-butylphthalocyanine ($CuPc(t\text{-}Bu)_4$) was dissolved in toluene at a concentration of 10 mg/mL, and a 20 µL droplet of the solution was applied to the graphene pixels. The spin coating process was performed using an L2001A3 Ossila spin coater with a custom-made chuck (as seen in **Chapter 3.3.1.2**). To ensure that only the graphene pixels of the sensor arrays were functionalized, the metal contacts at the bottom of the devices were temporarily covered with Parafilm.

The spin-coating parameters were as follows:

	Step 1
Time (s):	30.0
Spin speed (rpm):	2000

Spin-coating parameters were selected based on those found in published literature on spin-coating CuPc films [321], [335].

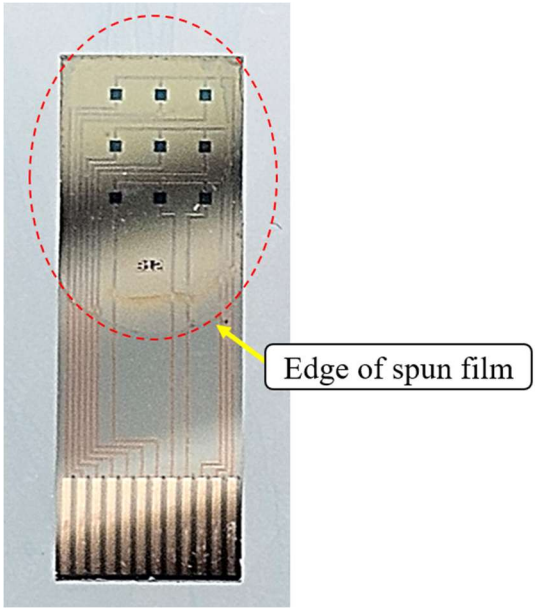


***Figure 6.18**: Image demonstrating complete coverage of the graphene pixels using a spun film on a 3x3 graphene pixel array sensor.*

6.6.3.4. Atomic Force Microscopy

Atomic force microscopy (AFM) was utilized to analyse the surface morphology of the spin-coated CuPc(t-Bu)$_4$ films, which were prepared according to the spin-coating procedure detailed in the previous sub-section (**6.6.3.3**).

The surface topography before and after spin coating was characterised using a *Bruker Dimension icon XR* scanning probe microscope with a SCANASYST-AIR probe in tapping mode (probe specifications and scan parameters are provided in **Chapter 3.4.4**). The surface of the bare graphene wafer before and after spin coating with CuPc(t-Bu)$_4$ showed clear changes in surface roughness and topography (**Figure 6.19**). An examination of the spin-coated film image reveals distinct, 'rice grain'

features not observed on the bare graphene wafer. The average root mean square (RMS) roughness of three measurements taken the of bare graphene wafer was 0.196 nm which increased to 1.749 nm after CuPc(t-Bu)$_4$ was spin coat onto the wafer.

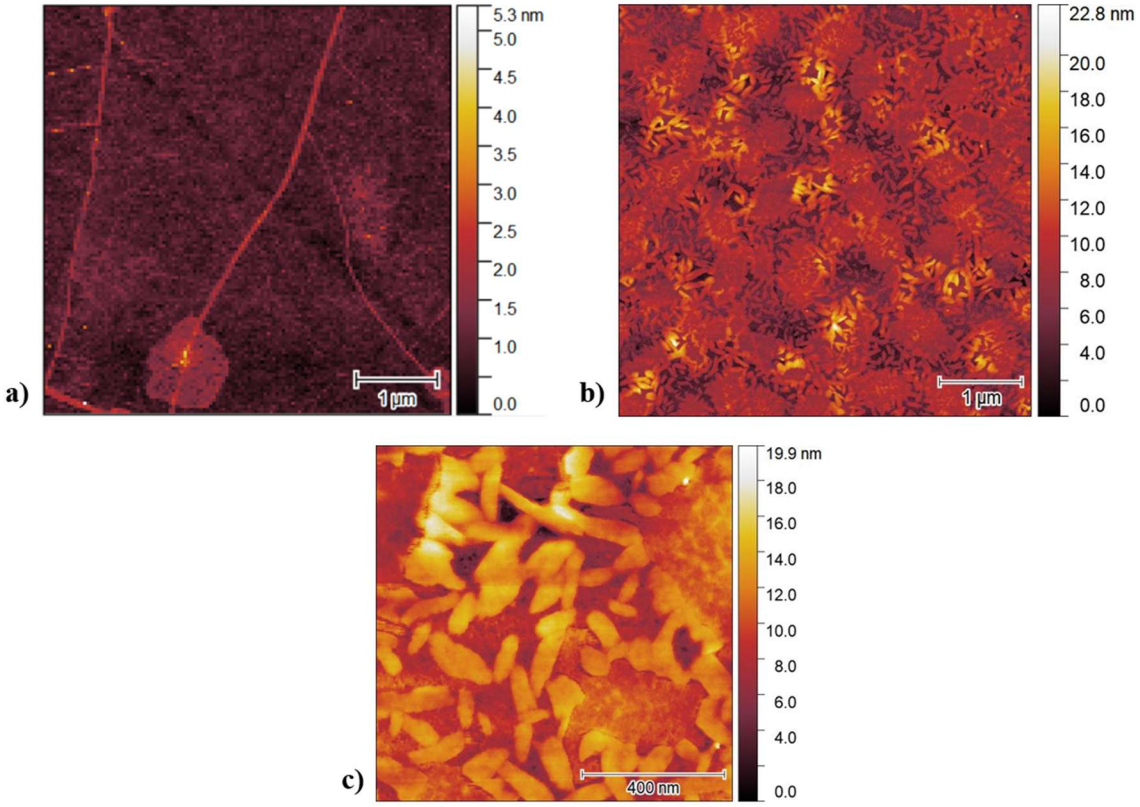


***Figure 6.19**: AFM morphology of **(a)** bare graphene wafer (5 µm spot size). CuPc(t-Bu)$_4$ spin coat graphene wafer **(b)** 5 µm spot size and **(c)** 1 µm spot size.*

6.6.3.5. Ellipsometry

Variable angle spectroscopic ellipsometry was utilized to estimate the thickness of the spin-coated CuPc(t-Bu)$_4$ films. Scans were performed at three different angles: 65°, 70°, and 75°. A Cauchy film optical model was employed to fit the data obtained from these measurements. The average film thickness from three measurements was measured to be 5.47 ± 0.007 nm.

6.6.3.6. *Raman Spectroscopy*

Raman spectroscopy was used to monitor changes in the graphene structure following the functionalization process. Single point extended scan spectra and 60 µm x 60 µm maps were taken of bare graphene and CuPc(t-Bu)$_4$ modified samples. The acquired spectrum (**Figure 6.20a**) was cross-referenced with other spectra and peak positions (**Table 23**) found in relevant literature sources [333], [336].

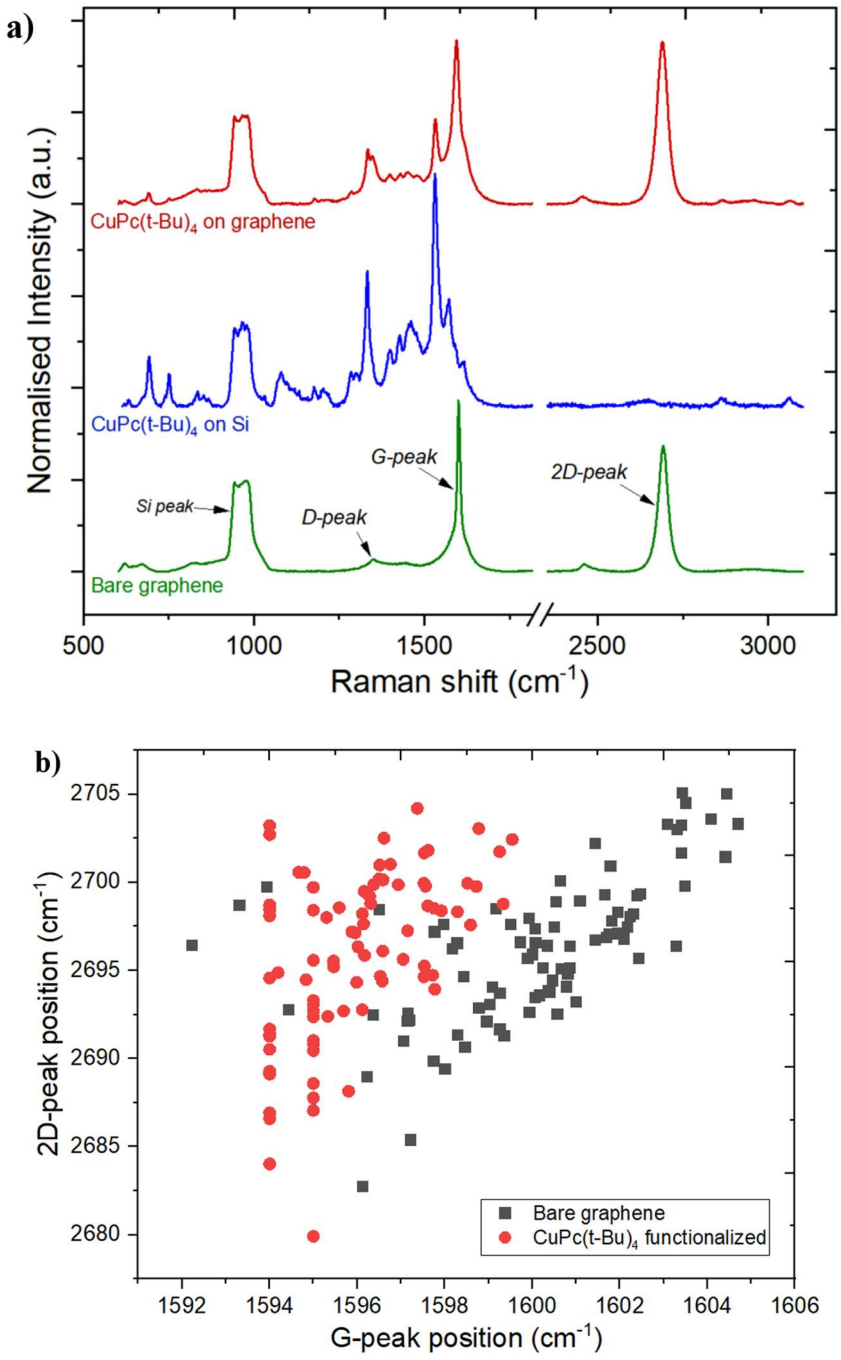


***Figure 6.20**: **(a)** Experimentally obtained Raman spectrum of pristine (bare) graphene and tetra tert-butyl copper phthalocyanine functionalized graphene. **(b)** Scatter plot displaying the G- and 2D-peak positions in the bare graphene and CuPc(t-Bu)$_4$-functionalized samples.*

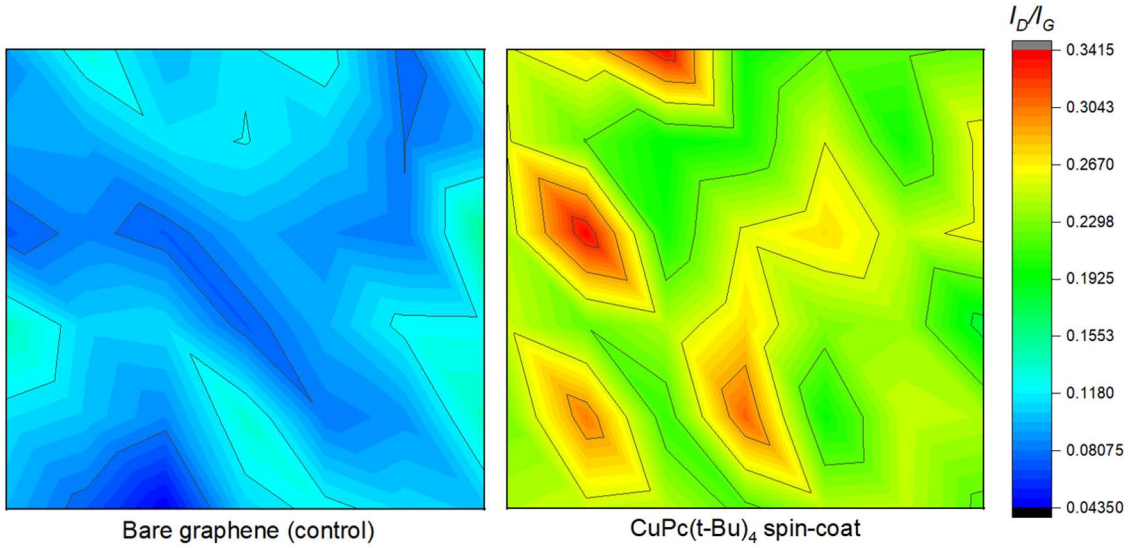


***Figure 6.21**: 60 µm x 60 µm Raman maps displaying the intensity ratio of the D-peak/G-peak (I_D/I_G).*

In the pristine (bare) graphene sample, the characteristic G- and 2D-peaks are located at ~1599 cm^{-1} and ~2691 cm^{-1}, respectively (**Figure 6.20a**). A small D-peak, located at ~1351 cm^{-1} in the pristine graphene sample is observable. The D-peak, also known as the defect or disorder peak, is attributed to the 'breathing mode' of sp^2 carbons and becomes Raman active when a defect is present adjacent to a sp^2 carbon [244], [246]. The average intensity ratio between the D- and G-peak (I_D/I_G) for pristine graphene was approximately 0.103, a low ratio indicating high-quality, well-ordered graphene (**Figure 6.21**).

In the CuPc(t-Bu)$_4$ sample, G- and 2D-peaks are found at ~1594 cm^{-1} and ~2688 cm^{-1}, respectively (**Figure 6.20a**). The G- and 2D peaks in the CuPc(t-Bu)$_4$ spectrum are slightly red-shifted (downshifted) compared to pristine graphene, indicating there could be n-type doping [337]–[339] induced by the CuPc(t-Bu)$_4$ molecules (**Figure 6.20b**). This proposed doping effect is further corroborated by the electrical characterization data presented in the following section (**6.6.3.7**), which also confirms an n-type doping influence.

The I_D/I_G ratio increased following CuPc(t-Bu)$_4$ functionalization (from 0.103 to 0.248), indicating increasing disorder within the graphene structure, due to the aromatic molecules on the surface [340]. The increasing intensity ratio can be easily

observed in **Figure 6.21** where the colour contour maps transition from cooler colours to warmer colours following the functionalization process.

Peak positions in the CuPc(t-Bu)$_4$ spectrum were compared to relevant literature sources [333], [336] for peak assignments (**Table 23**). The peaks at 1335, 1447, and 1533 cm^{-1} are associated with stretching vibrations in the pyrrole and isoindole rings, as well as displacement of the C-N-C bridge bond due to the central metal ion [333]. Specifically, the peak at 1335 cm^{-1} is a characteristic feature of a phthalocyanine spectrum, corresponding to the stretching vibration of the pyrrole group [336].

***Table 23**: Peak positions of acquired spectrum compared to literature values* [333], [336].

Acquired spectrum (cm^{-1})	Literature (cm^{-1})
831	826
1181	1187
1198	1199
1214	1219
1304	1307
1335	1335,1343
1447	1446,1455
1531	1527,1531

6.6.3.7. I-V Sweep Pre- and Post-Functionalization

The resistance of the graphene pixels was measured before and after CuPc(t-Bu)$_4$ functionalization to monitor any changes. **Figure 6.22** shows an increase in the resistance of graphene pixels following CuPc(t-Bu)$_4$ functionalization. The mean resistance prior to functionalization was approximately 4.6 kΩ, which increased to around 5.0 kΩ after surface modification. The observed increase in resistance indicates that the deposited CuPc(t-Bu)$_4$ film is doping the graphene. Since graphene on SiO_2 is p-type [99], [300], the electron-donating properties of CuPc(t-Bu)$_4$ [328] lead to an n-type doping effect on graphene, reducing the number of charge carriers. This reduction in the number of charge carriers results in an increase in resistance.

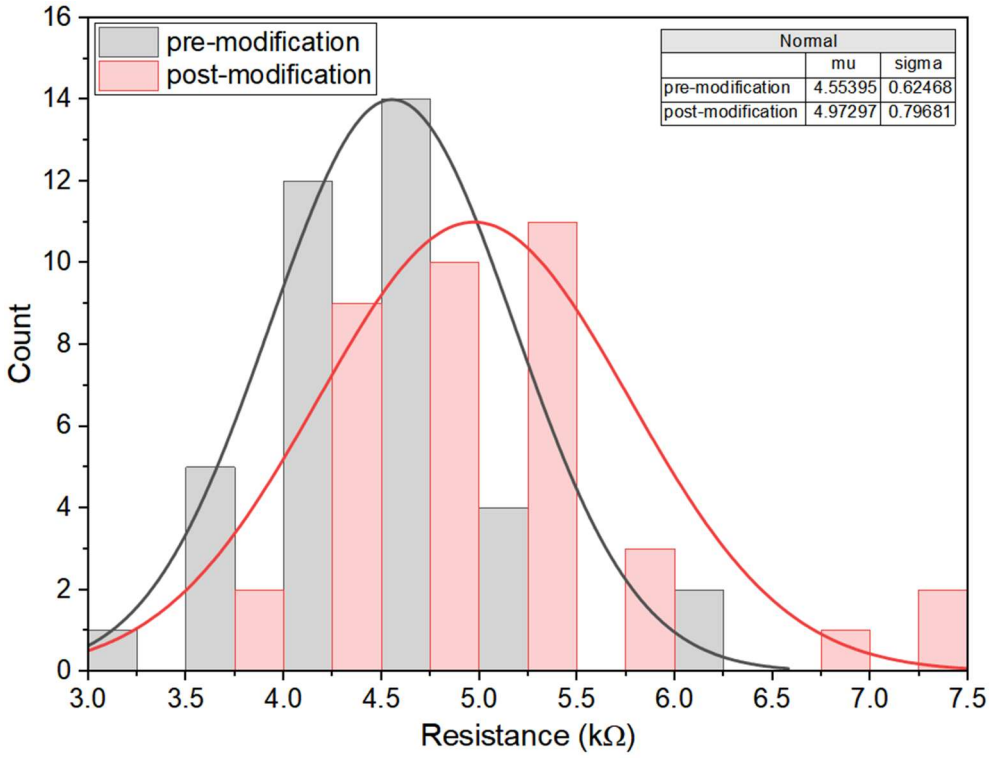


***Figure 6.22**: Distribution plot displaying the resistance of graphene pixels from 3x3 graphene sensor array devices before and after functionalization with CuPc(t-Bu)$_4$.*

6.7. Gas Sensing with CuPc(t-Bu)$_4$

Real-time resistance measurements were performed in the gas sensing rig (Phase 3) on CuPc(t-Bu)$_4$-functionalized 3x3 graphene pixel array sensors. All experiments were performed at RT and atmospheric pressure using a constant flow rate of 1000 mL/min. Sensor recovery, selectivity and different target gas concentrations were analysed. The findings were compared with bare graphene and drop-casted CuPc graphene sensors.

6.7.1. Nitrogen Dioxide Sensing and Recovery Performance

The gas sensing performance of the CuPc(t-Bu)$_4$-functionalized sensor was initially tested with NO_2 gas. **Figure 6.23a** illustrates seven repeat real-time resistance measurements of a CuPc(t-Bu)$_4$-functionalized 3x3 graphene pixel array sensor subjected to the following exposure sequence: (1) 10 minutes of air, (2) 10 minutes of 5 ppm nitrogen dioxide (NO_2), (3) 10 minutes of air, and (4) an 8-minute vacuum-

assisted UV exposure (not shown in real-time). The measurements reveal a consistent trend across repeats, with the sensor response magnitude gradually increasing. Initially, the sensor response (Test 0) was -10.8%, which rose to -15.9% by the final repeat (Test 6) (**Figure 6.23b**). The fluctuations in sensor response may be attributed to the removal of additional ambient adsorbates from the graphene surface. Alternatively, a study by Newton et al. [341] demonstrated that pre-doping CuPc films with NO_2 increased the magnitude of the sensor response. The researchers suggested that pre-doping prevents NO_2 from diffusing into the bulk of the film, allowing the more rapid surface adsorption mechanism to dominate and thereby enhancing conductivity gains. This phenomenon could explain the gradually increasing sensor response observed with the CuPc(t-Bu)$_4$-functionalized sensor.

Figure 6.23b displays the trend in sensor response repeats compared to those obtained using the drop-cast unsubstituted CuPc-functionalized DipChipX sensor as detailed in **Section 6.5.1.1**. The CuPc(t-Bu)$_4$-functionalized sensor achieved 147% of the initial sensor response, suggesting recovery following UV light exposure. In contrast, the CuPc sensor only recovers 19% of its initial sensor response. This finding aligns with the work of Lee et al. [328], who reported improved recovery for CuPc(t-Bu)$_4$ films compared to CuPc films.

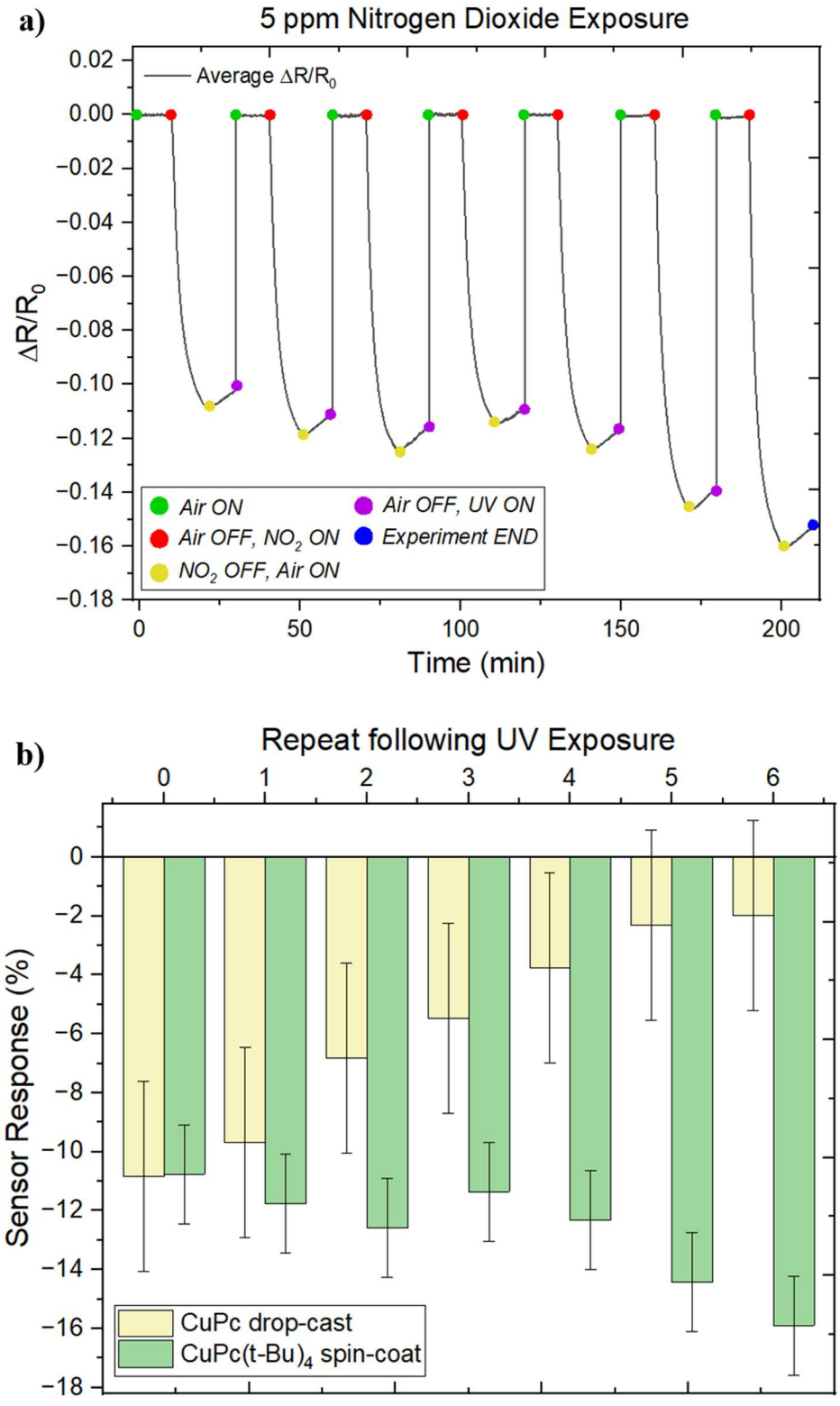


***Figure 6.23**: **(a)** Seven repeat real-time resistance measurements (expressed as $\Delta R/R_0$) of a 3x3 graphene pixel array sensor exposed to 5 ppm NO_2 and subsequent exposure to UV light for 8 minutes (not shown). **(b)** Bar chart comparing the sensor response to nitrogen dioxide of a drop-cast CuPc and spin-coat CuPc(t-Bu)$_4$ sensor following repeat exposures to UV light.*

To investigate how different concentrations of nitrogen dioxide affect sensor response, a CuPc(t-Bu)$_4$-functionalized 3x3 graphene pixel array sensor was tested with a range of NO_2 concentrations: 100 ppb, 250 ppb, 500 ppb, 750 ppb, 1 ppm, 2.5 ppm, and 5 ppm. The NO_2 gas cylinder was diluted to the desired concentrations following the procedure outlined in **Chapter 5.5.2**.

Figure 6.24a displays the real-time resistance measurements of the CuPc(t-Bu)$_4$-functionalized sensor when exposed to different concentrations of NO_2. For each concentration, the sensor was exposed to NO_2 and then recovered using an 8-minute vacuum-assisted UV recovery period. The data for each concentration, along with the subsequent UV treatment (indicated by purple shaded areas on the graph), are combined on the same graph for comparison. The graph shows that each graphene pixel exhibits a similar response to the tested concentrations, with the response magnitude increasing as the concentration increases

Figure 6.24b displays the average sensor response across pixels for the various concentrations tested. The data shows that as the concentration of nitrogen dioxide increases, the sensor response also increases. This can be attributed to a greater number of NO_2 molecules interacting with the graphene. The logarithmic scale demonstrates a linear relationship between NO_2 concentration and sensor response, suggesting that the original data follows a power law relationship. The sensor response of individual graphene pixels for each concentration is shown in the **Appendix** (**Figure A7**).

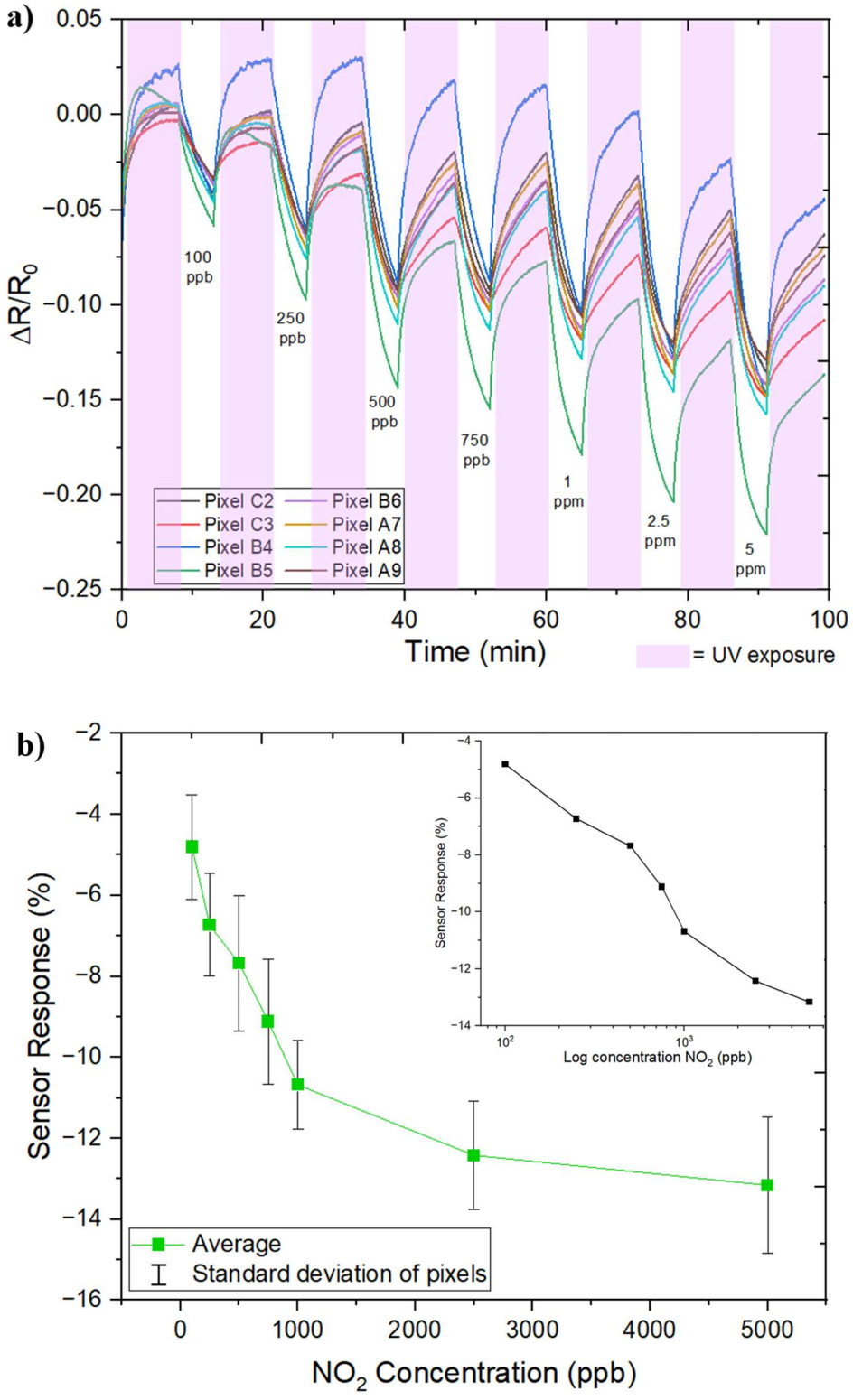


***Figure 6.24**: **(a)** Real-time resistance response profile of a CuPc(t-Bu)$_4$-functionalized 3x3 graphene pixel array sensor exposed to different concentrations of NO_2. **(b)** Sensor response (%) versus parts per billion (ppb) NO_2 concentration at various concentrations ranging from 100 ppb to 5000 ppb of a CuPc(t-Bu)$_4$-functionalized 3x3 graphene pixel array sensor. **Inset**: Sensor response (%) versus ppb NO_2 concentration displayed on a logarithmic scale.*

6.7.1.1. Recovery Time Estimation

Although the recovery period for each repetition was fixed at 8 minutes to ensure complete sensor recovery, the actual recovery time—defined as the time at which the baseline (or initial resistance) is restored [256], [257]—can still be approximated. This estimation was performed by identifying the point within the 8-minute recovery period where the baseline was recovered. **Figure 6.25** provides a graphical representation of this approximation process.

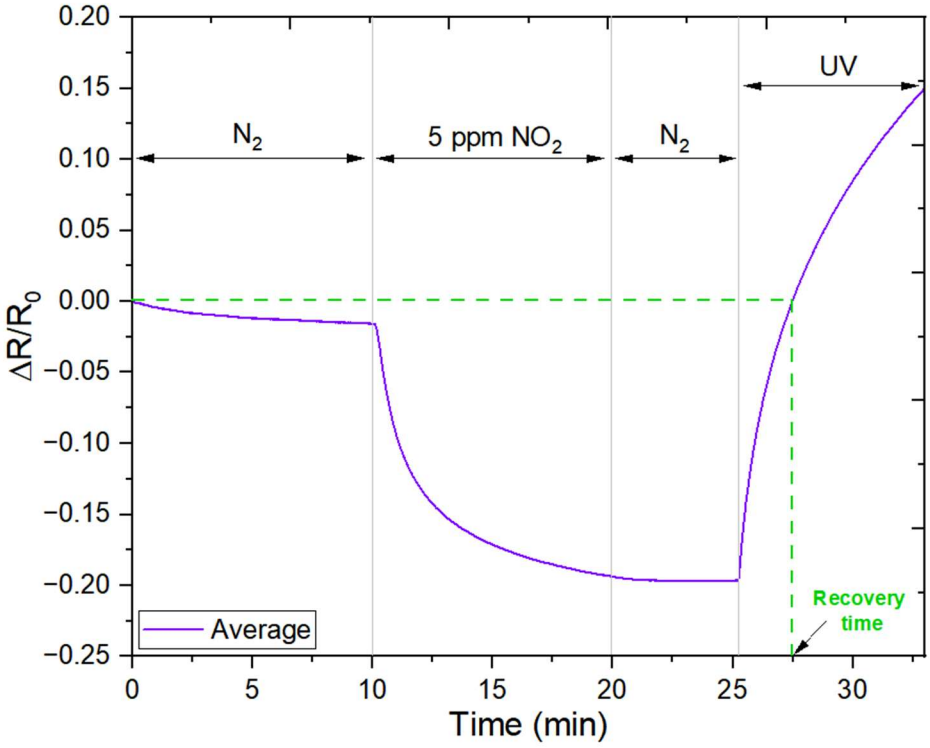


***Figure 6.25**: Graphical representation of recovery time estimation. The graph illustrates the average normalized resistance ($\Delta R/R_0$) of each graphene pixel during the following exposure sequence: (1) 10 minutes N_2, (2) 10 minutes 5 ppm NO_2, (3) 5 minutes N_2 and (4) 8 minutes UV exposure. From these data points, the recovery time—when the baseline resistance is restored—can be approximated.*

The normalized resistance ($\Delta R/R_0$) for each graphene pixel on a device was averaged over three repetitions, and from this average, the recovery time was estimated. **Table 24** displays a rapid average recovery time of 67 s with some variability between repetitions for the CuPc(t-Bu)$_4$-functionalized sensor. **Section 6.7.3** provides a detailed comparison of gas sensing performance parameters with those of other sensors reported in the published literature.

***Table 24**: Recovery times (s) for three repetitions of the CuPc(t-Bu)$_4$-functionalized sensors exposed to 5 ppm NO_2 and recovered with UV light.*

Recovery time (s)			
Repeat 1	**Repeat 2**	**Repeat 3**	**Average**
55	46	99	67

6.7.2. Selectivity

The capability to distinguish between different gases is a crucial parameter for gas sensing. The selectivity of the CuPc(t-Bu)$_4$-functionalized sensor was evaluated by exposing it independently to various gases and measuring the sensor response: 25 ppm ammonia (NH_3), 5 ppm nitric oxide (NO), 100 ppm methane (CH_4), and 450 ppm carbon dioxide (CO_2).

The CuPc(t-Bu)$_4$-functionalized sensor demonstrates a strong selectivity towards NO_2 gas, showing a significant sensor response of -13.2% (**Figure 6.26**). In comparison, the sensor response to NO is -3.3% and to NH_3 is 0.47%, with no measurable response to CH_4 or CO_2. This notable variation in sensor response across different gases indicates that the sensor possesses good selectivity.

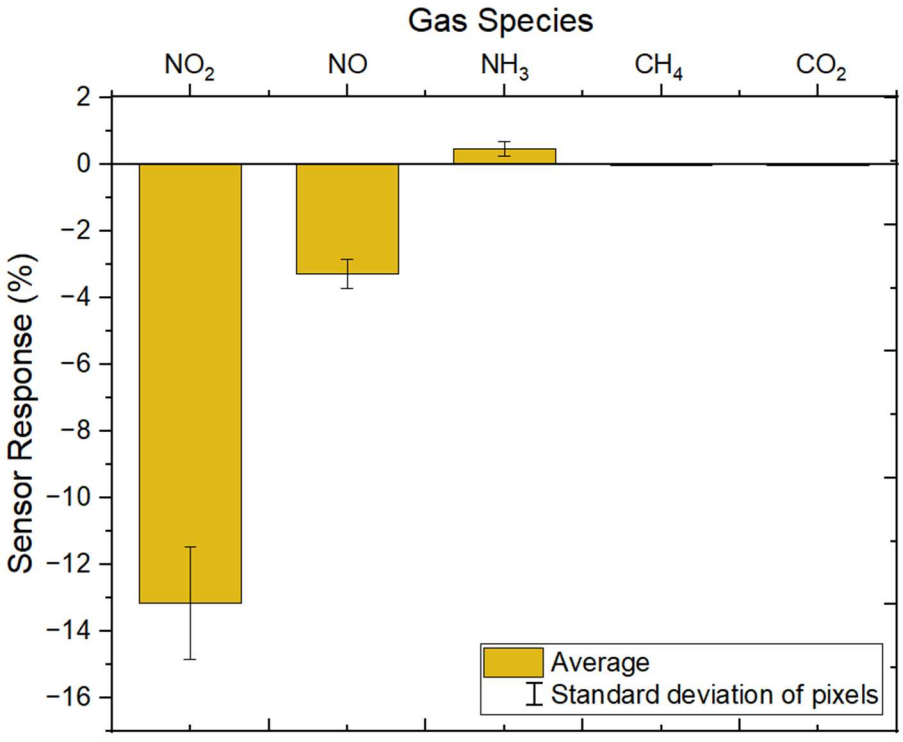


***Figure 6.26**: Bar chart demonstrating the selectivity of the CuPc(t-Bu)$_4$-functionalized 3x3 graphene pixel array sensor exposed to various gases: 5 ppm nitrogen dioxide (NO_2), 25 ppm ammonia (NH_3), 5 ppm nitric oxide (NO), 100 ppm methane (CH_4), and 450 ppm carbon dioxide (CO_2).*

6.7.3. Gas Sensing Performance Comparison

The sensing performance of the CuPc(t-Bu)$_4$-functionalized sensor was evaluated against a bare graphene sensor and the unsubstituted CuPc graphene sensor. All three iterations of the graphene sensors were tested using the 3x3 graphene pixel array sensors. The bare graphene sensor, the CuPc drop-casted sensor and the CuPc(t-Bu)$_4$-functionalized sensor were exposed to NO_2 gas at a concentration of 5 ppm for 5 minutes for 3 repeat measurements each.

Figure 6.27 illustrates the sensor response across all pixels on a device exposed to 5 ppm NO_2. The bare graphene sensor shows an average response of -7.2%. This response increases to -9.6% when unsubstituted CuPc is drop-cast onto the surface. The CuPc(t-Bu)$_4$ spin-coated device exhibits the highest average response at -14.2%, indicating it is the most effective for sensing NO_2. This improvement suggests that the CuPc(t-Bu)$_4$-functionalized sensor is superior for NO_2 detection. The enhanced sensor response could be attributed to the four tert-butyl groups on the molecule, which act as electron donor groups [328]. These groups may increase the sensor's response to an electron-withdrawing gas such as NO_2. Additionally, the spin-coated CuPc(t-Bu)$_4$ film on the graphene sensor is expected to be significantly more uniform compared to the drop-cast CuPc. This improved uniformity could offer a greater number of accessible gas adsorption sites, thereby enhancing the sensor's overall response.

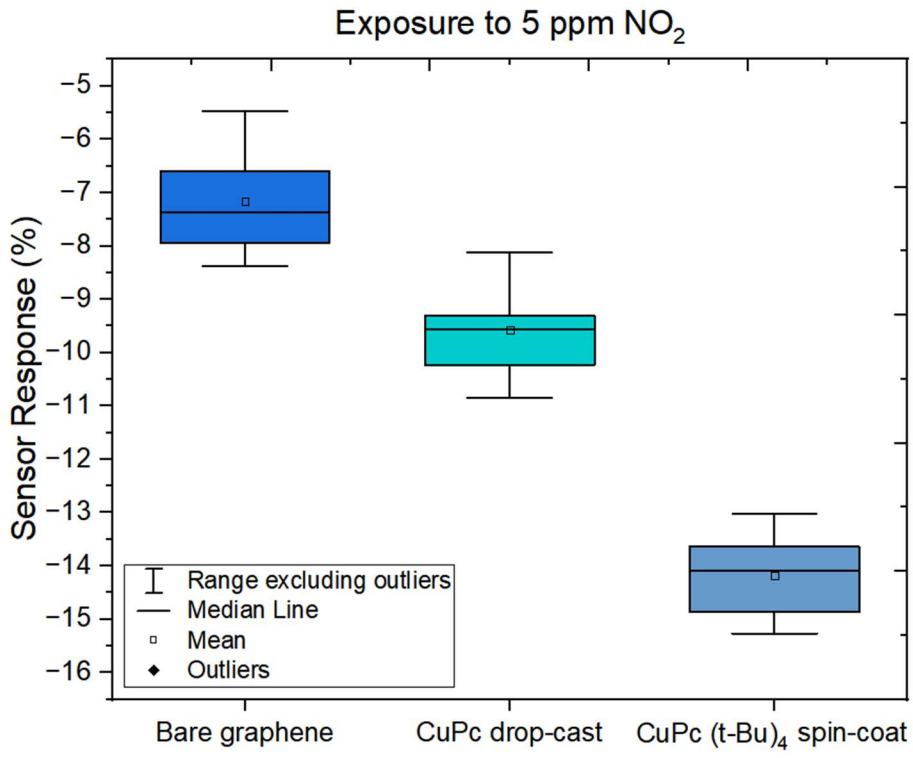


***Figure 6.27**: Box plot showing the sensor response (%) of three different 3x3 graphene pixel array sensors: bare graphene, CuPc drop-cast, and CuPc(t-Bu)$_4$ spin-coat.*

Response times for individual graphene pixels were determined over the 5-minute exposure period, and the average for each repeat measurement was plotted. Additional data on response times for individual graphene pixels for each repeat can be found in the **Appendix** (**Figure A8**). **Figure 6.28** presents a comparison of the response times for repeated measurements of bare graphene, CuPc-functionalized, and CuPc(t-Bu)$_4$-functionalized sensors exposed to 5 ppm NO_2. The data show that both the bare graphene and CuPc drop-cast sensors respond approximately 20 seconds faster than the CuPc(t-Bu)$_4$-functionalized sensor. The average response times across the repeats were 251, 250, and 271 seconds for the bare graphene, CuPc drop-cast, and CuPc(t-Bu)$_4$ sensors, respectively. The increased response time observed with the CuPc(t-Bu)$_4$ sensor could be due to the film structure. Lee et al. [159] and Newton et al. [341] discuss that the structure of a phthalocyanine film significantly impacts response and recovery times by the slow penetration of molecules into the bulk between individual crystallites. Therefore, the CuPc(t-Bu)$_4$ film on the graphene devices may reduce transfer kinetics by impeding the penetration of molecules to the graphene layer.

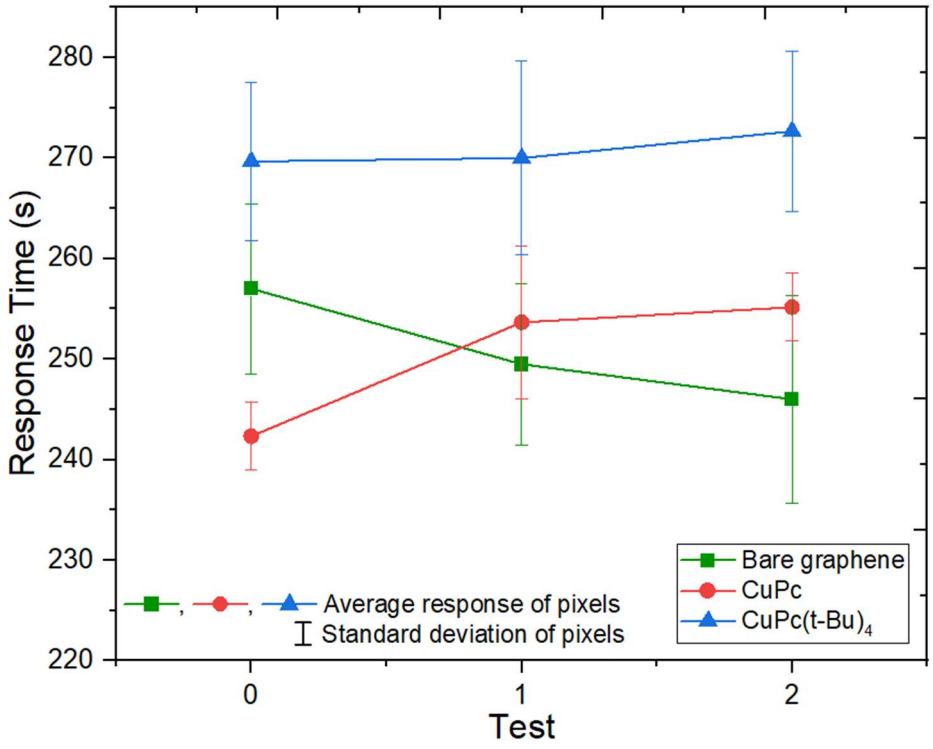


***Figure 6.28**: Average response times (s) for repeated measurements of bare graphene, CuPc-functionalized, and CuPc(t-Bu)$_4$-functionalized 3x3 pixel array sensors.*

Table 25 compares the gas sensing performance of the CuPc(t-Bu)$_4$-functionalized 3x3 graphene pixel array sensor for nitrogen dioxide detection with similar sensors reported in the literature. It is important to note that the lowest concentration tested (as listed in the table) is not the limit of detection (LOD) but rather the lowest concentration reported for that particular study.

In similar studies using either CuPc or pristine graphene, the lowest concentration tested is comparable to that of the CuPc(t-Bu)$_4$-functionalized sensor in this work. The restriction to 100 ppb in this work was due to the available gas cylinder concentration and the minimum flow rate of the mass flow controllers. However, the signal-to-noise ratio (SNR) at 100 ppb NO_2 was estimated to be 7.2, suggesting that lower concentrations may be detectable. Furthermore, the LOD and limit of quantification (LOQ) were estimated to be 31 ppb and 103 ppb, respectively. Formulas for LOD, LOQ and SNR are provided in **Chapter 3.6**. Additionally, the calibration curve fitting is provided in the **Appendix** (**Figure A9**). A direct comparison of the CuPc(t-Bu)$_4$ film [328] in the table demonstrates that the CuPc(t-Bu)$_4$-graphene sensor developed

in this work is superior in every aspect, notably due to its room temperature operation and significantly reduced recovery time. Overall, the $CuPc(t\text{-}Bu)_4$-graphene sensor shows promise as an NO_2 sensor.

Table 25: Comparison of NO_2 sensors using different sensing materials.

Sensor Description	Sensing Material	Operating Temperature (°C)	Lowest Concentration Tested	Recovery Time (min)	Ref.
CVD monolayer graphene on SiO_2/Si substrate	$CuPc(t\text{-}Bu)_4$ (spin-coat) on graphene	RT	100 ppb	1	***This work***
$CuPc(t\text{-}Bu)_4$ and CuPc thin films on interdigitated Au electrodes	$CuPc(t\text{-}Bu)_4$ and CuPc thin films	125-225	10 ppm	90	[328]
cobalt phthalocyanine -graphene quantum dot on interdigitated electrodes	2,9,16,23-tetracarboxylic cobalt phthalocyanine/graphene	RT	50 ppb	2	[180]
CuPc thin films on interdigitated Au electrodes	CuPc thin film	RT	10 ppm	20-90[a]	[160]
CuPc thin films on interdigitated Au electrodes	CuPc thin film	RT	50 ppb	2[b]	[175]
CuPc thin films on interdigitated Au electrodes	CuPc thin film doped with NO_2	RT	500 ppb	28	[341]
Epitaxial graphene on SiC	Pristine graphene	RT	2.5 ppm	120	[342]
Epitaxial graphene on SiC	Pristine graphene	70 - 100°C	10 ppb	Overnight recovery	[185]
Epitaxial graphene on SiC	Pristine graphene	RT	500 ppb	5	[120]

a. Depending on crystal phase and temperature deposited.
b. Did not recover within time allowed.

6.8. Conclusions

In this chapter, the gas sensing performance of various metal phthalocyanines deposited on graphene sensors was investigated. Metal phthalocyanines have shown potential in gas sensing applications due to their sensitivity to different target gases based on their metal centres and functional groups on the ring. Thus, applying them to graphene to enhance sensor selectivity and sensitivity was explored.

The performance using the drop-cast functionalization technique was investigated with the unsubstituted cobalt, copper, iron, metal-free and zinc phthalocyanine.

Exposure of both the unsubstituted CuPc and bare graphene devices to 100 ppm NO_2 decreased the resistance of the devices, with subsequent exposures underscoring the necessity for a reliable recovery method. Despite the enhanced sensor performance due to the CuPc, it did not fully recover to its initial baseline state following UV exposure. Exposure to NH_3 increased resistance due to electron donation, with bare graphene showing variable responses and CuPc-functionalized sensors showing lower but more consistent responses. Neither sensor type responded to methane, which is attributed to low adsorption energies.

The metal centre significantly impacts gas sensitivity and selectivity. Neither the bare graphene nor the metal phthalocyanine-functionalized sensors exhibited significant changes in response to CH_4 and CO_2.

The different types of metal phthalocyanines are ranked for the following gases:

- NO_2 response: H_2Pc > CuPc > FePc > bare graphene > CoPc > ZnPc
- NO response: CuPc > H_2Pc > bare graphene > CoPc > ZnPc > FePc
- NH_3 response: CoPc > CuPc > bare graphene > FePc > H_2Pc > ZnPc

While drop-casting is an easier approach to graphene device functionalization, MPc distribution is non-uniform, which leads to a varying signal response. A soluble phthalocyanine, $CuPc(t\text{-}Bu)_4$, was synthesized to test its film performance on graphene sensors. The $CuPc(t\text{-}Bu)_4$-functionalized sensor had the largest sensor response to NO_2 gas, with the sensor response magnitude gradually increasing with repeat measurements.

Comparisons with bare graphene and unsubstituted CuPc showed CuPc(t-Bu)$_4$-functionalized graphene sensor had the highest response (-14.2%) but longer average response times. When compared with similar sensors reported in the literature, these results are competitive. The low LOD and LOQ values indicate significant potential for a highly sensitive NO_2 detector. Additionally, the CuPc(t-Bu)$_4$-functionalized sensor's ability to achieve rapid, complete recovery outperforms other reported sensors. Overall, the CuPc(t-Bu)$_4$-functionalized graphene sensor shows considerable promise as an NO_2 detector due to its enhanced response, straightforward functionalization process, and selectivity.

Chapter 7 : Enhanced Nitrogen Dioxide Detection Using Graphene Sensors Modified with Polymers of Intrinsic Microporosity

7.1. Introduction

Polymers of Intrinsic Microporosity (PIMs) are a class of polymers that possess a unique molecular architecture enabling them to exhibit intrinsic microporosity. This means they inherently contain a network of extremely small pores (micropores, < 2 nm) within their structure [343]. This structural characteristic renders PIMs highly suitable for applications in gas separation [233], leveraging their ability to selectively adsorb and transport gases based on size and chemical properties.

Despite their established utility in gas separation [344], PIMs have not been extensively explored for gas sensing applications. The integration of a PIM membrane onto a graphene sensor holds the potential to enhance both sensitivity and selectivity, thereby advancing the development of more precise and reliable gas sensors.

This chapter focuses on evaluating the gas sensing performance of 3x3 graphene pixel array sensors coated with PIMs. By exploring this novel application, the study aims to uncover the potential benefits of PIMs in enhancing the functionality of graphene-based sensors for gas detection.

Lastly, this work explores the potential of using a hybrid material, specifically a Mixed Matrix Membrane (MMM), for gas sensing applications. MMMs typically consist of an inorganic or inorganic-organic hybrid material embedded within a polymer matrix. By combining materials with distinct gas transport properties, the resulting composite may exhibit enhanced performance, leveraging the strengths of both components for improved gas sensing capabilities [345].

7.2. Polymers Employed in this Study

Three distinct polymers were investigated in this chapter: PIM-1, PIM-EA-TB, and Matrimid (all supplied from the M. Carta research group at Swansea University). PIM-1, known as the 'first polymer of intrinsic microporosity,' is extensively studied and synthesized through the polycondensation of tetra-fluorophthalonitrile and a spirobisindane component [346]. PIM-EA-TB is another PIM synthesized using ethanoanthracene (EA) and Tröger base coupling (TB) [347]. Matrimid, on the other hand, is a commercially available polyimide thermoplastic polymer widely used in gas separation applications [348], [349] and was utilized as a comparison with the PIMs. **Figure 7.1** illustrates the molecular structures of these three polymers.

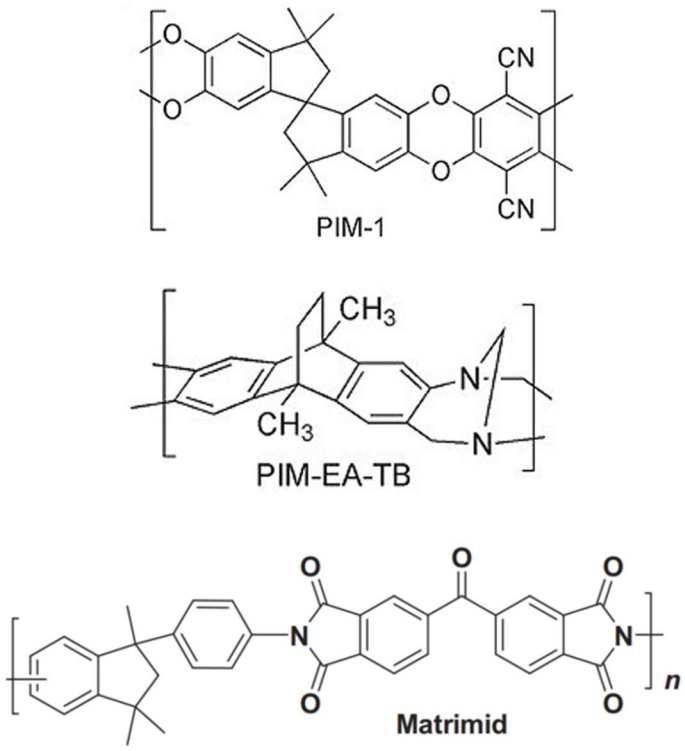


***Figure 7.1**: Molecular structure of the three polymers used in this study: PIM-1, PIM-EA-TB and Matrimid.*

7.3. Graphene Functionalization with PIMs and Matrimid

This section outlines the procedure for modifying the graphene surface with PIMs and Matrimid. For sensor functionalization, each of the three 3x3 graphene pixel array devices were coated with one of the PIMs or Matrimid using spin-coating. Polymer solutions were prepared by dissolving each polymer powder in chloroform with a concentration of 1 mg/mL. Spin coating was performed using an L2001A3 Ossila spin coater with a custom-made chuck (as seen in **Chapter 3.3.1.2**). The spin parameters were as follows:

	Step 1
Time (s):	30.0
Spin speed (rpm):	2500

Spin coating parameters were based on those for a PMMA spin-coat film found in published literature [350]. However, after observing the viscosity of the polymer solutions, the spin speed was reduced to 2500 rpm to prevent the formation of an extremely thin film that could hinder the film's sensing capabilities.

During the spin-coating process, the metal contacts at the bottom of the devices were temporarily covered with Parafilm to prevent them from being coated. This ensured that the functionalization was applied only to the desired areas of the sensor arrays. Characterization of the spin-coat polymer films was performed using silicon wafer fragments.

7.4. Sensor Recovery Methods

In this chapter, three different recovery methods were investigated for use with the polymer-functionalized 3x3 graphene pixel array sensors to determine the most effective way to return the devices to their initial baseline state. The recovery methods tested were UV exposure, methanol treatment (described below), and heating. This section outlines the procedures used for each recovery method.

7.4.1. UV exposure

The method is discussed in detail in **Chapter 5.5.1.5.1**.

7.4.2. Methanol Treatment

Over time and with repeated use, PIMs can undergo a relaxation of polymeric chains to a more energetically favourable state. This relaxation significantly impacts their gas separation properties, typically reducing gas permeability and increasing selectivity [213]. Methanol treatment followed by vacuum exposure has been shown to restore the micropore structure of PIMs by removing traces of previous gas exposure [213], making it a viable sensor recovery method.

For methanol treatment, polymer-functionalized sensors were submerged in methanol for 30 minutes, then soaked for an additional hour in fresh methanol. After removal from the solvent, sensors were allowed to dry at room temperature before being placed in a vacuum desiccator overnight (~0.027 MPa).

7.4.3. Heating

After exposure to the target gas, the sensors were removed from the sensing chamber and placed on a hot plate at 175°C for 5 minutes. This temperature was selected based on the findings from the investigation conducted in **Chapter 5.6.2.2**.

7.5. Surface Morphology and Film Thickness

The surface topography and film thickness of the spin-coat polymer films were investigated using atomic force microscopy and ellipsometry.

7.5.1. Atomic Force Microscopy

Atomic force microscopy (AFM) was utilized to analyse the surface morphology of the spin-coated polymer films, which were prepared according to the procedure detailed in **Section 7.3.**

The surface topography before and after spin coating was characterised using a *Bruker Dimension icon XR* scanning probe microscope with a SCANASYST-AIR probe in tapping mode (probe specifications and scan parameters are provided in **Chapter 3.4.4**). The surface of a bare silicon wafer, compared to those spin-coated with the polymers, exhibited changes in surface roughness (**Table 26**) and topography (**Figure 7.2**).

Figure 7.2 displays AFM images (250 nm x 250 nm) of a bare silicon wafer and three silicon wafers spin-coated with different polymers. The microstructures of PIM-1 and PIM-EA-TB are distinctly visible compared to the bare silicon wafer, featuring apparent micropores across their surfaces. While the Matrimid polymer exhibits less pronounced surface features, it shows an increase in surface roughness, with an RMS roughness of 0.213 nm compared to 0.112 nm for the bare silicon wafer (**Table 26**). The PIM-1 and PIM-EA-TB polymers exhibit even greater increases in surface roughness, with RMS roughness values of 0.285 nm and 0.293 nm, respectively.

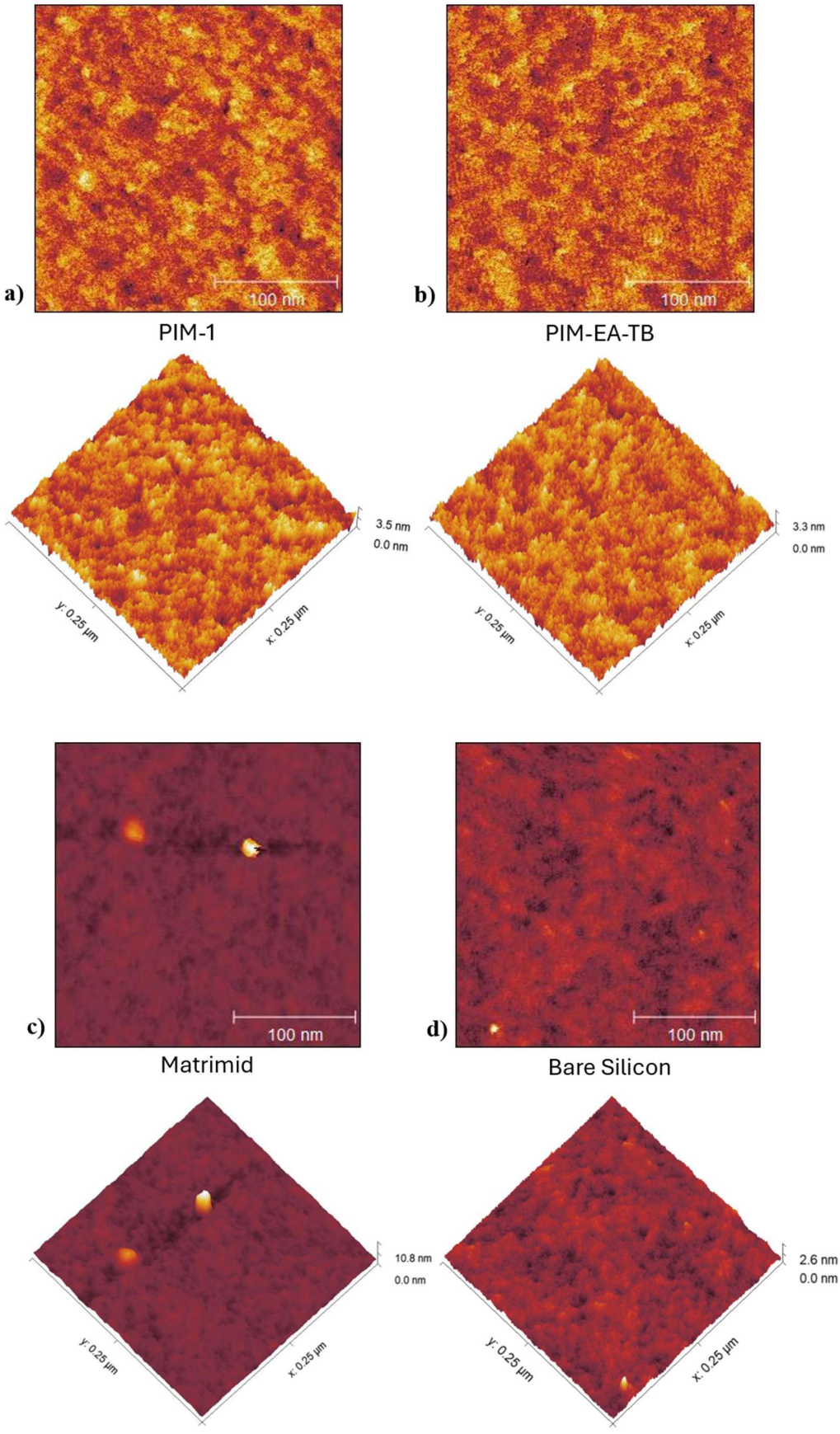


***Figure 7.2**: AFM images with accompanying 3D images for a 250 nm spot size of **(a)** PIM-1 **(b)** PIM-EA-TB and **(c)** Matrimid and. **(d)** bare Silicon wafer.*

***Table 26**: Average roughness and RMS roughness measurements from three measurements on bare silicon, PIM-1, PIM-EA-TB and Matrimid.*

Sample	Average Roughness (nm)	Average RMS Roughness (nm)
Bare Silicon	0.089	0.112
PIM-1	0.227	0.285
PIM-EA-TB	0.229	0.293
Matrimid	0.168	0.213

7.5.2. Ellipsometry

Variable angle spectroscopic ellipsometry was utilized to estimate the thickness of the spin-coated polymer films. Scans were performed at three different angles: 65°, 70°, and 75°. A Cauchy film optical model was employed to fit the data obtained from these measurements. The average film thickness from these three measurements is presented in **Table 27** below. The film thicknesses of the three spin-coated polymers are quite similar, ranging from 8.55 nm to 11.45 nm, with only a 2.9 nm difference between Matrimid and PIM-EA-TB.

***Table 27**: Average film thickness of spin-coat PIM-1, PIM-EA-TB and Matrimid films on Si substrates.*

Polymer	**Thickness (nm)**
PIM-1	10.56 ± 0.031
PIM-EA-TB	11.45 ± 0.023
Matrimid	8.55 ± 0.019

7.6. Gas Sensing Performance

Real-time resistance measurements were performed in the gas sensing rig on PIM-1, PIM-EA-TB and Matrimid-functionalized 3x3 graphene pixel array sensors. All experiments were performed at room temperature and atmospheric pressure using a constant flow rate of 1000 mL/min. This section reports on sensor recovery, selectivity, responses to different target gas concentrations, and comparisons with bare graphene, the CuPc(t-Bu)$_4$-functionalized sensor (**Chapter 6.7**), and similar sensors documented in the literature.

7.6.1. Nitrogen Dioxide Sensing

Functionalized devices were placed in the gas sensing chamber and exposed to 5 ppm nitrogen dioxide in nitrogen. Each experiment commenced with a 10-minute exposure to 20% oxygen/nitrogen gas (air) to establish a baseline, followed by a 10-minute exposure to the target gas, and concluded with a 10-minute exposure to air. **Figure 7.3** displays the real-time gas sensing response of the three polymer-functionalized sensors exposed to 5 ppm nitrogen dioxide (NO_2). The responses for each pixel on a device were averaged and expressed as $\Delta R/R_0$, representing normalized resistance. Upon exposure to NO_2, there was a sharp decrease in the resistance of the sensor arrays, indicating a strong sensor response. However, subsequent exposure to air did not restore the sensors to their initial resistance values, suggesting incomplete recovery after NO_2 exposure.

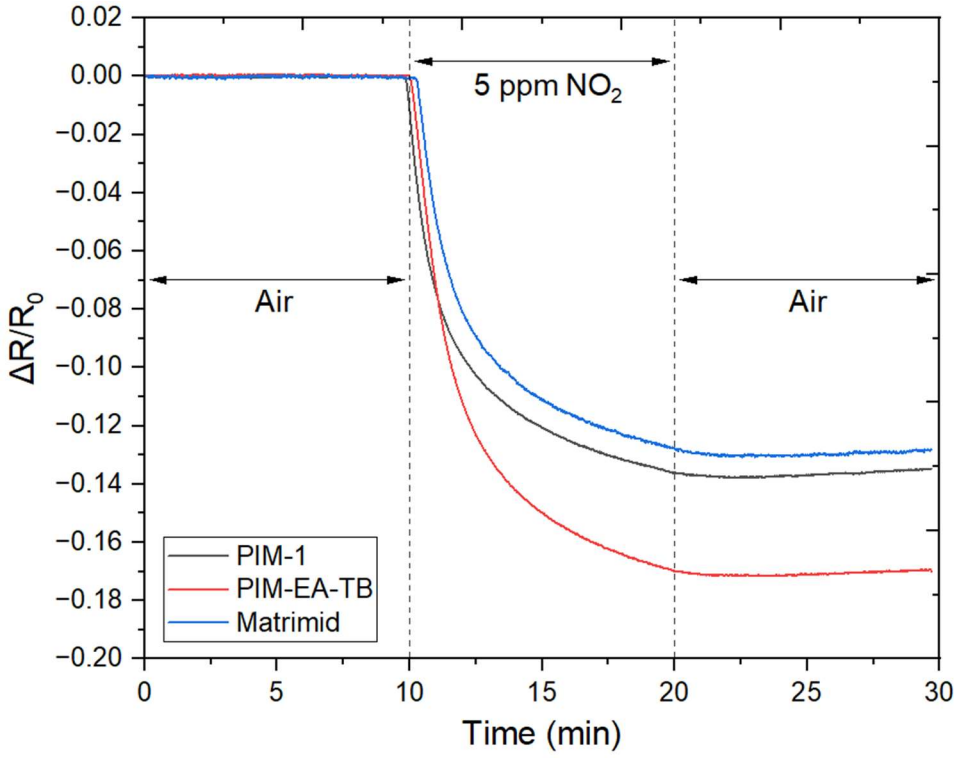


***Figure 7.3**: Real-time resistance measurements of three 3x3 graphene pixel array sensors functionalized with PIM-1, PIM-EA-TB and Matrimid exposed to 5 ppm nitrogen dioxide expressed as $\Delta R/R_0$, where $\Delta R/R_0 = [R_{device} - R_0]/R_0$, and R_0 is the resistance at T = 0.*

Figure 7.4 shows the average sensor response and the response time of three functionalized sensors exposed to 5 ppm NO_2. The sensors functionalized with the polymers demonstrated significantly better performance than the bare graphene sensor, exhibiting both an increased sensor response and a quicker response time.

The bare graphene sensor, when exposed to 5 ppm NO_2, showed a sensor response of -10.8% with a response time of 412 seconds. However, surface modification using PIM-1, PIM-EA-TB, and Matrimid notably improved the sensor performance. The average sensor response for these functionalized sensors were -20.2%, -25.7% and -21.5% respectively, while their response times decreased by approximately 56 seconds compared to the bare graphene sensor.

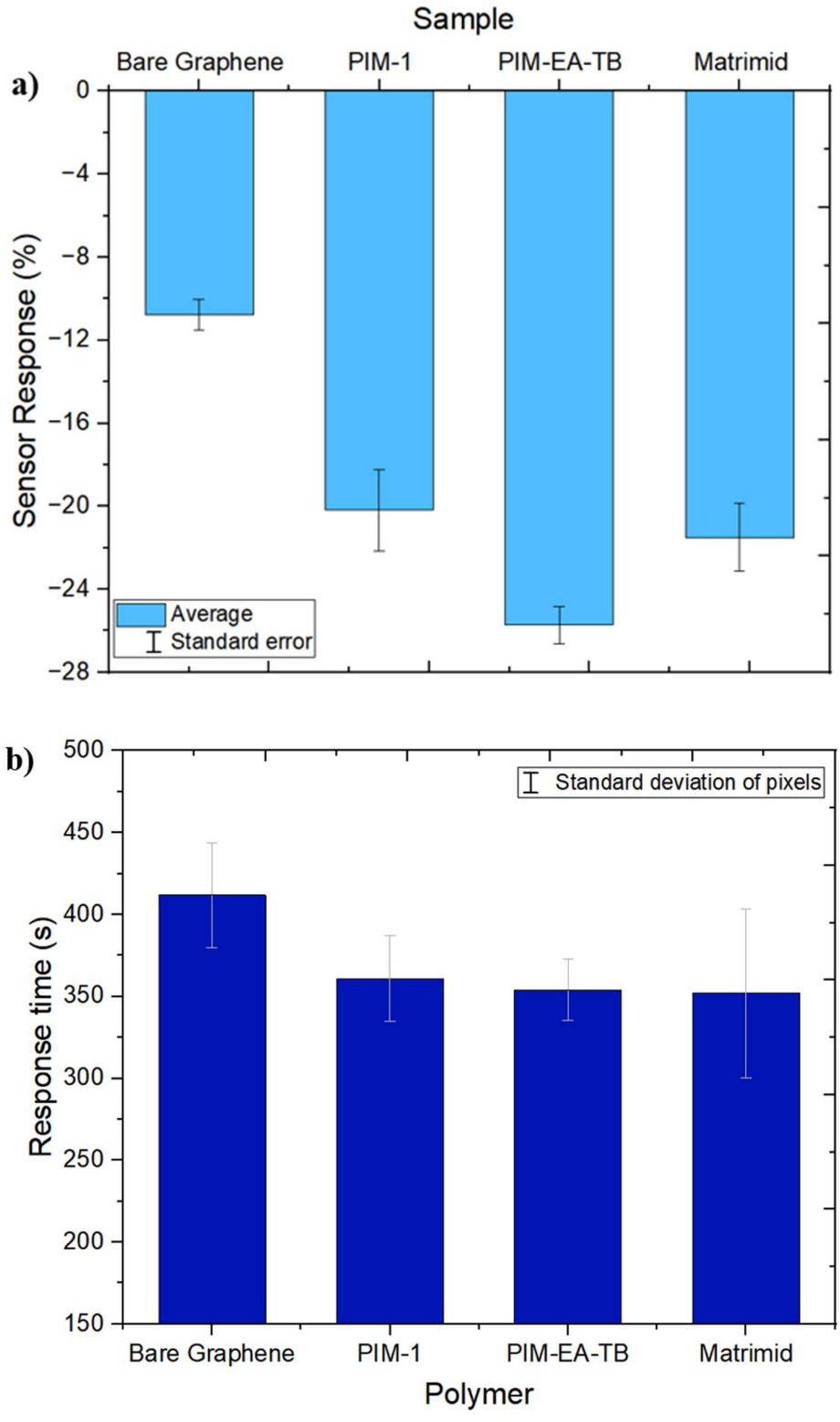


***Figure 7.4**: Bar chart displaying the **(a)** average sensor response (%) and **(b)** response time (s) of polymer-functionalized 3x3 graphene pixel arrays sensors exposed to 5 ppm NO_2 compared to the response of a bare graphene sensor.*

The increase in sensor performance in the PIM-functionalized sensors can be attributed to the kinetic diameter of the nitrogen dioxide molecule, which is 3.3 Å [351], [352]—identical to that of the highly permeable carbon dioxide (CO_2) molecule in PIMs. PIMs demonstrate enhanced diffusivity selectivity towards molecules with smaller kinetic diameters [233]. Compared to nitrogen (N_2) and oxygen (O_2) molecules, with kinetic diameters of 3.64 Å and 3.46 Å respectively, the smaller kinetic diameter of NO_2 allows it to pass through the membrane more easily. This molecular sieve effect provided by PIMs enhances the sensor's performance by preferentially allowing smaller molecules to diffuse through, thus increasing sensitivity to NO_2.

To investigate how different concentrations of nitrogen dioxide affect sensor response, the three polymer-functionalized 3x3 graphene pixel array sensors were tested with a range of NO_2 concentrations: 1 ppm, 2.5 ppm, 5 ppm, 10 ppm, 25 ppm and 50 ppm. The NO_2 gas cylinder was diluted to the desired concentrations following the procedure outlined in **Chapter 5.5.2**. Following exposure to each concentration, the sensors were recovered using an 8-minute vacuum-assisted UV recovery period. Details on the recovery methods tested with the polymer-functionalized sensors are provided in the next section (**7.6.2**).

Figure 7.5 displays the sensor responses to various NO_2 concentrations for each polymer-functionalized sensor. All three sensors exhibit an increase in response with increasing NO_2 concentration up to 25 ppm, beyond which the polymer membranes begin to saturate. At 25 ppm, the Matrimid-functionalized sensor shows a significant decrease in response, the PIM-EA-TB sensor shows a slight decrease, and the PIM-1 sensor decreases similarly at 50 ppm.

Given the film thickness of the polymer membranes (~9 nm to 11 nm), this trend suggests that the polymers are likely saturating with NO_2 at higher concentrations. Additionally, at these elevated concentrations, the vacuum-assisted UV treatment may not be effectively removing all the NO_2 from the polymer membranes and graphene surface. This could result in a diminished sensor response during subsequent exposures.

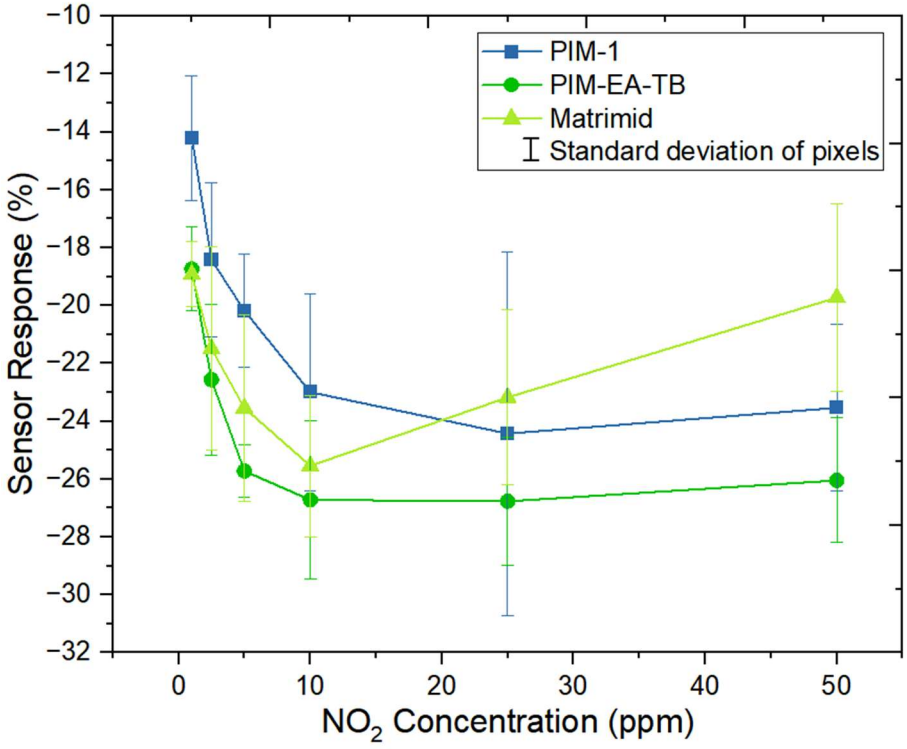


***Figure 7.5**: Sensor response (%) versus parts per million (ppm) NO_2 concentration at various concentrations ranging from 1 ppm to 50 ppm for PIM-1, PIM-EA-TB and Matrimid-functionalized 3x3 graphene pixel array sensors.*

7.6.2. Sensor Recovery

Three different sensor recovery methods were evaluated for the polymer-functionalized sensors: UV exposure, methanol treatment, and heating. Details of the procedures used for each recovery method can be found in **Section 7.4**. To evaluate each recovery method, the sensors were exposed to a 10-minute period of 5 ppm NO_2, 5 minutes of nitrogen and were followed by one of the recovery methods.

Figure 7.6 displays the average sensor response of the graphene pixels on each polymer-functionalized sensor exposed to 5 ppm NO_2 following the use of each recovery method. Compared to the initial response, the use of heat and methanol resulted in significantly lower sensor responses. The term 'initial sensor response' refers to the sensor's response during its first exposure to 5 ppm NO2, prior to any UV exposure. **Table 28** shows the percentage recovery of the initial response. The PIM-functionalized sensors only recovered 41-48% of their initial response, while Matrimid recovered 55-56% of its initial response after using either heating or methanol for recovery. This suggests that these recovery methods are not effectively

desorbing the molecules and returning the sensor to its initial baseline state. In contrast, the use of an 8-minute vacuum-assisted UV treatment on the polymer-functionalized sensors showed a significant increase in sensor response, surpassing the initial response. A discussion on the potential reasons for this increase is provided after the additional UV repeats. The UV treatment demonstrated a recovery of 169%, 147%, and 169% for the PIM-1, PIM-EA-TB, and Matrimid sensors, respectively.

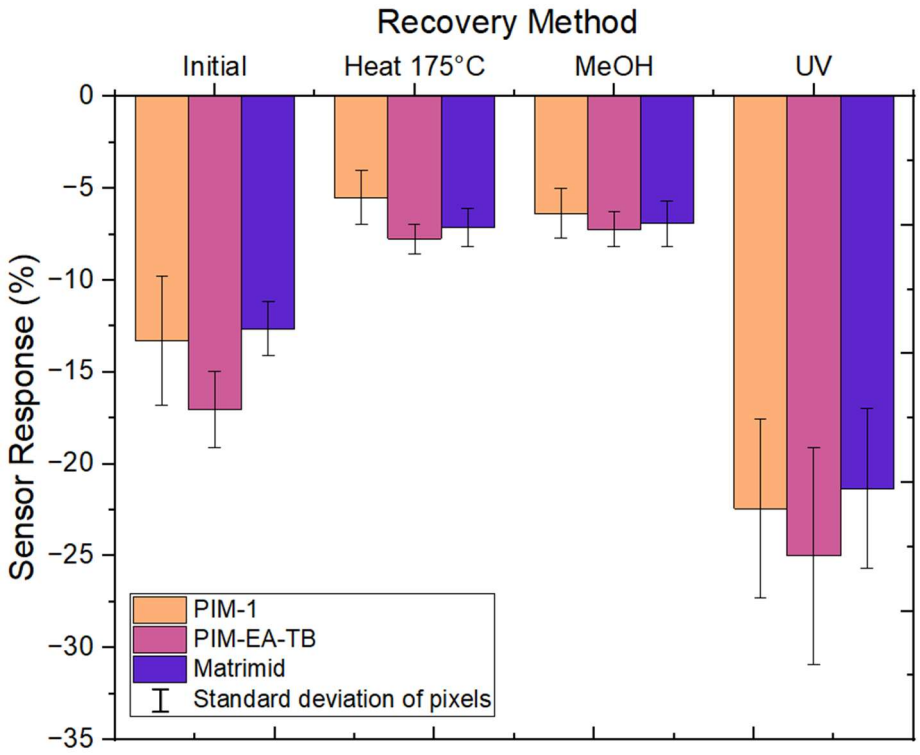


***Figure 7.6**: Bar chart comparing the sensor responses of various recovery methods for the polymer-functionalized 3x3 graphene pixel array sensors.*

***Table 28**: Percentage recovery of the initial response of the polymer-functionalized sensors. The formula for calculating percentage recovery is provided in **Chapter 3.6.3**.*

Method	Recovery of Initial Response (%)		
	PIM-1	PIM-EA-TB	Matrimid
Heat 175°C	41	45	56
MeOH	48	42	55
UV	169	147	169

Although the data suggests that UV exposure is effectively desorbing the NO_2 molecules, there is notable variability in sensor response between individual graphene pixels. This variability is unexpected given that PIMs typically exhibit uniformity due to their rigid molecular structures. While spin-coating usually results in good film thickness uniformity, several factors, including spin speed and duration, solution viscosity, and solvent evaporation rate, can affect the outcome [353]. The spin parameters used for coating the polymers were initially chosen to assess the potential of PIMs for gas sensing applications. However, further optimization and investigation may be necessary to ensure uniform polymer film deposition on the sensors, as any inconsistency might be contributing to the variability in sensor response across the pixels of the same device.

Additionally, it is important to note that the positioning of the UV light over the sensor significantly impacts its effectiveness in removing adsorbed molecules from individual pixels. Although the beam angle of the UV LED covers all the graphene pixels, the intensity is not uniform and is most intense at the centre of the LED. This variation in intensity is demonstrated in **Chapter 5.6.2.1.1**, where a Hall Bar exposed to UV light shows a variable response between channels due to the large spacing between the graphene channels. A potential solution to this issue would be to develop a UV LED array that provides more uniform illumination across a larger area.

To verify the results from the UV treatment recovery test, a further four tests were performed in the same manner described above. **Figure 7.7** displays the repeat measurements of sensor response of the polymer-functionalized sensors compared to the initial sensor response. Compared to the initial sensor response, the response after UV exposure initially increases and then stabilizes at a relatively constant level. For instance, the initial sensor response of PIM-1, PIM-EA-TB and Matrimid was -13.3%, -17.0% and -12.6%, respectively. This increases to an average sensor response across the five repeat measurements of -20.2%, -25.7% and -21.5% for PIM-1, PIM-EA-TB and Matrimid, respectively. The increase in sensor response following UV exposure could be attributed to the rearrangement of the PIM structure. Studies have shown [354], [355] that UV irradiation causes polymer chains to undergo a 1,2-migration reaction, forming a new rearranged structure. The new PIM structure has been shown to exhibit superior gas separation properties, particularly for the H_2/CO_2 gas pair [354],

[355]. As mentioned previously, NO_2 shares a very similar kinetic diameter to CO_2, and this suggests that the selectivity towards NO_2 has increased in a similar way.

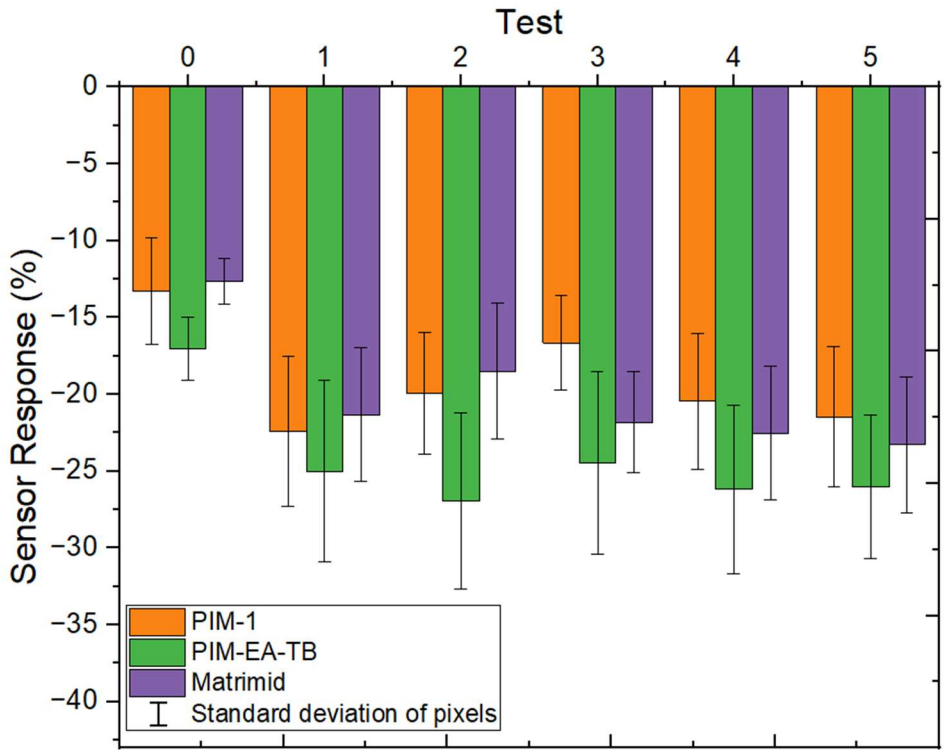


***Figure** 7.7: Bar chart displaying the sensor response (%) of polymer-functionalized 3x3 graphene pixel array devices exposed to 5 ppm NO_2 and recovered using UV exposure. 'Test 0' represents the initial exposure to the target gas with no prior exposure to UV light.*

7.6.2.1. Recovery Time Estimation

Although the recovery period for each repetition was fixed at 8 minutes to ensure complete sensor recovery, the actual recovery time for exposure to 5 ppm NO_2 was still estimated. This estimation was performed by identifying the point within the 8-minute recovery period where the baseline was recovered. **Chapter 6.7.1.1** provides a graphical representation of this approximation process (**Figure 6.25**).

The normalized resistance ($\Delta R/R_0$) for each graphene pixel on a device was averaged over three repetitions, and from this average, the recovery time was estimated. **Table 29** lists average recovery times of 114 s, 149 s, and 153 s for the PIM-1, PIM-EA-TB and Matrimid functionalized sensors, respectively. While there is some variability between repetitions—particularly for Matrimid, which shows a significant increase after repeated UV exposures—the recovery times in **Table 29** are excellent compared to other NO_2 graphene-based sensors reported in the literature [356]–[361]. A detailed

comparison of gas sensing performance with these sensors is discussed in **Section 7.6.4**.

***Table 29**: Recovery times (s) for three repetitions of the polymer-functionalized sensors exposed to 5 ppm NO_2 and recovered with UV light.*

Polymer	Recovery time (s)			
	Repeat 1	Repeat 2	Repeat 3	Average
PIM-1	148	110	84	114
PIM-EA-TB	149	139	159	149
Matrimid	59	135	265	153

7.6.3. Selectivity

The selectivity of the PIM-1, PIM-EA-TB and Matrimid-functionalized sensors were evaluated by exposing them independently to various gases and measuring the sensor response: 5 ppm ammonia (NH_3), 5 ppm nitric oxide (NO), 100 ppm methane (CH_4), and 450 ppm carbon dioxide (CO_2).

Figure 7.8 compares the selectivity of polymer-functionalized sensors to various gases with those of bare graphene and the CuPc(t-Bu)$_4$-functionalized sensor from **Chapter 6.7**. The polymer-functionalized sensors exhibited the highest selectivity towards NO_2, with sensor responses of -20.2%, -25.7% and -21.5% for PIM-1, PIM-EA-TB, and Matrimid, respectively. This represents a significant improvement in selectivity compared to bare graphene (-10.8%) and the CuPc(t-Bu)$_4$-functionalized sensor (-13.1%). The enhanced selectivity is attributed to the molecular sieve effect of the PIMs, which allows more NO_2 molecules to reach and interact with the graphene surface, resulting in a larger response [233].

The polymer-functionalized sensors showed no measurable response to NO and only small responses to NH_3 (ranging from 2.0% to 2.2%), although these were higher than the responses of bare graphene (0.63%) and the CuPc(t-Bu)$_4$-functionalized sensor (1.6%). This indicates that the polymers do not significantly enhance the selectivity for NH_3 or NO, and as graphene inherently exhibits low adsorption energy for both NH_3 [295] and NO [362], this leads to a minimal response.

While the responses to CH_4 and CO_2 were low compared to NO_2, this is the first instance in this thesis where either gas has been detectable using a graphene sensor. This suggests the polymer membranes are selectively allowing these gases to pass through more easily than O_2 and N_2, thereby eliciting a response from the underlying bare graphene.

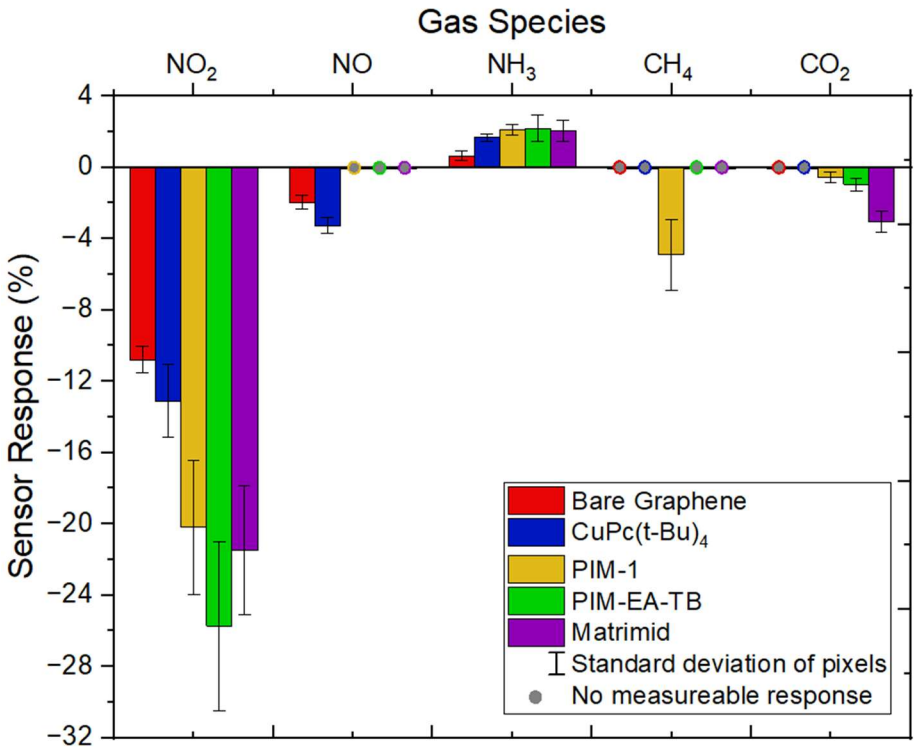


***Figure 7.8**: Bar chart comparing the selectivity of bare graphene and CuPc(t-Bu)$_4$, PIM-1, PIM-EA-TB and Matrimid-functionalized 3x3 graphene pixel array sensors exposed to various gases: 5 ppm nitrogen dioxide (NO_2), 5 ppm ammonia (NH_3), 5 ppm nitric oxide (NO), 100 ppm methane (CH_4), and 450 ppm carbon dioxide (CO_2).*

7.6.4. Gas Sensing Performance Comparison

The sensing performance of the polymer-functionalized sensors was evaluated in comparison to bare graphene, the CuPc(t-Bu)$_4$ sensor, and similar sensors documented in the literature. **Table 30** compares sensor response, recovery time, and percentage recovery for the sensors in this study with other room temperature NO_2 sensors using graphene materials [356]–[361].

***Table 30**: Comparison of graphene-based NO_2 sensors using different sensing materials.*

Sensing materials	NO_2 response	Recovery time (s)	Recovery (%)	Ref.
CVD graphene/*PIM-1*	20% at 5 ppm	114	100	***This work***
CVD graphene/*PIM-EA-TB*	26% at 5 ppm	149	100	***This work***
CVD graphene/*Matrimid*	22% at 5 ppm	153	100	***This work***
CVD graphene/*CuPc(t-Bu)$_4$*	13% at 5 ppm	67	100	***This work***
CVD graphene	11% at 5 ppm	93	100	***This work***
4-aminoquinoline-rGO	74% at 10 ppm	3300	80	[356]
CVD graphene	32% at 200 ppm	>1440	Did not recover in time allowed.	[357]
rGO coated nanofibrous mesh fabrics	14% at 1 ppm	10000	Not reported.	[358]
ME graphene	5% at 1.5 ppm	1200	Not reported.	[359]
CVD graphene	20% at 1 ppm	900	97	[360]
CVD graphene-AlGaN/GaN	19% at 5 ppm	>600	Full recovery observed after overnight.	[361]
SnO_2-rGO hybrid	2% at 1 ppm	100	Not reported.	[363]

A comparison of the polymer-functionalized sensors with other sensors demonstrates their potential for highly sensitive, selective, and rapid recovery devices. While some studies have reported larger sensor responses [356] , [360], often at higher concentrations, the recovery times achieved in this work (ranging from 67 s to 153 s) and the complete 100% recovery of the devices are superior. Although the metal oxide sensor (SnO_2-rGO hybrid) demonstrates a slightly quicker recovery time compared to the polymer-functionalized sensors, its response magnitude to NO_2 is significantly lower. This suggests that the sensors reported in this work exhibit a higher level of

sensitivity. Notably, the PIM-functionalized sensors also show impressive selectivity towards NO_2, further highlighting their superior performance in detecting this gas. Furthermore, the limit of detection (LOD) and limit of quantitation (LOQ) were estimated for each of the polymer-functionalized sensors and are shown in **Table 31**. The low LOD and LOQ values, in the range of a few parts per billion (ppb), further suggest that these sensors have the potential to be highly sensitive NO_2 detectors.

***Table 31**: Estimated Limit of Detection (LOD) and Limit of Quantification (LOQ) for each polymer-functionalized 3x3 graphene pixel array sensor.*

Polymer	LOD (ppb)	LOQ (ppb)
PIM-1	1.0	3.4
PIM-EA-TB	0.7 *(700 ppt)*	2.3
Matrimid	1.0	3.3

7.7. Mixed Matrix Membranes

Mixed Matrix Membranes (MMMs) are composite membranes that combine organic polymer matrices with inorganic fillers, such as nanoparticles, metal-organic frameworks (MOFs), or zeolites [345], [364]. The integration of these materials aims to enhance the performance of the membrane by leveraging the advantages of both the organic and inorganic components.

Given the enhanced selectivity of $CuPc(t\text{-}Bu)_4$ towards NO_2, combining this phthalocyanine with a PIM offers an intriguing opportunity to explore the gas sensing capabilities of the hybrid material. Since PIM-EA-TB showed the highest sensor response increase towards NO_2 among the tested polymers, it was chosen to form the MMM with $CuPc(t\text{-}Bu)_4$.

7.7.1. Graphene Functionalization and Preparation of MMMs

The preparation methods for each hybrid mixture are presented in this section. The hybrid material consisted of PIM-EA-TB and $CuPc(t\text{-}Bu)_4$ blended in two different

volume-to-volume (v/v) and weight-to-weight (w/w) ratios, chosen based on the ranges reported in the literature [365].

The two blending ratios chosen for comparison were 50:50 and 80:20 PIM-EA-TB: CuPc(t-Bu)$_4$. To prepare the w/w ratio mixtures, powdered PIM-EA-TB and CuPc(t-Bu)$_4$ were first weighed in the desired ratios and then dissolved in chloroform to create a 1 mg/mL solution. For the v/v ratio mixtures, a 1 mg/mL PIM-EA-TB solution in chloroform was combined with a 10 mg/mL CuPc(t-Bu)$_4$ solution in toluene (as prepared in **Chapter 6.6.3.3**), mixed in the desired ratios.

The prepared solutions of mixed matrix membranes were applied to 3x3 graphene pixel array devices using the same spin-coating procedure and parameters as described in **Section 7.3**.

7.7.2. Gas Sensing Performance

Four spin-coated MMM sensors were evaluated for their gas sensing performance upon exposure to NO_2. Given the previous finding (**Section 7.6.2**) that sensor response can improve following exposure to UV light due to polymer rearrangement [354], [355], all functionalized devices were pre-exposed to UV light before the sensing experiments began. The functionalized devices were placed in a gas sensing chamber and exposed to 5 ppm NO_2 in nitrogen. Each experiment started with a 10-minute exposure to N_2 to establish a baseline, followed by a 10-minute exposure to the target gas, and concluded with a 10-minute exposure to N_2. All tests were conducted at room temperature and atmospheric pressure, with a constant flow rate of 1000 mL/min. Real-time resistance measurements are supplied in the **Appendix** (**Figure A11a**).

Figure 7.9 illustrates the average sensor response of four prepared MMMs with different compositions (50:50 v/v, 80:20 v/v, 50:50 w/w, and 80:20 w/w of PIM-EA-TB:CuPc(t-Bu)$_4$) when exposed to 5 ppm NO_2, compared to bare graphene, a CuPc(t-Bu)$_4$-functionalized sensor, and a PIM-EA-TB-functionalized sensor. The sensor responses for individual graphene pixels are supplied in the **Appendix** (**Figure A11b**).

The MMMs showed a slight increase in sensor response (ranging from -11.5% to -14.5%) compared to the bare graphene sensor (-10.8%). However, only one MMM (80:20 w/w) exhibited a higher sensor response than the CuPc(t-Bu)$_4$-functionalized

sensor. Importantly, none of the MMMs matched the sensor response of the pure PIM-EA-TB membrane.

This suggests that the addition of CuPc(t-Bu)$_4$ may have disrupted the micropore structure of the PIM, leading to reduced permeability and selectivity, and consequently, a diminished sensor response. Dong et al. [366] highlight several challenges in constructing an effective MMM without compromising selectivity and separation performance. They explain that a lack of compatibility between the two blended phases or agglomeration of particles within the polymer matrix can negatively impact the quality and performance of the resulting MMM. Moreover, because CuPc(t-Bu)$_4$ is dispersed within the polymer, its NO_2 binding sites may be obstructed, reducing the amount of adsorbed NO_2 and consequently lowering the sensor response.

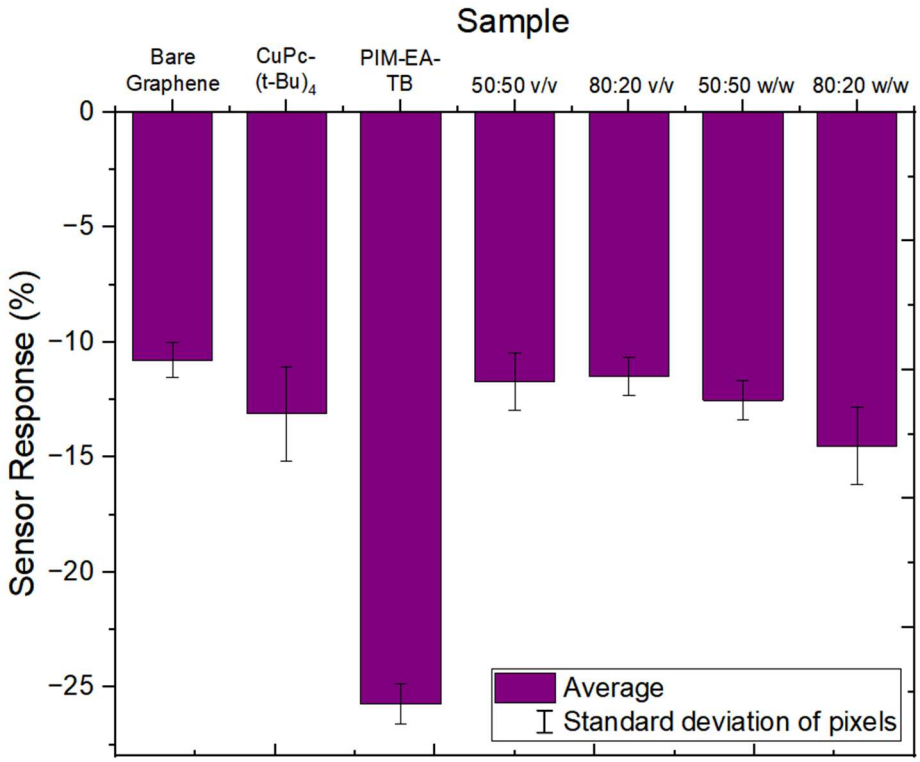


***Figure 7.9**: Bar chart demonstrating the sensor response (%) of four mixed matrix membranes (50:50 v/v, 80:20 v/v, 50/50 w/w and 80:20 w/w PIM-EA-TB:CuPc(t-Bu)$_4$) compared to the response of bare graphene, CuPc(t-Bu)$_4$ and PIM-EA-TB.*

7.8. Conclusions

In this work, the gas sensing performance of PIM-1, PIM-EA-TB, and Matrimid was investigated using 3x3 graphene pixel array sensors. Polymers of intrinsic microporosity (PIMs) are known for their excellent gas separation properties due to their rigid structures [233]. As PIMs have not been frequently investigated for gas sensing applications, this study explores the potential of combining their excellent gas transport properties with graphene gas sensors.

The PIMs and Matrimid demonstrated excellent selectivity towards NO_2 gas, with sensor responses 9-15% higher than that of bare graphene and reduced response times. Compared to the CuPc(t-Bu)$_4$-functionalized sensor discussed in Chapter 6, the polymer-functionalized sensors showed increased sensor responses and exhibited rapid recovery times, outperforming similar sensors reported in the literature. The estimated LOD and LOQ values were in the range of a few ppb, which is highly relevant for real-life applications, as even small concentrations of NO_2 can cause damage to respiratory organs. For instance, the World Health Organization (WHO) has set an annual exposure limit to NO_2 of 21 ppb [224], highlighting the need for highly sensitive NO_2 detectors.

Additionally, it is notable that this is the first instance in this thesis where both CO_2 and CH_4 gases were detected using a graphene sensor, facilitated by the polymer membranes. This demonstrates the versatility of the polymer-functionalized sensors in detecting multiple gases, further highlighting their potential in various applications.

This work also explored the possibility of creating a mixed matrix membrane (MMM) using CuPc(t-Bu)$_4$ and PIM-EA-TB. Unfortunately, this particular blend did not demonstrate improved gas sensing performance, indicating that more engineering is needed to address the challenges of creating an effective MMM.

Overall, the polymer-functionalized 3x3 graphene pixel array sensors demonstrate promising characteristics as reversible NO_2 gas sensors. They are highly sensitive, selective, and exhibit quick response and recovery times, making them suitable for practical applications.

Chapter 8 : Electrochemical Functionalization of Graphene Sensors

8.1. Introduction

This chapter reports the electrochemical functionalization of 3x3 graphene pixel array sensors and their subsequent gas sensing performance. Two distinct graphene functionalization processes were evaluated: the electrochemical polymerization of 1,5-diaminonaphthalene and electrochemical oxidation. The chapter begins by outlining the methodology for each process, followed by a detailed characterization of the resulting graphene surface modifications. A significant challenge encountered during these processes was device damage due to the corrosive electrolyte solutions utilized, which is discussed in the final section of the chapter.

The research on poly-(1,5-diaminonaphthalene) was conducted in collaboration with undergraduate student Owen Wade.

8.2. Electrochemical Polymerization of 1,5-diaminonapthalene

Conductive π-stacking polymers have gained significant attention for biosensor development, particularly in conjunction with graphene, due to their aromatic π-stacking interactions [155], [367]. Conducting polymers like polyaniline (PANi), poly(diaminonaphthalene) (pDAN), polypyrrole (PPy), poly(o-phenylenediamine), poly(3,4-ethylenedioxythiophene) (PEDOT), and polythiophene (PTh) have been widely utilized in the design of biosensors and gas sensors [146], [367], [368]. Their electrical conductivity, redox properties, and effective operation at room temperature make them ideal candidates for integration with nanomaterials, such as graphene [367].

The addition of amine groups (-NH_2) is particularly important in biofunctionalization processes, as they enable crosslinking through amide bond formation between the NH_2 groups and carboxyl groups on bioreceptors. This is typically achieved using coupling agents, such as EDC (1-ethyl-3-(3-dimethylaminopropyl)carbodiimide) and NHS (N-hydroxysuccinimide), to attach bioreceptor molecules like antibodies [133], [369], proteins/enzymes [149], aptamers [213], [370], and peptides [371]. Consequently, the use of 1,5-diaminonaphthalene for graphene functionalization on 3x3 pixel array devices was evaluated to investigate the potential for achieving varying degrees of graphene pixel functionalization. This study aims to demonstrate how graded levels of functionalization might influence the sensor response of individual graphene pixels. If successful, this surface modification technique could be applied to a future sensor array, where distinct receptor molecules are attached to specific graphene pixels, effectively creating an 'electronic nose.'

8.2.1. Cyclic Voltammetry Methodology

CVD graphene on 3x3 graphene pixel array sensors was electrochemically functionalized with 1,5-diaminonaphthalene (DAN) monomers, converting them into the polymer pDAN (**Figure 8.1**) using a cyclic voltammetry method previously established by the research group [372]. The procedure was performed with a *PGSTAT30 Autolab* system and **Nova 2.1.2** software, as described in detail in **Chapter 3.3.1.3**.

Fathi et al. [373] suggest a six-step mechanism (**Figure 8.1**) for DAN polymerization: (a) The process begins with the oxidation of the monomer to generate a radical cation. (b) This radical cation then reacts with another monomer, resulting in the formation of (c) a neutral radical and a protonated monomer. (d) The neutral radical is further oxidized, producing a cationic species. (e) This species undergoes an irreversible chemical reaction, forming a dihydrodimer that is subsequently deprotonated to yield an aromatic dimer. (f) The aromatic dimer is oxidized to form a dication, which then combines with another monomer (as in step b) and undergoes deprotonation, forming a trimer. This cycle repeats to produce a tetramer and higher oligomers.

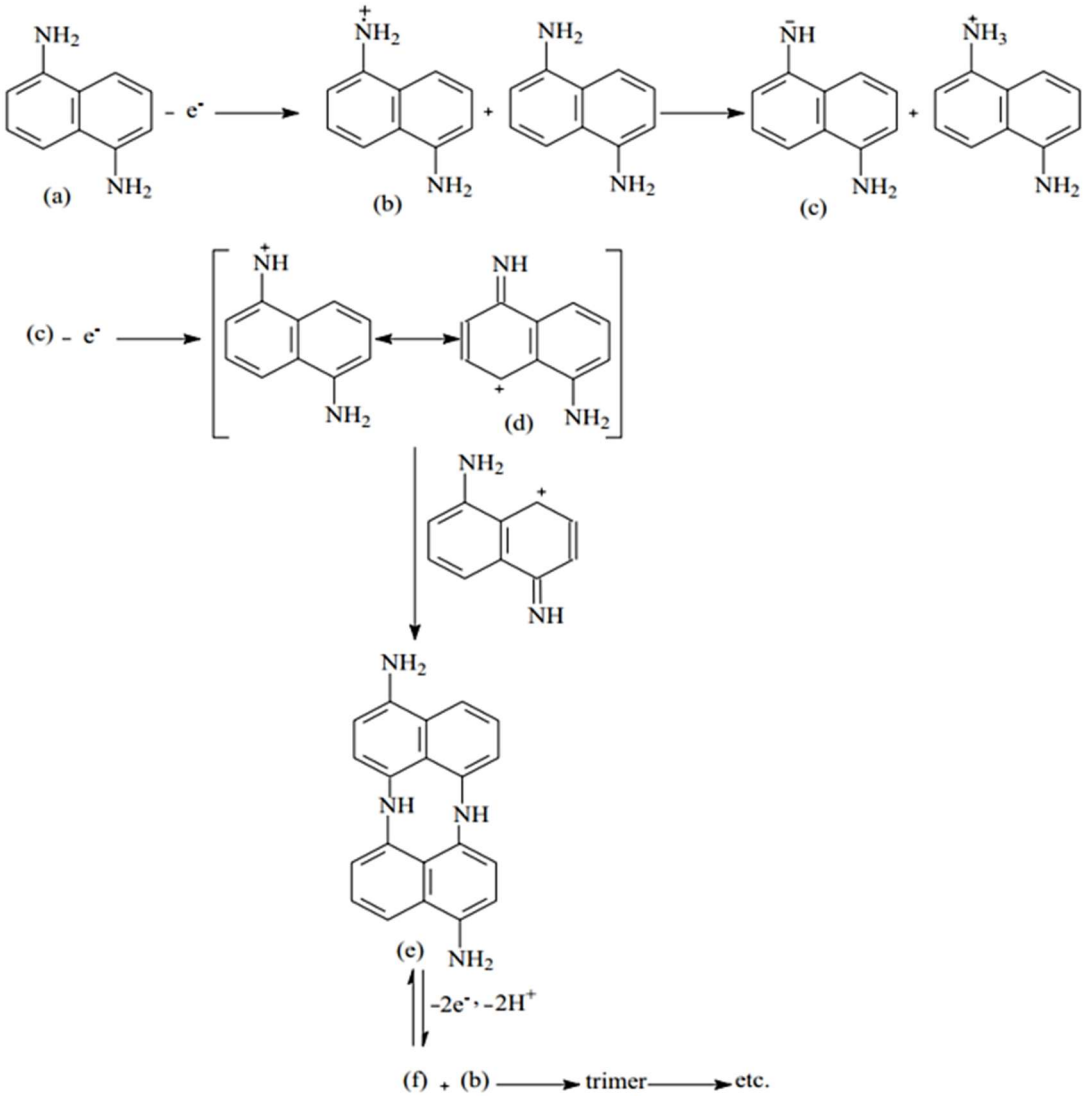


***Figure 8.1**: Proposed mechanism for the synthesis of pDAN from DAN monomers. Reproduced from reference* [373].

A 3-electrode cell setup was used with a platinum wire as the counter electrode (CE), silver/silver chloride (Ag/AgCl) (saturated in 3M sodium chloride) reference electrode (RE) and CVD graphene on Si/SiO_2 (using a platinum wire probe) or a 3x3 graphene pixel array sensor as the working electrode (WE) (**Figure 8.2**). While the graphene sensor was acting as the working electrode, a USB C PCB connector was used to electrically connect the sensor to the working electrode. An electrolyte solution containing 10 mM DAN in 0.25 M sulphuric acid (H_2SO_4) was prepared and DAN underwent electropolymerization using a scan rate of 50 mV/s, a potential window of 0.9 to -0.6 V and a set number of scan cycles. The number of scan cycles was investigated and therefore was varied from 5 to 30 cycles. CVD graphene on Si/SiO_2

substrates were used for characterization purposes, while gas sensing was performed using 3x3 graphene array sensors.

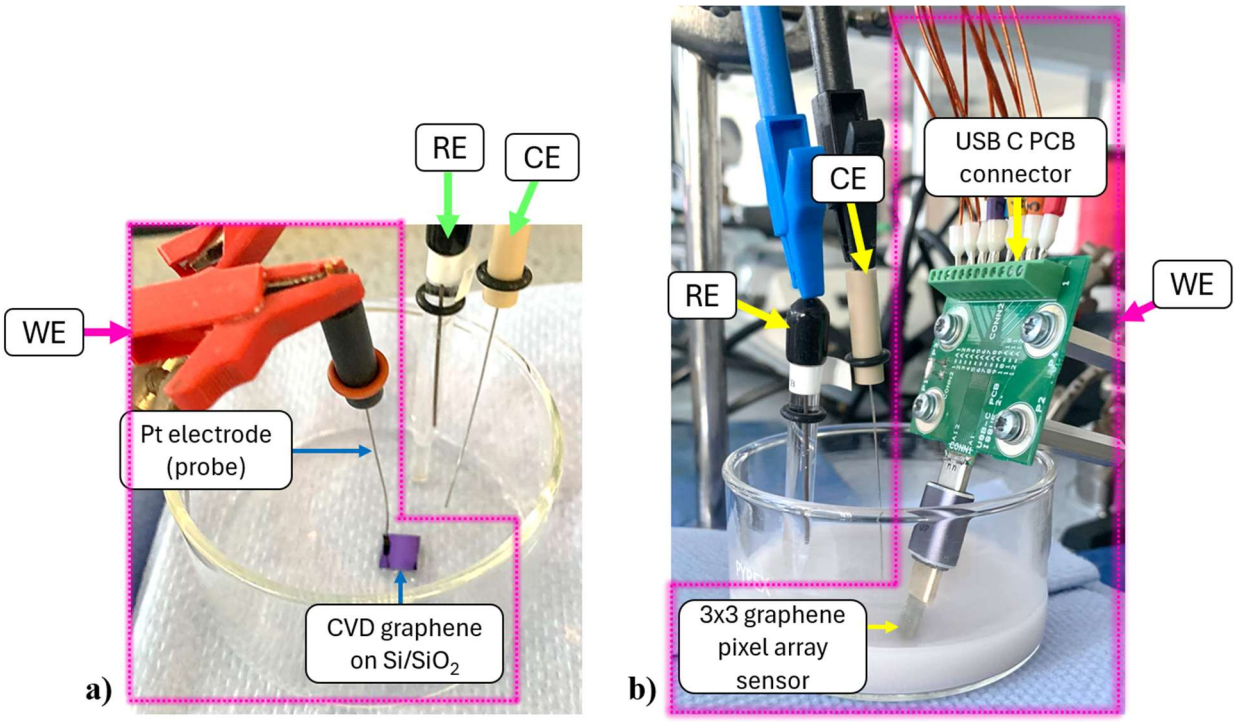


Figure 8.2: 3-electrode cell electrochemical set-up for the polymerization of DAN onto ***(a)*** *CVD graphene on Si/SiO2 and* ***(b)*** *3x3 graphene pixel array sensors. The working electrode (WE) is highlighted by pink circled areas in both setups.*

Electrochemical functionalization of the graphene sensor arrays was achieved by submerging individual rows of pixels in the electrolyte solution, allowing for unique functionalization of each row while preventing unintended surface modification of the other pixel rows. Two independent graphene sensor arrays were functionalized, varying the number of scan cycles per row in each case. In both experiments, Rows B and C were functionalized with pDAN, while Row A, left as bare graphene, served as a control (**Figure 8.3**) and was never submerged in the electrolyte solution.

In Experiment 1, Row C was submerged in the electrolyte solution first, and 10 cycles were performed. Subsequently, Row B was lowered into the solution, and 5 cycles were conducted. For Experiment 2, using a different device, Row C and Row B were functionalized with 20 and 15 cycles, respectively. After functionalization, the sensor arrays were rinsed with deionized water and dried with compressed air.

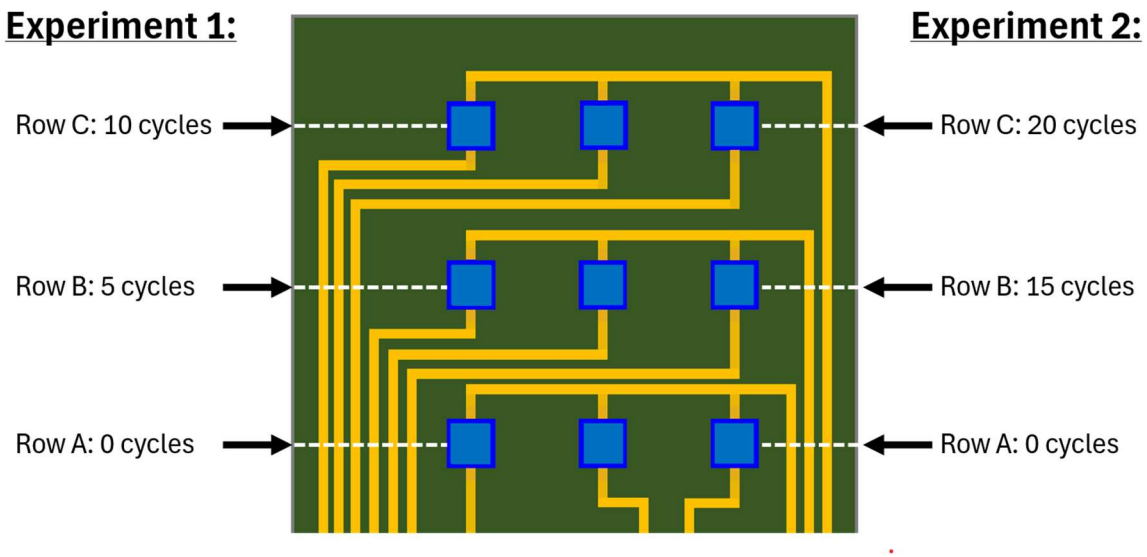


***Figure 8.3**: Schematic illustrating the number of scan cycles applied to each row of the 3x3 graphene pixel array devices during electrochemical functionalization in both experiments.*

8.2.1.1. Cyclic Voltammetry Profile

Each functionalization procedure yielded a cyclic voltammogram exhibiting a similar trend, as described below.

Figure 8.4 demonstrates that as the number of cycles increases, the peak current increases due to the pDAN forming on the graphene surface. Large oxidation and reduction peaks are seen at 0.01 and -0.38 V respectively which both increase in amplitude. Zooming in on the voltammogram in the region around 0.4 V reveals additional peaks. Specifically, two oxidation peaks initially observed at 0.40 V and 0.46 V which coalesce into a single peak at 0.43 V with increasing cycle count. Furthermore, an extra reduction peak emerges at 0.42 V. The observed peaks are characteristic of the DAN polymerization reaction, with their increasing height corresponding to successive cycles of DAN polymerization. Moreover, these peaks are consistent with previous findings from previous research within the group [149], [372].

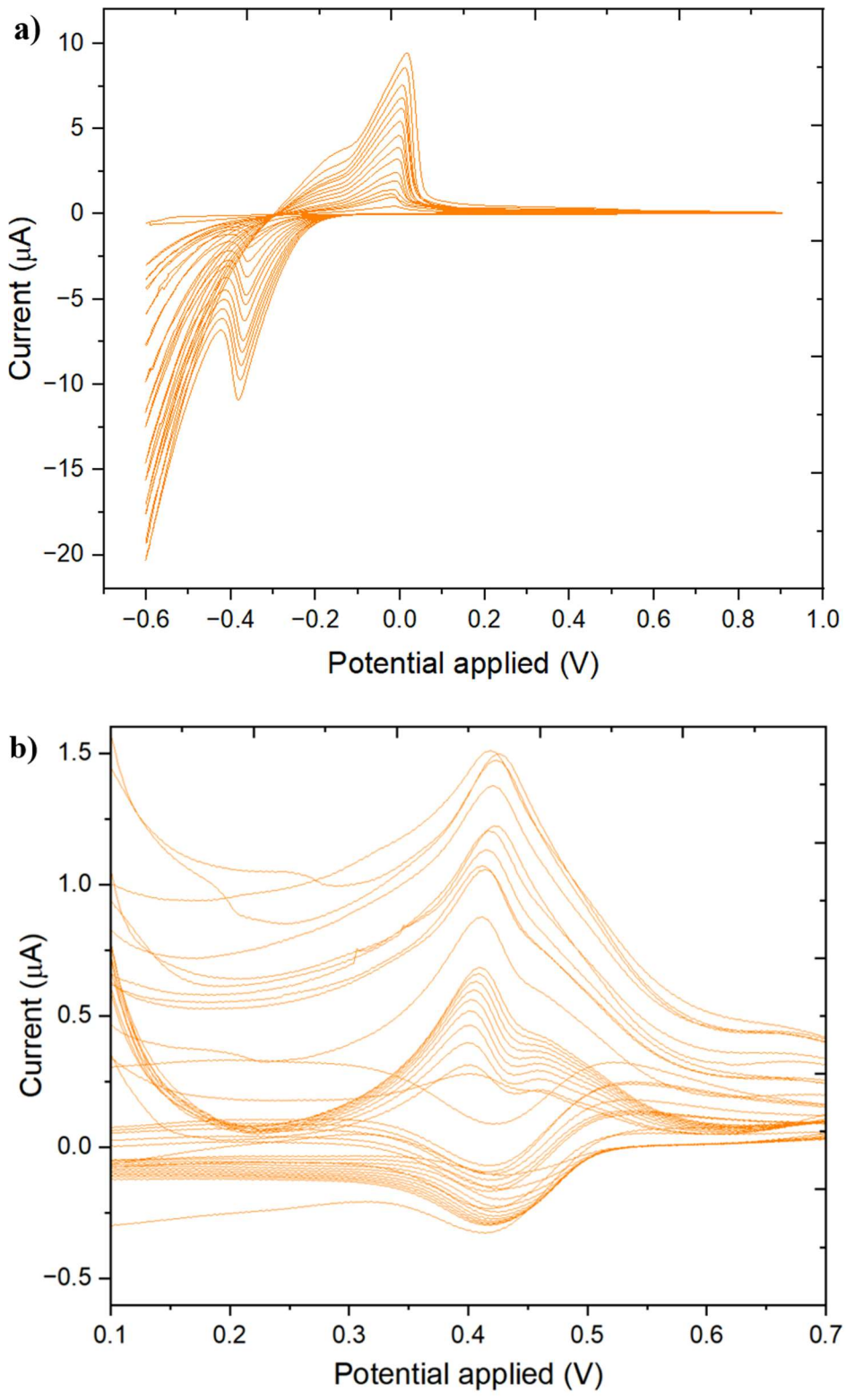


***Figure 8.4**: Cyclic voltammograms of **(a)** the electropolymerization of 1,5-diaminonapthalene at a scan rate of 50 mV/s over 15 cycles and **(b)** zoomed in region of the voltammogram revealing additional oxidation and reduction peaks.*

8.2.2. Characterization of pDAN films

This section describes the characterization of the pDAN films on graphene-SiO_2/Si wafer fragments and 3x3 graphene pixel array sensors.

8.2.2.1. Surface Morphology

An obvious colour change was observed upon completion of the electropolymerization and was used as an initial indicator that the experiment was successful. This change in colour is attributed to variations in light absorption and reflection on the samples, presumably influenced by the presence of the pDAN film.

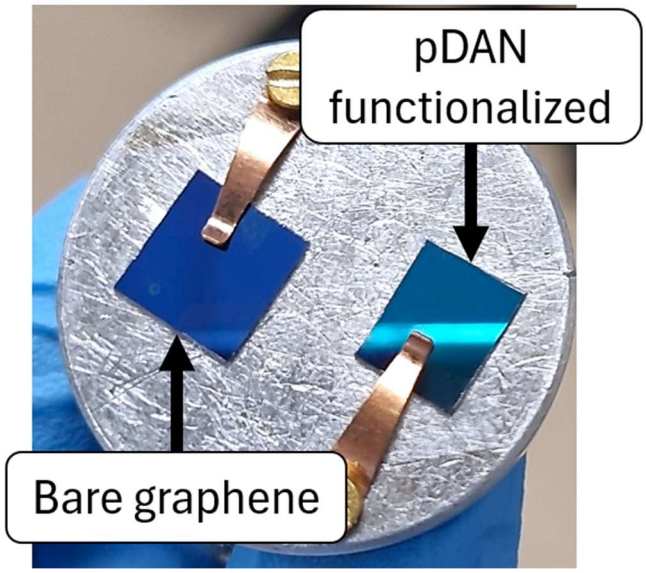


***Figure 8.5**: Image of a bare and pDAN functionalized graphene-SiO_2/Si wafers.*

An optical light microscope was used to observe surface changes following the electropolymerization of pDAN. **Figure 8.6** illustrates a gradual evolution in surface colour and appearance with each successive scan cycle. In the bare graphene image, visible "lines" likely represent graphene grain boundaries. After the application of the pDAN film, new surface features appear as distinct "spots" that were not present before the modification. These features suggest changes in surface morphology or composition resulting from the modification.

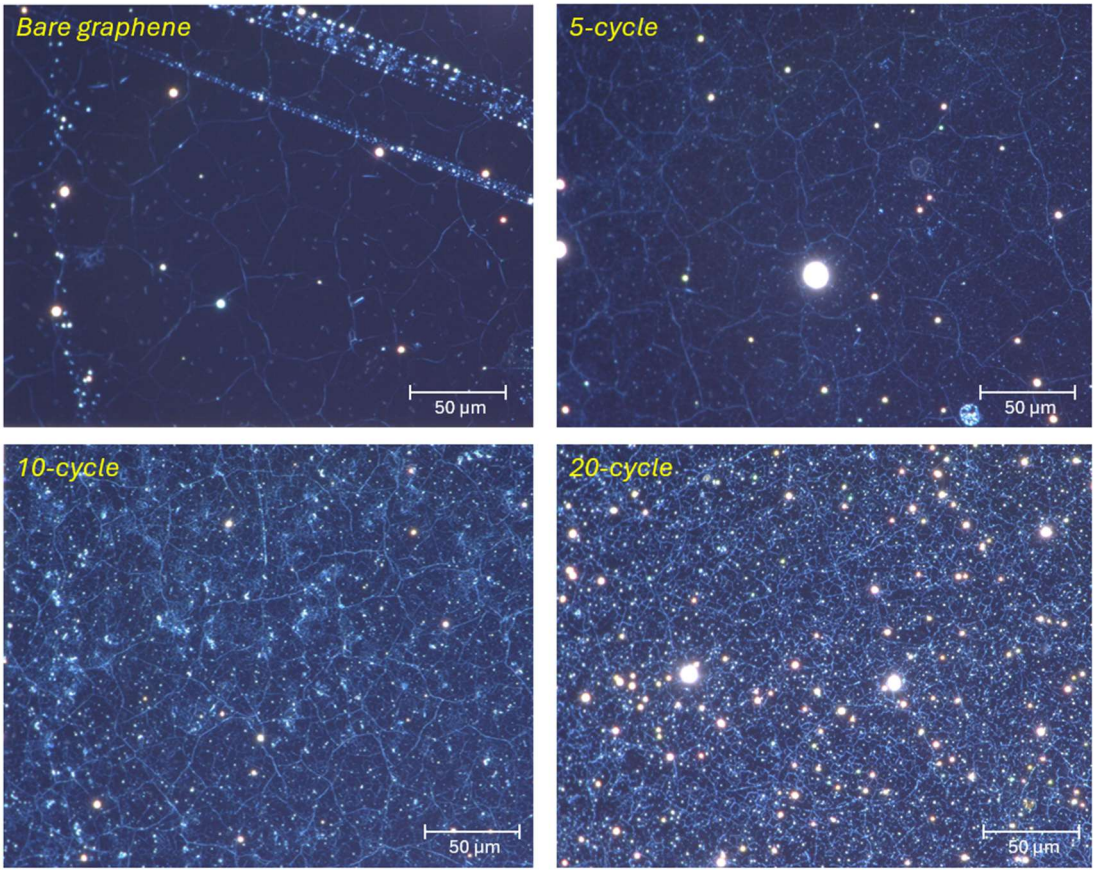


***Figure 8.6**: Optical images of bare graphene, 5-cycles, 10-cycles, and 20-cycles of pDAN on the surface.*

A scanning electron microscope (SEM) (**Figure 8.7**) was used in conjunction with the optical microscope to verify the observed surface changes. Similar to the optical images, the bare graphene image (**Figure 8.7a**) shows lines that likely indicate grain boundaries. Additionally, the darker "spots" in the image may correspond to regions with multiple graphene layers.

Although the pDAN film seems to cover the entire surface, its thickness appears non-uniform across the sample at 5 scan cycles (**Figure 8.7b**). The lighter areas likely indicate regions with a thicker film, while the darker areas may represent exposed graphene. The varying density of these lighter and darker regions suggests an uneven distribution of the pDAN film on the graphene surface. This suspected non-uniformity was confirmed in the subsequent paragraph using atomic force microscopy.

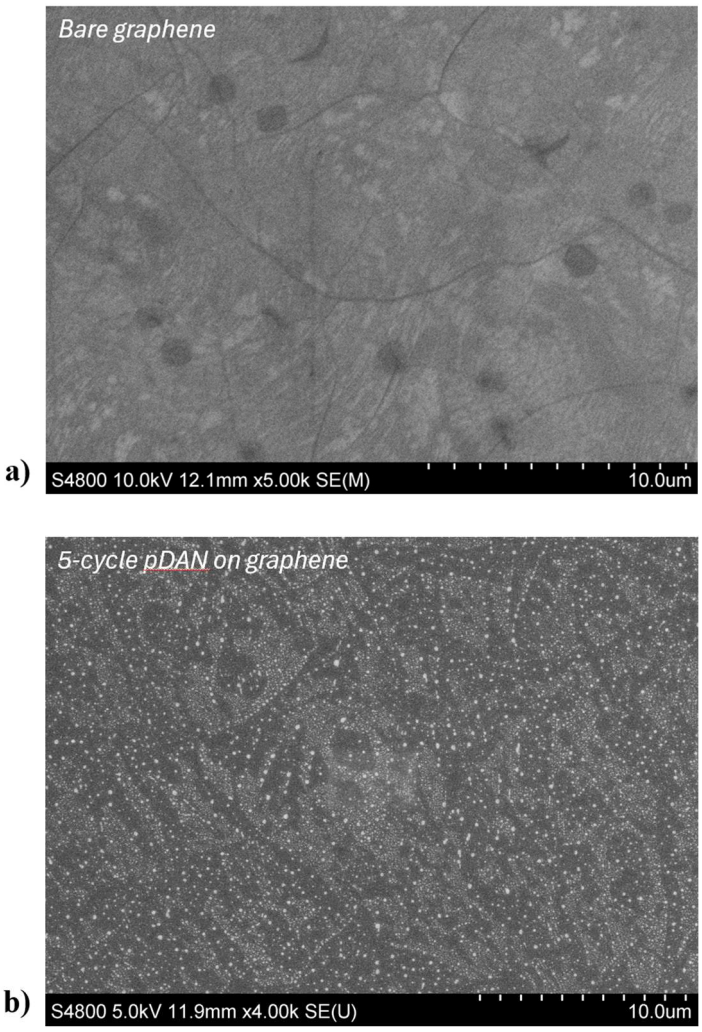


***Figure 8.7**: SEM images of **(a)** bare graphene and **(b)** 5 cycles of pDAN on graphene.*

The surface topography before and after electropolymerization of pDAN on a graphene wafer was characterized using AFM on a 1 µm x 1 µm scan area. The surface of the bare graphene wafer before and after functionalization showed clear changes in surface roughness and topography (**Figure 8.8**). An examination of the pDAN film image reveals distinct features not observed on the bare wafer. Fissures are observed in the 5-cycle pDAN film, confirming the non-uniformity observed in the SEM image. These cracks disappear as the number of cycles increase, with only a few holes in the film observable at 20 cycles. The average root mean square (RMS) roughness of three measurements taken of the bare graphene wafer was 0.536 nm which increased to 3.135 nm after 5 cycles of pDAN. However, the RMS roughness decreased to 1.981 nm at 20 cycles, suggesting the formation of a smoother film after increased deposition cycles.

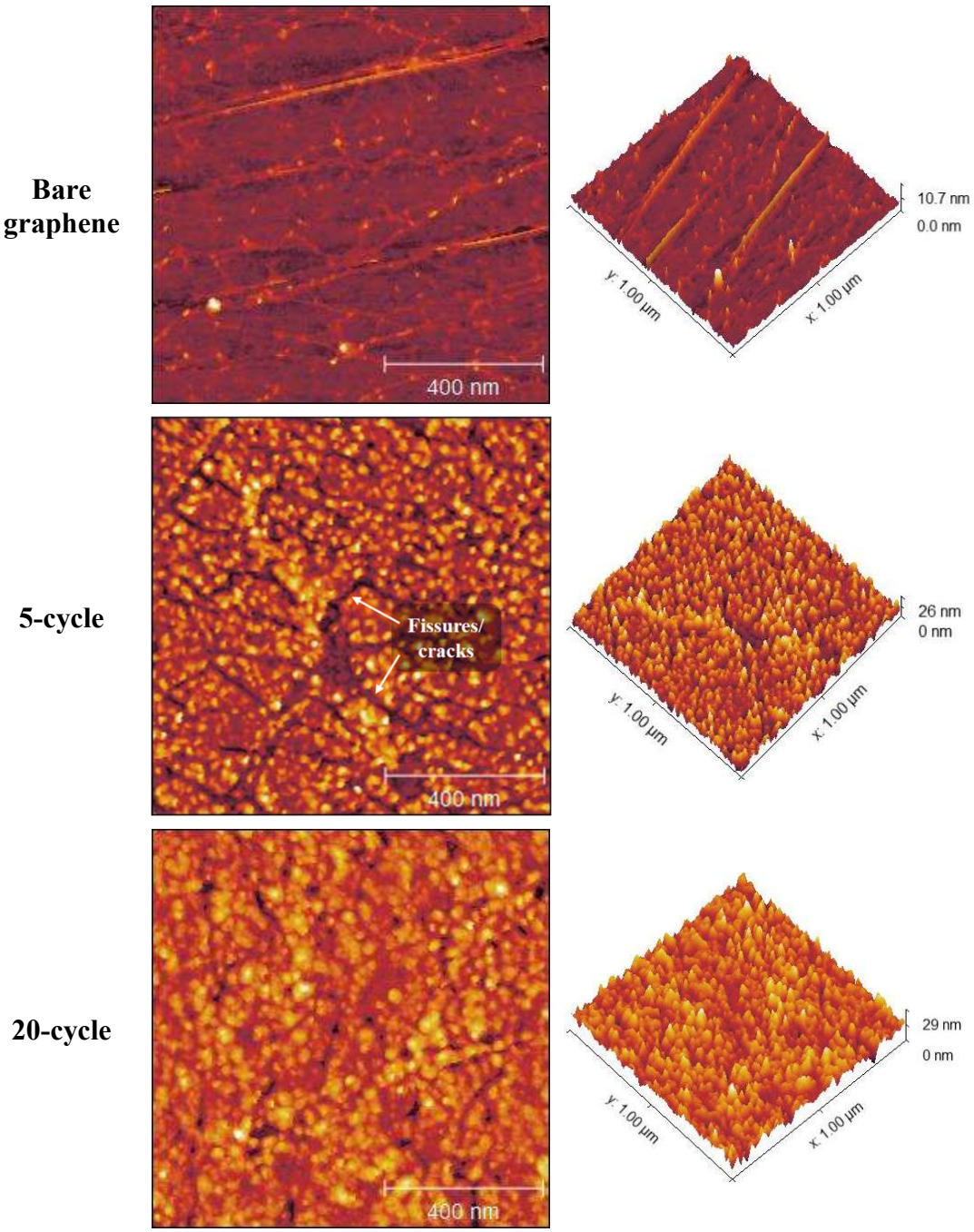


***Figure 8.8**: AFM surface morphology of bare graphene, 5-cycle, and 20-cycle pDAN functionalized samples.*

8.2.2.2. Film Thickness

Polymer film thickness was determined using variable angle spectroscopic ellipsometry. Three measurements were performed after 5, 10, 15, 20, 25 and 30 cycles of pDAN deposition and the average was calculated. The data illustrates that the film

thickness of the pDAN film increases linearly with an increasing number of cycles (**Figure 8.9**).

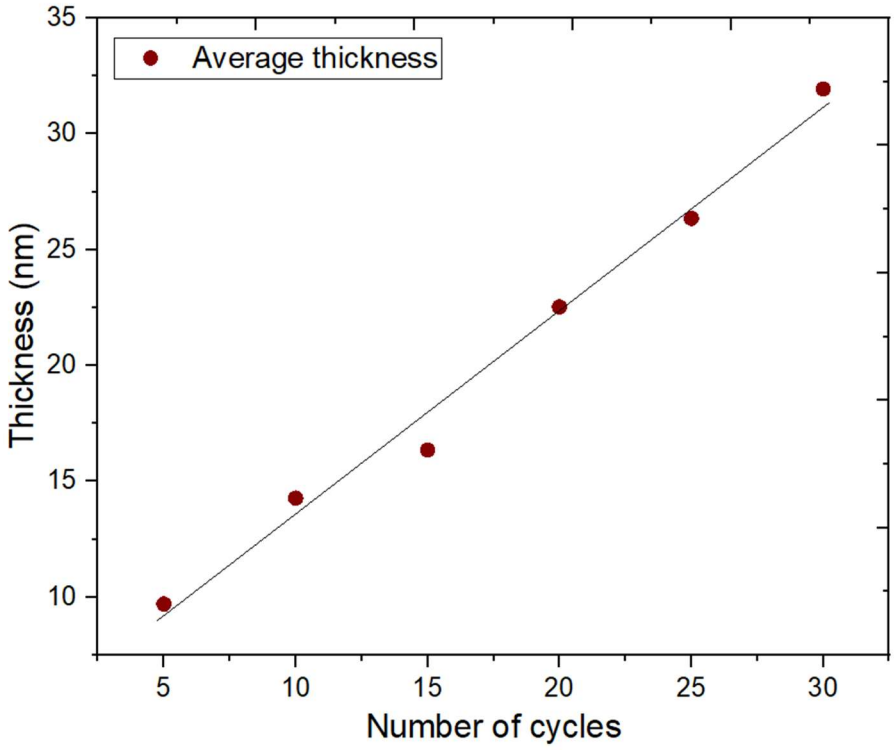


***Figure 8.9**: Thickness of pDAN films measured on CVD graphene samples with 5, 10, 15, 20, 25 and 30 cycles.*

8.2.2.3. Raman Spectroscopy

Raman spectroscopy was used to monitor changes in the graphene structure and pDAN film following the functionalization process. Single point extended scan spectra and 60 µm x 60 µm maps were taken of bare graphene and pDAN functionalized samples.

In the pristine (bare) graphene sample, the characteristic G- and 2D-peaks are located at ~1593 cm^{-1} and ~2689 cm^{-1}, respectively (**Figure 8.10a**). The full width at half maximum (FWHM) (**Figure 8.11c**) of the G-peak of the bare graphene sample was 11 cm^{-1}, suggesting very little doping [374]. The FWHM of the 2D-peak in the pristine sample was 28 cm^{-1}, the small value indicative of high-quality single-layer graphene [246], [375]. A small D-peak, located at ~1350 cm^{-1} in the pristine graphene sample is observable which could be attributed to minor defects or contaminants on the graphene surface. The D-peak, also known as the defect or disorder peak, is attributed to the 'breathing mode' of sp^2 carbons and becomes Raman active when a defect is

present adjacent to a sp^2 carbon [244], [246]. The average intensity ratio between the D- and G-peak (I_D/I_G) for pristine graphene was approximately 0.110, a low ratio indicating high-quality, well-ordered graphene.

In the pDAN samples, G- and 2D-peaks are found at ~1593-1594 cm^{-1} and ~2686 cm^{-1}, respectively (**Figure 8.10a**). The 2D-peak is slightly red-shifted compared to pristine graphene, indicating there could be n-type doping [339] from the pDAN molecules. This is further supported by the electrical characterization data presented in **Section 8.2.2.5**, which also demonstrates the n-type doping effect induced by pDAN.

As the number of pDAN cycles increase, the D- and G- peaks broaden and a D'-peak (~1620cm^{-1}) is first observable at 10 cycles. The asymmetrical nature of the G- and D-peaks could be due to overlapping peaks from the pDAN component of the Raman spectra (**Figure 8.10b**), consistent with a previous study [372]. Furthermore, a band at 1371 cm^{-1} is associated with C-N vibrations (from the DAN molecule) and could be contributing to the broadening of the D-peak [376]. The I_D/I_G ratio increased with increasing pDAN cycles (from 0.110 to 0.281), indicating increasing disorder within the graphene structure, due to the aromatic molecules on the surface [340]. The increasing intensity ratio can be easily observed in **Figure 8.11d** where the colour contour maps transition from cooler colours to warmer colours as the number of cycles increase.

The broadening of the G-peak and the increase in its full width at half maximum (FWHM) from 11 cm^{-1} for pristine graphene to 95 cm^{-1} after 15 pDAN cycles indicate increased disorder or strain in the graphene lattice. The FWHM of the G-peak continues to rise with more pDAN cycles, eventually plateauing (**Figure 8.11c**). In contrast, the FWHM of the 2D peak remains consistently stable at 28-30 cm^{-1} even with the introduction of pDAN. This stability suggests minimal strain on the graphene lattice, implying that the pDAN molecules did not form covalent bonds with the graphene [372].

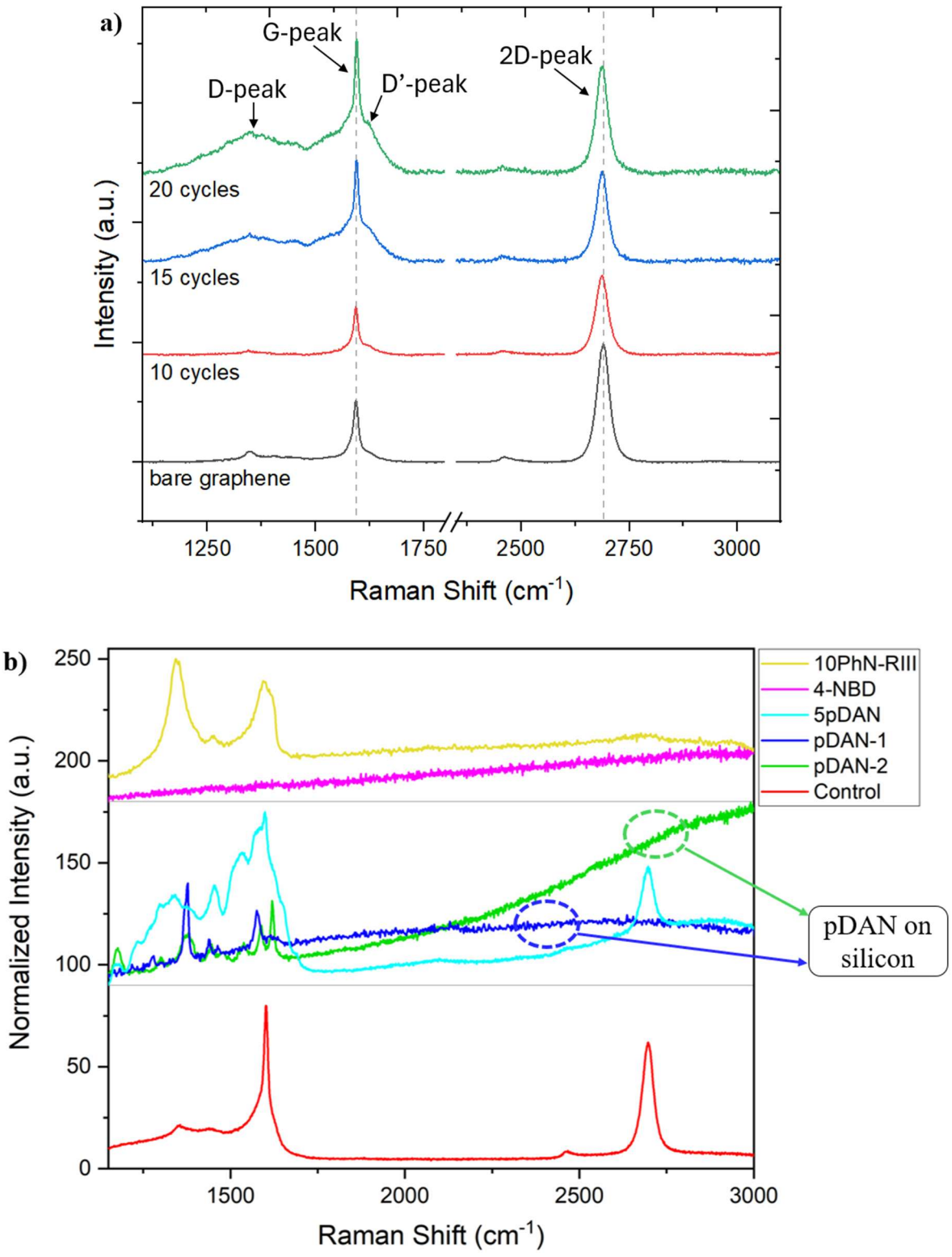


***Figure 8.10**: **(a)** Raman spectra of bare graphene, 10-cycle, 15-cycle, and 20-cycle pDAN samples. **(b)** Raman spectra of pDAN on silicon: relevant spectra circled and labelled (reproduced from Supplementary Information, reference* [372].

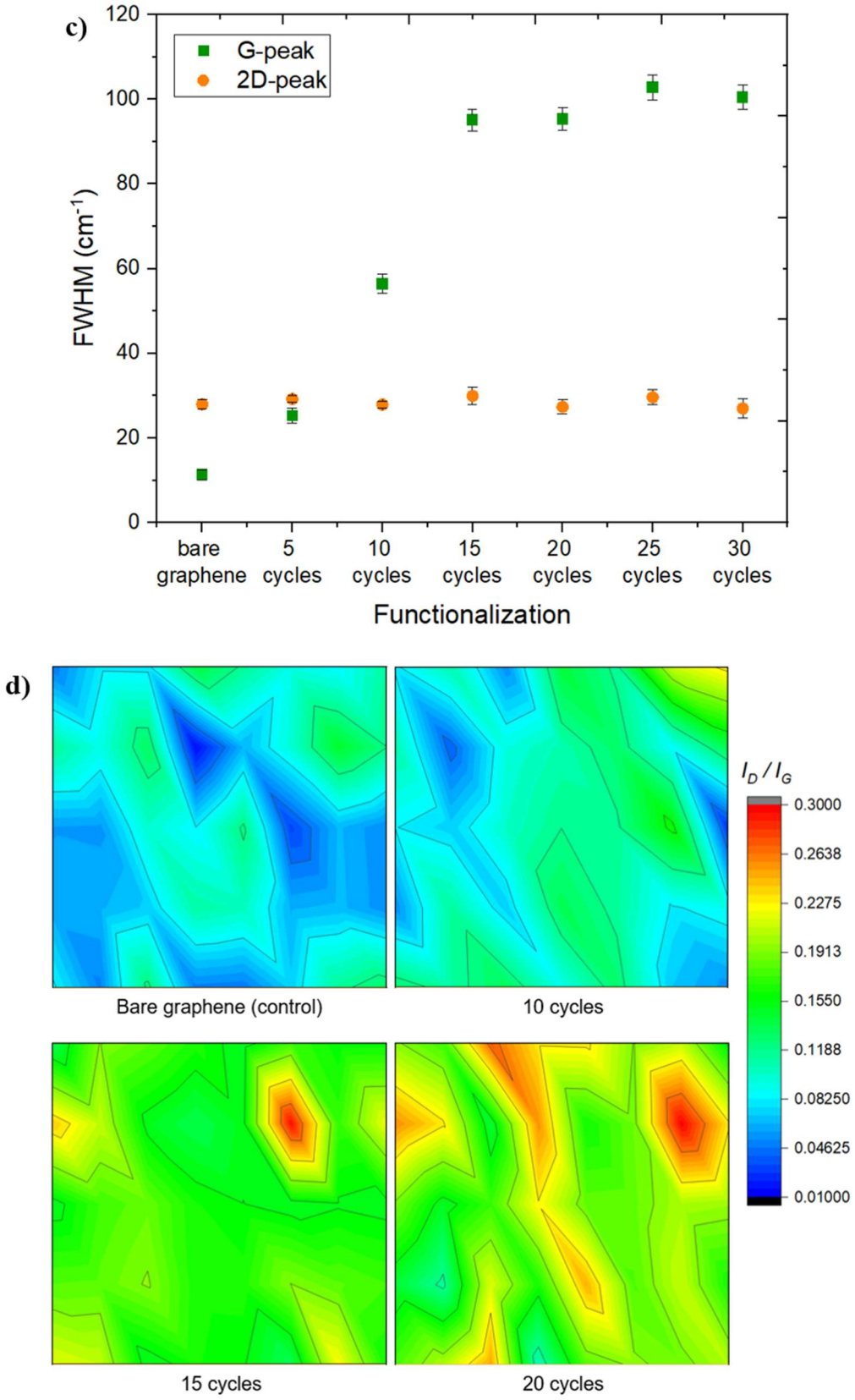


***Figure 8.11**: **(c)** Full width at half maximum (FWHM) of the G- and 2D-peaks of bare graphene and 5, 10, 15, 20, 25, 30 cycles of pDAN. **(d)** 60 µm x 60 µm Raman maps displaying the intensity ratio of the D-peak/G-peak (I_D/I_G).*

8.2.2.4. Surface Chemistry

XPS analysis was conducted on bare graphene and 5- to 30-cycle pDAN samples to validate the data obtained from other characterization techniques. Initially, wide scans were acquired (**Figure 8.12**) to confirm the presence of all elements. Subsequently, high-resolution scans were conducted on the identified key elements.

The atomic concentrations and spectra of carbon (C), oxygen (O), and nitrogen (N) indicate increasing pDAN film thickness. Specifically, the atomic concentrations of carbon and nitrogen rise with the number of cycles due to the formation of pDAN on the surface (**Table 32**). There were five peaks identified in the C 1s spectra (**Figure 8.13a**): sp^2 carbon (~284.5 eV), sp^3 carbon (~285 eV), C-N/C-O (~287 eV), C=O (~288 eV) and O-C=O (~289 eV). Peaks were fitted with Gaussian/Lorentzian peak shapes and atomic concentrations calculated using relative sensitivity factors.

As the number of cycles increase, the C 1s peak broadens as peaks related to C-N and sp^3 carbon become more prominent. The N 1s spectra (**Figure 8.14c**) displays a very small peak in the bare graphene sample (most likely due to surface contaminants). The N peak becomes more prominent as the number of cycles are increased, and nitrogen is introduced to the graphene surface due to pDAN molecules. In contrast, the atomic concentration of oxygen decreases with additional cycles, primarily because the majority of the oxygen originates from the underlying SiO_2 layer, which becomes increasingly shielded by the growing pDAN layer. This trend is further corroborated by the O 1s spectra (**Figure 8.13b**), where the oxygen peak is prominent in the bare graphene sample but decreases in intensity as the number of cycles increases. At 15 cycles, the atomic concentrations start to fluctuate with minimal changes. This fluctuation can be attributed to the limitations of XPS instrumentation, which can only analyse to a depth of 10 nm, while the polymer thickness exceeds this depth.

***Table 32**: Atomic concentrations of carbon, oxygen, and nitrogen in bare graphene and pDAN samples.*

Sample	Atomic Concentration (%)		
	C	O	N
Bare graphene	40.43 ± 0.58	59.15 ± 0.57	0.42 ± 0.02
5 cycles	54.51 ± 2.40	40.47 ± 2.62	5.02 ± 0.55
10 cycles	72.17 ± 0.34	20.16 ± 0.68	7.68 ± 0.49
15 cycles	74.54 ± 3.22	18.07 ± 3.35	7.39 ± 0.13
20 cycles	76.95 ± 0.27	15.66 ± 0.46	7.53 ± 0.31
25 cycles	77.66 ± 1.01	12.70 ± 1.28	9.63 ± 0.29
30 cycles	77.08 ± 0.72	14.18 ± 1.14	8.73 ± 0.44

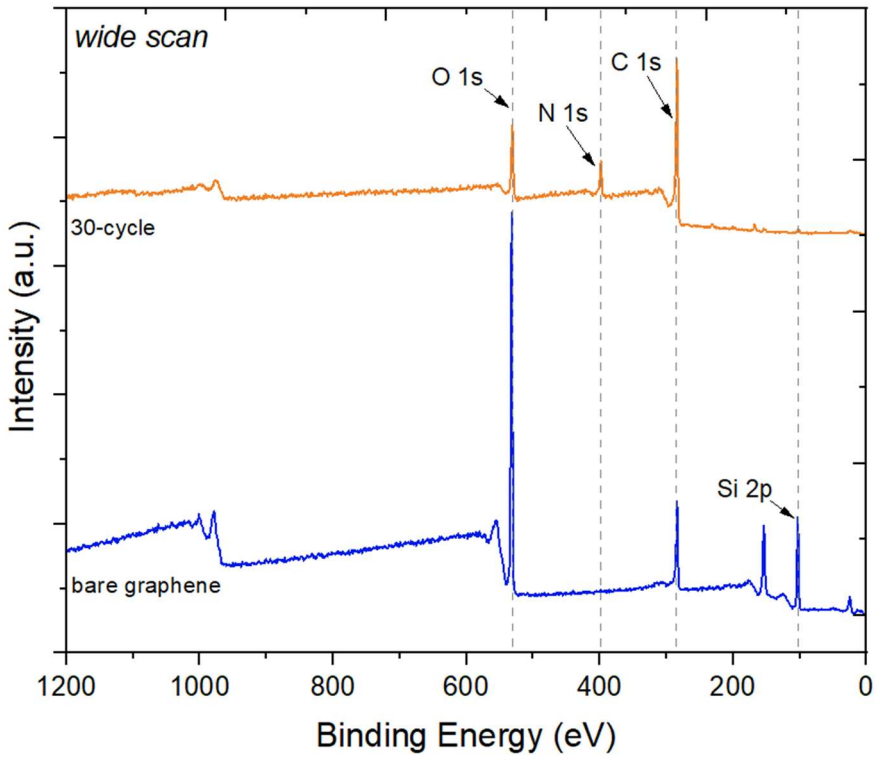


***Figure 8.12**: Wide scan XPS spectra of bare graphene and 30-cycle pDAN samples.*

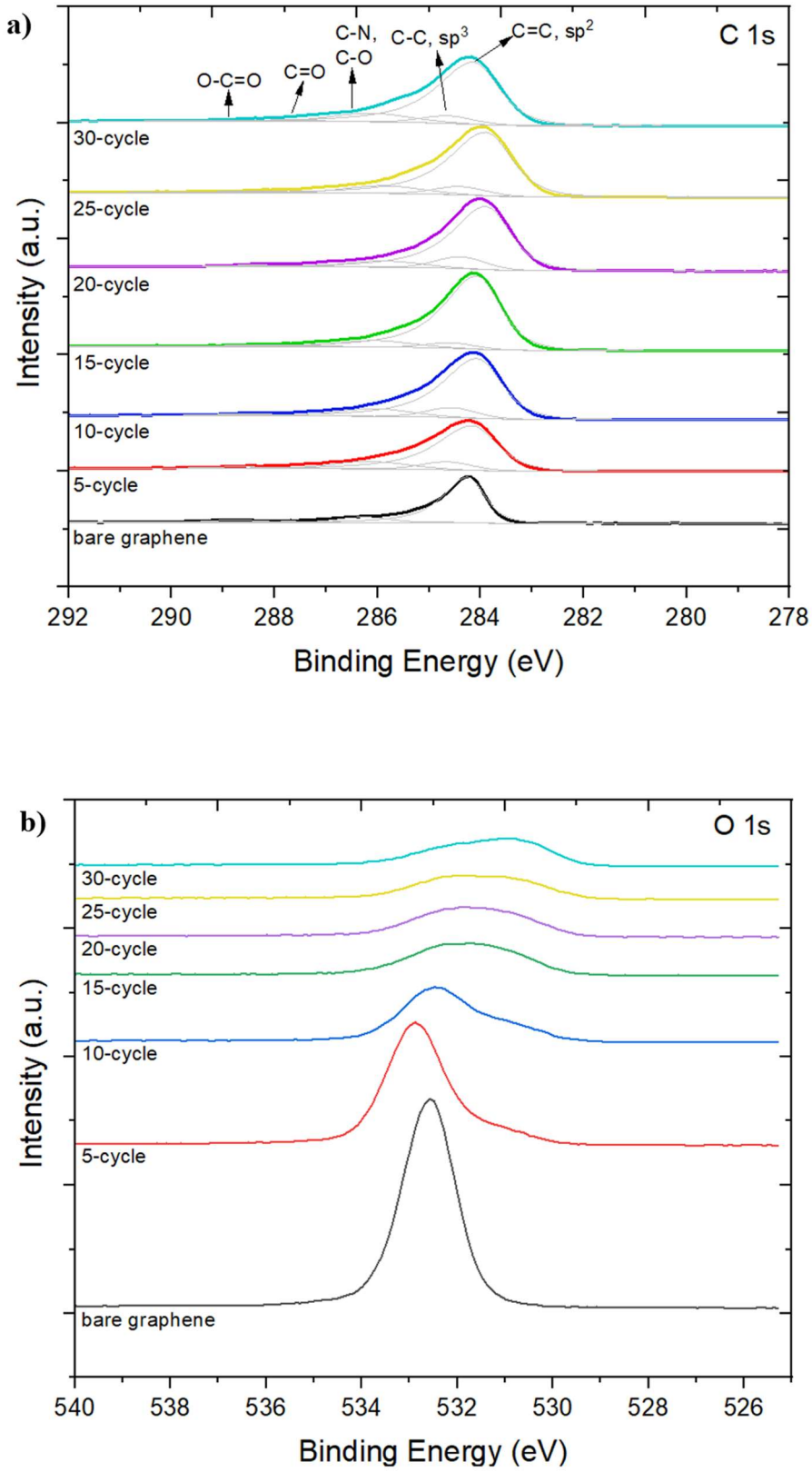


***Figure 8.13**: High resolution XPS spectra of **(a)** C 1s, **(b)** O 1s of bare graphene and 5 to 30-cycle pDAN samples.*

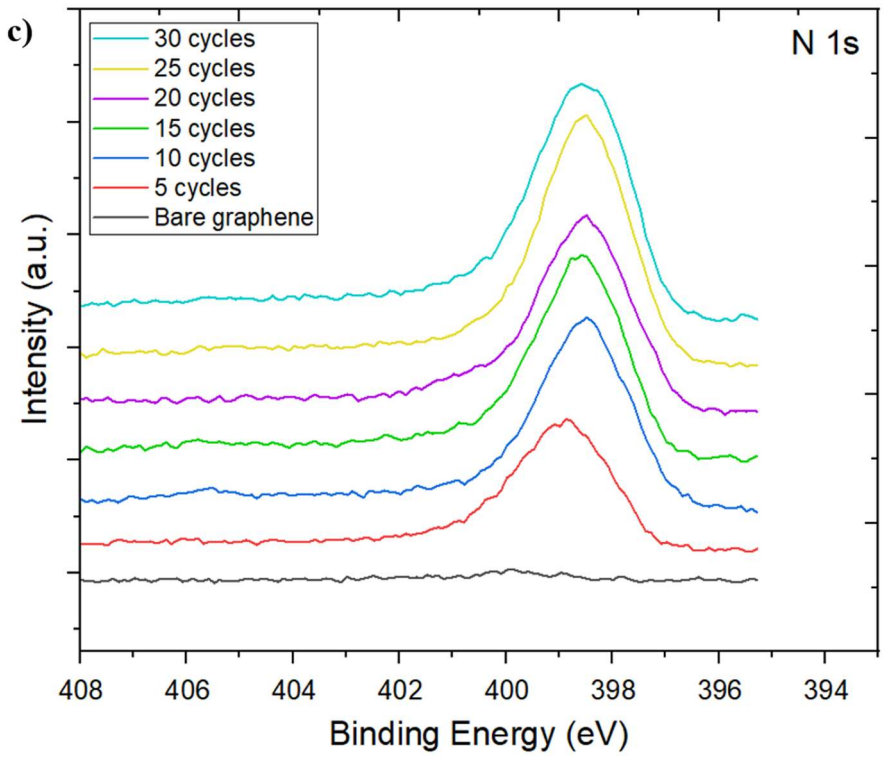


***Figure 8.14**: **(c)** High resolution XPS spectra of **(c)** N 1s of bare graphene and 5 to 30-cycle pDAN samples.*

8.2.2.5. I-V Sweep Pre- and Post-Functionalization

The resistance of the graphene pixels was measured before and after pDAN functionalization to monitor any changes. **Figure 8.15** shows a slight increase in the resistance of graphene pixels following pDAN functionalization. The mean resistance prior to functionalization was approximately 1.9 kΩ, which increased to around 2.2 kΩ after surface modification. The observed increase in resistance indicates that the electrodeposited pDAN film is doping the graphene, a phenomenon also reported in a related study by the research group [155]. Since graphene on SiO_2 is p-type [99], [300], the electron-donating properties of DAN [377] lead to electron donation that combines with the existing holes in the graphene. This reduction in the number of charge carriers results in a small increase in resistance.

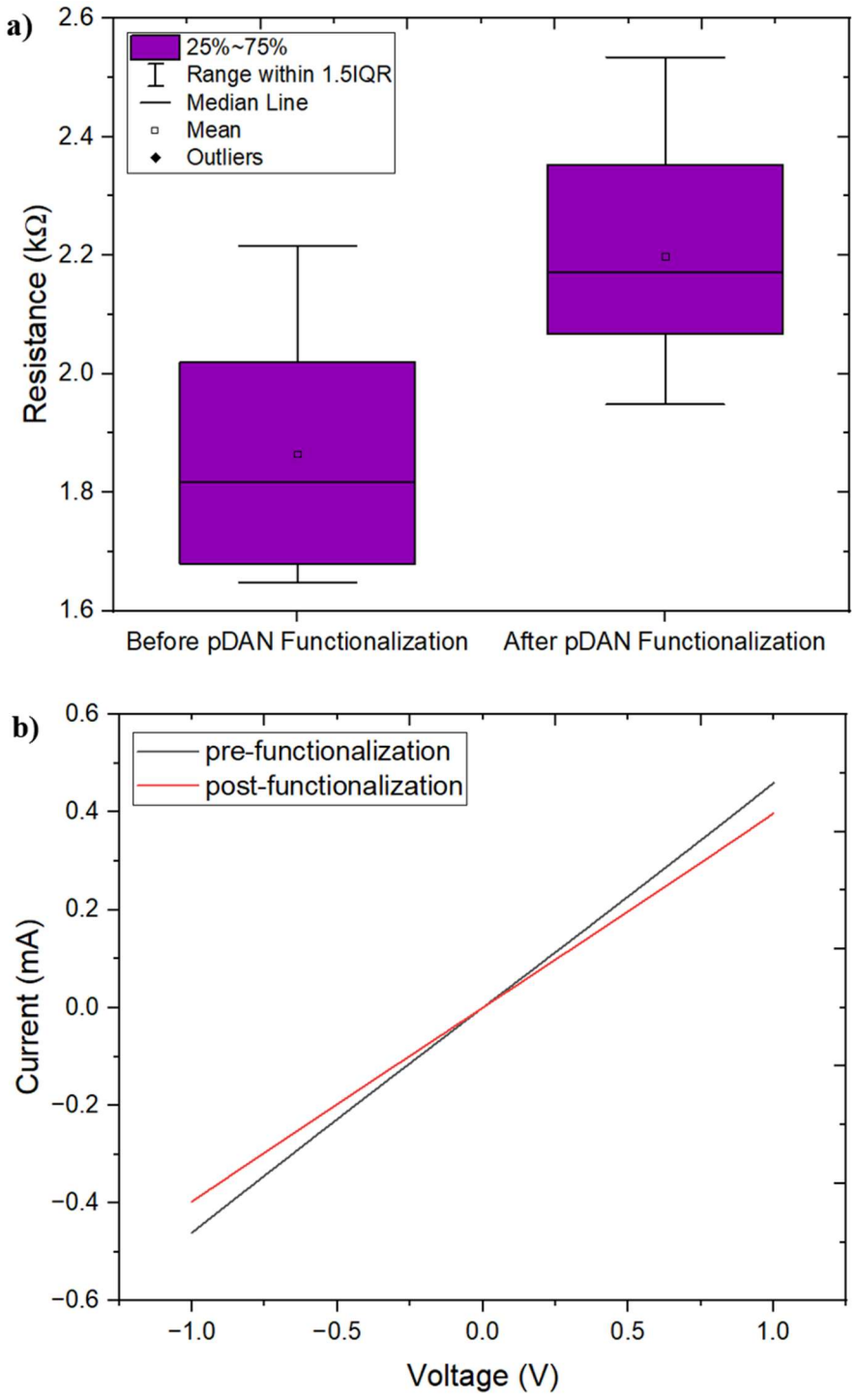


***Figure 8.15**: **(a)** Box plot displaying the resistance of graphene pixels from 3x3 graphene sensor array devices before and after functionalization with pDAN. **(b)** I-V sweep of a graphene pixel before and after pDAN functionalization.*

8.2.3. Gas Sensing Performance

The gas sensing performance of pDAN films deposited on 3x3 graphene pixel array devices was investigated using the Phase 3 gas system. Modified devices were placed in the gas sensing chamber and tested with five different target gases: 5 ppm nitrogen dioxide (NO_2), 10 ppm nitric oxide (NO), 50 ppm ammonia (NH_3), 5000 ppm methane (CH_4) and 580 ppm carbon dioxide (CO_2). Each experiment commenced with a 10-minute exposure to nitrogen gas to establish a baseline, followed by a 10-minute exposure to the target gas, and concluded with a 5-minute exposure to nitrogen gas. The flow rate for all gas exposures was maintained at 1000 mL/min and experiments were performed at room temperature and atmospheric pressure.

The real-time gas sensing response for each target gas is displayed below. The responses for each pixel in a row were averaged and expressed as $\Delta R/R_0$, normalized resistance. Subsequent to nitrogen exposure, both NO_2 and NO exposure resulted in a sharp decrease in the resistance of the sensor arrays. **Figure 8.16a** and **b** highlight differences in response to the same gas with varying numbers of cycles, suggesting that the pDAN film affects the sensing performance. Ammonia exposure (**Figure 8.16c**) increased the resistance of the devices and showed a distinct response between bare graphene and pDAN-modified graphene. Upon exposure to CH_4 and CO_2 (**Figure 8.16d** and **e**), neither the bare graphene nor the pDAN-modified graphene exhibited any response to these gases.

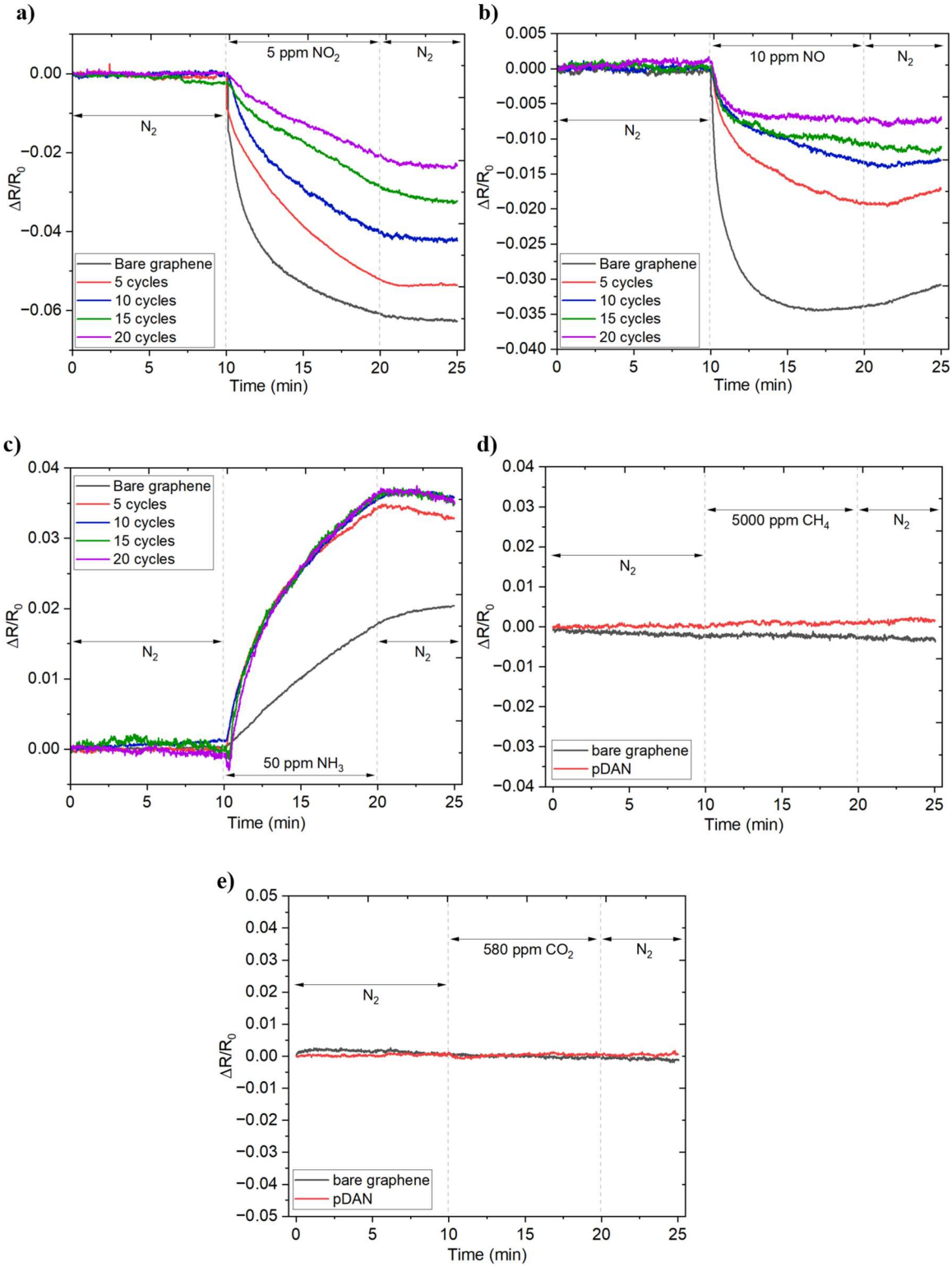


***Figure 8.16**: Real-time resistance measurements, expressed as $\Delta R/R_0$, of a 3x3 graphene pixel array sensor functionalized with pDAN exposed to **(a)** 5 ppm NO_2, **(b)** 10 ppm NO, **(c)** 50 ppm NH_3, **(d)** 5000 ppm CH_4, and **(e)** 580 ppm CO_2.*

The sensor responses (%), depicted in **Figure 8.17**, were calculated for each target gas and number of cycles. For both NO_2 and NO, the sensor response decreases as the number of pDAN cycles increases, suggesting that the pDAN film acts as a barrier, preventing some gas molecules from reaching the graphene surface. Conversely, the pDAN film enhances the sensor response to ammonia, rising from 1.8% to 3.5% after just 5 cycles, with additional cycles showing minimal impact on further response. This enhancement is likely due to hydrogen bonding between the amine groups ($-NH_2$) on the polymer and ammonia molecules. Since the surface has a finite number of available $-NH_2$ groups, increasing the number of cycles beyond this point does not significantly boost the sensor response. Moreover, it is important to consider that a thicker film may have reduced charge transport compared to a thinner film. This was demonstrated by Valaski et al., [378] who showed that polypyrrole films experienced reduced charge transport properties due to space charge limitations.

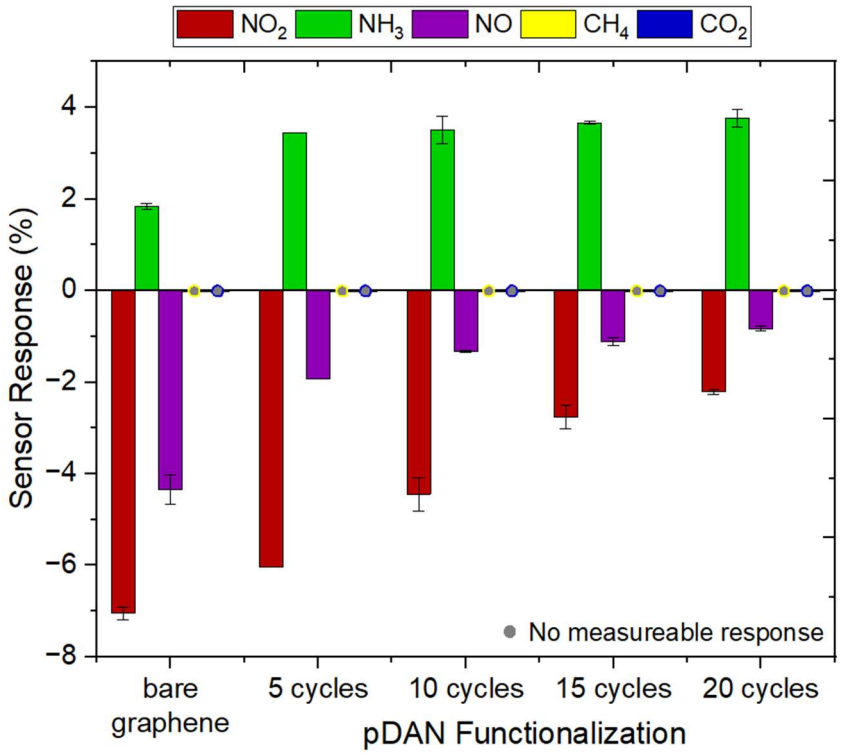


***Figure 8.17**: Comparison of sensor response (%) of a 3x3 graphene array sensor exposed to NO_2, NH_3, NO, CH_4 and CO_2.*

The variations in sensor response due to different levels of pDAN functionalization are crucial for establishing a proof-of-concept sensor array. Notably, effective gas

discrimination does not require a high response to all gases; instead, response variability plays a key role in distinguishing between different gases. Applying varying degrees of functionalization to the same sensor can enhance selectivity, sensitivity, and robustness, resulting in more reliable sensor performance.

Principal Component Analysis (PCA) was employed to evaluate the performance of the 3x3 graphene gas sensor array (for details on PCA refer to **Chapter 3.6.9**). **Figure 8.18** presents the PCA bi-plot with a cumulative variance of 100%, indicating that all variance in the data is captured by the principal components. In the plot, eigenvectors are shown as blue lines with arrowheads. For example, the eigenvectors corresponding to bare graphene, 15-cycle, and 20-cycle functionalization methods are positioned in the bottom right quadrant, reflecting their sensitivity to NH_3 gas. Conversely, the eigenvectors for 5-cycle and 10-cycle methods are located in the upper right quadrant, while the data points for NO and NO_2 are situated in the upper left and bottom left quadrants, respectively.

The distinct placement of NO and NO_2, separate from the eigenvectors, implies that these gases are not significantly influenced by the functionalization methods represented by the eigenvectors. However, the separation of gases into different quadrants demonstrates that the sensor array produces unique response patterns for each gas. This distinct quadrant distribution indicates that the array effectively distinguishes between the gases.

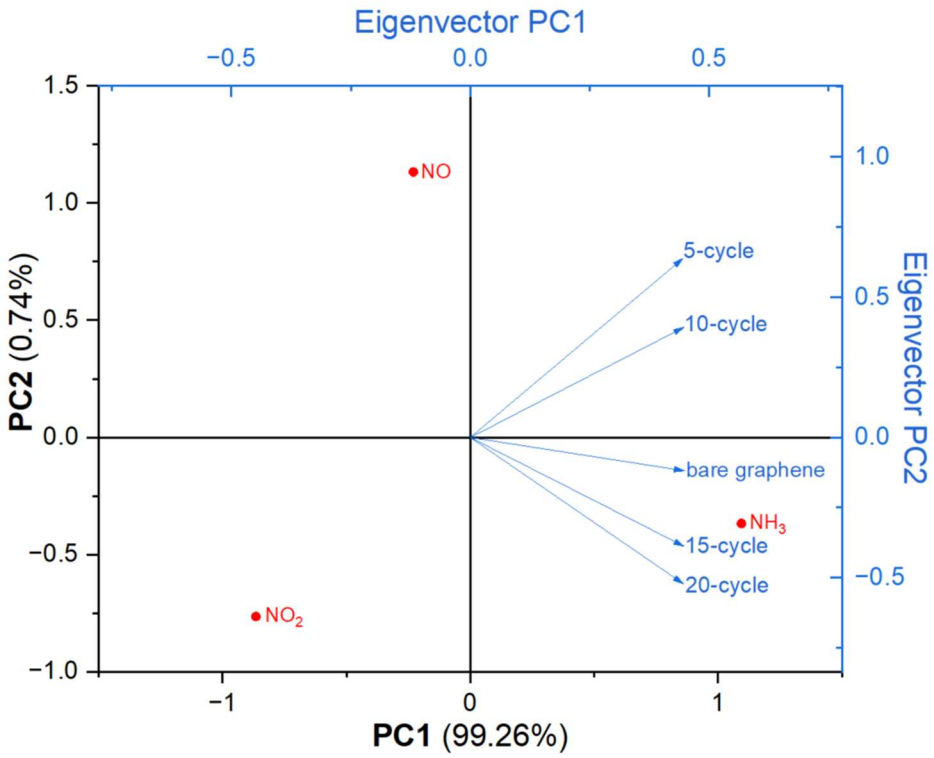


***Figure 8.18**: PCA bi-plot demonstrating the eigenvectors of the sensor array response to NO, NO_2 and NH_3 gases. Origin 'Multivariate Analysis' Principle Component Analysis tool was used to generate PCA results.*

This proof-of-concept utilized different thicknesses of the same pDAN molecule, demonstrating that the sensor response can be quantitatively correlated to the thickness of the pDAN layer. PCA results support this by showing that the sensor array generates distinct response patterns for different gases, suggesting effective differentiation between them. This approach highlights the potential to integrate variable responses from PCA with pattern-recognition software, which uses the transformed data to classify or identify different gases based on their distinct response patterns, thereby accurately identifying unknown gases. Future developments could involve using diverse functionalization species to enable simultaneous detection of multiple analytes.

8.3. Electrochemical Oxidation

The oxidation of graphene is a versatile and effective technique for tailoring its surface properties to meet the demands of various applications. Graphene oxide (GO) and

reduced graphene oxide (rGO) are readily prepared and highly tuneable materials. They introduce functional groups, such as hydroxyl (-OH), epoxy (C-O-C), carboxyl (COOH), and carbonyl (C=O), which enhance interactions with gas molecules and modify the surface's hydrophilicity [20], [379]. Given these advantages, graphene oxidation was investigated to assess its impact on gas sensing performance. This section focuses on the electrochemical oxidation of graphene-based sensors, aiming to develop a controllable process for functionalizing graphene channels/pixels to varying degrees, thereby enabling distinct responses to different gas molecules.

Electrochemical oxidation of graphene-based sensors was performed with a cyclic voltammetry procedure employing different concentrations of sulfuric acid. This section details the procedure and presents the findings obtained. The procedure was carried out using a *PGSTAT30 Autolab* and *Nova 2.1.2* software, as detailed in **Chapter 3.3.1.3**.

8.3.1. Cyclic Voltammetry Methodology

CVD graphene on '3x3 pixel array' and 'Hall Bar' sensors were electrochemically oxidized using sulphuric acid (H_2SO_4) utilizing a cyclic voltammetry (CV) method found in published literature [380]. A 3-electrode cell setup was employed, consisting of a platinum wire as the counter electrode (CE), a silver/silver chloride (Ag/AgCl) reference electrode (RE) saturated in 3 M sodium chloride, and either a 3x3 graphene pixel array sensor or a Hall Bar as the working electrode (WE). **Figure 8.19** provides a schematic of this configuration. When the graphene sensor functioned as the working electrode, a connector was used to establish an electrical connection. Various concentrations of H_2SO_4, ranging from 0.01 M to 1 M, were tested in this investigation. The cyclic voltammetry procedure was conducted with a scan rate of 50 mV/s, within a potential range of -0.2 to 1.2 V, and with a specified number of scan cycles. The impact of the number of scan cycles was investigated by conducting trials at 10, 20 and 30 cycles. The following sub-section provide a detailed description of the procedure used for the Hall Bars. The procedure for the 3x3 graphene pixel arrays is discussed later in **Section 8.3.4.2**.

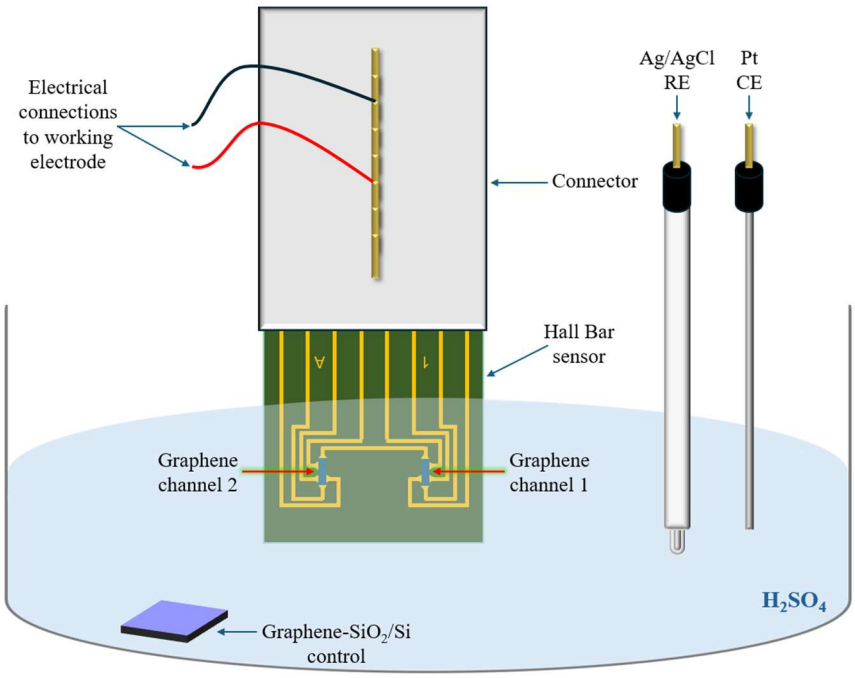


***Figure 8.19**: Schematic depicting the electrochemical oxidation setup, featuring a Hall Bar sensor and a graphene-Si/SiO_2 wafer as the control*

8.3.1.1. Hall Bar Sensors

Hall Bar sensors were initially investigated to evaluate the feasibility of applying this procedure to 3x3 graphene pixel array sensors. Varying the number of scan cycles on individual channels made it possible to evaluate whether graphene channels on the same device could be oxidized to different degrees. The results from this investigation would inform the procedure for the 3x3 graphene pixel array sensors, with the aim of selectively oxidizing graphene pixels to varying extents.

Four different Hall Bar sensors were used to trial varying concentrations of H_2SO_4: 0.1 M, 0.25 M, 0.5 M, and 0.75 M. Both graphene channels on a Hall Bar device, situated adjacent to each other, were submerged simultaneously in the electrolyte solution. Channel 1 and Channel 2 were sequentially exposed to CV cycles as only one electrochemical process could be performed at a time. Channel 1 was subjected to 10 cycles, followed by channel 2, which underwent 20 cycles. Additionally, graphene-SiO_2/Si wafer pieces were submerged in the electrolyte solution for the same duration as the Hall Bar sensors to serve as a control representing '0 cycles' (i.e. exposure to H_2SO_4 only, but no electrochemical oxidation) (**Figure 8.19**). After each

electrochemical functionalization process, the samples were removed from the electrolyte solution, rinsed with deionized water, and dried using compressed air.

Initially, a 1M H_2SO_4 concentration was used as the starting point, following the method reported by [380]. However, this resulted in catastrophic damage to both types of graphene sensors (see images in **Section 8.4**). Consequently, the concentration was reduced. The details of the device damage are discussed later in this chapter (see **Section 8.4**).

8.3.2. Cyclic Voltammetry Profile

Each electrochemical oxidation produced a cyclic voltammogram displaying a similar trend, as described below. Additional cyclic voltammograms are provided in the **Appendix** (**Figure A12** to **Figure A15**).

Figure 8.20 shows that as the number of cycles increases, the peak currents also increase. Two reduction peaks are observed at 0.40 V and 0.70 V, both of which increase with increasing cycles. The reduction peak at 0.40 V is consistent with the findings of Liu et al. [380], whereas the oxidation peak reported at 0.8 V is notably absent. Instead, a flatter region of increasing current is observed from 0.54 V to 0.96 V. The reasons for these discrepancies are discussed in **Section 8.4**. Surface characterization was conducted to verify the outcome of the electrochemical oxidation. The results are reported in the following section.

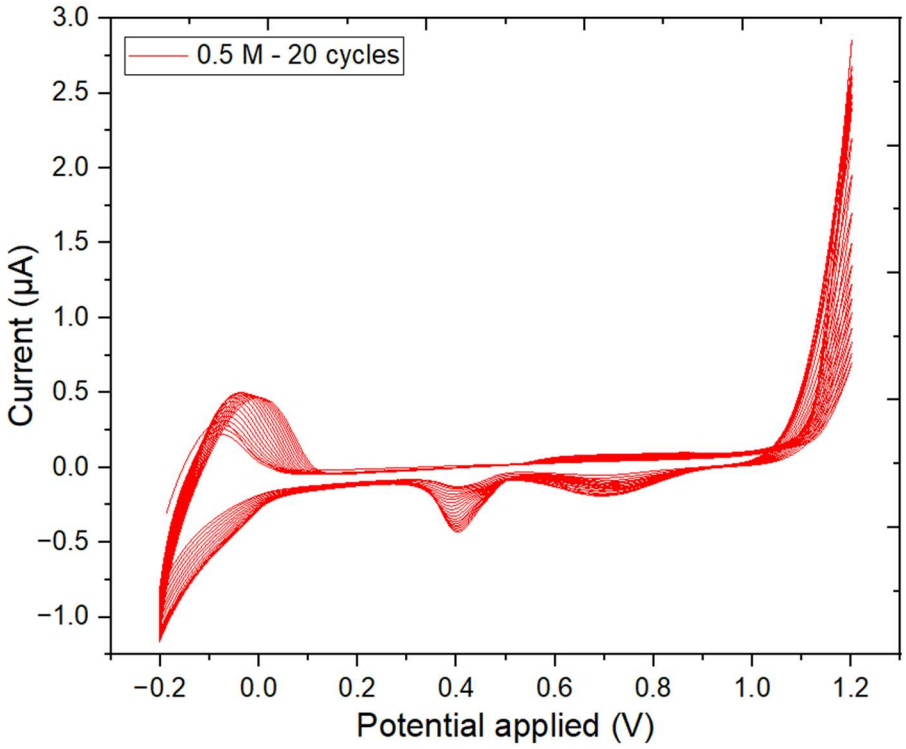


***Figure 8.20**: Cyclic voltammogram of the electrochemical oxidation of a graphene Hall Bar sensor in 0.5 M H_2SO_4 for 20 cycles.*

8.3.3. Surface Chemistry

XPS analysis was performed on bare graphene-SiO_2/Si wafer pieces, graphene-SiO_2/Si wafer control samples exposed to various H_2SO_4 concentrations, and Hall Bar sensors to validate the data obtained from the cyclic voltammetry profiles. Initially, wide scans were acquired to confirm the presence of all elements. Subsequently, high-resolution scans were conducted on the identified elements.

The spectra from the C 1s carbon (**Figure 8.21a**) and O 1s oxygen (**Figure 8.22**), along with the atomic concentrations of oxygen-containing peaks in the C 1s region (**Table 33**), indicate that the graphene channels on the Hall Bar sensors were oxidized. Specifically, the increase of atomic concentration of the oxygen-containing functional groups in C 1s (C-OH, C-O-C, C=O, and O-C=O) (see **Table 33**) confirm this oxidation. The C 1s spectra revealed five distinct peaks: sp^2 carbon (~284.5 eV), sp^3 carbon (~285 eV), C-OH/O-C-O (~286 eV), C=O (~288 eV), and O-C=O (~289 eV). These peaks were fitted using Gaussian/Lorentzian peak shapes, and the atomic concentrations were calculated based on relative sensitivity factors.

As the number of cycles increases, the C 1s peak (**Figure 8.21**-**Figure 8.22**) broadens, indicating an increasing presence of oxygen-containing groups and sp^3 carbon. Similarly, the O 1s spectra (**Figure 8.23**) exhibit a broader oxygen peak around ~532 eV in samples with 10 or 20 cycles, in contrast to bare graphene and control samples, which show a prominent but sharper oxygen peak primarily due to the underlying SiO_2 layer. Although slight variations in peak shapes are observed across different H_2SO_4 concentrations, no clear trend is evident.

The atomic concentration of oxygen in the C 1s region for bare graphene was measured at 5.92 ± 0.15% (**Table 33**). This value, aside from the 0.1 M/0 cycle control sample, is lower than the oxygen levels found in other control samples exposed to 0.25 M, 0.5 M, and 0.75 M H_2SO_4. The increase in oxygen content suggests that the graphene undergoes some limited oxidation in the electrolyte solution, even without an applied potential, a process that has been observed in several studies [381]–[383].

Comparing the control samples for each acid concentration with the Hall Bar sensors after 10 and 20 cycles shows a notable increase in oxygen content. For example, the 0.25 M/0 cycle control sample had an atomic oxygen concentration of 8.00 ± 0.10%, which rose to 12.88 ± 0.29% and 13.97 ± 0.25% after 10 and 20 cycles, respectively. The data indicates that varying H_2SO_4 concentrations do not significantly influence the oxidation level, as the oxygen content fluctuates across samples. Notably, the 0.75 M/10 cycle and 20 cycle samples exhibited lower oxygen content compared to other concentrations tested.

However, when comparing the oxidation levels between the 10-cycle and 20-cycle samples for each acid concentration, a more substantial increase in oxygen-containing groups is observed at higher acid concentrations. The increase in oxygen content between the 10-cycle and 20-cycle samples was approximately:

- 0.1 M: ~0.88%
- 0.25 M: ~1.09%
- 0.5 M: ~2.43%
- 0.75 M: ~2.55%

Overall, the data suggests that electrochemical oxidation was effective, with the level of oxidation increasing as the number of cycles increases.

***Table 33**: Atomic concentrations of the carbon-only and oxygen-containing peaks in C 1s carbon peak.*

H_2SO_4 Concentration (M)	Number of Cycles	Atomic Concentrations (%) C 1s	
		C=C, sp2 C-C, sp3	C-OH, C-O-C C=O O-C=O
N/A – bare graphene	0	91.99 ± 0.20	5.92 ± 0.15
0.1	0	94.47 ± 0.56	5.54 ± 0.16
	10	86.33 ± 0.57	13.66 ± 0.43
	20	85.45 ± 0.28	14.54 ± 0.28
0.25	0	92.01 ± 0.77	8.00 ± 0.10
	10	87.12 ± 1.48	12.88 ± 0.29
	20	86.04 ± 0.91	13.97 ± 0.25
0.5	0	93.50 ± 0.71	6.51 ± 0.17
	10	84.61 ± 0.74	15.39 ± 0.62
	20	82.18 ± 0.30	17.82 ± 0.25
0.75	0	91.94 ± 0.69	8.06 ± 0.18
	10	89.53 ± 0.19	10.47 ± 0.27
	20	86.98 ± 0.16	13.02 ± 0.19

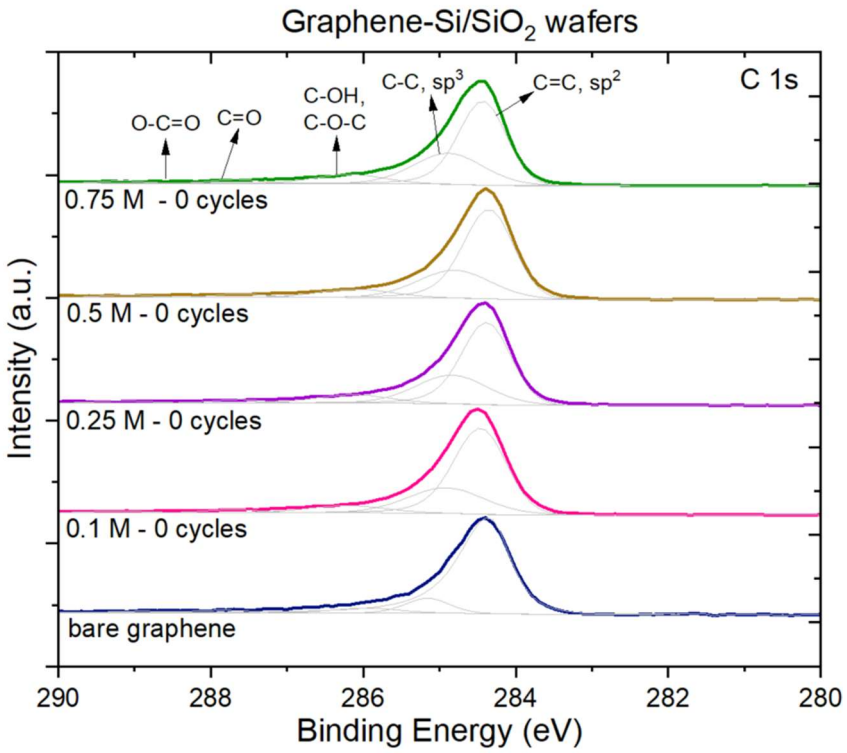


***Figure 8.21**:High resolution C 1s XPS spectra of bare graphene-SiO_2/Si and graphene-SiO_2/Si wafers exposed to 0.1 M, 0.25 M, 0.5 M and 0.75 M H_2SO_4 (labelled '0 cycles').*

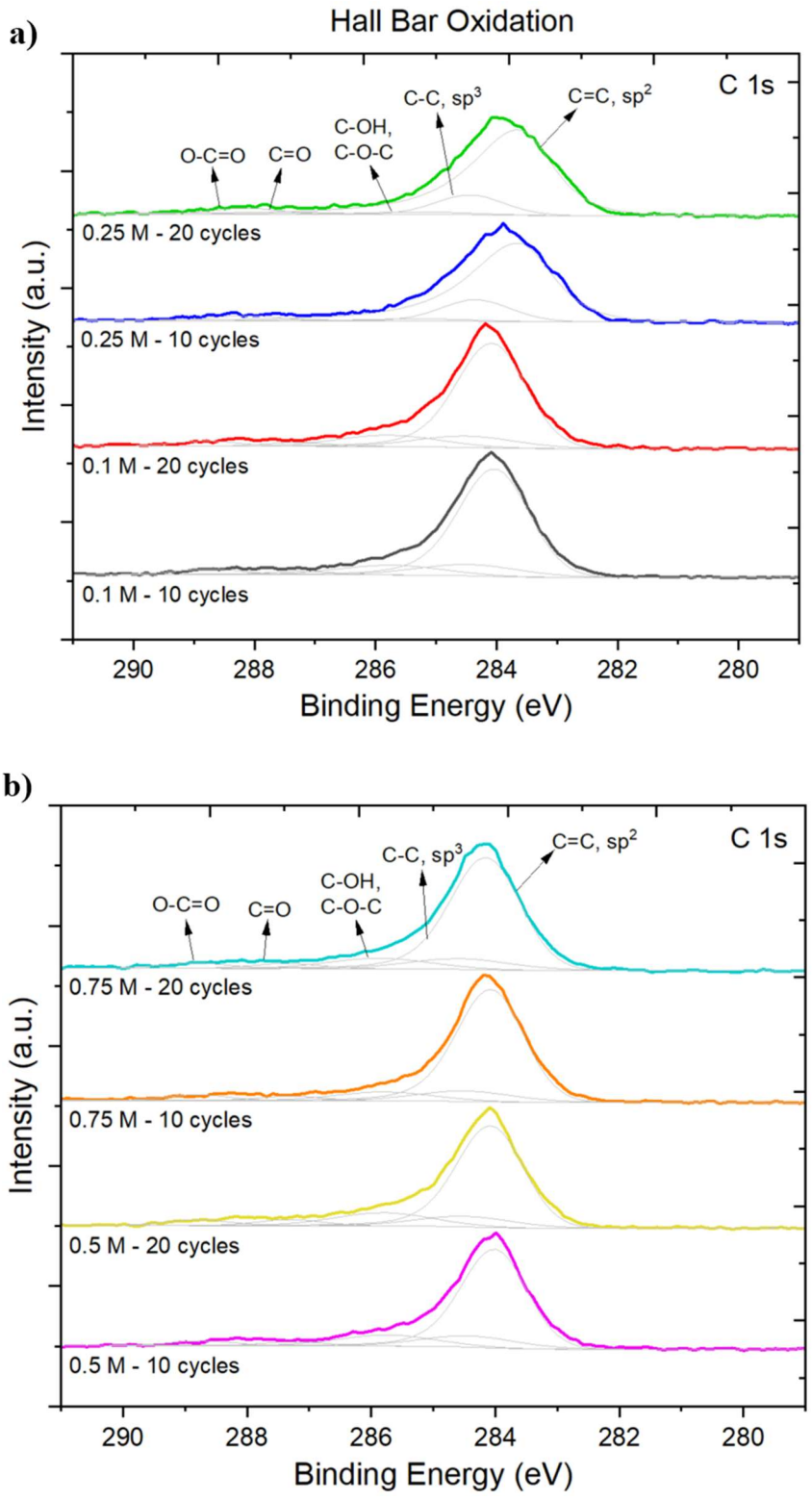


***Figure 8.22**: High resolution C 1s XPS spectra of **(a)** Graphene 'Hall Bar' sensors exposed to 0.1 M and 0.25 M H_2SO_4, with each channel on individual sensors exposed for 10- and 20 cycles. **(b)** Graphene 'Hall Bar' sensors exposed to 0.5 M and 0.75 M H_2SO_4, with each channel on individual sensors exposed for 10- and 20 cycles.*

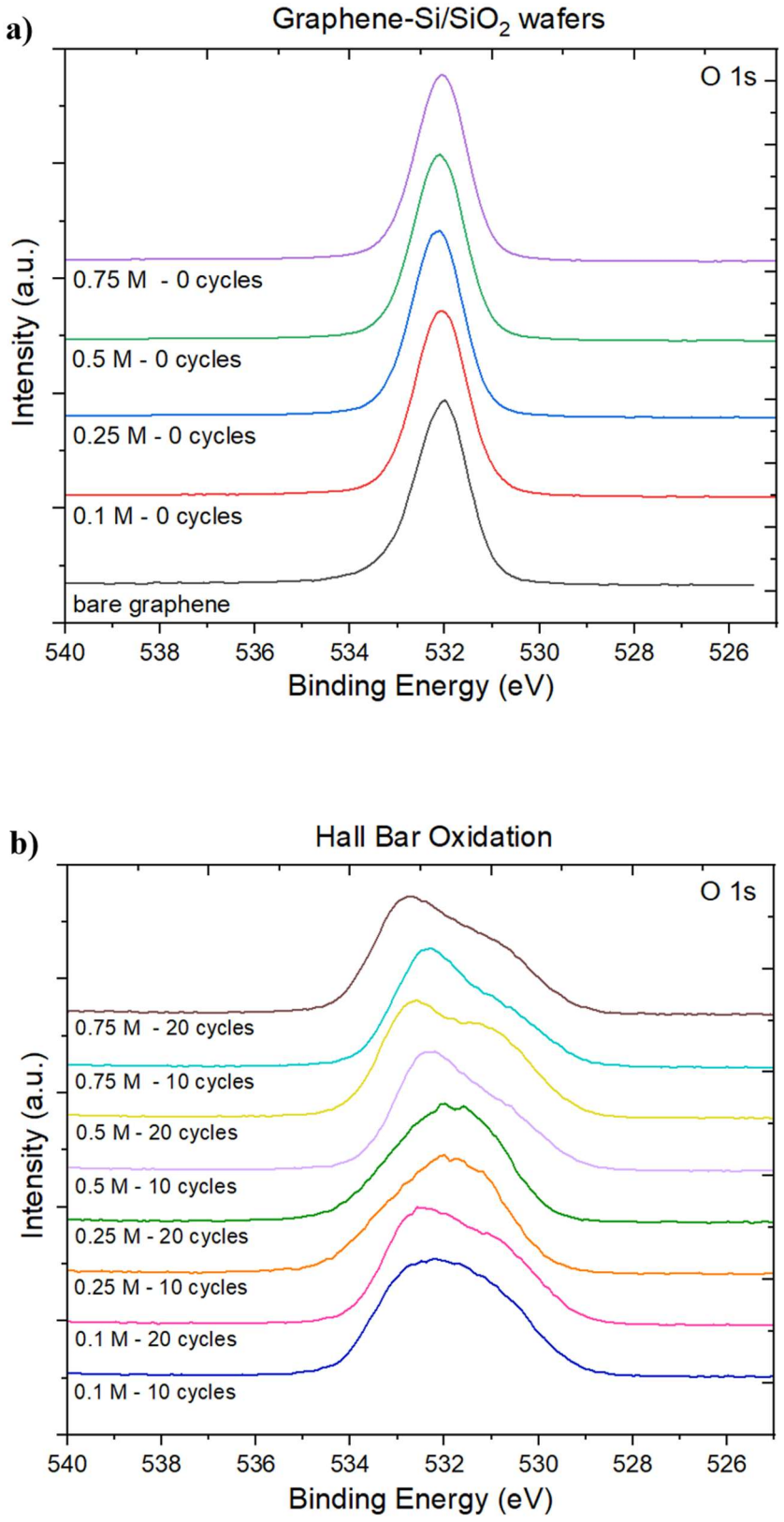


***Figure 8.23**: High resolution O 1s XPS spectra of **(a)** bare graphene-SiO_2/Si and graphene-SiO_2/Si wafers exposed to 0.1 M, 0.25 M, 0.5 M and 0.75 M H_2SO_4 (labelled '0 cycles'). **(b)** Graphene 'Hall Bar' sensors exposed to 0.1 M, 0.25 M, 0.5 M and 0.75 M H_2SO_4, with each channel on individual sensors exposed for 10- and 20 cycles.*

8.3.4. Gas Sensing Performance

The gas sensing performance of the electrochemically oxidized Hall Bar and 3x3 graphene pixel array sensors were evaluated through a controlled sequence of exposures. Each experiment began with a 10-minute nitrogen gas exposure to establish a baseline, followed by a 10-minute exposure to the target gas, and concluded with a 5-minute return to nitrogen gas. The gas flow rate was consistently maintained at 1000 mL/min, and all experiments were conducted at room temperature and atmospheric pressure.

8.3.4.1. Hall Bar Sensors

The oxidized Hall Bar devices were placed in the gas sensing chamber and exposed to 50 ppm ammonia (NH_3) and 5 ppm nitrogen dioxide (NO_2). Ammonia was selected for testing because graphene oxide is known to exhibit a detectable response to this gas [384]–[386]. Nitrogen dioxide was used for comparison, as it typically elicits a strong response from graphene-based sensors. Moreover, NO_2 was chosen due to its electron-withdrawing nature [301], which produces a response opposite to that of NH_3, providing a contrasting behaviour for analysis. Before exposing the sensors to the next target gas, they were recovered outside the sensing chamber by heating on a hot plate at 175°C for 5 minutes. Since the recovery process occurred outside the sensing chamber, real-time measurements of resistance changes during recovery were not possible.

The real-time gas sensing response for each target gas is shown below (**Figure 8.24**), expressed as $\Delta R/R_0$, representing the normalized resistance. When exposed to NH_3, the sensors exhibit an increase in resistance ($\Delta R/R_0$ shifts in a positive direction) due to ammonia's electron-donating nature and the inherently p-type graphene [166], [169]. Minor fluctuations in $\Delta R/R_0$ can be observed among devices that were functionalized using different acid concentrations, with the most notable difference seen in the response of bare graphene, which shows a significantly reduced sensitivity compared to its oxidized counterparts (**Figure 8.24a**).

In contrast, upon exposure to NO_2, the sensors' resistance decreases ($\Delta R/R_0$ shifts in a negative direction) as NO_2 readily withdraws electrons from the graphene (**Figure 8.24b**). Here, the bare graphene sensor demonstrates a significantly larger response

compared to the oxidized sensors, highlighting the impact of oxidation on the gas sensing performance.

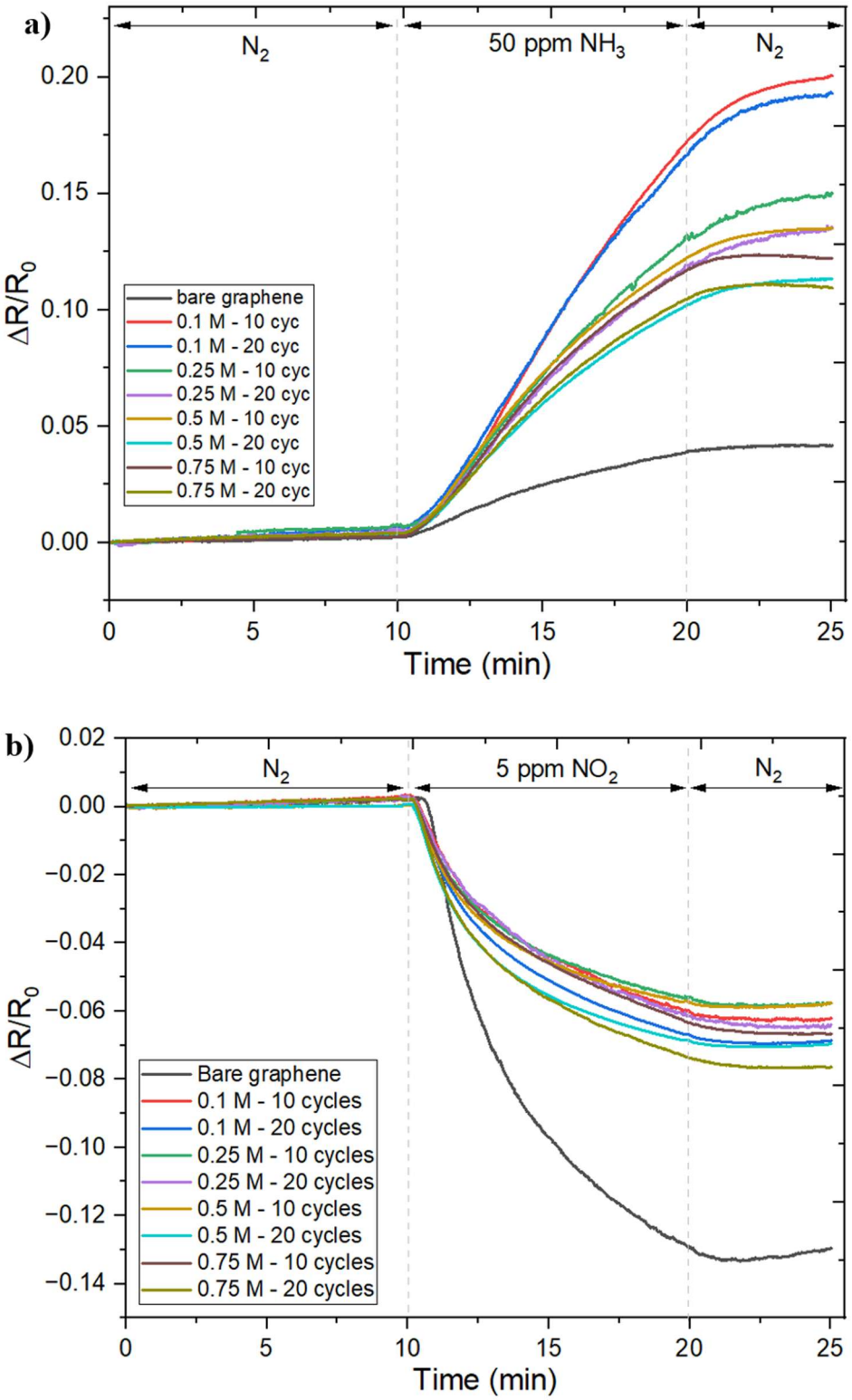


***Figure 8.24**: Real-time resistance measurements, expressed as $\Delta R/R_0$, of electrochemically oxidized Hall Bar sensors sensors—oxidized in four different concentrations of H_2SO_4 (0.1 M, 0.25 M, 0.5 M, and 0.75 M) with either 10 or 20 cycles—when exposed to **(a)** 50 ppm NH_3 and **(b)** 5 ppm NO_2.*

Figure 8.25 presents the sensor response to 50 ppm NH_3 of the Hall Bar sensors oxidized at different acid concentrations and cycle scans, compared to a bare graphene sensor. In **Figure 8.25a**, a significant increase in sensor response is observed for the oxidized Hall Bar sensors, with responses ranging from 10.3% to 18.0%, in contrast to the bare graphene sensor, which shows a response of only 3.8%. The difference in sensor response between graphene channels subjected to 10 cycles versus 20 cycles is minimal; for instance, the 0.25 M-10 cycle sensor shows a response of 11.8%, which increases slightly to 12.9% with 20 cycles. The sensor response remains relatively consistent across the 0.25 M, 0.5 M, and 0.75 M samples, while the 0.1 M sample displays a notably larger response, suggesting a potential anomaly. However, it is important to note that a balance must be achieved between a useful degree of oxidation and excessive oxidation. Too much oxidation can significantly decrease the electrical conductivity of graphene, reducing its effectiveness in detecting resistance changes upon gas exposure [130], [386]–[388].

Figure 8.25b presents the sensing response to 5 ppm NO_2, showing a contrasting trend where the bare graphene sensor exhibits a significantly larger response (-14.1%) compared to the oxidized Hall Bar sensors, which display responses ranging from -5.9% to -7.7%. Additionally, there is a slight, random variation in sensor response between graphene channels subjected to 10 cycles versus 20 cycles. The sensor response remains relatively consistent across the different acid concentrations used during oxidation.

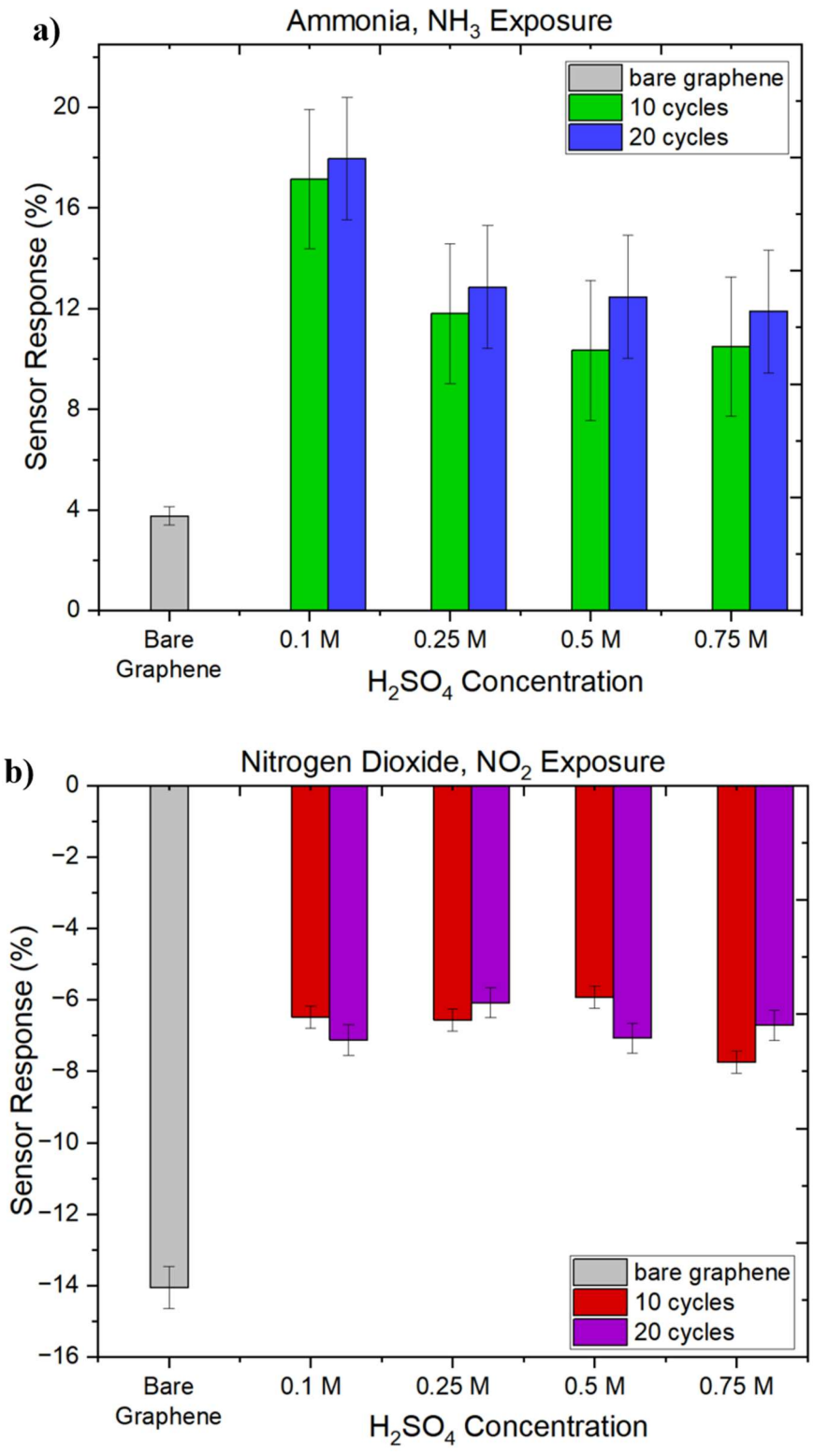


***Figure 8.25**: Bar charts illustrating the sensor response (%) of bare graphene sensors and electrochemically oxidized graphene Hall Bar sensors—oxidized in four different concentrations of H_2SO_4 (0.1 M, 0.25 M, 0.5 M, and 0.75 M) with either 10 or 20 cycles—when exposed to **(a)** 50 ppm NH_3 and **(b)** 5 ppm NO_2.*

The increased sensor response to ammonia gas observed with the oxidized Hall Bar sensors can be attributed to the additional functional groups and defects present on the graphene oxide (GO) surface. Compared to pristine graphene, GO has a higher density of defects, which serve as active sites for gas adsorption [385], [389]. The GO surface typically contains functional groups such as hydroxyl (-OH), epoxy (C-O-C), carboxyl (COOH), and carbonyl (C=O) groups. The NH_3 molecule can coordinate with these groups, with nitrogen in NH_3 forming interactions with hydrogen in hydroxyl groups and also engaging with carbonyl groups [385]. The presence of oxygen-containing functional groups and a higher defect density in GO increases its reactivity, enhancing its sensitivity to NH_3.

Additionally, Toda, K. et al. [379] report a binding energy of 0.1 eV for NH_3 on pristine graphene, compared to binding energies of 0.5 eV, 0.6 eV, and 0.8 eV for interactions with oxygen-containing functional groups on GO. This increase in binding energy indicates a stronger affinity for NH_3 on GO, further explaining the improved sensor response.

The decreased sensor response to NO_2 gas is unexpected, given that NO_2 is known to interact with defects and functional groups on the surface similarly to NH_3 [389]. While the binding energies of NO_2 molecules with pristine graphene are relatively low (0.05-0.4 eV), they are significantly higher when interacting with oxygen-containing groups on GO (0.4-8 eV) [379]. One possible explanation for the reduced sensor response is the incomplete desorption of NH_3 molecules from the previous test. Since GO has higher binding energies than pristine graphene for NH_3, resulting in stronger bonds, the standard recovery methods effective for bare graphene may be insufficient for GO. Further investigation into more effective recovery methods for GO-based sensors is necessary to confirm this hypothesis.

8.3.4.2. 3x3 Graphene Pixel Array Sensors

As a different number of scan cycles demonstrated a different level of oxidation in the Hall Bar sensors, resulting in different sensor responses, this was attempted on the 3x3 graphene pixel array sensor. To hopefully elicit a larger difference in the level of oxidation and thus, sensor response, 10 cycles and 30 cycles were employed in this

case. To minimize the damage caused by the electrolyte solution, an H_2SO_4 concentration of 0.1 M was employed initially.

Two independent 3x3 graphene sensor arrays were functionalized with varying numbers of scan cycles per row (**Figure 8.26**). In Experiment 1 the first sensor array was treated with a 0.1 M H_2SO_4 solution, with Row C subjected to 30 cycles, Row B to 10 cycles, and Row A serving as the control with no applied potential (**Figure 8.26**). All rows were submerged in the electrolyte solution simultaneously. After functionalization, the sensor arrays were rinsed with deionized water and dried using compressed air.

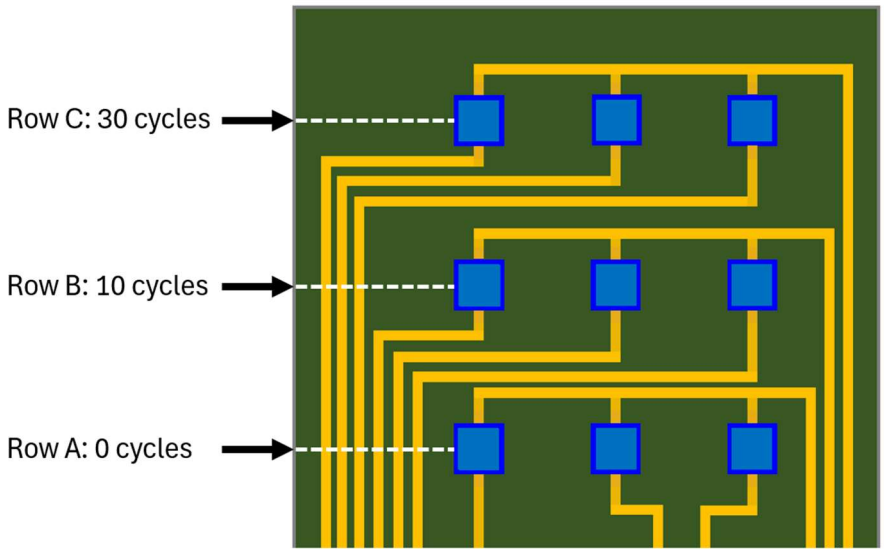


***Figure 8.26**: Schematic illustrating the number of scan cycles applied to each row of the 3x3 graphene pixel array devices during electrochemical oxidation in both experiments.*

Gas sensing tests were conducted on the bare graphene sensor (no H_2SO_4 exposure) prior to the oxidation procedure to establish a baseline for comparison. Since XPS analysis was not performed on these devices, an increase in sensor response to NH_3 gas was used as an indicator of successful oxidation. Ammonia gas was utilized as findings from **Section 8.3.4.1.** revealed an increase of sensor response to this gas following graphene oxidation.

Figure 8.27 compares the sensor response to 50 ppm NH_3 gas between the bare graphene sensor and the response following electrochemical oxidation in 0.1 M H_2SO_4. The average responses of the graphene pixels in each row, subjected to 0

cycles, 10 cycles, and 30 cycles, were 7.1%, 7.5%, and 5.7%, respectively. While these results indicate an increased response compared to the bare graphene sensor (1.7%), suggesting successful oxidation, it was anticipated that the graphene pixels exposed to 30 cycles would exhibit the highest response to NH_3. However, the findings for 30 cycles could also suggest that the graphene may have been over-oxidized, thereby reducing its sensitivity [388].

Notably, the significant increase from 1.7% (bare graphene) to 7.1% for the row that had no potential applied indicates that a substantial amount of oxidation occurred without the need for an applied potential. This suggests that the acid concentration might be too high, especially considering the smaller surface area of the graphene pixels (1.60 mm^2) on the 3x3 pixel array compared to the graphene channels (2.45 mm^2) on the Hall Bar sensors. Consequently, the experiment was repeated using a 10x diluted H_2SO_4 acid concentration of 0.01 M and a new 3x3 graphene pixel array sensor.

The average sensor responses of the graphene pixels in each row after oxidation in 0.01 M H_2SO_4 were 3.9%, 3.6%, and 3.9% for 0, 10, and 30 cycles, respectively (see **Figure 8.27**). The graphene pixels show a reduced sensor response compared to those exposed to 0.1 M H_2SO_4, suggesting that the lower acid concentration of 0.01 M has resulted in a lower degree of oxidation. There is minimal variation in sensor responses between rows subjected to different numbers of scan cycles, particularly when compared to the row with no applied potential. This suggests that the cyclic voltammetry procedure has a negligible effect on the degree of oxidation experienced by the graphene pixels. Therefore, the observed oxidation seems to be primarily due to exposure to H_2SO_4 rather than the cyclic voltammetry process itself. This could be attributed to the smaller surface area of the graphene pixels compared to the Hall Bar sensors. In the Hall Bar sensors, a more consistent trend was observed: as the number of scan cycles increased, the level of oxidation—and consequently the sensor response—also increased.

Further research is needed to determine if this process can be optimized to achieve a controllable and variable level of oxidation across individual graphene pixels.

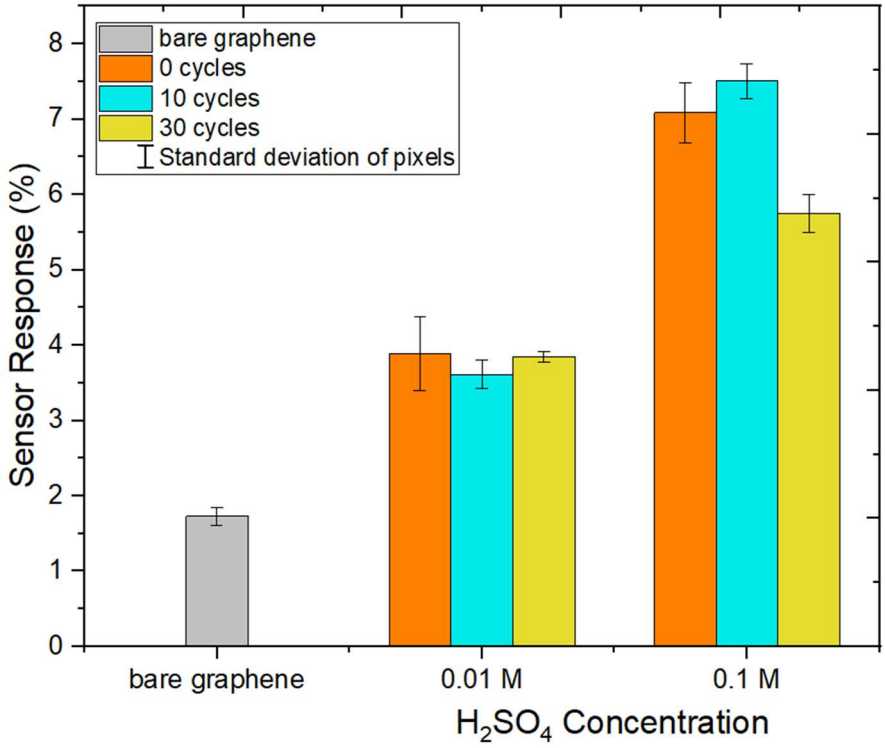


***Figure 8.27**: Bar chart illustrating the sensor response (%) of two different 3x3 graphene pixel array sensors exposed to 50 ppm NH_3, following electrochemical oxidation in 0.1 M and 0.01 M H_2SO_4, with varying scan cycles per row (0, 10 and 30 cycles).*

8.4. Device Damage

During both electrochemical functionalization processes described in this chapter, damage was observed on the metal tracks at various locations on both the Hall Bar and 3x3 graphene pixel array devices. Although a 50 nm layer of Al_2O_3 was applied to passivate the devices, the corrosive nature of the electrolyte solution still appeared to interact adversely with the metal tracks submerged in the solution. Most of the damage was concentrated near the edges of the passivation windows adjacent to the graphene pixels or channels; however, some damage was also detected at sites more distant from these passivation windows.

Pinholes in the passivation layer may have allowed the acid to penetrate, leading to localized corrosion of the metal. **Figure 8.28** shows images of the damage observed on the 3x3 graphene pixel array and Hall Bar devices during the electrochemical functionalization processes.

As a temporary measure, a photoresist mask was applied during electrochemical functionalization to provide extra protection to the metal regions of the sensor. This approach proved to be an effective solution.

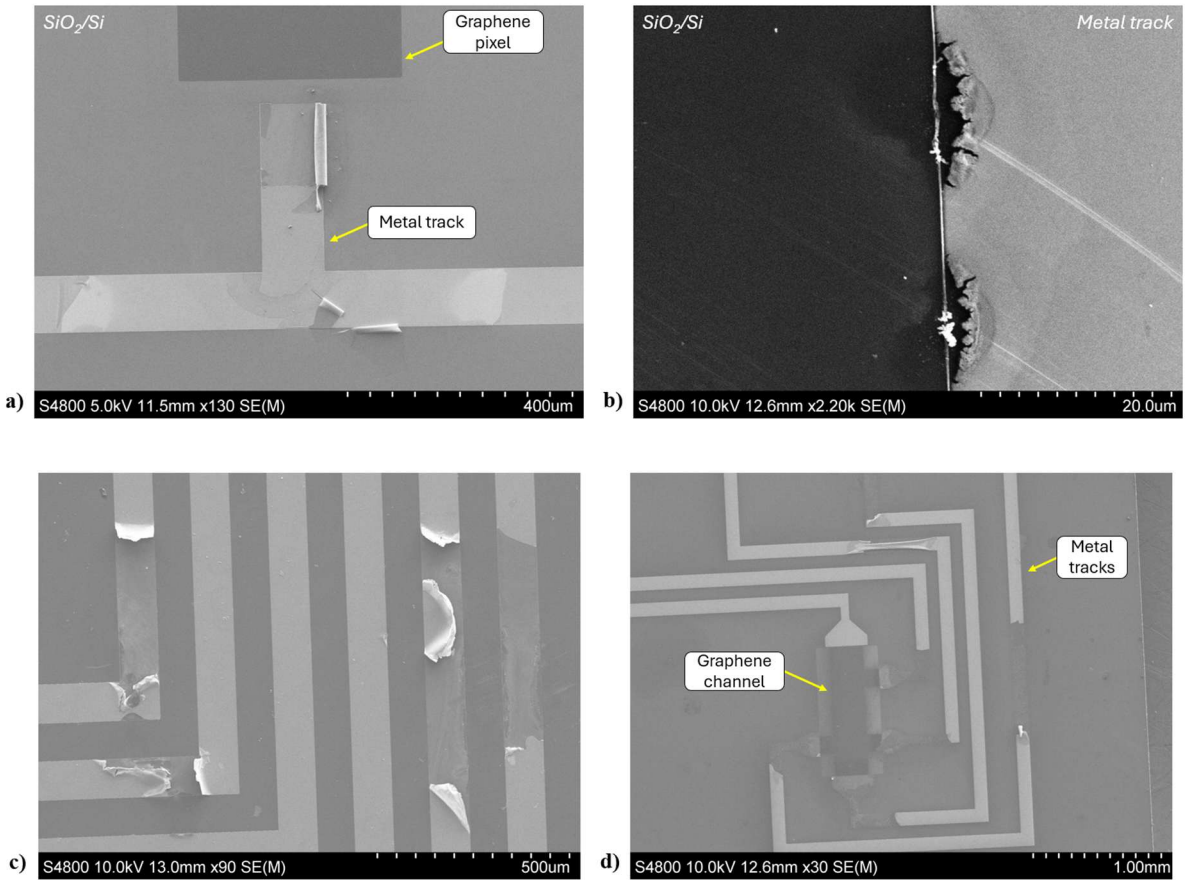


***Figure 8.28**: SEM images of damage observed on Hall Bar and 3x3 graphene pixel array devices during electrochemical functionalization of pDAN and electrochemical oxidation. **(a)** – **(c)** 3x3 graphene pixel array devices and **(d)** Hall Bar device.*

During the electrochemical oxidation process of graphene sensors, the CV profile exhibited similarities to the voltammetry profile reported by Liu et al. [380]. However, the oxidation peak at 0.8 V, as reported by Liu et al., was absent. Instead, a region of increasing current was observed between 0.54 V and 0.96 V. Given that the metal tracks consist of a Pd-Cr stack and considering the evidence of an additional reaction occurring concurrently with graphene oxidation, it is expected that the CV profile from these reactions would closely resemble the profile associated with palladium oxidation.

Figure 8.29a presents the CV profile reported by Grden et al. [390], detailing the electrochemical oxidation, electrodissolution, and ionic absorption of a palladium electrode in H_2SO_4. Their study [390] identifies several processes, including hydrogen (H) adsorption, anion absorption, and surface oxidation and reduction. A comparison between their CV profile and the one obtained in this work (**Figure 8.29b**) reveals several similarities, further confirming that palladium oxidation occurs concurrently with graphene oxidation.

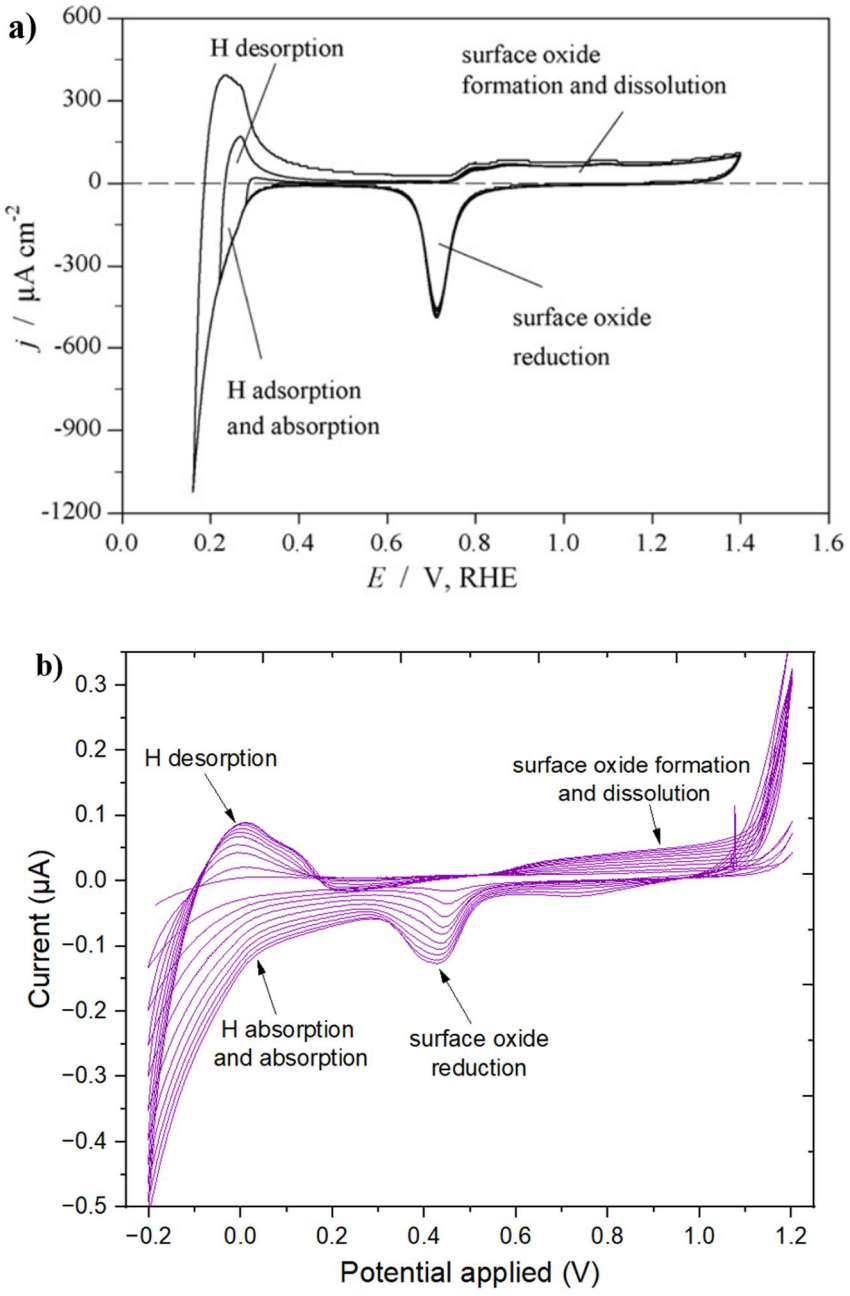


***Figure 8.29**: **(a)** CV profile of the electrochemical oxidation, electrodissolution, and ionic absorption of a palladium electrode, adapted from Grden, et al.* [390]. ***(b)** CV profile from this study, with labels highlighting similarities to **(a)**.*

8.4.1. Pinhole Investigation

To confirm the presence of pinholes in the passivation layer, SEM, EDS, and conductive-AFM were performed.

8.4.1.1. Scanning Electron Microscopy (SEM)

SEM was initially employed to detect potential pinhole defects on the metal tracks of newly fabricated Hall Bar and 3x3 graphene pixel array devices, which may appear as darker regions within the passivation layer above the metal tracks. **Figure 8.30** presents SEM images from these graphene devices, highlighting potential defects in the Al_2O_3 passivation layer above the metal tracks.

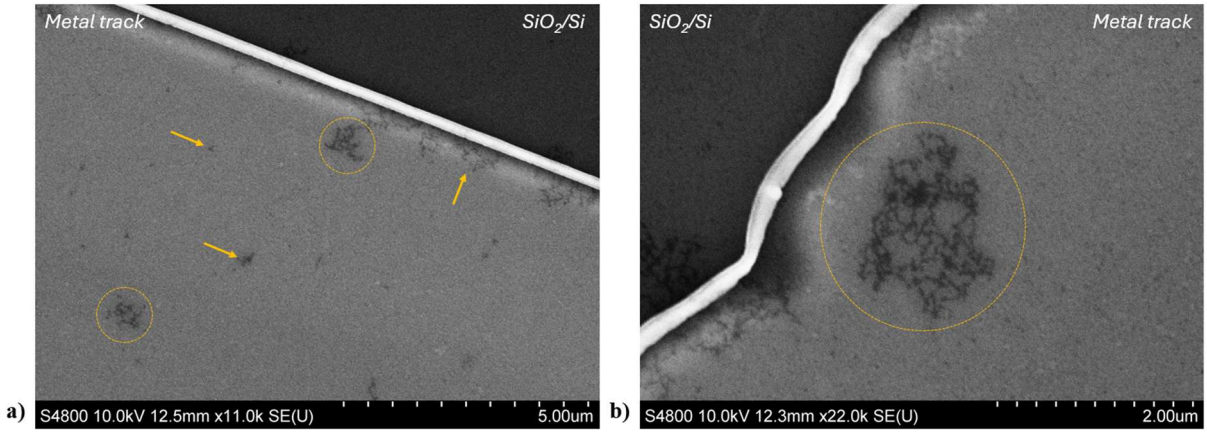


***Figure 8.30**: SEM images of graphene devices revealing potential defects in the Al_2O_3 passivation layer over the metal tracks.*

8.4.1.2. Energy-Dispersive X-ray Spectroscopy (EDS)

EDS mapping was conducted using an acceleration voltage of 15 keV to perform elemental analysis on the identified potential defect areas, aiming to determine the presence of pinholes in the passivation layer. A ~1.25 μm^2 scan (**Figure 8.31**) was initially performed over a graphene pixel, including the metal tracks, to detect any possible pinholes. The individual element maps (**Figure 8.31b**) reveal silicon (Si) in regions devoid of metal tracks, while palladium (Pd) is detected on the metal tracks, and chromium (Cr) is present but less distinctly concentrated. The aluminium (Al) from the Al_2O_3 passivation layer is detected as well, with a slightly visible 'square' in

the centre of the map, corresponding to the etched passivation window above the graphene pixel. These images do not provide clear evidence of pinholes in the metal tracks, and the aluminium oxide layer appears to be relatively uniform across the surface.

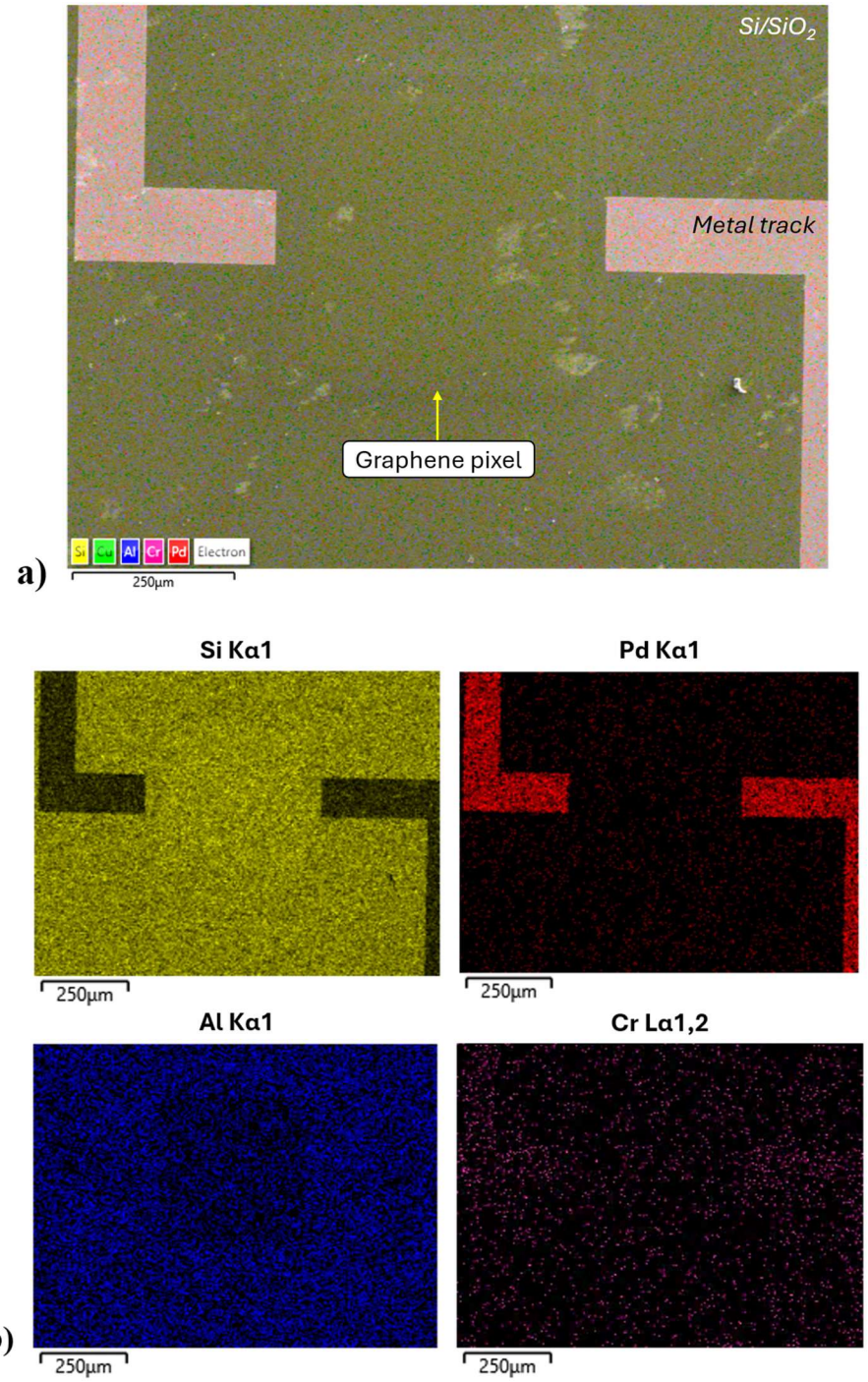


***Figure 8.31**: EDS mapping images of a graphene pixel and metal tracks on a 3x3 graphene pixel array device. **(a)** Overlaid elemental SEM image and **(b)** individual elemental maps for Si, Pd, Al, and Cr.*

Subsequently, a ~40 μm^2 scan (**Figure 8.32**) was performed after identifying potential defects in the passivation layer above a metal track. However, the elemental maps (**Figure 8.32b**) did not reveal any non-uniformities in the passivation layer (Al elemental map), nor were there any 'brighter areas' in the palladium or chromium maps that would suggest the presence of holes in the passivation layer above. As a result, the EDS data was inconclusive and did not provide sufficient evidence to confirm the presence of pinholes in the passivation layer. To further investigate the possibility of pinholes, conductive AFM was subsequently performed and is reported in the next section.

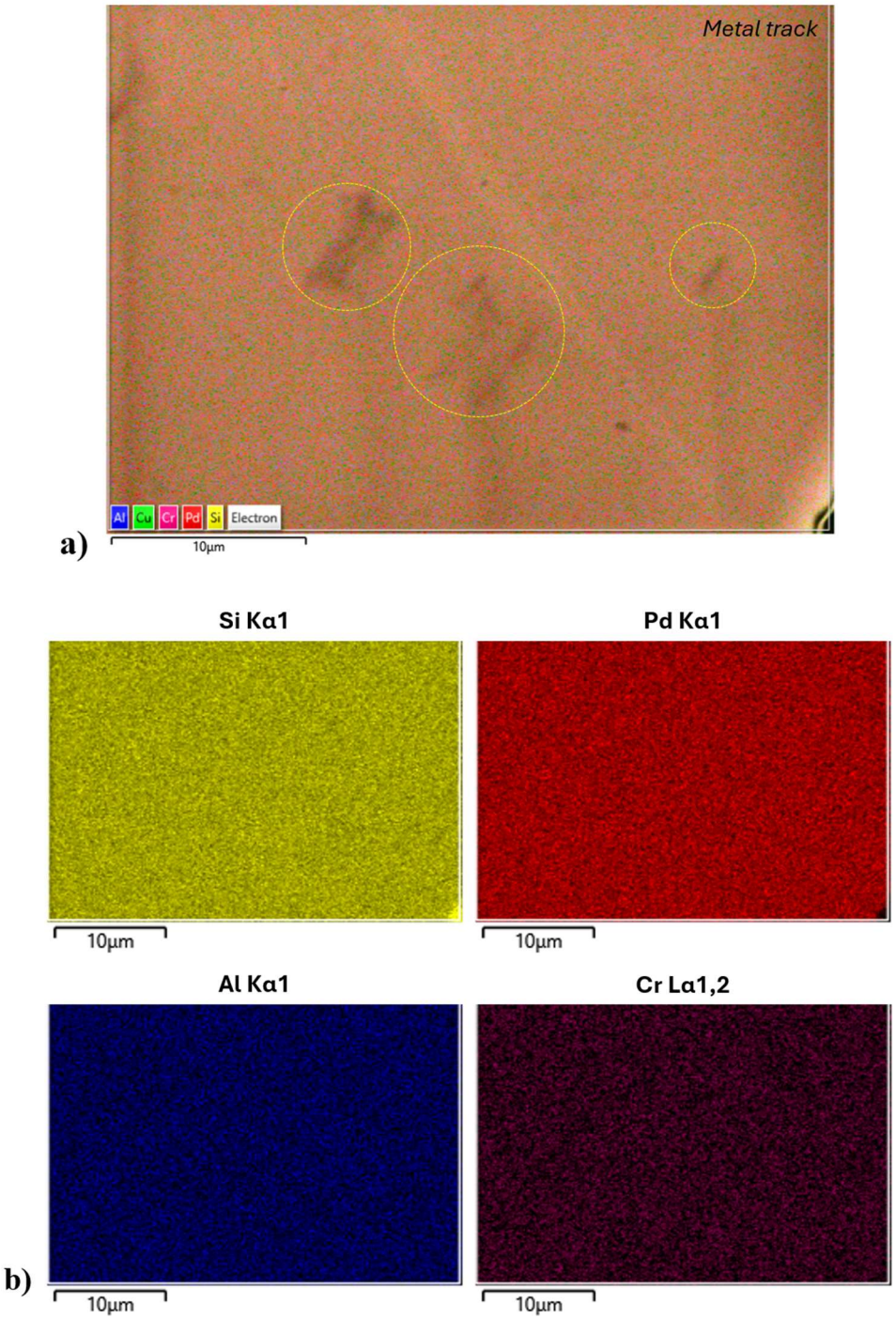


***Figure 8.32**: EDS mapping images of a metal track on a 3x3 graphene pixel array device. **(a)** Overlaid elemental SEM image and **(b)** individual elemental maps for Si, Pd, Al, and Cr.*

8.4.1.3. Conductive Atomic Force Microscopy (C-AFM)

Conductive atomic force microscopy (C-AFM) was employed to analyse the passivation layer on graphene devices, aiming to identify areas of varying conductivity that could suggest the presence of pinhole defects. The analysis was conducted using a *JFK Nanowizard 3* AFM system equipped with a gold SHR300 probe (detailed probe specifications and scan parameters are provided in **Chapter 3.4.4**).

Figure 8.33 shows AFM images of a 10 µm x 10 µm area on the Al_2O_3 passivation layer over a metal track in a Hall Bar device, specifically in a region where defects were suspected. **Figure 8.33a** presents the surface topography, revealing an amorphous surface covered with 'particle-like' structures, with a maximum height of 57.3 nm and an average RMS roughness of 0.763 nm based on three measurements. **Figure 8.33b** illustrates the conductivity variations over the same area. The largest conductivity value recorded was 251 mV, with the highest values observed in regions with the greatest height. Notably, there is no clear evidence of pinholes, as higher conductivity values would have been expected in the lower regions (i.e., exposed metal) of the topography map if pinholes were present.

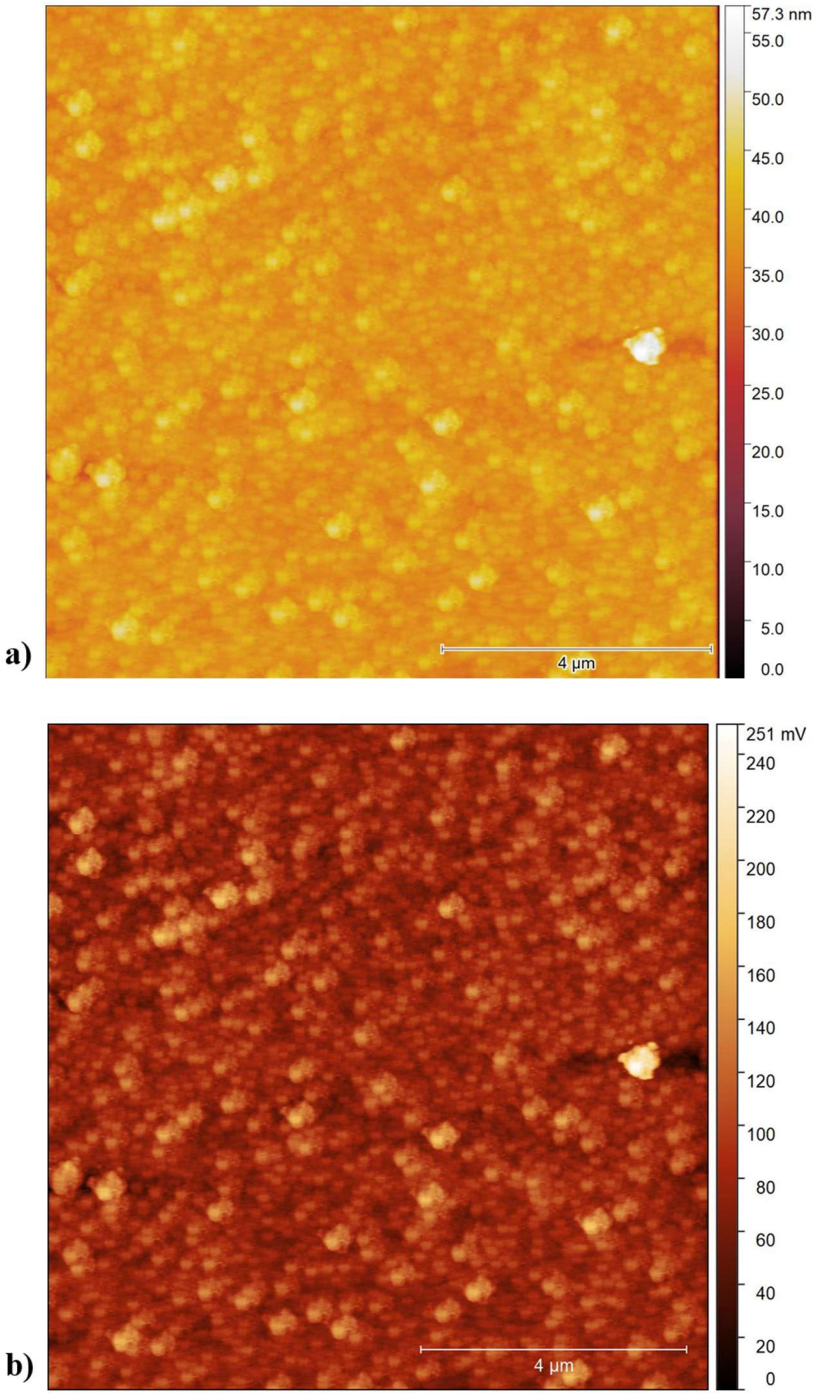


***Figure 8.33**: AFM images of the passivation layer above a metal track on a Hall Bar device (10 µm x 10 µm): **(a)** surface topography and **(b)** corresponding conductive measurements of the same area.*

Although the AFM data does not provide direct evidence of pinholes in the passivation layer, the penetration of acidic solutions and their reaction with the underlying metal suggest the presence of defects. Chang et al. [391] investigated defect formation in Al_2O_3 films deposited by atomic layer deposition (ALD) and identified the defect

mechanism. Their study found that defects manifest as a "looser microstructure" compared to the surrounding material, rather than as direct substrate exposure like pinholes. These defect areas create diffusion pathways that allow aggressive molecules to penetrate the film. The study [391] further identified two sources of defects: (1) extrinsic defects originating from sample surface preparation and (2) intrinsic defects resulting from incomplete reactions between TMA (trimethylaluminium) and -OH species during deposition. Both growth mechanisms lead to slower growth around the defect site, resulting in a looser microstructure.

These findings help explain the absence of visible pinholes while suggesting a mechanism for defect formation. The Al_2O_3 films utilized in this thesis were deposited via molecular vapor deposition (MVD) at 100°C. Previous studies have shown that higher deposition temperatures [391], such as 225°C [392] and 300°C [393], produce films with better corrosion resistance and fewer defects. Therefore, to ensure effective corrosion protection for graphene devices, it may be necessary to deposit Al_2O_3 passivation layers at elevated temperatures.

Finally, most of the observed damage was concentrated near the edges of the graphene passivation windows, indicating that the TMAH (tetramethylammonium hydroxide) wet etching process compromises the integrity of the remaining Al_2O_3 passivation layer. This likely increases the porosity of the residual layers, facilitating the diffusion of aggressive entities into the film and potentially leading to further defects that undermine the coating's effectiveness [392]. Additional Al_2O_3 etching techniques may need to be investigated to ensure that the film's integrity is maintained after the graphene surfaces are exposed.

8.5. Conclusions

This chapter explores two electrochemical functionalization methods for use in graphene-based sensors: the polymerization of 1,5-diaminonaphthalene (DAN) and electrochemical oxidation.

The electrochemical polymerization of DAN on graphene revealed that increasing the number of scan cycles results in a thicker pDAN film. The 3x3 graphene pixel array sensors were functionalized by varying the number of scan cycles in each row, allowing for different degrees of functionalization across the array. Gas sensing measurements showed variable responses to NO_2, NO, and NH_3 depending on the pDAN film thickness. PCA results show that the sensor array produces distinct response patterns for each gas, facilitating effective differentiation.

Compared to a bare graphene sensor, the pDAN film decreased the sensor's response to NO_2 and NO, suggesting that the film acts as a barrier, limiting the interaction of these molecules with the graphene surface. Conversely, the pDAN film slightly enhanced the sensor's response to NH_3, likely due to hydrogen bonding with the amine groups on the surface.

Electrochemical oxidation of graphene Hall Bar sensors revealed a small variation in the level of oxidation corresponding to the number of scan cycles. Notably, oxidation of graphene was also observed without the application of any potential. The different oxidation levels affected the sensor responses to NH_3 gas, with more scan cycles resulting in a higher response, likely due to the introduction of functional groups on the surface that facilitate additional interactions with gas molecules. However, when the experiment was repeated with 3x3 graphene pixel array sensors, this relationship between oxidation level and sensor response was not observed. Further research is needed to develop a method for achieving a controllable level of oxidation across different graphene pixels.

The varying magnitudes of sensor response to the same gas highlight the impact of different levels of functionalization on the graphene surface. With the right functional molecule, this technique could be employed to fine-tune the selectivity and sensitivity of a graphene sensor for specific applications. Additionally, unique responses from a sensor array can be integrated with pattern recognition software to identify unknown

gases. In this proof-of-concept, the sensor array was functionalized with the same molecule to different extents; however, this approach could be further improved by functionalizing with different species, enabling the detection of multiple analytes simultaneously.

A significant challenge in employing these functionalization methods was the damage to devices caused by exposure to the corrosive electrolyte solution. Despite the presence of a 50 nm Al_2O_3 passivation layer intended to protect the metal tracks, localized damage was still observed. It was hypothesized that pinholes in the passivation layer might be allowing aggressive molecules to diffuse through and react with the underlying metal. However, an investigation into the presence of pinholes was inconclusive, with no direct evidence found. Nonetheless, literature [391] suggests that defects in Al_2O_3 films often manifest as a looser microstructure, allowing molecules to diffuse in without direct substrate exposure. Further development is required to create a passivation layer capable of withstanding corrosive electrolyte solutions.

Chapter 9 : Detection of Odorants Using Human Olfactory Receptor 2AG1

9.1. Introduction

This chapter was adapted from Danielle M. Goodwin, Ffion Walters, Muhammad Munem Ali, Ehsaneh Daghigh Ahmadi and Owen J. Guy, “Graphene Bioelectronic Nose for the Detection of Odorants with Human Olfactory Receptor 2AG1”.

https://doi.org/10.3390/chemosensors9070174 [190]

Although the liquid-sensing experiments using the 'DipChipX' design were conducted earlier than the other research discussed in this thesis, they are presented last to highlight the sensor array's potential future applications.

Utilisation of odorant binding proteins and olfactory receptors in biosensors to develop a ‘bioelectronic nose’, resulting in a device that mimics the human olfactory system, dates back to 1961 [394]. Conceptually, the bioelectronic nose is analogous to the human olfactory system. Whereas the human olfactory system consists of olfactory receptors located in olfactory epithelium in the nose, bioelectronic noses contain these receptors immobilized on a support matrix (e.g., graphene, carbon nanotubes, silicon nanowires, etc.). Binding between the odorant molecule and its respective olfactory receptor/odorant-binding protein results in signal transduction produced by a conformational change in the receptor protein. Signals are detected as a change in resistance as conformational changes can alter charge transfer [395].

Traditional diagnosis techniques, although reliable and well-established, often require skilled personnel, expensive equipment and time-consuming sample preparation. Biosensors are becoming the present-day solution for rapid, reliable, sensitive, selective and cost-effective detection methods. Current research includes the use of several different types of biosensors: optical, potentiometric, impediametric, amperometric [396] and piezoelectric [397].

Although widely researched, graphene has not frequently been employed in these bioelectronic nose sensors to date. Graphene, a 2D nanomaterial composed of a single layer of sp^2 hybridised carbons, possesses superior electrical properties such as high carrier mobility and electron transfer rates at room temperature [398], which present opportunities for applications in a diverse range of fields such as medical, solar cells, energy storage, transparent electrodes, transistors and nanocomposites [399]. In particular, graphene-based sensing devices have features such as label-free detection, high sensitivity and selectivity, biocompatibility and ease of functionalization [145], [148], [155]. The ability to fabricate graphene devices using standard lithographic processes presents significant advantages over CNT-based sensors in terms of reliability of device platforms and potential multiplexing capability for any bioelectronic nose.

This chapter reports the fabrication, real-time functionalization and performance of a graphene resistor capable of selectively and sensitively detecting amyl butyrate (AB), an odorant specific to OR2AG1.

9.2. Graphene Functionalization

This section outlines the functionalization procedure for the DipChipX devices.

9.2.1. DAN functionalization

10 mM DAN solution was prepared in 70% ethanol in DI water. A 20 µL droplet was drop-cast onto the graphene channel and incubated at room temperature (RT) for 1 h. The droplet was topped with a 20 µL droplet during the hour to avoid evaporation. After incubation, devices were washed three times with a 20 µL droplet of 70% ethanol followed by washing three times with a 20 µL droplet of DI (deionized) water.

9.2.2. Olfactory Receptor Attachment

To deposit the OR2AG1 protein, a solution of 2% (v/v) glutaraldehyde (condensing agent) in 1 × phosphate buffered saline (PBS) (pH 7.4) was prepared, and 20 µL of this was drop-cast onto the graphene channel and incubated at RT for 30 min. Devices

were subsequently washed three times with 20 µL of DI water, before applying a 16 µL droplet of OR2AG1 (0.01 µg/µL in 50 mM Tris-HCI, 10 mM reduced glutathione, pH = 8.0 in the elution buffer) onto the activated DAN-modified graphene channel and incubating for 1 h at RT. Functionalized devices were washed three times with 20 µL of DI water. The graphene functionalization is illustrated in **Figure 9.1**.

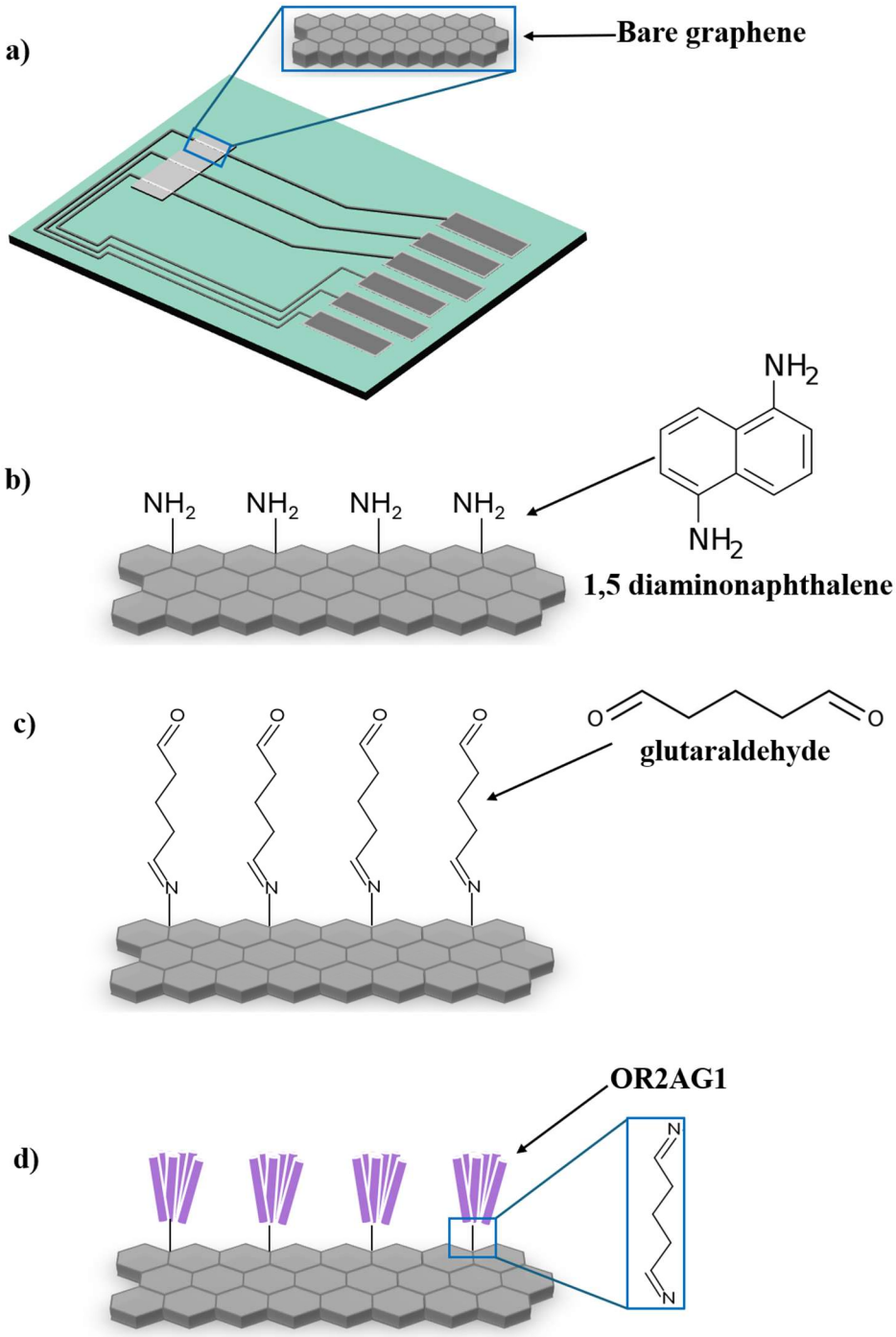


***Figure 9.1**: Functionalization of graphene: **(a)** schematic of graphene resistor chip (18,200 µm × 9700 µm), **(b)** 1,5 diaminonaphthalene chemical modification of the bare graphene surface, **(c)** addition of glutaraldehyde, **(d)** immobilization of olfactory receptor 2AG1.*

9.2.3. Blocker Attachment

Following functionalization of the graphene channel with OR2AG1, blocking agents were used to mop up any non-specific binding sites on the graphene channel device.

A 1% 20 µL droplet of bovine serum albumin (BSA) blocker solution diluted in DI water was thus drop-cast onto the OR2AG1/glutaraldehyde/DAN functionalized graphene devices and was incubated for 30 min at RT. Devices were washed three times with 20 µL of DI water and gently dried with N_2.

9.3. Electrical Measurements

Real-time current–voltage resistance measurements were performed using the 'DipChipX' graphene sensor chips, consisting of three discrete CVD graphene devices on a single chip. The three graphene resistor devices were measured simultaneously by sliding the chips into the 'Sensor-Connect' connector, supplied by Biovici Ltd.; see **Figure 9.2**. Measurements were carried out under ambient conditions (temperature 20 °C, normal atmospheric pressure), monitoring current in response to a constant voltage of 40 mV applied across the graphene devices. Real-time resistance measurements were carried out by in situ drop-casting: starting with a 'blank' measurement (no solution), followed by PBS, negative controls (pentyl valerate, butyl butyrate and propyl butyrate) and finally, the target odorant, amyl butyrate at increasing concentrations.

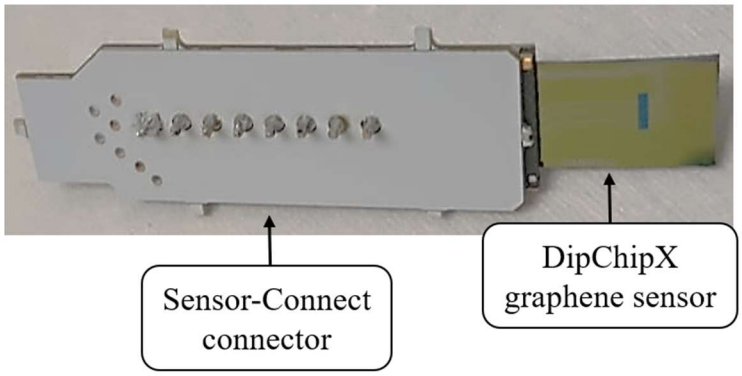


***Figure 9.2**: Image of a passivated chip in the Biovici 'Sensor-Connect' connector for real-time resistance measurements.*

Below is a depiction of signal transduction for this bioelectronic nose (Figure 3). The binding event between the odorant and receptor causes a conformational change in the receptor. The transducer (graphene resistor chip) converts the biorecognition event into a measurable electrical signal, which in this case is a current measurement [395].

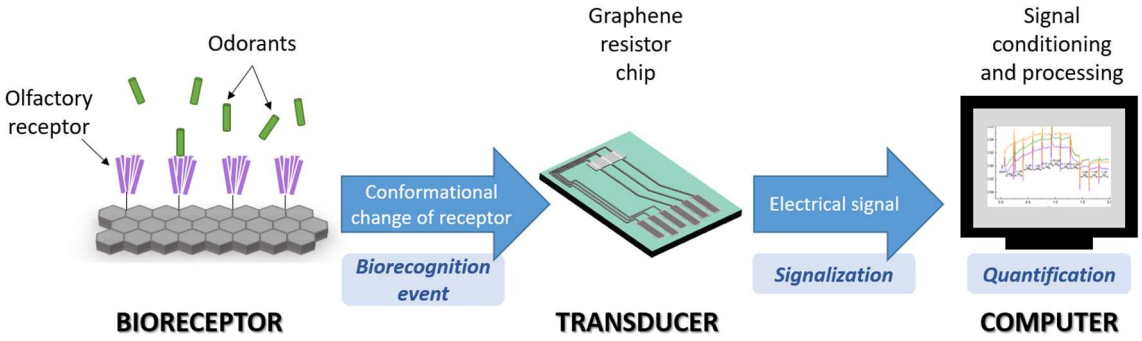


Figure 9.3: Schematic representation of signal transduction in the bioelectronic nose.

9.4. Surface Characterization

9.4.1. Atomic Force Microscopy

The surface topography of graphene before and after functionalization with DAN was characterised using atomic force microscopy (AFM), performed using a JPK NanoWizards II Dimension-3100 Multimode (*Bruker*, USA), using a non-contact AFM tip with resonant frequency, spring constant and tip radius of 320 kHz, 40 N/m and 8 nm, respectively, operated in AC mode. The surface graphene before and after functionalization with DAN (**Figure 9.4**) showed clear changes in surface topology and surface roughness. The root mean square (RMS) roughness of 0.534 nm (**Figure 9.4a**) of bare graphene dramatically increased to 2.315 nm (**Figure 9.4b**) after functionalization of graphene by DAN drop-casting.

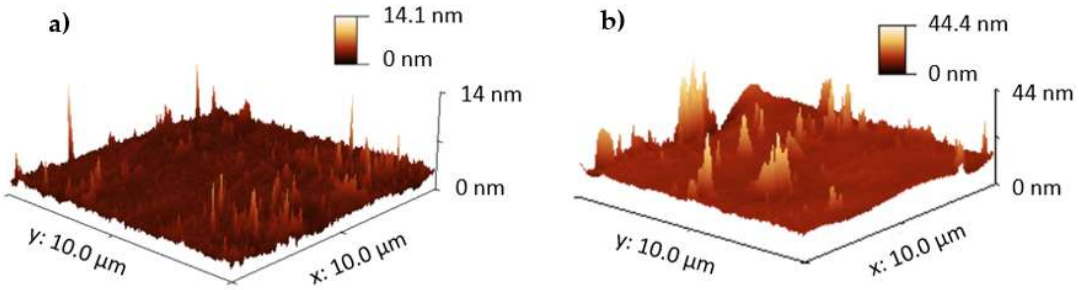


*Figure 9.4: AFM morphology of the **(a)** the non-functionalized (intrinsic graphene) surface, and **(b)** the functionalized graphene surface with DAN.*

9.4.2. Raman Spectroscopy

Raman spectroscopy was performed using a Renishaw inVia Raman microscope with a 532 nm laser at 2 mW power and a x100 objective lens. This spectroscopic technique was used to characterize the changes in the graphene surface after each functionalization stage. Extended point scans were performed on the graphene, (**Figure 9.5a**). For the pristine graphene, the average intensity ratio between the D- and G-peaks, located at ~1350 cm^{-1} and ~1590 cm^{-1}, respectively, was close to 0.079. This ratio increased with each surface modification step due to the presence of additional aromatic molecules on the graphene surface. After the DAN modification step, the intensity and FWHM of the D-peaks and G-peaks changed significantly. The D-band produced an asymmetrical peak, influenced by the stretching of C–N vibrational modes, found in the DAN structure [155]. An additional peak was present at ~1460 cm^{-1} and ~1620 cm^{-1} due to the vibrational modes created by the aromatic rings found in DAN [400]. The peak ~1620 cm^{-1} started to broaden due to the C=O and amide stretching caused by the glutaraldehyde and OR2AG1 receptor protein [401] surface modification steps. With each attachment step, the additional peaks broadened due to the influence of the different functional groups present on the graphene surface, and began merging with the graphene G-peak, increasing the FWHM. These changes in the Raman spectrum indicated successful graphene functionalization after each step. Using a custom script, the Raman peak positions of the G-peaks and 2D-peaks were obtained after each functionalization stage and were placed into a scatter plot (**Figure 9.5b**). The shifts in the G-peak positions, with respect to the shifts in the 2D-peak position, after each functionalization stage could be used to analyse the changes in stress or strain in the graphene crystalline structure and alterations in the charge carrier doping [402]. The application of DAN resulted in electron donation between the DAN and the graphene surface, introducing an n-doping effect on the graphene, shown by the blue-shifting of the Raman peaks [155], [244], [403]. However, once the glutaraldehyde and OR2AG1 receptor proteins were attached, the Raman peaks shifted again in the opposite direction, indicating that a p-doping effect was taking place. This p-doping effect occurred due to the charge transfer occurring between the glutaraldehyde/protein layers and the graphene buried underneath [244], [402]–[405]. After the final functionalization step, the doping level

of the graphene was shown to be p-doped overall, resulting in the graphene being further away from the charge neutrality point.

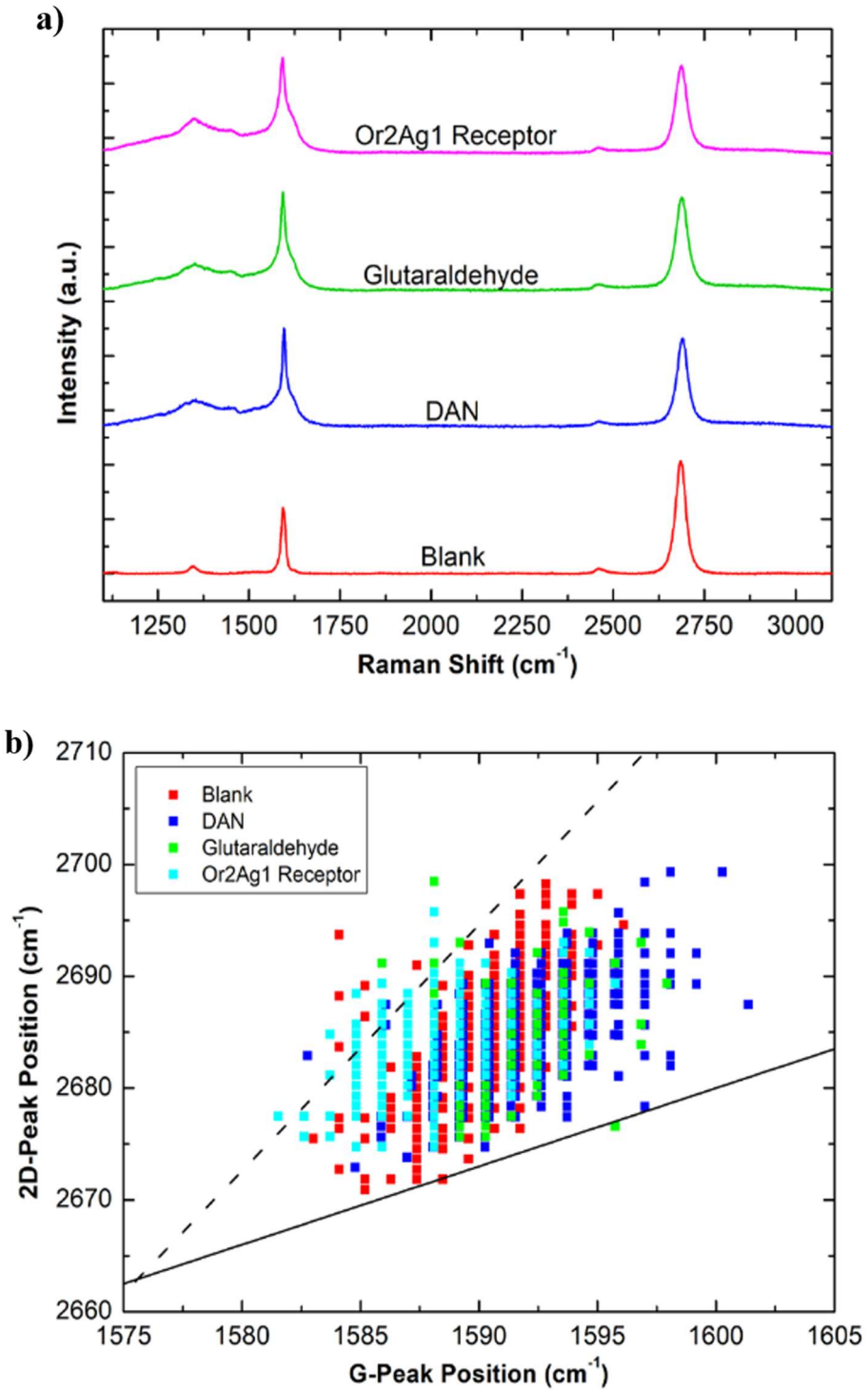


***Figure 9.5**: **(a)** Raman spectroscopy of unmodified graphene (red) and graphene after each functionalization step (drop-casting of DAN (blue), followed by glutaraldehyde attachment (green) and lastly OR2AG1 protein receptor (pink). **(b)** Scatter plot showing the shifting in the G-peak and 2D-peak positions, at each functionalization stage, unmodified graphene (red), drop-cast DAN (dark blue), glutaraldehyde attachment (green) and OR2AG1 protein receptor (light blue), indicative of changes in doping and applied strain of the graphene structure, after each functionalization stage.*

9.5. Real-time Functionalization

Real-time resistance measurements during the functionalization process were carried out with drop-casting and in situ washing followed by 45-min relaxation/drying periods after each functionalization stage. The requirement for graphene to relax under ambient conditions was investigated in the research group's previous work [155] and is perhaps related to the redistribution of charges within the graphene surface absorbates and Si/SiO_2 substrate [95], [145].

Figure 9.6 shows a dramatic increase in resistance after DAN (in 70% ethanol) was drop-cast onto the graphene devices, relative to the resistance of the dry pristine graphene device. During the 1 hour incubation period, in which graphene became saturated with DAN, spikes in resistance were seen, which corresponded to the topping up of the droplet to avoid evaporation. Following DAN modification, devices were washed (3 × 20 µL of 70% ethanol, followed by 3 × 20 µL of DI water) and allowed to relax/dry for 45 min. Following drying, the resistance was higher than the initial resistance of the pristine graphene device, indicating modification with DAN resulted in a resistance change. A second increase in resistance was observed with the addition of glutaraldehyde, which was subsequently washed (3 × 20 µL of DI water) and allowed to dry. Addition of the ORA2G1 receptor, followed by BSA blocker (the blocker reduces non-specific binding to unused graphene sites) also produced slight changes in resistance when compared to the previous functionalization steps and to the pristine graphene. The final resistance after completion of functionalization remained higher than the pristine (unmodified) graphene surface.

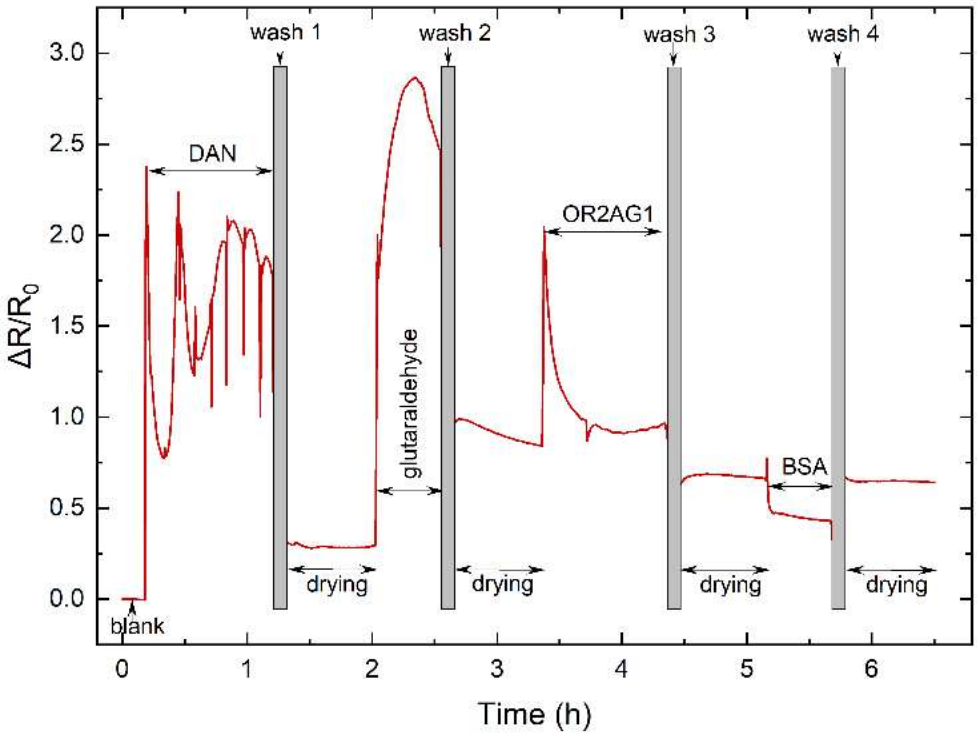


***Figure 9.6**: Real-time resistance measurements of the graphene functionalization process, where $\Delta R/R_0 = [R_{device} - R_0]/R_0$, and R_0 is the resistance at T = 0 (resistance of bare (intrinsic) graphene).*

9.6. Detection of Amyl Butyrate

A schematic of the functionalized sensor is shown in **Figure 9.1**. OR2AG1 has a high affinity towards amyl butyrate (AB), demonstrated in previous studies [158], [406]–[409], where OR2AG1 produced no response on exposure to non-specific, structurally similar molecules of aliphatic alcohols, aldehydes, ketones, ketals and esters, including, for example, pentyl valerate, butyl butyrate and propyl butyrate (**Figure 9.7**).

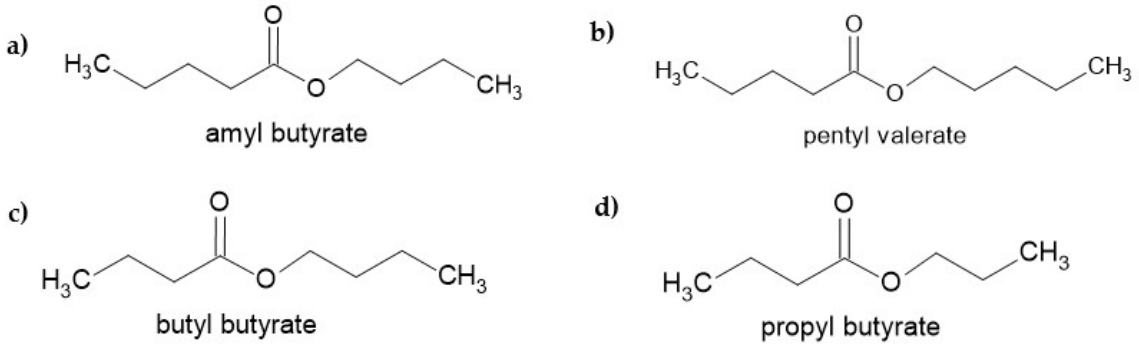


***Figure 9.7**: Structure of **(a)** amyl butyrate (target odorant), **(b)** pentyl valerate, **(c)** butyl butyrate and **(d)** propyl butyrate.*

Figure 9.8a shows the real-time resistance measurement profiles for three OR2AG1 graphene sensors on the same chip. Addition of 0.5 pM AB caused a sharp decrease in resistance ($\Delta R/R_0$ in a negative direction) in all three devices, and subsequently, sensor saturation was observed after addition of 1 pM AB. Two structurally similar odorants were employed to assess sensor selectivity: pentyl valerate (PV) and butyl butyrate (BB). No significant changes of $\Delta R/R_0$ in a negative direction were observed with the addition of the non-target odorants. **Figure 9.8b** represents normalised device resistance against AB concentrations. Concentration dependence was observed at 0.5 pM, followed by a plateau, representing device saturation. Additional AB concentrations (0.1, 0.2, 0.3, 0.4, 0.75, 250, 500 pM) in the linear detection region are displayed in **Figure 9.9c**, which demonstrates a linear sensor response. **Figure 9.9d** displays the device's reaction time at 0.5 pM, presenting a response time of approximately 350 s. **Figure 9.9e** shows a comparison of the obtained signal after drop-casting of 1 µM AB or the three control odorants. The response signals (% difference in relation to PBS) showed a significantly larger signal change for the AB

specific analyte, with only very small changes seen for all three negative control odorants run. Therefore, these results indicate that the functionalised graphene biosensor offered high selectivity towards amyl butyrate.

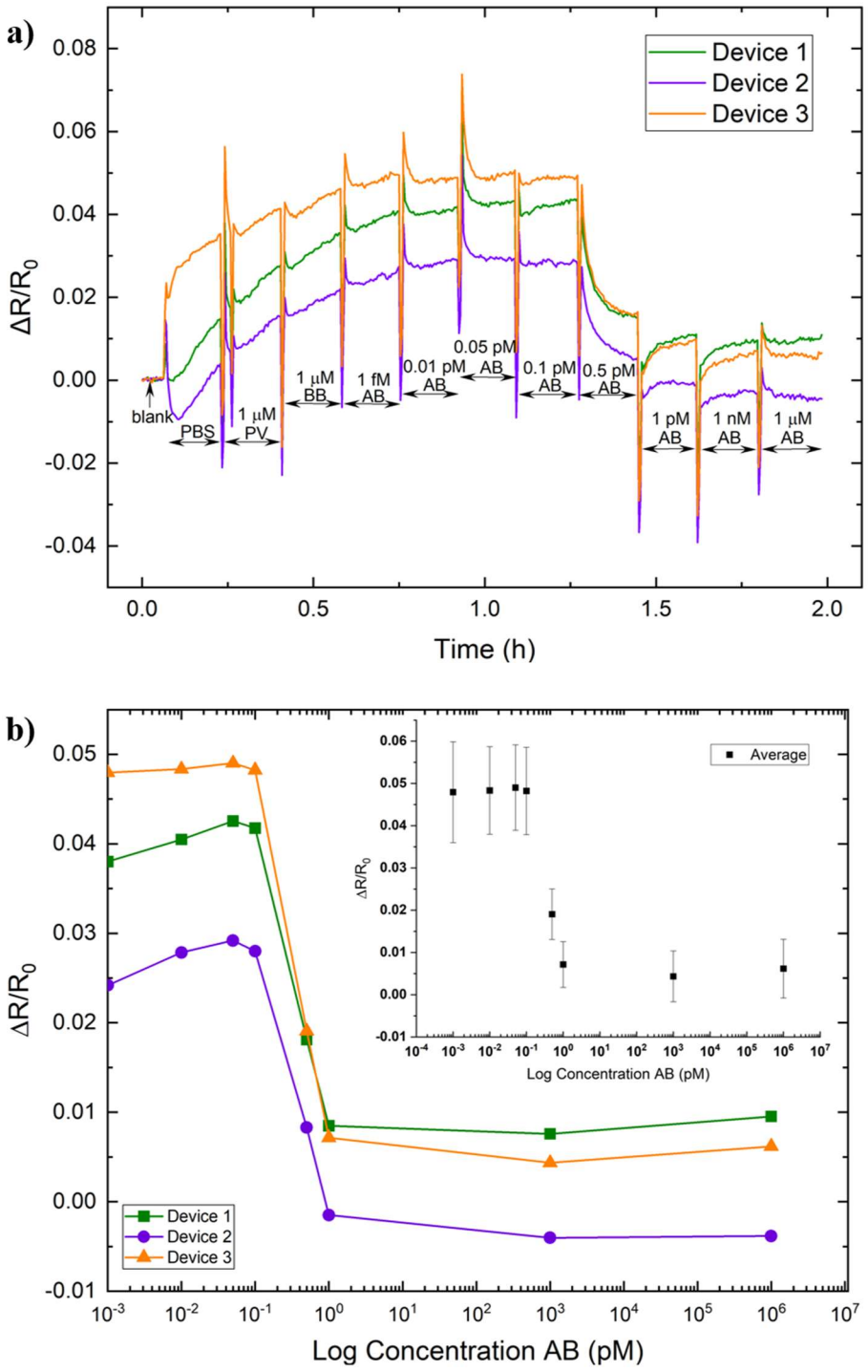


***Figure 9.8**: **(a)** Real-time resistance measurements of the OR2AG1 functionalized sensor, where $\Delta R/R_0 = [R_{device} - R_0]/R_0$, and R_0 is the resistance at T = 0 (resistance of OR2AG1 functionalized graphene). A concentration range of 10^{-15} to 10^{-6} M in PBS was used for the target odorant, amyl butyrate (AB), and 10^{-6} M in PBS was used for pentyl valerate (PV) and butyl butyrate (BB) controls (all prepared using 1 M stock solutions in DMSO). **(b)** Picomolar amyl butyrate concentration (logarithmic scale) plotted against resistance with inset error bars.*

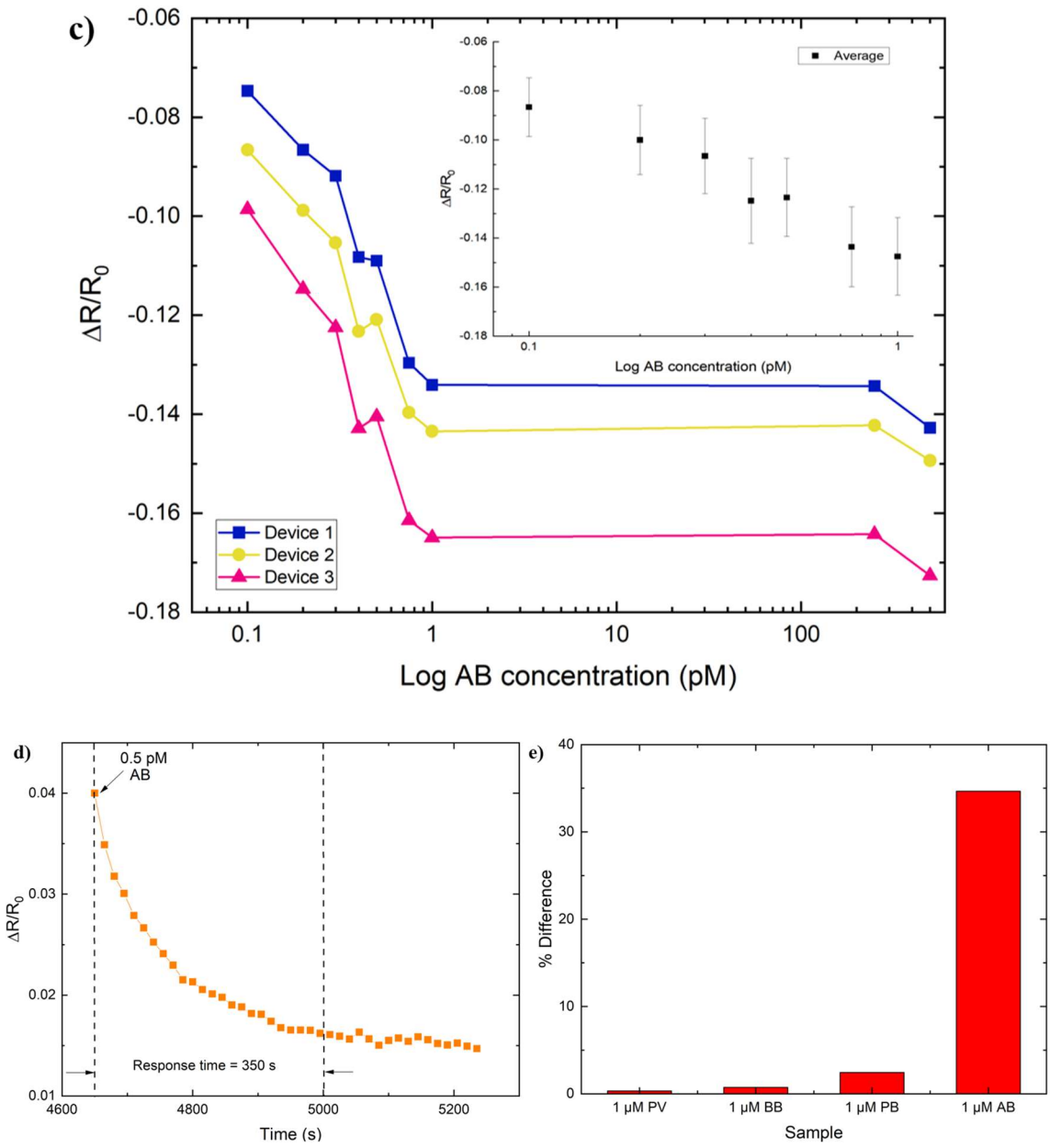


***Figure 9.9**: **(c)** Picomolar amyl butyrate concentration (logarithmic scale) repeats with additional concentrations (0.1, 0.2, 0.3, 0.4, 0.75, 250, 500 pM) plotted against resistance with inset error bars. **(d)** Real-time reaction time graph showing response time after adding the target odorant (amyl butyrate, 0.5 pM). **(e)** Selectivity graph of the negative controls (1 μM PV, BB, PB) and target odorant (1 μM AB) with respect to PBS.*

In similar studies, where nanovesicles were used to amplify sensing signals [406], and the working concentration of the olfactory receptor was higher (0.05 μg/μL) [158], sensitivity was reported at 10^{-15} M. However, the reported device contains a working concentration of the OR2AG1 receptor of 0.01 μg/μL, with a sensitivity of 10^{-13} M;

this shows that good sensitivity can still be achieved even with low working concentrations of receptor, indicating lower potential development costs.

9.7. Conclusions

In this chapter, a graphene resistor bioelectronic nose was fabricated and its performance evaluated using real-time I–V characterization. The sensor was realized using non-covalent surface functionalization of graphene resistor devices with DAN using a drop-cast technique and subsequent immobilization of OR2AG1 protein. The resulting sensor selectively detected the target odorant, amyl butyrate, at a concentration of 0.5 pM even with a low working concentration of the olfactory receptor 2AG1 (0.01 μg/μL), indicating the potential for a bioelectronic nose design using combinations of olfactory receptors. The facile functionalization method allows for simple, quick, and cost-effective fabrication of selective and sensitive sensing devices.

Chapter 10 : Conclusions and Future Work

This chapter summarizes the key findings of the thesis and outlines potential avenues for future research.

10.1. Summary of Key Results

This thesis focussed on developing and optimizing a gas sensing system, including the creation of a 3x3 graphene array sensing device. The research explored various functionalization methods to enhance sensor performance, leading to several key findings:

- **Chapter 4**: Detailed the design and fabrication of the 3x3 graphene pixel array sensor, aimed at enabling multiplexed gas sensing.
- **Chapter 5**: Developed a gas sensing system capable of measuring real-time resistance across multiple graphene channels simultaneously.
- **Chapter 6**: Evaluated the performance of different phthalocyanines in combination with graphene sensors. The study highlighted the impact of different metal centres on gas sensing capabilities, with various phthalocyanines showing different responses to gases. The poor solubility of phthalocyanines led to the synthesis of tetra-tert-butyl copper phthalocyanine, which demonstrated competitive gas sensing performance and a notable recovery time of 60 seconds.
- **Chapter 7**: The integration of Polymers of Intrinsic Microporosity (PIMs) with graphene sensors was investigated, presenting a novel approach that combines the gas separation properties of PIMs with the exceptional conductivity of graphene. The study demonstrated a substantial improvement in selectivity and sensitivity toward nitrogen dioxide, with the polymers achieving a limit of detection in the low parts per billion range. These results highlight the polymers' significant potential for practical gas sensing applications.
- **Chapter 8**: Demonstrated the feasibility of electrochemical functionalization using polymer 1,5-diaminonaphthalene and oxidation. The study showed that

variations in sensor response could be attributed to the degree of functionalization applied to the graphene array. PCA results supported this by showing that the sensor array generates distinct response patterns for different gases, suggesting effective differentiation between them. Device damage was observed during the electrochemical functionalization processes which was attributed to defects in the passivation layer.

- **Chapter 9**: Presented a proof-of-concept bioelectronic nose incorporating human olfactory receptor 2AG1. The sensor successfully detected analytes down to 0.5 pM, highlighting the potential for future applications involving the modification of the sensor array with different olfactory receptors to enable simultaneous detection of multiple analytes.

Table 34 summarises the electronic interactions between graphene and each functionalization method employed (where measurements were available).

***Table 34**: Summary of electronic interactions with each functionalization technique.*

Functionalization	Electronic Interaction	Chapter
copper (II) 2,9,16,23-tetra-tert-butylphthalocyanine ($CuPc(t\text{-}Bu)_4$)	Electron-donating	6
Polymers of intrinsic microporosity	N/A – not measured	7
poly-1,5 diaminonaphthalene (pDAN)	Electron-donating	8
3-part functionalization: (1) pDAN, (2) glutaraldehyde and (3) OR2AG1.	(1) Electron-donating (2) Electron-donating (3) Electron-accepting	9

10.2. Comparison of Nitrogen Dioxide Sensor Performance

The table below (**Table 35**) provides a summary of the comparison between the top-performing NO_2 sensors developed in this work, other nitrogen dioxide sensors reported in the literature, and one commercial sensor (highlighted in green).

***Table 35**: Comparison between the top-performing NO_2 sensors developed in this work and notable NO_2 sensors reported in the literature.*

Sensing Materials	NO_2 Response	Operation Temperature (°C)	LOD (ppb)	Recovery time (s) (Percentage recovery)	Ref.
CVD graphene/PIM-1	20% at 5 ppm	RT	1.0	114 (100%)	***This work***
CVD graphene/PIM-EA-TB	26% at 5 ppm	RT	0.7	149 s (100%)	***This work***
CVD graphene/Matrimid	22% at 5 ppm	RT	1.0	153 s (100%)	***This work***
CVD graphene/CuPc(t-Bu)$_4$	13% at 5 ppm	RT	31	67 s (100%)	***This work***
CVD graphene	11% at 5 ppm	RT	NR	93 s (100%)	***This work***
CVD graphene	20% at 1 ppm	RT	NR	900s (97%)	[360]
4-aminoquinoline-rGO	74% at 10 ppm	RT	NR	3300 (80%)	[356]
SnO_2-rGO hybrid	2% at 1 ppm	RT	1000	100 (NR)	[363]
ZnO	NR at 1 ppm	RT	50	240-360 (NR)	[410]
CuPc(t-Bu)$_4$ and CuPc thin films on interdigitated Au electrodes	NR at 10 ppm	125-225	NR	5400 (NR)	[328]
CuPc thin films	NR at 20 ppb	80	10	3600 s (NR)	[411]
Solid polymer electrolyte (electrochemical sensor)	Sensing range: 0 – 50 ppm	RT	1000	NR	[412]

*Abbreviations: **RT** = Room Temperature, **NR** = Not Reported

A comparison of gas sensing performance metrics indicates that the NO_2 sensors developed in this work have the potential to be highly selective and sensitive, with performance metrics competitive with those reported in the literature. The comparison

also indicates that these sensors achieve low detection limits that rival those of commercially available options. Although the comparison was constrained by the available data, the polymer-functionalized sensors show the greatest overall potential as effective NO_2 sensors, particularly in terms of sensitivity, selectivity, and recovery times.

Additionally, it is important to note that the sensors in this work perform comparably to others, despite the absence of substantial optimization (e.g., channel dimensions, surface modification techniques, recovery system, operation at different temperatures). This highlights the promise of graphene-based sensors for gas sensing and multiplexing applications.

10.3. Future Work

This research successfully developed a graphene sensing array and gas sensing system, exploring various functionalization techniques to enhance gas sensing performance. However, several areas require improvement to advance the technology.

Software Interface

The current gas sensing system lacks an automated software interface, which limits its functionality. Future work should focus on integrating a system similar to LabVIEW. Such an integration would enable autonomous control of experimental parameters and automate the switching of mass flow controllers, improving the efficiency and ease of use.

Sensor Design

In terms of sensor design, a significant limitation was the redundancy of one channel for real-time resistance measurements. This issue arose from the oversight that USB-C plug types utilize outer tracks as grounds. Future developments should address this by optimizing connector designs to ensure all channels function effectively. Additionally, the 90 nm SiO_2 layer was insufficient for performing back-gated measurements with the current device design. Exploring the use of a thicker oxide layer, such as 300 nm, could facilitate back-gated measurements and yield more comprehensive gas sensing data.

Passivation Layer

Device damage to the metal tracks on sensors was observed when exposed to aggressive functionalization techniques. Improvements are needed in the passivation layer, including options such as a thicker layer, increased deposition temperature, or different dielectric materials, especially for devices used in electrochemical surface modifications.

Sensor Response Variability

While polymer-functionalized graphene array sensors demonstrated excellent selectivity and sensitivity towards nitrogen dioxide, significant response variations were noted between pixels. Investigating the sources of these variations or potentially restricting polymer applications to single graphene channels could enhance consistency in sensor performance.

Enhanced Functionalization

The diverse functionalization techniques showcased in this thesis highlight the potential for creating a robust graphene gas sensing array capable of simultaneous multi-gas detection. Future sensor designs could benefit from incorporating microfluidics to apply distinct functional modifications to different graphene channels. For instance, PIM-EA-TB could be used for nitrogen dioxide, PIM-1 for methane, and oxidation for ammonia detection.

Recovery Method Optimization

Challenges with recovery and variability among devices were observed, indicating a need for improved recovery methods. Employing UV light more evenly across all sensors or integrating an on-board heater system, similar to those in metal oxide sensors, could aid in more efficient recovery.

Commercialization Challenges

To advance towards commercialization, addressing issues such as device-to-device variability and graphene contamination is essential.

By addressing these areas, future work can enhance the functionality and reliability of graphene-based gas sensors, paving the way for more effective and versatile sensing applications.

Appendix

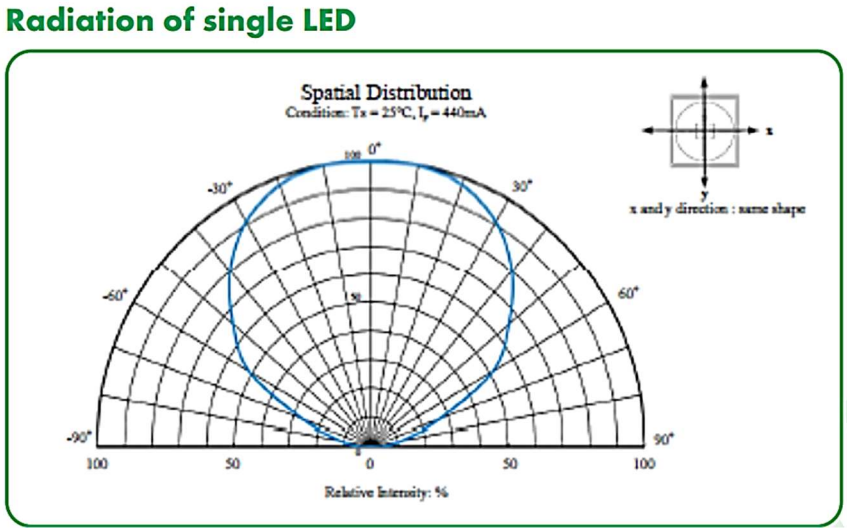


***Figure A1**: Polar radiation plot provided in the data sheet from RS Components for the UVC LED (ILR-ZZ01-Z265-LS025-SC201).*

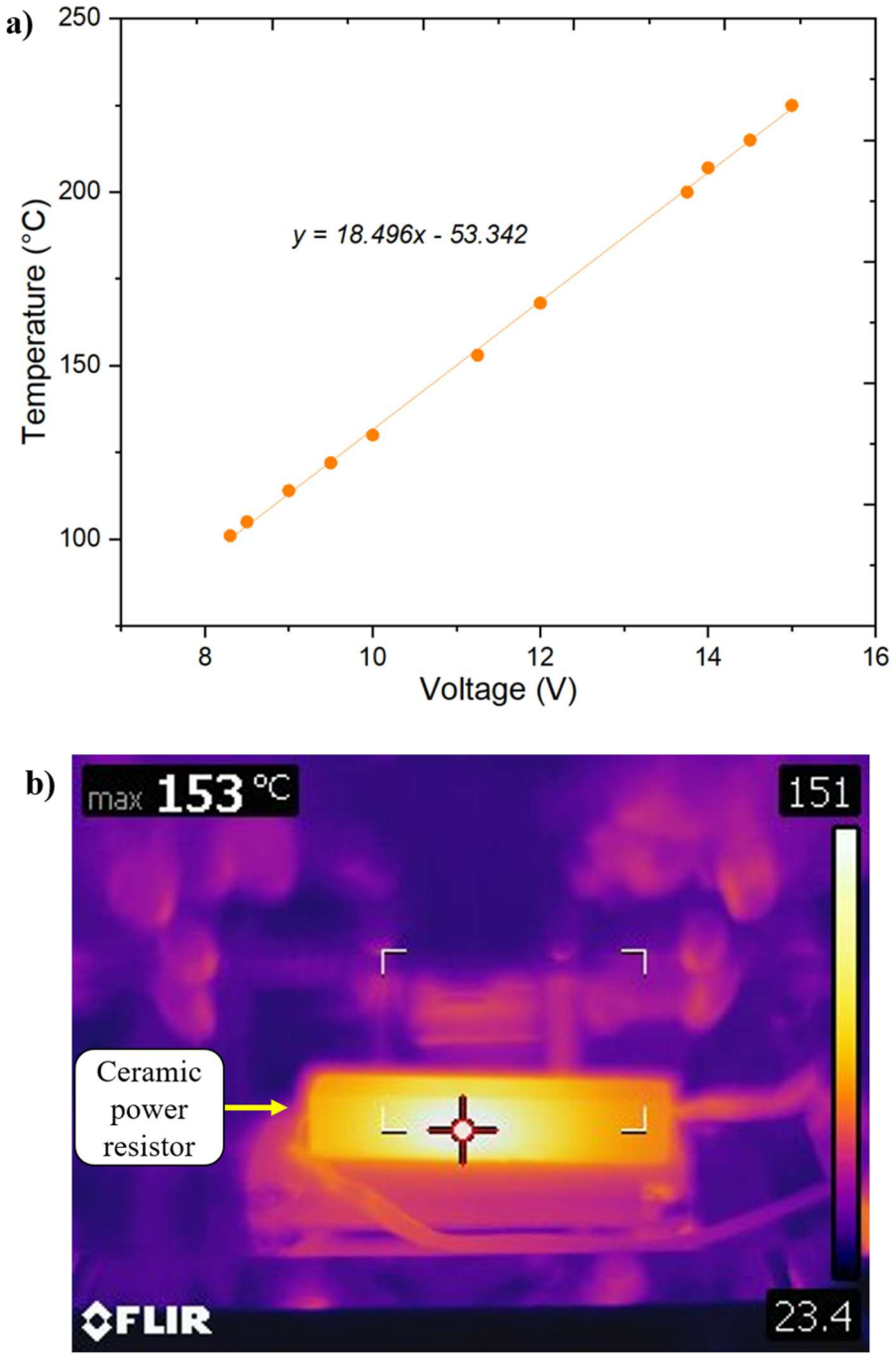


***Figure A2**: **(a)** Heater calibration plot displaying the temperatures measured for different voltage settings. **(b)** FLIR thermal imaging photo of the ceramic power resistor. Imaging performed by Robert John.*

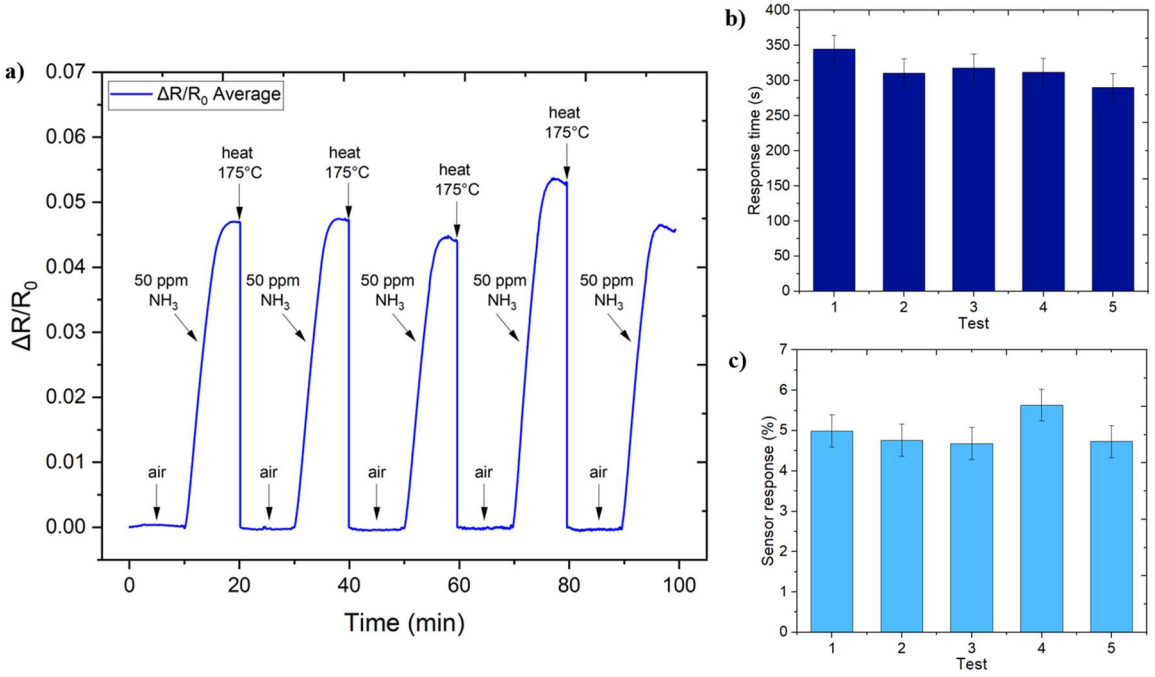


***Figure A3**: **(a)** Real-time resistance measurements (expressed as $\Delta R/R_0$) taken from a 2-channel graphene device exposed to 50 ppm NH_3 and heated to 175°C for four repetitions to assess recovery. **(b)** Response time (s) and **(c)** Sensor response (%) of four repeats.*

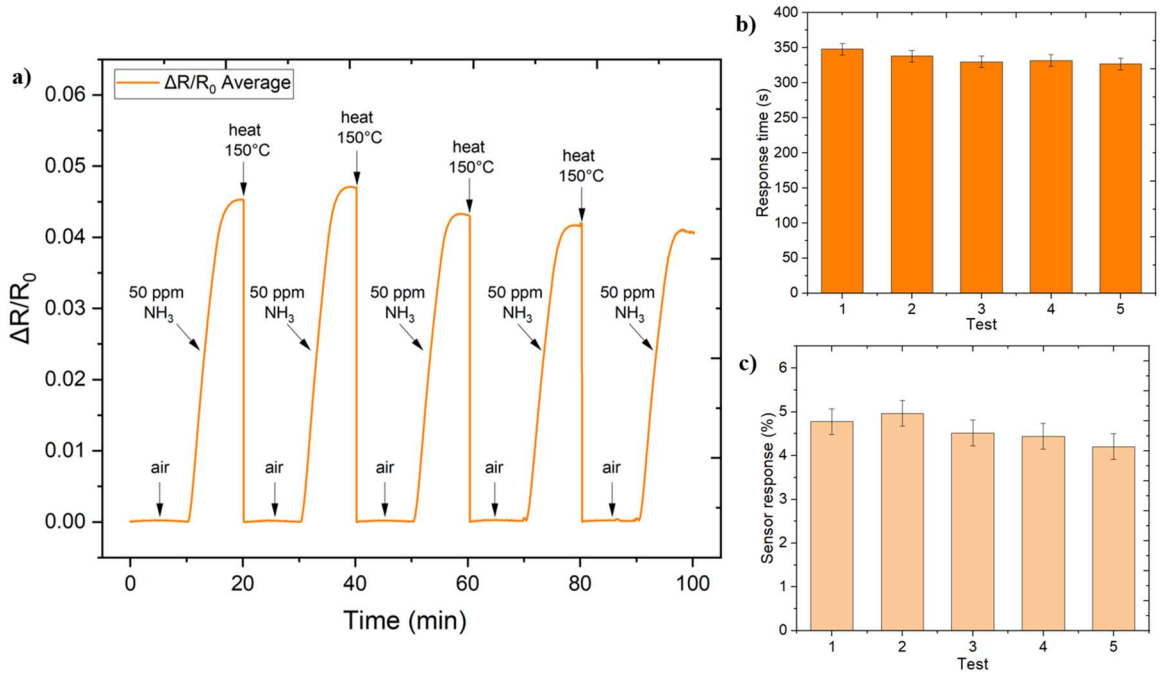


***Figure A4**: **(a)** Real-time resistance measurements (expressed as $\Delta R/R_0$) taken from a 2-channel graphene device exposed to 50 ppm NH_3 and heated to 150°C for four repetitions to assess recovery. **(b)** Response time (s) and **(c)** Sensor response (%) of four repeats.*

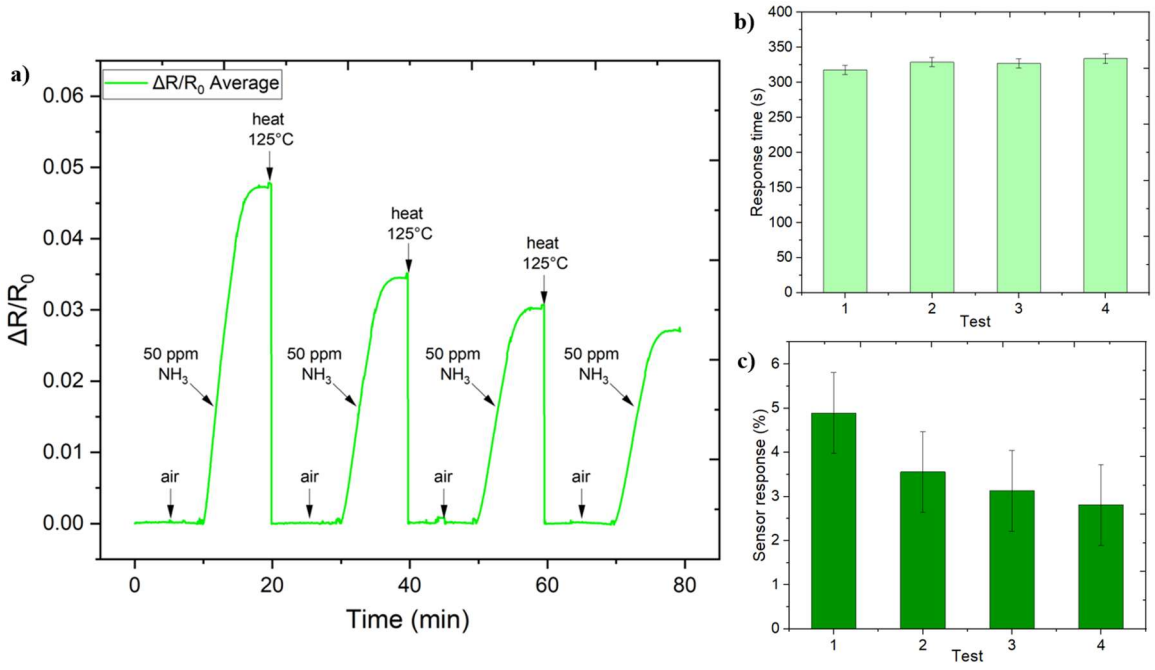


***Figure A5**: **(a)** Real-time resistance measurements (expressed as $\Delta R/R_0$) taken from a 2-channel graphene device exposed to 50 ppm NH_3 and heated to 125°C for four repetitions to assess recovery. **(b)** Response time (s) and **(c)** Sensor response (%) of four repeats.*

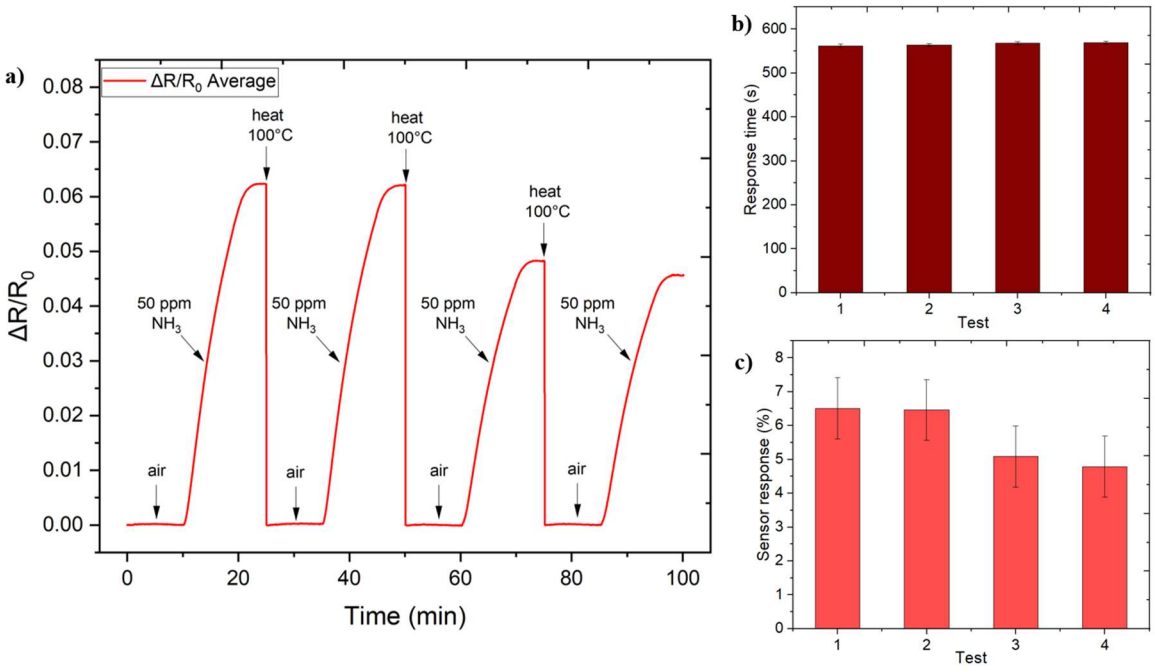


***Figure A6**: **(a)** Real-time resistance measurements (expressed as $\Delta R/R_0$) taken from a 2-channel graphene device exposed to 50 ppm NH_3 and heated to 100°C for four repetitions to assess recovery. **(b)** Response time (s) and **(c)** Sensor response (%) of four repeats.*

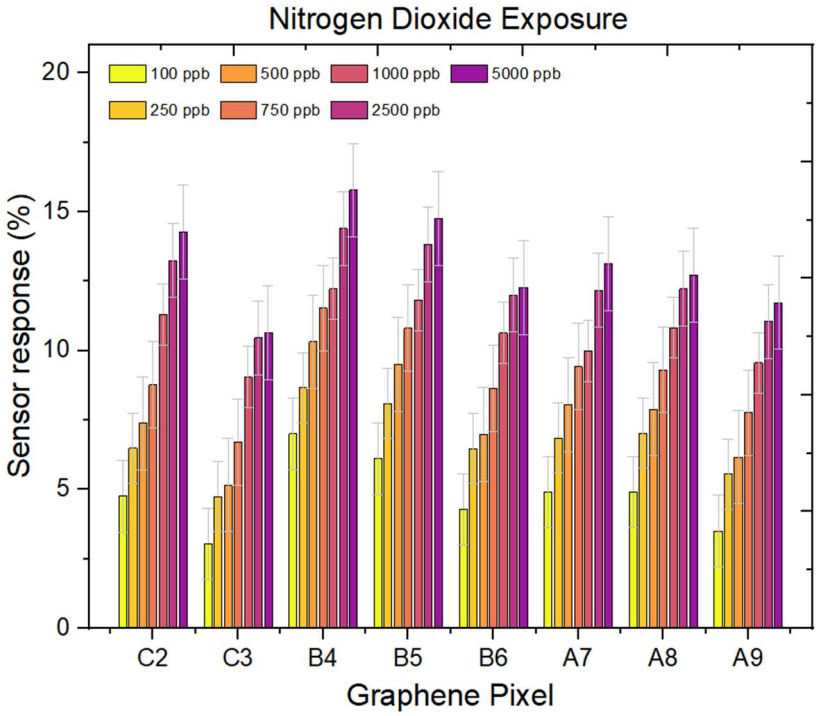


***Figure A7**: Individual sensor response (%) of graphene pixels on a 3x3 pixel array sensor exposed to different concentrations of NO_2: 100, 250, 500, 750, 1000, 2500 and 5000 ppb.*

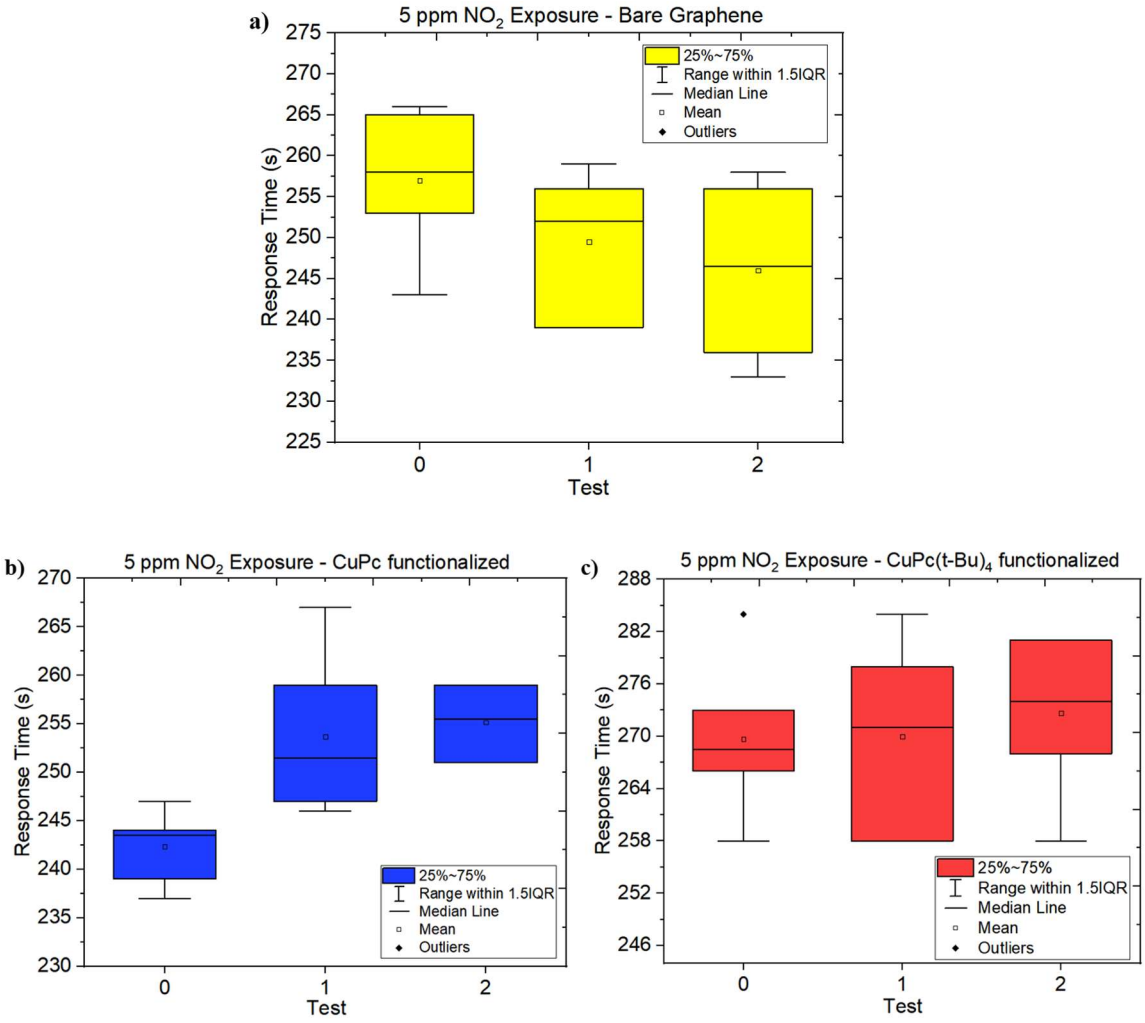


***Figure A8**: Box plot displaying the range of response times to 5 ppm NO_2 of the graphene pixels for each repeat of the **(a)** bare graphene, **(b)** CuPc-functionalized and **(c)** CuPc(t-Bu)$_4$-functionalized 3x3 pixel array sensors.*

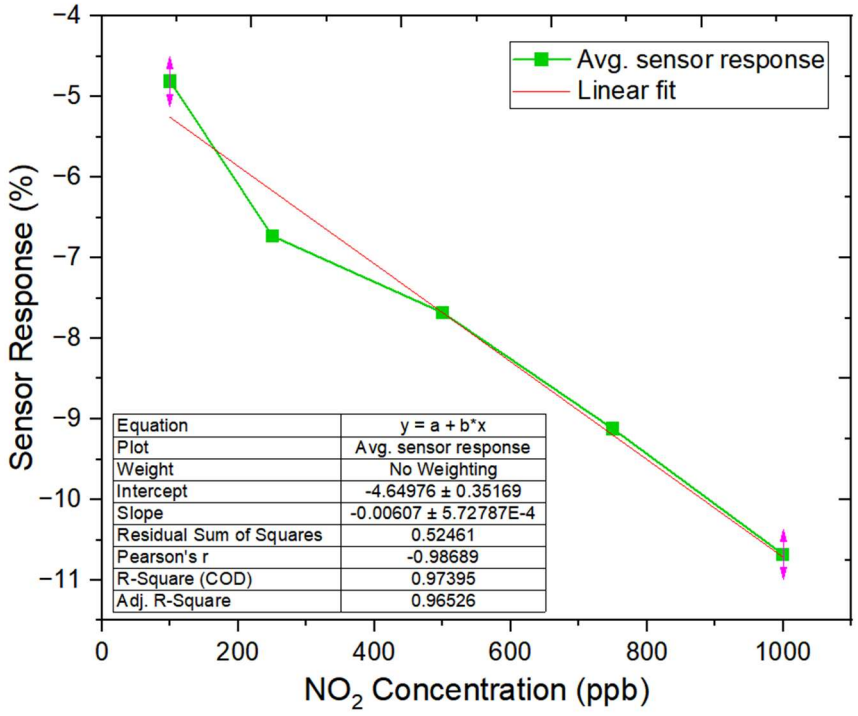


***Figure A9**: Linear fit for the linear portion of calibration curve obtained from the concentration range 100 ppb to 1 ppm using the CuPc(t-Bu)$_4$-functionalized 3x3 graphene pixel array sensor. Origin linear fitting software was used to perform the fit.*

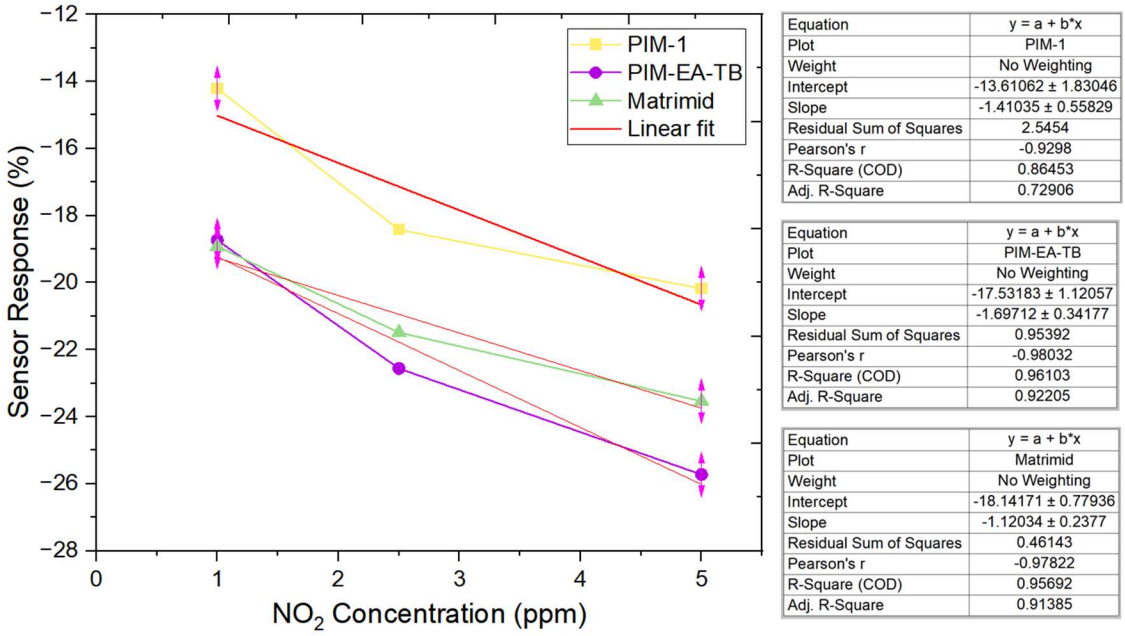


***Figure A10**: Linear fit for the linear portion of calibration curve obtained from the concentration range 1 ppm to 5 ppm using the polymer-functionalized 3x3 graphene pixel array sensors. Origin linear fitting software was used to perform the fit.*

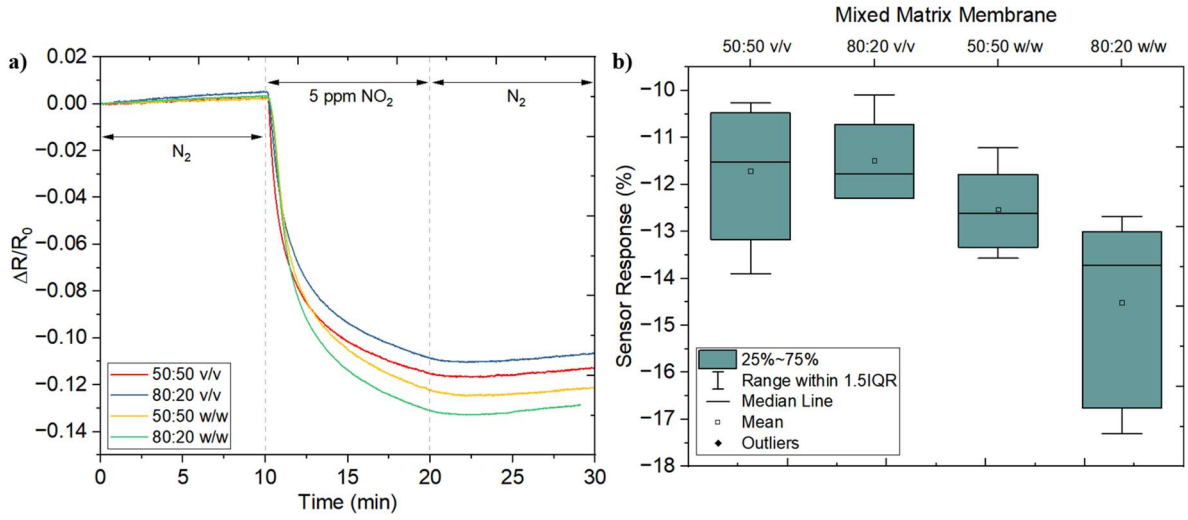


***Figure A11**: **(a)** Real-time resistance plot and **(b)** box plot displaying the range of sensor responses (%) to 5 ppm NO_2 of the graphene pixels for the four mixed matrix membrane-functionalized sensors (50:50 v/v, 80:20 v/v, 50/50 w/w and 80:20 w/w PIM-EA-TB:CuPc(t-Bu)$_4$).*

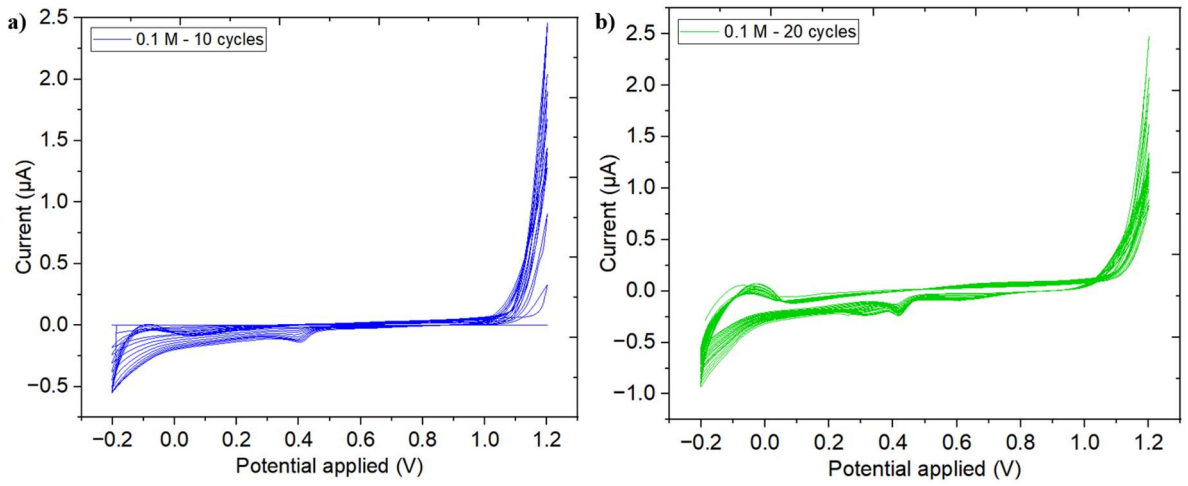


***Figure A12**: Cyclic voltammograms of the electrochemical oxidation for both graphene channels of a Hall Bar sensor in 0.1 M H_2SO_4 over **(a)** 10 cycles and **(b)** 20 cycles.*

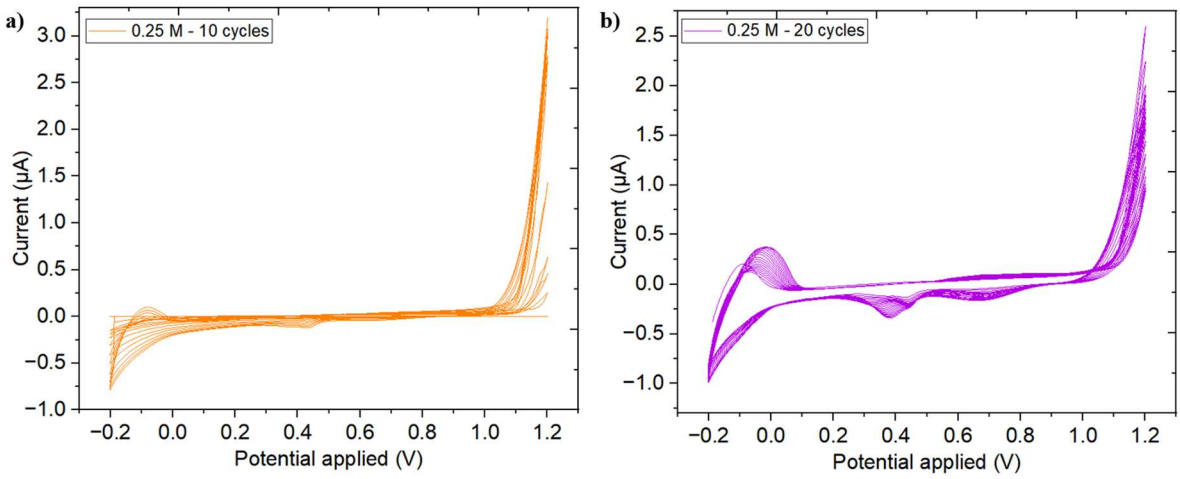


***Figure A13**: Cyclic voltammograms of the electrochemical oxidation for both graphene channels of a Hall Bar sensor in 0.25 M H_2SO_4 over **(a)** 10 cycles and **(b)** 20 cycles.*

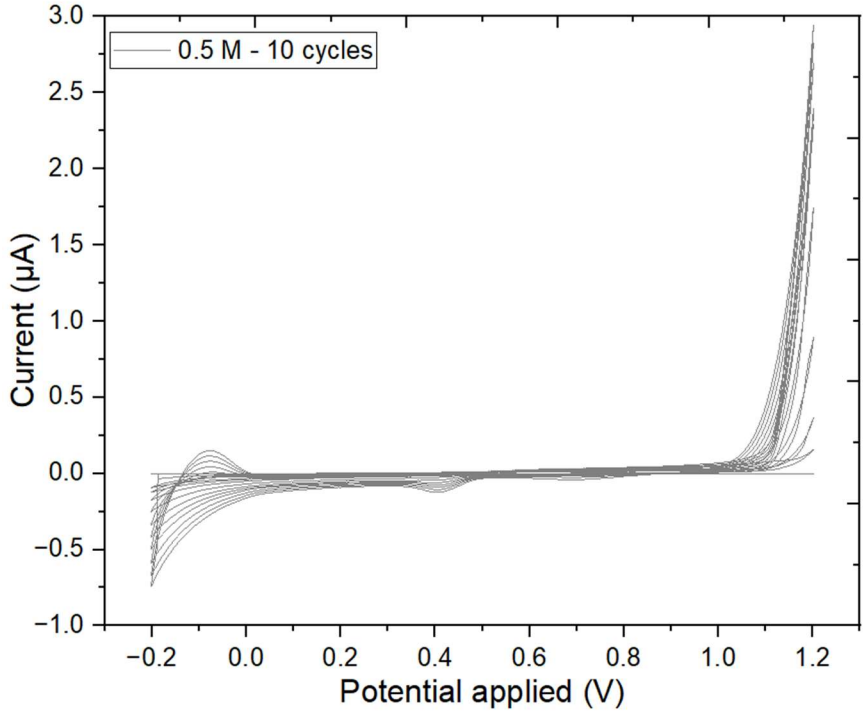


***Figure A14**: Cyclic voltammogram of the electrochemical oxidation for one graphene channels of a Hall Bar sensor in 0.5 M H_2SO_4 over 10 cycles. The CV profile for 20 cycles is located in **Section 8.3.2 (Figure 8.20)**.*

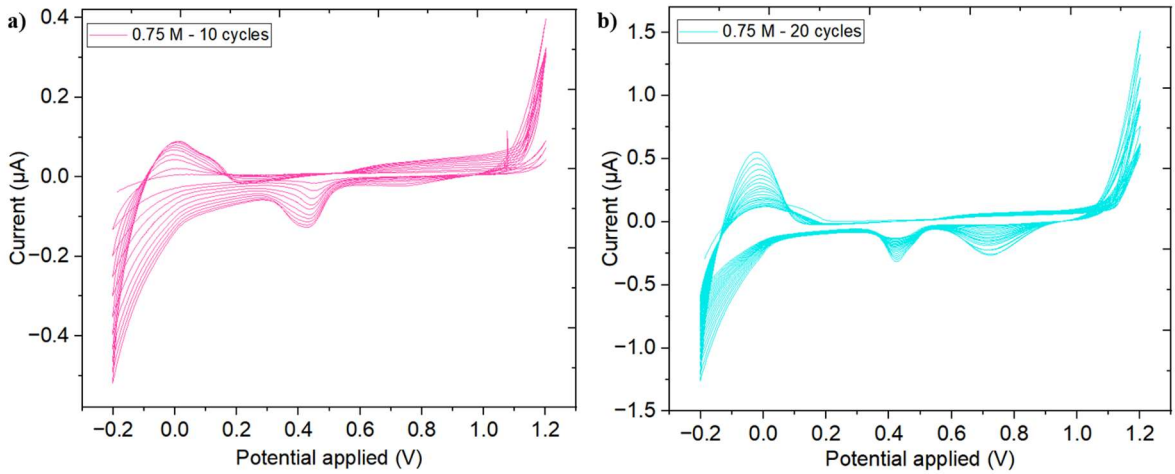


***Figure A15**: Cyclic voltammograms of the electrochemical oxidation for both graphene channels of a Hall Bar sensor in 0.75 M H_2SO_4 over **(a)** 10 cycles and **(b)** 20 cycles.*

Bibliography

[1] J. Hodgkinson *et al.*, “Gas sensors 2. The markets and challenges,” *Nanotechnol. Perceptions*, vol. 5, no. 1, pp. 83–107, 2009, doi: 10.4024/N36HO08A.ntp.05.01.

[2] U. Yaqoob, “Chemical Gas Sensors : Recent Developments , Challenges ,” *Sensors*, vol. 21, no. D, p. 2877, 2021.

[3] S. Kendler and A. Zuck, “The challenges of prolonged gas sensing in the modern urban environment,” *Sensors (Switzerland)*, vol. 20, no. 18, pp. 1–7, 2020, doi: 10.3390/s20185189.

[4] O. V. Cheremisina and S. Z. Al-Salim, “Modern methods of analytical control of industrial gases,” *J. Min. Inst.*, vol. 228, pp. 726–730, 2017, doi: 10.25515/pmi.2017.6.726.

[5] G. Rolla *et al.*, “Exhaled nitric oxide in asthma,” *Ital. J. Allergy Clin. Immunol.*, vol. 16, no. 4, pp. 141–150, 2006, doi: 10.1378/chest.07-2743.

[6] F. Schedin, A. K. Geim, S. V. Morozov, and E. W. Hill, “Detection of Individual Gas Molecules Adsorbed on Graphene,” *Nat. Mater.*, vol. 6, no. 9, pp. 652–5, 2017, doi: 10.1038/nmat1967.

[7] A. Nag, A. Mitra, and S. C. Mukhopadhyay, “Graphene and its sensor-based applications: A review,” *Sensors Actuators, A Phys.*, vol. 270, pp. 177–194, 2018, doi: 10.1016/j.sna.2017.12.028.

[8] Y. V. M. Reddy *et al.*, “Strategies, advances, and challenges associated with the use of graphene-based nanocomposites for electrochemical biosensors,” *Adv. Colloid Interface Sci.*, vol. 304, no. April, p. 102664, 2022, doi: 10.1016/j.cis.2022.102664.

[9] P. Recum and T. Hirsch, “Graphene-based chemiresistive gas sensors,” *Nanoscale Adv.*, vol. 6, no. 1, pp. 11–31, 2023, doi: 10.1039/d3na00423f.

[10] Anonymous, “Environmental Gas Sensor Market Size, Share, and Trends 2024 to 2034,” 2024.

[11] Anonymous, “Climate Change,” *United Nations*, 2024. [Online]. Available: https://www.un.org/en/global-issues/climate-change#:~:text=The Paris Agreement’s central aim,have ratified the Paris Agreement. [Accessed: 29-Aug-2024].

[12] Anonymous, “International Work on Climate Change,” *WWF-UK*, 2024. [Online]. Available: https://www.wwf.org.uk/what-we-do/projects/international-work-climate-change.

[13] S. Gujar and D. Vishwakarma, “Gas Sensor Market,” Selbyville, 2023.

[14] Anonymous, “Gas Sensor Market Size,” 2021.

[15] M. Ma, X. Yang, X. Ying, C. Shi, Z. Jia, and B. Jia, “Applications of Gas Sensing in Food Quality Detection: A Review,” *foods*, vol. 12, no. 3966, 2023.

[16] P. Chongthanaphisut, T. Seesaard, and T. Kerdcharoen, “Monitoring of microbial canned food spoilage and contamination based on e-nose for smart home,” *ECTI-CON 2015 - 2015 12th Int. Conf. Electr. Eng. Comput. Telecommun. Inf. Technol.*, 2015, doi: 10.1109/ECTICon.2015.7206960.

[17] Y. Xu, W. Cheung, C. L. Winder, and R. Goodacre, “VOC-based metabolic profiling for food spoilage detection with the application to detecting Salmonella typhimurium-contaminated pork,” *Anal. Bioanal. Chem.*, vol. 397, no. 6, pp. 2439–2449, 2010, doi: 10.1007/s00216-010-3771-z.

[18] J. Park *et al.*, “A bioelectronic sensor based on canine olfactory nanovesicle-carbon nanotube hybrid structures for the fast assessment of food quality,” *Analyst*, vol. 137, no. 14, pp. 3249–3254, 2012, doi: 10.1039/c2an16274a.

[19] S. Márquez-sánchez, J. Huerta-muñoz, and J. Herrera-santos, “Gas sensing in industry . A case study : Train hangar,” *Ad Hoc Networks*, vol. 148, no. May, p. 103205, 2023, doi: 10.1016/j.adhoc.2023.103205.

[20] K. R. Ratinac, W. Yang, S. P. Ringer, and F. Braet, “Toward Ubiquitous Environmental Gas Sensors s Capitalizing on the Promise of Graphene,” vol. 44, no. 4, pp. 1167–1176, 2010.

[21] W. Bourgeois, A. Romain, and R. M. Stuetz, “The use of sensor arrays for

environmental monitoring : interests and limitations," *J. Environ. Monit.*, vol. 5, pp. 852–860, 2003, doi: 10.1039/b307905h.

[22] N. Nasiri and C. Clarke, "Nanostructured Chemiresistive Gas Sensors for Medical Applications," *sensors*, vol. 19, no. 462, pp. 17–19, 2019, doi: 10.3390/s19030462.

[23] S. V Ryabtsev, A. V Shaposhnick, A. N. Lukin, and E. P. Domashevskaya, "Application of semiconductor gas sensors for medical diagnostics," *Sensors Actuators B. Chem.*, vol. 59, pp. 26–29, 1999.

[24] B. Brunekreef and S. T. Holgate, "Air pollution and health," *Lancet*, vol. 360, no. 9341, pp. 1233–1242, 2002, doi: 10.1016/S0140-6736(02)11274-8.

[25] T. Rajabloo, "Ammonia, production, applications, and the effect of its phase-out," 2022.

[26] Z. Guo and B. Wang, "A high-sensitive room temperature gas sensor based on cobalt phthalocyanines and reduced graphene oxide nanohybrids for the ppb-levels of ammonia detection," *RSC Adv.*, no. 2, pp. 37518–37525, 2019, doi: 10.1039/c9ra08065a.

[27] T. M. Chen, J. Gokhale, S. Shofer, and W. G. Kuschner, "Outdoor air pollution: Nitrogen dioxide, sulfur dioxide, and carbon monoxide health effects," *Am. J. Med. Sci.*, vol. 333, no. 4, pp. 249–256, 2007, doi: 10.1097/MAJ.0b013e31803b900f.

[28] "WHO guidelines for air quality.," vol. 35, no. 8, pp. 812–815, 1998.

[29] Kidde, "Carbon Monoxide Levels," 2024. [Online]. Available: https://www.kidde.com/home-safety/en/us/support/help-center/browse-articles/articles/what-are-the-carbon-monoxide-levels-that-will-sound-the-alarm.html#:~:text=Per these requirements%2C standard CO,suffering from pre-existing conditions. [Accessed: 30-Aug-2024].

[30] NIST, "How do Carbon Monoxide Detectors Work?," *How Do You Measure It?*, 2024. [Online]. Available: https://www.nist.gov/how-do-you-measure-it/how-do-carbon-monoxide-detectors-work. [Accessed: 30-Aug-2024].

[31] Safelincs, “Detection Low Level Carbon Monoxide (CO),” *Smoke, Fire & Gas Detection*, 2024. [Online]. Available: https://www.safelincs.co.uk/detecting-low-level-carbon-monoxide/. [Accessed: 30-Aug-2024].

[32] Anonymous, “Modern Breathalyzers,” *Drink Driving in the UK*, 2024. [Online]. Available: https://www.drinkdriving.org/drink_driving_information_breathalysers_modern.php#:~:text=Infrared optical sensor breathalysers use,start to absorb infrared light. [Accessed: 11-Sep-2024].

[33] M. Shouran and I. Elhedmi, “Handheld Evidential Breath Analyser Design,” *Int. J. Adv. Res. Electr. Electron. Instrum. Eng.*, vol. 9, no. 8, pp. 2247–2257, 2020.

[34] K. I. Ozoemena *et al.*, “Fuel cell-based breath-alcohol sensors: Innovation-hungry old electrochemistry,” *Curr. Opin. Electrochem.*, vol. 10, pp. 82–87, 2018, doi: 10.1016/j.coelec.2018.05.007.

[35] A. W. Jones, “Alcohol: Breath Analysis,” *Encycl. Forensic Leg. Med. Second Ed.*, vol. 1, pp. 119–137, 2015, doi: 10.1016/B978-0-12-800034-2.00011-2.

[36] S. Wilbur *et al.*, “Toxicological profile for carbon monoxide,” *U.S. Agency Toxic Subst. Dis. Regist.*, no. June, pp. 1–347, 2012.

[37] N. A. Mohd Bakri, S. A. M. Al Junid, A. H. A. Razak, M. F. Md Idros, and A. K. Halim, “Mobile Carbon Monoxide Monitoring System Based on Arduino-Matlab for Environmental Monitoring Application,” *IOP Conf. Ser. Mater. Sci. Eng.*, vol. 99, no. 1, 2015, doi: 10.1088/1757-899X/99/1/012009.

[38] C. Zhang, K. Xu, K. Liu, J. Xu, and Z. Zheng, “Metal oxide resistive sensors for carbon dioxide detection,” *Coord. Chem. Rev.*, vol. 472, p. 214758, 2022, doi: 10.1016/j.ccr.2022.214758.

[39] T. Aldhafeeri, M. K. Tran, R. Vrolyk, M. Pope, and M. Fowler, “A review of methane gas detection sensors: Recent developments and future perspectives,” *Inventions*, vol. 5, no. 3, pp. 1–18, 2020, doi: 10.3390/inventions5030028.

[40] G. B. Steventon, “Hydrogen sulphide,” *Mol. Death, Second Ed.*, vol. 46, no. 5, pp. 131–147, 2007, doi: 10.1142/9781860948381_0008.

[41] Ricardo Energy & Environment, “Pollutant Information: Sulphur Dioxide,” *National Atmospheric Emissions Inventory*, 2021. [Online]. Available: https://naei.beis.gov.uk/overview/pollutants?pollutant_id=8#:~:text=Sulphur dioxide emissions from fuel,content relative to other fuels. [Accessed: 18-Aug-2024].

[42] B. Beckerman, M. Jerrett, J. R. Brook, D. K. Verma, M. A. Arain, and M. M. Finkelstein, “Correlation of nitrogen dioxide with other traffic pollutants near a major expressway,” *Atmos. Environ.*, vol. 42, no. 2, pp. 275–290, 2008, doi: 10.1016/j.atmosenv.2007.09.042.

[43] Q. Li, W. Zeng, and Y. Li, “Metal oxide gas sensors for detecting NO2 in industrial exhaust gas: Recent developments,” *Sensors Actuators B Chem.*, vol. 359, no. 2, p. 131579, 2022, doi: 10.1016/j.snb.2022.131579.

[44] S. Vigneshvar, C. C. Sudhakumari, B. Senthilkumaran, and H. Prakash, “Recent advances in biosensor technology for potential applications - an overview,” *Front. Bioeng. Biotechnol.*, vol. 4, no. FEB, pp. 1–9, 2016, doi: 10.3389/fbioe.2016.00011.

[45] W. Li *et al.*, “Reduced graphene oxide electrically contacted graphene sensor for highly sensitive nitric oxide detection,” *ACS Nano*, vol. 5, no. 9, pp. 6955–6961, 2011, doi: 10.1021/nn201433r.

[46] C. J. Wysocki, P. Dalton, M. J. Brody, and H. J. Lawley, “Acetone odor and irritation thresholds obtained from acetone-exposed factory workers and from control (occupationally unexposed) subjects,” *Am. Ind. Hyg. Assoc. J.*, vol. 58, no. 10, pp. 704–712, 1997, doi: 10.1080/15428119791012342.

[47] A. Mirzaei, J. H. Kim, H. W. Kim, and S. S. Kim, “Resistive-based gas sensors for detection of benzene, toluene and xylene (BTX) gases: A review,” *J. Mater. Chem. C*, vol. 6, no. 16, pp. 4342–4370, 2018, doi: 10.1039/c8tc00245b.

[48] H. J. Kim, J. W. Yoon, K. Il Choi, H. W. Jang, A. Umar, and J. H. Lee, “Ultraselective and sensitive detection of xylene and toluene for monitoring indoor air pollution using Cr-doped NiO hierarchical nanostructures,” *Nanoscale*, vol. 5, no. 15, pp. 7066–7073, 2013, doi: 10.1039/c3nr01281f.

[49] D. R. Thevenot, K. Toth, R. A. Durst, and G. S. Wilson, “Electrochemical biosensors : recommended definitions and classification,” *Biosens. Bioelectron.*, vol. 16, pp. 121–131, 2001.

[50] S. R. Morrison, “Semiconductor Gas Sensors,” *Sensors & Actuators*, vol. 2, pp. 329–341, 1982, doi: 10.1016/C2017-0-00001-0.

[51] Z. Yunusa, M. N. Hamidon, A. Kaiser, and Z. Awang, “Gas Sensors : A Review,” *Sensors & Transducers*, vol. 168, no. 4, pp. 61–75, 2014.

[52] G. Coelho Rezende, S. Le Calvé, J. J. Brandner, and D. Newport, “Micro photoionization detectors,” *Sensors Actuators, B Chem.*, vol. 287, no. November 2018, pp. 86–94, 2019, doi: 10.1016/j.snb.2019.01.072.

[53] M. A. H. Khan, M. V. Rao, and Q. Li, “Recent advances in electrochemical sensors for detecting toxic gases: NO2, SO2 and H2S,” *Sensors (Switzerland)*, vol. 19, no. 4, 2019, doi: 10.3390/s19040905.

[54] K. Crozier, “An infrared microspectrometer redefining hazard detection,” *The University of Melbourne - Success stories*, 2023. [Online]. Available: https://research.unimelb.edu.au/partnerships/case-studies/infrared-microspectrometer-redefining-hazard-detection. [Accessed: 20-Aug-2024].

[55] M. A. Z. Chowdhury and M. A. Oehlschlaeger, “Deep Learning for Gas Sensing via Infrared Spectroscopy,” *Sensors*, vol. 24, no. 6, 2024, doi: 10.3390/s24061873.

[56] A. M. Azad, S. A. Akbar, S. G. Mhaisalkar, L. D. Birkefeld, and K. S. Goto, “Solid-State Gas Sensors: A Review,” *J. Electrochem. Soc.*, vol. 139, no. 12, pp. 3690–3704, 1992, doi: 10.1149/1.2069145.

[57] J. Wawrzyniak, “Advancements in Improving Selectivity of Metal Oxide Semiconductor Gas Sensors Opening New Perspectives for Their Application in Food Industry,” *sensors*, vol. 23, no. 9548, 2023.

[58] G. W. Hunter *et al.*, “Editors’ Choice—Critical Review—A Critical Review of Solid State Gas Sensors,” *J. Electrochem. Soc.*, vol. 167, no. 3, p. 037570, 2020, doi: 10.1149/1945-7111/ab729c.

[59] S. You, G. Li, Z. Fan, X. Li, L. Fu, and W. Wu, “Nanotechnology-assisted sensors for the detection of carbon monoxide : A review,” *Int. J. Electrochem. Sci.*, vol. 18, no. August, pp. 1–9, 2023, doi: 10.1016/j.ijoes.2023.100314.

[60] J. Y. Xuan *et al.*, “In-situ fabrication of ZnO nanoparticles sensors based on gas-sensing electrode for ppb-level H2S detection at room temperature,” *Chinese Phys. B*, vol. 30, no. 2, 2021, doi: 10.1088/1674-1056/abcf46.

[61] Y. Nagarjuna and Y.-J. Hsiao, “ CuO/ZnO Heterojunction Nanostructured Sensor Prepared on MEMS Device for Enhanced H 2 S Gas Detection ,” *J. Electrochem. Soc.*, vol. 168, no. 6, p. 067521, 2021, doi: 10.1149/1945-7111/ac0aa8.

[62] D. Wang *et al.*, “CO2-sensing properties and mechanism of nano-SnO2 thick-film sensor,” *Sensors Actuators, B Chem.*, vol. 227, pp. 73–84, 2016, doi: 10.1016/j.snb.2015.12.025.

[63] L. Mei *et al.*, “Ultrasensitive ethanol sensor based on 3D aloe-like SnO 2,” *Sensors Actuators, B Chem.*, vol. 166–167, pp. 7–11, 2012, doi: 10.1016/j.snb.2011.06.054.

[64] D. M. Ramos Gonzalez *et al.*, “CO2 sensing performance enhanced by Pt-catalyzed SnO2/porous-silicon hybrid structures,” *Sensors Int.*, vol. 3, no. January, pp. 3–11, 2022, doi: 10.1016/j.sintl.2022.100165.

[65] S. Liu, Z. Wang, H. Zhao, T. Fei, and T. Zhang, “Ordered mesoporous Co3O4 for high-performance toluene sensing,” *Sensors Actuators, B Chem.*, vol. 197, pp. 342–349, 2014, doi: 10.1016/j.snb.2014.03.007.

[66] N. Tamaekong, C. Liewhiran, A. Wisitsoraat, and S. Phanichphant, “Acetylene sensor based on Pt/ZnO thick films as prepared by flame spray pyrolysis,” *Sensors Actuators, B Chem.*, vol. 152, no. 2, pp. 155–161, 2011, doi: 10.1016/j.snb.2010.11.058.

[67] X. Li *et al.*, “Au@In2O3 core-shell composites: A metal-semiconductor heterostructure for gas sensing applications,” *RSC Adv.*, vol. 5, no. 1, pp. 545–551, 2015, doi: 10.1039/c4ra12467g.

[68] J. Wang, M. Yu, X. Li, and Y. Xia, “UV-enhanced NO2 gas sensing properties

of polystyrene sulfonate functionalized ZnO nanowires at room temperature," *Inorg. Chem. Front.*, vol. 6, no. 1, pp. 176–183, 2019, doi: 10.1039/c8qi01110a.

[69] B. Karunagaran, P. Uthirakumar, S. J. Chung, S. Velumani, and E. K. Suh, "TiO2 thin film gas sensor for monitoring ammonia," *Mater. Charact.*, vol. 58, no. 8-9 SPEC. ISS., pp. 680–684, 2007, doi: 10.1016/j.matchar.2006.11.007.

[70] A. D. Amico, G. Ferri, and A. Zompanti, "Sensor Systems for Breathprinting: A Review of the Current Technologies for Exhaled Breath Analysis Based on a Sensor Array With the Aim of Integrating Them in a Standard and Shared Procedure," in *Breath Analysis*, Academic Press, 2019, pp. 49–79.

[71] Y. Geng, W. J. Peveler, V. M. Rotello, and C. B. Program, "Array-based 'Chemical Nose' Sensing in Diagnostics and Drug Discovery," *Angew. Chemie Int. Ed.*, vol. 58, no. 16, pp. 5190–5200, 2019, doi: 10.1002/anie.201809607.Array-based.

[72] M. J. Szary, "Toward high selectivity of sensor arrays : Enhanced adsorption interaction and selectivity of gas detection (N2 , O2 , NO , CO , CO2 , NO2 , SO2 , AlH3 , NH3 , and PH3) on transition metal dichalcogenides (MoS2 , MoSe2 , and MoTe2)," *Acta Mater.*, vol. 274, no. February, 2024, doi: 10.1016/j.actamat.2024.120016.

[73] T. Seiyama, A. Kato, K. Fujiishi, and M. Nagatani, "A New Detector for Gaseous Components Using Semiconductive Thin Films," *Anal. Chem.*, vol. 34, no. 11, pp. 1502–1503, 1962.

[74] R. J. Rath, S. Farajikhah, F. Oveissi, F. Dehghani, and S. Na, "Chemiresistive Sensor Arrays for Gas / Volatile Organic Compounds Monitoring : A Review," *Adv. Eng. Mater.*, vol. 2200830, 2023, doi: 10.1002/adem.202200830.

[75] J. Lee *et al.*, "High-performance gas sensor array for indoor air quality monitoring : the role of Au nanoparticles on WO3, SnO2 and NiO-based gas sensors," pp. 1159–1167, 2021, doi: 10.1039/d0ta08743b.

[76] Y. Zhang, J. Zhao, T. Du, Z. Zhu, J. Zhang, and Q. Liu, "A gas sensor array for the simultaneous detection of multiple VOCs," *Sci. Rep.*, no. January, pp. 1–8, 2017, doi: 10.1038/s41598-017-02150-z.

[77] C. Mackin *et al.*, “Chemiresistive Graphene Sensors for Ammonia Detection,” *ACS Appl. Mater. Interfaces*, vol. 10, no. 18, pp. 16169–16176, 2018, doi: 10.1021/acsami.8b00853.

[78] A. Star, V. Joshi, S. Skarupo, D. Thomas, J. P. Gabriel, and V. Emery, “Gas Sensor Array Based on Metal-Decorated Carbon Nanotubes,” *J. Phys. Chem. B*, vol. 110, pp. 21014–21020, 2006.

[79] J. White, J. S. Kauer, T. A. Dickinson, and D. R. Walt, “Rapid Analyte Recognition in a Device Based on Optical Sensors and the Olfactory System,” *Anal. Chem.*, vol. 68, no. 13, pp. 2191–2202, 1996.

[80] H. Wang *et al.*, “Gas Biosensor Arrays Based on Single-Stranded DNA-Functionalized Single-Walled Carbon Nanotubes for the Detection of Volatile Organic Compound Biomarkers Released by Huanglongbing Disease-Infected Citrus Trees,” *Sensors*, vol. 19, no. 4795, 2019.

[81] K. S. Novoselov *et al.*, “Electric field in atomically thin carbon films,” *Science (80-.).*, vol. 306, no. 5696, pp. 666–669, 2004, doi: 10.1126/science.1102896.

[82] Y. Wang, Z. Li, J. Wang, J. Li, and Y. Lin, “Graphene and graphene oxide: Biofunctionalization and applications in biotechnology,” *Trends Biotechnol.*, vol. 29, no. 5, pp. 205–212, 2011, doi: 10.1016/j.tibtech.2011.01.008.

[83] A. K. Geim and K. S. Novoselov, “The rise of graphene,” *Nat. Mater.*, vol. 6, pp. 183–191, 2007, doi: https://doi.org/10.1038/nmat1849.

[84] R. Forsyth, A. Devadoss, and O. J. Guy, “Graphene Field Effect Transistors for Biomedical Applications: Current Status and Future Prospects,” *Diagnostics*, vol. 7, no. 3, p. 45, 2017, doi: 10.3390/diagnostics7030045.

[85] O. J. Guy, G. Burwell, Z. Tehrani, A. Castaing, K. A. Walker, and S. H. Doak, “Graphene nano-biosensors for detection of cancer risk,” *Mater. Sci. Forum*, vol. 711, pp. 246–252, 2012, doi: 10.4028/www.scientific.net/MSF.711.246.

[86] M. Z. Iqbal and A. U. Rehman, “Recent progress in graphene incorporated solar cell devices,” *Sol. Energy*, vol. 169, no. May, pp. 634–647, 2018, doi: 10.1016/j.solener.2018.04.041.

[87] A. Ali Tahir, H. Ullah, P. Sudhagar, M. Asri Mat Teridi, A. Devadoss, and S. Sundaram, "The Application of Graphene and Its Derivatives to Energy Conversion, Storage, and Environmental and Biosensing Devices," *Chem. Rec.*, pp. 1591–1634, 2016, doi: 10.1002/tcr.201500279.

[88] K. Rana, J. Singh, and J. H. Ahn, "A graphene-based transparent electrode for use in flexible optoelectronic devices," *J. Mater. Chem. C*, vol. 2, no. 15, pp. 2646–2656, 2014, doi: 10.1039/c3tc32264e.

[89] B. Zhan, C. Li, J. Yang, G. Jenkins, W. Huang, and X. Dong, "Graphene field-effect transistor and its application for electronic sensing," *Small*, vol. 10, no. 20, pp. 4042–4065, 2014, doi: 10.1002/smll.201400463.

[90] V. Dhand, K. Y. Rhee, H. Ju Kim, and D. Ho Jung, "A comprehensive review of graphene nanocomposites: Research status and trends," *J. Nanomater.*, vol. 2013, 2013, doi: 10.1155/2013/763953.

[91] M. S. Fuhrer, C. N. Lau, and A. H. MacDonald, "Graphene: Materially Better Carbon," *MRS Bull.*, vol. 35, no. 4, pp. 289–295, 2010, doi: 10.1557/mrs2010.551.

[92] H. Liu, H. Liu, and D. Zhu, "Chemical doping of graphene," *J. Mater. Chem.*, vol. 21, no. 10, pp. 3335–3345, 2011, doi: 10.1039/c0jm02922j.

[93] S. Peng, J. Zhang, Z. Jin, D. Zhang, J. Shi, and S. Wei, "Electric-Field Induced Doping Polarity Conversion in Top-Gated Transistor Based on Chemical Vapor Deposition of Graphene," *Crystals*, pp. 0–7, 2022.

[94] A. Das *et al.*, "Monitoring dopants by Raman scattering in an electrochemically top-gated graphene transistor," vol. 3, no. April, pp. 1–6, 2008, doi: 10.1038/nnano.2008.67.

[95] H. Pinto and A. Markevich, "Electronic and electrochemical doping of graphene by surface adsorbates," *Beilstein J. Nanotechnol.*, vol. 5, no. 1, pp. 1842–1848, 2014, doi: 10.3762/bjnano.5.195.

[96] D. Zhan, J. Yan, L. Lai, Z. Ni, L. Liu, and Z. Shen, "Engineering the electronic structure of graphene," *Adv. Mater.*, vol. 24, no. 30, pp. 4055–4069, 2012, doi: 10.1002/adma.201200011.

[97] K. Nagashio, T. Yamashita, T. Nishimura, K. Kita, and A. Toriumi, “Electrical transport properties of graphene on SiO2 with specific surface structures,” *J. Appl. Phys.*, vol. 110, no. 2, 2011, doi: 10.1063/1.3611394.

[98] P. Joshi, H. E. Romero, A. T. Neal, V. K. Toutam, and S. A. Tadigadapa, “Intrinsic doping and gate hysteresis in graphene field effect devices fabricated on SiO2 substrates,” *J. Phys. Condens. Matter*, vol. 22, no. 33, 2010, doi: 10.1088/0953-8984/22/33/334214.

[99] S. D. Costa, J. Weis, O. Frank, M. Fridrichova, and M. Kalbac, “Monitoring the doping of graphene on SiO2/Si substrates during the thermal annealing process,” *RSC Adv.*, vol. 00, pp. 1–6, 2016, doi: 10.1039/C6RA10764H.

[100] Y. Kang, J. Kang, and K. J. Chang, “Electronic structure of graphene and doping effect on SiO2,” *Phys. Rev. B*, no. April, pp. 1–5, 2008, doi: 10.1103/PhysRevB.78.115404.

[101] S. K. Jang, J. Jeon, S. M. Jeon, Y. J. Song, and S. Lee, “Effects of dielectric material properties on graphene transistor performance,” *Solid. State. Electron.*, vol. 109, pp. 8–11, 2015, doi: 10.1016/j.sse.2015.03.003.

[102] T. Hayasaka, Y. Kubota, Y. Liu, and L. Lin, “The influences of temperature, humidity, and O2 on electrical properties of graphene FETs,” *Sensors Actuators, B Chem.*, vol. 285, no. December 2018, pp. 116–122, 2019, doi: 10.1016/j.snb.2019.01.037.

[103] R. A. Nistor, M. A. Kuroda, A. A. Maarouf, and G. J. Martyna, “Doping of adsorbed graphene from defects and impurities in SiO 2 substrates,” vol. 041409, pp. 1–5, 2012, doi: 10.1103/PhysRevB.86.041409.

[104] S. Ryu *et al.*, “Atmospheric Oxygen Binding and Hole Doping in Deformed Graphene on a SiO 2 Substrate,” *Nano Lett.*, vol. 10, pp. 4944–4951, 2010, doi: 10.1021/nl1029607.

[105] Y. Yang, K. Brenner, and R. Murali, “The influence of atmosphere on electrical transport in graphene,” *Carbon N. Y.*, vol. 50, no. 5, pp. 1727–1733, 2011, doi: 10.1016/j.carbon.2011.12.008.

[106] Y. Yang and R. Murali, “Binding mechanisms of molecular oxygen and

moisture to graphene," *Appl. Phys. Lett.*, vol. 093116, pp. 2011–2014, 2011, doi: 10.1063/1.3562317.

[107] A. Adetayo and D. Runsewe, "Synthesis and Fabrication of Graphene and Graphene Oxide: A Review," *Open J. Compos. Mater.*, vol. 09, no. 02, pp. 207–229, 2019, doi: 10.4236/ojcm.2019.92012.

[108] X. Y. Wang, A. Narita, and K. Müllen, "Precision synthesis versus bulk-scale fabrication of graphenes," *Nat. Rev. Chem.*, vol. 2, no. 1, pp. 1–10, 2018, doi: 10.1038/S41570-017-0100.

[109] M. Lotya *et al.*, "Liquid phase production of graphene by exfoliation of graphite in surfactant/water solutions," *J. Am. Chem. Soc.*, vol. 131, no. 10, pp. 3611–3620, 2009, doi: 10.1021/ja807449u.

[110] Y. L. Zhong, Z. Tian, G. P. Simon, and D. Li, "Scalable production of graphene via wet chemistry: Progress and challenges," *Mater. Today*, vol. 18, no. 2, pp. 73–78, 2015, doi: 10.1016/j.mattod.2014.08.019.

[111] Y. B. Pottathara, Y. Grohens, V. Kokol, N. Kalarikkal, and S. Thomas, *Synthesis and processing of emerging two-dimensional nanomaterials*. Elsevier Inc., 2019.

[112] H. Tetlow, J. Posthuma de Boer, I. J. Ford, D. D. Vvedensky, J. Coraux, and L. Kantorovich, "Growth of epitaxial graphene: Theory and experiment," *Phys. Rep.*, vol. 542, no. 3, pp. 195–295, 2014, doi: 10.1016/j.physrep.2014.03.003.

[113] A. Gutiérrez-Cruz, A. R. Ruiz-Hernández, J. F. Vega-Clemente, D. G. Luna-Gazcón, and J. Campos-Delgado, "A review of top-down and bottom-up synthesis methods for the production of graphene, graphene oxide and reduced graphene oxide," *J. Mater. Sci.*, vol. 57, no. 31, pp. 14543–14578, 2022, doi: 10.1007/s10853-022-07514-z.

[114] X. Chen, L. Zhang, and S. Chen, "Large area CVD growth of graphene," *Synth. Met.*, vol. 210, pp. 95–108, 2015, doi: 10.1016/j.synthmet.2015.07.005.

[115] M. S. A. Bhuyan, M. N. Uddin, M. M. Islam, F. A. Bipasha, and S. S. Hossain, "Synthesis of graphene," *Int. Nano Lett.*, vol. 6, no. 2, pp. 65–83, 2016, doi: 10.1007/s40089-015-0176-1.

[116] K. Parvez, S. Yang, X. Feng, and K. Müllen, “Exfoliation of graphene via wet chemical routes,” *Synth. Met.*, vol. 210, pp. 123–132, 2015, doi: 10.1016/j.synthmet.2015.07.014.

[117] N. Camara *et al.*, “Selective epitaxial growth of graphene on SiC,” *Appl. Phys. Lett.*, vol. 93, no. 12, pp. 2006–2009, 2008, doi: 10.1063/1.2988645.

[118] C. Melios, V. Panchal, K. Edmonds, A. Lartsev, R. Yakimova, and O. Kazakova, “Detection of Ultralow Concentration NO2 in Complex Environment Using Epitaxial Graphene Sensors,” *ACS Sensors*, vol. 3, no. 9, pp. 1666–1674, 2018, doi: 10.1021/acssensors.8b00364.

[119] S. Novikov, N. Lebedeva, and A. Satrapinski, “Ultrasensitive NO2 Gas Sensor Based on Epitaxial Graphene,” *J. Sensors*, vol. 2015, 2015, doi: 10.1155/2015/108581.

[120] M. W. K. Nomani *et al.*, “Highly sensitive and selective detection of NO2 using epitaxial graphene on 6H-SiC,” *Sensors Actuators, B Chem.*, vol. 150, no. 1, pp. 301–307, 2010, doi: 10.1016/j.snb.2010.06.069.

[121] V. K. Nagareddy *et al.*, “Improved Chemical Detection and Ultra-Fast Recovery Using Oxygen Functionalized Epitaxial Graphene Sensors,” vol. 13, no. 8, pp. 2810–2817, 2013.

[122] R. R. Sagar, X. Zhang, and C. Xiong, “Growth of graphene on copper and nickel foils via chemical vapour deposition using ethylene,” *Mater. Res. Innov.*, vol. 18, no. August, pp. S4706–S4710, 2014, doi: 10.1179/1432891714Z.000000000771.

[123] M. I. Kairi, M. Khavarian, A. R. Mohamed, and S. A. Bakar, “Recent trends in graphene materials synthesized by CVD with various carbon precursors,” *J. Mater. Sci.*, vol. 53, no. 2, pp. 851–879, 2018, doi: 10.1007/s10853-017-1694-1.

[124] S. J. Chang *et al.*, “Graphene growth from reduced graphene oxide by chemical vapour deposition: Seeded growth accompanied by restoration,” *Sci. Rep.*, vol. 6, no. March, pp. 1–9, 2016, doi: 10.1038/srep22653.

[125] N. Alzate-carvajal and A. Luican-mayer, “Functionalized Graphene Surfaces

for Selective Gas Sensing," *ACS Omega*, vol. 5, pp. 21320–21329, 2020, doi: 10.1021/acsomega.0c02861.

[126] H. Y. Mao, Y. H. Lu, J. D. Lin, S. Zhong, A. T. S. Wee, and W. Chen, "Manipulating the electronic and chemical properties of graphene via molecular functionalization," *Prog. Surf. Sci.*, vol. 88, no. 2, pp. 132–159, 2013, doi: 10.1016/j.progsurf.2013.02.001.

[127] V. Georgakilas *et al.*, "Functionalization of graphene: Covalent and non-covalent approaches, derivatives and applications," *Chem. Rev.*, vol. 112, no. 11, pp. 6156–6214, 2012, doi: 10.1021/cr3000412.

[128] A. Criado, M. Melchionna, S. Marchesan, and M. Prato, "The Covalent Functionalization of Graphene on Substrates," *Angew. Chemie - Int. Ed.*, vol. 54, no. 37, pp. 10734–10750, 2015, doi: 10.1002/anie.201501473.

[129] D. Yoo, J. Kim, and J. H. Kim, "Direct synthesis of highly conductive poly (3 , 4- ethylenedioxythiophene): poly (4-styrenesulfonate) (PEDOT : PSS)/ graphene composites and their applications in energy harvesting systems," vol. 7, no. 5, pp. 717–730, 2014, doi: 10.1007/s12274-014-0433-z.

[130] S. Drewniak, R. Muzyka, A. Stolarczyk, and T. Pustelny, "Studies of Reduced Graphene Oxide and Graphite Oxide in the Aspect of Their Possible Application in Gas Sensors," *sensors*, vol. 16, no. 103, 2016, doi: 10.3390/s16010103.

[131] C. Chung, Y. Kim, D. Shin, S. Ryoo, B. H. E. E. Hong, and D. Min, "Biomedial Applications of Graphene and Graphene Oxide," *Acc. Chem. Res.*, vol. 46, no. 10, pp. 2211–2224, 2013.

[132] S. Teixeira, R. S. Conlan, O. J. Guy, and M. G. F. Sales, "Novel single-wall carbon nanotube screen-printed electrode as an immunosensor for human chorionic gonadotropin," *Electrochim. Acta*, vol. 136, pp. 323–329, 2014, doi: 10.1016/j.electacta.2014.05.105.

[133] S. Teixeira, G. Burwell, A. Castaing, D. Gonzalez, R. S. Conlan, and O. J. Guy, "Epitaxial graphene immunosensor for human chorionic gonadotropin," *Sensors Actuators, B Chem.*, vol. 190, pp. 723–729, 2014, doi:

10.1016/j.snb.2013.09.019.

[134] S. Teixeira, N. S. Ferreira, R. S. Conlan, O. J. Guy, and M. G. F. Sales, “Chitosan/AuNPs Modified Graphene Electrochemical Sensor for Label-Free Human Chorionic Gonadotropin Detection,” *Electroanalysis*, vol. 26, no. 12, pp. 2591–2598, 2014, doi: 10.1002/elan.201400311.

[135] J. Park and M. Yan, “Covalent Functionalization of Graphene with Reactive intermediates,” *Org. Synth. Highlights III*, vol. 46, no. 1, pp. 181–189, 2012, doi: 10.1021/ar300172h.

[136] A. Sinitskii, A. Dimiev, D. A. Corley, A. A. Fursina, D. V. Kosynkin, and J. M. Tour, “Kinetics of diazonium functionalization of chemically converted graphene nanoribbons,” *ACS Nano*, vol. 4, no. 4, pp. 1949–1954, 2010, doi: 10.1021/nn901899j.

[137] O. J. Guy, A. Castaing, Z. Tehrani, and S. H. Doak, “Fabrication of ultrasensitive graphene nanobiosensors,” *Proc. IEEE Sensors*, pp. 907–912, 2010, doi: 10.1109/ICSENS.2010.5690883.

[138] Z. Tehrani *et al.*, “Generic epitaxial graphene biosensors for ultrasensitive detection of cancer risk biomarker,” *2D Mater.*, vol. 1, no. 2, 2014, doi: 10.1088/2053-1583/1/2/025004.

[139] X. Zhang *et al.*, “Impact of chlorine functionalization on high-mobility chemical vapor deposition grown graphene,” *ACS Nano*, vol. 7, no. 8, pp. 7262–7270, 2013, doi: 10.1021/nn4026756.

[140] J. Wu *et al.*, “Controlled chlorine plasma reaction for noninvasive graphene doping,” *J. Am. Chem. Soc.*, vol. 133, no. 49, pp. 19668–19671, 2011, doi: 10.1021/ja2091068.

[141] K. J. Jeon *et al.*, “Fluorographene: A wide bandgap semiconductor with ultraviolet luminescence,” *ACS Nano*, vol. 5, no. 2, pp. 1042–1046, 2011, doi: 10.1021/nn1025274.

[142] P. T. Yin, S. Shah, M. Chhowalla, and K. B. Lee, “Design, synthesis, and characterization of graphene-nanoparticle hybrid materials for bioapplications,” *Chem. Rev.*, vol. 115, no. 7, pp. 2483–2531, 2015, doi:

10.1021/cr500537t.

[143] W. Fu, L. Jiang, E. P. van Geest, L. M. C. Lima, and G. F. Schneider, “Sensing at the Surface of Graphene Field-Effect Transistors,” *Adv. Mater.*, vol. 29, no. 6, pp. 1–25, 2017, doi: 10.1002/adma.201603610.

[144] J. Katoch *et al.*, “Structure of a peptide adsorbed on graphene and graphite,” *Nano Lett.*, vol. 12, no. 5, pp. 2342–2346, 2012, doi: 10.1021/nl300286k.

[145] F. Walters *et al.*, “Real-time detection of hepatitis B surface antigen using a hybrid graphene-gold nanoparticle biosensor,” *2D Mater.*, vol. 7, no. 2, 2020, doi: 10.1088/2053-1583/ab734c.

[146] L. Xia, Z. Wei, and M. Wan, “Conducting polymer nanostructures and their application in biosensors,” *J. Colloid Interface Sci.*, vol. 341, no. 1, pp. 1–11, 2010, doi: 10.1016/j.jcis.2009.09.029.

[147] H. Cheng, R. Shiue, C. Tsai, W. Wang, and Y. Chen, “High-Quality Graphene p−n Junctions via Resist-free Fabrication and Solution-Based Noncovalent Functionalization,” *ACS Nano*, vol. 5, no. 3, pp. 2051–2059, 2011.

[148] S. Teixeira, R. S. Conlan, O. J. Guy, and M. G. F. Sales, “Label-free human chorionic gonadotropin detection at picogram levels using oriented antibodies bound to graphene screen-printed electrodes,” *J. Mater. Chem. B*, vol. 2, no. 13, pp. 1852–1865, 2014, doi: 10.1039/c3tb21235a.

[149] A. Devadoss *et al.*, “Ultrathin Functional Polymer Modified Graphene for Enhanced Enzymatic Electrochemical Sensing,” *Biosensors*, vol. 9, no. 1, pp. 1–12, 2019, doi: 10.3390/bios9010016.

[150] H. Y. Abbasi *et al.*, “Graphene based electrochemical immunosensor for the ultra-sensitive label free detection of Alzheimer’s beta amyloid peptides Aβ(1-42),” *Nanoscale Adv.*, vol. 3, no. 8, pp. 2295–2304, 2021, doi: 10.1039/d0na00801j.

[151] B. H. Nguyen *et al.*, “Development of label-free electrochemical lactose biosensor based on graphene/poly(1,5-diaminonaphthalene) film,” *Curr. Appl. Phys.*, vol. 16, no. 2, pp. 135–140, 2016, doi: 10.1016/j.cap.2015.11.004.

[152] T. D. Nguyen *et al.*, "One-step Electrosynthesis of Poly(1,5-diaminonaphthalene)/Graphene Nanocomposite as Platform for Lead Detection in Water," *Electroanalysis*, vol. 28, no. 8, pp. 1907–1913, 2016, doi: 10.1002/elan.201501075.

[153] V. R. Cooper, L. C.N., Y. Wang, and B. G. Sumpter, "Noncovalent Interactions in Nanotechnology," in *Noncovalent Interactions in Quantum Chemistry and Physics*, Amsterdam: Elsevier, 2017, pp. 417–451.

[154] Z. Zhang, H. Huang, X. Yang, and L. Zang, "Tailoring Electronic Properties of Graphene by pi - pi Stacking with Aromatic Molecules," *J. Phys. Chem. Lett.*, vol. 2, pp. 2897–2905, 2011.

[155] F. Walters *et al.*, "A facile method for the non-covalent amine functionalization of carbon-based surfaces for use in biosensor development," *Nanomaterials*, vol. 10, no. 9, pp. 1–14, 2020, doi: 10.3390/nano10091808.

[156] D. H. Shin *et al.*, "Flower-like Palladium Nanoclusters Decorated Graphene Electrodes for Ultrasensitive and Flexible Hydrogen Gas Sensing," *Sci. Rep.*, vol. 5, no. July, pp. 1–11, 2015, doi: 10.1038/srep12294.

[157] N. J. de Mol and M. J. E. Fischer, "Amine Coupling Through EDC/NHS: A Practical Approach," *Life Sci.*, p. 255, 2010, doi: 10.1007/978-1-60761-670-2.

[158] S. H. Lee, H. J. Jin, H. S. Song, S. Hong, and T. H. Park, "Bioelectronic nose with high sensitivity and selectivity using chemically functionalized carbon nanotube combined with human olfactory receptor," *J. Biotechnol.*, vol. 157, no. 4, pp. 467–472, 2012, doi: 10.1016/j.jbiotec.2011.09.011.

[159] Y. L. Lee, C. Y. Sheu, and R. H. Hsiao, "Gas sensing characteristics of copper phthalocyanine films: Effects of film thickness and sensing temperature," *Sensors Actuators, B Chem.*, vol. 99, no. 2–3, pp. 281–287, 2004, doi: 10.1016/j.snb.2003.11.024.

[160] N. Padma *et al.*, "NO2 sensors with room temperature operation and long term stability using copper phthalocyanine thin films," *Sensors Actuators, B Chem.*, vol. 143, no. 1, pp. 246–252, 2009, doi: 10.1016/j.snb.2009.07.044.

[161] L. P. P. I, P. Part, and I. A. N. Type, "Part I. A new type of synthetic colouring

matters," no. 1016, pp. 1933–1934, 1933.

[162] A. B. Sorokin, "Phthalocyanine metal complexes in catalysis," *Chem. Rev.*, vol. 113, no. 10, pp. 8152–8191, 2013, doi: 10.1021/cr4000072.

[163] H. G. Wang, H. Wang, Y. Li, Y. Wang, and Z. Si, "A bipolar metal phthalocyanine complex for sodium dual-ion battery," *J. Energy Chem.*, vol. 58, pp. 9–16, 2021, doi: 10.1016/j.jechem.2020.09.023.

[164] Y. Terao, H. Sasabe, and C. Adachi, "Correlation of hole mobility, exciton diffusion length, and solar cell characteristics in phthalocyanine/fullerene organic solar cells," *Appl. Phys. Lett.*, vol. 90, no. 10, pp. 32–35, 2007, doi: 10.1063/1.2711525.

[165] R. M. Wang, H. Wang, Y. Wang, H. R. Li, Y. F. He, and E. X. Hao, "Preparation and photocatalytic activity of chitosan-supported cobalt phthalocyanine membrane," *Color. Technol.*, vol. 130, no. 1, pp. 32–36, 2014, doi: 10.1111/cote.12062.

[166] F. I. Bohrer *et al.*, "Comparative gas sensing in cobalt, nickel, copper, zinc, and metal-free phthalocyanine chemiresistors," *J. Am. Chem. Soc.*, vol. 131, no. 2, pp. 478–485, 2009, doi: 10.1021/ja803531r.

[167] T. A. Jones and B. Bott, "Gas-induced electrical conductivity changes in metal phthalocyanines," vol. 9, pp. 27–37, 1986.

[168] R. Jaisutti and T. Osotchan, "An investigation of molecular interactions between zinc phthalocyanine thin film and various oxidizing gases for sensor applications," *Adv. Mater. Res.*, vol. 403–408, no. 2, pp. 48–51, 2012, doi: 10.4028/www.scientific.net/AMR.403-408.48.

[169] B. Schöllhorn, J. P. Germain, A. Pauly, C. Maleysson, and J. P. Blanc, "Influence of peripheral electron-withdrawing substituents on the conductivity of zinc phthalocyanine in the presence of gases. Part 1: Reducing gases," *Thin Solid Films*, vol. 326, no. 1–2, pp. 245–250, 1998, doi: 10.1016/S0040-6090(98)00553-7.

[170] M. S. Nieuwenhuizen, A. J. Nederlof, and A. W. Barendsz, "Metallophthalocyanines as Chemical Interfaces on a Surface Acoustic Wave

Gas Sensor for Nitrogen Dioxide," *Anal. Chem.*, vol. 235, no. 35, pp. 230–235, 1988.

[171] T. V Basova, E. K. Kol, and I. K. Igumenov, "Spectral investigation of interaction of copper phthalocyanine with nitrogen dioxide," *Sensors Actuators B. Chem.*, vol. 105, no. 2, pp. 259–265, 2005, doi: 10.1016/j.snb.2004.06.007.

[172] J. D. Wright, "GAS ADSORPTION ON PHTHALOCYANINES AND ITS EFFECTS ON ELECTRICAL PROPERTIES," *Prog. Surf. Sci.*, vol. 31, pp. 1–60.

[173] L. Lozzi, S. Picozzi, S. Santucci, C. Cantalini, and B. Delley, "Photoemission and theoretical investigations on NO2 doping of copper phthalocyanine thin films," *J. Electron Spectrosc.*, vol. 140, no. 2, pp. 101–105, 2004, doi: 10.1016/j.elspec.2004.02.034.

[174] J. H. Park *et al.*, "Atomic Imaging of the Irreversible Sensing Mechanism of NO2 Adsorption on Copper Phthalocyanine," *J. Am. Chem. Soc.*, vol. 135, no. 2, pp. 14600–14609, 2013.

[175] L. S. Chia, Y. H. Du, S. Palale, and P. S. Lee, "Interaction of Copper Phthalocyanine with Nitrogen Dioxide and Ammonia Investigation Using X-ray Absorption Spectroscopy and Chemiresistive Gas Measurements," *ACS Omega*, vol. 4, no. 6, pp. 10388–10395, 2019, doi: 10.1021/acsomega.8b02108.

[176] B. Wang, X. Wang, X. Li, Z. Guo, X. Zhou, and Y. Wu, "The effects of amino substituents on the enhanced ammonia sensing performance of PcCo / rGO," *RSC Adv.*, vol. 8, pp. 41280–41287, 2018, doi: 10.1039/c8ra07509c.

[177] M. S. Polyakov *et al.*, "Effect of covalent and non-covalent linking of zinc (II) phthalocyanine functionalised carbon nanomaterials on the sensor response to ammonia," *Synth. Met.*, vol. 227, pp. 78–86, 2017, doi: 10.1016/j.synthmet.2017.02.024.

[178] W. Jiang *et al.*, "Room temperature DMMP gas sensing based on cobalt phthalocyanine derivative/graphene quantum dot hybrid materials," *RSC Adv.*, vol. 11, no. 24, pp. 14805–14813, 2021, doi: 10.1039/d1ra01975a.

[179] P. Jha *et al.*, "Functionalization of carbon nanotubes with metal phthalocyanine

for SELECTIVE gas sensing application," *Synth. React. Inorganic, Met. Nano-Metal Chem.*, vol. 44, no. 10, pp. 1551–1557, 2014, doi: 10.1080/15533174.2013.818021.

[180] W. Jiang *et al.*, "Enhancing room-temperature NO2gas sensing performance based on a metal phthalocyanine/graphene quantum dot hybrid material," *RSC Adv.*, vol. 11, no. 10, pp. 5618–5628, 2021, doi: 10.1039/d0ra10310a.

[181] S. Kumar *et al.*, "Room temperature highly sensitive chlorine sensor based on reduced graphene oxide anchored with substituted copper phthalocyanine," *Sensors Actuators, B Chem.*, vol. 327, no. September 2020, p. 128925, 2021, doi: 10.1016/j.snb.2020.128925.

[182] B. Wang, X. Zhou, Y. Wu, Z. Chen, and C. He, "Lead phthalocyanine modified carbon nanotubes with enhanced NH3 sensing performance," *Sensors Actuators, B Chem.*, vol. 171–172, pp. 398–404, 2012, doi: 10.1016/j.snb.2012.04.084.

[183] B. Wang, X. Wang, Z. J. Guo, S. Gai, Y. Li, and Y. Wu, "A highly sensitive ppb-level H2S gas sensor based on fluorophenoxy-substituted phthalocyanine cobalt/rGO hybrids at room temperature," *RSC Adv.*, vol. 11, no. 11, pp. 5993–6001, 2021, doi: 10.1039/d0ra08832c.

[184] F. Schedin, A. K. Geim, S. V. Morozov, E. W. Hill, and M. I. Blake, "Detection of Individual Gas Moelcules Adsorbed on Graphene," *Nat. Mater.*, vol. 6, no. 9, pp. 652–655, 2007.

[185] C. Melios, V. Panchal, K. Edmonds, A. Lartsev, R. Yakimova, and O. Kazakova, "Detection of Ultra-low Concentration NO2 in Complex Environment Using Epitaxial Graphene Sensors," *ACS Sensors*, vol. 3, no. 9, pp. 1666–1674, 2018, doi: 10.1021/acssensors.8b00364.

[186] F. Zhang *et al.*, "Recent advances on graphene: Synthesis, properties and applications," *Compos. Part A Appl. Sci. Manuf.*, vol. 160, no. April, p. 107051, 2022, doi: 10.1016/j.compositesa.2022.107051.

[187] D. Shahdeo, A. Roberts, N. Abbineni, and S. Gandhi, *Graphene based sensors*, 1st ed., vol. 91. Elsevier B.V., 2020.

[188] B. C. Janegitz *et al.*, “The application of graphene for in vitro and in vivo electrochemical biosensing,” *Biosens. Bioelectron.*, vol. 89, pp. 224–233, 2017, doi: 10.1016/j.bios.2016.03.026.

[189] N. Bhalla, P. Jolly, N. Formisano, and P. Estrela, “Introduction to biosensors,” *Essays Biochem.*, vol. 60, no. 1, pp. 1–8, 2016, doi: 10.1042/EBC20150001.

[190] D. M. Goodwin, F. Walters, M. M. Ali, E. Daghigh Ahmadi, and O. J. Guy, “Graphene bioelectronic nose for the detection of odorants with human olfactory receptor 2ag1,” *Chemosensors*, vol. 9, no. 7, pp. 1–12, 2021, doi: 10.3390/chemosensors9070174.

[191] H. D. Jang, S. K. Kim, H. Chang, K. M. Roh, J. W. Choi, and J. Huang, “A glucose biosensor based on TiO2-Graphene composite,” *Biosens. Bioelectron.*, vol. 38, no. 1, pp. 184–188, 2012, doi: 10.1016/j.bios.2012.05.033.

[192] A. Pandey, Y. Gurbuz, V. Ozguz, J. H. Niazi, and A. Qureshi, “Graphene-interfaced electrical biosensor for label-free and sensitive detection of foodborne pathogenic E. coli O157:H7,” *Biosens. Bioelectron.*, vol. 91, no. December 2016, pp. 225–231, 2017, doi: 10.1016/j.bios.2016.12.041.

[193] Z. Tao, J. Du, Y. Cheng, and Q. Li, “Electrochemical immune analysis system for gastric cancer biomarker carcinoembryonic antigen (CEA) detection,” *Int. J. Electrochem. Sci.*, vol. 13, no. 2, pp. 1413–1422, 2018, doi: 10.20964/2018.02.21.

[194] T. Beduk *et al.*, “Rapid Point-of-Care COVID-19 Diagnosis with a Gold-Nanoarchitecture-Assisted Laser-Scribed Graphene Biosensor,” *Anal. Chem.*, vol. 93, no. 24, pp. 8585–8594, 2021, doi: 10.1021/acs.analchem.1c01444.

[195] Y. Li, Y. Zhu, C. Wang, M. He, and Q. Lin, “Selective detection of water pollutants using a differential aptamer-based graphene biosensor,” *Biosens. Bioelectron.*, vol. 126, no. October 2018, pp. 59–67, 2019, doi: 10.1016/j.bios.2018.10.047.

[196] R. Sha, S. Badhulika, and A. Mulchandani, *Graphene-Based Biosensors and Their Applications in Biomedical and Environmental Monitoring*, vol. 16, no. July. Springer, Cham, 2017.

[197] W. Shi, X. Yu, Y. Zheng, and J. Yu, "DNA based chemical sensor for the detection of nitrogen dioxide enabled by organic field-effect transistor," *Sensors Actuators, B Chem.*, vol. 222, pp. 1003–1011, 2016, doi: 10.1016/j.snb.2015.09.040.

[198] Y. Takada, R. Otsuka, and K. Tsukada, "A Carbon Monoxide Sensing Film Based on Hemoglobin Allostery," *J. Biomed. Sci. Eng.*, vol. 07, no. 04, pp. 173–180, 2014, doi: 10.4236/jbise.2014.74021.

[199] J. Baranwal, B. Barse, G. Gatto, and G. Broncova, "Electrochemical Sensors and Their Applications : A Review," *Chemosensors*, vol. 10, no. 363, 2022.

[200] B. R. Adhikari, M. Govindhan, and A. Chen, "Sensitive detection of acetaminophen with graphene-based electrochemical sensor," *Electrochim. Acta*, vol. 162, pp. 198–204, 2015, doi: 10.1016/j.electacta.2014.10.028.

[201] A. Cernat, M. Tertiş, R. Săndulescu, F. Bedioui, A. Cristea, and C. Cristea, "Electrochemical sensors based on carbon nanomaterials for acetaminophen detection: A review," *Anal. Chim. Acta*, vol. 886, pp. 16–28, 2015, doi: 10.1016/j.aca.2015.05.044.

[202] X. Kang, J. Wang, H. Wu, J. Liu, I. A. Aksay, and Y. Lin, "A graphene-based electrochemical sensor for sensitive detection of paracetamol," *Talanta*, vol. 81, no. 3, pp. 754–759, 2010, doi: 10.1016/j.talanta.2010.01.009.

[203] A. Pandikumar *et al.*, "Graphene and its nanocomposite material based electrochemical sensor platform for dopamine," *RSC Adv.*, vol. 4, no. 108, pp. 63296–63323, 2014, doi: 10.1039/c4ra13777a.

[204] M. Du, T. Yang, and K. Jiao, "Immobilization-free direct electrochemical detection for DNA specific sequences based on electrochemically converted gold nanoparticles/graphene composite film," *J. Mater. Chem.*, vol. 20, no. 41, pp. 9253–9260, 2010, doi: 10.1039/c0jm01549k.

[205] R. S. Andre *et al.*, "Sensing Materials: Nanofibers Produced by Electrospinning and Solution Blow Spinning," in *Encyclopedia of Sensors and Biosensors*, Elsevier, 2023, pp. 521–541.

[206] X. Yan, Y. Wu, R. Li, C. Shi, and R. Moro, "High-Performance UV-Assisted

NO 2 Sensor Based on Chemical Vapor Deposition Graphene at Room Temperature," *ACS Omega*, vol. 4, pp. 14179–14187, 2019, doi: 10.1021/acsomega.9b00935.

[207] S. Hong *et al.*, "FET-type gas sensors: A review," *Sensors Actuators, B Chem.*, vol. 330, no. November 2020, p. 129240, 2021, doi: 10.1016/j.snb.2020.129240.

[208] M. Shimatani *et al.*, "Giant Dirac point shift of graphene phototransistors by doped silicon substrate current," *AIP Adv.*, vol. 6, no. 3, 2016, doi: 10.1063/1.4944622.

[209] M. Farahmandpour, H. Haghshenas, and Z. Kordrostami, "Blood glucose sensing by back gated transistor strips sensitized by CuO hollow spheres and rGO," *Sci. Rep.*, vol. 12, no. 1, 2022, doi: 10.1038/s41598-022-26287-8.

[210] D. Kwong Hong Tsang *et al.*, "Chemically Functionalised Graphene FET Biosensor for the Label-free Sensing of Exosomes," *Sci. Rep.*, vol. 9, no. 1, pp. 2–11, 2019, doi: 10.1038/s41598-019-50412-9.

[211] R. Kumar, D. K. Avasthi, and A. Kaur, "Fabrication of chemiresistive gas sensors based on multistep reduced graphene oxide for low parts per million monitoring of sulfur dioxide at room temperature," *Sensors Actuators, B Chem.*, vol. 242, pp. 461–468, 2017, doi: 10.1016/j.snb.2016.11.018.

[212] T. Hayasaka *et al.*, "An electronic nose using a single graphene FET and machine learning for water, methanol, and ethanol," *Microsystems Nanoeng.*, vol. 6, no. 1, 2020, doi: 10.1038/s41378-020-0161-3.

[213] J. Tu, Y. Gan, T. Liang, Q. Hu, Q. Wang, and T. Ren, "Graphene FET Array Biosensor Based on ssDNA Aptamer for Ultrasensitive Hg 2 + Detection in Environmental Pollutants," *Front. Chem.*, vol. 6, no. August, pp. 1–9, 2018, doi: 10.3389/fchem.2018.00333.

[214] Y. Ren *et al.*, "Detection of sulfur dioxide gas with graphene field effect transistor," *Appl. Phys. Lett.*, vol. 100, no. 16, pp. 1–5, 2012, doi: 10.1063/1.4704803.

[215] G. Lupina *et al.*, "Residual metallic contamination of transferred chemical

vapor deposited graphene," *ACS Nano*, vol. 9, no. 5, pp. 4776–4785, 2015, doi: 10.1021/acsnano.5b01261.

[216] L. Lin *et al.*, "Towards super-clean graphene," *Nat. Commun.*, vol. 10, no. 1, pp. 1–7, 2019, doi: 10.1038/s41467-019-09565-4.

[217] M. M. Ali, "The development and optimisation of graphene-based biosensors devices as a commercial biosensing platform," Swansea University, 2023.

[218] J. Chan *et al.*, "Reducing extrinsic performance-limiting factors in graphene grown by chemical vapor deposition," *ACS Nano*, vol. 6, no. 4, pp. 3224–3229, 2012, doi: 10.1021/nn300107f.

[219] X. Yang and M. Yan, "Removing contaminants from transferred CVD graphene," *Nano Res.*, vol. 13, no. 3, pp. 599–610, 2020, doi: 10.1007/s12274-020-2671-6.

[220] A. Pirkle *et al.*, "The effect of chemical residues on the physical and electrical properties of chemical vapor deposited graphene transferred to SiO2," *Appl. Phys. Lett.*, vol. 99, no. 12, pp. 2011–2014, 2011, doi: 10.1063/1.3643444.

[221] G. Xu, Y. Zhang, X. Duan, A. A. Balandin, and K. L. Wang, "Variability effects in graphene: Challenges and opportunities for device engineering and applications," *Proc. IEEE*, vol. 101, no. 7, pp. 1670–1688, 2013, doi: 10.1109/JPROC.2013.2247971.

[222] L. Liu, M. Qing, Y. Wang, and S. Chen, "Defects in Graphene: Generation, Healing, and Their Effects on the Properties of Graphene: A Review," *J. Mater. Sci. Technol.*, vol. 31, no. 6, pp. 599–606, 2015, doi: 10.1016/j.jmst.2014.11.019.

[223] A. Venugopal *et al.*, "Effective mobility of single-layer graphene transistors as a function of channel dimensions," *J. Appl. Phys.*, vol. 109, no. 10, 2011, doi: 10.1063/1.3592338.

[224] Q. Yu *et al.*, "Control and characterization of individual grains and grain boundaries in graphene grown by chemical vapour deposition," *Nat. Mater.*, vol. 10, no. 6, pp. 443–449, 2011, doi: 10.1038/nmat3010.

[225] X. Sun, Z. Wang, and Y. Q. Fu, “Adsorption and diffusion of sodium on graphene with grain boundaries,” *Carbon N. Y.*, vol. 116, pp. 415–421, 2017, doi: 10.1016/j.carbon.2017.01.024.

[226] B. C. Wood *et al.*, “Methane and carbon dioxide adsorption on edge-functionalized graphene: A comparative DFT study,” *J. Chem. Phys.*, vol. 137, no. 5, 2012, doi: 10.1063/1.4736568.

[227] N. Tit, K. Said, N. M. Mahmoud, S. Kouser, and Z. H. Yamani, “Ab-initio investigation of adsorption of CO and CO 2 molecules on graphene: Role of intrinsic defects on gas sensing,” *Appl. Surf. Sci.*, vol. 394, pp. 219–230, 2017, doi: 10.1016/j.apsusc.2016.10.052.

[228] Y. You *et al.*, “On the mechanism of gas adsorption for pristine, defective and functionalized graphene,” *Phys. Chem. Chem. Phys.*, vol. 19, no. 8, pp. 6051–6056, 2017, doi: 10.1039/c6cp07654h.

[229] A. Lipatov *et al.*, “Intrinsic device-to-device variation in graphene field-effect transistors on a Si/SiO2 substrate as a platform for discriminative gas sensing,” *Appl. Phys. Lett.*, vol. 104, no. 1, 2014, doi: 10.1063/1.4861183.

[230] N. B. Mc Keown and P. M. Budd, “Polymers of intrinsic microporosity (PIMs): Organic materials for membrane separations, heterogeneous catalysis and hydrogen storage,” *Chem. Soc. Rev.*, vol. 35, no. 8, pp. 675–683, 2006, doi: 10.1039/b600349d.

[231] J. Rouquerol *et al.*, “Recommendations for the characterization of porous solids,” 1994.

[232] N. B. McKeown and P. M. Budd, “Inducing Unoccupied Space in Polymers : From Excess Free Volume,” *John Wiley Sons, Inc.*, no. 1, 2009.

[233] M. Carta *et al.*, “An efficient polymer molecular sieve for membrane gas separations,” *Science (80-.).*, vol. 339, no. 6117, pp. 303–307, 2013, doi: 10.1126/science.1228032.

[234] M. Carta *et al.*, “Triptycene induced enhancement of membrane gas selectivity for microporous Tröger’s base polymers,” *Adv. Mater.*, vol. 26, no. 21, pp. 3526–3531, 2014, doi: 10.1002/adma.201305783.

[235] W. Yang, X. Wang, Z. Wang, W. Liang, and Z. Ge, “Light-powered microrobots: Recent progress and future challenges,” *Opt. Lasers Eng.*, vol. 161, no. 107380, 2023, doi: https://doi.org/10.1016/j.optlaseng.2022.107380.

[236] V. Gupta, “Sputtering technique,” in *Thin Film Science and Technology*, .

[237] R. Bigham, “Development of process technology for Silicon and Graphene biosensor devices,” 2019.

[238] W. Zhou, R. Apkarian, Z. L. Wang, and D. Joy, “Fundamentals of scanning electron microscopy (SEM),” *Scanning Microsc. Nanotechnol. Tech. Appl.*, pp. 1–40, 2007, doi: 10.1007/978-0-387-39620-0_1.

[239] A. Nanakoudis, “EDX Analysis with SEM: How Does it Work?,” 2019. [Online]. Available: https://www.thermofisher.com/blog/microscopy/edx-analysis-with-sem-how-does-it-work/. [Accessed: 16-Dec-2020].

[240] Bruker, “Guide to Raman Spectroscopy,” 2023. [Online]. Available: https://www.bruker.com/en/products-and-solutions/infrared-and-raman/raman-spectrometers/what-is-raman-spectroscopy.html#:~:text=The frequency shift is called,green laser (532 nm). [Accessed: 11-Oct-2023].

[241] J. Thyr and T. Edvinsson, “Evading the Illusions: Identification of False Peaks in Micro-Raman Spectroscopy and Guidelines for Scientific Best Practice,” *Angew. Chemie - Int. Ed.*, vol. 62, no. 43, 2023, doi: 10.1002/anie.202219047.

[242] T. Wenzel, “Raman Spectroscopy,” *Molecular and Atomic Spectroscopy*. [Online]. Available: https://chem.libretexts.org/Bookshelves/Analytical_Chemistry/Molecular_and_Atomic_Spectroscopy_(Wenzel)/5%3A_Raman_Spectroscopy. [Accessed: 19-Jul-2024].

[243] A. C. Ferrari and J. Robertson, “Interpretation of Raman spectra of disordered and amorphous carbon,” *Phys. Rev. B*, vol. 61, no. 20, pp. 632–645, 1999, doi: 10.1103/PhysRevB.61.14095.

[244] A. C. Ferrari and D. M. Basko, “Raman spectroscopy as a versatile tool for studying the properties of graphene,” *Nat. Publ. Gr.*, vol. 8, no. April, pp. 235–246, 2013, doi: 10.1038/nnano.2013.46.

[245] Z. Ni, Y. Wang, T. Yu, and Z. Shen, “Raman spectroscopy and imaging of graphene,” *Nano Res.*, vol. 1, no. 4, pp. 273–291, 2008, doi: 10.1007/s12274-008-8036-1.

[246] M. Wall, “The Raman Spectroscopy of Graphene and the Determination of Layer Thickness,” *Thermo Sci.*, p. 5, 2011.

[247] J. F. M. and G. E. M. P. C. C. D. Wanger, W. M. Riggs, L. E. Davis, *Handbook of X-ray Photoelectron Spectroscopy*. 1979.

[248] A. M. Venezia, “X-ray photoelectron spectroscopy (XPS) for catalysts characterization,” *Catal. Today*, vol. 77, no. 4, pp. 359–370, 2003, doi: 10.1016/S0920-5861(02)00380-2.

[249] ThermoFisher, “XPS: Table of Elements,” *Materials Science Learning Center*, 2024. [Online]. Available: https://www.thermofisher.com/uk/en/home/materials-science/learning-center/periodic-table. [Accessed: 17-Jul-2024].

[250] M. C. Biesinger, “X-ray Photoelectron Spectroscopy (XPS) Reference Pages.” [Online]. Available: https://www.xpsfitting.com/.

[251] A. V Naumkin, A. Kraut-Vass, S. W. Gaarenstroom, and C. J. Powell, “NIST X-ray Photoelectron Spectroscopy Database,” *National Institute of Standards and Technology*, 2023. [Online]. Available: https://srdata.nist.gov/xps/.

[252] A. Dutta, *Fourier Transform Infrared Spectroscopy*, vol. 2. Elsevier Inc., 2017.

[253] M. Rizwan and C. Gwenin, “Nanomaterials in renewable energy: UV-Visible spectroscopy characterization and applications,” in *In Micro and Nano Technologies, Nano Tools and Devices for Enhanced Renewable Energy*, Elsevier, 2021, pp. 103–120.

[254] N. J. Podraza and G. E. Jellison, “Ellipsometry,” in *Encyclopedia of Spectroscopy and Spectrometry*, Elsevier, 2017, pp. 482–489.

[255] J. A. Woollam, “Ellipsometry FAQ,” 2024. [Online]. Available: https://www.jawoollam.com/resources/ellipsometry-faq#toggle-id-1. [Accessed: 07-Jul-2024].

[256] Z. Zhang, Z. Gao, R. Fang, H. Li, W. He, and C. Du, "UV-assisted room temperature NO2 sensor using monolayer graphene decorated with SnO2 nanoparticles," *Ceram. Int.*, vol. 46, no. 2, pp. 2255–2260, 2020, doi: 10.1016/j.ceramint.2019.09.211.

[257] W. Chen, Q. Zhou, F. Wan, and T. Gao, "Gas sensing properties and mechanism of Nano-SnO2-based sensor for hydrogen and carbon monoxide," *J. Nanomater.*, vol. 2012, no. May, 2012, doi: 10.1155/2012/612420.

[258] M. Tonezzer and L. Van Duy, "Gas Sensors," in *Encyclopedia of Sensors and Biosensors*, First., R. Narayan, Ed. Elsevier, 2023, pp. 185–208.

[259] E. Stojanovska, M. Calisir, N. Ozturk, and A. Kilic, "Chapter 3: Carbon-based foams: Preparation and applications," in *Nanocarbon and its Composites*, Woodhead Publishing Series, 2019, pp. 43–90.

[260] W. T. Honeycutt, M. Tyler Ley, and N. F. Materer, "Precision and Limits of Detection for Selected Commercially Available, Low-Cost Carbon Dioxide and Methane Gas Sensors," *sensors*, vol. 19, pp. 3157–3172, 2019, doi: 10.3390/s19143157.

[261] M. Bouvet, P. Gaudillat, and J. M. Suisse, "Phthalocyanine-based hybrid materials for chemosensing," *J. Porphyr. Phthalocyanines*, vol. 17, no. 10, pp. 913–919, 2013, doi: 10.1142/S1088424613300073.

[262] A. Kubatova, "Determination of LODs (limits of detection) and LOQs (limit of quantification)," *University of Notre Dakota Department of Chemistry*, vol. 3. p. 3, 2008.

[263] G. L. Long and J. D. Winefordner, "Limit of Detection: A Closer Look at the IUPAC Definition," *Anal. Chem.*, vol. 55, no. 7, 1983.

[264] L. Li, "Principal Component Analysis for Dimensionality Reduction," *Medium*, 2019. [Online]. Available: https://towardsdatascience.com/principal-component-analysis-for-dimensionality-reduction-115a3d157bad. [Accessed: 13-Sep-2024].

[265] Z. Jaadi, "Principal Component Analysis (PCA): A Step-by-Step Explanation," *built in*, 2024. [Online]. Available: https://builtin.com/data-science/step-step-

explanation-principal-component-analysis. [Accessed: 13-Sep-2024].

[266] R. Wicklin, “How to interpret graphs in a principal component analysis,” *sas Blogs*, 2019. [Online]. Available: https://blogs.sas.com/content/iml/2019/11/04/interpret-graphs-principal-components.html. [Accessed: 13-Sep-2024].

[267] M. M. Ali *et al.*, “Application of molecular vapour deposited al2 o3 for graphene-based biosensor passivation and improvements in graphene device homogeneity,” *Nanomaterials*, vol. 11, no. 8, 2021, doi: 10.3390/nano11082121.

[268] J. J. Mitchell, “Towards A Graphene Chip System For Blood Clotting Disease Diagnostics,” 2020.

[269] Y. C. Lin, C. C. Lu, C. H. Yeh, C. Jin, K. Suenaga, and P. W. Chiu, “Graphene annealing: How clean can it be?,” *Nano Lett.*, vol. 12, no. 1, pp. 414–419, 2012, doi: 10.1021/nl203733r.

[270] C. Melios *et al.*, “Effects of humidity on the electronic properties of graphene prepared by chemical vapour deposition,” *Carbon N. Y.*, vol. 103, pp. 273–280, 2016, doi: 10.1016/j.carbon.2016.03.018.

[271] L. Zheng *et al.*, “Property transformation of graphene with Al2O3 films deposited directly by atomic layer deposition,” *Appl. Phys. Lett.*, vol. 104, no. 2, pp. 3–8, 2014, doi: 10.1063/1.4861861.

[272] H. Wang, Y. Wu, C. Cong, J. Shang, and T. Yu, “Hysteresis of electronic transport in graphene transistors,” *ACS Nano*, vol. 4, no. 12, pp. 7221–7228, 2010, doi: 10.1021/nn101950n.

[273] X. Tang, M. Debliquy, D. Lahem, Y. Yan, and J. P. Raskin, “A review on functionalized graphene sensors for detection of ammonia,” *Sensors*, vol. 21, no. 4, pp. 1–28, 2021, doi: 10.3390/s21041443.

[274] H. Momtazbaf, “Effect of Geometry and Gate Voltage on the Conductance of an Ideal Strip of Graphene,” no. April, 2015.

[275] A. T. Murdock *et al.*, “Controlling the orientation, edge geometry, and

thickness of chemical vapor deposition graphene," *ACS Nano*, vol. 7, no. 2, pp. 1351–1359, 2013, doi: 10.1021/nn3049297.

[276] S. J. Han, Z. Chen, A. A. Bol, and Y. Sun, "Channel-length-dependent transport behaviors of graphene field-effect transistors," *IEEE Electron Device Lett.*, vol. 32, no. 6, pp. 812–814, 2011, doi: 10.1109/LED.2011.2131113.

[277] J. Červenka and C. F. J. Flipse, "Structural and electronic properties of grain boundaries in graphite: Planes of periodically distributed point defects," *Phys. Rev. B - Condens. Matter Mater. Phys.*, vol. 79, no. 19, pp. 1–5, 2009, doi: 10.1103/PhysRevB.79.195429.

[278] H. Zhang, G. Lee, C. Gong, L. Colombo, and K. Cho, "Grain boundary effect on electrical transport properties of graphene," *J. Phys. Chem. C*, vol. 118, no. 5, pp. 2338–2343, 2014, doi: 10.1021/jp411464w.

[279] P. Vancsó, G. I. Márk, P. Lambin, A. Mayer, C. Hwang, and L. P. Biró, "Effect of the disorder in graphene grain boundaries: A wave packet dynamics study," *Appl. Surf. Sci.*, vol. 291, pp. 58–63, 2014, doi: 10.1016/j.apsusc.2013.09.127.

[280] T. Sizun, M. Bouvet, and J. M. Suisse, "Humidity effect on ammonia sensing properties of substituted and unsubstituted cobalt phthalocyanines," *Talanta*, vol. 97, pp. 318–324, 2012, doi: 10.1016/j.talanta.2012.04.037.

[281] B. Alemour, M. H. Yaacob, H. N. Lim, and M. R. Hassan, "Review of electrical properties of graphene conductive composites," *Int. J. Nanoelectron. Mater.*, vol. 11, no. 4, pp. 371–398, 2018.

[282] Y. J. Kim, Y. Kim, K. Novoselov, and B. H. Hong, "Engineering electrical properties of graphene: Chemical approaches," *2D Mater.*, vol. 2, no. 4, p. 42001, 2015, doi: 10.1088/2053-1583/2/4/042001.

[283] S. Ghosh, S. R. Polaki, P. K. Ajikumar, N. G. Krishna, and M. Kamruddin, "Aging effects on vertical graphene nanosheets and their thermal stability," *Indian J. Phys.*, vol. 92, no. 3, pp. 337–342, 2018, doi: 10.1007/s12648-017-1113-0.

[284] C. M. Yang, T. C. Chen, Y. C. Yang, and M. Meyyappan, "Annealing effect on UV-illuminated recovery in gas response of graphene-based NO2 sensors,"

RSC Adv., vol. 9, no. 40, pp. 23343–23351, 2019, doi: 10.1039/c9ra01295h.

[285] G. Lee, G. Yang, A. Cho, J. W. Han, and J. Kim, "Defect-engineered graphene chemical sensors with ultrahigh sensitivity," *Phys. Chem. Chem. Phys.*, vol. 18, no. 21, pp. 14198–14204, 2016, doi: 10.1039/c5cp04422g.

[286] X. Yan *et al.*, "High-Performance UV-Assisted NO2 Sensor Based on Chemical Vapor Deposition Graphene at Room Temperature," *ACS Omega*, vol. 4, no. 10, pp. 14179–14187, 2019, doi: 10.1021/acsomega.9b00935.

[287] T.-C. Chen, Y.-C. Yang, H.-L. Liu, C.-M. Yang, M. Meyyappan, and C.-S. Lai, "The Effect of Monolayer Graphene on the UV Assisted NO2 Sensing and Recovery at Room Temperature," no. 2, p. 461, 2017, doi: 10.3390/proceedings1040461.

[288] F. Yavari, E. Castillo, H. Gullapalli, P. M. Ajayan, and N. Koratkar, "High sensitivity detection of NO 2 and NH 3 in air using chemical vapor deposition grown graphene," *Appl. Phys. Lett.*, vol. 100, no. 20, pp. 2–5, 2012, doi: 10.1063/1.4720074.

[289] A. D. Smith *et al.*, "Resistive graphene humidity sensors with rapid and direct electrical readout," *Nanoscale*, vol. 7, no. 45, pp. 19099–19109, 2015, doi: 10.1039/c5nr06038a.

[290] X. Fan *et al.*, "Humidity and CO2 gas sensing properties of double-layer graphene," *Carbon N. Y.*, vol. 127, pp. 576–587, 2018, doi: 10.1016/j.carbon.2017.11.038.

[291] H. Bi *et al.*, "Ultrahigh humidity sensitivity of graphene oxide," *Sci. Rep.*, vol. 3, no. 5 V, pp. 1–7, 2013, doi: 10.1038/srep02714.

[292] Y. Dan, Y. Lu, N. J. Kybert, Z. Luo, and A. T. C. Johnson, "Intrinsic response of graphene vapor sensors," *Nano Lett.*, vol. 9, no. 4, pp. 1472–1475, 2009, doi: 10.1021/nl8033637.

[293] M. Gautam and A. H. Jayatissa, "Ammonia gas sensing behavior of graphene surface decorated with gold nanoparticles," *Solid. State. Electron.*, vol. 78, pp. 159–165, 2012, doi: 10.1016/j.sse.2012.05.059.

[294] A. I. Ayesh, A. F. S. Abu-Hani, S. T. Mahmoud, and Y. Haik, "Selective H2S sensor based on CuO nanoparticles embedded in organic membranes," *Sensors Actuators, B Chem.*, vol. 231, pp. 593–600, 2016, doi: 10.1016/j.snb.2016.03.078.

[295] Z. Zhang *et al.*, "Study on adsorption and desorption of ammonia on graphene," *Nanoscale Res. Lett.*, vol. 10, no. 1, 2015, doi: 10.1186/s11671-015-1060-7.

[296] S. M. Mortazavi Zanjani, M. M. Sadeghi, M. Holt, S. F. Chowdhury, L. Tao, and D. Akinwande, "Enhanced sensitivity of graphene ammonia gas sensors using molecular doping," *Appl. Phys. Lett.*, vol. 108, no. 3, pp. 1–6, 2016, doi: 10.1063/1.4940128.

[297] A. R. Cadore *et al.*, "Enhancing the response of NH3 graphene-sensors by using devices with different graphene-substrate distances," *Sensors Actuators, B Chem.*, vol. 266, pp. 438–446, 2018, doi: 10.1016/j.snb.2018.03.164.

[298] O. Tsymbalenko *et al.*, "High-sensitivity NH3 gas sensor using pristine graphene doped with CuO nanoparticles," *Microchim. Acta*, vol. 190, no. 4, pp. 1–11, 2023, doi: 10.1007/s00604-023-05717-y.

[299] A. Piazza *et al.*, "Graphene p-Type Doping and Stability by Thermal Treatments in Molecular Oxygen Controlled Atmosphere," *J. Phys. Chem. C*, vol. 119, no. 39, pp. 22718–22723, 2015, doi: 10.1021/acs.jpcc.5b07301.

[300] A. Piazza *et al.*, "Effect of air on oxygen p-doped graphene on SiO2," *Phys. Status Solidi Appl. Mater. Sci.*, vol. 213, no. 9, pp. 2341–2344, 2016, doi: 10.1002/pssa.201532909.

[301] S. S. Chauhan, D. Kumar, P. Chaturvedi, and M. R. Rahman, "Highly Sensitive and Stable NO2 Gas Sensors Based on SWNTs with Exceptional Recovery Time," *IEEE Sens. J.*, vol. 19, no. 24, pp. 11775–11783, 2019, doi: 10.1109/JSEN.2019.2937506.

[302] C. Y. Lee, C. M. Chiang, Y. H. Wang, and R. H. Ma, "A self-heating gas sensor with integrated NiO thin-film for formaldehyde detection," *Sensors Actuators, B Chem.*, vol. 122, no. 2, pp. 503–510, 2007, doi: 10.1016/j.snb.2006.06.018.

[303] N. D. Chinh, N. Van Toan, V. Van Quang, N. Van Duy, N. D. Hoa, and N. Van

Hieu, “Comparative NO2 gas-sensing performance of the self-heated individual, multiple and networked SnO2 nanowire sensors fabricated by a simple process,” *Sensors Actuators, B Chem.*, vol. 201, no. 2, pp. 7–12, 2014, doi: 10.1016/j.snb.2014.04.095.

[304] G. R. Yazdi *et al.*, “Effect of epitaxial graphene morphology on adsorption of ambient species,” *Appl. Surf. Sci.*, vol. 486, no. April, pp. 239–248, 2019, doi: 10.1016/j.apsusc.2019.04.247.

[305] J. Liu, Z. Liu, C. J. Barrow, and W. Yang, “Molecularly engineered graphene surfaces for sensing applications: A review,” *Anal. Chim. Acta*, vol. 859, pp. 1–19, 2015, doi: 10.1016/j.aca.2014.07.031.

[306] M. K. Rana, M. Sinha, and S. Panda, “Gas sensing behavior of Metal-Phthalocyanines : Effects of electronic structure on sensitivity,” *Chem. Phys.*, 2018, doi: 10.1016/j.chemphys.2018.06.021.

[307] F. I. Bohrer *et al.*, “Gas Sensing Mechanism in Chemiresistive Cobalt and Metal-Free Phthalocyanine Thin Films,” no. 11, pp. 5640–5646, 2007.

[308] Y. Li *et al.*, “The effects of central metals on ammonia sensing of metallophthalocyanines covalently bonded to graphene oxide hybrids,” no. x, pp. 34215–34225, 2017, doi: 10.1039/c7ra06081e.

[309] V. S. Anithaa, R. Shankar, and S. Vijayakumar, “DFT-based investigation on adsorption of methane on pristine and defected graphene,” pp. 1935–1952, 2017, doi: 10.1007/s11224-017-0988-x.

[310] R. Ghanbari, R. Safaiee, M. H. Sheikhi, and M. M. Golshan, “Graphene Decorated with Silver Nanoparticles as a Low- Temperature Methane Gas Sensor,” *ACS Appl. Mater. Interfaces*, 2019, doi: 10.1021/acsami.9b00625.

[311] K. C. Lam, “Room-temperature methane gas sensing properties based on in situ reduced graphene oxide incorporated with tin dioxide,” pp. 11131–11142, 2017, doi: 10.1039/c7ta01293d.

[312] N. Y. Id *et al.*, “The Effects of Graphene Stacking on the Performance of Methane Sensor : A First-Principles Study on the Adsorption , Band Gap and Doping of Graphene,” 2018, doi: 10.3390/s18020422.

[313] X. Chen *et al.*, “Density-Functional Calculation of Methane Adsorption on Graphenes,” *IEEE Electron Device Lett.*, vol. 36, no. 12, pp. 1366–1368, 2015, doi: 10.1109/LED.2015.2492580.

[314] R. A. Collins and K. A. Mohammed, “Gas sensitivity of some metal phthalocyanines,” *J. Phys. D. Appl. Phys.*, vol. 21, no. 1, pp. 154–161, 1988, doi: 10.1088/0022-3727/21/1/021.

[315] S. Pochekailov, J. Nožár, S. Nešpůrek, J. Rakušan, and M. Karásková, “Interaction of nitrogen dioxide with sulfonamide-substituted phthalocyanines: Towards NO 2 gas sensor,” *Sensors Actuators, B Chem.*, vol. 169, no. 2, pp. 1–9, 2012, doi: 10.1016/j.snb.2011.12.087.

[316] E. Yabaş, E. Biçer, and A. Altındal, “Novel reduced graphene oxide/zinc phthalocyanine and reduced graphene oxide/cobalt phthalocyanine hybrids as high sensitivity room temperature volatile organic compound gas sensors,” *J. Mol. Struct.*, vol. 1271, p. 134076, 2023, doi: 10.1016/j.molstruc.2022.134076.

[317] F. Ghani, J. Kristen, and H. Riegler, “Solubility Properties of Unsubstituted Metal Phthalocyanines in Different Types of Solvents,” *J. Chem. Eng. Data*, vol. 57, pp. 439–449, 2012.

[318] J. George, *Preparation of thin films*. New York: M. Dekker, 1992.

[319] M. M. El-Nahass, F. Bahabri, and R. Al-Harbi, “Optical properties of copper phthalocyanine (CuPc) thin films,” *J. Sol.*, vol. 24, no. 2, pp. 307–321, 2001.

[320] M. T. Hussein, K. A. Aadim, and E. K. Hassan, “Structural and Surface Morphology Analysis of Copper Phthalocyanine Thin Film Prepared by Pulsed Laser Deposition and Thermal Evaporation Techniques,” *Adv. Mater. Phys. Chem.*, vol. 06, no. 04, pp. 85–97, 2016, doi: 10.4236/ampc.2016.64009.

[321] S. M. Critchley *et al.*, “Deposition of Ordered Phthalocyanine Films by Spin Coating,” vol. 2, no. 2, pp. 157–159, 1992.

[322] S. M. Critchely, D. C. Davies, K. J. Markland, and M. R. Willis, “MORPHOLOGY AND ELECTRICAL PROPERTIES OF SPUN PHTHALOCYANINE FILMS,” *Synth. Met.*, vol. 43, pp. 1447–1450, 1991.

[323] B. Wang, X. Zuo, Y. Wu, Z. Chen, C. He, and W. Duan, “Comparative gas sensing in copper porphyrin and copper phthalocyanine spin-coating films,” *Sensors Actuators, B Chem.*, vol. 152, no. 2, pp. 191–195, 2011, doi: 10.1016/j.snb.2010.12.006.

[324] A. Kumar *et al.*, “Tetra-tert-butyl copper phthalocyanine-based QCM sensor for toluene detection in air at room temperature,” *Sensors Actuators, B Chem.*, vol. 210, pp. 398–407, 2015, doi: 10.1016/j.snb.2015.01.010.

[325] N. Kobayashi, S. I. Nakajima, H. Ogata, and T. Fukuda, “Synthesis, spectroscopy, and electrochemistry of tetra-tert-butylated tetraazaporphyrins, phthalocyanines, naphthalocyanines, and anthracocyanines, together with molecular orbital calculations,” *Chem. - A Eur. J.*, vol. 10, no. 24, pp. 6294–6312, 2004, doi: 10.1002/chem.200400275.

[326] V. N. Nemykina and E. A. Lukyanets, “Synthesis of substituted phthalocyanines,” *Arkivoc*, vol. 2010, no. 1, pp. 136–208, 2010, doi: 10.3998/ark.5550190.0011.104.

[327] J. Travis, A. K. Ray, S. C. Thorpe, M. J. Cook, and S. A. James, “Langmuir-Blodgett films of copper tetra-4-tert-butyl phthalocyanine molecules as NO2 gas sensors,” *Meas. Sci. Technol.*, vol. 6, no. 7, pp. 988–994, 1995, doi: 10.1088/0957-0233/6/7/021.

[328] Y. L. Lee, C. Y. Hsiao, C. H. Chang, and Y. M. Yang, “Effects of sensing temperature on the gas sensing properties of copper phthalocyanine and copper tetra-tert-butyl phthalocyanine films,” *Sensors Actuators, B Chem.*, vol. 94, no. 2, pp. 169–175, 2003, doi: 10.1016/S0925-4005(03)00329-0.

[329] K. K. Yadav, U. Narang, P. K. Sahu, and S. M. S. Chauhan, “Copper(II) phthalocyanine as an efficient and versatile catalyst for click reactions at room temperature,” *J. Iran. Chem. Soc.*, vol. 19, no. 11, pp. 4359–4375, 2022, doi: 10.1007/s13738-022-02609-5.

[330] T. Mateus *et al.*, “Fourier-Transform Infrared Spectroscopy as a Discriminatory Tool for Myotonic Dystrophy Type 1 Metabolism : A Pilot Study,” 2021.

[331] D. Lv, H. Sung, X. Li, X. Zhang, Z. Li, and D. Chen, “Dyes and Pigments

Effects of single layer graphene and graphene oxide modification on the properties of phthalocyanine blue pigments," *Dye. Pigment.*, vol. 180, no. January, p. 108449, 2020, doi: 10.1016/j.dyepig.2020.108449.

[332] A. A. M. Farag, "Optical absorption studies of copper phthalocyanine thin films," *Opt. Laser Technol.*, vol. 39, no. 4, pp. 728–732, 2007, doi: 10.1016/j.optlastec.2006.03.011.

[333] S. Kumar, N. Kaur, A. K. Sharma, A. Mahajan, and R. K. Bedi, "Improved Cl2 sensing characteristics of reduced graphene oxide when decorated with copper phthalocyanine nanoflowers," *RSC Adv.*, vol. 7, no. 41, pp. 25229–25236, 2017, doi: 10.1039/c7ra02212c.

[334] M. Rasyidi, A. Arsad, and S. Samahani, "Fourier Transforms Infrared Spectroscopy and X-ray Diffraction Investigation of Recycled Polypropylene / Polyaniline Blends," vol. 56, pp. 1015–1020, 2017, doi: 10.3303/CET1756170.

[335] S. M. Critchley, M. R. Willis, Y. Maruyama, S. Bandow, M. J. Cook, and J. Mcmurdo, "Preparation of smooth crystalline phthalocyanine films by spin coating," *Mol. Cryst. Liq. Cryst. Sci. Technol. Sect. A. Mol. Cryst. Liq. Cryst.*, vol. 229, no. 1, pp. 47–51, 1993, doi: 10.1080/10587259308032174.

[336] D. R. Deng and Q. H. Wu, "Raman spectroscopy of copper phthalocyanine/graphene and 2,3,5,6-tetrafluoro-tetracyano-quino-dimethane/graphene interfaces," *Surf. Interface Anal.*, vol. 53, no. 4, pp. 466–472, 2021, doi: 10.1002/sia.6934.

[337] A. Ali *et al.*, "Deep-Ultraviolet (DUV)-Induced Doping in Single Channel Graphene for Pn-Junction," *Nanomaterials*, vol. 11, no. 3003, 2021.

[338] Y.-M. Seo, W. Jang, T. Gu, and D. Whang, "Highly Efficient n -Type Doping of Graphene by Vacuum Annealed Amine-Rich Macromolecules," *Materials (Basel).*, vol. 13, no. 2166, pp. 1–11, 2020.

[339] C. Casiraghi, "Probing disorder and charged impurities in graphene by Raman spectroscopy," *Phys. Status Solidi*, vol. 177, no. 6, pp. 175–177, 2009, doi: 10.1002/pssr.200903135.

[340] I. Childres, Y. Qi, M. A. Sadi, J. F. Ribeiro, H. Cao, and Y. P. Chen, "Combined

Raman Spectroscopy and Magneto-Transport Measurements in Disordered Graphene: Correlating Raman D Band and Weak Localization Features," *Coatings*, vol. 12, no. 8, 2022, doi: 10.3390/coatings12081137.

[341] M. I. Newton, T. K. H. Starke, M. R. Willis, and G. McHale, "NO2 detection at room temperature with copper phthalocyanine thin film devices," *Sensors Actuators, B Chem.*, vol. 67, no. 3, pp. 307–311, 2000, doi: 10.1016/S0925-4005(00)00542-6.

[342] R. Pearce, T. Iakimov, M. Andersson, L. Hultman, A. L. Spetz, and R. Yakimova, "Epitaxially grown graphene based gas sensors for ultra sensitive NO2 detection," *Sensors Actuators B. Chem.*, vol. 155, no. 2, pp. 451–455, 2011, doi: 10.1016/j.snb.2010.12.046.

[343] N. B. McKeown, "Polymers of Intrinsic Microporosity (PIMs)," *Polymer (Guildf).*, vol. 202, p. 122736, 2020, doi: 10.1016/j.polymer.2020.122736.

[344] C. Ma and J. J. Urban, "Polymers of Intrinsic Microporosity (PIMs) Gas Separation Membranes: A mini Review," *Proc. Nat. Res. Soc.*, vol. 2, no. January, 2018, doi: 10.11605/j.pnrs.201802002.

[345] J. Dechnik, J. Gascon, C. J. Doonan, C. Janiak, and C. J. Sumby, "New Directions for Mixed-Matrix Membranes," *Angew. Chemie - Int. Ed.*, vol. 56, no. 32, pp. 9292–9310, 2017, doi: 10.1002/anie.201701109.

[346] P. Li, T. S. Chung, and D. R. Paul, "Gas sorption and permeation in PIM-1," *J. Memb. Sci.*, vol. 432, pp. 50–57, 2013, doi: 10.1016/j.memsci.2013.01.009.

[347] L. Wang *et al.*, "Polymer of intrinsic microporosity (PIM) films and membranes in electrochemical energy storage and conversion: A mini-review," *Electrochem. commun.*, vol. 118, no. June, p. 106798, 2020, doi: 10.1016/j.elecom.2020.106798.

[348] P. Evangelos, A. F. Favvas, R. Castro-Muñoz, V. Fíla, and X. He, "Chapter 1 - Polymeric Membrane Materials for CO2 Separations," in *Current Trends and Future Developments on (Bio-) Membranes*, Elsevier, 2018, pp. 3–50.

[349] X. H. Ma and S. Y. Yang, *Polyimide gas separation membranes*. Elsevier Inc., 2018.

[350] J. Hong, S. Lee, J. Seo, S. Pyo, J. Kim, and T. Lee, "A highly sensitive hydrogen sensor with gas selectivity using a PMMA membrane-coated Pd nanoparticle/single-layer graphene hybrid," *ACS Appl. Mater. Interfaces*, vol. 7, no. 6, pp. 3554–3561, 2015, doi: 10.1021/am5073645.

[351] Z. Wang *et al.*, "Highly Sensitive Capacitive Gas Sensing at Ionic Liquid-Electrode Interfaces," *Anal. Chem.*, vol. 88, no. 3, pp. 1959–1964, 2016, doi: 10.1021/acs.analchem.5b04677.

[352] Z. Li *et al.*, "SO2/NO2 Separation Driven by NO2Dimerization on SSZ-13 Zeolite Membrane," *J. Am. Chem. Soc.*, vol. 144, no. 15, pp. 6687–6691, 2022, doi: 10.1021/jacs.2c01635.

[353] R. G. Larson and T. J. Rehg, "Spin Coating," in *Liquid Film Coating*, Dordrecht: Springer, 1997.

[354] F. Y. Li, Y. Xiao, Y. K. Ong, and T. S. Chung, "UV-rearranged PIM-1 polymeric membranes for advanced hydrogen purification and production," *Adv. Energy Mater.*, vol. 2, no. 12, pp. 1456–1466, 2012, doi: 10.1002/aenm.201200296.

[355] F. Y. Li and T. S. Chung, "Physical aging, high temperature and water vapor permeation studies of UV-rearranged PIM-1 membranes for advanced hydrogen purification and production," *Int. J. Hydrogen Energy*, vol. 38, no. 23, pp. 9786–9793, 2013, doi: 10.1016/j.ijhydene.2013.05.056.

[356] R. Jia, P. Xie, Y. Feng, Z. Chen, A. Umar, and Y. Wang, "Dipole-modified graphene with ultrahigh gas sensibility," *Appl. Surf. Sci.*, vol. 440, pp. 409–414, 2018, doi: 10.1016/j.apsusc.2018.01.166.

[357] G. Yang, C. Lee, J. Kim, F. Ren, and S. J. Pearton, "Flexible graphene-based chemical sensors on paper substrates," *Phys. Chem. Chem. Phys.*, vol. 15, no. 6, pp. 1798–1801, 2013, doi: 10.1039/c2cp43717a.

[358] H. J. Park *et al.*, "Highly flexible, mechanically stable, and sensitive NO2 gas sensors based on reduced graphene oxide nanofibrous mesh fabric for flexible electronics," *Sensors Actuators, B Chem.*, vol. 257, no. 2, pp. 846–852, 2018, doi: 10.1016/j.snb.2017.11.032.

[359] F. Ricciardella *et al.*, “Effects of graphene defects on gas sensing properties towards NO2 detection,” *Nanoscale*, vol. 9, no. 18, pp. 6085–6093, 2017, doi: 10.1039/c7nr01120b.

[360] C. Yang, T. Chen, Y. Yang, and M. Meyyappan, “Annealing effect on UV-illuminated recovery in gas response of graphene-based NO2 sensors,” *RSC Adv.*, vol. 9, pp. 23343–23351, 2019, doi: 10.1039/c9ra01295h.

[361] K. Drozdowska *et al.*, “The effects of gas exposure on the graphene/AlGaN/GaN heterostructure under UV irradiation,” *Sensors Actuators B Chem.*, vol. 381, no. 2, 2023, doi: 10.1016/j.snb.2023.133430.

[362] Y. Zhang, Y. Chen, K. Zhou, C. Liu, J. Zeng, and H. Zhang, “Improving gas sensing properties of graphene by introducing doping and defect: a first principles study,” vol. 20, no. 185504, 2009.

[363] D. Zhang, J. Liu, and B. Xia, “Nitrogen Dioxide-Sensing Properties at Room Temperature of Metal Oxide-Modified Graphene Composite via One-Step Hydrothermal Method,” *J. Electron. Mater.*, vol. 45, no. 8, pp. 4324–4330, 2016, doi: 10.1007/s11664-016-4600-8.

[364] R. D. Noble, “Perspectives on mixed matrix membranes,” *J. Memb. Sci.*, vol. 378, no. 1–2, pp. 393–397, 2011, doi: 10.1016/j.memsci.2011.05.031.

[365] J. Sánchez-Laínez *et al.*, “Polymer engineering by blending PIM-1 and 6FDA-DAM for ZIF-8 containing mixed matrix membranes applied to CO2 separations,” *Sep. Purif. Technol.*, vol. 224, no. December 2018, pp. 456–462, 2019, doi: 10.1016/j.seppur.2019.05.035.

[366] G. Dong, H. Li, and V. Chen, “Challenges and opportunities for mixed-matrix membranes for gas separation,” *J. Mater. Chem. A*, vol. 1, no. 15, pp. 4610–4630, 2013, doi: 10.1039/c3ta00927k.

[367] G. Zamiri and A. S. M. A. Haseeb, “Recent Trends and Developments in Graphene / Conducting Polymer Nanocomposites,” *Materials (Basel).*, vol. 13, 2020.

[368] R. Bhatt, A. Mishra, and A. Kumar, “Role of diaminonaphthalene based polymers as sensors in detection of biomolecules : A review,” *Results Mater.*,

vol. 9, no. December 2020, p. 100174, 2021, doi: 10.1016/j.rinma.2021.100174.

[369] Z. Tehrani *et al.*, "Generic epitaxial graphene biosensors for ultrasensitive detection of cancer risk biomarker," *2D Mater.*, vol. 1, no. 2, 2014, doi: 10.1088/2053-1583/1/2/025004.

[370] doi: 10. 1021/acsami. 7b07684. Hao, Zhuang[1] Z. Hao et al., "Real-Time Monitoring of Insulin Using a Graphene Field-E ff ect Transistor Aptameric Nanosensor," ACS Appl. Mater. Interfaces, vol. 9, pp. 27504–27511, 2017 *et al.*, "Real-Time Monitoring of Insulin Using a Graphene Field-E ff ect Transistor Aptameric Nanosensor," *ACS Appl. Mater. Interfaces*, vol. 9, pp. 27504–27511, 2017, doi: 10.1021/acsami.7b07684.

[371] S. Noel, B. Liberelle, L. Robitaille, G. De Crescenzo, and C. Hc, "Quantification of Primary Amine Groups Available for Subsequent Biofunctionalization of Polymer Surfaces," *ACS Bioconjugate Chem.*, vol. 22, pp. 1690–1699, 2011.

[372] E. J. Legge *et al.*, "Understanding the bonding mechanisms of organic molecules deposited on graphene for biosensing applications," *J. Chem. Phys.*, vol. 155, no. 17, 2021, doi: 10.1063/5.0064136.

[373] A. M. Fathi and H. S. Mandour, "Electrosynthesized conducting poly(1,5-diaminonaphthalene) as a corrosion inhibitor for copper," *Polym. Bull.*, vol. 77, no. 6, pp. 3305–3324, 2020, doi: 10.1007/s00289-019-02913-w.

[374] L. Banszerus *et al.*, "Identifying suitable substrates for high-quality graphene-based heterostructures," *2D Mater.*, vol. 4, no. 2, 2017, doi: 10.1088/2053-1583/aa5b0f.

[375] L. Banszerus *et al.*, "Ultrahigh-mobility graphene devices from chemical vapor deposition on reusable copper," *Sci. Adv.*, vol. 1, no. 6, pp. 1–6, 2015, doi: 10.1126/sciadv.1500222.

[376] H. Chen, Y. Wang, J. Qu, and S. Dong, "Self-assembled silver nanoparticle monolayer on glassy carbon: an approach to SERS substrate," *J. Raman Spectrosc.*, vol. 38, pp. 1444–1448, 2007, doi: 10.1002/jrs.

[377] S. J. Rodríguez, L. Makinistian, and E. A. Albanesi, “Electronic Transport upon Adsorption of Biomolecules on Graphene,” vol. 6, pp. 767–792.

[378] R. Valaski, S. Ayoub, L. Micaroni, and I. A. Hümmelgen, “Influence of film thickness on charge transport of electrodeposited polypyrrole thin films,” *Thin Solid Films*, vol. 415, no. 1–2, pp. 206–210, 2002, doi: 10.1016/S0040-6090(02)00553-9.

[379] K. Toda, R. Furue, and S. Hayami, “Recent progress in applications of graphene oxide for gas sensing : A review,” *Anal. Chim. Acta*, vol. 878, pp. 43–53, 2015, doi: 10.1016/j.aca.2015.02.002.

[380] F. Liu and D. Xue, “An electrochemical route to quantitative oxidation of graphene frameworks with controllable C/O ratios and added pseudocapacitances,” *Chem. - A Eur. J.*, vol. 19, no. 32, pp. 10716–10722, 2013, doi: 10.1002/chem.201300679.

[381] Y. Y. Wang *et al.*, “Structural evolution in CVD graphene chemically oxidized by sulphuric acid,” no. September 2014, 2015, doi: 10.1002/jrs.4638.

[382] N. Grinceviciute, B. Snopok, and V. Snitka, “Functional two-dimensional nanoarchitectures based on chemically converted graphene oxide and hematoporphyrin under the sulfuric acid treatment,” *Chem. Eng. J.*, vol. 255, pp. 577–584, 2014, doi: 10.1016/j.cej.2014.06.081.

[383] R. Forsyth, “Graphene Biosensors for Detection of Biomarkers Related to Mental Health Conditions,” 2018.

[384] C. Wang *et al.*, “A reduced GO-graphene hybrid gas sensor for ultra-low concentration ammonia detection,” *Sensors (Switzerland)*, vol. 18, no. 9, 2018, doi: 10.3390/s18093147.

[385] F. Khurshid, M. Jeyavelan, T. Hussain, M. S. L. Hudson, and S. Nagarajan, “Ammonia gas adsorption study on graphene oxide based sensing device under different humidity conditions,” *Mater. Chem. Phys.*, vol. 242, p. 122485, 2020, doi: 10.1016/j.matchemphys.2019.122485.

[386] R. Ghosh, A. Midya, S. Santra, S. K. Ray, and P. K. Guha, “Chemically reduced graphene oxide for ammonia detection at room temperature,” *ACS Appl. Mater.*

Interfaces, vol. 5, no. 15, pp. 7599–7603, 2013, doi: 10.1021/am4019109.

[387] W. Liu and G. Speranza, "Tuning the Oxygen Content of Reduced Graphene Oxide and Effects on Its Properties," *ACS Omega*, vol. 6, no. 9, pp. 6195–6205, 2021, doi: 10.1021/acsomega.0c05578.

[388] S. Drewniak, M. Procek, R. Muzyka, and T. Pustelny, "Comparison of gas sensing properties of reduced graphene oxide obtained by two different methods," *Sensors (Switzerland)*, vol. 20, no. 11, pp. 1–18, 2020, doi: 10.3390/s20113175.

[389] Y. R. Choi *et al.*, "Role of oxygen functional groups in graphene oxide for reversible room-temperature NO2 sensing," *Carbon N. Y.*, vol. 91, no. 2, pp. 178–187, 2015, doi: 10.1016/j.carbon.2015.04.082.

[390] M. Grdeń, M. Łukaszewski, G. Jerkiewicz, and A. Czerwiński, "Electrochemical behaviour of palladium electrode: Oxidation, electrodissolution and ionic adsorption," *Electrochim. Acta*, vol. 53, no. 26, pp. 7583–7598, 2008, doi: 10.1016/j.electacta.2008.05.046.

[391] M. L. Chang, L. C. Wang, H. C. Lin, M. J. Chen, and K. M. Lin, "Investigation of defects in ultra-thin Al 2 O 3 films deposited on pure copper by the atomic layer deposition technique," *Appl. Surf. Sci.*, vol. 359, pp. 533–542, 2015, doi: 10.1016/j.apsusc.2015.10.144.

[392] B. Díaz *et al.*, "Failure mechanism of thin Al2O3 coatings grown by atomic layer deposition for corrosion protection of carbon steel," *Electrochim. Acta*, vol. 56, no. 26, pp. 9609–9618, 2011, doi: 10.1016/j.electacta.2011.07.104.

[393] P. Boryło *et al.*, "Structure and properties of Al2O3 thin films deposited by ALD process," *Vacuum*, vol. 131, pp. 319–326, 2016, doi: 10.1016/j.vacuum.2016.07.013.

[394] J. W. Gardner and P. N. Bartlett, "A Brief History of Electronic Noses," *Sensors Actuators B Chem.*, vol. 18, no. 19, pp. 211–220, 1994.

[395] D. Purves, G. Augustine, and D. Fitzpatrick, "The Transduction of Olfactory Signals," in *Neuroscience*, 2nd ed., Sunderland (MA): Sinauer Associates, 2001.

[396] A. Dalal, H. Mohan, and M. Prasad, “Detection methods for influenza A H1N1 virus with special reference to biosensors : a review,” vol. 0, no. February, pp. 1–18, 2020.

[397] H. Jean, T. Saha, T. Tey, W. Siang, and C. Wei, “Quartz crystal microbalance-based biosensors as rapid diagnostic devices for infectious diseases,” *Biosens. Bioelectron.*, vol. 168, no. June, p. 112513, 2020, doi: 10.1016/j.bios.2020.112513.

[398] P. Marconcini and M. Macucci, “Approximate calculation of the potential profile in a graphene-based device,” vol. 9, no. March 2014, pp. 30–38, 2015, doi: 10.1049/iet-cds.2014.0003.

[399] V. Singh, D. Joung, L. Zhai, S. Das, S. I. Khondaker, and S. Seal, “Graphene based materials: Past, present and future,” *Prog. Mater. Sci.*, vol. 56, no. 8, pp. 1178–1271, 2011, doi: 10.1016/j.pmatsci.2011.03.003.

[400] D. Lin-Vien, N. Colthup, W. Fateley, and J. Grasselli, “Aromatic and Heteroaromatic Rings,” in *The Handbook of Infrared and Raman Characteristic Frequencies of Organic Molecules*, 1991, pp. 277–306.

[401] D. Lin-Vien, N. Colthup, W. Fateley, and J. Grasselli, “Compounds Containing the Carbonyl Group,” in *The Handbook of Infrared and Raman Characteristic Frequencies of Organic Molecules*, 1991, pp. 117–154.

[402] T. Vincent, V. Panchal, T. Booth, S. R. Power, and A. Jauho, “Probing the nanoscale origin of strain and doping in graphene-hBN heterostructures,” 2019.

[403] C. Casiraghi, S. Pisana, K. Novoselov, A. Geim, and A. Ferrari, “Raman fingerprint of charged impurities in graphene,” vol. 233108, no. September, pp. 1–4, 2007, doi: 10.1063/1.2818692.

[404] L. Banszerus, M. Schmitz, K. Watanabe, C. Neumann, S. Reichardt, and M. Dro, “Raman spectroscopy as probe of nanometre-scale strain variations in graphene ¨,” no. May, pp. 1–7, 2015, doi: 10.1038/ncomms9429.

[405] E. Sitsanidis, J. Schirmer, and A. Lampinen, “Tuning protein adsorption on graphene surfaces via laser-induced oxidation,” 2021, doi: 10.1039/d0na01028f.

[406] H. J. Jin *et al.*, “Nanovesicle-based bioelectronic nose platform mimicking human olfactory signal transduction,” *Biosens. Bioelectron.*, vol. 35, no. 1, pp. 335–341, 2012, doi: 10.1016/j.bios.2012.03.012.

[407] T. H. Kim *et al.*, “Single-carbon-atomic-resolution detection of odorant molecules using a human olfactory receptor-based bioelectronic nose,” *Adv. Mater.*, vol. 21, no. 1, pp. 91–94, 2009, doi: 10.1002/adma.200801435.

[408] H. Yoon *et al.*, “Polypyrrole Nanotubes Conjugated with Human Olfactory Receptors: High-Performance Transducers for FET-Type Bioelectronic Noses,” *Angew. Chemie*, vol. 121, no. 15, pp. 2793–2796, 2009, doi: 10.1002/ange.200805171.

[409] E. M. Neuhaus, A. Mashukova, W. Zhang, J. Barbour, and H. Hatt, “A specific heat shock protein enhances the expression of mammalian olfactory receptor proteins,” *Chem. Senses*, vol. 31, no. 5, pp. 445–452, 2006, doi: 10.1093/chemse/bjj049.

[410] Y. Song *et al.*, “Chemical Fabrication of highly sensitive and selective room-temperature nitrogen dioxide sensors based on the ZnO nano fl owers,” *Sensors Actuators B. Chem.*, vol. 287, no. December 2018, pp. 191–198, 2019, doi: 10.1016/j.snb.2019.01.146.

[411] J. Brunet, V. P. Garcia, A. Pauly, C. Varenne, and B. Lauron, “An optimised gas sensor microsystem for accurate and real-time measurement of nitrogen dioxide at ppb level,” *Sensors Actuators B Chem.*, vol. 134, no. 2, pp. 632–639, 2008, doi: 10.1016/j.snb.2008.06.010.

[412] SGX-SENSORTECH, “Nitrogen Dioxide Sensor Datasheet.” Katowice, 2024.